Ferropicrites as evidence for lithological heterogeneity in the mantle source of continental flood basalts

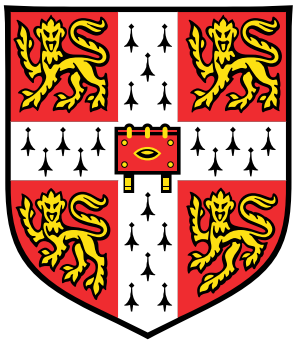

Eleanor Sarah Jennings
Department of Earth Sciences
University of Cambridge

This dissertation is submitted for the degree of
Doctor of Philosophy

Girton College

January 2016

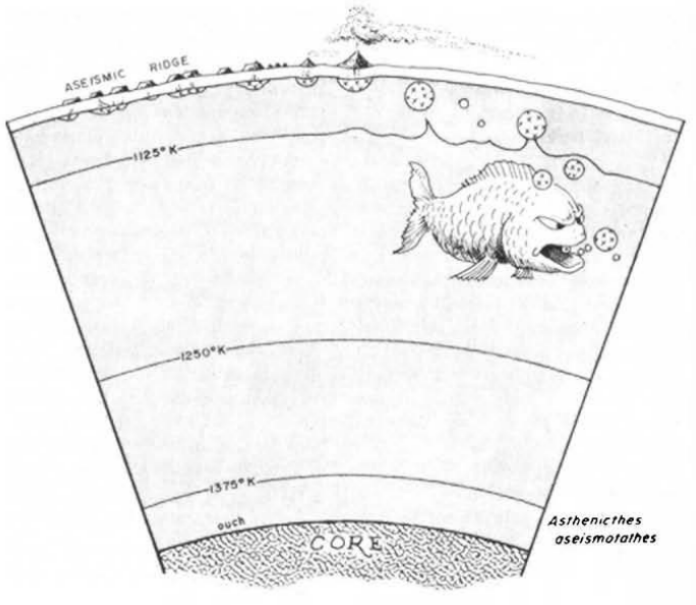

"Alternative to mantle plume theory"
Holden and Vogt (1977).

Declaration

This dissertation is the result of my own work and includes nothing which is the outcome of work done in collaboration, except where specifically indicated in the text. My supervisors Sally Gibson and John Maclennan provided comments and proofreading on drafts of various chapters, and additional comments and proofreading were provided by Tim Holland and David Neave. Chapter 3 is based on a draft prepared for publication, and as such was edited according to comments from co-authors (Jussi Heinonen in addition to my supervisors), and includes minor content from them. Chapter 4 is based in part on a published manuscript towards which Tim Holland provided significant content and comments, which is discussed explicitly at the start of that chapter.

This work has not previously been submitted in part or in whole for consideration for any other degree or qualification at this, or any other University. In accordance with the Department of Earth Sciences guidelines, this thesis is does not exceed 275 numbered pages, of which no more than 225 pages are of text, appendices (except data tables), illustrations and bibliography.

Eleanor Sarah Jennings

January 2016

Acknowledgements

I would like to thank my supervisor Sally Gibson for giving me an interesting problem to work on, for support throughout my project, and for above and beyond proofreading of early drafts of this thesis. I would also like to thank John Maclennan, my second supervisor, for always being available for constructive discussions and advice, and for encouraging me to model my data. Additionally, I am indebted to Tim Holland, who gave me the fantastic opportunity of being able to work with him on his mantle melting model, and to publish it. I am grateful to Tim and also to Mike Bickle for informal mentoring and interesting discussions. I would also like to thank my collaborator Jussi Heinonen for lively debate and for teaching me that a paper can be submitted in under a month.

I would like to acknowledge the excellent technical staff in the Earth Sciences department in Cambridge who have always been very helpful and have gone out of their way for me. Iris Buisman was skilled and helpful on the probe and spent days analysing and processing QEMSCAN data for me. I would especially have struggled to complete much of my work without the help and expertise of Martin Walker, who made himself available no matter how busy he was. Rob Clarke, Chris Parish and Jason Day have also given me technical support, for which I am grateful. Help from Sarah Humbert and Andy Buckley is also acknowledged. Outside of our department, Cees-Jan de Hoog looked after me for my three visits to the NERC IMF lab. As well as teaching me to use the probe and perform the necessary data corrections, he also made my visits to Edinburgh enjoyable and introduced me to many people. Lawrence Coogan sent me his Al-in-olivine thermometer paper before it was published and gave me technical advice. I also thank Konstantin Ignatyev at DLS for providing technical assistance for the XANES work. Jussi and Teal Riley kindly provided additional samples for my project.

Many of the methods that I used and interpretations that I made were guided by discussions, suggestions and encouragement from other people. I learned a lot from David Neave and Oliver Shorttle, who were frequently my first port of call for advice, especially in coding and modelling. Interesting discussions and helpful suggestions also came from Margaret Hartley, Eve Rooks, Svetlana Sibic and Mike, amongst others. I am very grateful for the encouragement and emotional support from some excellent friends in the department. Alex Maskell and Iris are two of the most generous people that I have ever met, and I will always be grateful for the daily encouragement and support that I received from them and the patience with which they sat through my 'afternoon rants'. Beyond the people already mentioned, I had interesting and useful science chats, friendly advice, or was generally helped

in one way or another by the following people: Lydia Gibson, Lois Salem, Llewellyn Pilbeam, Andrew Gilbert, Simon Matthews, Ben Mandler, Marthe Klöcking, Kat Daniels, Kerrie Taylor-Jones, Brendan McCormick and the rest of the Earth Sciences graduate student community. Eve kept the synchrotron night shifts bearable, and I am also grateful to James Bryson for helping out at the first beamtime. Alex Pietrowski has been a good academic friend to me. David, Marthe, Shaun Brace and Irene Jennings kindly proofread chapters of this thesis.

Finally, I would have struggled to enjoy the PhD process without the continuous love and support of Shaun.

Abstract

The sublithospheric mantle must be chemically heterogeneous as a consequence of billions of years worth of continuous subduction. Evidence for heterogeneity is strong in ocean island settings, where variability in isotopic, major and trace element composition is frequently attributed to variability in the mantle source. In continental flood basalt (CFB) provinces, signals of mantle-derived heterogeneity are obscured by fractionated and contaminated nature of CFB magmas. However, outcrops of primitive magmas that more closely represent primary mantle melts are found in some CFB provinces. This study focuses on picrites and ferropicrites from the Paraná-Etendeka CFB province, and also examines ferropicrites from the Karoo CFB province, which are found as dykes and thin flows. Ferropicrites are Fe-rich, Al-poor magmas equally primitive and Mg-rich as the peridotite-derived picrites, but cannot have formed from peridotite melting.

The sample sets are investigated by supplementing published whole-rock and mineral analyses with new mineral chemistry and melt inclusion data. Incompatible trace element compositions of their olivine-hosted melt inclusions are very homogeneous, suggesting that their primary fractional mantle melts underwent extensive mixing prior to the onset of crystallisation. Compared with primitive melt inclusions from other settings, inclusions in these and other CFB provinces are well-mixed. The crystallisation temperatures of olivine phenocrysts in these samples were determined by Al-in-olivine thermometry, with maximum crystallisation temperatures of $\sim$ 1500 °C identified in some Etendeka picrites. These require a very high mantle potential temperature (T_P); the ferropicrites crystallised at somewhat lower temperatures. XANES analyses confirmed that the spinel Fe^{3+}/Fe_T were within the thermometer's calibrated range.

Ferropicrite has been suggested to originate from high pressure, low fraction melting of mantle pyroxenite. The Etendeka ferropicrite geochemistry is examined with the aid of a new thermodynamic model in order to interrogate its mantle source lithology and melting conditions. Modelling indicates that both the major and trace element composition of ferropicrite is indeed more compatible with garnet clinopyroxenite melting than peridotite melting, and that elevated T_P plume conditions are required in its formation. By comparison, picrite major element chemistry is consistent with a high T_P depleted peridotite melt. If a depleted peridotite and hybrid pyroxenite source mineralogy are used for picrite and Etendeka ferropicrite, respectively, then they both represent $\sim$ 10–20% mantle melting.

Two principal conclusions are drawn. Firstly, ferropicrites are almost pure partial melts of garnet clinopyroxenite. Given that they are present in at least six CFBs globally, the presence of pyroxenite is a common feature of mantle plume starting heads. Pyroxenite could derive from peridotite that was metasomatised by partial melts of eclogite. This has implications for the presence for recycled crustal materials in plume nucleation regions. Secondly, the Etendeka picrites and ferropicrites derive from high T_P melting ($\sim$ 1400 and 1575 °C, respectively) under a thinned lithosphere of $\sim$ 70–80 km. Given that ferropicrites often represent the first expression of magmatism in CFB provinces, it is proposed that they form by melting of fusible pyroxenite in the leading edge of the upwelling plume head, shortly before picrite production in the plume core.

Table of contents

List of figures

List of tables

Acronyms and Notation

Variables

D	partition coefficient
F	melt fraction
P	pressure
T	temperature
T'	dimensionless scaled temperature
T_P	potential temperature
W_i	mass fraction of i
X	composition
X_i	mole fraction of i

Acronyms

AFC	assimilation fractional crystallisation
BSE	back-scattered electron
CFB	continental flood basalt
CMB	core-mantle boundary
DML	Dronning Maud Land
EPMA	electron probe microanalyser
FMQ	fayalite-magnetite-quartz fO_2 buffer
Fo	olivine forsterite content (mol. %)
KDE	kernel density estimate
LILE	large ion lithophile element
LIP	large igneous province
LLSVP	large low shear velocity zone

Mg#	magnesium number, = Mg/(Mg+Fe^{2+})
MORB	mid ocean ridge basalt
OIB	ocean island basalt
PCA	principal component analysis
REE	rare earth element (L, light; M, medium; H, heavy)
SCLM	subcontinental lithospheric mantle
SIMS	secondary ion mass spectrometry
TTG	tonalite-trondhjemite-granodiorite
XANES	x-ray absorption near edge structure

Chapter 1

Introduction

The presence of lithologically heterogeneous domains within the convecting mantle is a necessary consequence of the subduction of oceanic crust. Despite extensive study, the compositions of partial melts of this recycled material are not well resolved, and thus quantifying the proportion of recycled crust in the mantle source of melts is both difficult and controversial. In this study, a unique suite of primitive mantle melts from Continental Flood Basalt (CFB) provinces known as picrites and ferropicrites is studied and mantle melting scenarios are modelled in order to further our understanding of melting processes in a lithologically heterogeneous mantle. This chapter begins with reviews of the concepts and scientific developments in the fields of a) mantle heterogeneity, b) CFB generation and c) ferropicrite genesis, followed by a summary linking the three concepts together and a statement of the intent of this research.

1.1 Mantle heterogeneity

1.1.1 Plume reservoirs

Mantle plumes have long been accepted as the origin of ocean island chains and continental flood basalts (Morgan, 1971; Richards *et al.*, 1989). Traditionally, differences in the major, trace element and isotopic geochemistry between Ocean Island Basalt (OIB) and Mid Ocean Ridge Basalt (MORB), beyond those expected from the different pressure (P) and temperature (T) of melting, have been attributed to plumes advecting 'primordial' (i.e. non-depleted) lower mantle (Morgan, 1971). The presence of such a reservoir was favoured by mass balance calculations (O'Nions *et al.*, 1979), which indicated that less than half of the primordial mantle would need to be depleted by the extraction of the continental crust (White, 2010). The validity of this simplistic model is unclear, and more recently, observations of chemical differences between MORB and OIB have arisen that cannot be explained by this theory (van Keken *et al.*, 2002). Additionally, heterogeneity is observed between and within MORB, OIB and CFB from different locations on a variety of scales, indicating more

complex geodynamic processes in the mantle. Compositional heterogeneity in primitive melts, phenocrysts, and their trapped melt inclusions that cannot be attributed to dynamic melting and crustal processes reflects heterogeneity in the underlying mantle source.

1.1.2 Observations of mantle heterogeneity in MORB and intra-plate basalts

Isotopic heterogeneity

Radiogenic isotope ratios cannot be fractionated by melting or crystallisation processes, so isotopic variability is entirely attributable to variations in the mantle source composition. This provides the most compelling evidence for mantle heterogeneity. Isotopic variations between different OIBs are commonly accepted to show that heterogeneity is ubiquitous in mantle plumes and are often grouped into different mantle reservoirs, e.g. EM1, EM2 and HIMU (Hart *et al.*, 1992; Hofmann, 1997, 2003; Zindler and Hart, 1986). Samples from various ocean islands often show binary mixing trends between any one of these end-members and a common end-member known as 'FOZO' or 'C', presumably representing a common plume-source mantle (Hanan and Graham, 1996; Hart *et al.*, 1992; Stracke *et al.*, 2005). Because similar end-members are identified in different locations (e.g. EM2 is identified in both Samoa and the Society Islands, Hofmann, 1997), the process which drives isotopic heterogeneity must operate globally. However, assigning origins to end-members is not straightforward. EM1, observed in melts from the Tristan plume and others, has a poorly constrained origin and has variably been assigned to: recycled old oceanic crust and pelagic sediment (e.g. Andres *et al.*, 2002; Chauvel *et al.*, 1992); delaminated, subducted or in-situ metasomatised subcratonic lithospheric mantle (e.g. Gibson *et al.*, 2005; Konter and Becker, 2012); recycled lower crustal material (e.g. Regelous *et al.*, 2009; Willbold and Stracke, 2006) or upper crust/sediment (e.g. Jackson and Dasgupta, 2008). Additionally, if melts from end-members of these arrays have undergone mixing prior to eruption, their compositions will be damped and may not represent the true mantle end-member compositions; this mixing effect can produce misleading vectors towards end-member compositions (Rudge *et al.*, 2013; Stracke and Bourdon, 2009).

Trace element heterogeneity

Variations in incompatible trace element compositions have been observed in basaltic lavas in a variety of settings (e.g. Gibson *et al.*, 2012; Hart *et al.*, 1992; Koornneef *et al.*, 2012; Pietruszka *et al.*, 2013; Shorttle *et al.*, 2013; Slater *et al.*, 2001; Willbold and Stracke, 2006), as well as at the smaller length scale of melt inclusions (e.g. Kent, 2008; Maclennan, 2008a; Maclennan *et al.*, 2003b; Neave *et al.*, 2013; Norman *et al.*, 2002; Ren *et al.*, 2005; Slater *et al.*, 2001; Yaxley *et al.*, 2004). Unlike isotopic ratios, incompatible trace elements are fractionated by dynamic melting in a plume, especially if low fraction melts are efficiently extracted at depth (e.g. Elliott *et al.*, 1991). The trace

element composition of subducted material should be unique and impart a detectable signal in mantle melting. Incompatible trace element heterogeneity is therefore a function of both melting processes and source composition, so identifying lithological heterogeneity in the source is dependent on understanding both processes. Trace element anomalies have been linked to isotopic end-members and used to try to constrain their origin (e.g. Elkins *et al.*, 2008; Gibson *et al.*, 2005; Kawabata *et al.*, 2011; Weaver, 1991; Willbold and Stracke, 2006), though mixing processes of incremental mantle melts complicates the combined use of the two types of data (Stracke and Bourdon, 2009).

The realisation that compatible trace element abundances in melts should be insensitive to fractionation during melting has led Sobolev *et al.* (2005) and Sobolev *et al.* (2007) to suggest that elevated Ni and low Mn are characteristic of melts from mantle pyroxenite, and Gurenko *et al.* (2009) to use these elements to quantify the recycled contribution. However, elevated Ni could also result from the temperature sensitivity of the Ni partition coefficient in olivine (Matzen *et al.*, 2013; Putirka *et al.*, 2011) and has alternatively been suggested to originate from interactions with the core (Herzberg *et al.*, 2013). Mn partitioning in garnet is sensitive to temperature and the presence of water, which provides an alternative mechanism for varying its concentrations (Balta *et al.*, 2011).

Major element heterogeneity

Easiest to measure but hardest to interpret is the major element chemistry of mantle derived melts. Major elements present an extra layer of complexity relative to trace elements, as their abundance controls source phase equilibria and melting relations, and the liquid composition will change as a function of melting extent and crystallisation. Alongside isotopic and trace element differences, major element variations in OIB and MORB that cannot be explained by peridotite melting, for example high FeO and TiO_2 and low CaO for a given MgO, are well documented (Dasgupta *et al.*, 2010; Hauri, 1996; Herzberg, 2011a, 2006; Hirschmann and Stolper, 1996; Jackson and Dasgupta, 2008; Kawabata *et al.*, 2011; Prytulak and Elliott, 2007; Shorttle and Maclennan, 2011; Sobolev *et al.*, 2005). The realisation that recycled eclogite or pyroxenite is present in upwelling mantle plumes has led to decades worth of experimental work in order to predict the major element chemistry of eclogite and pyroxenite melts in the mantle and interpret the major element deviations observed in plume-derived melts (Hirschmann *et al.*, 2003; Keshav *et al.*, 2004; Kogiso *et al.*, 1998; Kogiso and Hirschmann, 2006; Kogiso *et al.*, 2003, 2004a; Mallik and Dasgupta, 2012; Pertermann and Hirschmann, 2003a,b; Pertermann *et al.*, 2004; Yaxley and Sobolev, 2007; Yaxley and Green, 1998). The validity of identifying pyroxenite partial melts from their major element chemistry is examined by Lambart *et al.* (2013), and identification schemes have been proposed, such as applying MgO and CaO thresholds to primitive melts (Herzberg and Asimow, 2008). Major element heterogeneity in mantle melts is also documented in continental settings by the presence of ferropicrite in various CFB

provinces (Gibson, 2002), which are too iron-rich to form by peridotite melting, and are a focus of this thesis.

Length scales of compositional variability

Compositional heterogeneity has been observed on all length scales between: different tectonic settings; magmas from different plumes; and magmas from the same plume. Iceland is a well-studied example of this, where often extreme isotopic, trace element and/or major element variability is observed between volcanic systems, within lava flows and down to the melt inclusion scale. This is usually interpreted to reflect both dynamic melting processes and the presence of discrete units of lithologically distinct material in the mantle plume source (Gurenko and Chaussidon, 1995; Maclennan, 2008a,b; Maclennan *et al.*, 2003b; Moune *et al.*, 2012; Neave *et al.*, 2014b, 2013; Shorttle *et al.*, 2013; Slater *et al.*, 2001).

When hosted in a high-temperature liquidus phase such as olivine, melt inclusions provide evidence of the nature and composition of primitive mantle melts soon after they escape the mantle. Pooling and mixing of fractional mantle melts is expected; it is thought that primitive olivine-hosted melt inclusions trap melt prior to the complete mixing of melts in lower crustal magma chambers (Maclennan, 2008a). Trapped melts should be more variable and better reflect the range of mantle melts than whole-rock samples, although mixing by mantle transport processes and by convection during cooling and crystallisation act to dampen variability and mask the true extent of initial melt heterogeneity from the mantle. Olivine-hosted melt inclusions from primitive melts in oceanic settings frequently display variability in major and trace elements, and perhaps most strikingly, in isotopic composition (Jackson and Hart, 2006; Kent, 2008; Maclennan, 2008a,b; Maclennan *et al.*, 2003b; Neave *et al.*, 2013; Norman *et al.*, 2002; Saal *et al.*, 1998; Slater *et al.*, 2001; Sobolev *et al.*, 2011; Sours-Page *et al.*, 2002), showing that inclusions retain a record of mantle lithological heterogeneity as well as the melting process.

1.1.3 Origin of mantle heterogeneity

It was first suggested by Hofmann and White (1982) and White and Hofmann (1982) that subducted slabs in mantle plumes were the cause of the geochemically distinctive nature of OIB. The idea has since become widely (but not universally) accepted, with observations of natural samples supplemented by experimental and theoretical models to determine the nature, composition and proportion of this recycled material. Alternative models are proposed, such as delamination of oceanic or continental lithospheric mantle (e.g. McKenzie and O'Nions, 1983; Niu, 2003; Pilet *et al.*, 2005; see discussion in White, 2010); this is volumetrically minor relative to the global subduction flux. According to evidence from theoretical calculations (Hirose *et al.*, 1999) and tomographic observations

(e.g. Grand, 2002; van der Hilst *et al.*, 1997), many subducting oceanic slabs are thought to sink to the base of the mantle.

As the basaltic crust descends through the peridotite mantle, it first metamorphoses to eclogite (a 'stage 1 pyroxenite' in the scheme of Herzberg, 2011a), whilst undergoing some extent of subduction-modification, then progresses through a further series of high P phase transitions en route to the lower mantle (Hirose *et al.*, 2005). These reverse back to eclogite upon decompression. The eclogite is silica-saturated (bearing free-silica) and, as such, cannot be in equilibrium with peridotite. The consequences of this, discussed in detail by Yaxley and Green (1998), Herzberg (2011b) and Kogiso *et al.* (2004b), are as follows:

1. A solid-state reaction will occur at the interface between eclogite and the surrounding peridotite: olivine + free silica = orthopyroxene (or Ca-poor clinopyroxene at higher pressures) i.e. quartz/coesite in the eclogite, along with a proportion of olivine in the peridotite, is lost, creating a silica-undersaturated pyroxenite ('stage 2 pyroxenite', Herzberg, 2011a). Equivalent reactions apply for lower mantle assemblages. If the eclogite is stretched and thinned by convective mixing to lengthscales accessible by diffusion, a block of subducted slab could react to completion.

2. Remaining unreacted eclogite will have its solidus intersected and partially melt at higher pressure than peridotite. The resultant silica-rich partial melt will buoyantly rise and come into contact with overlying peridotite. The melt will be in strong disequilibrium with the surrounding peridotite, which will react with it and transform as above, replacing some proportion of olivine with pyroxene and creating a silica-undersaturated ('stage 2') pyroxenite (Sobolev *et al.*, 2005; Yaxley and Green, 1998).

Pyroxenites produced by both mechanisms are silica-undersaturated and will go on to produce silica-undersaturated melts. Viscous SiO_2-rich partial melts of quartz-bearing recycled MORB will react with peridotite to form pyroxenite and therefore should not reach the surface. Most OIB primary melts, even those for which a pyroxenite source is invoked, are not SiO_2-rich (e.g. Herzberg, 2006). As such, for the remainder of this thesis, 'pyroxenite' refers to the silica-undersaturated reaction product described above. The two formation methods of pyroxenite have subtly different implications in terms of major, compatible and incompatible trace element chemistry and mineral assemblage.

Plumes and slabs: a lower mantle link?

It is often thought that mantle plumes nucleate at the core-mantle boundary (CMB) and consist predominantly of advected lower mantle material (e.g. Campbell, 2007; Griffiths and Campbell, 1990; Figs. 1.1a and 1.1b). While some proposed plumes have been imaged down to the CMB (e.g. Boschi

et al., 2007; Wolfe *et al.*, 2009; Zhao, 2004), poor spatial resolution in lower mantle seismic imaging makes their detection difficult (Sleep, 2006; Styles *et al.*, 2011). According to fluid dynamic modelling, plume tails are not thought to entrain ambient mantle material (Farnetani *et al.*, 2002; Griffiths and Campbell, 1990). By extension, recycled crustal material within the plume must also have been advected from the base of the mantle. Despite the density of subducted slabs being higher than that of peridotite at lower mantle conditions (Hirose *et al.*, 1999), computational simulations indicate that plumes are able to carry slab material to the surface (Farnetani, 2005; Farnetani *et al.*, 2012; Lin and van Keken, 2006a; Tackley, 2011).

Some intriguing observations link plumes, slabs and lower mantle seismic structure. Two broad, steep-sided features known as Large Low Shear Velocity Provinces (LLSVPs) are identified at the base of the mantle; these enigmatic regions may be thermal or chemical in origin (e.g. a 'slab graveyard' or primordial mantle), partially molten, or laterally focused by slab penetration (Davies *et al.*, 2012; Garnero *et al.*, 2007; Lassak *et al.*, 2010; Li *et al.*, 2014; McNamara and Zhong, 2005; Tackley, 2012). LLSVPs may or may not be implicated as the chemical reservoir sampled by plumes. The margins of LLSVPs have been spatially correlated with the reconstructed positions of LIPs and kimberlites (Steinberger and Torsvik, 2012; Torsvik *et al.*, 2006), which (assuming that they upwelled with little lateral displacement) is suggested to imply that mantle plumes are triggered by interaction of subducted slabs with LLSVPs (Tackley, 2011). Some authors further propose that island chains with bilateral geochemical asymmetry (e.g. the 'Loa' and 'Kea' trends of Hawaii) are generated by a laterally bimodal plume from the LLSVP margin, orientated so that the side bearing the recycled component faces the LLSVP (Farnetani *et al.*, 2012; Jackson *et al.*, 2014; Weis *et al.*, 2011). These observations are compelling but the interpretations are not robust, with alternative explanations presented (e.g. Ballmer *et al.*, 2013; Pietruszka *et al.*, 2013; Ren *et al.*, 2005; Rudolph and Zhong, 2013; Shorttle *et al.*, 2013). The observation of recycled slab material in plume-derived melts would strengthen the suggestion of plume-slab interactions in the lowermost mantle. Whole-mantle convective processes are summarised in Fig. 1.1c, which assumes that the mantle is not layered.

1.2 Continental flood basalt provinces

1.2.1 Origin and characteristics of CFBs

CFBs constitute the bulk of subaerial Large Igneous Provinces (LIPs; Coffin and Eldholm, 1994). They are characterised by enormous volumes of magma ($> 10^5$ km^3, Bryan and Ernst, 2008), the bulk of which is erupted over very short time scales ($< \sim$ 1-5 Myr, Courtillot and Renne, 2003) with individual eruptive units emplaced on the order of tens of thousands of years (Barry *et al.*, 2013). The main phase of flood basalt emplacement is characterised by pulsed eruptive episodes on the order of <

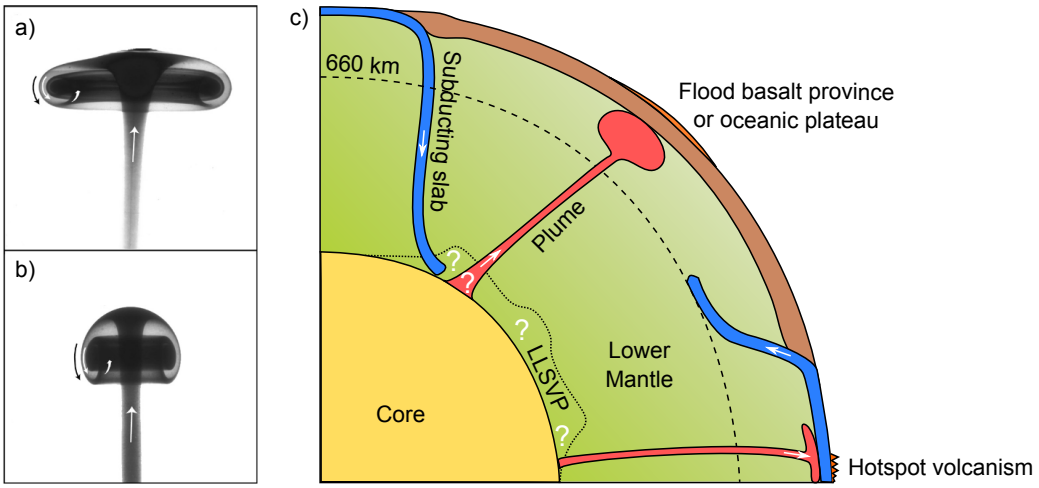

Figure 1.1: a) Experimental upwelling thermal plume head flattening at the top of its ascent and b) upwelling thermal plume head earlier in its ascent; both are photographs of experimental plumes in glucose syrup from Campbell (2007), originally from Griffiths and Campbell (1990). Arrows indicate the direction motion, and entrainment of ambient material is seen. c) Simplified schematic diagram of whole-mantle cycling systematics. Slabs may stall at 660 km and/or penetrate to the base of the mantle, and plumes in this figure are suggested to nucleate at the core-mantle boundary. The role of LLSVPs in the nucleation of plumes and the transfer of slab material to the plume is unclear at present. Not to scale.

1 Myr (e.g. Schoene *et al.*, 2015; Self *et al.*, 2014). Examples of these exceptionally high melt fluxes are provided by the Grande Ronde Basalt Formation in the Columbia River CFB province, where an emplacement rate of 0.375 km^3/year was sustained for 400,000 years (Barry *et al.*, 2013). In the Paraná-Etendeka CFB province a lower magmatic flux sustained over 4 Myr resulted in extruded volumes in excess of 10^6 km^3 (Dodd *et al.*, 2015).

Morgan (1971) first identified the link between hot spot tracks and CFBs, linking the two to convective plumes in the mantle. Richards *et al.* (1989) extended this interpretation by suggesting that CFB provinces and oceanic plateaus represent melting within a hot, upwelling, enlarged mantle plume starting head. The transition to a long-lived but narrow stationary plume tail results in hotspot tracks. More recently, it was shown that plumes may have more complex morphologies and/or mixed lithologies (Farnetani, 2005; Lin and van Keken, 2006b), but this basic model for the origin of CFBs is robust. CFBs are often spatially and temporally linked to rifting and continental breakup, although it is not necessarily true that plumes trigger this breakup (Hill, 1991). This means that CFB provinces often experience extensive rifting; both lithospheric thinning and elevated temperatures are important in the generation of large-volume CFB magmatism (White and McKenzie, 1989, 1995).

1.2.2 Primitive melts in CFB provinces

CFB provinces are dominated by basalt and basaltic andesite compositions of around 4-6 wt.% MgO that are thought to have formed by extensive fractional crystallisation and assimilation of higher MgO primary mantle-derived melts, with correspondingly large volumes of dense cumulate material in the crust (e.g. Farnetani *et al.*, 1996; Karlstrom and Richards, 2011; Morrison *et al.*, 1985; Neumann *et al.*, 2011; Ridley and Richards, 2010). In many CFB provinces, small volumes of primitive melts are found alongside the vast flood basalts (e.g. Chung and Jahn, 1995; Erlank *et al.*, 1984; Riley *et al.*, 2005; Rogers, 2006). These melts derive from the same high temperature plume source and represent parental or closely related liquids to the large volume flood basalts. They avoided extensive fractionation in lower crustal reservoirs and are found as narrow sills, dykes and flows. The Etendeka portion of the Paraná-Etendeka and the Antarctic portion of the Karoo province are examples of two CFB provinces where such primitive rocks are found (e.g. Heinonen *et al.*, 2010; Riley *et al.*, 2005; Thompson *et al.*, 2001, 2007). This thesis focuses on such primitive samples in order to better understand the mantle source and melting processes involved in the generation of CFBs.

The presence of primitive melts in CFB settings provides an opportunity to search for evidence of mantle heterogeneity, as some may have a pyroxenite-derived melt component. The thick lithosphere means that CFB provinces are ideal settings for identifying such melts, which is an advantage over OIBs. Pyroxenite is more fusible than peridotite, and will melt deeper and more productively in an upwelling plume head. The thick lithosphere means that in the early stages of plume upwelling and rifting, melting can be restricted to fusible lithologies only. Specifically, picrite and ferropicrite are two primitive melt types found in some CFB settings (Gibson, 2002). These equally primitive melt types have different chemistries and cannot derive from the same mantle source. Their presence is strong evidence that mantle heterogeneity is a feature of CFB plume sources, and understanding their origin is a focus of this thesis.

1.3 The origin of ferropicrite

Ferropicrite is a rare magma type found exclusively associated with thick lithosphere in some CFBs. Its origin has been linked to high pressure melting of lithologically distinct domains within the mantle (Gibson, 2002). Better constraining the origin of this unique magma type is central to this thesis.

1.3.1 Definition and characteristics

Ferropicrite, as the name suggests, is an iron-rich picrite. It is defined by a bulk composition of >12 wt. % MgO (some samples in this study have lower MgO and are strictly ferrobasalt). Early Proterozoic picrites from Pechenga with FeO_T = 14.8 wt% were first described as ferropicrites by Hanski

and Smolkin (1989); Gibson (2002) has since noted a decrease in FeO_T of ferropicrites through to the present. The MgO and FeO concentrations of ferropicrite and picrite samples used in this thesis are compared with global OIB and MORB samples in Fig. 1.2. Ferropicrite is defined by Heinonen and Luttinen (2008) and in this study as having a threshold 13 wt.% FeO_T, which should be paired with a characteristic low Al_2O_3 (e.g. < 10 wt.%) relative to picrite. Ferropicrites are subalkaline, enriched in incompatible trace elements and isotopic characteristics, and have a strong 'garnet signature' (high MREE (medium rare earth element) to HREE (heavy REE) ratios, e.g. $[Gd/Yb]_N$ of around 2-3.5 in Phanerozoic and Proterozoic samples and 1.7-3 in Archaean samples (Gibson, 2002)). They can have high TiO_2 contents of around 1-5 wt.%. If ferropicrite whole-rock analyses represent primary or near-primary melts, these characteristics should reflect mantle processes. Elevated high field strength element (HFSE) concentrations are common amongst Archaean ferropicrites, as well as high concentrations of compatible elements (Ni, Cr), which is particularly apparent in samples with surviving olivine phenocrysts (e.g. Goldstein and Francis, 2008).

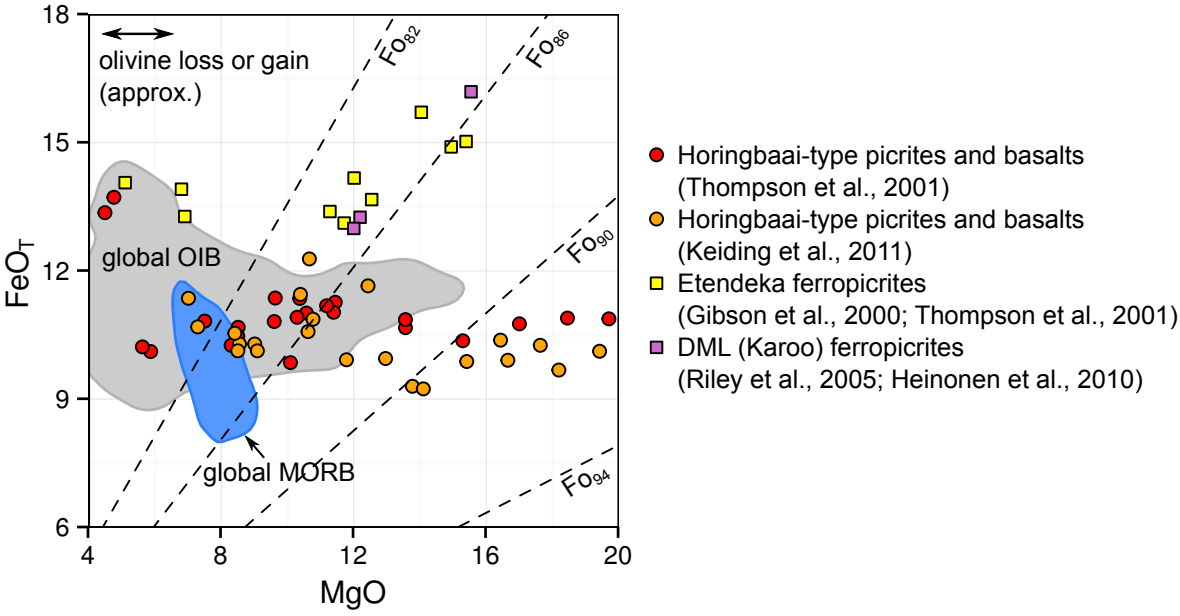

Figure 1.2: Weight % FeO_T (total Fe expressed as FeO) as a function of MgO of Etendeka picrites, Etendeka and Karoo ferropicrites, global OIBs, and MORBs, truncated at 4 wt.% MgO. The ferropicrites are characterised by an elevated FeO at a given MgO. The OIB and MORB fields are 90% density contours calculated from compositions from the PetDB database (MORB $n = 956$, OIB $n = 1482$). Dashed lines show the equilibrium olivine compositions, assuming $K_D = 0.32$ and $Fe^{3+}/\Sigma Fe = 0.1$ in the samples.

Is ferropicrite a primary melt?

To date, fresh ferropicrite glass has not been discovered, and all ferropicrite analyses are of whole-rock samples. It is important to evaluate whether these whole-rock compositions represent a unique

ferropicrite primary magma, or are a function of crystal accumulation, fractionation or crustal assimilation. Unaltered Phanerozoic ferropicrites invariably contain a high load of Fo_{76-86} olivine phenocrysts, sometimes accompanied by a smaller mode of clinopyroxene, orthopyroxene and/or plagioclase phenocrysts, reflecting the high-Mg nature of the melt (e.g. Gibson *et al.*, 2000). Accumulated olivine will drive a bulk composition towards higher MgO and FeO, making a high-Fe basalt appear ferropicritic. Published ferropicrite whole-rock compositions were examined by Heinonen and Luttinen (2008). They found that some are indeed cumulate, but many samples have olivine phenocrysts in approximate Fe-Mg equilibrium with the whole-rock composition, indicating that they have neither accumulated nor fractionated olivine, so the whole-rock composition approximates that of the initial melt. In some cases, olivine phenocrysts are out of Fe-Mg equilibrium with the whole-rock analyses, but not by such an extent as to explain the observed high FeO and MgO. This is explored further for samples in this study in Chapter 2. Additionally, a high modal proportion of groundmass oxides (Cr-spinel, ilmenite, magnetite) is common, indicating that the melt was iron-rich. In contrast, Archaean and Proterozoic samples tend to have lost their primary igneous assemblage through metamorphic overprinting and may be cumulates in some cases (Goldstein and Francis, 2008), although evidence of spinifex olivine in Pechenga indicate that those samples are not cumulates (Hanski and Smolkin, 1995).

The isotopic signatures of Phanerozoic samples indicate that most have a sublithospheric mantle source. This can be somewhat variable, from unradiogenic and MORB-like through to radiogenic and OIB-like. Levels of crustal and/or lithospheric mantle contamination can be modelled using the isotopic compositions. Some ferropicrites from the Etendeka province have positive εNd so are not thought to be significantly contaminated by crustal or lithospheric mantle material (Gibson *et al.*, 2000). Ferropicrites from Ahlmannryggen, Antarctica (part of the Karoo CFB) also have high, MORB-like positive εNd which, in conjunction with Sr, Pb and Os isotopes, has been modelled to indicate just 1% contamination by Archaean crust (Heinonen *et al.*, 2014). Although some ferropicrite samples in the literature have more contaminated isotopic and trace element compositions, assimilation does not account for the compositional difference between picritic and ferropicritic melts.

1.3.2 Spatio-temporal distribution

The spatio-temporal distribution of ferropicrites is shown in Fig. 1.3 and Table 1.1. Ferropicrite outcrops are rare globally (Fig. 1.3), often found as small-volume flows and dykes. Phanerozoic outcrops are exclusively associated with CFB provinces (Gibson, 2002), whereas Archaean ferropicrites are part of greenstone belts and are identified by their whole-rock chemistry, as their primary mineralogy is heavily altered by metamorphic overprinting (e.g. Goldstein and Francis, 2008). In many CFB provinces, ferropicrites are found at the base of the magmatic sequence, indicating their formation

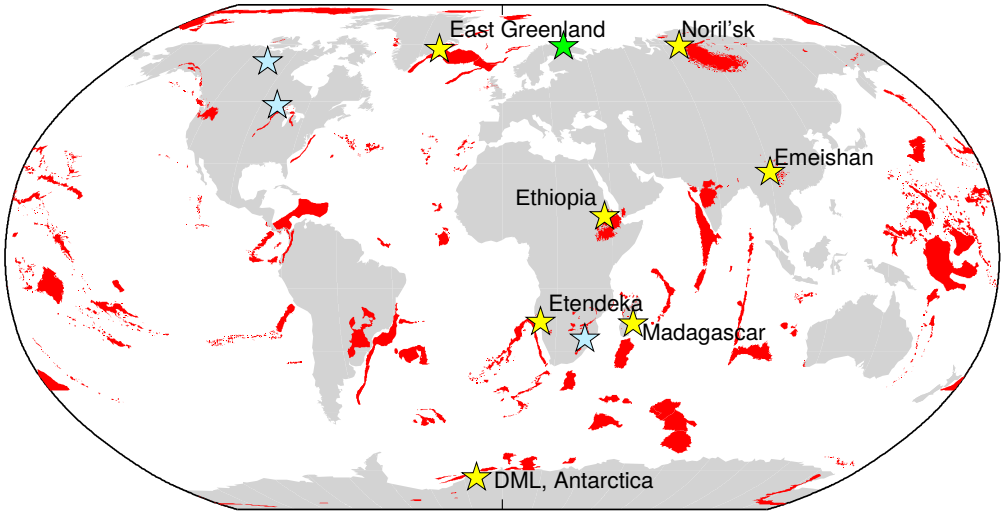

Figure 1.3: Map of global LIP and ferropicrite distribution. LIPs marked in red, after Coffin and Eldholm (1994); data from Coffin *et al.* (2006) and references therein. Ferropicrite locations marked by stars, where light blue is Archaean, green is Proterozoic and yellow with labels is Phanerozoic (ferropicrite compilation adapted from Heinonen, 2011)

Location	Age	References
Sandspruit Fm., Onverwacht Group, South Africa*	Archaean	Jahn *et al.* (1982), samples 5048-5050
Western Superior Province, Canada (various localities)	Archaean	Goldstein and Francis (2008); Stone *et al.* (1995)
Slave province, Canada	Archaean	Francis *et al.* (1999)
Pechenga, Russia	Proterozoic	Hanski and Smolkin (1989, 1995)
Emeishan CFB province, China**	Permian	Zhang *et al.* (2006), sample DJ-26
Noril'sk, Gudchikhinsky fm., Siberian Traps CFB, Russia*	Permo-Triassic	Lightfoot *et al.* (1990); Sobolev *et al.* (2009); Wooden *et al.* (1993)
Dronning-Maud Land, Antarctica, Karoo LIP	Jurassic	Heinonen *et al.* (2010); Heinonen and Luttinen (2008); Riley *et al.* (2005)
Etendeka, Namibia*	Cretaceous	Ewart *et al.* (1998); Gibson *et al.* (2000)
Madagascar*	Cretaceous	Storey *et al.* (1997), samples MAN90-45, -47
Miki Fm., East Greenland (NAVP)*	Palaeogene	Fram and Lesher (1997)
Lalibela, Ethiopia	Oligocene	Desta *et al.* (2014)

Table 1.1: Ferropicrite occurrences, identified originally or retrospectively as ferropicrite. Sample suites tend to include a small number of ferropicrite analyses amongst a larger number of other lithologies.
*First identified as ferropicrite by Gibson *et al.* (2000) and/or Gibson (2002)
**First identified as ferropicrite by Heinonen (2011)

close to the onset of magmatism (Gibson, 2002), although some ferropicrite dykes cross-cut Karoo flood basalts in Antarctica (Heinonen and Luttinen, 2008).

Ferropicrites span most of geological time. Archaean ferropicrites tend to be misidentified as komatiites, and ferropicrite compositions through to the present day have tended to decrease in Fe and Mg, reflecting deeper melting in the hotter Archaean mantle (Gibson, 2002).

1.3.3 Origin of ferropicrites

It is generally agreed that ferropicrites are mantle-derived, and that their unusual chemistry is a primary feature reflecting mantle process rather than later assimilation and alteration (e.g. Gibson *et al.*, 2000; Hanski and Smolkin, 1995; Heinonen *et al.*, 2014). There is also a consensus that the trace element chemistry of ferropicrites reflects the involvement of garnet in some form, where HREE are fractionated during mantle melting by the presence of residual or fractionating garnet. Beyond this, there is significant disagreement about the mechanism of ferropicrite formation, with a divide between studies of Precambrian samples and studies of Phanerozoic samples.

Origin of ferropicrite: a Precambrian perspective

Melting of an olivine-dominated, Fe-rich mantle

A simple explanation is that ferropicrites derive from melting of an Fe-rich mantle, an idea first proposed by Hanski and Smolkin (1995). This was subsequently supported by Francis *et al.* (1999) and Gibson *et al.* (2000). Goldstein and Francis (2008) tested this hypothesis by comparing the composition of ferropicrites with experimental partial melt compositions. They noted that experiments on the Fe-rich xenolith HK-66 give melts which are too high in Al_2O_3 at a given FeO, and melts from a hypothesised Martian mantle (Homestead) also give conflicting major element trends. They suggested that by interpolating between the melts of Homestead and KLB-1, a composition approximating ferropicrite could be achieved.

An Fe-enriched mantle requires a viable mechanism by which mantle domains can become enriched in Fe ($\pm$ LREE and Ti), which is not fully resolved in the literature. At the time of publication, Francis *et al.* (1999) noted that the only ferropicrites identified as such in the literature were Archaean to Proterozoic in age, leading them to conclude that the Earth's mantle was initially Fe-rich, having gradually sequestered Fe over time to the core and/or lower mantle. However, with the discovery of Phanerozoic ferropicrites, this idea was dismissed (Gibson *et al.*, 2000). Alternative models for Fe-enrichment of the mantle include a possible core contribution (Gibson *et al.*, 2000), although this is unlikely as Archaean ferropicrites are depleted in Pt-group elements relative to komatiites (Stone *et al.*, 1995).

Some authors propose that in addition to being Fe-rich, the mantle source must also be olivine-dominated, to explain both the high MgO and high Ni of ferropicritic melts (Goldstein and Francis, 2008; Hanski and Smolkin, 1995). High-degree, high-temperature melting of such a source would result in a high modal proportion of olivine in the melt. In this model, garnet does not have to be present in the source (Goldstein and Francis, 2008; Hanski and Smolkin, 1995); the 'garnet-signature' could be produced by a previous garnet fractionation event. For example, the segregation of olivine crystallising simultaneously with garnet during primordial magma ocean solidification could produce an

olivine-rich layer, from which subsequent melts would be depleted in HREE and Al_2O_3 (Goldstein and Francis, 2008). This model, proposed for Archaean ferropicrites, is difficult to invoke for modern samples as such layers in the mantle would not survive large-scale convective mixing processes. HREE depletion is far more commonly interpreted in terms of buffering by residual garnet in the mantle source in a wide range of mantle-derived melts, including OIB, MORB and CFB (e.g. Hirschmann and Stolper, 1996).

Origin of ferropicrite: a Phanerozoic perspective

Crystal fractionation and immiscible melts

After a high degree of crystal fractionation, basaltic melts become immiscible and split into Si-rich and Fe-rich liquids (e.g. Jakobsen *et al.*, 2005). It has been proposed that the Fe-rich portion has the trace element characteristics of ferropicrite (Veksler *et al.*, 2006). To match the high MgO content, the dense Fe-rich immiscible liquid would need to sink and mix with primitive picritic melts in order to produce the final ferropicritic composition (Jakobsen *et al.*, 2005; Veksler *et al.*, 2006). However, Goldstein and Francis (2008) point out several inconsistencies with this model, effectively ruling it out for ferropicrite genesis. Ferropicritic melts are far hotter than the basalt miscibility gap at 1000-1150 °C (Tuff *et al.*, 2005, determined a 1 atm liquidus temperature of a Phanerozoic ferropicrite as 1350-1375 °C), and mixed melts would have too low MgO at the required FeO. Voluminous counterpart silicic magmatism is expected, which is not observed in the Western Superior Province (Goldstein and Francis, 2008). In addition, there is no published petrographic evidence for melt immiscibility or mixing in any ferropicrite.

Garnet-pyroxenite dominated mantle source

The most frequently published model for Phanerozoic ferropicrite petrogenesis is melting of a garnet pyroxenite source, requiring the mantle to be lithologically heterogeneous. Both mantle pyroxenite and eclogite would be enriched in incompatible elements, which would explain the high concentrations in ferropicrites. This is consistent with the observation that the global distribution of ferropicrites coincides with continental lithosphere and CFBs: melting in the sublithospheric mantle is restricted to high pressures and will be biased towards, or even isolate, more fusible lithologies (such as pyroxenite or eclogite) that have solidus curves offset to lower temperatures relative to peridotite (e.g. Kogiso *et al.*, 1998).

Gibson (2002) first suggested that mantle garnet pyroxenite was the source for ferropicrites, noting that in the sandwich layered peridotite/eclogite experiments of Yaxley and Green (1998), the hybrid pyroxenite produced by the enrichment of peridotite by partial melts of eclogite is enriched in FeO and would potentially melt to produce an Fe-rich picrite. Alternatively, the FeO_T and trace

element enrichment could be explained by recycled Fe-Ti gabbro rather than a generic subduction-modified MORB composition, as suggested by Ichiyama *et al.* (2006) and Heinonen and Luttinen (2008). This would result in an Fe-rich eclogite or pyroxenite mantle source.

The pyroxenite or eclogite source hypothesis is supported by the subsequent experiments of Tuff *et al.* (2005), who examined high-pressure supersolidus phase relations of a natural ferropicrite (sample 97SB68 of Gibson *et al.*, 2000). It was found that the melt was doubly-saturated in ol + cpx at 2.2 GPa, or cpx + grt at > 5 GPa; the clear garnet signature of the natural samples favours the higher pressure scenario. This implies that the melt last equilibrated with a garnet and clinopyroxene bearing source. Heinonen *et al.* (2010, 2014, 2013) argue for a pyroxenite source for ferropicrites from Vestfjella and Ahlmannryggen, Dronning Maud Land (DML, Antarctica), based on major, trace element and isotopic chemistry. They show that their highly radiogenic Os isotopic ratios cannot be obtained through melting of unradiogenic mantle peridotite. However, several authors point out that no eclogite-peridotite mixed experiment or similar setup has ever produced a melt high enough in FeO at a given MgO for this model to work (Goldstein and Francis, 2008; Ichiyama *et al.*, 2006). Whilst being true, this reflects the difficulty in performing experimental work at the high pressures and low melt fractions appropriate for ferropicrite genesis, along with poor constraint on an appropriate pyroxenite bulk composition.

A similar eclogite or pyroxenite source is frequently invoked in OIB formation (e.g. Herzberg, 2011b; Hofmann and White, 1982; Sobolev *et al.*, 2007, 2005). OIB has lower FeO and MgO than ferropicrite, so if the recycled source argument is correct, it must be consistent with both OIB and ferropicrite geochemistry. The fact that experimental partial melts of pyroxenite currently available do not match ferropicrite compositions well may reflect the lower pressure range of pyroxenite melting experiments, which tend to be performed with the aim of understanding OIB geochemistry. There is also little consensus on the composition of mantle pyroxenite, meaning that a wide range of melt compositions can produced in different studies (Lambart *et al.*, 2013). The origin of the major element chemistry of ferropicrite is reassessed in Chapter 4.

1.4 Summary

CFB provinces derive from high temperature, high degree melting in mantle plume starting heads. The lithosphere beneath CFBs is thicker than in OIB settings, especially in the early stages of plume head impingement, prior to significant rifting and lithospheric thinning. This increases the likelihood of isolating and sampling melts that formed at pressures above that of the peridotite solidus, where only recycled materials (eclogite or pyroxenite) would begin to melt. This contrasts with OIB and especially MORB settings, where pyroxenite partial melts are subsequently diluted by higher fraction peridotite melts due to the shallower extent of the melt column. CFB provinces are therefore well

placed to identify mantle heterogeneity. However, CFB magmas have suffered extensive fractionation and assimilation, making it difficult to gain much resolution on their mantle source characteristics. Rare primitive melts found in CFB provinces include picrites and ferropicrites, where ferropicrites cannot be explained by peridotite melting.

Ferropicrite petrogenesis is unresolved in the literature, although it is generally agreed that the composition reflects a primary mantle-derived melt that equilibrated with garnet. Studies of Archaean samples tend to favour an Fe-rich peridotite model, whereas studies of Phanerozoic samples favour a recycled eclogite or pyroxenite mantle source. It would be unsatisfactory to invoke two separate formation mechanisms for the same unusual rock composition. However, this may have to be the case, as questions about the timing of subduction recycling and the onset of plate tectonics make the recycled crustal option difficult to invoke for the oldest Archaean samples (Van Kranendonk, 2011), and arguments for an Fe-rich mantle lack a mechanism for Fe-enrichment and are poorly applicable to the better characterised modern ferropicrites.

The recycled mafic crust argument is considered the most likely answer, at least for modern ferropicrites. If true, this has important implications in terms of geodynamics, demonstrating that deeply subducted material can indeed be returned from the core-mantle boundary to the surface by mantle plumes. Ferropicrite would also represent an important endmember to aid with identifying the contribution of melts from recycled materials in other settings with elevated melting pressure and temperature conditions, such as OIB. In order to test this hypothesis and strengthen this conclusion, the origin of ferropicrite is revisited in this thesis.

1.4.1 Research statement

The purpose of this thesis is to better understand source lithology and melting processes in mantle plume starting heads, that ultimately produce continental flood basalts. The approach is both forward (prediction of major and trace elements of melts of various lithologies expected from plume melting) and inverse (investigating natural samples from CFB provinces which represent the end-product of mantle melting to understand their mode of formation in the mantle, along with their subsequent mixing, assimilation and fractionation in the crust). A particular focus is on the presence of recycled material and its link with the origin of ferropicrite, in order to test and strengthen previous interpretations. If ferropicrites originate in the high pressure melting of recycled slab material, then they should form an end-member in our understanding of the behaviour of recycled material in the mantle. This will have implications for the search of such material in melts from different tectonic settings, and ultimately informing our knowledge of the interaction between subducted slabs and the triggering of new mantle plumes. Picrites and ferropicrites from the Etendeka province, part of the Paraná-

Etendeka CFB, are the main focus of this thesis, and the ferropicrite samples are supplemented by samples from the Antarctic portion of the Karoo province.

1.4.2 Thesis structure

The petrology of the natural samples is examined in Chapter 2, with a focus on primary melt compositions and crustal processing. Olivine-hosted melt inclusions are then investigated in Chapter 3 to determine whether these samples represent a well-mixed combination of fractional mantle melts, and to investigate melt accumulation processes in CFB provinces. Chapter 4 introduces and applies a new thermodynamic model to explore both the subsolidus assemblages and the partial melt compositions of peridotite as well as range of other potential mantle lithologies, from harzburgite through to MORB. The unusual major element characteristics of ferropicrite are then explored by forward modelling of fractional melting of different lithologies. The potential temperatures of the respective mantle plumes are determined from novel thermometery work on these samples in Chapter 5. Trace element compositions of the different samples in this study are similarly examined in Chapter 6 through forward modelling of melting of different mantle lithologies. The concluding chapter (7) brings together the findings of the previous chapters in order to make a compelling case for the origin of ferropicrite in partial melting of recycled crustal material in the Tristan and Karoo mantle plume starting heads, and provides revised T_P and lithospheric thickness estimates to inform a model for the early evolution of the Paraná-Etendeka CFB province. The broader implications of these findings are discussed. Details of all analytical methods, model input parameters and data tables are provided in the appendices.

Chapter 2

Petrology and geological context

The whole-rock elemental and isotopic compositions and some of the mineral chemistry of samples from the Paraná-Etendeka and Karoo CFB provinces described in this chapter were previously analysed and published by various groups. It is supplemented with new analyses of mineral chemistry here. The geological backgrounds and petrological characteristics of both sample sets are discussed to provide context for this thesis, with a focus on the Etendeka samples. The compositions of samples considered in this thesis are supplemented by additional published compositions of Etendeka Horingbaai-type picrites from Keiding *et al.* (2011) and Keiding *et al.* (2013).

2.1 Geological background

2.1.1 The Paraná-Etendeka CFB province

The Paraná-Etendeka CFB province, which is today split by the South Atlantic, formed as a single magmatic province (Erlank *et al.*, 1984). Although the majority of the flood basalts outcrop in South America, a small proportion of the magmatic volume crops out in the Etendeka province of Namibia and southern Angola (Fig. 2.1). The Etendeka region includes a greater variety of magma types than the Paraná, as well as exposure of the basal contact and magmatic plumbing systems, making it important for understanding the evolution and origin of the province (Erlank *et al.*, 1984; Marsh *et al.*, 2001; Peate, 1997). The Paraná-Etendeka CFB province covers at least 1.2×10^6 km^2 with an average thickness of 0.7 km in Paraná and has an aerial extent of 0.8×10^5 km^2 in Namibia (Peate, 1997). The flood basalts in Etendeka are mostly situated in the north (the 'southern Etendeka volcanics' of Fig. 2.2); these are bimodal in composition, with significant volumes of mafic and silicic material (Ewart *et al.*, 2004). The southern part of the Etendeka CFB contains igneous complexes, dyke swarms and other subvolcanic intrusives, many of which have been correlated to magmas in Paraná (Ewart *et al.*, 1998; Marsh *et al.*, 2001; Milner and le Roex, 1996; Peate, 1997; Thompson *et al.*, 2001).

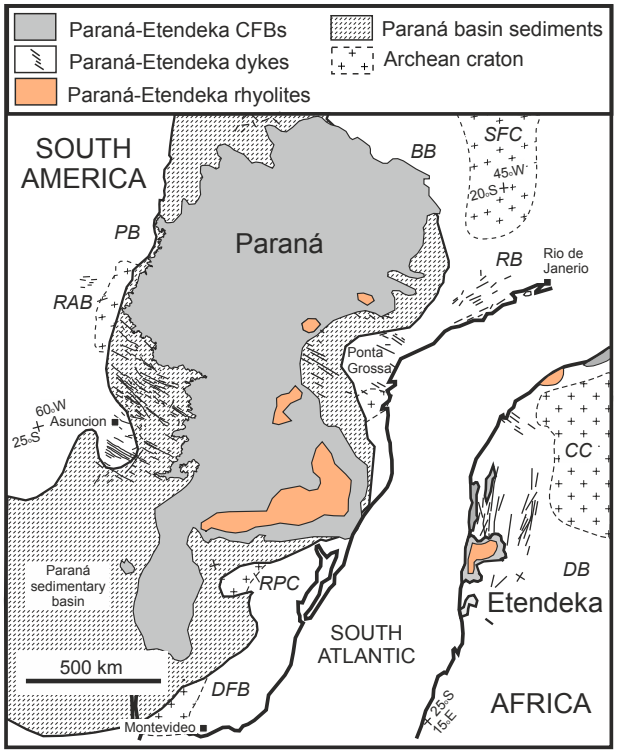

Figure 2.1: Paraná-Etendeka CFB province with tectonic reconstruction to 133 Ma, modified from Gibson *et al.* (2006). The distribution of the grey region shows that the majority of the CFB outcrops in South America. Abbreviations: BB, Brasilia Belt; DB, Damara Belt; DFB, Dom Feliciano Belt; PB, Paraguai Belt; RB, Ribeira Belt; CC, Congo Craton; LA; Luis Alves Craton; RAB, Rio Apa Block; RPC, Rio de la Plata Craton; SFC, São Francisco Craton

The timing and extrusion rate of the Paraná-Etendeka CFB province are heavily debated, and lack consensus at present. Milner *et al.* (1995) used Rb-Sr and $^{40}Ar/^{39}Ar$ dating to place the bulk of magmatic activity in the Etendeka province at 137–124 Ma. Shortly after, however, Renne *et al.* (1996) dated plagioclase crystals from the Etendeka flood basalts by $^{40}Ar/^{39}Ar$ and obtained an age range of 131.7–132.3 ($\pm$0.7) Ma, and combined these dates with palaeomagnetic data to argue for a short duration of peak magmatism. More recently, it was suggested on the basis of magnetostratigraphy that the peak of flood basalt emplacement in Etendeka occurred over > 4 Ma from 135–130 Ma, which is a rather long duration relative to other CFBs (Dodd *et al.*, 2015). In Paraná, Turner *et al.* (1994) used $^{40}Ar/^{39}Ar$ laser spot dating to determine that the flood basalts erupted over 11 Myr, from 140–129 Ma. However, a recent re-analysis of the samples of Turner *et al.* (1994) reveals that their ages are in fact indistinguishable from each other, placing the Paraná extrusion at 134.6 ± 0.6 (Thiede and Vasconcelos, 2010) with an average eruption rate of 2 km^3/yr, which is comparable with extrusion rates of the Emeishan, Siberian, and Deccan traps. The extrusion rate, which is a function of eruption duration, is of great interest as it may (or may not) explain the notable lack of a major extinction event associated with emplacement of the Paraná-Etendeka CFB province (e.g. Wignall,

2001). The onset of magmatism in the province as a whole is represented by older (up to 145 Ma) small-fraction alkaline magmas from lithospheric melting in Paraná (Gibson *et al.*, 2006).

Both sides of the Paraná-Etendeka CFB province are temporally associated with rifting and the opening of the South Atlantic Ocean during the breakup of the Gondwana supercontinent. They are also linked to the island of Tristan da Cuhna, thought to be the result of melting in the modern Tristan mantle plume, by aseismic ridges (the Walvis ridge on the African side and the Rio Grande Rise on the South American side), leading various authors to conclude that the upwelling Tristan plume starting head was responsible for the formation of the province (e.g. Gallagher and Hawkesworth, 1994; White and McKenzie, 1989). Some studies consider that conductive heating and melting of the overlying subcontinental lithospheric mantle (SCLM) by an impinging plume produced much of the CFB (e.g. Erlank *et al.*, 1984; Garland *et al.*, 1996; Hawkesworth *et al.*, 1992; Peate, 1997; Turner *et al.*, 1994). More recent studies consider the bulk of magmatism to derive from melting within the sublithospheric mantle, from the plume head itself (Ewart *et al.*, 2004, 1998; Gibson *et al.*, 1999; Hawkesworth *et al.*, 1999; Milner and le Roex, 1996; Milner *et al.*, 1995; Thompson *et al.*, 2001, 2007), although some high Ti/Y basaltic units are proposed to derive from melting of delaminated lithospheric mantle (Peate *et al.*, 1999). Ewart *et al.* (2004) suggest that aspects of some Etendeka basalt types are consistent with that plume source being heterogeneous. For example, low Nb/Nb* and enriched radiogenic isotopes in the 'Khumib type' basalts are interpreted by Ewart *et al.* (2004) as being indicative of recycled sediment in the plume source, rather than resulting from crustal contamination.

Sample background and field relations

Both picrites and ferropicrites from the Etendeka are situated in the Proterozoic Damara mobile belt between the Kalahari and Congo cratons on the west coast of Namibia. A detailed map of sample locations, including those of Keiding *et al.* (2011), is given in Fig. 2.2.

Horingbaai-type picrites and basalts

The Horingbaai-type basalts and picrites, first described by Erlank *et al.* (1984), were originally identified in a dyke swarm close to the Horingbaai coast and are distinctively MORB-like in terms of their trace element geochemistry and isotopic composition (Erlank *et al.*, 1984; Ewart *et al.*, 2004; Thompson *et al.*, 2001). Most are defined as picrite as they contain > 12 wt. % MgO (Thompson *et al.*, 2001), and are referred to hereafter as the 'Etendeka picrites' for simplicity, as they are the only Etendeka rock type examined other than the ferropicrites. They occur to the south of the main CFB outcrops in Etendeka (Fig. 2.2). The Etendeka picrites in this study have been characterised in terms of whole-rock major-, trace-element and isotope geochemistry and phenocryst geochemistry in Thompson and Gibson (2000) and Thompson *et al.* (2001). Although not dated directly, a Horingbaai-type picrite dyke cross-cuts a flood basalt dated 132 $\pm$ 0.7 Ma by Renne *et al.* (1996), constraining the maximum

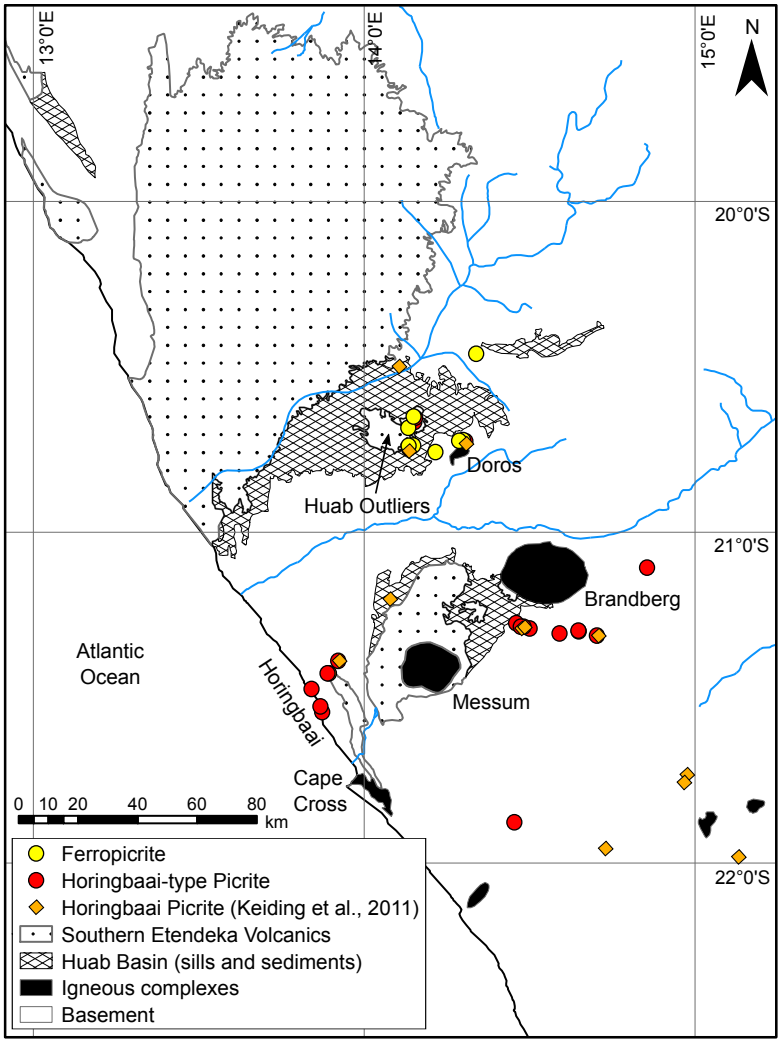

Figure 2.2: Geological map of Southern Etendeka, Namibia, after Thompson *et al.* (2001). Sample locations of Horingbaai-type picrites from Thompson *et al.* (2001) and Keiding *et al.* (2011) and of ferropicrites from Gibson *et al.* (2000) and Thompson *et al.* (2001).

age of the picrite, which is itself intersected by granites suggested to be 131 $\pm$ 1 Ma by Thompson *et al.* (2001) based on the geochronology work of Schmitt *et al.* (2000). Thompson *et al.* (2001) therefore proposed an age of 132 Ma for the picrites, which is younger than the ferropicrites, consistent with field stratigraphic evidence, and approximately coeval with the main basalt emplacement phase. These age estimates suffer reasonably large uncertainties.

Etendeka ferropicrites

In the Etendeka province, ferropicrite dykes and thin flows represent the earliest magmatic activity associated with the arrival of the proto-Tristan mantle plume. They underlie and slightly pre-date the main CFB sequence, including the picrites (Gibson *et al.*, 2000; Thompson *et al.*, 2001). Some basal lava flows, which are interbedded with Aeolian sands (known collectively as the Tafelkop-Interdune Member, part of the Awahab Fm. in the Huab Outliers; Jerram *et al.*, 1999), have ferropicritic compo-

sitions. The oldest flow of this unit is dated at 132.9 ± 0.3 Ma (Renne, 1999, pers. comm., in Jerram *et al.*, 1999) and as such, Thompson *et al.* (2001) assume that all ferropicrites have a similar age. Some ferropicrite samples are strictly ferrobasalt as they contain < 12 wt. % MgO.

2.1.2 The Karoo CFB province

The Karoo CFB province, like the Paraná-Etendeka, formed during the breakup of Gondwana, albeit in the earliest stages ($\sim$ 184–179 Ma; Duncan *et al.*, 1997; Riley and Knight, 2001). Outcrops of Karoo magmatic material are found over a vast area of southern Africa (Erlank, 1984), with a smaller volume in Dronning Maud Land (DML) in East Antarctica. The Karoo CFB is now heavily eroded but may have had an initial volume of up to around 2×10^6 km^3 (Richards *et al.*, 1989) and a high peak magmatic flux (e.g. 367,000 km^3 of magma extruded over just 0.47 Myr, Svensen *et al.*, 2012). It is temporally coincident with both the Ferrar province (which also formed in response to Gondwanan breakup) and the Pliensbachian-Toarcian extinction (Duncan *et al.*, 1997; Riley and Knight, 2001).

As for the Paraná-Etendeka, the origin of the Karoo CFB province has been heavily debated. Varying levels of importance are assigned to rifting vs. a mantle thermal anomaly being the main cause of melt production, and there has been disagreement about whether the bulk of the voluminous CFB was sourced from within the mantle plume itself and/or from partial melting of the overlying sub-continental lithospheric mantle (SCLM) by conductive heating and rifting (Ellam and Cox, 1991; Erlank, 1984; Hawkesworth *et al.*, 1999; Riley *et al.*, 2005; White and McKenzie, 1989). Most recently, it was suggested that the different CFB groups all originated from the same sublithospheric MORB-source mantle and were subsequently contaminated to varying extents by SCLM and/or crust (Luttinen *et al.*, 2015). The elevated mantle temperature for the Karoo, as with other CFB provinces, has traditionally been interpreted in the context of the thermal mantle plume paradigm. However, recently, a thermal insulation model has also been invoked in which the Gondwana supercontinent insulates underlying mantle, allowing it to build up heat and then partially melt during subsequent rifting (Coltice *et al.*, 2007; Hole, 2015; Rolf *et al.*, 2012).

Although most samples of the Karoo, especially in Africa, have strong lithospheric geochemical overprints (Erlank, 1984), a small number of more depleted, primitive outcrops are found in DML that have been linked to a sublithospheric mantle origin, including basalt, meimechite (MgO > 18 wt.%, TiO_2 > 1 wt. %; Le Bas, 2000) and ferropicrite (Heinonen *et al.*, 2010; Heinonen and Kurz, 2015; Heinonen and Luttinen, 2008, 2010; Luttinen and Furnes, 2000; Luttinen *et al.*, 2015; Riley *et al.*, 2005); some of these samples are examined in this thesis.

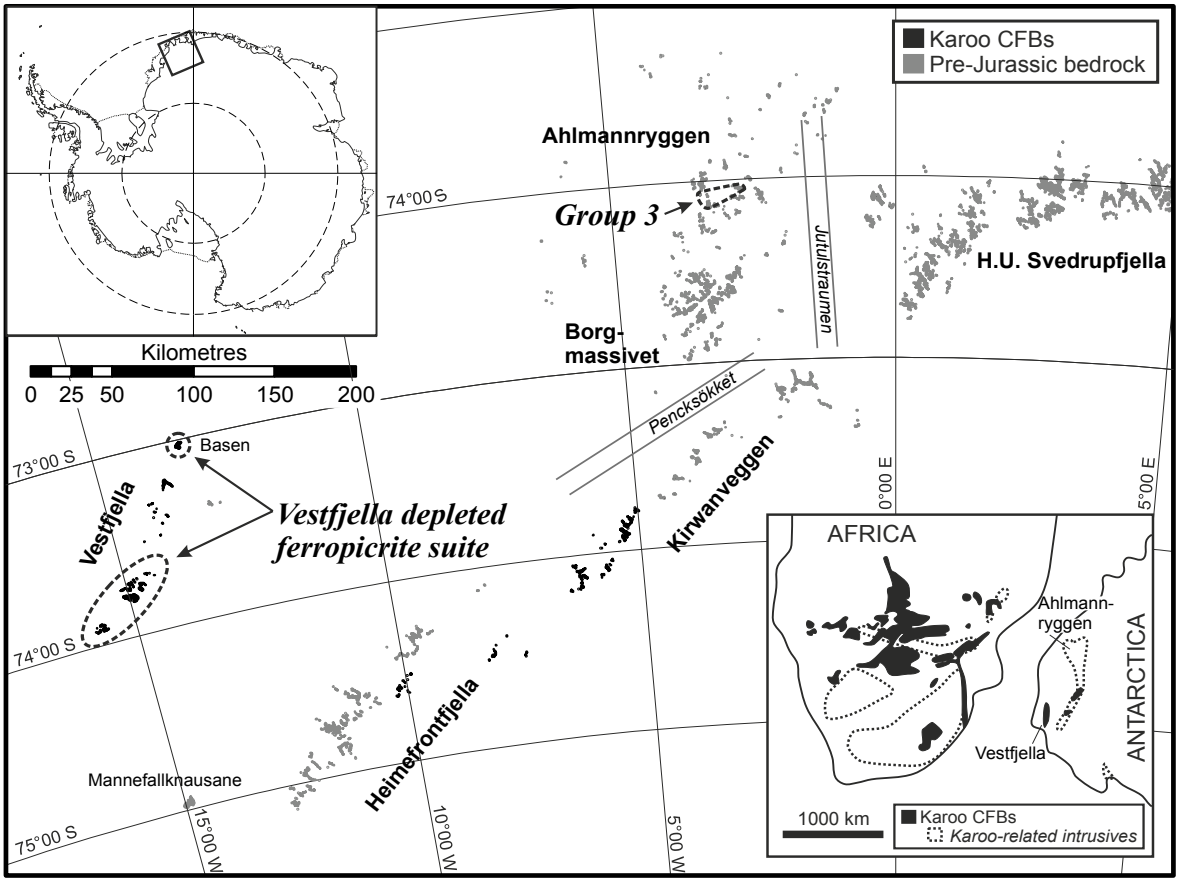

Figure 2.3: Outcrop map of Dronning Maud Land, Antarctica (from Heinonen *et al.*, 2015), showing sample locations. Three samples used in this study are from the 'Group 3' samples in Ahlmannryggen and one sample is from Basen in Vestfjella.

Sample background and field relations

Dronning Maud Land ferropicrites

Karoo ferropicrites are found as dykes in DML, Antarctica (hereafter called the 'DML ferropicrites' to distinguish them from the Etendeka ferropicrites). The four samples (three 'Group 3 picrites', Z1813.1, Z1816.3 and Z1817.2, from Ahlmannryggen, Riley *et al.*, 2005; one 'enriched ferropicrite', JSH-B006, from Basen in Vestfjella, Heinonen *et al.*, 2010) included in this study have previously been characterised in terms of whole-rock major and trace elements, Sr, Nd, Pb and Os isotopic composition and mineral chemistry (Heinonen *et al.*, 2010, 2014, 2013; Riley *et al.*, 2005). Their locations are given in Fig. 2.3. The Ahlmannryggen samples have been dated by $^{40}Ar/^{39}Ar$ and are approximately 187 Ma (Riley *et al.*, 2005). The age of the Vestfjella sample is unknown, although other Vestfjella lavas span 182.2–189.2 Ma (Luttinen *et al.*, 2015). The Vestfjella ferropicrite dykes cross-cut the Karoo CFBs (Heinonen *et al.*, 2010; Luttinen *et al.*, 2015), and the Ahlmannryggen ferropicrites form isolated dykes intruded into the underlying sedimentary and volcanic sequence of

the Neoproterozoic Ritscherflya Supergroup (Riley *et al.*, 2005). Both overlie the Archaean basement of the Grunehogna craton close to its south-eastern margin.

2.2 Petrology and Geochemistry

The samples used in this study are primitive, high MgO magmatic rocks emplaced as small dykes, sills or flows which are temporally associated with the voluminous CFBs. Photomicrographs of a selection of these samples are shown in Fig. 2.9.

2.2.1 Whole-rock chemistry

A table of the whole-rock chemistry of the samples used in this study is provided in Appendix C. Fig. 2.4 illustrates the probability distribution of whole-rock MgO compositions of the two provinces. The major flood basalt units are clearly shown by the large peaks at 4–6 wt.% MgO. The bimodalality of Etendeka rocks, where voluminous siliceous and mafic samples are found, is also clear, and it is also apparent that the combined Karoo and Ferrar CFB provinces contain significant volumes of more evolved rocks. The samples of this study are in the high MgO tail of the distribution (the highest MgO samples have suffered olivine accumulation); they are different to the bulk of the extrusive materials and are volumetrically minor.

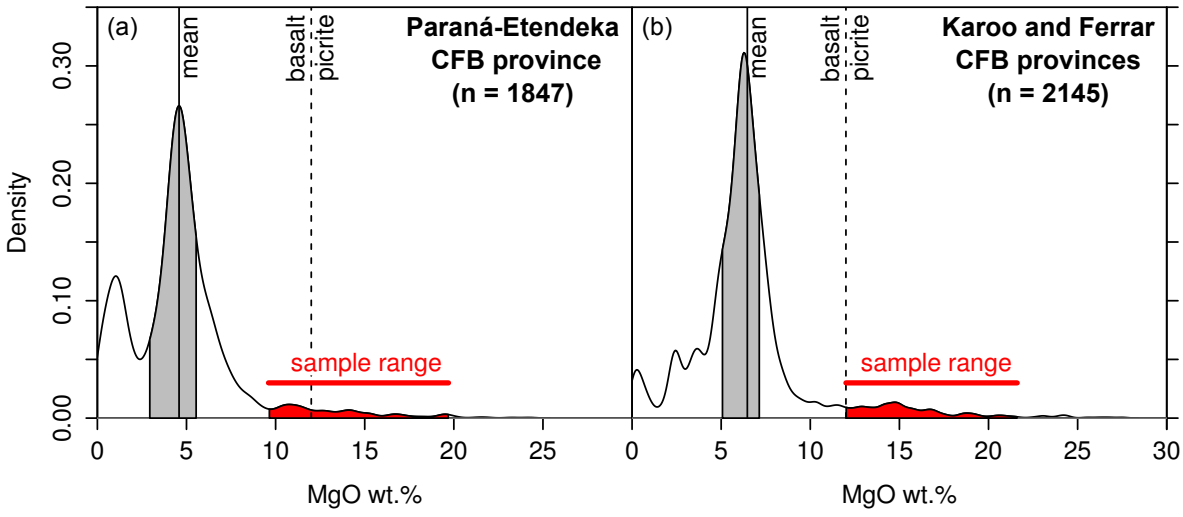

Figure 2.4: Probability distribution of MgO wt.% of whole-rock and glass analyses of samples from the GEOROC database (Sarbas and Nohl, 2008), excluding exotic compositions, from a) the Paraná-Etendeka CFB province and b) the related Karoo and Ferrar CFB provinces. The peak at around 5 wt.% MgO is a result of sampling of the voluminous flood basalts; for context, the range of samples of this study is shown by the red bar. Grey region shows lower and upper quartile.

Etendeka picrites

On a total alkali versus silica (TAS) plot (Fig. 2.5) the Etendeka picrites, which are olivine tholeiites, mostly classify as subalkaline basalts. The whole-rock samples have basaltic to picritic MgO concentrations. Primitive mantle normalised incompatible trace element patterns are approximately flat, with a slight garnet signature seen in $[MREE/HREE]_N > 1$ (Fig. 2.6). Isotopic compositions (high but varied εNd of 3.7–8.7 and low $^{87}Sr/^{86}Sr$ of 0.703–0.708) have been interpreted as ranging from depleted and convecting mantle-like to crustally overprinted or indicating a minor melt contribution from the SCLM (Thompson *et al.*, 2001).

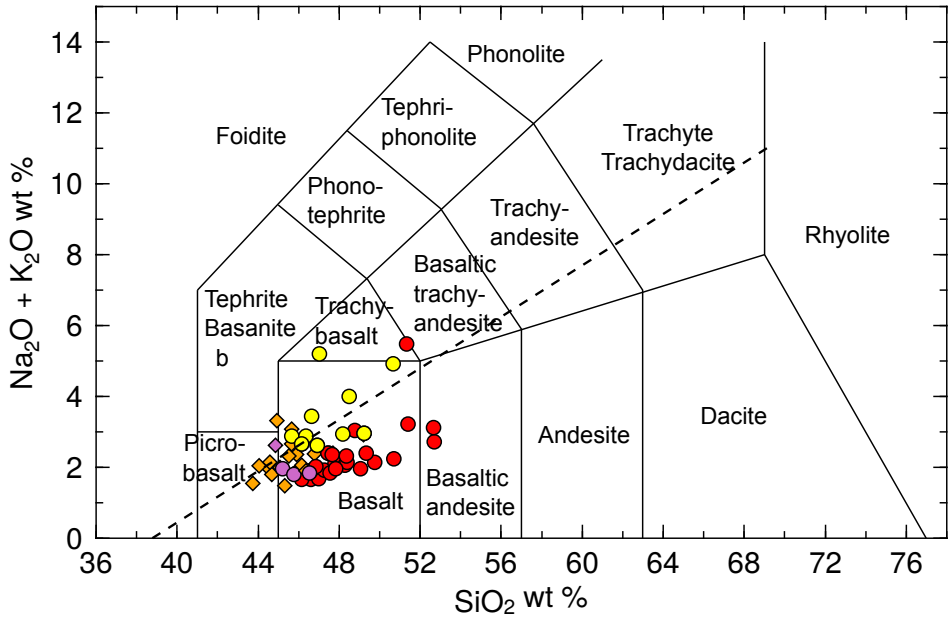

Figure 2.5: TAS classification diagram (Le Bas *et al.*, 1986) with the dashed line showing the alkaline/subalkaline divide of Macdonald (1968), from the coordinates of Rickwood (1989). Whole-rock data is plotted, showing most samples to be primitive and subalkaline. Data sources: Gibson *et al.* (2000); Heinonen *et al.* (2010); Keiding *et al.* (2011); Riley *et al.* (2005); Thompson *et al.* (2001). Legend as in Fig. 2.11.

The whole-rock composition of the Etendeka picrites has been used to infer low degrees (0–6 %) of crustal contamination (Thompson *et al.*, 2001). $^{87}Sr/^{86}Sr$, εNd, Rb/Nb ratio and Pb isotopic systematics all show mixing trends towards Damara belt sediments and granites, i.e. the local upper crust. Samples with the most irregular trace element patterns in Fig. 2.6a are those most affected by contamination and hydrothermal alteration (Thompson *et al.*, 2001). Recent measurements of olivines from six similar picrites from the Etendeka province show their $\delta^{18}O$ to be 4.92–5.96 ‰ (Harris *et al.*, 2015); by comparison, mantle olivine has $\delta^{18}O = 5.2$. $\delta^{18}O$ correlates with whole-rock $^{87}Sr/^{86}Sr$, εNd and Pb isotope ratios, which was interpreted by Harris *et al.* (2015) as showing

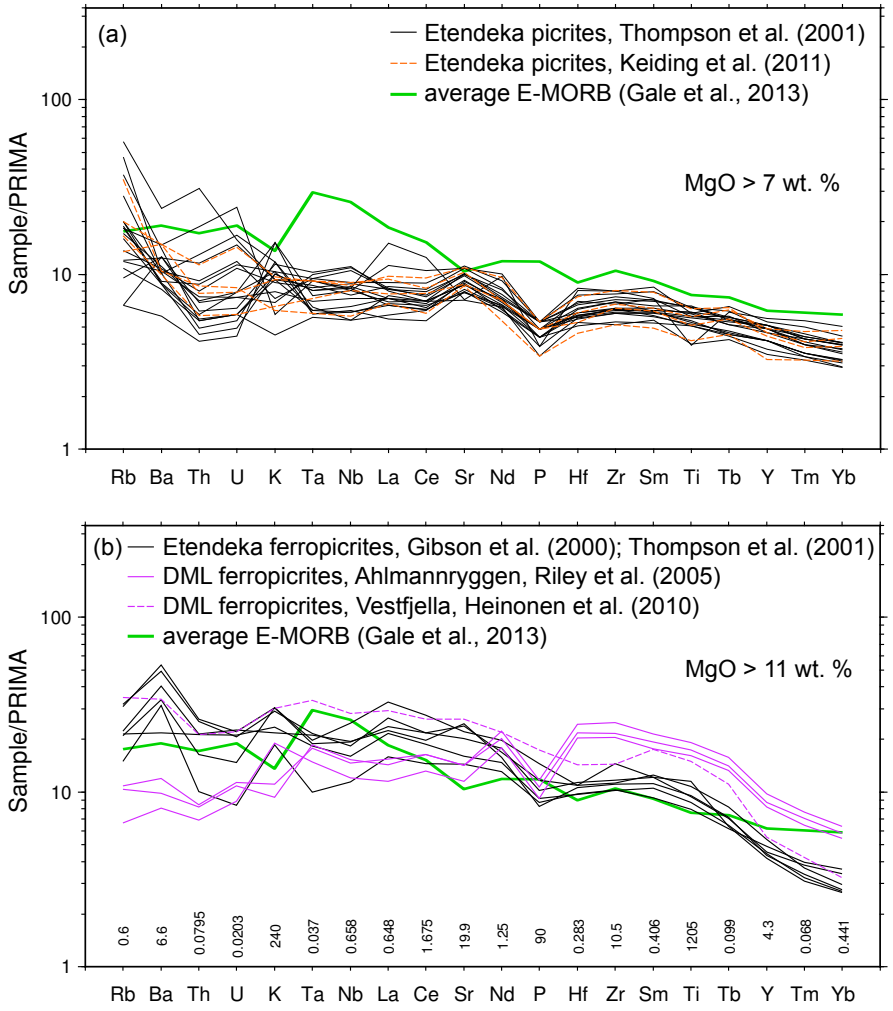

Figure 2.6: Primitive mantle normalised (PRIMA; McDonough and Sun, 1995) multi-element plot for a) Etendeka picrites (and basalts; Thompson *et al.*, 2001, used in this thesis) and Keiding *et al.* (2011), with MgO > 7 wt. %; b) Etendeka and DML ferropicrites with MgO > 11 wt. % (Gibson *et al.*, 2000; Heinonen *et al.*, 2010; Riley *et al.*, 2005; Thompson *et al.*, 2001). Thick green lines are the average E-MORB composition of Gale *et al.* (2013). Numbers along x-axis are normalisation values.

magmatic assimilation. The relative timing of crustal assimilation and crystallisation is examined at higher resolution using olivine-hosted melt inclusions in Chapter 3.

When plotted against whole-rock MgO, the Horingbaai whole-rock compositions of Thompson *et al.* (2001) and Keiding *et al.* (2011) define a clear liquid line of descent, indicating their genetic relationship to one another (Fig. 2.7). The linear trend at high MgO is attributed to both olivine fractionation and modal olivine loss or accumulation. Petrographic evidence indicates that the kink in the trends at lower MgO are due to plagioclase joining the crystallising assemblage, and later clinopyroxene.

Both Petrolog3 (Danyushevsky and Plechov, 2011) and MELTS (Ghiorso and Sack, 1995) were used to determine whether the phase relationships could be modelled well enough to discriminate be-

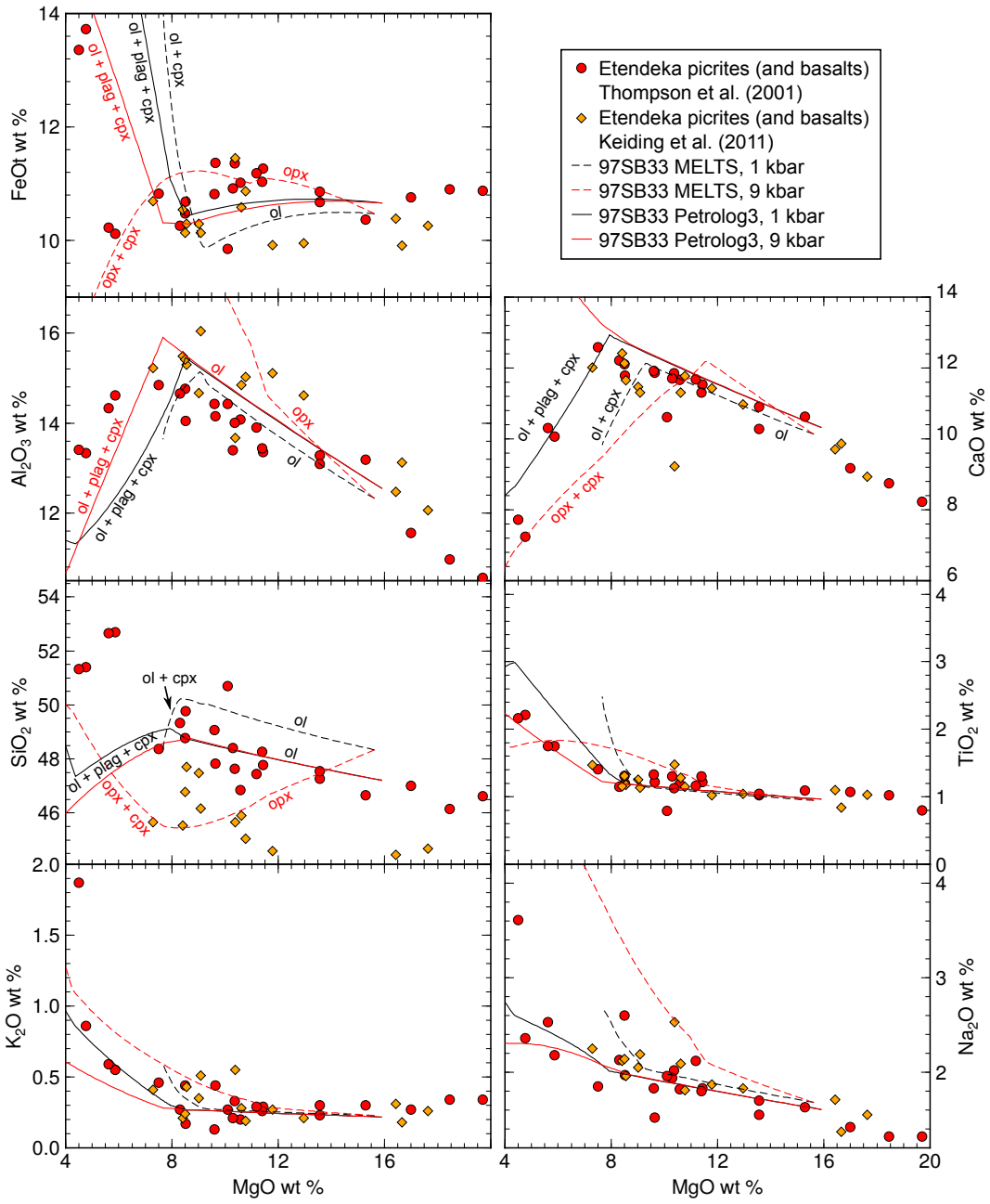

Figure 2.7: Etendeka picrite whole-rock oxide wt.% vs. MgO. Data: Red circles, Thompson *et al.* (2001); orange diamonds, Keiding *et al.* (2011). Lines are modelled melt evolution calculated from the composition of sample 97SB33 in MELTS (Ghiorso and Sack, 1995, dashed lines, calculations performed in alphaMELTS, Smith and Asimow, 2005) and Petrolog3 (Danyushevsky and Plechov, 2011, solid lines) where black lines are calculated at 1 kbar and red at 9 kbar, all at the QFM oxygen fugacity buffer.

tween high and low pressure fractionation. Although no model reproduces the observed petrography, Petrolog3 did an acceptable job of reproducing the whole-rock chemistry trend at 1 kbar (Fig. 2.7). However, it predicts early clinopyroxene crystallisation along with olivine and plagioclase, which is not observed in the samples. It should be noted that the systematic offset in Al_2O_3 and SiO_2 between

the data of Thompson *et al.* (2001) and Keiding *et al.* (2011) is not due to the sample sets being different (as shown in Fig. 2.2, some samples were taken from the same dykes); rather, this offset is attributed to inter-laboratory analytical bias.

Etendeka ferropicrites

Etendeka ferropicrites have similarly high MgO but higher FeO (> 13 wt. %) and lower Al_2O_3 and CaO than is typical in picrites. They are also subalkaline olivine tholeiites (Fig. 2.5). Similarly to the Etendeka picrites, not all of the ferropicrite whole-rock samples are in FeO-MgO equilibrium with their olivine macrocrysts, and whole-rock MgO contents reflect gain of olivine as well as how fractionated a sample is relative to the primary melt (Fig. 2.10b).

Most Etendeka ferropicrites have smooth normalised incompatible trace element patterns which show a very strong garnet signature ($[MREE/HREE]_N$ = 3–6) and are enriched in highly incompatible elements relative to picrite (Fig. 2.6b). Their isotopic compositions (εNd =-2.9-+3.7 and $^{87}Sr/^{86}Sr$ = 0.704-0.705) are thought to indicate derivation from the sublithospheric mantle and < 10 % contamination by lower crustal material (Gibson *et al.*, 2000).

The relationship between different ferropicrite samples within the Etendeka is not clear and does not obviously define a liquid line of descent (Fig. 2.8). This may be due to: i) too few samples; ii) samples with more olivine accumulation than is seen in the picrites; or iii) the possibility of a slightly different origin for each sample, i.e. rather than being derived from one deep crustal magma chamber, they represent different primary mantle melts, for example the proportion of pyroxenite-derived melt represented may vary. For this reason, melt evolution is not modelled for ferropicrites, although the trends seen in the olivine Ni–Fo relationships mean that the samples are linked, to some extent, by crystal fractionation (Fig. 2.11).

Dronning Maud Land ferropicrites

The DML Ahlmannryggen ferropicrites of Riley *et al.* (2005) and the single Vestfjella ferropicrite sample of Heinonen *et al.* (2010) are somewhat similar to those from the Etendeka in terms of whole-rock geochemistry. They are also high MgO, subalkaline olivine tholeiites with elevated FeO and low Al_2O_3 and CaO relative to picrites. Both DML ferropicrite groups have distinctively high TiO_2 (3–4 wt. %), which is even higher than the 2–3 wt. % of the Etendeka ferropicrites (Fig. 2.8). From a major element perspective, both DML sample sets are very similar to each other. Again, there are too few samples to identify a liquid line of descent, but it is assumed on the basis of very similar trace elements, mineral chemistries and isotopic ratios that the three Ahlmannryggen samples are closely linked and differ only through the modal proportion of olivine.

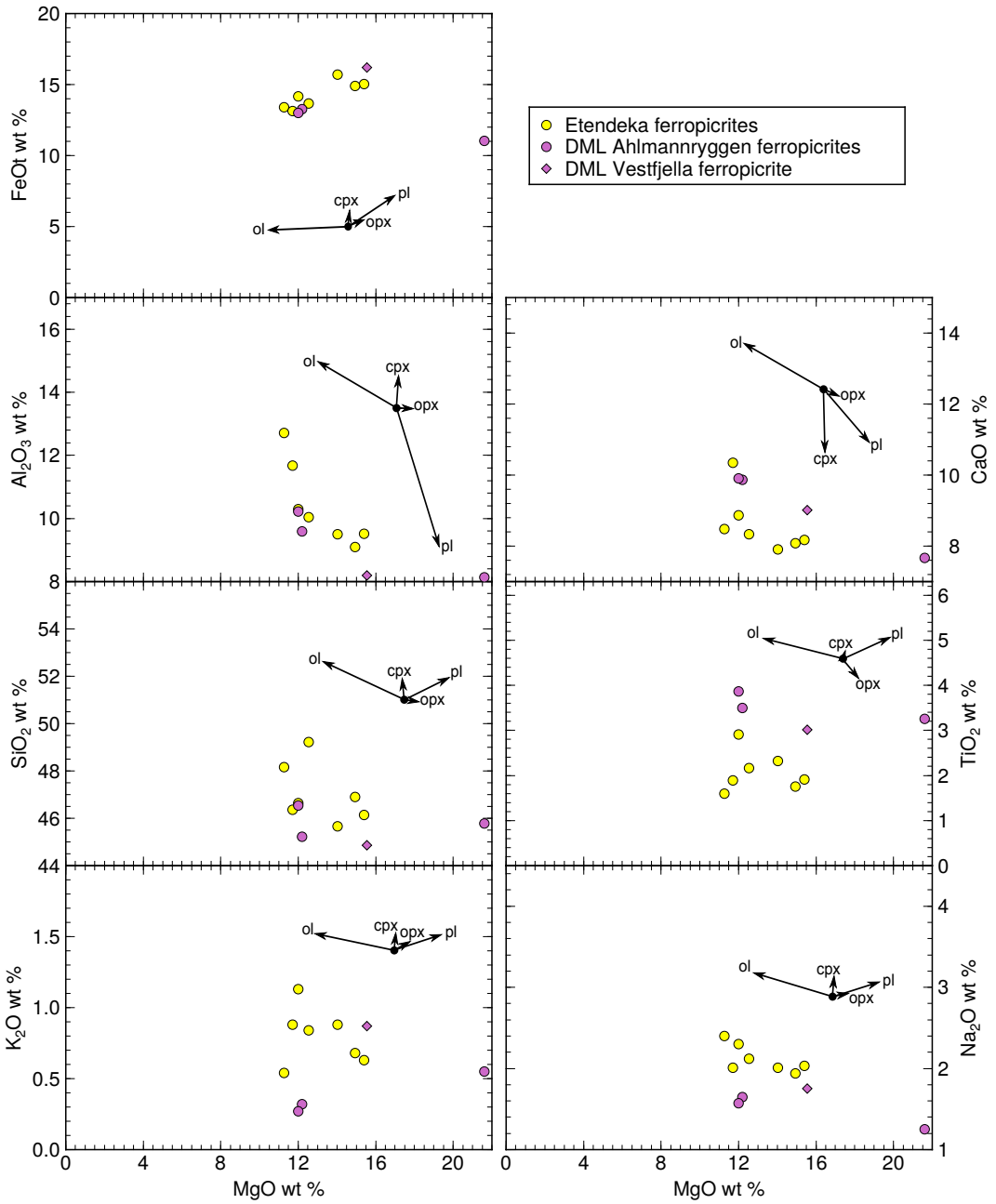

Figure 2.8: Ferropicrite whole-rock oxide wt.% vs. MgO. Yellow, Etendeka ferropicrites (Gibson *et al.*, 2000; Thompson *et al.*, 2001); purple circles, Ahlmannryggen ferropicrites (Riley *et al.*, 2005); purple diamonds, Vestfjella ferropicrite (Heinonen *et al.*, 2010). Vectors indicate the effect of fractionation of individual phases on the liquid composition. The liquid line of descent was not modelled because the small number of samples here do not form clear trends and the sample groups are not genetically related.

The DML ferropicrites from Ahlmannryggen are depleted in highly incompatible trace elements relative to more moderately incompatible trace elements (e.g. $[Th/La]_N < 1$) and also have fractionated HREE relative to MREE $[Gd/Lu]_N > 1]$. This gives a concave-down trace element pattern, which could be created by melting of a more depleted mantle source deep within the garnet stability field

(Fig. 2.6). The Vestfjella sample is more enriched and resembles the Etendeka ferropicrites in terms of incompatible trace elements, with even higher $[MREE/HREE]_N$. This difference in trace element enrichment might reflect a more subtle difference in the mantle origin of ferropicrites at the two DML locations, for example, a previous depletion event or higher extent of melting at Ahlmannryggen.

The three Ahlmannryggen samples have near-identical εNd of 7.0–7.2 (Riley *et al.*, 2005), whereas εNd = 3.5 in the somewhat more enriched Vestfjella sample (Heinonen *et al.*, 2010); both indicate an affinity with the sublithospheric mantle. Modelling of the whole-rock Nd, Sr, Pb and Os isotopic compositions of the Ahlmannryggen ferropicrites indicates that the magma originated in a mixture of recycled crust ($\sim$ 0.7-0.8 Ga) and depleted MORB-source mantle, and assimilated less than 1% Archaean crust (Heinonen *et al.*, 2014). Two other Group 3 Ahlmannryggen samples (picrites, not ferropicrites) have olivine $\delta^{18}O$ = 5.67 and 5.90, which is slightly higher than mantle olivine and the Etendeka mean (Harris *et al.*, 2015).

2.2.2 Petrography and mineral chemistry

The mineral chemistry of the Etendeka samples is published in Gibson *et al.* (2000) and Thompson *et al.* (2001), and for DML samples by Heinonen *et al.* (2014); it is supplemented with new EPMA mineral chemistry data in this thesis. Details of the analytical method and the new analyses are provided in Appendix A and Appendix C, respectively.

Etendeka picrites

The Etendeka picrites are medium to fine grained porphyritic rocks, often with a subophitic groundmass. This indicates a two stage cooling history of initial phenocryst crystallisation in deeper magma reservoirs followed by shallow emplacement and groundmass crystallisation at moderate cooling rates. Olivine phenocrysts (0.5–4 mm) have cores in the compositional range Fo_{86-93} (Fo = molar $Mg/(Mg+Fe^{2+})$, expressed as %). They usually have a narrow, lower Fo rim and are occasionally accompanied by plagioclase phenocrysts. The olivine phenocrysts frequently contain small Cr-spinel inclusions (their chemistry is discussed in Chapter 5), although spinel is rarely identified in the groundmass. Olivine Fo is not always in equilibrium with the whole-rock Mg-Fe composition, i.e. it falls outside of an appropriate $K_{D_{Fe-Mg}}^{ol-liq}$ range of 0.31–0.35 (Fig. 2.10a), so in some cases the whole-rock composition does not properly represent the parental liquid composition. As the olivine phenocryst compositional range is quite similar across all samples, the large range in whole-rock MgO must be partly accounted for by varying modal olivine. The pressure of phenocryst formation in the Horingbaai picrites is not tightly constrained, although the co-crystallisation of plagioclase and olivine implies relatively shallow evolution (Thompson *et al.*, 2001).

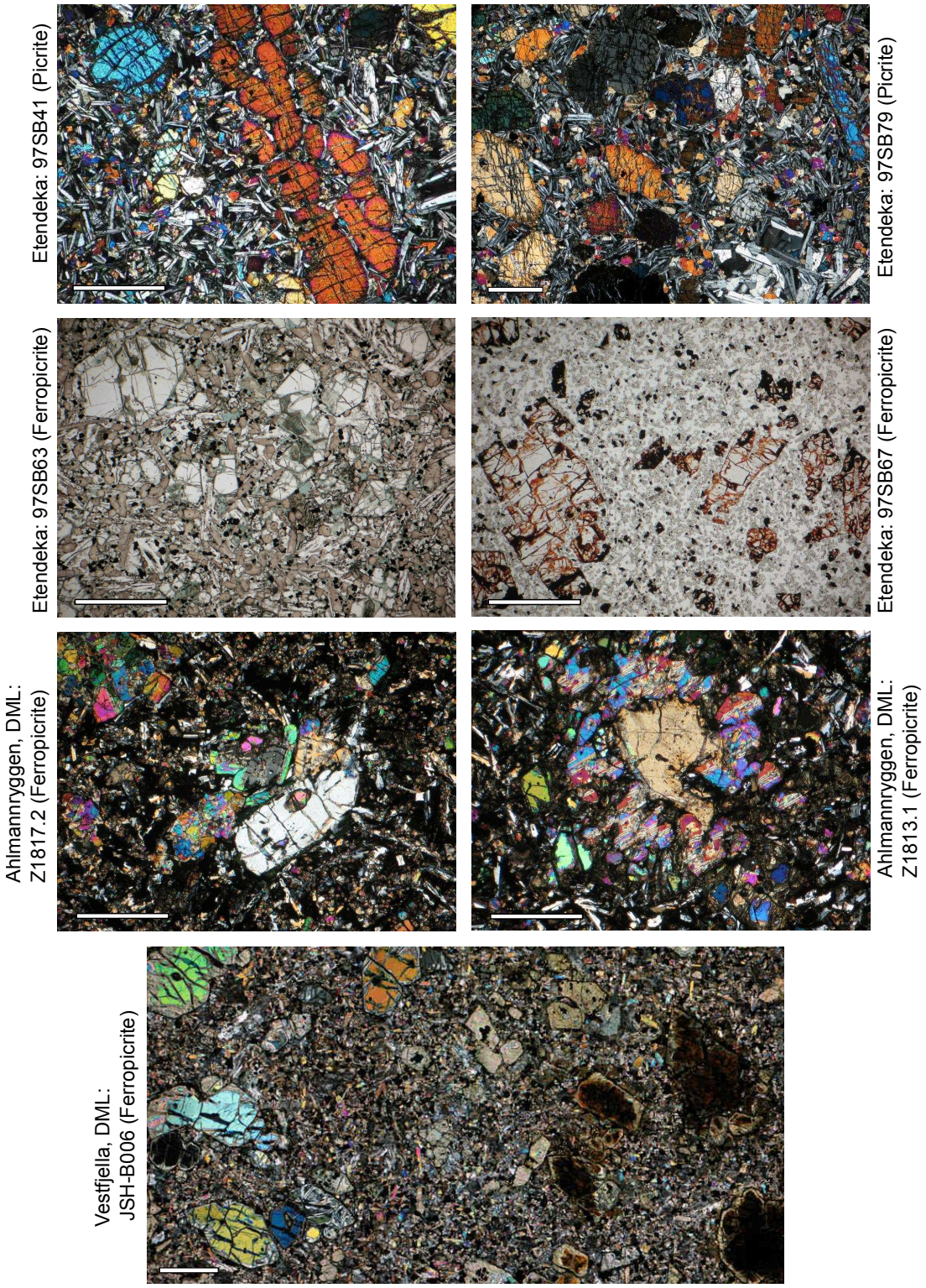

Figure 2.9: Photomicrographs of various samples, scale bars are 1 mm. Clockwise from top left: two picrite samples with a range of olivine phenocryst morphologies; olivine phenocrysts with haematite coatings in an Etendeka ferropicrite sample; a cpx rim around resorbing opx, DML (Antarctica) ferropicrite; olivine phenocrysts in DML ferropicrite showing progressive alteration; fresh opx phenocryst next to fresh olivine and cpx-filled pseudomorph; most primitive Etendeka ferropicrite with purple titanaugite, plagioclase and some secondary chlorite in the groundmass.

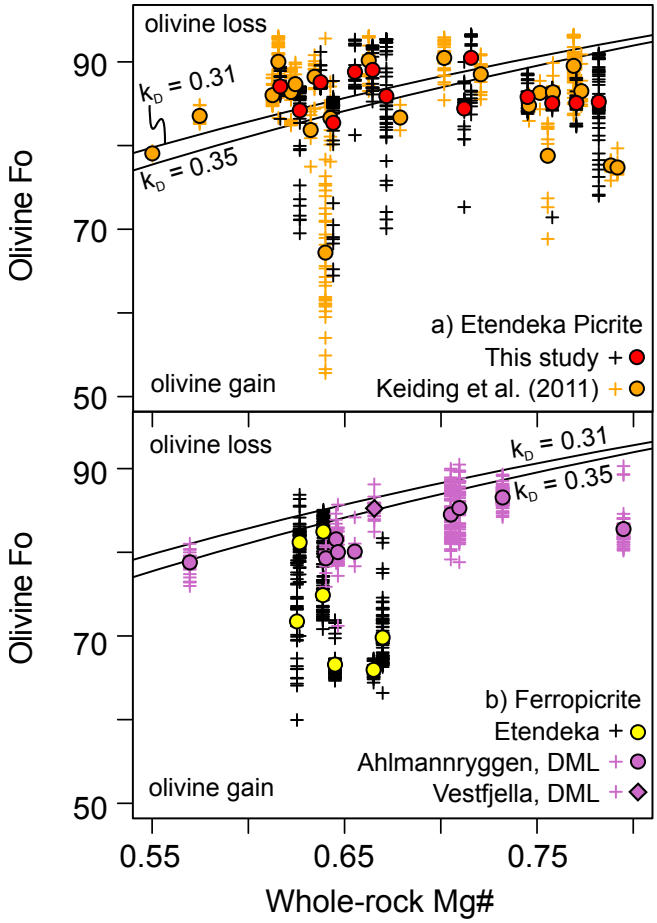

Figure 2.10: Forsterite content of olivine phenocrysts as a function of whole-rock Mg#. + show individual olivine analyses, filled circles are sample averages. Data sources: new data (this study), Gibson *et al.* (2000); Heinonen and Luttinen (2010); Heinonen *et al.* (2013); Keiding *et al.* (2011); Thompson *et al.* (2001). The two curves show equilibrium forsterite for a given Mg# calculated at a suggested reasonable k_D range of 0.31-0.35 (this parameter is sensitive to pressure, temperature and composition *PTX*; see Chapter 4). Mg# = molar Mg/(Mg + Fe^{2+}), where is is assumed that Fe^{2+}/Fe_T = 0.9 in whole-rock analyses. Points above the curve indicate that the whole-rock Mg# has been reduced through olivine loss (fractionation) and points beneath the curve show that samples have accumulated excess olivine, raising whole-rock Mg#. The whole-rock analysis approximately represents the liquid composition if points lie on or near the equilibrium curve.

The highest Fo olivines contain $\sim$ 3000-4000 ppm Ni, which decreases with decreasing Fo (Fig. 2.11) as is expected from crystal fractionation. The high Ni contents, in conjunction with high Fo, indicate a mantle origin for the melts. The CaO content of the highest Fo olivine is also high (> 0.2 wt. %), confirming that their origin is magmatic and that they are not mantle xenocrysts (Thompson and Gibson, 2000); this is in agreement with the lack of observed sub-grain domains within the olivine, which would be indicative of strain.

Bimodal olivine population

Thompson and Gibson (2000) observed that some Horingbaai picrite samples have both texturally

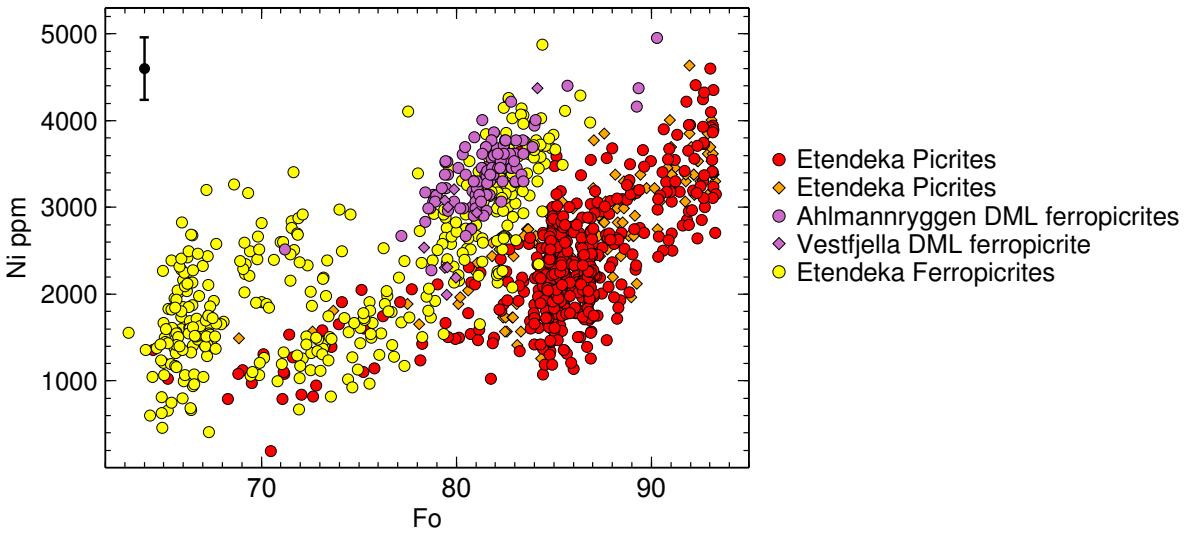

Figure 2.11: Ni content of olivine phenocrysts in Etendeka Horingbaai-type picrites (red filled circles, new data and Thompson *et al.* (2001); orange filled diamonds, Keiding *et al.*, 2011), Etendeka ferropicrites (yellow filled circles, new data and Gibson *et al.*, 2000) and DML ferropicrites (purple filled circles, Ahlmannryggen samples, new data and Heinonen *et al.*, 2013; purple filled diamonds, Vestfjella samples, new data). Error bar shows $\pm 1\sigma$ based on repeat analyses.

and compositionally bimodal olivine macrocryst populations, where the main phenocrysts population is at Fo $_{<89}$ and a second group is $Fo_{91-93.3}$. They suggest that the compositionally grouped olivine phenocrysts also have distinctive morphologies, where the higher Fo population are larger, subhedral and can have morphologies indicative of rapid crystallisation (tubular, elongate, hopper), whereas the lower Fo olivines are smaller and more prismatic. The hypothesis of Thompson and Gibson (2000) states that the highest Fo olivine macrocrysts are antecrysts (terminology as reviewed by Thomson and Maclennan, 2013) from a more Mg-rich, komatiitic primary melt, which pooled at the Moho due to its high density. Lower Fo olivine, with euhedral forms, crystallised directly from the picritic melt, making them phenocrysts. This would have implications for interpretations of the present study: for example, melt and spinel in the high Fo olivines would have to be interpreted separately to the whole-rock data and the phenocryst population.

A histogram and kernal density estimate (KDE) of olivine core Fo from Horingbaai-type picrites and basalts is shown in Fig. 2.12, consisting of around twice as much data as was available to Thompson and Gibson (2000). This plot does not show the bimodal distribution of Thompson and Gibson (2000), which should result in a dip at around Fo_{90}. Instead, the frequency of olivine measurements are skewed to high Fo and plateau from Fo_{88-93}. There are instead two resolvable peaks at Fo_{85} and Fo_{87}. This distribution across all samples is difficult to interpret. It may to some extent reflect sampling bias because a small number of samples (most data is from ten samples) are measured a large number of times. The high count frequency at $Fo_{93.0-93.5}$ may be the result of sampling bias, where the highest Fo olivines, which are observable in back-scattered electron (BSE) images, are sought

out during EPMA point selection. The abrupt upper limit of compositions at $Fo_{93.3}$ sets a maximum Fo in equilibrium with the primary melt and means that higher Fo olivine never crystallised. Olivine rims tend to be narrow and have the composition range Fo_{65-82}, and are excluded from Fig. 2.12. Whether or not the reported bimodality about Fo_{90} exists within individual samples can be assessed from Fig. 2.13. Most samples have a unimodal Fo distribution with a peak at Fo_{85-87} and few $Fo_{>90}$ olivines. Sample 97SB33 contains almost exclusively $Fo_{>92}$ olivines. Samples 97SB35, 46, 62 and 79 do appear to be bimodal, with varying proportions of $Fo_{>90}$ and $Fo_{<90}$ groups.

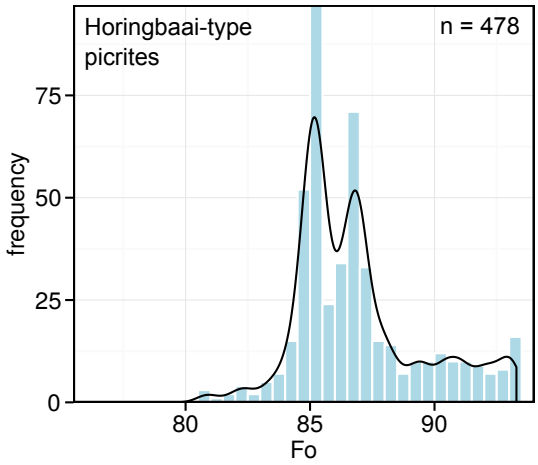

Figure 2.12: Histogram (0.5 Fo bins) and kernal density estimate (KDE) of Fo from 478 analyses of olivine cores from Horingbaai-type picrites and basalts (data from this work, including olivines picked for melt inclusion analysis, and from Thompson *et al.*, 2001). KDE normalised to frequency.

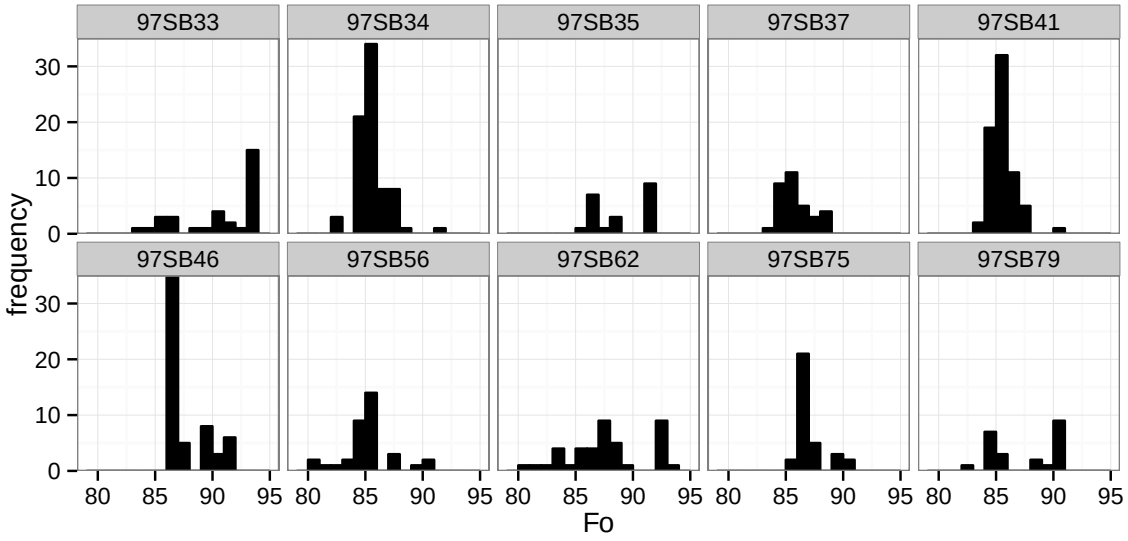

Figure 2.13: Histograms of measured Fo for olivine cores of individual Etendeka picrite samples, shown for samples with at least 20 analyses (1 Fo bins). Data as for Fig. 2.12.

The morphologies of the olivine macrocrysts must also be considered. Photomicrographs of two samples which contain both highly elongate and more equant grains, 97SB41 and 97SB79, are shown in Fig. 2.9. The relationship between grain size, shape and composition of olivines in the Etendeka Horingbaai-type picrites is further examined by QEMSCAN® analysis (FEI, University of Cambridge, with the assistance of Dr. Iris Buisman), which provides semi-quantitative chemical analysis and mineral identification on a pixel by pixel basis (Fig. 2.14). For each sample, the complete QEMSCAN is shown along with just the olivines, which are identified as individual particles by the software and placed on a grid in approximately size order. Three picrite samples are chosen: 97SB33, which contains the highest Fo olivines of any sample; 97SB35, which contains apparently bimodal Fo olivine in a variety of sizes and morphologies; and 97SB79, which contains olivine macrocrysts with a range of morphologies, from elongate euhedral crystals to equant subhedral grains, both of which have occasional hopper overgrowths. Fig. 2.14 shows that, in all samples, there is not an obvious relationship between crystal size, shape and chemistry. Some elongate and delicate crystals are high Fo, making it unlikely that they were entrained and moved (i.e. they are probably not entrained antecrysts from an unsampled komatiite). Sample 97SB35 has only euhedral morphologies but with a wide range in grain sizes and aspect ratios. This sample highlights the difficulty in distinguishing between phenocrysts and groundmass olivine, as the size contrast is small and the size distribution continuous, as is the case with many picrite samples. Some very small highly elongate grains have compositions of $Fo_{>90}$ (e.g. the very thin, horizontally-orientated crystal in the centre of the QEMSCAN® of 97SB35). In conjunction with the low modal proportion of olivine, these show that the parental melt of this sample was high MgO, as opposed to the whole-rock analysis being high MgO because of accumulated olivine. Small, high aspect ratio crystals must have crystallised in-situ in the final dyke emplacement, as they would not have survived extensive transport processes.

For each olivine grain, the area and maximum forsterite were determined from the QEMSCAN® images (Fo has poor precision and accuracy compared with EPMA data), and aspect ratios were estimated by fitting ellipses to grains in the ImageJ software. This does not always distinguish between olivines in polycrystalline clusters or identify optically continuous crystals which are visually discontinuous. Fig. 2.15a shows aspect ratio as a function of crystal area for the three samples. In each sample, both the crystal sizes and aspect ratios have skewed normal distributions. Points do not form two distinct clusters, which does not suggest a bimodal morphology distribution. When the maximum olivine Fo is plotted against grain size (Fig. 2.15b), the same conclusion is drawn: samples 97SB33 and 97SB79 have unimodal maximum Fo distributions, although 97SB35 does appear slightly bimodal, or at least has a broader spread of data. However, no distinct two clusters of points in any samples argues against having two groups of olivine grains with different parental melts and cooling histories.

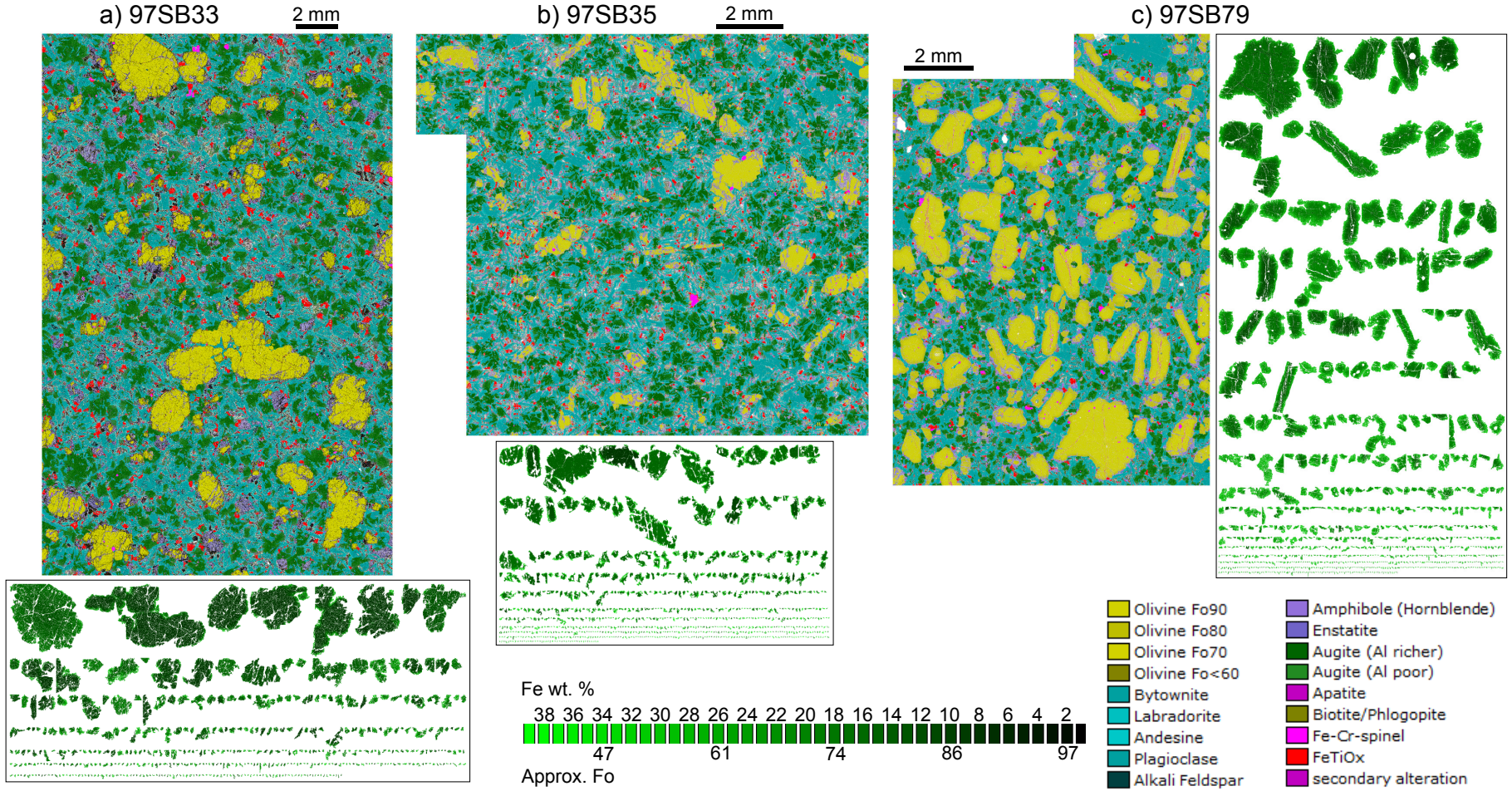

Figure 2.14: QEMSCAN® images of three Horingbaai-type picrite samples: a) 97SB33, b) 97SB35, c) 97SB79, with each pixel identified as a particular phase (colour code legend is shown). In the second image for each sample, individual olivines are identified as particles and lined up approximately in size order, with colour scaled from bright green to black with decreasing wt.% Fe (black is 0 Fe, i.e. Fo_{100}); an approximate conversion to Fo is shown. In these plots, olivine grains with an area of < 50 μm^2 are excluded.

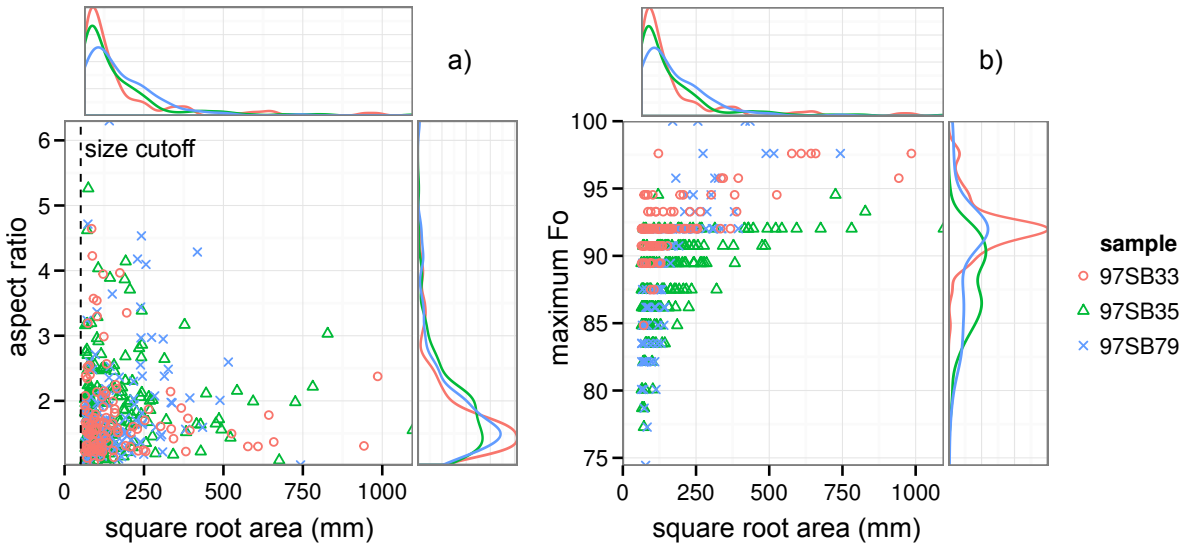

Figure 2.15: a) Olivine aspect ratio and b) maximum Fo content as a function of the square root of grain area for three Etendeka picrites. A KDE is shown for each axis, colour coded to sample. The individual olivines grains are shown in Fig. 2.14, and aspect ratios are calculated by fitting ellipses to grains. Maximum Fo is binned in 1 wt.% Fe steps. QEMSCAN compositional data is obtained by short count time EDS and has lower precision and accuracy than EPMA data. Only olivine grains > 50 µm^2 were considered.

Thompson and Gibson (2000) hypothesise that the two olivine populations exist in the Etendeka picrites, where the $Fo_{>90}$ olivines are antecrysts inherited from an unsampled parental komatiite. They argue on this basis for a very high mantle T_P of 1680 °C or more. The new evidence presented in this chapter does not support their conclusion, because olivine Fo and morphology distribution does not show two distinct populations. However, it is also not straightforward to explain by closed-system crystallisation and cooling. A variety of morphologies, grain sizes and compositions must reflect some combination of different samples experiencing diverse thermal histories and degrees of fractionation. Varying degrees of undercooling cause a range of morphologies to develop and crystal mush disaggregation events can return olivines with higher Fo than equilibrium to a melt (e.g. Thomson and Maclennan, 2013). The smallest most elongate olivine crystals seen in Fig. 2.14b probably crystallised in-situ after final emplacement of the magma in a dyke. This simpler model, which does not require a second hidden melt, is supported by a continuum in olivine-hosted melt inclusion compositions with host olivine Fo (Chapter 3), although thermometry data does not clearly distinguish between either hypothesis (Chapter 5).

Etendeka ferropicrites

The ferropicrites are highly olivine-phyric (Fo_{74-85}) and sometimes also contain augite phenocrysts showing sector zoning, along with a high proportion of oxide phases. Olivine phenocrysts (0.5–2

mm) contain small Cr-spinel inclusions ($\sim$ 10 μm), although less frequently than in the picrite samples; none is identified outside of olivine. Olivine phenocrysts are euhedral, without the high aspect ratios observed in some picritic olivines, and sometimes have a surface veneer of haematite caused by oxidation during or after emplacement. Typical ferropicrite sample 97SB63 and the haematite-coated olivine of atypical sample 97SB67 are shown in Fig. 2.9. Samples show limited to extensive secondary alteration in the groundmass and in the serpentinisation of olivine phenocrysts. As with the picrites, the Etendeka ferropicrites show $K_{D_{Fe-Mg}}^{ol-liq}$ disequilibrium between whole-rock chemistry and olivine phenocrysts, where all samples show evidence of olivine accumulation (Fig. 2.10b). Although olivines of the ferropicrite samples are lower Fo than those of the picrite samples, they have similar Ni concentrations (up to 4000 ppm Ni; Fig. 2.11), suggesting that the ferropicrites are not necessarily more evolved than the picrite samples. Rather, the lower Fo content of the phenocrysts simply reflects a higher Fe/Mg of the parental melt.

A ferropicrite subset typified by sample 97SB67 (also 97SB68 and 96SB48) have more fayalitic, evolved phenocrysts (Fo_{64-72}) yet similar whole-rock compositions, leading Heinonen and Luttinen (2008) to describe them as having a ferropicritic composition only because of accumulated olivine. Whilst this appears true to some extent (Fig. 2.10 shows this group to be far from $K_{D_{Fe-Mg}}^{ol-WR}$ equilibrium), the Fo-Ni systematics of these low Fo olivines indicate higher Ni than would be expected from fractionation alone (Fig. 2.11) and appears to define a higher Ni trend. This enigmatic sample subset also has melt inclusions with unexpected major element compositions, which are discussed further in Chapter 3.

Compositional zonation of augite is observed in some ferropicrites, as shown in sample 97SB73 in Fig. 2.16. In this particular back scattered electron (BSE) image, 3 principle zones are observed, along with a clear irregular resorption surface. Major element chemistry was analysed orthogonal to the zones, and one SIMS point was analysed in each of the three major zones. The major elements indicate that this clinopyroxene experienced disequilibrium events, caused by either magma recharge or crystal mush disaggregation. The innermost zone (1) has low Cr_2O_3 due to previous Cr-spinel fractionation, and decreasing Mg# ($= Mg/Mg + Fe^{2+}$) towards the rim. The next, brighter zone is more REE-rich. The start of the 3rd major zone in the BSE image is marked by a jump to a more primitive major element composition (Fig. 2.16), with higher Mg#, higher Cr_2O_3 and lower REE concentrations. This could indicate a magma recharge event, which would be responsible for the resorption surface inferred from the BSE image, and is followed by several similar major element jumps to more primitive compositions towards the crystal rim. The 500 μm clinopyroxene macrocryst here is a glomerocryst of evolved crystals in the core bound by a shared more primitive overgrowth, which could indicate that the crystals were in contact in a mush zone before being partially disaggregated by a more primitive melt.

The reconstructed REE content of the melt from the different cpx zones have the same slope and are parallel to the whole-rock composition (Fig. 2.16b). The recharge magma must therefore have been derived from the same initial mantle melt, and reflects varying levels of fractionation, which concentrates REEs, deeper in the system. Such complex zoning is not observed in olivine.

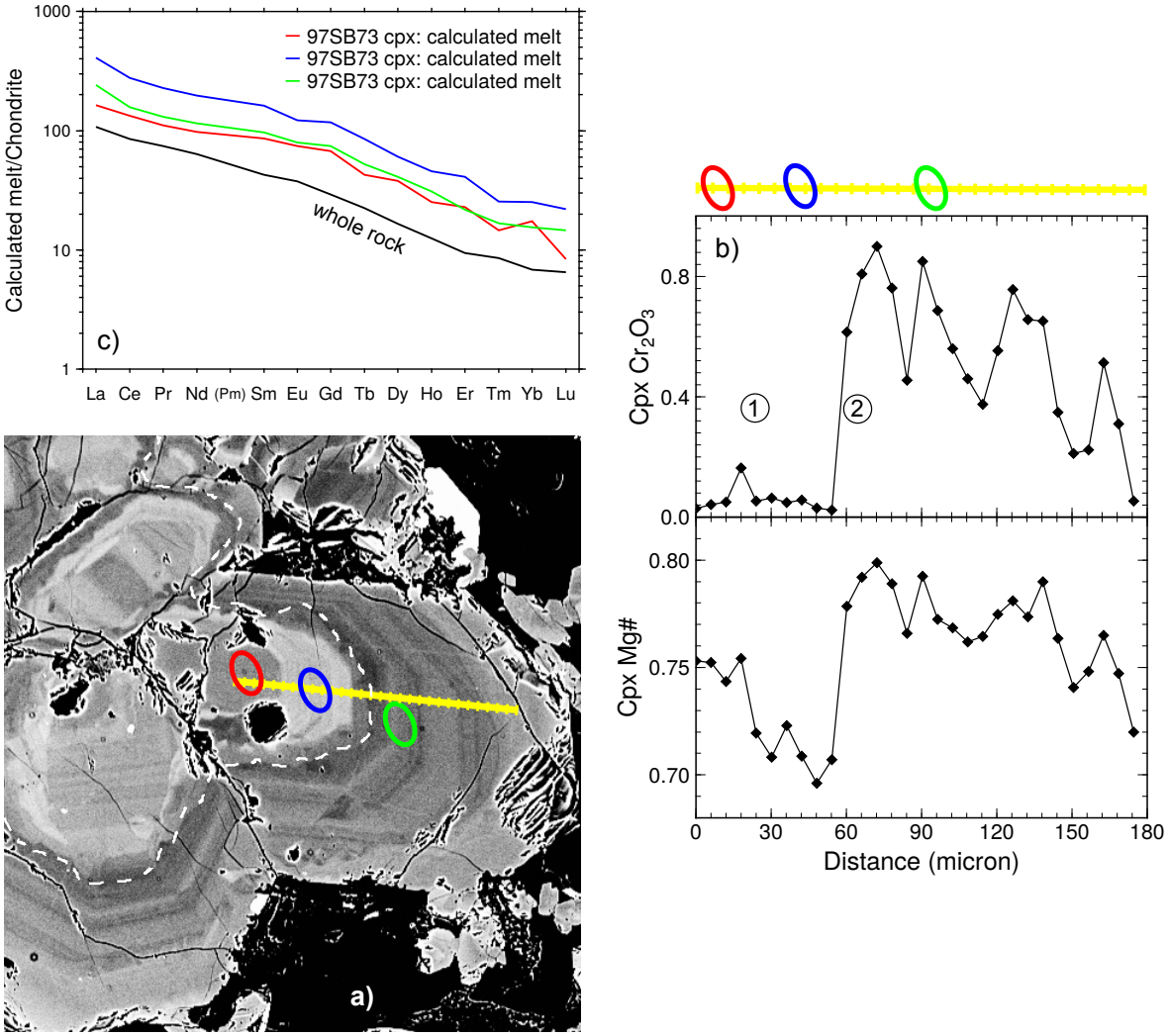

Figure 2.16: Zoned cpx glomerocryst from Etendeka ferropicrite sample 97SB73. a) high-contrast BSE image showing locations of analyses. White dashed line shows a resorption surface. b) EPMA major element profile taken at 6 micron intervals along the yellow line. The innermost area (1) is suggested to indicate initial crystallisation following chrome spinel fractionation; (2) may show magma recharge and/or crystal mush disaggregation event. c) REE profiles are equilibrium liquid compositions reconstructed from the three SIMS spot analyses (red, green and blue lines correspond to the three circles in a) using the partition coefficients of McKenzie and O'Nions (1991), normalised to chondrite (McDonough and Sun, 1995).

Based on the presence of high pressure titanaugite in some samples, Gibson *et al.* (2000) interpreted the ferropicrites to have crystallised their olivine phenocrysts at high pressures in the crust. The lack of adequate barometric methods for basalt crystallisation makes it difficult to improve upon

this assessment, but it should be noted that the high density of ferropicritic melts would predispose them to reach neutral buoyancy and pool at high crustal pressures.

Dronning Maud Land ferropicrites

The four DML ferropicrites are somewhat similar to the Etendeka ones in that they contain abundant olivine phenocrysts (0.5–1.5 mm, Fo_{77-86}) and are variably affected by secondary alteration. One sample, Z1816.3, also has extremely rare higher Fo_{89-90} olivines. Similarly to the Etendeka ferropicrites, the DML ferropicrites have $K_{D_{Fe-Mg}^{ol-WR}}$ that are too high, indicating some olivine accumulation (Fig. 2.10b). The olivine phenocryst cores have high Ni ($< \sim 4000$ ppm) with Fo-Ni systematics similar to that of the Etendeka ferropicrites (Fig. 2.11).

The three DML Ahlmannryggen samples studied here also contain orthopyroxene macrocrysts (1–2 mm), sometimes alone but more commonly mantled by clinopyroxene. Clinopyroxene is also found as macrocrystic polycrystalline clusters of 1–3 mm. The presence of orthopyroxene phenocrysts, along with olivine, has been modelled by Heinonen *et al.* (2013) with MELTS (Ghiorso and Sack, 1995) to indicate a high crystallisation pressure of > 6 kbar, in a slightly hydrous melt (0.25–1 wt.% H_2O). The presence of clinopyroxene rims around orthopyroxene could be interpreted in terms of a change in melt H_2O content or pressure of crystallisation, reflecting some combination of polybaric crystallisation and melt recharge and/or crystal mush disaggregation events.

The single Vestfjella sample contains no opx, although it does contain tiny (< 0.05 mm) kaersutite crystals in the groundmass, indicating that the melt was water-bearing. This sample is particularly similar to Etendeka ferropicrites both in terms of petrography and mineral chemistry.

2.3 Primary melt compositions

To understand the mantle source characteristics and melting regime that produced the picrites and ferropicrites, it is necessary to define a primary melt composition, i.e. the composition of the batch or mixed incremental fractional melts that emerge from the melting column. Most erupted primitive melts are not thought to be primary, rather, they have fractionated olivine at some point between creation in the mantle and final emplacement. This can be corrected for by adding equilibrium olivine back into the liquid composition (inverse modelling), or by extrapolating from compositions that have only experienced olivine fractionation to higher MgO.

It is difficult to know exactly how much olivine was fractionated and how far to correct the inferred liquid composition. Commonly, melts are corrected to an arbitrary primitive MgO such that they are directly comparable to one another (e.g. at MgO = 8 wt. % for MORB, Klein and Langmuir, 1987; Langmuir *et al.*, 1992). One way in which a melt can be fractionation-corrected to a primary composition is by back-calculating major elements along a LLD such that the Mg# of the corrected

melt is in equilibrium with mantle olivine (e.g. Albarède, 1992). Peridotite melting is fairly well understood, and detailed parametrisations of experimental melting results allow forward modelling of mantle melt compositions as a function of PT. This forms the basis of an alternative method for calculating a primary melt composition: such parametrisations define an array of modelled mantle melt MgO and FeO, and the point at which this array intersects an inverse modelled olivine control line (or LLD) for a given primitive sample can be found (Herzberg and O'Hara, 2002). Recently updated parametrisations in the software PRIMELT3 (Herzberg and Asimow, 2015) allow modelling of accumulated fractional melts. This method has the advantage of solving a primitive melt composition for mantle potential temperature (T_p, the temperature of the mantle extrapolated along an adiabatic gradient to the surface, McKenzie and Bickle, 1988) and melt fraction (F), but relies on the intrinsic assumption of anhydrous peridotite melting, and that peridotite melting is well enough understood that large errors are not propagated. Primary melts can alternatively be calculated by correcting along an olivine control line until a liquid composition is in $K_{D_{Fe-Mg}}^{ol-liq}$ equilibrium with the highest Fo phenocryst present, which provides a minimum estimate of the primary melt MgO (e.g. Thompson and Gibson, 2000). All methods rely on $K_{D_{Fe-Mg}}^{ol-liq}$ being precisely known and having either negligible or well-characterised PTX dependency.

In this study, tentative primary melt compositions, suggested in Table 2.1, are calculated by different methods. The preferred values are given in bold. After correction for olivine accumulation or loss to bring whole-rock compositions into $K_{D_{Fe-Mg}}^{ol-liq}$ equilibrium, the highest MgO sample for each group, listed under method 0, must represent the minimum primary melt MgO. The highest MgO picrite sample is 97SB33 (16.45 wt. %, corrected by +0.09 X_{ol}, the weight fraction of mean olivine added to the composition) and the highest MgO Etendeka ferropicrite sample is 97SB63 (11.79 wt. %, -0.07 X_{ol}). DML ferropicrites are not corrected in this way as the most primitive samples contain olivine, cpx and opx macrocrysts, although sample Z1813.1 is already close to equilibrium with its olivine phenocryst population. The highest MgO sample (Z1816.3) is not used as it has accumulated a large fraction of macrocrysts. If these magmas had fractionated olivine prior to their emplacement, the primary melts would be higher in MgO (higher Fo olivines may no longer be present or have re-equilibrated to lower Fo). PRIMELT3 suggests a primary magma for the corrected picrite 97SB33 of 17.7wt. % MgO, corresponding to T_p = 1505 °C and a melt fraction of 0.26, where 97SB33 (corrected) represents a magma that has fractionated 3 wt.% olivine. Since PRIMELT3 is only calibrated for a peridotite source, it is not applied to the ferropicrites.

Method 2 in Table 2.1 shows the result of adding olivine to the starting composition until it is in equilibrium with the highest identified olivine Fo of the sample type. 16% olivine is added to the picrite, giving a high-MgO primary melt of 21.6 wt.% MgO; amounts added to the ferropicrites are more moderate (Etendeka ferropicrite X_{ol} + 10%, primary melt MgO = 15.1 wt.%; DML Ahlmannryggen ferropicrite X_{ol} + 0.01, primary melt MgO = 13.0 wt.%). For comparison, Gibson *et al.*

(2000) suggest 10-25% olivine fractionation for the Etendeka ferropicrites, assuming a melt derive from a peridotite source. This method is considered preferred and it is suggested that these results are the best estimate of ferropicrite primary melt MgO. Alternatively, method 3 is used to illustrate the effects of fixing both ferropicrite groups to 15 wt.% MgO to make them directly comparable, and to illustrate the effect of a higher MgO Vestfjella sample.

Type	Etendeka Picrite			Etendeka Ferropicrite			DML Vestfjella Ferropicrite		
Sample	97SB33 corrected (+0.09 Ol)			97SB63 corrected (-0.07 Ol)			Z1813.1 uncorrected		
Method	0	**1**	2	0	3	**2**	0	3	**2**
SiO_2	46.75	46.96	46.27	46.14	46.14	46.12	45.22	46.57	46.97
TiO_2	0.94	0.92	0.81	2.50	2.31	2.30	3.50	3.40	3.61
Al_2O_3	12.22	11.93	10.54	10.24	9.43	9.41	9.59	9.31	9.88
FeO_T	10.56	10.58	10.20	15.66	15.78	15.78	13.25	13.72	13.79
MnO	0.17	0.17	0.16	0.19	0.19	0.19	0.17	0.18	0.18
MgO	16.45	17.69	21.62	11.79	15.00	15.07	12.19	15.00	13.01
CaO	10.05	9.82	8.69	8.49	7.83	7.81	9.87	9.59	10.17
Na_2O	1.56	1.53	1.35	2.17	1.99	1.99	1.65	1.60	1.70
K_2O	0.21	0.21	0.18	0.95	0.87	0.87	0.32	0.31	0.33
P_2O_5	0.08	0.08	0.07	0.32	0.30	0.30	0.22	0.21	0.23
X_{ol}	-	0.03	0.16	-	0.10	0.10	-	0.07	0.01
Fo	90.5	91.6	93.3	82.5	86.0	86.0	-	87.6	86.0

Table 2.1: Various estimates of primary melt compositions; those highlighted in bold are the preferred estimates. FeO_T is total Fe expressed as FeO. All correction calculations performed assuming $Fe^{3+}/Fe_T = 0.1$. X_{ol} indicates the mass proportion of olivine added or removed from the whole-rock composition. Methods: 0) Starting composition used, which is the whole-rock composition of the most MgO-rich sample for that group (excluding Z1816.3 which is a cumulate), which may or may not be corrected for olivine accumulation or loss by adding or removing the average olivine phenocryst composition until the recalculated whole-rock composition is in equilibrium with it (at $K_D = 0.32$). 1) The primary melt composition predicted by PRIMELT3 (Herzberg and Asimow, 2015). 2) Composition obtained by adding equilibrium olivine until the composition is in equilibrium with the highest Fo olivine found in thin section. 3) Melt composition of the most MgO-rich sample corrected to 15 wt.% MgO by adding equilibrium olivine. Equilibrium olivine addition is performed in PRIMELT3.

These primary melts show essentially the same compositional features as the whole-rock samples discussed previously. The picrites are high in MgO and are consistent with melt compositions found experimentally from high-fraction peridotite melting at moderate pressure (e.g. Walter, 1998). Ferropicrite primary melts are lower in MgO, which is consistent with pyroxenite melting (Chapter 4). Ferropicrite primary melts are higher in FeO and TiO_2 and lower in Al_2O_3 than picrites, with similar concentrations of SiO_2. This indicates that, similarly to peridotite, their mantle source must be silica-undersaturated, as suggested by Tuff *et al.* (2005). The primary Etendeka ferropicrite is richer in FeO than the primary DML Ahlmannryggen ferropicrite and appears to be a more distinct composition from picrite, although the Ahlmannryggen primary melt has the highest TiO_2. The single Vestfjella ferropicrite sample (not shown) is similar to the Etendeka ferropicrite primary melt, but with higher MgO and FeO, and in many respects is the ferropicrite composition which is furthest removed from

picrite. The ferropicrite primary compositions are inconsistent with peridotite partial melting and are compared with forward models of silica-undersaturated pyroxenite melting in Chapter 4.

2.4 Previous work: Petrogenesis

2.4.1 The origin of the Etendeka picrites

The high MgO content of the whole-rocks in combination with the high forsterite content of olivine phenocrysts and MORB-like isotopic characteristics has led previous workers to interpret the Horingbaai-type picrites to represent near-primary melts deriving from a hot, sublithospheric mantle source (Keiding *et al.*, 2011; Thompson and Gibson, 2000; Thompson *et al.*, 2001). Even studies which invoke a SCLM source for the Etendeka CFB suggest that the Horingbaai picrites are from the convecting mantle, where adiabatic decompression melting within the plume was increased by rifting of Gondwana (Peate, 1997).

Thompson *et al.* (2001) calculated the primary melt composition by assuming that MgO = 15 wt.% and recalculating whole-rock analyses accordingly, and applied the major element modelling method of Langmuir *et al.* (1992). They found that the picrite major element compositions can be mimicked by 12% dry decompression melting of KLB-1 peridotite from 4 GPa to 3 GPa, corresponding to $T_p \sim 1560$ °C. The high Fo population of olivine macrocrysts is suggested by extrapolation to be entrained from a parental melt from a hotter source mantle (Thompson and Gibson, 2000), although this interpretation is contested (Keiding *et al.*, 2011). REE inversion modelling by Thompson *et al.* (2001) approximately matches the major element model, requiring a melt fraction of 22% and melting from 3.5 to 1.8 GPa with T_p = 1470-1500 °C. This technique exploits the 'garnet signature' observed in the HREE as a proxy for pressure. Both approaches require a convecting mantle source with a significantly elevated temperature over the ambient MORB-source mantle.

Lithospheric thickness estimates from these studies help to constrain the relative timing of plume arrival, melt production and rifting. The lithosphere at the Horingbaai coast, a mobile belt between two cratons, is around 160 km thick today (Fernàndez *et al.*, 2010), which has cooled and recovered from the peak of rifting. According to REE inversions, the Etendeka picrites record an upper melting limit (a rheological boundary layer) at around 55-95 km (Thompson *et al.*, 2001). This is shallower than the depth required for the earlier ferropicrite production in the Etendeka province (Gibson *et al.*, 2000), indicating that significant rifting was concurrent with the formation of the CFB province.

2.4.2 The origin of the Etendeka and DML ferropicrites

Previous work on the origin of ferropicrites in general is discussed in Chapter 1, section 1.3. A large proportion of published literature on Phanerozoic ferropicrites is based on the samples described in

this chapter. In summary, it is thought that the Etendeka ferropicrites represent early high pressure melting as the proto-Tristan mantle plume approached the base of the lithosphere (Gibson *et al.*, 2000), preferentially sampling fusible mantle lithologies such as pyroxenite (Gibson, 2002). This is likewise the case for the DML ferropicrites, although the presence of a mantle plume as opposed to other mechanisms for heating and upwelling the mantle in the Karoo CFB province is debated (e.g. Coltice *et al.*, 2007; Heinonen and Kurz, 2015; Rolf *et al.*, 2012). Partial melting of pyroxenite at high pressures produces an Fe-rich melt, with $[MREE/HREE]_N$ ratios increased by the high modal abundance of garnet. A more trace element and isotopically enriched melt results from the higher concentrations of incompatible trace elements in the recycled crust. This interpretation is also in accordance with the high Ni in ferropicrite olivine (Fig. 2.11). High Ni olivine was suggested by Sobolev *et al.* (2007, 2005) to be an indicator of a pyroxenite source, although elevated Ni in olivine can alternatively be explained by the temperature sensitivity of D_{Ni}^{ol-liq} and the temperature contrast between the mantle solidus and melt liquidus (Matzen *et al.*, 2013; Putirka *et al.*, 2011).

2.5 Summary

Sample groups, petrology and previous interpretations described in this chapter are summarised in Table 2.2, along with a representative sample from each group which is primitive, relatively uncontaminated and not too affected by olivine accumulation. The subalkaline Etendeka picrite samples are porphyritic, containing high Ni, high Fo olivine and occasionally feldspar phenocrysts, in a fine- to medium-grained groundmass. They are found as sills and dykes that cross-cut flood basalts in southern Etendeka and are thought to be $\sim$ 132 Ma. Their whole-rock and olivine phenocryst compositions have been used to argue for a high temperature sublithospheric mantle peridotite source, which melted extensively at moderate pressure in the core of the Tristan proto-plume starting head as it upwelled beneath extensively rifted continental lithosphere during the opening of the South Atlantic. This phase of melting would also have produced the flood basalts. As such, the picrites represent the parental melts to the voluminous CFBs. They also provide an example of peridotite partial melts with which to compare ferropicrite compositions.

This contrasts with the ferropicrites, which in the Etendeka province are an early expression of CFB magmatism that pre-dates much of the rifting. Outcrops of ferropicrites in the Etendeka occur as thin dykes and occasional flows, and in DML as dykes that cross-cut Karoo CFBs. The Etendeka and DML ferropicrites (along with other Phanerozoic ferropicrites) are high in FeO and MgO and low in CaO and Al_2O_3 relative to picrites, with high $[MREE/HREE]_N$ and enriched highly incompatible trace elements and radiogenic isotopic ratios relative to picrites. Olivine phenocrysts in the ferropicrites are as high in Ni as those from the picrites, and the forsterite contents are lower (because the primary melt Fe/Mg is higher). These characteristics, as well as their early emplacement in

several CFB provinces (when the lithosphere was thicker), has led to the interpretation that ferropicritic compositions form as a result of high pressure, low fraction melting of silica-undersaturated mantle pyroxenite, which also explains the observation that ferropicrite has only been found in CFB provinces. Pyroxenite could be entrained in a rising plume, and begin to melt on the leading edge prior to the peridotite solidus being reached (Gibson, 2002; Heinonen *et al.*, 2013; Tuff *et al.*, 2005). This theory is, however, controversial, not conclusively proved, and is complicated by the existence of Archaean ferropicrites elsewhere (e.g. Fiorentini *et al.*, 2008; Goldstein and Francis, 2008; Hanski and Smolkin, 1995; Jakobsen *et al.*, 2005; see Chapter 1, section 1.3).

A goal of this thesis is to revisit previous interpretations and to test the working petrogenetic model for picrite and ferropicrite genesis with new data and the application of new modelling techniques, thus demonstrating that whole-mantle convection is able to return evidence of ancient deeply-subducted crust to the Earth's surface. Previous work has convincingly demonstrated mantle peridotite to be a reasonable source for the Etendeka picrites, so they serve as a useful comparative scenario with which to understand the unusual aspects of ferropicrite chemistry.

CFB province	Paraná-Etendeka		Karoo	
Location	Southern Etendeka		Ahlmannryggen, DML	Vestfjella, DML
Type	Picrite	Ferropicrite	Ferropicrite	Ferropicrite
Age (Ma)	$\sim$ 132 (Renne *et al.*, 1996)	$\sim$ 133 (Jerram *et al.*, 1999)	187.3 $\pm$ 3.6 (sample Z1816.3)	$\sim$ 182.2-189.2
Reference	Thompson *et al.*, 2001	Gibson *et al.*, 2000; Thompson *et al.*, 2001	Heinonen *et al.* (2010, 2014, 2013); Luttinen *et al.* (2015); Riley *et al.* (2005)	
εNd	3.7-8.7	-2.9-+3.7	7.0-7.2	3.5
Petrography	Ol $\pm$ Plag phenocrysts, medium to fine grained groundmass	Ol $\pm$ Cpx phenocrysts, medium to fine grained groundmass	Ol + Opx $\pm$ Cpx phenocrysts, medium to fine grained groundmass	Ol $\pm$ Cpx phenocrysts, medium to fine grained groundmass
Olivine chemistry	Fo_{86-93}, 1000-4500 ppm Ni	Fo_{74-85}, 1000-4500 ppm Ni	Fo_{78-86}, 2500-4000 ppm Ni	Fo_{78-85}, 2000-4000 ppm Ni
Source lithology*	Peridotite	Pyroxenite	Pyroxenite	Pyroxenite
F*	0.12-0.22	$\sim$ 0.1	low	low
T_p* (°C)	$\sim$ 1470-1560 (Thompson *et al.*, 2001); $\sim$ 1700 for highest Fo olivine (Thompson and Gibson, 2000)	$\sim$ 1550	not determined, assumed high	not determined, assumed high
Lithospheric thickness (km)*	55-95	$\sim$ 115	high	high
Representative sample	97SB33	97SB63	Z1813.1	JSH-B006
SiO_2	47.27	45.66	45.22	44.86
TiO_2	1.02	2.32	3.50	3.01
Al_2O_3	13.28	9.50	9.59	8.19
FeO_T	10.67	15.71	13.25	16.19
MnO	0.17	0.19	0.17	0.21
MgO	13.56	14.04	12.19	15.54
CaO	10.90	7.90	9.87	9.02
Na_2O	1.70	2.01	1.65	1.75
K_2O	0.23	0.88	0.32	0.87
P_2O_5	0.09	0.30	0.22	0.36

Table 2.2: Summary of sample groups, petrology and previous interpretations. Representative sample is a primitive sample chosen from each set which shows low contamination, that represents an ideal example of that group.
*literature interpretations (Etendeka ferropicrite F, lithospheric thickness and T_p estimates based on peridotite assumption).

Chapter 3

Melt inclusion variability: Deep mixing of incremental mantle melts in CFB provinces

Collaborative work declaration

The data and interpretations presented in this chapter have been prepared for publication, and most of the text and figures presented below are taken directly from an early draft of the manuscript. The co-authors (Sally Gibson, John Maclennan and Jussi Heinonen) helped to formulate my ideas, were involved with editing the text of the manuscript and improving the clarity of arguments. Jussi Heinonen performed the EC-AFC modelling shown in Table 3.3. The data collection, figures, interpretation and most of the text are my own work.

3.1 Introduction

Fractional melting of adiabatically upwelling mantle is expected to produce incipient melts with highly variable incompatible trace element compositions. This contrasts strongly with the relatively homogeneous chemistry of suites of samples from individual lava flows or even from extensive volcanic provinces (Arndt *et al.*, 1993; Cox, 1980; Duncan *et al.*, 1997; Erlank *et al.*, 1984; Reidel and Tolan, 2013; Wooden *et al.*, 1993). Olivine-hosted melt inclusions from primitive rocks provide a link to deeper within the igneous plumbing system, and are often studied in order to understand the processes by which these melts recombine, homogenise and crystallise (e.g. Maclennan, 2008a). These inclusions are droplets of melt that become trapped in growing olivine crystals. Melt inclusions have the advantage over whole-rock samples of isolating and preserving initial melts in a relatively closed

system, providing a window through subsequent assimilation, hydrothermal alteration and crystal accumulation processes which may compromise the whole-rock data (Kent, 2008).

In oceanic settings, olivine-hosted melt inclusions from primitive magmas often display incompatible trace element variability. This was first noted in melt inclusions from mid-ocean ridges by Sobolev and Shimizu (1993), who attributed it to fractional melting in the mantle. Similar observations and interpretations have since been made in a variety of other settings (Gurenko and Chaussidon, 1995; Maclennan, 2008a; Maclennan *et al.*, 2003b; Norman *et al.*, 2002; Shimizu, 1998; Slater *et al.*, 2001; Sobolev, 1996; Sours-Page *et al.*, 2002). Variability that cannot be attributed to melting processes has also been identified in the isotopic composition of olivine-hosted melt inclusions and indicates that high amplitude, short length scale isotopic heterogeneity is present in the mantle source regions of individual basaltic volcanoes (Jackson and Hart, 2006; Maclennan, 2008b; Saal *et al.*, 1998; Sakyi *et al.*, 2012; Sobolev *et al.*, 2011). Consequently, incompatible trace element variability in melt inclusions is now commonly interpreted as a product of both melting process and compositional heterogeneity in the mantle (Norman *et al.*, 2002; Rudge *et al.*, 2013; Sobolev *et al.*, 2011, 2000). Evidence for initially heterogeneous melts is quickly destroyed by convective mixing in lower crustal sills where melts may pool, and Maclennan (2008a) demonstrated that this process is concurrent with crystallisation: high forsterite olivine crystallises early on and captures melt inclusions from heterogeneous melt, whereas lower forsterite olivines trap homogeneous inclusion populations from thoroughly mixed melts. Although well established in Iceland (Maclennan, 2008a; Maclennan *et al.*, 2003b; Neave *et al.*, 2013), the controls over the timing of this process in different tectonic settings are less well known.

This chapter presents a large number of olivine-hosted melt inclusion analyses from the primitive Paraná-Etendeka and Karoo rocks (described in Chapter 2). These rare, near-primary samples contain high-Fo phenocrysts. They are therefore better placed than the associated voluminous lower MgO CFB lavas to examine the way in which variable primary melts from fractional mantle melting recombine in lower crustal magma chambers. CFB lavas tend to have rather monotonous major element compositions and represent well mixed mantle melts which have undergone subsequent fractionation and crustal assimilation (e.g. Morrison *et al.*, 1985).

Only a few melt inclusion studies have been undertaken on samples from CFB provinces, including the North Atlantic Igneous Province, Yemen, Emeishan and the Siberian Traps (Kamenetsky *et al.*, 2012; Kent *et al.*, 2002; Peate *et al.*, 2012; Sobolev *et al.*, 2009; Starkey *et al.*, 2012; Yaxley *et al.*, 2004). This reflects the relative scarcity of suitable flood basalt samples that represent primitive melts. This Chapter investigates whether the same magmatic processes modify melt inclusion variability in continental settings as in the more commonly studied oceanic settings. New major and trace element data for olivine-hosted melt inclusions from the picrites and ferropicrites of the Paraná-Etendeka and Karoo CFB provinces are presented. These new melt inclusion analyses are compared with those

from other CFB provinces and the much larger global database of OIB and MORB in order to examine the role of the lithosphere and tectonic setting on melt inclusion chemical variability and the timing of mantle melt mixing.

3.2 Samples and methods

The samples used for melt inclusion analysis are a subset of those described in Chapter 2, including the four Dronning Maud Land (DML) ferropicrite samples and most of the Etendeka picrite and ferropicrite samples. Although chromian spinel is the true liquidus phase in the picrites and ferropicrites, olivine is the first volumetrically significant phase to crystallise. The most forsteritic olivines therefore trap melts whose compositions represent the closest approximation to the true initial liquid composition.

Olivine-hosted melt inclusions in the samples are partially to fully crystalline, which is consistent with the doleritic textures of their host rocks and reflects their moderately slow cooling history. The morphologies of crystals within the inclusions vary from sample to sample and equant, elongate and spinifex habits occur. The mineral assemblage reflects the rock groundmass assemblage, with varying proportion of olivine, including daughter olivine on inclusion rims, clinopyroxene, orthopyroxene, plagioclase and oxide phases. An irregular void from the original shrinkage bubble is often seen (Figs. 3.1b and c). Many melt inclusions also contain chromian spinels that were trapped with the melt and do not disappear on rehomogenisation (Fig. 3.1d). This association reflects the heterogeneous trapping of the melt and the liquidus phase (e.g. spinel on an olivine growth surface may cause a melt-trapping cavity to form). The hydrous phases amphibole (kaersutite) and biotite were found in a single Etendeka ferropicrite melt inclusion, and kaersutite is also found in the groundmass of the Vestfjella ferropicrite sample, indicating that the parental ferropicrite melt contained a small proportion of water. Hydrous phases are otherwise not seen in the whole-rock samples.

The sample rehomogenisation, preparation and analytical procedures are described fully in Appendix A, and are summarised here. Batches of olivine were placed in a gas-mixing furnace for 20 minutes in order to rehomogenise any melt inclusions present. The temperature was selected such that a visual loss of all daughter phases was achieved, which occurred at 1200–1280 °C. The inclusion compositions of similar Etendeka picrites examined by Keiding *et al.* (2011), which are included in this chapter, were heated to 1350 °C for 15 minutes. Samples were mounted, polished and analysed for major elements by EPMA and incompatible trace elements by SIMS. Major and trace element compositions of 154 rehomogenised olivine-hosted melt inclusions from picrites and ferropicrites were measured, and more melt inclusions were analysed for major elements alone.

Major and trace element concentrations of melt inclusions uncorrected for post-entrapment crystallisation (cf. Danyushevsky *et al.*, 2000) are given in Appendix C.

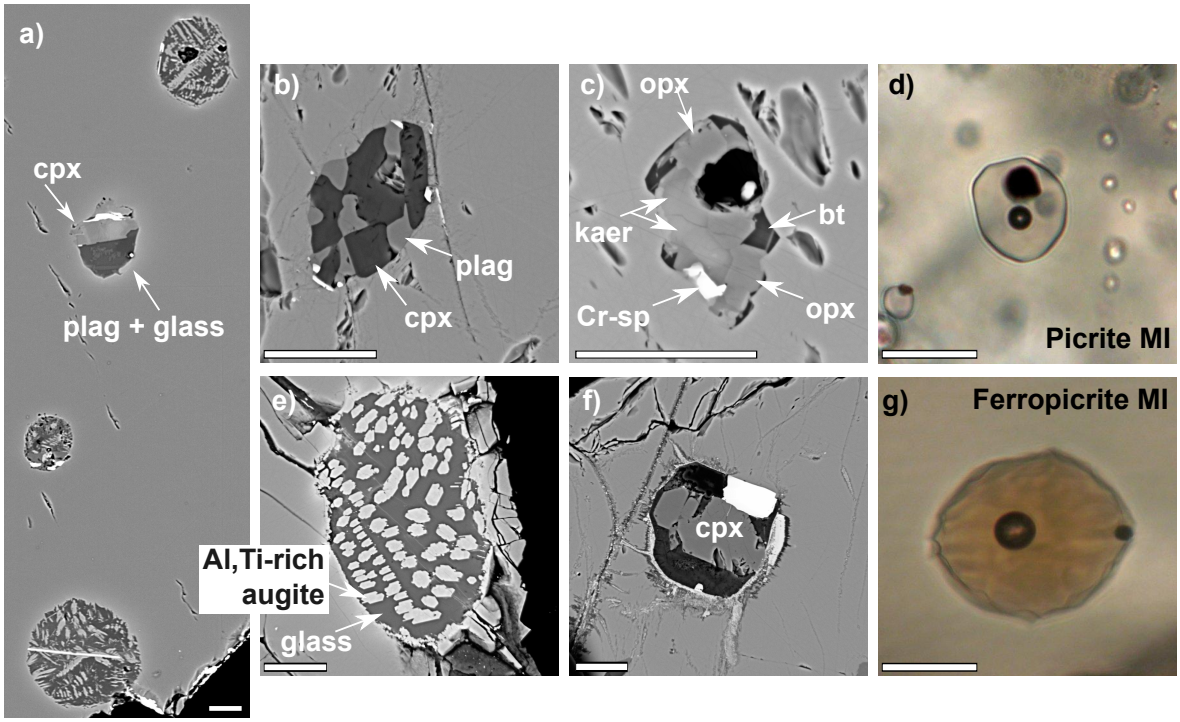

Figure 3.1: Images of melt inclusions. Scale bars all 20 µm. a) Four pristine inclusions from a single olivine grain of (DML ferropicrite sample Z1816-1): three are melt inclusions with skeletal crystals (the bright white needle in the bottom inclusion is magnetite), one is zoned clinopyroxene and melt that were heterogeneously trapped. b) Ferropicrite melt inclusion (sample 97SB67) pre-homogenisation bearing plagioclase and clinopyroxene. c) Ferropicrite melt inclusion pre-homogenisation (sample 97SB80) bearing hydrous phases (kaersutite and biotite) as well as Cr-spinel, orthopyroxene and a void which once contained a vapour bubble. d) Picrite melt inclusion post-homogenisation consisting of glass, a vapour bubble and a 'prisoner' Cr-spinel. e) Picrite melt inclusion (sample 97SB34) pre-homogenisation bearing Al- and Ti-rich augite and a low Fe and Mg glass. The alignment of augite suggests that a small number of spinifex crystals are present, formed through fast cooling at the olivine edge. A clear Fe-rich halo of olivine is seen around the inclusion. f) a pre-homogenisation breached inclusion (ferropicrite sample 97SB67); secondary phases fill fractures, hydrous phases occupy the dark area, and the Cr-sp appears replaced by haematite. g) Ferropicrite melt inclusion post-homogenisation; the glass often has a darker colour than in picrite melt inclusions. a–c and e–f are BSE images; d) and g) are photomicrographs.

3.3 Results

3.3.1 Major element compositions

Generally, the olivine-hosted melt inclusions have major element compositions that do not match their respective whole-rock composition well (Fig. 3.2). Some features of the whole-rock data are mirrored by the melt inclusion data. For example, in the DML samples, both whole-rock and melt inclusion compositions have particularly low Al_2O_3 concentrations, with the most primitive picrites having the highest Al_2O_3. However, many aspects are different. Whereas the whole-rock data for the Etendeka picrites define a clear liquid line of descent (Chapter 2, Fig. 2.7), i.e. the series are related through

fractional crystallisation alone, the same is not true of the major elements of olivine-hosted melt inclusions. None of the elements shown in Fig. 3.2 behave in a way that is clearly related to fractional crystallisation, and they show a high degree of variation at a given Fo content. For example, Na_2O and most other elements should negatively correlate with Fo as they are concentrated in the melt during olivine fractionation; this is not obviously the case in Fig. 3.2a. These enigmatic trends, especially in the lowest Fo samples, cannot be explained by normal fractionation processes, and the relationship between melt inclusion major element chemistry and host olivine Fo is puzzling.

The lowest Fo olivines (Fo_{63-75}) are from the Etendeka ferropicrite samples 97SB67 and 97SB68. Their melt inclusions reach extremely high FeO concentrations of up to 32 wt. % (Fig. 3.2b), which is more than double the 13.7 wt. % of the whole-rock composition (Fig. 3.2g). Such high FeO cannot represent any primary or subsequently fractionated composition derived by partial melting of mantle peridotite or pyroxenite. The FeO enrichment is responsible for lowering the wt. % concentration of all other major elements in the lowest Fo samples, explaining, for example, the positive correlation of Na_2O and Fo in Etendeka ferropicrites (Fig. 3.2a). The smooth trend exhibited by melt inclusion FeO with host Fo across all samples is intriguing.

The rehomogenisation process as a possible mechanism for modifying melt inclusion major element compositions

The distinction between picrite and ferropicrite reflects a step difference in the FeO contents of the whole-rock samples; this step is conspicuously lacking in Fig. 3.2b. The major element compositions of these melt inclusions may in fact have been significantly modified by post-entrapment crystallisation and rehomogenisation. Post-entrapment crystallisation causes successively more fayalite-rich layers of olivine from the trapped melt inclusion to crystallise on its host wall. These layers quickly re-equilibrate with the surrounding olivine crystal and effectively vanish (Danyushevsky *et al.*, 2000). During rehomogenisation in a furnace, some unknown amount of wall olivine remelts. If the temperature is too low, not enough olivine will remelt, whereas if the temperature is too high, excess olivine will be added to the melt. It is difficult to quantify the result of this process given the possibility of an unknown extent of partial re-equilibration of wall olivine during melting. The majority of the inclusions are under-heated, as they were judged to be homogeneous once all daughter phases except for olivine had disappeared. This has concentrated elements that are incompatible in olivine in the melt inclusion so that their concentrations are high relative to the associated whole-rock. The lowest Fo samples (97SB67 and 97SB68) were likely overheated as the haematite coating on the crystals, the dark melt colour and low frequency of inclusions made it difficult to visually assess the homogenisation temperature.

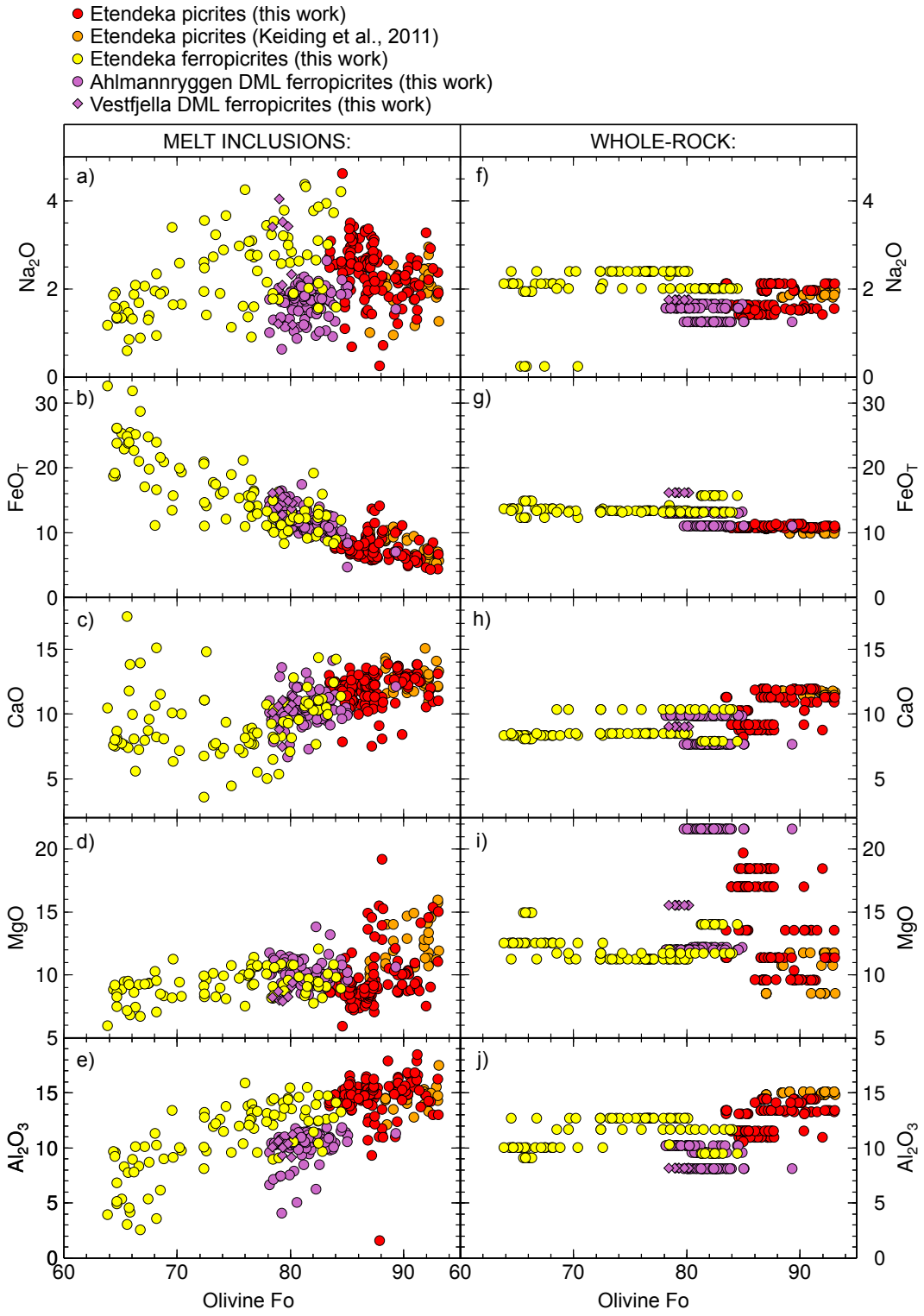

Figure 3.2: Major element compositions of rehomogenised melt inclusions, not corrected for post-entrapment crystallisation (cf. Danyushevsky *et al.*, 2000), plotted against host olivine forsterite content (a-e). In plots f-j, the Fo content of the same olivine hosts as in a-e are shown on the x-axis, plotted with their respective bulk rock composition (Gibson *et al.*, 2000; Heinonen *et al.*, 2010; Keiding *et al.*, 2011; Riley *et al.*, 2005; Thompson *et al.*, 2001) on the y-axis. Legend at top of figure.

It is expected that low forsterite olivines would be more overheated than high-forsterite olivines. The addition of excess olivine results in a dilution trend, accounting for some of the major element trends observed in Fig. 3.2. The FeO_T trend, however, cannot be explained in this way. Perhaps excess heating has resulted in the opposite effect of the 'Fe-loss' process (Danyushevsky *et al.*, 2000), in which: 1) excess MgO and FeO from the relatively Fe-rich olivine is added to the melt inclusion by olivine melting, then 2) the melt re-equilibrates with the surrounding olivine to maintain the correct $K_{D_{Fe-Mg}}^{ol-liq}$, swapping Fe^{2+} cations in the crystal with Mg^{2+} cations from the melt. This relies on adequate diffusion occurring over the 20 minute heating period. The hypothesis that melt inclusion FeO and MgO is buffered by the host olivine in this way is supported by the smooth trend in FeO_T with forsterite observed in Fig. 3.2f, in contrast with the discontinuous trends in other major and trace elements between picrites and ferropicrites. It is also supported by the observation of a ~ 5 μm high-Fo rim around reheated melt inclusions, compared with a broader low Fo-rim around non-heated inclusions. Gaetani and Watson (2000) observed that excess heating resulted in an increase in MgO as well as FeO in higher Fo olivine-hosted inclusions. It is difficult to assess MgO gain in inclusions in the low Fo olivines ($Fo_{<75}$) of samples 97SB67 and 97SB68 as the parental melt composition is poorly constrained (see Chapter 2). Alternatively, given the lower forsterite, more evolved nature of the olivine host, the high FeO could result from the partial resorption of another phase (such as magnetite) caught in heterogeneous trapping, again as a result of heating above the trapping temperature, in agreement with the suggestion of Heinonen and Luttinen (2008) that sample 97SB67 and 97SB68 contains a large proportion of accumulated crystals and is a lower temperature, more fractionated sample. This could also contribute to the variability observed in some major elements at low Fo.

Across all sample types, FeO in olivine-hosted melt inclusions varies smoothly with host olivine Fo (Fig. 3.2f), which is not true of their host rock compositions. This effect is an artefact and serves as a warning that rehomogenised melt inclusions are not reliable indicators of the original melt Fe/Mg, and thus are unsuitable material for the application of Fe-Mg-based thermometers (cf. Keiding *et al.*, 2011).

3.3.2 Incompatible trace elements

Trace element data for all analysed olivine-hosted melt inclusions is shown on primitive mantle normalised multi-element plots in Figs. 3.3 and 3.4. Some melt inclusions have elevated concentrations of fluid-mobile elements (commonly K, Rb and/or Sr) and are outliers in the inclusion population; the origin of their chemistry is discussed in the next section. Except for this subgroup, the compositions of melt inclusions of all sample types approximate the equivalent whole-rock compositions, where their average concentrations tend to converge on those of the whole-rock. All samples have a rather uniform melt inclusion population, which is especially true of the ferropicrites. The REE

contents of Etendeka picrites are somewhat depleted, with flat, MORB-like profiles, and deep melting is indicated by their fractionated HREEs. All ferropicrite inclusions have low concentrations of HREEs relative to the picrite inclusions. The Etendeka and Vestfjella ferropicrites are more enriched in highly incompatible trace elements than the picrites, whereas the Ahlmannryggen ferropicrites are quite depleted.

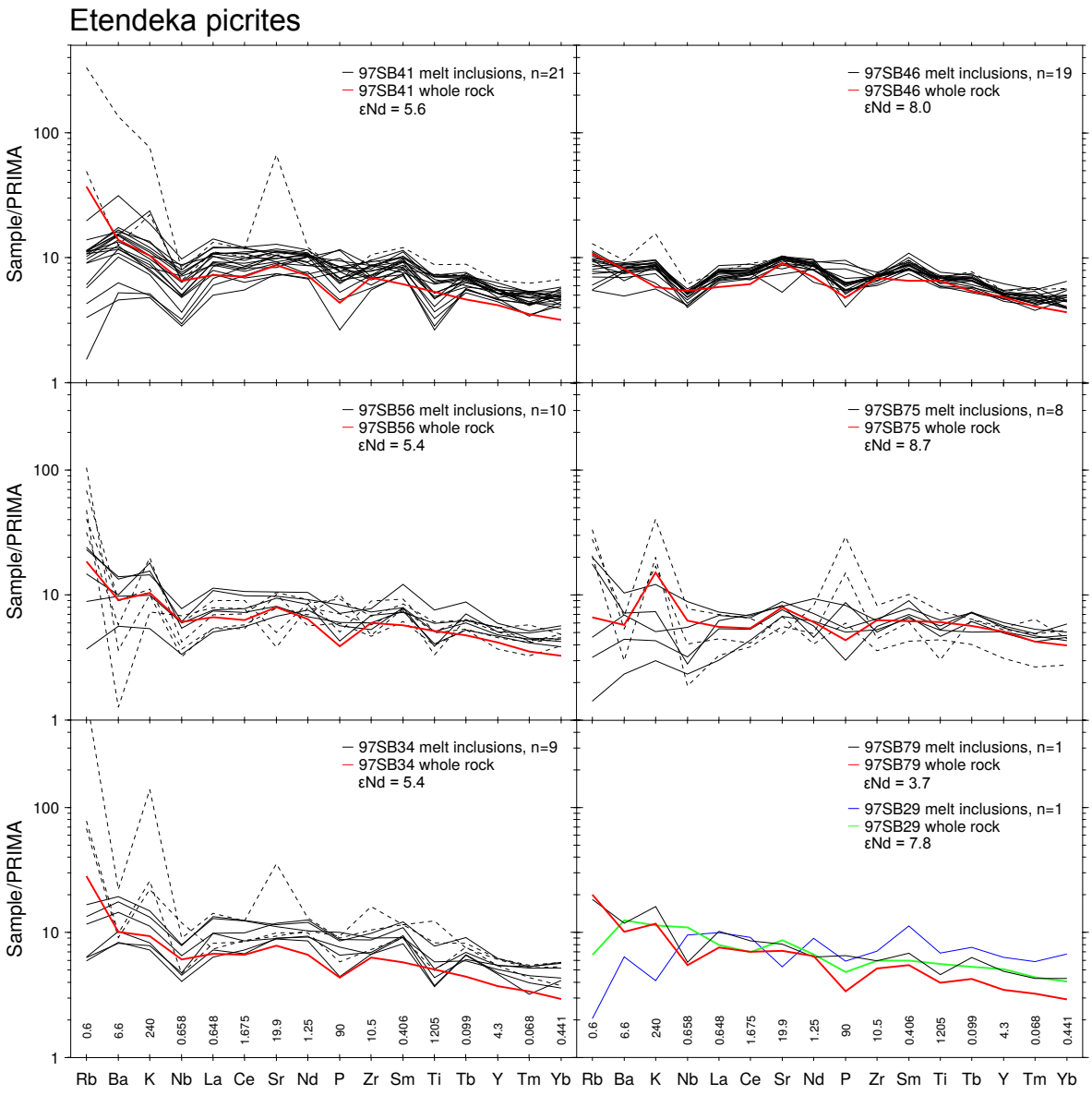

Figure 3.3: Primitive mantle (McDonough and Sun, 1995) normalised multi-element plots showing selected REE and other trace element concentrations in the Etendeka picrites, measured by SIMS, except P, which was measured by EPMA. Solid black lines, melt inclusions; dotted black lines, melt inclusions showing signs of alteration; red lines, host whole-rock composition. Each plot represents one whole-rock sample. Numbers along base denote normalisation values.

Shifts in normalised concentration patterns to higher or lower values relative to whole-rock patterns can be attributed to several processes. The rehomogenisation process, where variable amounts

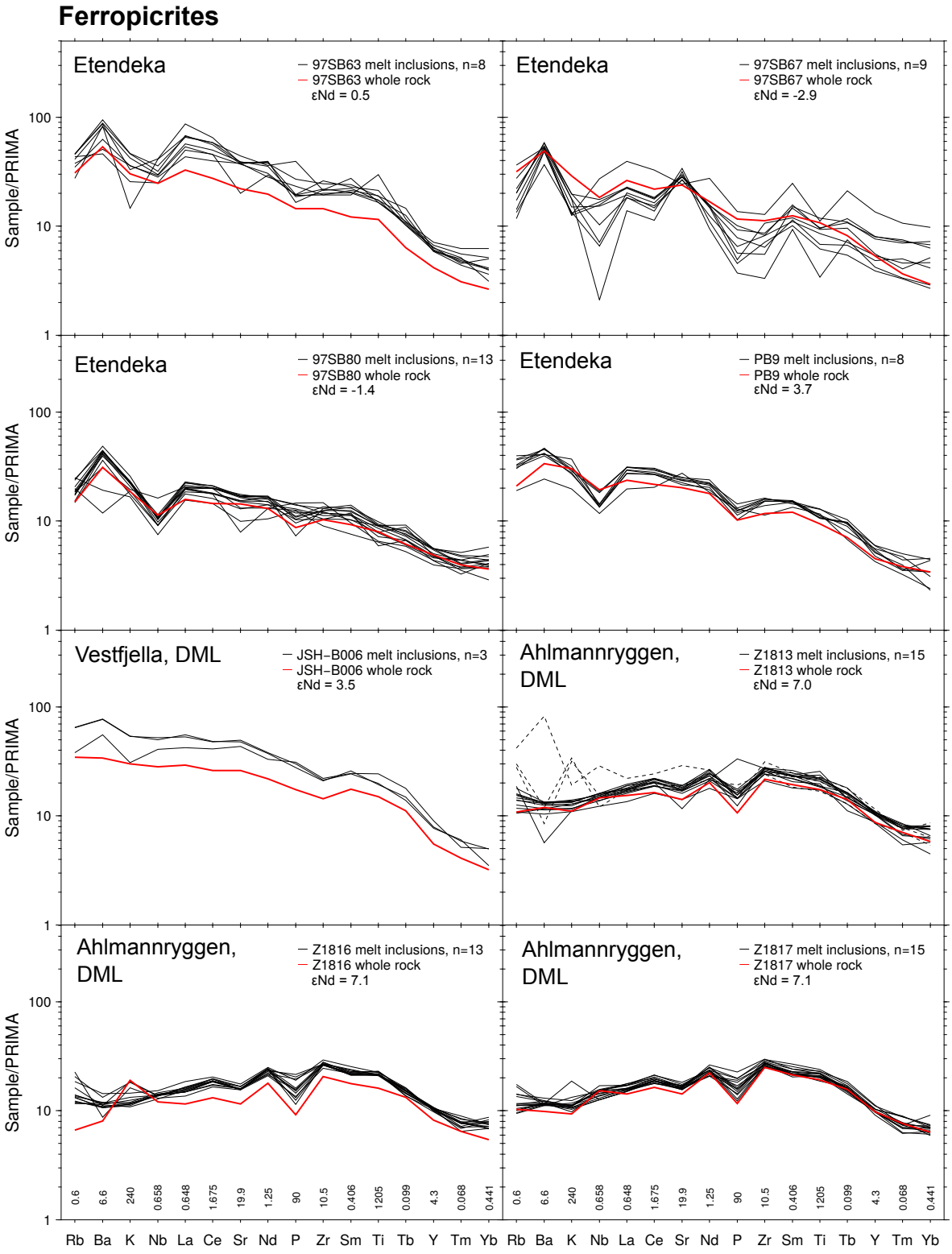

Figure 3.4: Primitive mantle (McDonough and Sun, 1995) normalised multi-element plots showing selected REE and other trace element concentrations in the Etendeka ferropicrites and Antarctic (Ahlmannryggen and Vestfjella) ferropicrites, measured by SIMS, except P, which was measured by EPMA. Lines as in Fig. 3.3. Numbers along base denote normalisation values.

of remelted olivine from the melt inclusion rim act to dilute or concentrate all other elements, shifts values in melt inclusions relative to the parental liquid. As discussed above, the majority of inclusions are under-heated and so incompatible trace elements are concentrated relative to parental liquid values. Similarly, accumulation or loss of olivine phenocrysts in the whole-rock samples also shifts whole-rock compositions relative to the initial liquid. Assuming that all of the analysed trace elements are fully incompatible in olivine, these effects should not affect their relative concentrations. For this reason, trace element ratios are preferred to absolute concentrations when interpreting rehomogenised melt inclusion data.

The trace element ratios plotted in Fig. 3.5 are insensitive to secondary hydrothermal alteration. The Etendeka and Vestfjella ferropicrites show elevated LREE/MREE ratios (La/Sm, Fig. 3.5b) ratios relative to the depleted, MORB-like Etendeka picrites and Ahlmannryggen ferropicrites ($[La/Sm]_N \sim 1$). The Etendeka ferropicrite samples may derive from slightly different primary melts and are not strictly linked to one another by fractionation. The trend of decreasing LREE/MREE with decreasing Fo may reflect mantle processes, because crystallisation is not expected to significantly alter REE ratios. Melt inclusions in the Vestfjella ferropicrite have similar trace element ratios to the Etendeka ferropicrites ones and therefore probably originated from a similar parental melt.

All ferropicrite melt inclusions have higher LREE/HREE, LREE/MREE and MREE/HREE ratios (Fig. 3.5a–c) than those from picrites, reflecting the lower fraction of melting and/or more enriched source, and the presence of garnet within the residual mantle. There is a strong contrast in the Sc/Zr ratio (Fig. 3.5d) between high Fo ferropicrites and picrites. Sc is moderately compatible in both clinopyroxene and garnet, so this difference may reflect an elevated clinopyroxene and/or garnet content in the ferropicrite source (e.g. garnet clinopyroxenite rather than peridotite, Chapters 4 and 6). The alternative explanation that magmatic clinopyroxene fractionation reduced the melt Sc/Zr is probably not correct as no correlation is seen with Fo in the Fo > 70 samples. Finally, the very tight distribution of ratios on Figure 3.5 shows that there is little variability between melt inclusions, particularly within the Etendeka picrites and Ahlmannryggen ferropicrites.

3.4 Discussion

3.4.1 Anomalous melt inclusions: magmatic assimilation or secondary alteration?

Some olivine-hosted melt inclusions have more irregular trace element patterns than others (highlighted in Figs. 3.3 and 3.4), and than would be expected for a mantle-derived melt, showing that they may have undergone some form of chemical alteration since derivation from the mantle. These inclusions frequently have large peaks in fluid-mobile elements such as Rb, Ba, K and/or Sr. However, they do not have particularly elevated levels of other highly similarly incompatible elements such as

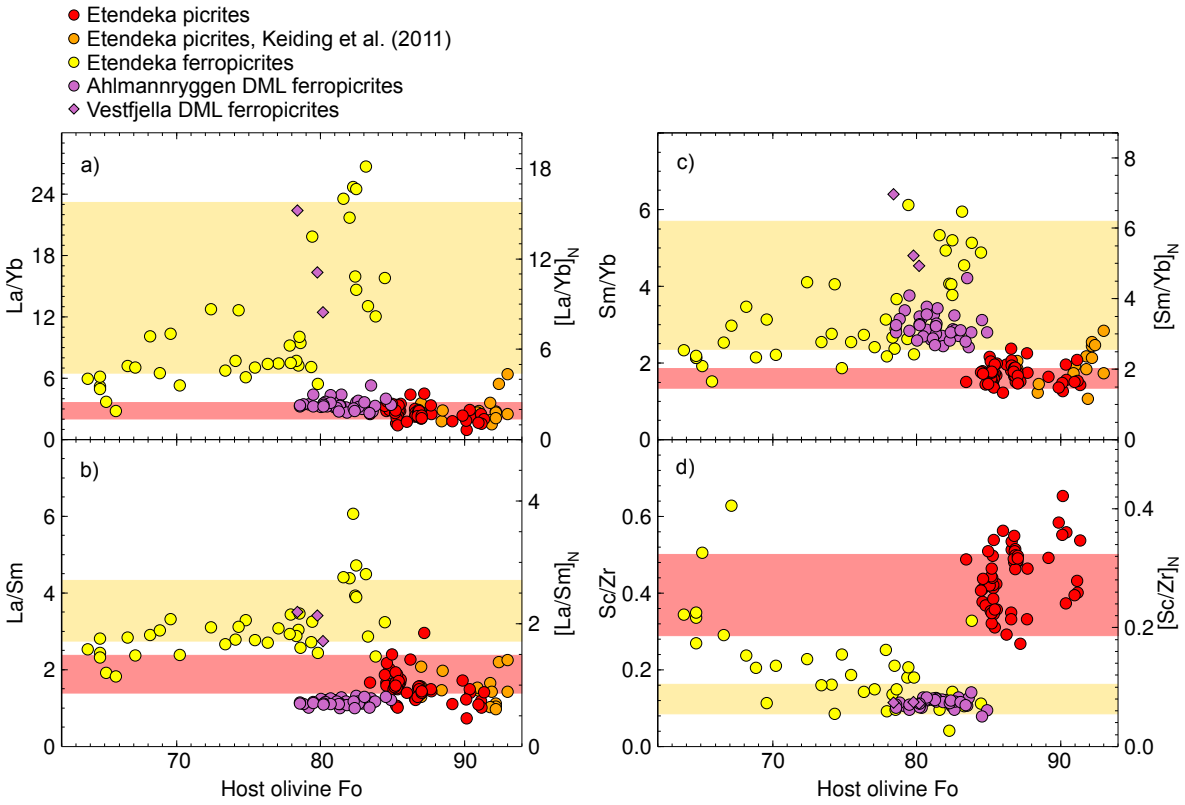

Figure 3.5: Trace element ratios of homogenised melt inclusions (excluding those identified as contaminated in Figs. 3.3 and 3.4), measured by SIMS, plotted against host olivine forsterite. Shaded pale red field shows the picrite whole-rock range and shaded yellow field shows the ferropicrite whole-rock range.

La, which should have higher concentrations in the continental crust than in mantle melts, and thus become elevated during crustal assimilation.

The large ion lithophile element (LILE) elevation in these inclusions may either be caused by magmatic assimilation of crustal material or secondary hydrothermal alteration, i.e. the inclusion may have sampled a liquid contaminated by crustal melts and preserved it as a closed system, or have been breached post-entrapment and have suffered hydrothermal alteration. The elevated LILE relative to other highly incompatible trace elements implies that alteration of melt inclusions by a hydrous fluid, rather than by partial melting of crustal rocks, is the likely cause of the chemical change. Some whole-rock samples in this study show evidence of secondary hydrothermal alteration: chlorite in the groundmass, olivine serpentinisation, and elevated concentrations of fluid-mobile elements relative to similarly incompatible elements. In thin section, a large proportion of melt inclusions (up to $\sim 50\%$ in some samples) show evidence of breaching: they contain secondary hydrous phases and/or are obviously fractured (e.g. Fig. 3.1f).

Whether the inclusions are altered by assimilation or hydrothermal processes can be further interrogated by examining the relationship between crystallisation progress and sensitive trace element

ratios. The upper crust local to the Etendeka samples is represented by a Damarara Belt granite (VB12, Thompson *et al.*, 2007), and its composition is used to consider the effects of crustal assimilation on these magmas. The incompatible trace element compositions of some potential contaminant reservoirs for the Etendeka samples are shown in Fig. 3.6. Although basement outcrop is scarce in the DML province of Antarctica, the ferropicrites there were probably emplaced through a predominantly tonalite–trondhjemite–granodiorite (TTG) basement (Heinonen *et al.*, 2010). This is represented by an average TTG composition from the Kaapvaal Craton (Kreissig *et al.*, 2000), that is contemporaneous with the Grunehogna craton where Ahlmannryggen is situated (Marschall *et al.*, 2010).

If the anomalous compositions of melt inclusions were due to crustal assimilation, then the ratios of elements sensitive to this process should correlate with Fo. Combined assimilation and fractional crystallisation (AFC; DePaolo, 1981) modelling defines curves of sensitive ratios with Fo, where contamination increases with crystallisation along different curves depending on the mass ratio of assimilated to crystallised material (M_a/M_c). Fig. 3.7 shows that this is not the case. Only a small subset of inclusions have highly elevated Rb/Zr or Ba/Zr, which do not correlate with Fo or follow the modelled curves. These ratios are sensitive to both crustal assimilation and hydrothermal alteration. Note that the Etendeka ferropicrites are thought to crystallise in the lower crust, so the curves modelled for granite assimilation are just for comparison; assimilation of lower crust, which has very low Rb and Rb/Zr, would cause no perceptible change in the Rb/Zr ratio.

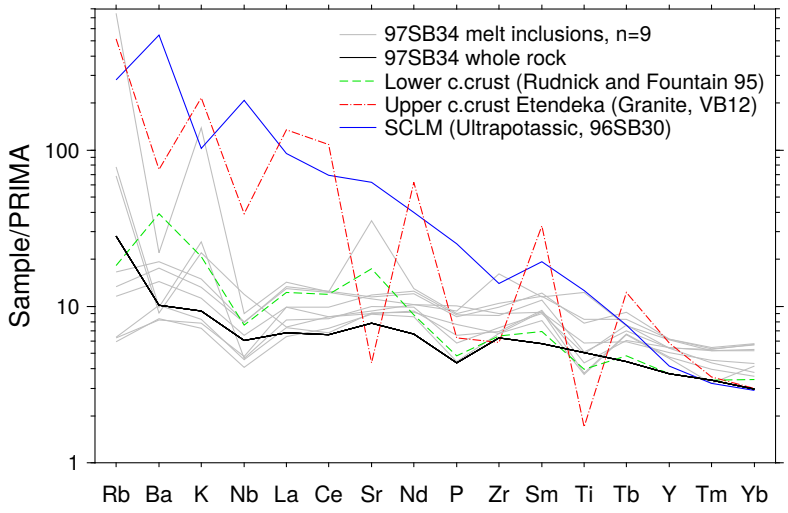

Figure 3.6: Multi-element plot of potential Etendeka contaminants normalised to primitive mantle (McDonough and Sun, 1995). Also shown are the composition of upper crust (Granite sample VB12, Thompson *et al.*, 2007) and SCLM (Lamprophyre sample 96SB30, Thompson *et al.*, 2001) local to the Etendeka province and estimated lower crustal composition of Rudnick and Fountain (1995). Melt inclusions and whole-rock composition of Etendeka picrite sample 97SB34 are shown for comparison. No inclusions show a good match with the combination of peaks and troughs of the upper crust and SCLM. Lower crust contains these elements in too low abundance to greatly influence inclusion composition.

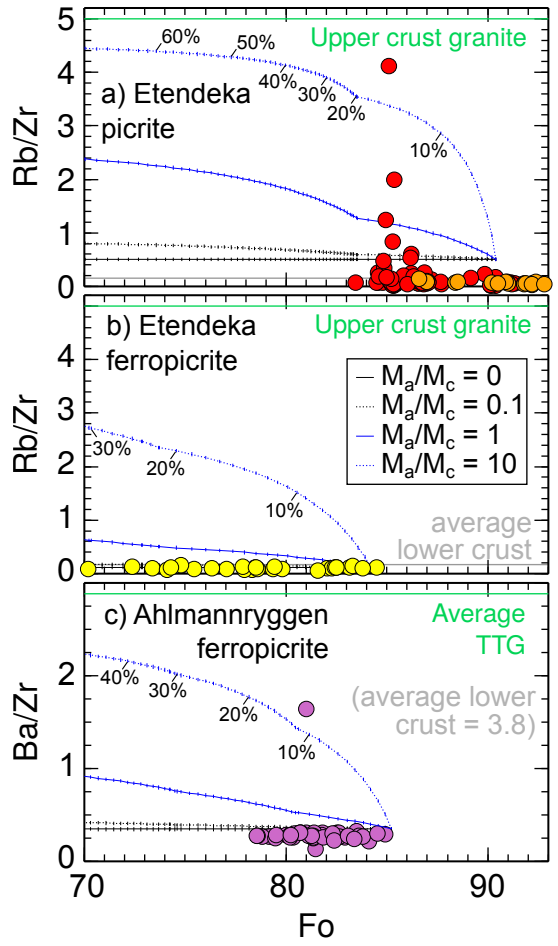

Figure 3.7: AFC modelling of melt Rb/Zr ratio plotted with melt inclusion compositions (filled circles) for: a) Etendeka picrite samples (this study in red; Keiding *et al.*, 2011 in orange, model is 97SB33 whole-rock composition corrected for olivine accumulation, QFM, 3kbar; b) Etendeka ferropicrites (model from 97SB63 whole-rock composition, QFM, 5kbar); c) AFC modelled Ba/Zr ratio of Ahlmannryggen DML ferropicrites (model is Z1813.1, QFM, 5kbar plotted with melt inclusion compositions). Melt compositions are plotted against equilibrium Fo. 1% crystallisation increments are shown with vertical dashes and 10% increments are labelled. Fractional crystallisation is modelled in Petrolog3 (Danyushevsky and Plechov, 2011). Curves are modelled melt compositions with simultaneous assimilation, where M_a/M_c is the ratio of assimilated to crystallised mass. Assimilant composition given by green horizontal line: Etendeka upper crustal granite, sample VB12, Thompson *et al.* (2007); average TTG is average of samples from Kreissig *et al.* (2000) (which is taken to be the dominant basement in DML); average lower crust, Rudnick and Fountain (1995).

The lack of a systematic change in Rb/Zr or Ba/Zr with Fo means that a random selection of inclusions have been altered. The inclusions with elevated Rb/Zr and Ba/Zr are those that are elevated in other LILE, which is consistent with inclusion breaching and secondary hydrous alteration. The unbreached inclusions do not increase in Rb/Zr or Ba/Zr with progressive crystallisation, and so for Etendeka picrites and Ahlmannryggen ferropicrites provide evidence that the magma was not assimilating significant levels of crustal material over this crystallisation interval, i.e. $M_a/M_c < 0.1$. This is consistent with the low levels of contamination observed in the whole-rock samples of this study, which show isotopic and trace element evidence of 0-6% magmatic assimilation (Gibson *et al.*, 2000; Heinonen *et al.*, 2010, 2014; Thompson *et al.*, 2001).

The olivine-hosted melt inclusions in all samples show little evidence of crustal contamination, and are no more contaminated than the host whole-rock samples (in contrast with melt inclusions from Yemen, Kent *et al.*, 2002). The picrites and ferropicrites of both the Paraná-Etendeka and Karoo CFB provinces record $M_a/M_c < 0.1$, which is slightly lower than that of Mull (0.1-0.3, Peate *et al.*, 2012) and much lower than the extremely contaminated inclusions found in primitive melts from Yemen (1-10, Kent *et al.*, 2002). It was suggested by Kent *et al.* (2002) that localised wall-rock melt

was preferentially trapped by fast growing olivine in the case of the Yemen samples, which does not appear to be the case here (Kent *et al.*, 2002).

3.4.2 Primary variability in incompatible elements of olivine-hosted melt inclusions

The trace element contents of the olivine-hosted melt inclusions in the Paraná-Etendeka and Karoo CFBs do not vary greatly from their whole-rock values; the ferropicrite samples display particularly little variability (Figs. 3.3 and 3.4).

Origin of the (limited) melt inclusion variability

The little variability observed in trace element abundances in the olivine-hosted melt inclusions from the Paraná-Etendeka and Karoo CFB provinces is examined through principal component analysis (PCA, e.g. Albarède, 1996). For this analysis, samples are grouped into Etendeka picrites, Etendeka ferropicrites (excluding 97SB67 and 97SB68), and the Ahlmannryggen DML ferropicrites; Vestfjella ferropicrites are excluded because of the low number of analyses. Altered melt inclusions that have elevated LILE are also excluded. The origins of various principal components (PCs) are assigned by considering the loadings of each element in each PC, which is shown, along with the relative importance of each PC, in Fig. 3.8. The % variability in each group accounted for by each PC is given in Table 3.1.

Group	% Variability from olivine dilution (PC1)	% Variability from mantle processes (PC2)
Etendeka picrites*	39.4	19.1
Etendeka ferropicrites	69.9	10.0
Ahlmannryggen ferropicrites**	35.4	12.9

Table 3.1: Sources of variability in the Paraná-Etendeka and Karoo melt inclusions, calculated by PCA. Percentage of variability accounted for by PC1 and PC2. Remaining variability is mostly accounted for by analytical uncertainty. *Variability low; composition of principal components has high uncertainty and origin of variability is tentatively assigned. **Variability very low; composition of principal components has high uncertainty and origin of variability is tentatively assigned. PC1 and PC2 both somewhat convoluted with crustal contamination signal.

The greatest source of variability seen in all samples, PC1, is attributed to the dilution effect of adding or subtracting varying proportions of olivine to the melt, which affects all trace element concentrations but not their relative proportions (Table 3.1). As discussed above, a number of processes can generate the PC1 signal, including post-entrapment crystallisation and experimental rehomogenisation of the inclusions, and variable amounts of fractional crystallisation of olivine. Therefore, PC1, which dominates the trace element concentrations, may reflect processes that occurred after the entrapment of the inclusion. In contrast, PC2 shows opposing behaviour of highly incompatible elements and HREE+Y. This component is likely to be the result of a variable garnet signature, i.e.

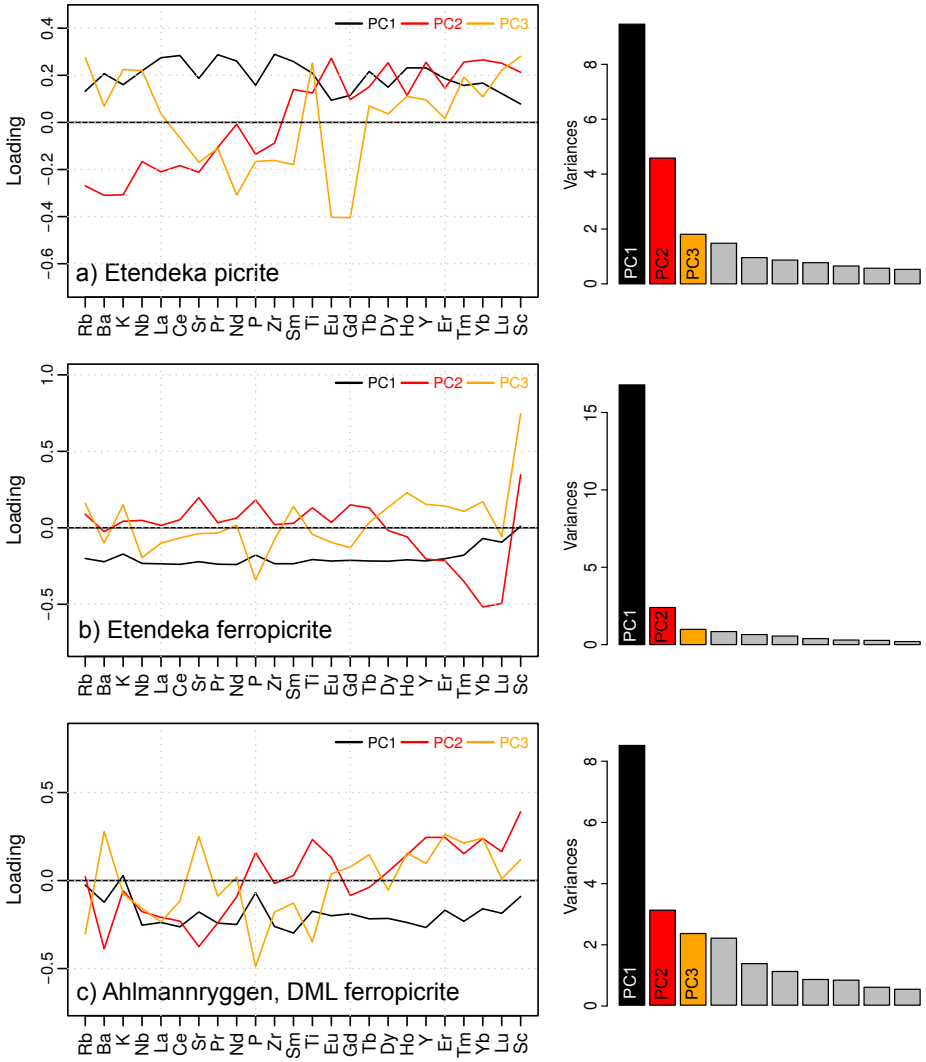

Figure 3.8: Loadings (composition of principal components (PCs) and variance (relative amount of variance in each sample group explained by each PC) for each sample group; PC1, 2 and 3 are highlighted, although 3 is already very noisy. Noise is high in all PCs because the overall variability is very low.

lithology and/or depth of melting, and the effect of different extents of fractional melting within a progressively depleting mantle source, where melts segregate at different depths in the melting column (Gast, 1968). However, it is difficult to confidently assign the origin of PC3 and beyond, especially in the Etendeka picrites and Ahlmannryggen ferropicrites where low trace element variability results in a low signal to noise ratio.

Comparison of melt inclusion variability with global CFB, OIB and MORB datasets

The level of trace element variability observed in melt inclusions from the primitive Paraná-Etendeka and Karoo CFB rocks is compared with datasets from MORB, OIB and other CFB provinces in Fig. 3.9 (datasets are filtered to remove contaminated and low Fo inclusions, $Fo_{<82}$ inclusions in

basalts and picrites and $Fo_{<76}$ inclusions in ferropicrites). Samples are individual hand specimens, usually from different lava flows and dykes, but occasionally from the same flow. The different ratios and concentrations shown in Fig. 3.9 are moderately insensitive to fractionation and hydrothermal alteration, and were selected to examine variability originating in the mantle source and melting process.

Olivine-hosted melt inclusion variability is highest in Mid Atlantic Ridge (MAR) and Icelandic samples, regardless of the element or ratio chosen. The range in standard deviations is also large in both, showing that the degree of variability is not consistent between whole-rock samples. Globally, there appears to be a tectonic setting control, where intra-sample melt inclusion variability follows the general pattern MOR > Iceland > OIB and CFB provinces > ferropicrites (as a subset of compositions within some CFBs). Note that Iceland is treated as a separate category to MAR and OIB in this analysis. The number of whole-rock samples in the global dataset that passed the criteria for inclusion is relatively small (n = 63–69, depending on element, where over a third of the samples are from Hawaii), so this pattern may not be robust. Mid-ocean ridge magmas are more variable than Icelandic magmas in terms of LREE, but less so in Sm/Zr and Ti/Zr. Samples from OIBs and CFB provinces have a similar low level of variability as samples in this study. Peate *et al.* (2012) also noted that melt inclusions from the North Atlantic Igneous Province (Mull) were rather homogeneous in those elements insensitive to contamination. The fact that variability in melt inclusions from Yemen is slightly higher than in those from other CFB provinces reflects the fact that some inclusions with lower levels of assimilation may not have been effectively removed during data filtering. Olivine-hosted melt inclusions from ferropicrite samples are the least heterogeneous group.

To put the degree of heterogeneity shown in Fig. 3.9 into context, it is useful to consider the maximum variability expected in incremental fractional mantle melts. For this purpose, La concentrations are used. By assuming a one dimensional melting column and a mantle source composition, C_0, and given that the partition coefficient of La (D_{La}) $\ll 1$, the fraction of melting, F, required to match the mean melt inclusion La concentration of a given sample type can be calculated using the approximate relationship $F \approx C_0/C_{\mathrm{L}}$. Assuming perfect fractional modal melting, equation D.6 of Rudge *et al.* (2013) can then be used to predict the variance of incremental melts:

$$\sigma^2 = \frac{C_0^2}{2FD} \tag{3.1}$$

The bulk partition coefficient D was calculated using the mineral-melt partition coefficients of Gibson and Geist (2010) and the 30 kbar peridotite solidus phase proportions of Davis *et al.* (2011). The results of this calculation are given in Table 3.2. Observed, σ, and predicted standard deviation, σ_0, are presented as a percentage of the relevant mean melt inclusion concentration. This is also used to calculate F. σ_0 ranges from 149% to 234%, which is much higher than the observed values (Fig.

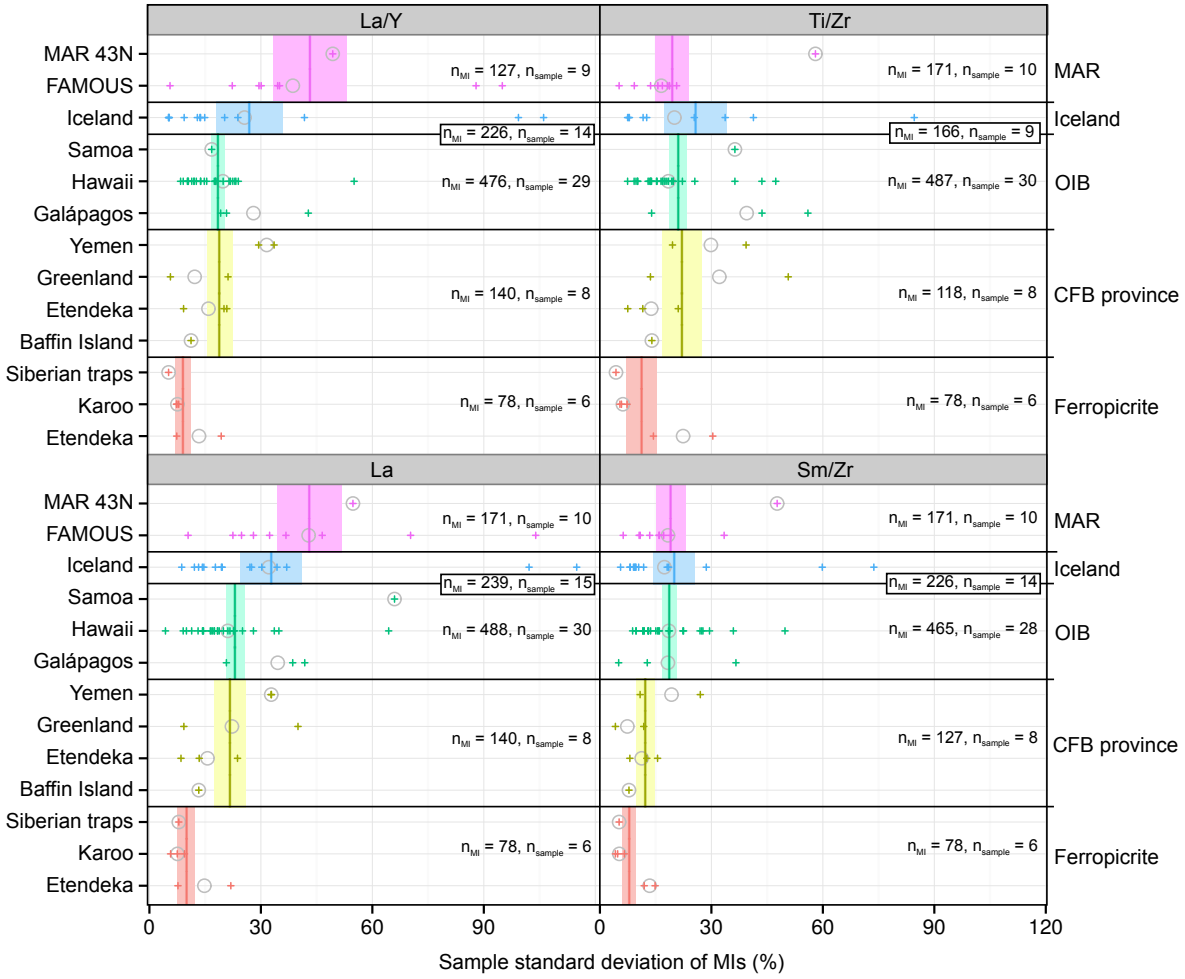

Figure 3.9: La/Y, La, Ti/Zr and Sm/Zr variability in melt inclusions from samples from the global dataset. Arbitrary filters are applied to remove inclusions with altered LILE concentrations (Rb/Zr > 0.25 or Ba/Zr > 3 or K2O > 2.0 wt.%, depending on which elements are provided), evolved inclusions (Fo < 82, basalts and picrites; < 76, ferropicrites), and samples with fewer than 8 inclusions after those filters are applied. Points (+) represent the standard deviation of melt inclusions in a single sample expressed as a percentage of the mean, such that all samples are directly comparable; circles represent the weighted mean standard deviation of all samples for a given location; vertical lines represent the mean standard deviation of samples for a given grouping. Rectangle is the standard error of the mean. Samples refer to hand specimens in all cases, where a sample code is given in the published source data. Data sources: FAMOUS, Laubier *et al.* (2012) and Shimizu (1998); 43 °N MORB, Kamenetsky *et al.* (1998); Iceland, compilation of Maclennan (2008a), Neave *et al.* (2014b, 2013); Hawaii, Norman *et al.* (2002), Sobolev *et al.* (2011) and Sides *et al.* (2014); Galápagos, Koleszar *et al.* (2009); Samoa, Jackson and Hart (2006); Baffin Island, Starkey *et al.* (2012); Greenland, Nielsen *et al.* (2006); Starkey *et al.* (2012); Yemen, Kent *et al.* (2002); Siberian Traps ferropicrites, Sobolev *et al.* (2009), Gudchikhinsky fm. samples from Noril'sk, identified as ferropicrite by Gibson (2002); Etendeka and Karoo, this study and Keiding *et al.* (2011)

3.9; Table 3.2); for example, the observed La variability on Iceland (33%) is a large reduction from that predicted for incremental fractional mantle melts (234%), and reflects extensive mixing after melt formation. The extent to which these incremental melts would have had to mix (M) in order to

reduce their variability down to that recorded in melt inclusions can be calculated using the equation of Maclennan (2008a):

$$M = 1 - \frac{\sigma^2}{\sigma_0^2} \tag{3.2}$$

	MI mean La	MI σ (%)	C_0	F	Model σ_0 (%)	M	n_{MI} (n_{sample})
MAR	2.9	42.9	0.23	0.08	187	0.947	171 (10)
Iceland	5.0	32.9	0.65	0.13	234	0.980	239 (15)
OIB	12.5	23.1	0.65	0.05	149	0.976	488 (30)
CFB province	6.4	21.7	0.65	0.10	208	0.989	140 (8)
Ferropicrite	14.1	10.0	1.16	0.08	188	0.997	78 (6)

Table 3.2: Degree of mixing (M) calculated for different groups using La concentration, where $M = 1$ is completely homogeneous and $M = 0$ refers to the range observed in modelled unmixed incremental mantle melts. Melt fractions are calculated from melt inclusion mean value (host Fo > 82 only, or Fo > 76 for ferropicrite). n_{MI} is the number of melt inclusion analyses considered, with the number in brackets indicating the corresponding number of samples. The concentration of La in the primitive mantle of McDonough and Sun (1995) is used for C_0, except in the case of the Mid Atlantic Ridge (MAR) and ferropicrite, for which the depleted mantle concentration of Salters and Stracke (2004) is used, and a 1:1 mixture of primitive mantle and subduction-modified igneous crust (Stracke *et al.*, 2003) is used, respectively.

In all cases, the vast majority of mixing occurred prior to the onset of crystallisation and melt inclusion entrapment. This calculation relies on a heavily simplified model and assumes that incipient melts are isolated from the moment of their formation, which may overestimate the expected variability of the outward flux of melt from the mantle melting region. Melt inclusions from all CFB provinces are rehomogenised and some variability in La concentrations is due to the dilution effect. All melts have been significantly mixed since their formation in the mantle, and CFB province and ferropicrite samples especially so.

Comparison between the timescale of mixing processes in CFB provinces and Iceland

There are many detailed studies of melt variability, especially from melt inclusions, on Iceland (Gurenko and Chaussidon, 1995; Maclennan, 2008a,b; Maclennan *et al.*, 2003b; Moune *et al.*, 2012; Neave *et al.*, 2014a, 2013; Slater *et al.*, 2001), so the effect of mantle and crustal processes on this compositional heterogeneity is now well understood. This provides an opportunity to compare melt inclusion variability from Etendeka and DML with that from a well characterised system.

Melt inclusion La/Yb, a proxy for all incompatible element variability, is plotted against host olivine Fo in Fig. 3.10. La/Yb for a given inclusion is normalised to the mean of melt inclusions in that whole-rock sample. This removes inter-sample offsets in La/Yb (e.g. as a consequence of differences in the extent of partial melting or fractionation), which allows the variability of the relatively small number of inclusions from each sample to be considered together. In Iceland, melt inclusion

variability is extremely large at high forsterite contents (La/Yb ranges from 0 to 3.5 of the sample mean at Fo > 86) and funnels towards little variability at low forsterite (La/Yb range of 0.7 to 1.3 of sample mean at Fo < 80; Fig. 3.10a). This reduction in variability with decreasing forsterite content of the olivine hosts is attributed to concurrent crystallisation and melt mixing (Maclennan, 2008a). Melt inclusions are trapped in crystallising olivine before the melt has completely homogenised through convective mixing. The large variability at high Fo represents primary differences in mantle-derived melts caused by different extents of fractional melting, and perhaps to a lesser extent, diversity of source lithology (e.g. Shorttle and Maclennan, 2011). These melts subsequently accumulate and mix in near-Moho and crustal sills. In Table 3.2, this level of detail is lost, where $M = 0.980$ reflects an average of inclusions from all olivine from > Fo_{82} host olivine, which is the threshold Fo applied to all data.

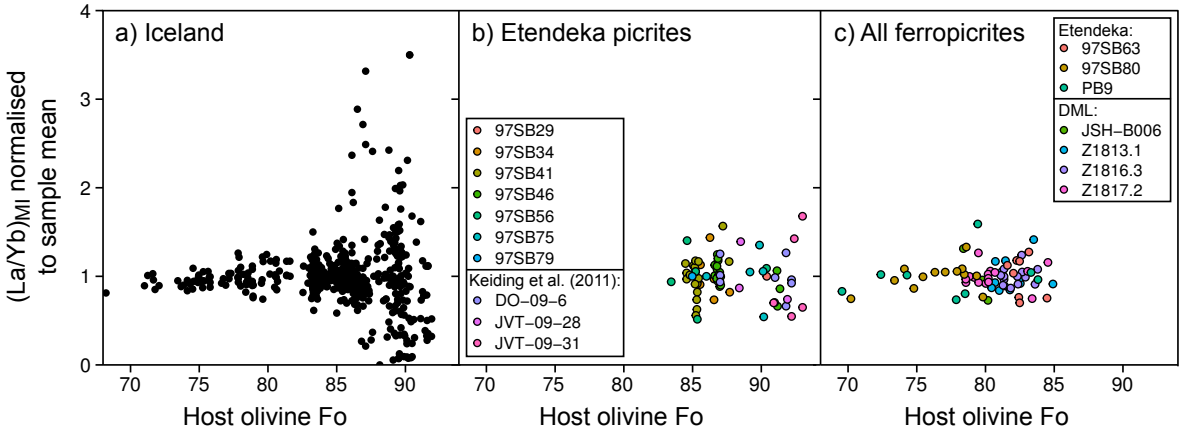

Figure 3.10: La/Yb of individual melt inclusions normalised to the mean La/Yb of all melt inclusions from a given sample, plotted against host olivine forsterite. a) Icelandic melt inclusions, from the analyses and literature compilation of Maclennan (2008a); b) All uncontaminated Etendeka picrites, including those of Keiding *et al.* (2011); c) All uncontaminated Etendeka and Karoo DML ferropicrites, excluding samples 97SB67 and 97SB68.

The Etendeka picrite melt inclusions occur in olivines with a compositional range of Fo_{84-93}, which is similar to that of the most variable Icelandic inclusions (most are Fo_{71-92}). However, the relative deviation of the Etendeka picrite inclusions at high Fo is much lower than that in the Icelandic samples (Fig. 3.10b). The observed La/Yb of individual inclusions range from 0.5-1.7 of the sample mean. The ferropicrites are similarly lacking in variability, especially at high Fo, where the higher Fe/Mg of the primary melt means that the forsterite content of liquidus olivine is offset to lower values relative to picrite. In further contrast to Icelandic inclusions, the deviation from the mean of both picrites and ferropicrites does not change systematically with forsterite content: rather than crystallisation-concurrent mixing occurring, the melts must have mixed to a greater extent prior to the onset of crystallisation. A signal to noise ratio for uncontaminated inclusions of 2.2 for the picrites (n = 71) and 1.3 for the ferropicrites (n = 72) means that the variability in La/Yb, i.e. the deviation

of melt inclusions from the sample mean, is statistically significant at the 95% confidence level (99% for picrites), so the variability is greater than that expected from analytical uncertainty alone.

Finally, it is noted that in Iceland, variable trace element and isotopic compositions are observed at all length scales, including different melt inclusion compositions found within the same olivine as well as different glass compositions between samples from the same flow (Maclennan, 2008b; Maclennan *et al.*, 2003b), and that lava flow isotopic compositions exhibit significant spatial variability (Shorttle *et al.*, 2013). These observations are in contrast with the results of this study, where melt inclusions are homogeneous, and the voluminous CFB lavas are relatively uniform across large geographical extents. Any heterogeneity in CFB flows must be gained through subsequent crustal assimilation and fractionation, and is not inherited from the primary melts.

Origin of melt inclusion incompatible trace element homogeneity in primitive CFB rocks

Fractional melts extracted from a melting column at different depths are expected to be compositionally heterogeneous, and even more so if the mantle source is lithologically heterogeneous. Melts from different heights and/or lithologies in a melting column may be isolated during transport (Kelemen *et al.*, 1997), and recombined by injection into the same magma body. In the analogous Laki system (which had historical eruption rates of similar magnitude to those estimated for CFB emplacement, Thordarson and Self, 1993), heterogeneous melts pond in lower crustal sills, and after some initial mixing and crystallisation, magmas rise through a complex plumbing system into shallower reservoirs (Neave *et al.*, 2013). In CFB provinces, such magmas may subsequently pool in large shallow crustal magma chambers where they further fractionate and assimilate country rock. Melt inclusions record the state of magma throughout crystallisation, where varied inclusions show that the host magma body was heterogeneous; subsequent mixing acts to destroy this variability. In Iceland, similar timescales of mixing and crystallisation mean that melt inclusions record a variable melt, with a reduction in variance correlating with proxies for crystallisation (Maclennan, 2008a). This is not the case for samples in this study. The existence of both picrite and ferropicrite in the same CFB provinces show that their associated mantle sources can consist of several lithologies, so how do melts from a heterogeneous mantle result in homogeneous melt inclusion populations?

Initially heterogeneous fractional mantle melts must have mixed to near completion prior to the liquidus temperature being reached, so that liquidus olivines sample a melt that has already homogenised. This mixing could happen both during transport through the convecting and lithospheric mantle and within deep crustal sills. As shown in Table 3.2, CFB melts must have already mixed by 98.9% prior to the onset of olivine crystallisation and inclusion entrapment. The Etendeka picrites derive from melting at elevated mantle potential temperature (T_P) under lithosphere of similar thickness to that of some OIBs, and ferropicrites derive from deeper melting, constrained to low fraction

melting beneath a thick continental lithosphere (Thompson *et al.*, 2001). These conditions result in hot, high-MgO melts that may have a moderate super-liquidus cooling interval when emplaced in the crust because of the large pressure drop experienced during ascent through the lithosphere: during ascent melts follow a liquid adiabat with a shallower PT gradient than the melt liquidus. Superliquidus melts can therefore undergo convective mixing as they cool to their liquidus temperatures. This would be the case for all melts formed under thick lithosphere, explaining the high degree of mixing observed in intra-plate ferropicrite, CFB and OIB samples. The plumbing systems of CFB provinces must also carry a higher melt flux, transferring heat into the crust and altering the geothermal gradient to promote deep melt mixing. Thinner lithosphere promotes shallower melting, resulting in both a smaller pressure drop between melt production and emplacement (so smaller liquidus temperature overstep), and cooler, less MgO-rich melts, which are more viscous and thus convect less easily. Although the Icelandic mantle is $\sim$ 150 °C hotter than the MORB-source mantle (e.g. Shorttle and Maclennan, 2011), both melting regimes terminate at lower pressures than melting in intra-plate settings, explaining their lower degrees of recorded mixing.

The physical properties of picrite and ferropicrite support convective mixing prior to the onset of crystallisation. At their respective liquidii, both picrite and ferropicrite melts have a lower dynamic viscosity than that of MORB, and Etendeka ferropicrite has a viscosity even lower than picrite. For example, MELTS calculations indicate that, while the liquidus dynamic viscosity of primary MORB at 1 kbar is 5.4 Pa s (composition calculated from Siqueros primitive MORB by Herzberg and Asimow, 2015), that of ferropicrite 97SB63 at 5 kbar is 0.7 Pa s and that of picrite 97SB33 at 5 kbar is 1.1 Pa s (Ghiorso and Sack, 1995). The liquidus temperatures of the Etendeka and DML samples of this study are demonstrated to be hotter than those of MORBs by Al-in-olivine thermometry (Chapter 5 and Heinonen *et al.*, 2015). The ferropicrites (both Etendeka and DML) may actually have been emplaced at a superliquidus temperature, allowing these hot, low viscosity melts to convect prior to the onset of crystallisation (Chapter 5). If this mixing was efficient, melt inclusions would record a homogeneous melt composition.

The effects of the melt transport style on the mixing of incremental mantle melts and/or segregation prior to emplacement of melts in crustal or near-Moho sills must also be considered. During adiabatic decompression melting, high porosity channels are likely to form through reactive transport processes; these serve to segregate incipient melts close to their source and deliver heterogeneous melts to magma chambers (Spiegelman and Kelemen, 2003). In addition, lithological heterogeneity may promote the formation of channelised flow (Katz and Weatherley, 2012; Weatherley and Katz, 2012). However, prior to channel nucleation (i.e. at low melt fraction), incipient melts may be trapped in-situ, promoting equilibrium melting conditions and/or homogenisation. The extent to which channelised flow develops during the high pressure, low fraction melting that produces ferropicrite is likely

to be limited, especially at pressures above the peridotite solidus, where Rudge *et al.* (2013) suggest a significant permeability barrier may exist.

The lack of crustal assimilation in primitive CFB melts

If the primitive melts studied here were effectively mixed in crustal sill-like magma chambers within continental lithosphere, it is important to consider why they show only limited geochemical evidence of interaction with lithospheric materials, as indicated by the whole-rock data and melt inclusions. Spera and Bohrson (2001) provided energy-constrained assimilation-fractional crystallisation (EC-AFC) equations to estimate the thermodynamics of magmas that crystallise in contact with crustal wall-rocks. The parameters and results of the modelling are presented in Table 3.3. To constrain the model parameters for the melt, the parental melt major element composition estimated for the Etendeka picrites by Thompson and Gibson (2000) and a liquidus temperature of 1450 °C were used, which corresponds to the highest temperatures recorded in CFB province primitive magmas by Al-in-olivine thermometry (Coogan *et al.*, 2014). To demonstrate the effect of a superliquidus melt temperature, initial temperature of the melt was taken as 1550 °C as an illustrative example. For the crustal wallrocks, the standard upper and lower crustal parameters provided by Bohrson and Spera (2001) were used, and additional models were performed with initial contaminant temperatures that take into account the heating effect of mafic underplating in a continental rift environment (Bohrson and Spera, 2001). Using high equilibration temperatures and high initial melt and contaminant temperatures ensures that the amount of crystallisation prior to initiation of wall-rock melting is not overestimated. The models using standard and continental rift parameters for upper crust suggest that 28 wt.% of cumulates form before the picritic magma has experienced 1 wt.% (relative to initial magma mass) of contamination from the wall rock. There is therefore ample opportunity for the mantle melts to mix and crystallise within the sills before crustal contamination takes place. This is equivalent to $M_a/M_c = 0.04$, which is consistent with melt inclusion evidence. The models are also compatible with the observation that picrites in CFBs tend to be uncontaminated whereas more evolved basalts and basaltic andesites with MgO of 4–6 wt.% often have a significant crustal overprint (e.g. Peate, 1997; Thompson *et al.*, 2007).

3.4.3 Comparison of melt inclusions and magma composition

In each of the samples from this study, the average incompatible trace element composition of the olivine-hosted melt inclusions approximates to the respective whole-rock analysis. This is especially true for incompatible trace element ratios, whereas the absolute concentrations in the melt inclusions can be offset from the whole-rock values (Figs. 3.3 and 3.4). This offset is consistent with the dilution or concentration of i) inclusions relative to whole-rock values due to under or over-heating of

	PM	Upper crust		Lower crust	
		standard	rift	standard	rift
Magma liquidus T (°C)	1450	-	-	-	-
Magma initial T (°C)	1550	-	-	-	-
Assimilant liquidus T (°C)	-	1000	1000	1100	1100
Assimilant initial T (°C)	-	300	600	600	800
Solidus T (°C)	-	850	850	950	950
Equilibration T (°C)	-	980	980	1080	1080
Isobaric specific heat (J/kg K)	1650	1370	1370	1388	1388
Crystallisation enthalpy (J/kg)	470000	-	-	-	-
Enthalpy of fusion (J/kg)	-	270000	270000	350000	350000
Amount of crystallisation at $M_a/M_0 = 1$ (wt.%)	-	59	28	32	8

Table 3.3: EC-AFC modelling parameters and results (modelling performed by J. Heinonen). Sources for the parental melt parameters: liquidus based on Fo > 90 Al-in-olivine crystallisation temperatures for Etendeka picrites (Chapter 5); initial T is an illustrative example high T to demonstrate the effect of a superliquidus melt temperature; isobaric specific heat calculated on the basis of major element composition estimated for the Etendeka picrites parental melt (Thompson and Gibson, 2000) using the partial molar isobaric heat capacities listed by Spera and Bohrson (2001); crystallisation enthalpy estimated using equilibrium crystallisation model for the major element composition at 5 kbar with the MELTS model. Thermodynamic parameters represent the standard crustal values of Bohrson and Spera (2001) with additional modelling performed with initial temperatures compatible with active continental rift environment.

melt inclusions, and/or ii) whole-rock values relative to inclusions i.e. from accumulation or loss of phenocrysts, as implied by olivine Fo vs. whole-rock Mg# disequilibrium. The similarity between incompatible trace element compositions of inclusions and whole-rocks occurs despite olivine accumulation and the potential of trace element disturbances by primary contamination and secondary hydrothermal alteration. Olivine-hosted melt inclusions sample the near-liquidus magmatic liquid and it is concluded that in these samples, the whole-rock incompatible trace element chemistry is a good approximation of the original liquid composition, which represents the well-mixed average of primary fractional mantle melts which accumulated in near-Moho sills. However, major element chemistry systematics in melt inclusions are different to whole-rock samples due to post-entrapment processes.

3.5 Conclusion

The major and trace element compositions of 154 olivine-hosted melt inclusions have been analysed from primitive magmas (picrites and ferropicrites) from the Paraná-Etendeka and Karoo CFB provinces. These melt inclusions were crystalline prior to re-homogenisation and their major element compositions have been altered by the rehomogenisation process, such that the compositions are difficult to account for. In contrast, incompatible trace element compositions of melt inclusions mirror

whole-rock compositions and small systematic variations reflect dilution processes, resulting from the addition or subtraction of olivine into the melt inclusion during homogenisation. This implies that whole-rock analyses for similar older, fully crystalline rocks can still provide a meaningful approximation of the initial liquid chemistry. The trace element compositions are not affected by crustal assimilation and only a small subset are affected by hydrothermal alteration (i.e. they were breached prior to rehomogenisation). Discounting hydrothermally altered melt inclusions, the trace element compositions of the trapped melts are surprisingly homogeneous relative to the variability seen in olivine-hosted melt inclusions from primitive melts in Iceland and other ridge samples.

This homogeneity, even when hosted in very high Fo olivine, shows that primitive melts from which olivine crystallised were already well mixed with respect to their source fractional melts by the onset of olivine crystallisation. In Iceland, primitive mantle melts, which are initially heterogeneous, mix concurrently with crystallisation (Maclennan, 2008a); such a process is not observed in samples from this study, where mixing has reached near-completion prior to the onset of crystallisation. Disregarding inclusions showing signs of crustal assimilation or hydrothermal alteration, high degrees of melt inclusion homogeneity are also observed globally in datasets from other CFB province and some OIB settings (Hawaii, Galápagos, Samoa). These settings are characterised by moderately thick lithosphere, which restrict adiabatic decompression melting to higher pressures, producing hot, high MgO melts that rise through the lithosphere over a large depth interval. This could result in a liquidus temperature overstep, meaning that the melts have significant time to convectively mix prior to inclusion entrapment in liquidus olivine. In contrast, melts in Iceland and mid-ocean ridges pond in sills at pressures closer to that of their mantle melting region, resulting in a smaller liquidus temperature overstep and less extensive mixing and trace element homogenisation prior to crystallisation. The increased melt flux in CFB settings and differences in melt physical properties may also play a role in promoting early mixing.

It is often thought that flood basalts homogenise during the extensive fractionation and assimilation processes that take place in crustal sills (e.g. Cox, 1980; Morrison *et al.*, 1985). The Etendeka picrite samples derive from the same mantle plume source as the more voluminous evolved Paraná-Etendeka CFB, and are probably closely related. The olivine-hosted melt inclusions in the picrites are homogeneous, and as such, the incremental mantle melts which were ultimately parental to the Etendeka CFB would also have been well mixed prior to undergoing extensive fractionation and assimilation, which leads to the final emplaced CFB compositions. Any observed chemical heterogeneity in CFB provinces must be accounted for by subsequent fractionation and assimilation of country rock in crustal magma reservoirs. Exceptions to this are the primitive ferropicrites, which form from melting of mantle pyroxenite, and alkaline magmas from small fraction melting of the lithospheric mantle (e.g. Gibson *et al.*, 2006).

This chapter demonstrates that the Etendeka and Karoo primitive melts used in this thesis represent well mixed mantle melts. In chapters 4 and 6, their major and trace element compositions are modelled accordingly.

Chapter 4

Understanding the origin of mantle melts: A major element approach

Collaborative work declaration

The first half of this chapter discusses a new thermodynamic model for mantle melting in the system NCFMASOCr, which includes a new melt model and the addition of Cr and ferric iron end-members to solid phases. The model development was done by Tim Holland, where I was involved in testing, making adjustments to some activity-composition relationships, and using the model to make observations on mantle melting. This work is published (Jennings and Holland, 2015) and parts of this chapter are taken verbatim from this paper. Because of Tim Holland's role in developing the model, this chapter is restricted to a brief summary of the model development followed by a more detailed discussion of the application of the model to peridotite melting, pyroxenite melting, and an investigation into the origin of ferropicrite compositions from a major element perspective.

4.1 Introduction

The coexistence of both picrite and ferropicrite, two primitive melts with rather different major element compositions, is strong evidence for lithological heterogeneity in the mantle source of CFB provinces. Although the unusual major element composition of ferropicrite is its most conspicuous feature, it is also the most difficult to interpret, hampering a clearer understanding of the nature and origin of exotic lithologies in the mantle.

Many experimental studies have been performed on pyroxenite melting, although none have produced a ferropicrite-like melt (Keshav *et al.*, 2004; Kogiso *et al.*, 1998; Kogiso and Hirschmann, 2006; Kogiso *et al.*, 2003; Lambart *et al.*, 2009; Mallik and Dasgupta, 2012; Takahashi and Nakajima, 2002; Yaxley and Green, 1998). Although these experiments are performed on a wide range

of bulk pyroxenite compositions, they are usually performed at < 3 GPa. This reflects the motivation of these studies, which is to understand the major element characteristics of OIBs, as well as the increased technical difficulty associated with performing higher pressure experiments. Primary ferropicrite is high in MgO and is thought to derive from pressures deeper than those of relevance to most OIB petrogenesis (Gibson, 2002; Tuff *et al.*, 2005). The experimental partial melt with a composition most similar to Etendeka ferropicrite sample 97SB63 was from a 5 GPa experiment on a silica-undersaturated pyroxenite (B-ECL1-OL) by Kogiso and Hirschmann (2006) (determined using the method and partial melt database of Shorttle and Maclennan, 2011). However, experiments on composition MIX1G (an intermediate composition from the array of lithospheric mantle pyroxenites; Hirschmann *et al.*, 2003) at 5 GPa by Kogiso *et al.* (2003) did not produce a ferropicritic melt. This may be because the bulk composition has particularly high Al_2O_3 and CaO and low MgO compared to that used in many other studies, as discussed by Tuff *et al.* (2005). Experiments only determine equilibrium melt compositions at fixed pressure P, temperature T and composition X. Because mantle melting is fractional and primitive melts are thought to be mixed accumulated melts, a more flexible modelling approach is required to investigate the major element composition of the ferropicrites.

Perhaps counterintuitively, the major element melt composition of mantle-derived melts is more difficult to model than the trace element composition; major element oxides are abundant and so control mantle phase equilibria, rather than passively tracing it. In order to predict mantle melt compositions, there are two options: 1) to use a thermodynamic model, where the source major element composition is used to predict phase equilibria at given PT conditions, or 2) apply empirical relationships between melt compositions and pressure for a generic mantle composition. Both approaches are anchored in experimental data, and both have strengths and weaknesses.

Empirical relationships derived from parametrisations of the many experimental melting studies performed on peridotite can be very effective for interpolating between experimental conditions, and so converting experimental results into a useful tool for exploring the origin of basalts. Examples include: i) the eight component parametrisation of Kinzler and Grove (1992) and its updates, given separately for plagioclase, spinel and garnet lherzolites (Grove *et al.*, 2013; Till *et al.*, 2012); and ii) the CMAS parametrisation of Herzberg and O'Hara (2002), with its various updated forms and software (e.g. Herzberg, 2006; Herzberg and Asimow, 2008). Results from the Till *et al.* (2012) and Grove *et al.* (2013) parametrisations are included for comparison in some plots of this chapter.

Thermodynamic approaches are more flexible and allow the effects of compositional variation to be interrogated. The most commonly applied existing approach is to use pMELTS, part of the MELTS family of thermodynamic models, which is optimised for mantle melting conditions (Ghiorso *et al.*, 2002). pMELTS/MELTS is flexible, convenient and frequently used to examine crystallisation as well as melting. However, it suffers some limitations which mean that it cannot yet be used to explore melting of enriched olivine-poor compositions, cannot be used above 40 kbar, and does not reproduce

low fraction melt compositions well. Results from pMELTS are shown in some plots of this chapter for comparison. The strengths and weaknesses of pMELTS are reviewed elsewhere (Ghiorso *et al.*, 2002; Jennings and Holland, 2015). Most recently, a thermodynamic model was published for spinel lherzolite melting in the FCMASO subsystem by Ueki and Iwamori (2014), which appears moderately effective but is not tested in this chapter.

In this chapter, a new thermodynamic model in the system NCFMASOCr is used (Jennings and Holland, 2015) and calculations are performed in THERMOCALC, a program more commonly applied to metamorphic systems that determines equilibrium phase stability by solving sets of non-linear equations (Powell *et al.*, 1998; as opposed to free energy minimisation as used by MELTS, Ghiorso and Sack, 1995). The model is validated throughout by comparison with experimental data. The currently available methods described above predict peridotite partial melts well, but are generally not flexible in terms of source lithology and are not applicable to pyroxenite melting, particularly if the pyroxenite is olivine-free. The present model seeks to provide a more flexible approach to understanding the control of mantle PTX on partial melt composition, and is ultimately used to test the working hypothesis that picrite and ferropicrite derive from different mantle source lithologies.

4.2 A thermodynamic melting model for the mantle in the system NCFMASOCr

The model consists of a set of thermodynamic parameters of end-members for various phases and a set of activity-composition relationships that describe the mixing behaviour of those end-members. The model is in the 8 component system NCFMASOCr, which should be complex enough to begin to approximate natural systems. The development of the model, outlined below, is described in detail in Jennings and Holland (2015), along with a complete list of values for the end-member thermodynamic properties and mixing parameters.

Solid phases are built upon the self-consistent thermodynamic dataset of Holland and Powell (2011). Garnet, pyroxene and spinel models appropriate to mantle pressures in the NCFMAS system are from Holland *et al.* (2013). Cr and Fe^{3+} were added to the model specifically to constrain realistic spinel and garnet stability fields in the mantle. For this, new end-member properties and mixing models were required. Fe^{3+} and Cr-bearing garnet end-members from Holland and Powell (2011) were used. The garnet mixing model is an extension of that of Holland *et al.* (2013). Pyroxene Cr and Fe^{3+} end-member properties and mixing relationships are poorly constrained. They were derived by the method of Powell *et al.* (2014) and a simultaneous consideration of the natural mineral compositions of Canil *et al.* (1994) and Woodland (2009), and a requirement to match the position of the peridotite opx-boundary to that of Walter (1998). Spinel was modelled after Bryndzia and Wood (1990), who assume random mixing of cations across all cation sites.

A new model for a melt phase is used, which is specifically calibrated for basaltic liquids. It is an extension of the simple model of Holland and Powell (2001) to basaltic compositions by using eight end-members which cover the NCFMASOCr system. The liquid model describes melts in terms of pseudo-sites (much like a solid phase), which incorporates end-members in a simple hypothetical structure composed of octahedral-like melt sites (M) set in a largely aluminosilicate framework (F) with additional larger cation sites (A). The number and occupancy of sites vary with composition; the structure of the liquid model is described fully in Jennings and Holland (2015). The model was developed by setting approximate interaction properties to six end-members in NCFMAS from the Holland and Powell (2001) dataset, and refining the interaction parameters and end-member enthalpies using Monte Carlo simulations to match the solidus temperature and melt compositions within certain bounds of KLB-1 fertile peridotite (after Takahashi *et al.*, 1993 and Davis *et al.*, 2011). Some parameters were assigned small pressure dependencies. Addition of Cr and Fe^{3+} was achieved with two additional end-members (assuming ideal mixing of these components). The haematite end-member was constrained using the calibration of Kress and Carmichael (1991) of the equilibrium expression 4 hm + q = 2 fa + O_2 (all melt components), which required a small enthalpy adjustment. Cr was approximately adjusted to match KLB-1 melting experiments. Finally, Fe and Mg were adjusted for a better fit to known olivine-liquid partitioning behaviour.

4.3 Application to peridotites: validation and observations

This section demonstrates the validity of the model by comparing it with experimental data, and uses it to make original observations about peridotite subsolidus and melting phenomena. The following examples take the bulk composition of KLB-1 (Davis *et al.*, 2009) with 0.3 wt.% Fe_2O_3 ($Fe^{3+}/\sum Fe$ = 0.033 and the appropriate adjustment to FeO), as representative of fertile upper mantle peridotite. 0.3 wt.% Fe_2O_3 was chosen on the basis of peridotite xenolith data presented by Canil *et al.* (1994), who report values in the range 0.1–0.4 wt.%. The phase diagram for mantle peridotite calculated for KLB-1 is given in Fig. 4.1. When bulk compositions KR4003 and MM-3 are considered, the respective compositions of Walter (1998) and Falloon *et al.* (2008) are used with 0.3 wt.% Fe_2O_3. Calculations for the same bulk compositions are also performed in pMELTS (Ghiorso *et al.*, 2002) using the alphaMELTS software (Smith and Asimow, 2005, input files given in appendix B), and using the melt composition parametrisation of Till *et al.* (2012) and Grove *et al.* (2013) for comparison.

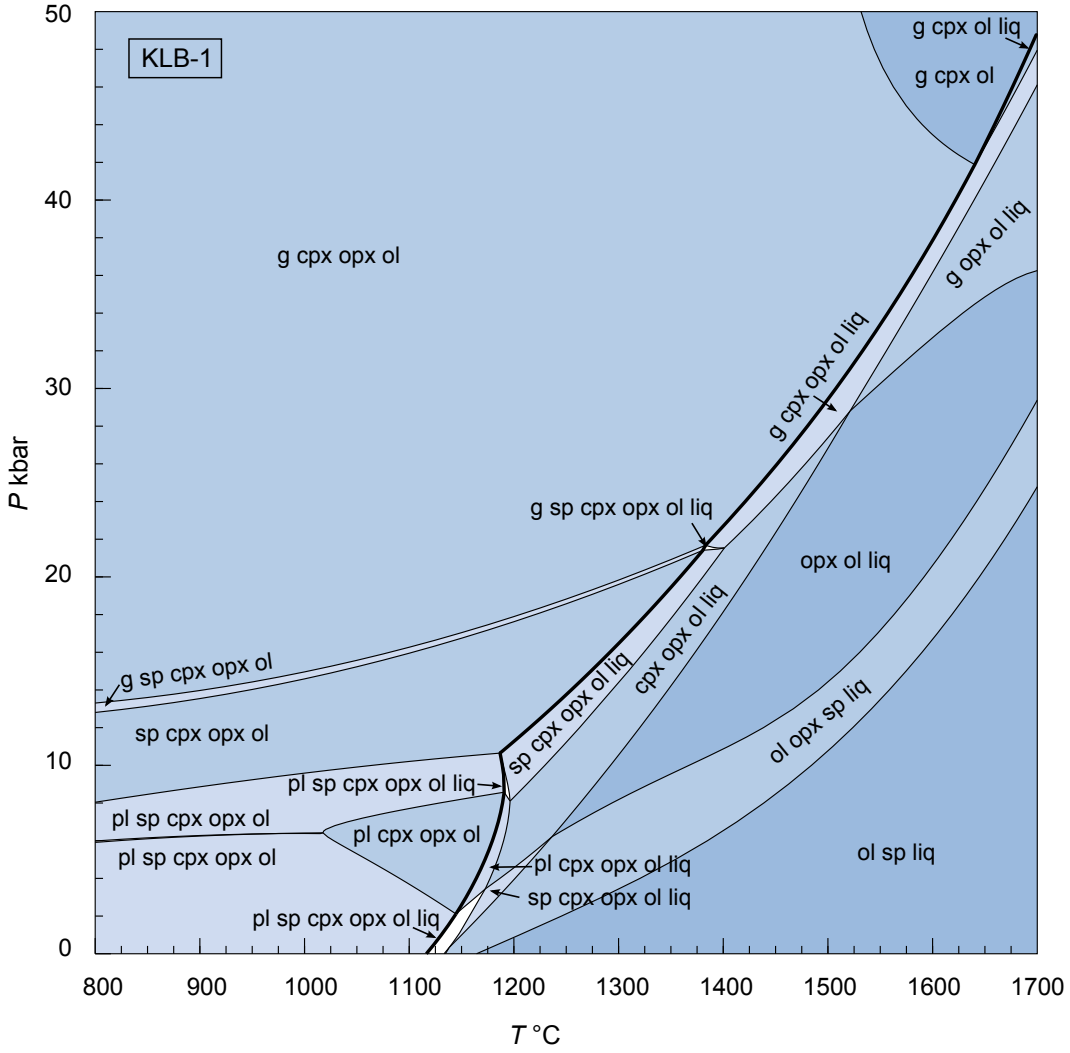

Figure 4.1: *PT* pseudosection calculated for KLB-1 in the NCFMASOCr system. Phases: g, garnet; sp, spinel; pl, plagioclase; ol, olivine; cpx, clinopyroxene; opx, orthopyroxene; liq, liquid. Lines denote phase boundaries, the thick line indicates the solidus (liq-out). Progressively darker fields indicate increasing variance, so decreasing number of phases. At subsolidus conditions, Cr-rich and Al-rich spinel are separated by a miscibility gap, where Cr-rich spinel occurs at lower pressures. At increasing temperatures, Al-rich spinel is lost in a melting assemblage, and re-appears as Cr-rich spinel in low modal proportion (< 0.01) in the high melt fraction assemblages (ol opx sp liq) and (ol sp liq), which may be an artifact of the simplified melt model.

4.3.1 Solidus phase relationships

Pressure of the spinel to garnet transition

With the present model, the spinel to garnet transition in KLB-1 peridotite is at somewhat lower pressure on the solidus than previously thought, i.e. the transition occurs at shallower depths, at around 22 kbar, where the pressure interval over which the transition occurs is also small (< 1 kbar; Fig. 4.1). This result is consistent with experimental studies in the system MAS (e.g. Gasparik and

Newton, 1984) extended to the more complex system, and is inconsistent with those performed on natural samples (Robinson and Wood, 1998; see discussion in Green *et al.*, 2012 and Jennings and Holland, 2015). The effects of variable Fe^{3+} and Cr on this transition in terms of position and width are shown in the *PX* pseudosections at 1100 °C and 1400 °C (Fig. 4.2). At 1100 °C (Fig. 4.2a, b) the spinel-garnet field is extremely narrow at the composition of KLB-1, but widens significantly as the amount of Fe^{3+} and Cr increases. The pressure at which garnet appears is almost independent of Cr content (Fig. 4.2a), whereas garnet-in moves to higher pressures with increasing Fe^{3+} content (Fig. 4.2b). The spinel-out boundary is sensitive to both increasing Cr and Fe^{3+}, with the transition becoming over 10 kbar wide at high Cr contents (Fig. 4.2a).

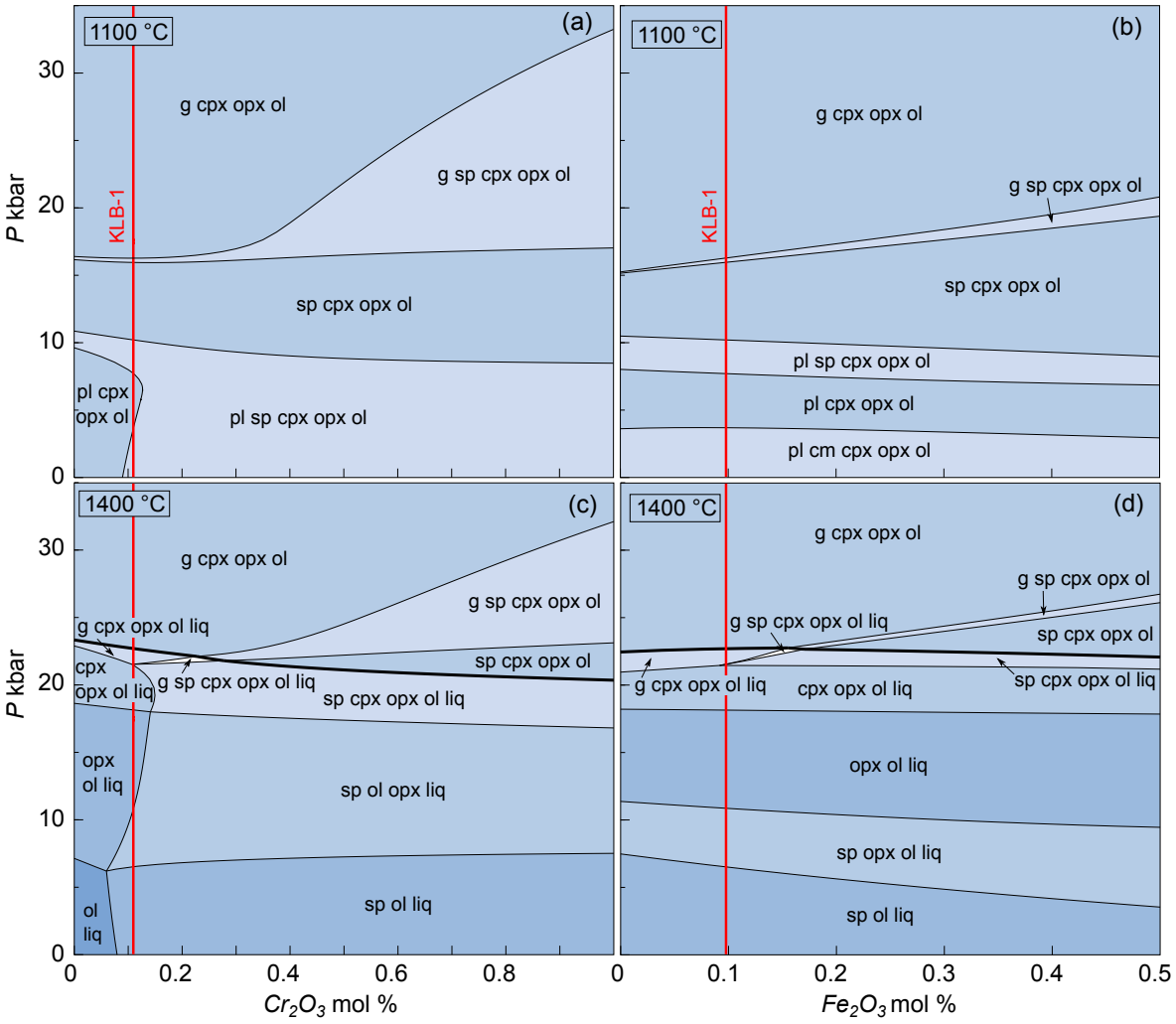

Figure 4.2: *PX* pseudosections for KLB-1 showing the effect of varying the molar proportions of Cr_2O_3 and Fe_2O_3 in the bulk composition on phase equilibria in isothermal sections. Red lines indicate the molar proportion of the oxide used in the KLB-1 composition. Thick black lines are the solidus, phase labels as in Fig. 4.1. (a) varied Cr_2O_3, 1100 °C, (b) varied Fe_2O_3, 1100 °C, (c) varied Cr_2O_3, 1400 °C, (d) varied Fe_2O_3, 1400 °C. Both oxides have the effect of stabilising spinel at higher pressures. Note that the x-axis range in (b) and (d) is half that of (a) and (c).

At 1400 °C, the spinel–garnet transition is of negligible width for the published Cr content of KLB-1 but widens to higher values with increasing Cr (Fig. 4.2c). Increasing Fe^{3+} contents move the transition zone to higher pressures, as at 1100 °C, but the zone remains rather narrow at all Fe^{3+} contents (Fig. 4.2d). Through thermodynamic analysis of experiments in the MASCr system, Klemme (2004) predicts a similar widening of the transition zone with increased Cr content, caused predominantly by the increasing stability of spinel at higher pressures. The pMELTS model shows a stronger effect of bulk Cr_2O_3 on garnet-in than this study (see also Smith and Asimow, 2005): for the KLB-1 bulk composition, pMELTS matches the calculated garnet-in pressure well (21.5-22 kbar on the solidus), whereas for a doubled Cr_2O_3 content, the boundary shifts to 24-24.5 kbar. pMELTS predicts spinel stability over a far wider pressure range for KLB-1 than this study, reflecting the absence of any host other than spinel for Cr_2O_3 in the pMELTS model.

Chromium in spinel

Isopleths of Cr in spinel in *PT* space (Fig. 4.3a) show that Cr in spinel is highly pressure sensitive when plagioclase is present in the assemblage and highly insensitive when plagioclase is absent, indicating its potential as a low pressure barometer for plagioclase spinel lherzolites. The convergence of X_{Cr} isopleths at 6 kbar highlights the presence of a miscibility gap between Cr-rich spinel at low pressure and Cr-poor spinel at high pressure also shown in Fig. 4.1, although at this pressure the spinel mode is negligible.

Aluminium in orthopyroxene

Fig. 4.3(b) shows the calculated isopleths for Al in orthopyroxene in the garnet, spinel, and plagioclase fields KLB-1 composition. Isopleths are very steep in the spinel field and have modest positive slopes in the garnet field, as is known from experimental studies (e.g. Perkins III and Newton, 1980). More surprising is the flat negative slope of isopleths in the plagioclase field (as noted by Gasparik and Newton, 1984), providing a potential barometer for low pressure peridotites. However, it is important to note that these isopleths are affected by the amounts of Fe^{3+} and Cr in the pyroxene M1 sites. Sample 313-106 from Vitim (Siberia) has a bulk composition close to KLB-1 (Ionov, 2004) and contains orthopyroxene with 0.18 Al on a 6-oxygen formula basis. Assuming that this is evenly divided between the T and M1 sites, a value of X_{Al}, opx(M1) of 0.09 on Fig. 4.3(b) corresponds extremely closely with published barometry and thermometry of 21–23 kbar and 950–1050 °C for the garnet peridotite samples (Ionov, 2004).

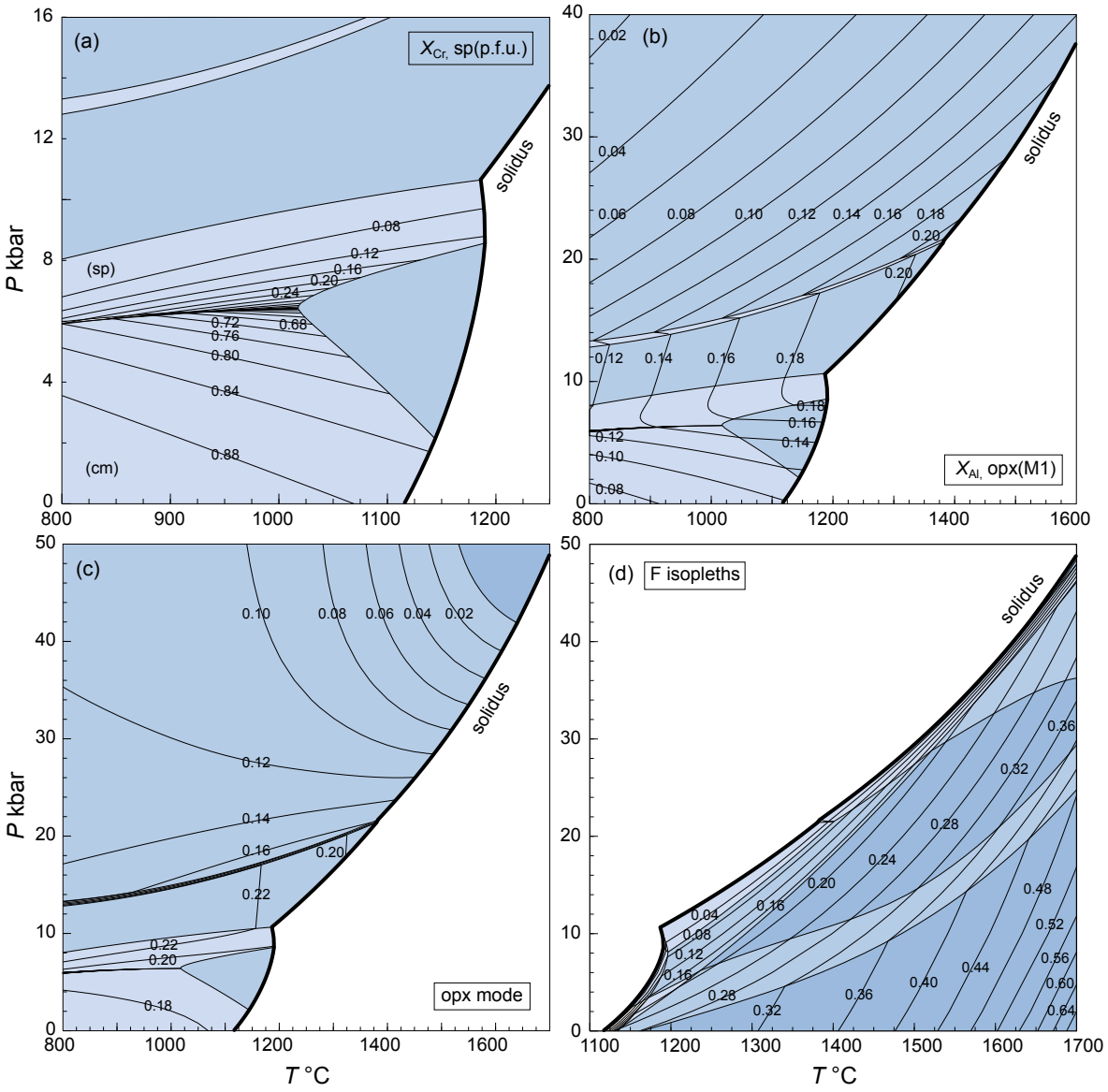

Figure 4.3: Isopleths of constant modes or phase compositions in *PT* space, calculated for KLB-1. Phase fields correspond to those in Fig. 4.1. (a) Molar proportion of Cr in spinel, per formula unit (p.f.u.). Two sets of isopleths appear to intersect at around 6 kbar, highlighting a narrow miscibility gap where Cr-rich and Al-rich spinel compositions can coexist. (b) Molar proportion of Al in the opx M1 site. (c) Modal proportion of opx. (d) Modal proportion of liquid (melt fraction, F). Note that the x- and y-axis ranges differ for each plot.

Disappearance of orthopyroxene at high temperatures

The pressure at which orthopyroxene disappears from the solidus in experimental studies is controversial (e.g. Canil, 1992; Herzberg *et al.*, 1990; Takahashi, 1986; Walter, 1998; Zhang and Herzberg, 1994). In Fig. 4.1 the calculated orthopyroxene-out boundary meets the solidus at 42 kbar and 1647 °C, in good agreement with the experiments of Zhang and Herzberg (1994) and Walter (1998). The modal proportion of orthopyroxene in KLB-1 is illustrated in Fig. 4.3(c), where it decreases rapidly

with increasing P and T in garnet-bearing assemblages. In a previous thermodynamic study (Holland *et al.*, 2013) it was shown that this boundary is highly sensitive to bulk composition, helping to explain the variation seen in experimental studies. The highest modal proportion of orthopyroxene occurs in the spinel lherzolite field, decreasing up-pressure in the garnet field and down-pressure in the plagioclase field.

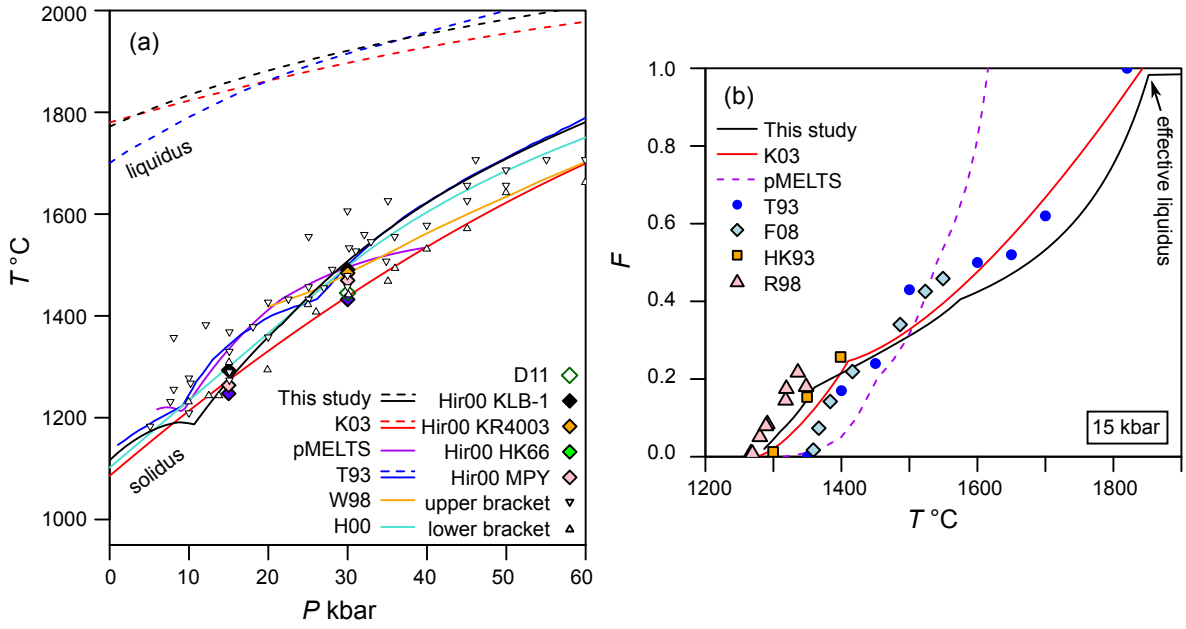

Figure 4.4: (a) Solidus (solid lines) and liquidus (dashed lines) temperature as a function of pressure, calculated in this study for KLB-1 and shown with experimental data and other parametrisations for comparison. Abbreviations: K03, Katz *et al.* (2003); pMELTS, KLB-1 in the system NCFMASOCrTi calculated in pMELTS; T93, KLB-1, Takahashi *et al.* (1993); W98, KR4003, Walter (1998); H00, KLB-1, Herzberg *et al.* (2000); D11, KLB-1, Davis *et al.* (2011). Hir00 indicates solidus position calculated by Hirschmann (2000) for given bulk compositions. Upper bracket and lower bracket are experimental data points which bracket the solidus position from the compilation of post-1988 experiments of Hirschmann (2000). There is good agreement between this study and others. (b) Isobaric melt fraction (F) as a function of temperature at 15 kbar calculated in this study for KLB-1 and shown with experimental data and other parametrisations for comparison. Additional abbreviations: F08, MM-3, Falloon *et al.* (2008) and references therein; HK93, KLB-1, Hirose and Kushiro (1993) recalculated by Hirschmann (2000); R98, MPY, Robinson *et al.* (1998). The cusp at around $F = 0.2$ seen in the three lines (this study, K03 and pMELTS) is caused by the exhaustion of clinopyroxene, and the cusp at $F = 0.4$ in this study is from the exhaustion of orthopyroxene. 'Effective liquidus' is the olivine-out boundary in this study, beyond which a small mode ($\sim 1\%$) of spinel persists to high temperatures; this behaviour is probably a model artifact.

4.3.2 Peridotite melting

The onset and productivity of melting

The calculated solidus across the pressure range of Fig. 4.4(a) shows excellent agreement with experimental data and published parametrisations. This is expected, as the liquid model is calibrated so that the onset of melting is bracketed by the experiments of Takahashi *et al.* (1993). The cusp in the solidus of this study and the pMELTS calculation at 10 kbar is caused by an increased albite content of plagioclase, and therefore an increased fusibility of plagioclase just before the plagioclase-out pressure is reached; this geochemical feature is also observed experimentally by Borghini *et al.* (2010) and its effect on the solidus is also predicted by the pHMELTS model (e.g. Smith and Asimow, 2005).

Unlike the solidus temperature, the temperature of the liquidus (Fig. 4.4a) and that of intermediate melt fractions (Fig. 4.4b) are not used in the liquid model calibration. It is encouraging to see that both of these properties predicted by this model match published experimental parametrisations well. In particular, Fig. 4.4(b) shows a cusp in melt productivity at around 20% melt. This change in melt productivity is a result of cpx exhaustion, i.e. the lherzolite to harzburgite transition, and both the position of the cusp and the slope of the curve on either side match the parametrisation of Katz *et al.* (2003) well. The fit is less good at high melt fractions. At 1750 °C, the melt fraction predicted in this study is 0.16 lower than that predicted by Katz *et al.* (2003), and looks lower than that expected by interpolating between the experimental observations of Takahashi *et al.* (1993). This is a result of the higher liquidus temperature in this study, which in turn may reflect the lack of K_2O and volatile phases in the system, which is not the case for natural samples. The 'effective liquidus' of Fig. 4.4(b) is the point at which olivine is lost from the assemblage; a small fraction (<1%) of spinel persists in the melt to higher temperatures, indicating a possible model shortcoming at liquidus temperatures.

Fig. 4.3(d) shows that melt isopleths are compressed at higher pressure, i.e. higher melt fractions are reached over a smaller temperature increase. This feature is also predicted in the Katz *et al.* (2003) parametrisation. Greater melt productivity at higher pressures in the mantle reduces the requirement for fusible recycled material to be present in order to account for excess crustal thickness observed at the surface at some hot spots (cf. Foulger and Anderson, 2005).

Mineral modes along the solidus

Mineral modes calculated along the solidus for KLB-1 are shown in Fig. 4.5. They are in good agreement with experimental data for lherzolite; modes at the KLB-1 solidus at 30 kbar determined by Davis *et al.* (2011) are shown for comparison. There is general agreement with the pMELTS model, except in the pyroxenes and in the persistence of spinel to high pressure (Fig. 4.5; see also Smith and Asimow, 2005). The garnet–spinel transition occurs over a narrow pressure range, with the two

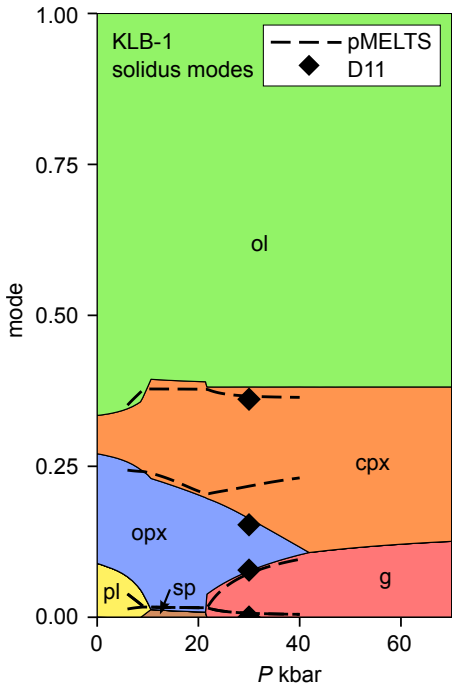

Figure 4.5: A modebox diagram for KLB-1 bulk composition at pressures along the solidus, showing modal phase proportions (normalised molar) as a function of pressure. Phase labels as for Fig. 4.1. Although Fig. 4.1 indicates the presence of Cr-rich spinel on the solidus at 0–2.2 kbar, it can be seen here that its modal proportion is negligible. Diamonds show experimentally determined modes at 30 kbar on the KLB-1 from Davis *et al.* (2011). Dashed lines are the same mode boundaries calculated along the solidus of KLB-1 in pMELTS in the system NCFMASOCrTi, which are in general agreement with the model presented here except for the clinopyroxene:orthopyroxene ratio in garnet-bearing assemblages.

phases coexisting at the solidus at 21.4-21.7 kbar; the position and the width is sensitive to bulk Cr_2O_3 and Fe_2O_3. Fig. 4.5 shows that the spinel to garnet transition consumes significant orthopyroxene, some clinopyroxene, and precipitates some olivine. The orthopyroxene mode decreases with pressure along the solidus, disappearing completely at 42 kbar. At elevated T_P, where the adiabat intersects the solidus at greater than 42 kbar, the melting assemblage would be orthopyroxene-free.

Melt composition

It is important to model the 0% melt fraction composition well, as it represents the composition of melts at the onset of melting for fractional melting of the mantle. If these melt compositions also hold true at somewhat more depleted bulk compositions, this melting model can effectively be used to model a realistic fractional melting scenario. With this in mind, the model 0% melt fraction composition for KLB-1 is compared with those determined experimentally by Falloon *et al.* (2008), for MM-3, and Herzberg and Zhang (1996) and Davis *et al.* (2011), for KLB-1 (Fig. 4.6a). Falloon *et al.* (2008) and Davis *et al.* (2011) employ iterative techniques to constrain the putative melt composition, whereas Herzberg and Zhang (1996) make use of the experimental temperature gradient and apply crystal/liquid partition coefficients in conjunction with an assumed SiO_2 content to calculate liquid composition. The 30 kbar composition of Davis *et al.* (2011) was, in part, used in the model calibration. Even so, the fit to all points in Fig. 4.6 is very good, and demonstrates the effectiveness of the model in interpolating between the fixed *PT* conditions of individual experiments, making them applicable to a wide range of mantle *PT* conditions. For comparison, Fig. 4.6(b) and 4.6(c) show the

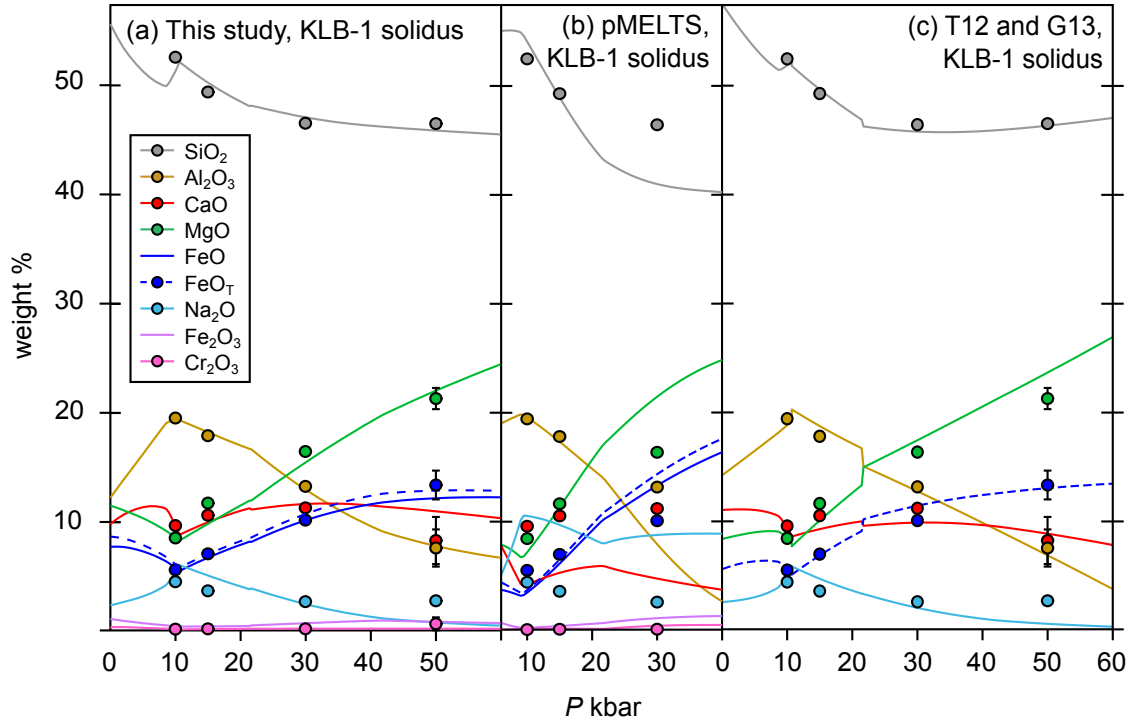

Figure 4.6: Calculated composition in weight % oxide of melts of KLB-1 along the solidus (i.e. for a nominal zero melt mole fraction) as a function of pressure. Filled circles are experimental zero melt fraction compositions: 10 kbar and 15 kbar points from bulk composition MM-3, Falloon *et al.* (2008) and references therein; 30 kbar points from KLB-1, Davis *et al.* (2011), error bars smaller than symbol; 50 kbar points from KLB-1, Herzberg and Zhang (1996), published uncertainties shown, except for Na_2O, which has a high uncertainty. FeO_T denotes total Fe reported as FeO. Experimental Fe is given as FeO_T only, as $Fe^{3+}/\Sigma Fe$ is unknown. For ease of comparison, model results in (a) and (b) are given both as (i) FeO and Fe_2O_3 individually (solid lines) and (ii) recalculated as FeO_T (dashed line). (a) KLB-1 bulk composition, melts at $F = 0$, this study. MM-3 and KLB-1 have similar compositions, resulting in a good model fit to both. (b) KLB-1 bulk composition in NCFCMASOCrTi, melts at F = 0.005, calculated in pMELTS. (c) T12 (Till *et al.*, 2012, plagioclase and spinel lherzolite models for $P < 20.7$ kbar) and G13 (Grove et al., 2013, garnet lherzolite model for $P > 20.7$ kbar). Steps in the curves result from three models being used for the different lithologies, where the compositions at phase boundaries from two models do not perfectly match. For the calculation, some melt chemical components must be known, such as Mg#, NaK#, K_2O, TiO_2 or P_2O_5. Mg# and NaK# are taken from the present model output at $F = 0$ (i.e. (a)); K_2O = 0.01, TiO_2 = 0.85 and P_2O_5 = 0. For this reason, the good fit in some elements is a result of combining the model of this study with T12 and G13 and is not independently predicted.

predicted KLB-1 solidus liquid composition of pMELTS, Till *et al.* (2012) and Grove *et al.* (2013). pMELTS does not predict this very low melt fraction well, particularly in terms of CaO and at high pressure. The Till *et al.* (2012) and Grove *et al.* (2013) parametrisations do a very good job, although in order to calculate these compositions, Mg# and NaK# were required from the THERMOCALC output, so the good fit is not entirely independently predicted.

Noteworthy features of Fig. 4.6 include the cusps in compositions at 10 kbar (at the plagioclase-spinel transition), and the Na_2O content of the melt, which decreases with increasing pressure (the

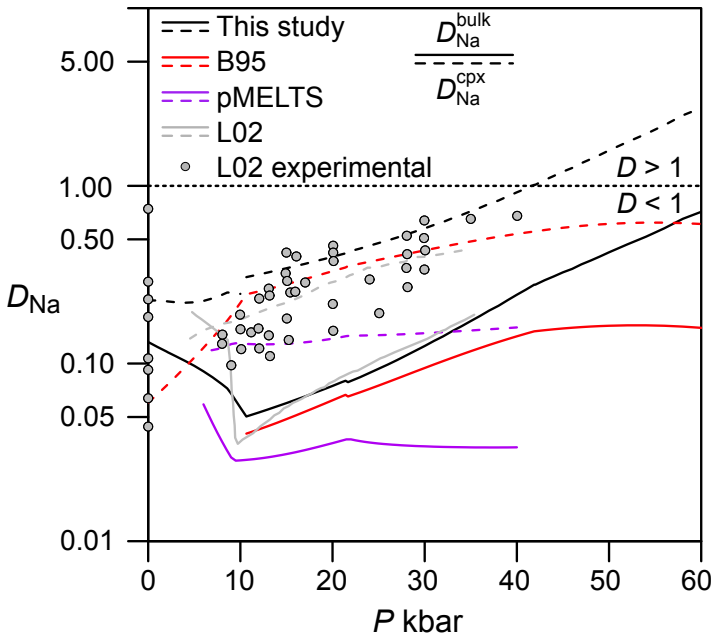

Figure 4.7: Effective D_{Na}^{cpx} (dashed lines) and bulk D_{Na}^{bulk} (solid lines) as a function of pressure along the solidus of KLB-1. Calculations are performed on KLB-1 for this study. Below 10 kbar, bulk D_{Na}^{bulk} is controlled by both plagioclase and cpx. B95; Blundy *et al.* (1995): D_{Na}^{cpx} calculated using P and T of the KLB-1 solidus of the present model. Bulk D_{Na}^{bulk} was calculated using modelled modal proportion of cpx from KLB-1 along the solidus, assuming Na is fully incompatible in all other phases. This assumption makes the model of this study and B95 comparable, and will result in an underestimated bulk D_{Na}^{bulk} in both. Above 40 kbar, the two models diverge and Na becomes compatible ($D > 1$) in cpx in the model of this study, but not in B95. Shown for comparison are the pMELTS solution along the KLB-1 solidus, and L02, the calculated values for DPUM $F = 0.01$ of Longhi (2002). Experimental data is a compilation of D_{Na}^{cpx} from L02.

uncertainty on the 50 kbar melt Na_2O of Herzberg and Zhang, 1996 is very large). Changes in Na_2O can be described by a pressure-dependent effective bulk partition coefficient (D_{Na}^{bulk}). The only solid phases in the presented simplified model which include Na-bearing end-members are plagioclase and cpx; therefore, above 10 kbar, cpx is the sole phase controlling melt Na_2O. It follows that D_{Na}^{cpx} must increase with increasing pressure, as proposed by Blundy *et al.* (1995). Fig. 4.7 shows the calculated bulk/liquid and cpx/liquid D_{Na} of this model, that of Blundy *et al.* (1995) and that of pMELTS, all calculated along the solidus of KLB-1. It is seen that the pressure dependence of both parameters in the present model is similar to those of Blundy *et al.* (1995), with both showing similar absolute values and a similar pressure dependence up to around 40 kbar, where they diverge. The pMELTS model has a weaker pressure dependence. The pressure dependence of D_{Na}^{cpx} in the present model results in melts with the highest alkali/silica ratio being produced at moderately low pressures and low melt fractions, specifically around the plagioclase–spinel transition (10 kbar). Understanding Na partitioning in peridotite is vital for investigating the origin of alkali basalts.

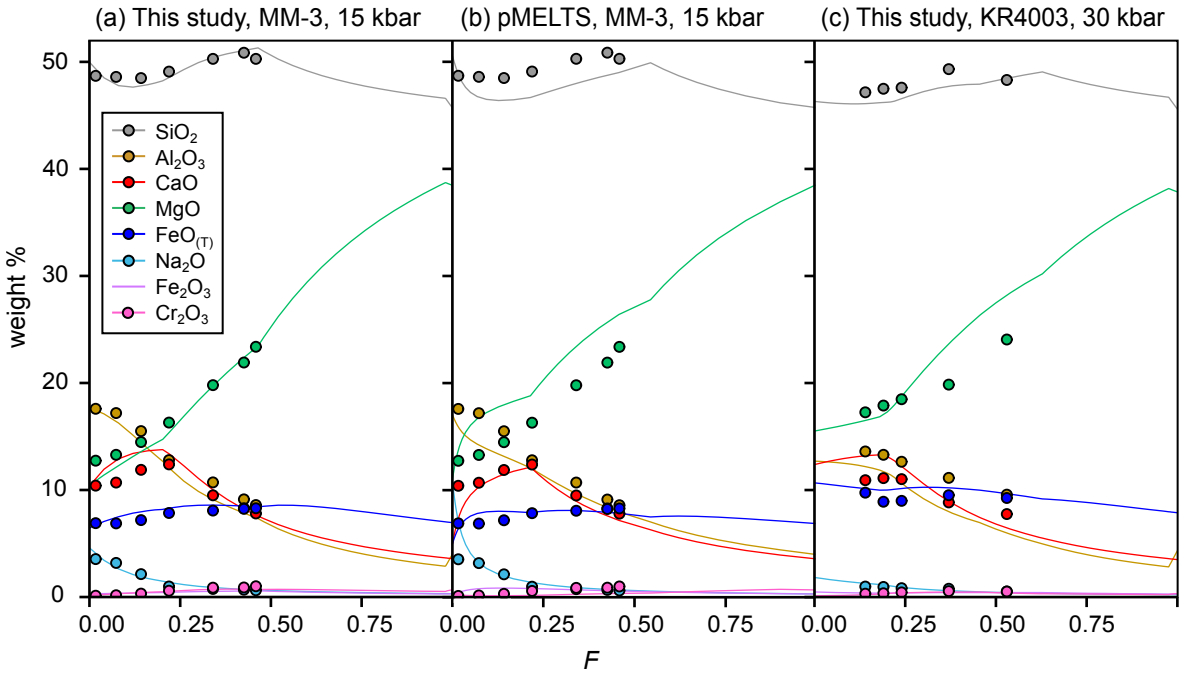

Figure 4.8: Calculated isobaric melt composition, for the bulk compositions (a) MM-3 (Falloon *et al.*, 2008) at 15 kbar, this study; (b) MM-3 at 15 kbar calculated in pMELTS in NCFCMASOCrTi (details of the calculation are given in appendix B), and (c) KR4003 at 30 kbar, this study. All plots show composition as a function of temperature (expressed as melt fraction F). Lines are calculated values, where each colour relates to a particular weight % oxide. For comparison, circles show the experimental melt compositions for MM-3 (Falloon *et al.*, 2008 and references therein), and KR4003 (Walter, 1998). The agreement with the experimental data for MM-3 is good, that with KR4003 slightly less so. In all cases, calculated FeO is FeO only, whereas experimental FeO is FeO_T, i.e. no allowance is made for Fe_2O_3 and no experimental Fe_2O_3 is reported.

The liquid model can be tested further by examining the compositions of higher fraction melts in relation to experimental studies. Fig. 4.8(a) shows isobaric melt composition (15 kbar) calculated at a range of temperatures (expressed as melt fraction F), for bulk composition MM-3. This involves a spinel-lherzolite solidus assemblage and is directly comparable with the study of Falloon *et al.* (2008). A good fit to the data is observed. Major inflections are caused by the exhaustion of cpx at around $F = 0.22$. The equivalent of Fig. 4.8(a) with calculations performed using pMELTS rather than the present model, also on MM-3 at 15 kbar, is shown in Fig. 4.8(b) for comparison. The fit to experiments is also close, except in MgO. At very low melt fraction the fit deteriorates, as is also indicated by Fig. 4.6(b). At 30 kbar (Fig. 4.8c; garnet-lherzolite solidus assemblage), the model melt composition at a range of melt fractions calculated for the bulk composition KR4003 is compared with those of Walter (1998). The fit is less close but still reasonable, more so at lower melt fractions, where the present model indicates perhaps a greater effect of cpx-out on the liquid composition. At low melt fraction there is an offset between modelled and experimentally determined CaO in the melt.

In summary, the liquid compositions predicted by this simple model are in good agreement with experimentally-produced liquids. The model is effective at low melt fractions, making it valuable for exploring fractional melting of the mantle, with application to the origin of basalt.

Olivine-liquid Fe-Mg partitioning along the solidus

$K_{D_{Fe\text{-}Mg}}^{ol\text{-}liq}$ was defined by Roeder and Emslie (1970) to characterise Fe–Mg exchange between olivine and liquid. Recent experiments and an evaluation of published data place the 1 atm $K_{D_{Fe\text{-}Mg}}^{ol\text{-}liq}$ at 0.34 for tholeiitic compositions (Matzen *et al.*, 2011), although the PT-dependence of this parameter is much less well constrained. Fig. 4.9 shows the $K_{D_{Fe\text{-}Mg}}^{ol\text{-}liq}$ of this model for KLB-1 calculated at the solidus (i.e. for a 0% melt fraction) and at a 12% melt fraction. Individual experimental data points and published composition-dependent parametrisations (using calculated melt compositions) are given for comparison. At the plagioclase-out boundary around 10 kbar, the solidus melt reaches an unusual composition (Fig. 4.6). The high Na_2O and Al_2O_3 in the melt affects $K_{D_{Fe\text{-}Mg}}^{ol\text{-}liq}$, albeit in an opposite sense to the published parametrisations of Herzberg and O'Hara (2002) and Toplis (2005). The 10 kbar 0% melt is Na- and Al- rich and Mg-poor, and may not be represented in the calibration range of these studies. The resulting cusps in the $K_{D_{Fe\text{-}Mg}}^{ol\text{-}liq}$–$P$ relationship vanish at higher melt fractions, where melt compositions vary more smoothly. At pressures below 40 kbar, the melt model agrees with experimental data and published parametrisations. Above this, the model $K_{D_{Fe\text{-}Mg}}^{ol\text{-}liq}$ values are too high, especially given that experimental evidence indicates $K_{D_{Fe\text{-}Mg}}^{ol\text{-}liq}$ plateauing (Herzberg and Zhang, 1996; Taura *et al.*, 1998) or even reducing (Mibe *et al.*, 2006) at higher pressures of up to 150 kbar.

4.3.3 Summary: Model predictions for peridotite melting

The presented model allows exploration of the phase equilibria and melting behaviour of mantle peridotite (in particular KLB-1 composition), and provides interesting observations that may not easily be accessible through experimental petrology or from natural samples. A miscibility gap between Al-rich and Cr-rich spinels has been identified at low temperature, in agreement with the observation that Cr-rich spinel is often found as the liquidus phase in primitive melts (low pressure), whereas Al-rich spinel is the stable phase found in spinel-bearing xenoliths (higher pressure). The model predicts that no mineral compositions are particularly pressure-sensitive in garnet-free spinel lherzolites (where there is no garnet or plagioclase to provide a density contrast with other silicates) illustrating the difficulty in finding a suitable barometer for spinel lherzolite xenoliths. The model also indicates that the spinel-garnet transition may be rather narrow in the mantle, and at lower pressures than suggested by previous studies; increasing bulk Cr and Fe^{3+} broadens the transition and shifts it to higher pressures. A cusp in solidus temperature is identified at the plagioclase-spinel transition, caused by

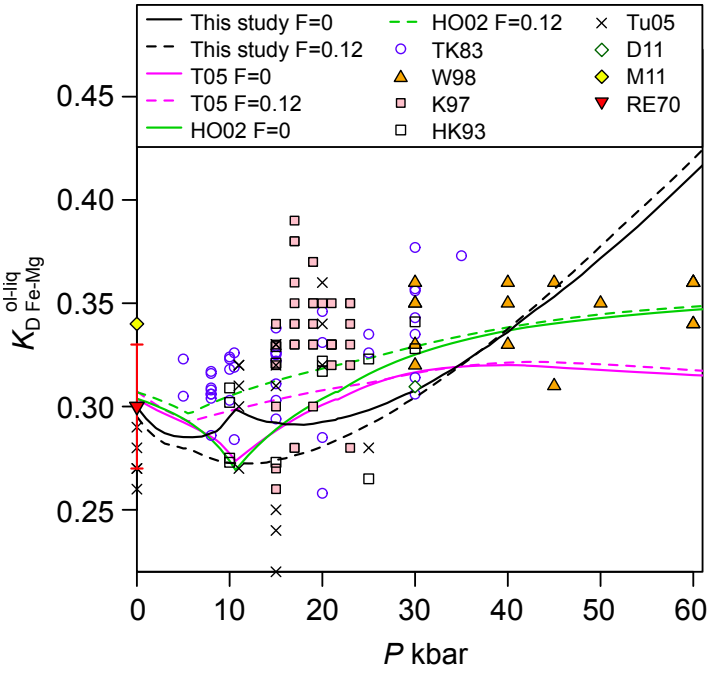

Figure 4.9: $K_{D_{Fe\text{-}Mg}}^{ol\text{-}liq}$ as a function of pressure. Solid lines are calculated along the KLB-1 solidus (a nominal zero melt fraction), dashed lines are calculated along a 12% melt fraction isopleth, black lines from this study. Points are experimental measured values. Experimental data point abbreviations: TK83, Takahashi and Kushiro (1983); W98, Walter (1998); K97, Kinzler (1997); HK93, Hirose and Kushiro (1993); Tu05, Tuff *et al.* (2005); D11, Davis *et al.* (2011); M11, Matzen *et al.* (2011); RE70, Roeder and Emslie (1970). All experiments are peridotite melting experiments, except Tu05, RE70 and M11, which are from basalt crystallisation. The range of ± 0.03 on the RE70 point is as suggested by Takahashi and Kushiro (1983). Lines for T05 and HO02 are calculated from the liquid compositions of this study at $F = 0$ (solidus) and 0.12 melt fraction from the expressions of T05, Toplis (2005) and HO02, Herzberg and O'Hara (2002). The downward inflection seen in T05 and HO02 $F = 0$ at 10 kbar reflects the unusual low fraction liquid composition close to the plagioclase-out boundary. A good agreement in $K_{D_{Fe\text{-}Mg}}^{ol\text{-}liq}$ is seen between this study and experimental points and previous formulations up to 40 kbar.

the increasing albite component of high pressure plagioclase. The model can also be used to explore fO_2 during melting (Jennings and Holland, 2015), which is not discussed in this chapter.

4.4 Application to other bulk compositions

4.4.1 Validation of liquid model with pyroxenite and eclogite bulk compositions

The liquid model is calibrated for basaltic melt compositions in equilibrium with peridotitic bulk compositions. It is not known whether the model is applicable for more Si-rich bulk compositions, i.e. pyroxenite and eclogite. The performance of the model for such compositions can be judged by its ability to reproduce experimental equilibrium partial melt compositions. Eclogite and pyroxenite are treated separately here, where eclogite is a high pressure basalt, which may contain quartz or

coesite, and pyroxenite is seen as a ultramafic composition with a low modal proportion of olivine, which is some eclogite-peridotite hybrid in terms of bulk composition (see Chapter 1 for a discussion of pyroxenite formation and composition).

Pyroxenite: KG1 composition

Like peridotite, pyroxenite has never been directly sampled in the convecting mantle. Different theoretical and experimental studies of pyroxenite melting have used different approaches to assign it a bulk composition. These include: selecting a measured pyroxenite whole-rock composition from the natural array of those sampled from ophiolites or xenoliths (Keshav *et al.*, 2004; Kogiso *et al.*, 2003; Lambart *et al.*, 2009); using a hypothetical composition (e.g. KG1 and KG2, which are blended mixes of KLB-1 peridotite and average MORB in 1:1 or 2:1 ratios respectively, Kogiso *et al.*, 1998, or a mix of an eclogite partial melt and peridotite, Mallik and Dasgupta, 2012); or sandwich layer experiments of eclogite wedged between two peridotite layers (Mallik and Dasgupta, 2012; Rosenthal *et al.*, 2014; Takahashi and Nakajima, 2002; Yaxley and Green, 1998), which show how melt composition evolves with progressive melt-rock reaction. These compositions vary greatly, making it difficult to compare between experiments. The implications of pyroxenite melting experiments were recently reviewed by Lambart *et al.* (2013).

For simplicity, the composition KG1 is used here to represent mantle pyroxenite, which falls somewhere in the middle of the experimental range. The bulk composition here is created by calculating a 1:1 mix of KLB-1 and the average N-MORB composition (after Gale *et al.*, 2013, with $Fe^{3+}/\Sigma Fe = 0.16$ after Cottrell and Kelley, 2011) and is very similar to the published bulk of Kogiso *et al.* (1998). It is unclear what this composition represents in reality; it could be some average composition in a melting region consisting of mixed eclogite and peridotite, or sheared slivers of eclogite that have equilibrated with surrounding peridotite.

In order to test the validity of the liquid model in this more Si-rich composition, the experiments of Kogiso *et al.* (1998) on KG1 are reproduced. To predict the liquid compositions at various PT conditions, the coexisting solid phase assemblage must first be constrained; the phase diagram in Fig. 4.10 is constructed for guidance in calculating the isobaric compositions of partial melts of KG1 over a range of temperatures, shown in Fig. 4.11. A moderate temperature offset of 20–60 °C is observed between the KG1 melting experiments of Kogiso *et al.* (1998) and the calculated melts for a given melt fraction F. This could indicate a model shortcoming, or alternatively reflect to the difficulty in accurately measuring experimental T (or F). The compositions of partial melts are expressed as a function of F for clearer comparison in Fig. 4.11. The model melt compositions show the same trends with pressure and melt fraction as the experimental melt compositions for all elements. The highest pressure (30 kbar) experimental and modelled melts are higher in FeO and MgO and lower

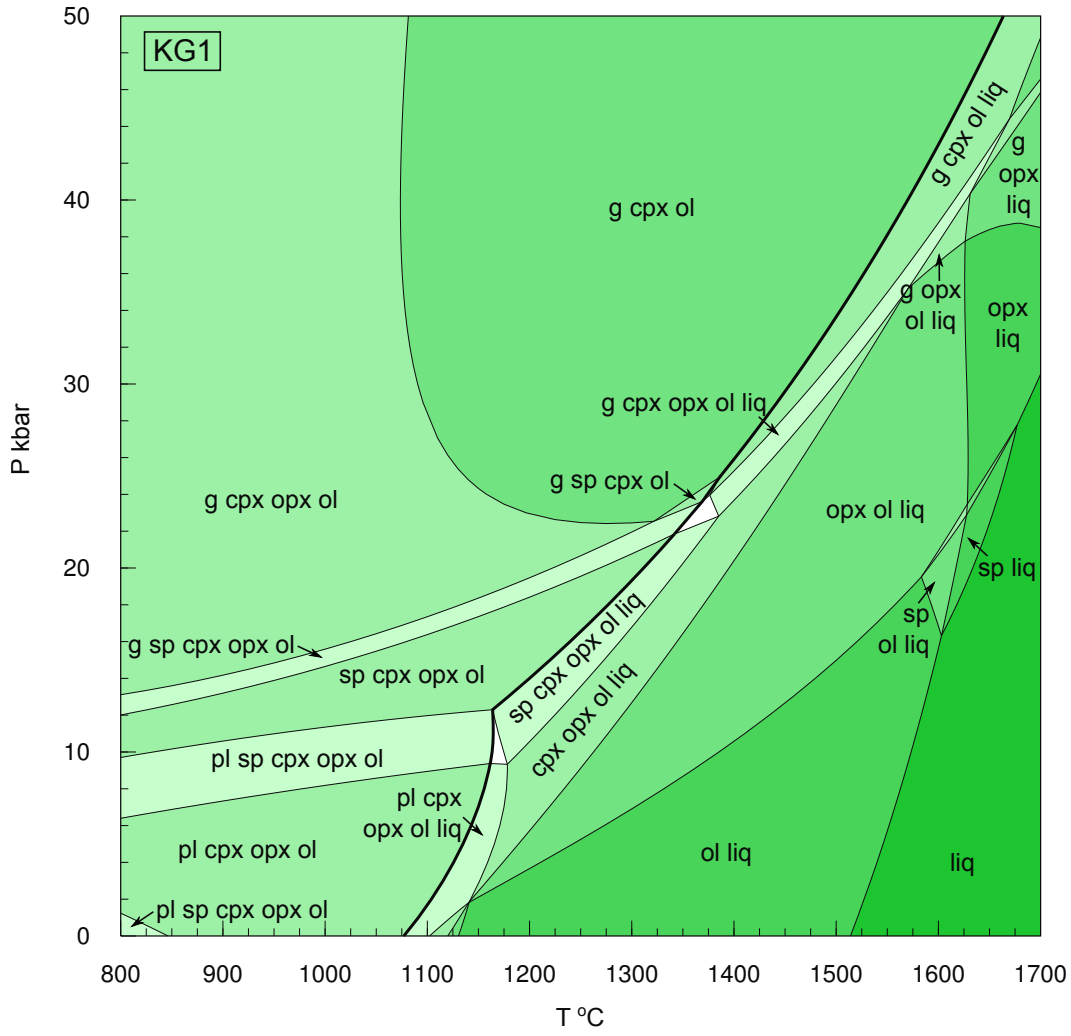

Figure 4.10: *PT* pseudosection calculated for bulk composition of hypothetical pyroxenite KG1 in the NCFMASOCr system. Legend as for Fig. 4.1. There is a small spinel field on the liquidus at 18-26 kbar; this is much smaller than in KLB-1 but may still be a model artefact.

in SiO_2 than the lowest pressure (15 kbar) melts, and the highest fraction melts are richer in MgO and Cr_2O_3 and lower in most other elements. Overall, it appears that the modelled melts do an acceptable job of predicting the experimental melts, which are themselves subject to reasonably large uncertainties (including in the estimation of F). The 30 kbar experimental melt SiO_2 at 43 wt. % is probably unrealistically low. Apart from this, the match in SiO_2 is acceptable. However, some clear offsets exist in other oxides. The model is overestimating melt CaO, and to a lesser extent FeO. It is suggested that, overall, the model performs well enough for a pyroxenite bulk composition to be used.

It is not too surprising that the model works well for the KG1 pyroxenite bulk composition, as although it is more Si-rich than KLB-1 peridotite, olivine is still present in the subsolidus, and the KG1 *PT* pseudosection (Fig. 4.10) to some extent resembles that of the KLB-1 (Fig. 4.1). Melting

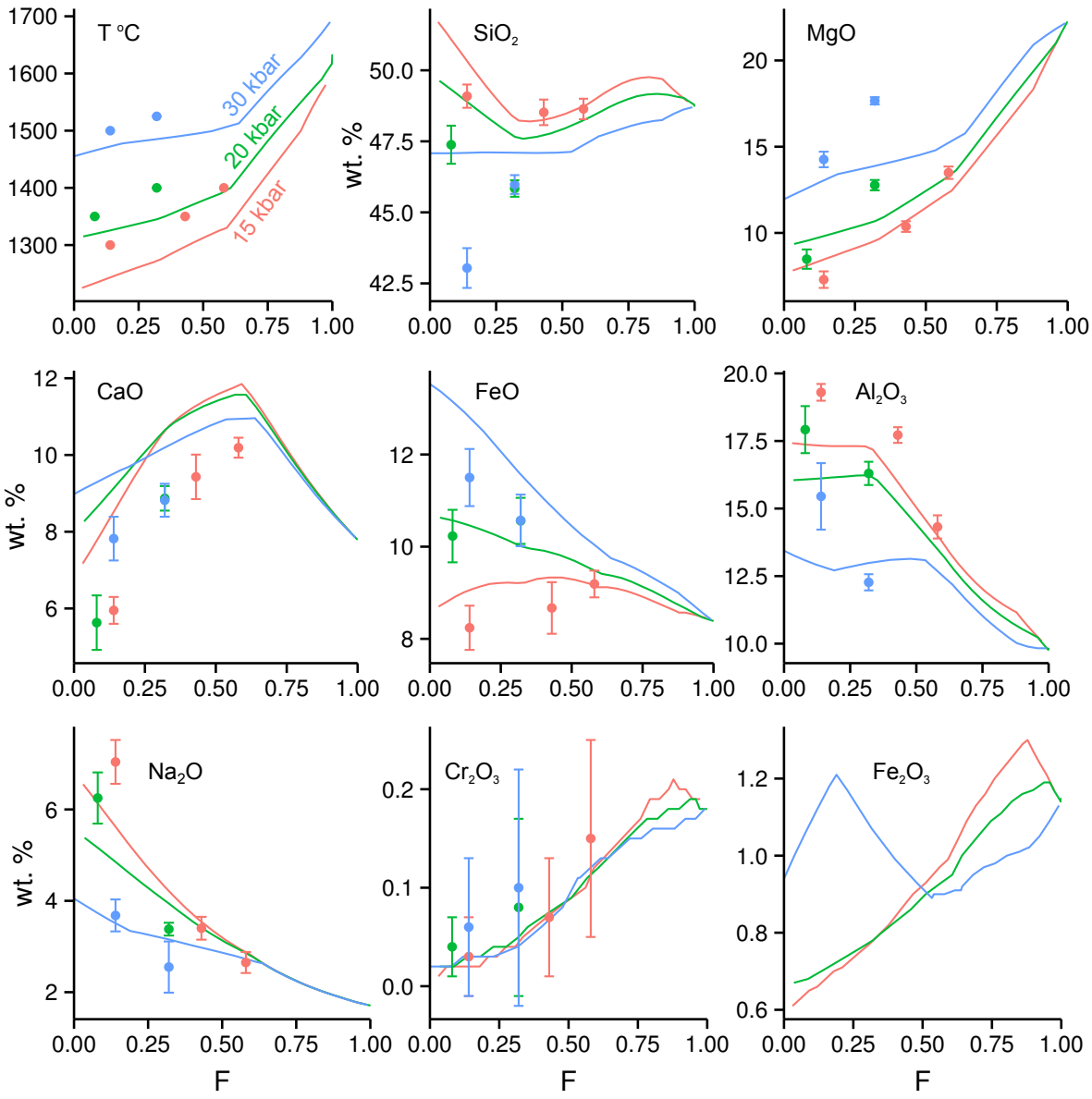

Figure 4.11: Comparison of model results with experiments of Kogiso *et al.* (1998) for bulk composition KG1. Red, experiments and model at 15 kbar; green, 20 kbar; blue, 30 kbar. Experimental compositions and uncertainties of Kogiso *et al.* (1998).

is still between the same phases, albeit at different proportions and with slightly different mineral chemistries. Partial melt compositions are still basalts to picrites and are not too dissimilar to those produced in peridotite melting. The FeO at a given MgO is noticeably higher than for typical primitive magma compositions.

Eclogite: average MORB and natural eclogite composition

Although the model functioned well for silica-undersaturated pyroxenite, it is not obvious that it should function at all well for silica-saturated compositions, i.e. olivine-free eclogite. Again, the

model is tested against experimental results from MORB and eclogites. As with pyroxenites, a variety of bulk compositions are used, although the range is narrower because there is better consensus (and direct measurements) of the composition of subducting basalt (Lambart *et al.*, 2009; Pertermann and Hirschmann, 2003a; Rosenthal *et al.*, 2014; Spandler *et al.*, 2008; Takahashi and Nakajima, 2002; Takahashi *et al.*, 1998; Yasuda *et al.*, 1994; Yaxley and Sobolev, 2007; Yaxley and Green, 1998). The average MORB composition of Gale *et al.* (2013) is used to approximate the average subducted crust in the remainder of this chapter. It is well-characterised and has the advantage of forming a binary compositional join with KG1 and KLB-1.

A *PT* pseudosection of this average MORB is calculated in Fig. 4.12a. In contrast to that of peridotite and the pyroxenite KG1, olivine is absent across the whole *PT* space except at < 7 kbar. Above 11 kbar, quartz, or at higher pressures, coesite, is present in all assemblages, and kyanite is also present (in low modal abundance) in the subsolidus from around 20 to 40 kbar. Kyanite is lost almost instantly at the onset of melting, and quartz soon after, but their presence influences the composition of low fraction melts. The prominent bulge on the solidus at around 10 kbar reflects a thermal divide, where the three-phase [pl cpx opx] assemblage melts at a higher temperature than the four-phase eutectic from quartz or olivine joining the assemblage above and below this field, respectively. Another difference with the peridotite and pyroxenite phase relations is the loss of liquidus olivine, i.e. this basalt would crystallise plagioclase first at shallow crustal levels, or clinopyroxene in the deeper crust. The pseudosection calculated here is similar to those determined in some basalt experimental studies (e.g. Spandler *et al.*, 2008; Takahashi and Nakajima, 2002), where the presence of K_2O and TiO_2 in the bulk composition stabilised rutile and K-feldspar in the experiments of Spandler *et al.* (2008). More MgO-rich basalts or picrites tend to have olivine on the experimental liquidus at low pressure, e.g. Tuff *et al.* (2005).

A pseudosection of the G2 (a natural eclogite) bulk composition of Pertermann and Hirschmann (2003a) is shown in Fig. 4.12b. G2 contains 1.5 mol.% less SiO_2 than average MORB, resulting in the lower limit of quartz stability on the solidus occurring at higher pressure (18.3 kbar) than in average MORB (13 kbar). Calculated isobaric equilibrium partial melt compositions from G2 are shown in Fig. 4.13, with G2 experimental melts from Pertermann and Hirschmann (2003a) and other melts from similar MORB-like eclogites are shown for comparison. During isobaric melting of G2 at 20 kbar, quartz is lost almost instantly from the melting assemblage on the solidus so the melting behaviour is effectively quartz-free. However, by 30 kbar, quartz stability is increased and is present to $F = 0.14$; this is also true of the observed melting assemblages of Pertermann and Hirschmann (2003a). This leads to a significant difference in the partial melt compositions between the two pressures, where melting at the quartz-present eutectic (melting at 30 kbar) produces melts which are much higher in SiO_2 and lower in FeO than melting of the effectively quartz-free assemblage. At melt fractions above 0.14, where quartz is exhausted from the high-pressure assemblage, the melt compositions at the two

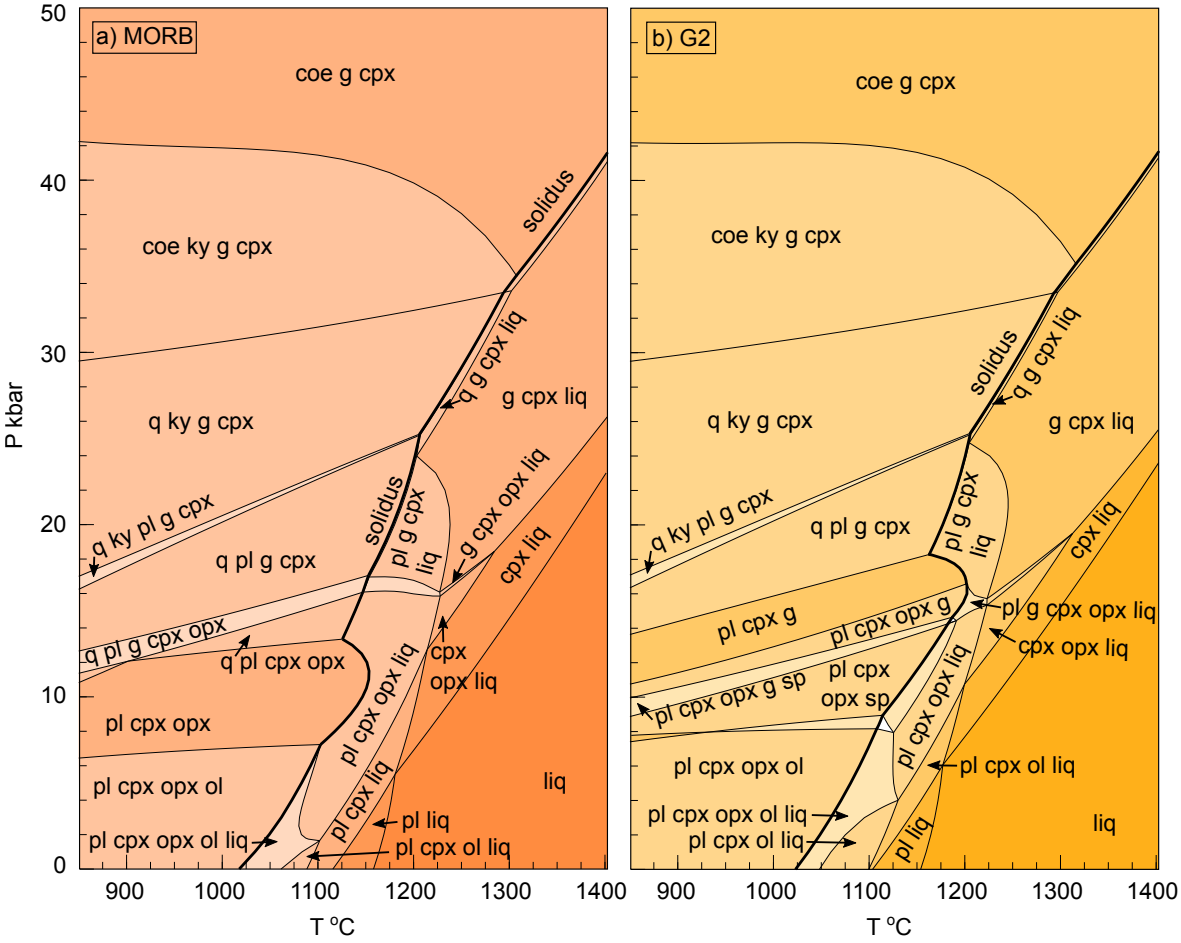

Figure 4.12: *PT* pseudosection calculated for a) average MORB bulk composition of Gale *et al.* (2013) and b) G2 eclogite bulk composition of Pertermann and Hirschmann (2003a), both in the NCFMASOCr system with $Fe^{3+}/\Sigma Fe = 0.16$. Legend as for Fig. 4.1; additional phases: q, quartz; coe, coesite; ky, kyanite. Spinel is not present in a).

pressures converge. These two low fraction melting behaviours can account for much of the range in melt SiO_2, CaO, FeO and Al_2O_3 produced in other experimental studies, along with their different bulk composition and pressures.

Despite the same solid phase assemblages reported by Pertermann and Hirschmann (2003a) (plus rutile at low F) being present in the modelled melting assemblages, Fig. 4.13 shows that the G2 partial melts at 30 kbar follow the quartz-absent trend of the 20 kbar calculated melts, whereas only the two data points from G2K (a slightly more Si- and K-rich bulk composition) produce melts on the modelled quartz-present trend. It is not clear why this is the case. Overall, the model effectively reproduces experimental melt compositions, even at silica-saturated conditions where melts reach > 70 wt.% SiO_2: melt compositions from Pertermann and Hirschmann (2003a) and a range of other experimental studies can be matched by melting in the presence or absence of a silica polymorph.

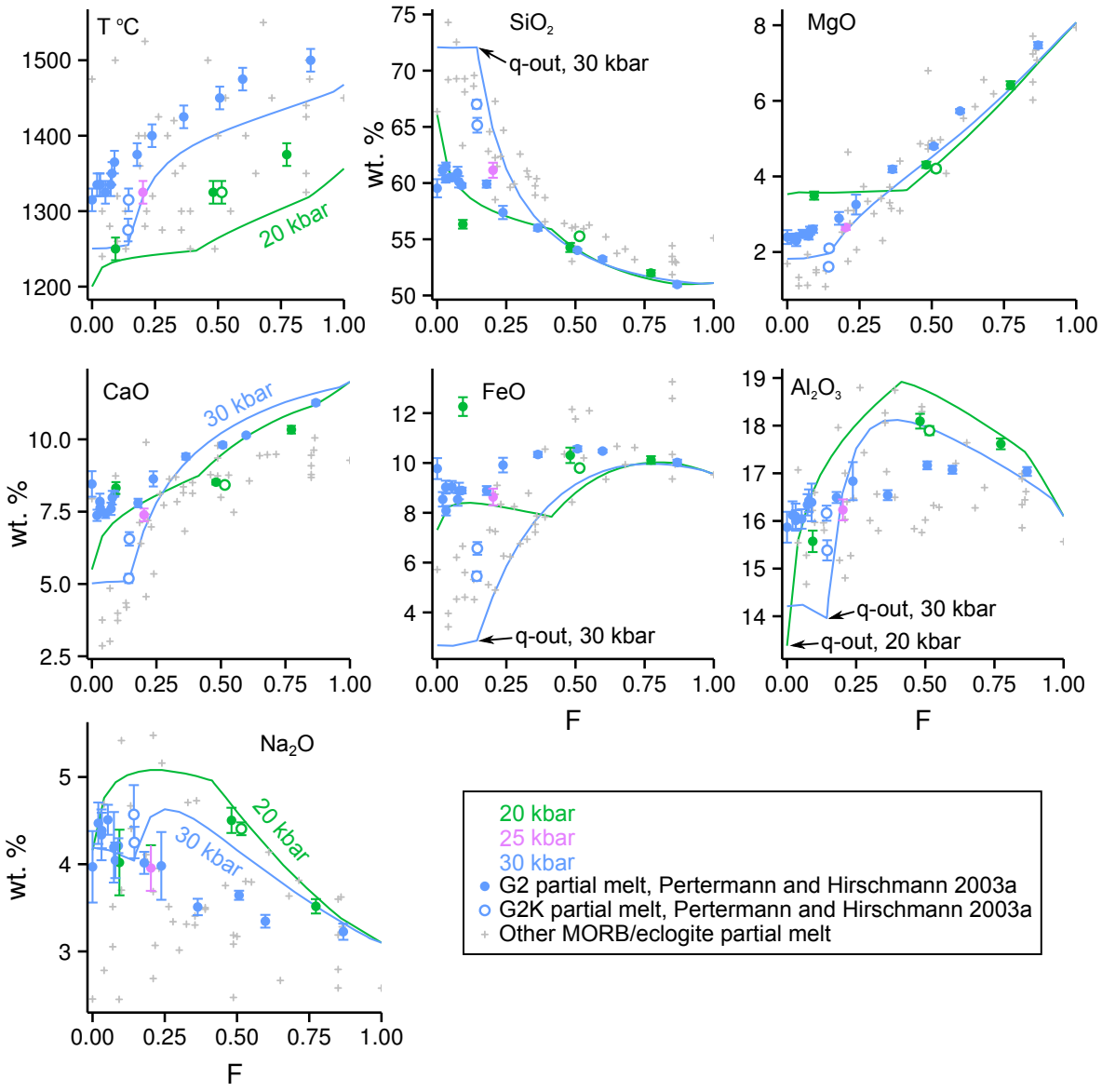

Figure 4.13: Comparison of model results with experiments of Pertermann and Hirschmann (2003a) for bulk composition G2 (experimental melts of G2K are also shown, which is a bulk composition somewhat higher in K_2O and SiO_2 than G2). Green, experiments and model at 20 kbar; purple, 25 kbar; blue, 30 kbar. Experimental compositions and uncertainties of Pertermann and Hirschmann (2003a). The G2 bulk composition is projected into the system NCFMASCr, and O is neglected for better comparability with experiments, which are buffered by graphite. Large differences in melt compositions at low F are explained by the presence or absence of quartz. Experimental melts from other studies using eclogite or MORB compositions at a range of pressures are shown with grey crosses, from the compilation of Shorttle and Maclennan (2011).

The melting productivity (dF/dT) of eclogite is also reproduced with an absolute offset in T of ~ 50 °C, as seen in Fig. 4.13.

The subsolidus assemblage for eclogite G2 switches from being olivine-bearing at at low pressure to quartz-bearing at > 18.3 kbar; this appearance of the thermal divide (which in CMAS is defined by

the En-CaTs-Di plane, i.e. a plane on to which garnet and pyroxenes project) is consistent with recent literature estimates of $\sim$ 20 kbar (Kogiso *et al.*, 2004a; Lambart *et al.*, 2013) and results in higher pressure partial melting of G2 at the lower temperature quartz-bearing eutectic. G2 is a 'silica-excess pyroxenite' according to the scheme of Kogiso *et al.* (2004a). It should be noted that the pressure at which the thermal divide becomes active is dependent on the non-CMAS bulk composition (Lambart *et al.*, 2013) and is lower in average MORB (Fig. 4.12). In the CMAS projections, the appearance of the thermal divide in silica-excess pyroxenites and the switching of olivine to quartz is univariant (O'Hara, 1968). In the present higher component system it is divariant, where a [pl cpx opx] field divides quartz and olivine-bearing field, and an olivine-free and quartz-free interval exists between 7 and 13 kbar near the solidus of average MORB (Fig. 4.12). Therefore, in natural systems, the thermal divide does not appear instantaneously at a given pressure, although it should still be defined by a sharp compositional divide. In summary, the presence or absence of quartz/coesite in the melting assemblage is the dominant control on the composition of eclogite partial melts, and is a function of whether the melting pressure is above or below the pressure at which the thermal divide becomes important.

Harzburgite

Finally, a more depleted bulk composition is examined (1 KLB-1 - 0.1 MORB). Depletion of a peridotite by partial melting will preferentially exhaust fusible phases such as cpx or the relevant aluminous phase, and it is usually considered that around $\sim$ 20% of partial melting is required to create a clinopyroxene-free harzburgite. Further partial melting is not often considered because, during decompression-driven fractional melting, melting should cease at clinopyroxene exhaustion as the residue solidus shifts to higher temperatures.

Wasylenki *et al.* (2003) performed melting experiments on a depleted upper (MORB-source) mantle composition (DMM1), which still contains a small fraction of clinopyroxene, lost at 10% melting. The melt compositions are very similar (except in more incompatible elements such as Na_2O) to somewhat higher fraction melts of KLB-1. Melting of more depleted bulk compositions, where clinopyroxene is not present on the solidus, would create melts with similar compositions as higher fraction and/or higher pressure melts of KLB-1, which function well in the current melt model. It is therefore concluded that depleted peridotite or harzburgite melting can be modelled effectively with the present melt model.

4.4.2 The effect of varying bulk composition on melting

It has been demonstrated that the melt model should be effective from depleted peridotite through to basaltic bulk compositions, so can be used to explore the control of bulk composition on melt chem-

istry. To simplify this, the bulk compositions are conveniently chosen to be linear combinations of KLB-1 peridotite (X = 0) and average MORB (X = 1), which are both normalised in NCFMASOCr, as illustrated in Fig. 4.14. This approximation reflects natural mafic-ultramafic systematics to a first order. As basalt (approximated by average MORB) is extracted from a primitive mantle lherzolite (KLB-1), the lherzolite bulk composition loses basalt and moves to negative X. Conversely, if subducted average MORB is added to peridotite in some proportion through subduction, the mantle moves to positive X. This allows a complete range of potential mantle lithologies to be investigated. In reality, this system does not account for the fact that MORB represents fractionated, accumulated incremental melts, whose parental primary melt is more Mg-rich than average subducted MORB.

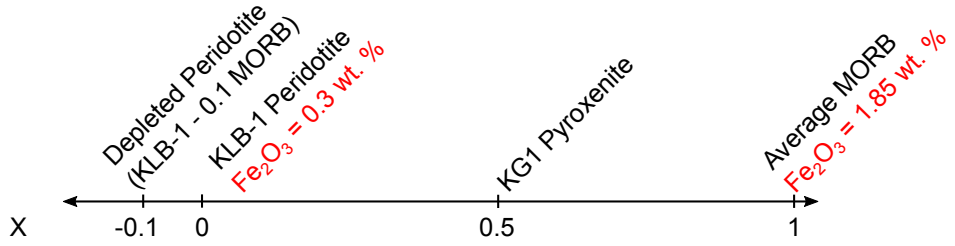

Figure 4.14: Illustration of the binary compositional range described by the compositional parameter X, where X = 0 is the enriched peridotite KLB-1 (Davis *et al.*, 2009, with 0.3 wt.% Fe_2O_3), X = 1 is average MORB (Gale *et al.*, 2013 with 1.85 wt.% Fe_2O_3). Other X values are linear combinations of KLB-1 and MORB.

The *PT* pseudosections shown in Figs. 4.1, 4.10 and 4.12 were used for guidance in calculating the intermediate phase assemblages, because in order to correctly predict an equilibrium melt composition, the correct phase assemblage must be given. A *PT* pseudosection was also calculated for the depleted end-member composition (KLB-1 minus 10.25% average MORB, which is the X at which Na_2O is zero). It is not shown here, but its key features are: i) it is very similar to that of KLB-1 in most respects; ii) opx is present at all pressures along the solidus until its transformation to hpx (high-pressure pyroxene, at $\sim$ 80 kbar, Holland *et al.*, 2013); iii) the high-temperature supersolidus spinel stability field is expanded.

Thermal properties: solidus and melt productivity

Experimental determinations of the onset of melting in various lithologies indicate that pyroxenite should begin to melt at higher pressure (or lower temperature) than peridotite, and eclogite at higher pressure still (Herzberg *et al.*, 2000; Hirschmann, 2000; Kogiso *et al.*, 1998; Pertermann and Hirschmann, 2003a; Yasuda *et al.*, 1994; Yaxley and Green, 1998). However, the lower pressure pyroxenite solidus may represent a low melt fraction region where volatiles and other fusible components are quickly lost to the melt, followed by the onset of significant melting at a similar temperature to that of peridotite. Perhaps a more important difference with peridotite is the melt productivity, i.e.

the amount of melting achieved over a given temperature interval. This is proposed to be much higher in pyroxenites, meaning that at near-solidus conditions, pyroxenite would melt more than peridotite and melt compositions from a mixed lithology mantle would be heavily biased towards pyroxenite (Kogiso *et al.*, 2004a; Lambart *et al.*, 2013; Shorttle *et al.*, 2014). Eclogites (described elsewhere as silica-excess pyroxenites) have been shown to have much lower temperature solidi, although the impact of the high pressure pyroxene-garnet thermal divide on the solidus temperature is not fully resolved (Kogiso *et al.*, 2004a). Because the compositions here are examined in an 8-component system, the solidus should represent the onset of the main phase of melting and be comparable in meaning to the peridotite solidus, rather than reflecting lower temperature incipient potassic or wet melts.

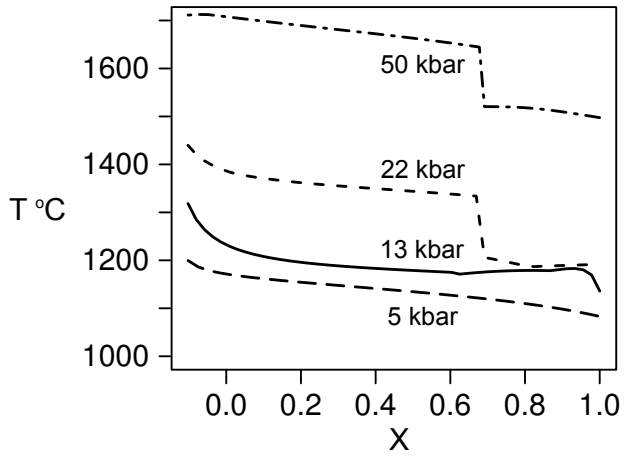

Figure 4.15: Solidus temperature as a function of composition (X, see Fig. 4.14 for explanation) and pressure. The jump in solidus at high pressure is caused by the presence of quartz in the solidus assemblage at X > 0.69.

Fig. 4.15 shows the calculated solidus temperature for a continuous range of compositions at four pressures. Melting occurs at higher temperature for higher pressures. At low pressures (5 and 13 kbar) across the full compositional range, the solidus temperature is not very sensitive to bulk compositions, where an increase in basalt content only slightly lowers the solidus temperature. Between X = 0 (peridotite) and X = 0.5 (KG1 silica-undersaturated pyroxenite), there is almost no difference in the solidus temperature. In reality, a higher concentration of K_2O, volatiles and other components not considered in this model will result in a larger offset in solidus temperature between peridotite and olivine-bearing pyroxenites (Kogiso *et al.*, 2004a). At pressures above that at which the thermal divide becomes important ($\sim$ 20 kbar, Kogiso *et al.*, 2004a; Lambart *et al.*, 2013; dependent on bulk composition, e.g. as shown in Fig. 4.12), compositions which stabilise a free silica phase (X > 0.69) experience a large drop in solidus temperature of around 150 °C. This is a result of melting jumping to the lower temperature quartz/coesite-bearing eutectic and reflects the fact that X = 0.69 represents the first 'silica-excess' bulk composition. The large jump in solidus temperature at the thermal divide is contrary to the suggestion of Kogiso *et al.* (2004a) that subsolidus phase assemblages do not have

an obvious influence on solidus temperatures. This means that subducted MORB would indeed begin to melt much deeper than other mantle lithologies in upwelling plumes. However, during fractional melting, this deeper melting will be self-limiting, as after the free-silica phase is exhausted (at $\sim$ 0-20% melting, depending on pressure and bulk composition), melting will cease and only restart once the quartz-free solidus is reached.

Although pyroxenites with a composition similar to KG1 do not have a solidus temperature that is particularly offset from that of peridotite, their melt productivity contrasts strongly with peridotite. Fig. 4.16 shows the isobaric melt fraction as a function of temperature for four lithologies. The contrasting behaviour is clearer at 25 kbar. Peridotite and depleted peridotite, after clinopyroxene exhaustion (the first inflection), have a shallow dF/dT slope. This contrasts with MORB and KG1, which have steep slopes, meaning that they will melt more over a given temperature interval. At 25 kbar, KG1 has a solidus 50 °C lower than that of KLB-1 (Fig. 4.16). Within that 50 °C interval, by the onset of peridotite melting, KG1 will already have melted by 60%. At the onset of melting, MORB melt productivity is even more extreme until the loss of quartz from the residue. The same is true at 50 kbar. At a T_P of 1500 °C, typical for an upwelling plume, MORB will be 25% molten at 50 kbar, and no other lithology will have begun to melt. By 25 kbar, peridotite will be 25% molten, KG1-type pyroxenite 75%, and MORB 100%.

When melting a mantle containing mixed pyroxenite and peridotite, the resultant magma will therefore contain a greater contribution of pyroxenite-derived melt than peridotite-derived melt, giving a biased perspective on the volume proportion of these lithologies in the plume source, in agreement with previous understanding (Shorttle *et al.*, 2014). However, if the two lithologies are in thermal equilibrium, the final melt contributions from pyroxenite relative to peridotite is higher still, because heat flow from the unmelted peridotite will further increase the melting productivity of the more fusible pyroxenite (Phipps Morgan, 2001).

Solidus phase assemblage

A good constraint on the solidus phase assemblage is important for understanding the trace element geochemistry of mantle melts, as well as for predicting their major element composition. Phase assemblages at the solidus for various pressures as a function of composition are shown in Fig. 4.17. This figure confirms that the temperature step in the solidus at X = 0.69 at 22 and 50 kbar (Fig. 4.15) coincides with the loss of olivine and the appearance of quartz/coesite in the solidus assemblage, caused by the high pressure thermal divide. Plagioclase is stable in more basalt-rich compositions to higher pressures on the solidus, whereas opx is stable to the highest pressures in the most depleted compositions. Of particular importance for trace element modelling is the stability of garnet. Although the various PT pseudosections presented in this chapter indicate a similar lower pressure limit

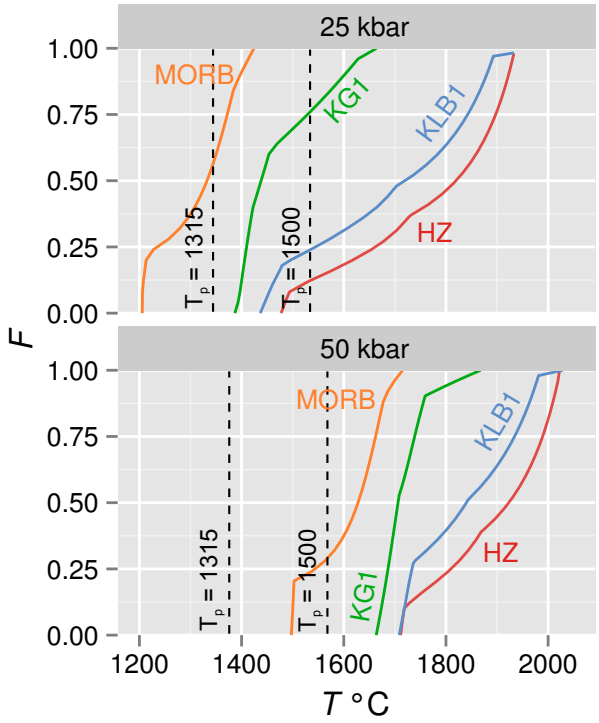

Figure 4.16: Melt fraction F as a function of temperature at 25 and 50 kbar. Orange, average MORB (X = 1); green, pyroxenite KG1 (X = 0.5); blue, peridotite KLB-1 (X = 0), red HZ, harzburgite (X = -0.1). Dashed lines indicate the mantle temperature, where potential temperature T_P is 1315 and 1500 °C, at the given pressure.

for garnet on the solidus in KLB-1, KG1 and average MORB, it can be seen here that the modal proportion of garnet in high pressure assemblages (50 kbar) increases from just 5% to almost 40% from harzburgite through to average MORB. Pyroxenite KG1 (X = 0.5) contains 29% modal olivine at 5 kbar, decreasing to 11% at 50 kbar, making this composition an olivine websterite.

Near-solidus melt composition

The compositions of a nominal 0% melt fraction along the solidus as a function of bulk composition are shown in Fig. 4.18, at 5, 13, 22 and 50 kbar, along with the respective bulk compositions. For compositions which do not contain a free silica phase (all compositions at pressures of 5 and 13 kbar, and compositions of X < 0.69 at higher pressures), compositional changes in the melt are muted relative to the change in bulk composition. For example, in MgO, CaO and Al_2O_3, the melt composition is almost constant over a broad compositional range. These elements appear to be buffered by the residual mineral assemblage, as increases or decreases in the bulk composition change the modal proportions of minerals but have a limited affect on melting reaction and mineral chemistry. CaO actually shows an opposite sense of change, where increasing CaO in the bulk is matched by a slight reduction in the CaO of the low fraction partial melt, presumably because the overall change in bulk composition has increased the relative stability of cpx. These effects make the difference between pyroxenite and peridotite partial melts muted and difficult to spot, which has also been suggested from experimental results (Lambart *et al.*, 2013). The exception to this rule is FeO, where the melt

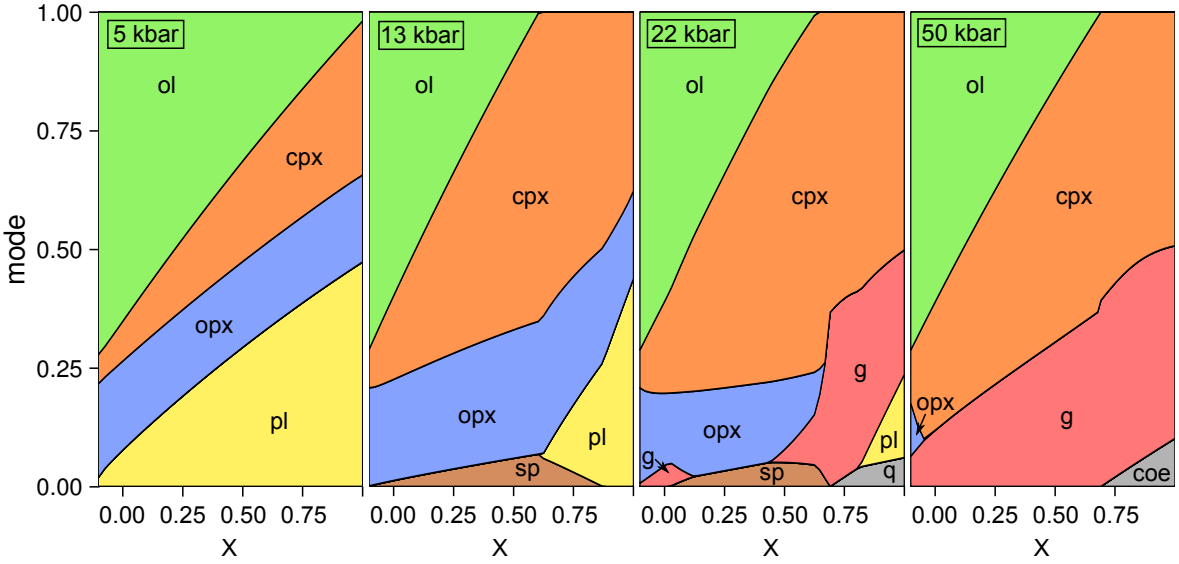

Figure 4.17: Solidus modes (normalised to one oxide molar, similar to volume percent) as a function of composition (X, see Fig. 4.14) for four different pressures. Phase labels as in previous figures. The appearance of garnet twice at 22 kbar is a product of the narrow [g+sp] stability field moving slightly up in pressure, and then down again, with increasing X; a diagram at 23 kbar would also show garnet present at X = 0.25.

experiences a larger change in FeO concentration than the change in the whole-rock composition. For many oxides, the differences in melt composition caused by pressure are greater than those caused by composition (Al_2O_3 and Na_2O being clear examples); the pressure vs. compositional effect is somewhat convoluted in pyroxenite vs. peridotite melting, since pyroxenites will melt at higher pressure and have a more enriched composition.

In contrast, MORB-rich compositions at high pressures begin to melt on the Si-excess side of the thermal divide. The effect of this on the melt composition is obvious and, in SiO_2 and FeO, dramatic. The compositions will only hold until quartz is exhausted from the residue. The likelihood of these dacitic liquids reaching the surface and undergoing no chemical reaction is slim, given that they would form deep, are far from equilibrium with peridotite and would have high viscosity.

The origin of mantle pyroxenite

The model of Yaxley and Green (1998), and later Sobolev *et al.* (2005), describes a two-step process whereby i) eclogite partially melts at depth, then ii) those partial melts metasomatise the surrounding peridotite to create pyroxenite, which itself melts deeper than peridotite. This process is consistent with the solidus pressures and melt productivities found in this section, although it is critically controlled by the ability of the high-silica melts to flow from their source. During fractional melting, the eclogite will stop melting once the free silica phase is consumed. The solid residue that is left behind will have a composition similar to that at the onset of the thermal divide (X = 0.69). At 30

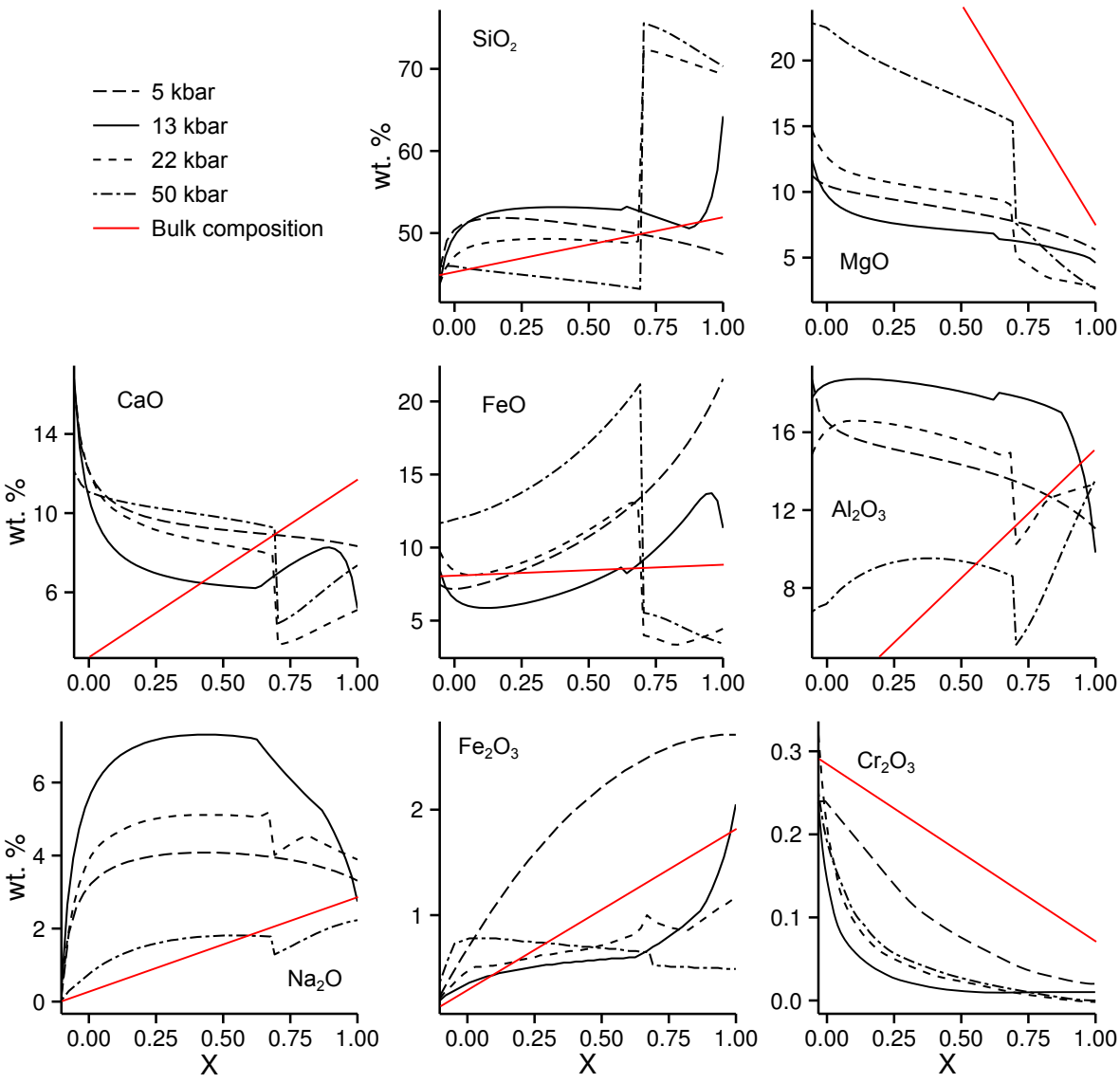

Figure 4.18: Calculated solidus melt composition for a nominal zero melt fraction as a function of bulk composition (from harzburgite through to eclogite), calculated at the solidus at 5, 13, 22 and 50 kbar.

kbar, G2 loses all of its quartz by $F = 0.14$ in equilibrium melting, or at lower F by fractional melting. If this $F = 0.14$ equilibrium dacitic melt is extracted, the residual solid is 48 wt.% SiO_2, 9 wt.% MgO 11 wt.% FeO, 16 wt.% Al_2O_3 and 13 wt.% CaO. This composition is low in MgO and high in Al_2O_3 compared with KG1 (22 wt.% MgO, 10 wt.% Al_2O_3), although it is not too dissimilar from composition MIX1G (17 wt.% MgO, 15 wt.% Al_2O_3, 12 wt.% CaO; Hirschmann *et al.*, 2003) which was created as an intermediate composition within the natural mantle pyroxenite array. The melting residue of mantle eclogite could therefore also be considered as a pyroxenite source for melts, although such melts may have a depletion in the highly incompatible trace elements.

Summary

The model functions well for compositions in addition to the mantle peridotite (KLB-1) on which it was first calibrated. Tests against experimental data indicate that it functions even in basaltic bulk compositions at pressures where the thermal divide is active, at which point quartz is present in the subsolidus assemblage and small fraction partial melts are dacitic in composition. It should be appropriate for use in pyroxenite and eclogite partial melting calculations.

The change from a quartz-free, olivine-bearing subsolidus assemblage to a quartz-bearing, olivine-free one (a divariant reaction in this eight-component system) causes a large shift in the major element composition of the melt towards SiO_2-rich compositions, and has long been identified as the result of a high pressure thermal divide (O'Hara, 1968). It is accompanied by a significant drop in solidus temperature, indicating that quartz/coesite-bearing eclogites will begin to melt deep in the mantle. These melts are far from equilibrium with peridotite and are unlikely to exit the mantle unchanged. The model of Yaxley and Green (1998) and Sobolev *et al.* (2005) where these melts metasomatise overlying peridotite to pyroxenite seems most feasible. The resulting pyroxenite will not contain quartz, and, according to the model presented here, will partially melt slightly deeper and much more productively than peridotite. The melt compositions will be slightly different to those of peridotite, but the subtle differences may be difficult to detect. FeO is one oxide which shows promise, where pyroxenite-derived melts are significantly richer in FeO than peridotite-derived ones. In the following section, the possibility that ferropicrite represents a rare occurrence of deep pyroxenite-derived melts on the Earth's surface is examined in greater detail.

4.5 The origin of ferropicrite from a major element perspective

The unusual major element chemistry of ferropicrites is their most conspicuous compositional feature. Yet, because major element modelling requires thermodynamic analysis (and an appropriate thermodynamic tool for pyroxenite melting was not previously available), its investigation has thus far been restricted to i) comparison with experimental melt compositions (Gibson, 2002; Goldstein and Francis, 2008); ii) comparison with published major element markers of pyroxenite partial melts (Heinonen *et al.*, 2013, after Herzberg and Asimow, 2008); and iii) experimental examination of the high pressure liquidus phase relationships (Tuff *et al.*, 2005). Whilst many (not all) of these studies conclude that a pyroxenite source is required to produce ferropicrite, this conclusion remains contentious.

4.5.1 Fractional melting simulations

Mantle melting is fractional and polybaric, meaning that the resultant aggregated melt compositions will not necessarily match the equilibrium compositions identified in Figs. 4.11, 4.13 or 4.18, for example. Fractional melting simulations were therefore performed to investigate the melt compositions expected from peridotite and pyroxenite partial melting in an adiabatically decompressing mantle. Calculations using the present model are implemented in THERMOCALC, which unlike alphaMELTS does not yet have the capability to automate fractional melting or calculate self-consistent isentropic *PT* paths. A stepwise equilibrium melting regime is therefore used, where melt is extracted at a threshold fraction, and these incremental melts are integrated for a final mixed melt composition. At every step, the bulk composition must be recalculated by removing the previous melt. For the following calculations, a melt fraction step of $F = 0.01$ was chosen. This step size was found to be an appropriate compromise between resolution (a repeat of a calculation run at $F = 0.02$ resulted in only a small change in integrated composition) and time efficiency. An accumulated stepped melting approach is broadly consistent with the idea that mantle melting may require a residual or threshold porosity for melt extraction to occur, although U-series disequilibrium suggests that porosities may be small (on the order of $\sim 0.1\%$, reviewed by Kelemen *et al.*, 1997).

Four scenarios were modelled: i) peridotite melting at ambient mantle T_P (1315 °C, McKenzie *et al.*, 2005); ii) pyroxenite melting at ambient T_P; iii) peridotite melting at T_P = 1500 °C; iv) pyroxenite melting at T_P = 1500 °C. KLB-1 was used for peridotite simulations. Because ferropicrite compositions show no sign of elevated SiO_2, the silica-deficient composition KG1 (1:1 KLB-1:MORB) was used to investigate pyroxenite melting. Melting at ambient mantle T_P will begin at shallower pressures and shows the melt compositions expected from passive upwelling in rift scenarios. For plume-type active upwelling, T_P 1500 °C is used as a general representation of the effect of elevated temperature, so deeper melting. This value is broadly applicable to many known plumes, where their mantle potential temperatures have a large uncertainty (see Chapter 5). The T_P of the proto-Tristan plume beneath the Etendeka province is somewhat higher than this value but is not well constrained.

Thermal structure

An isentropic *PT* path was manually imposed. *P* and *T* steps for $F = 0.01$ melt fraction intervals were calculated using the thermal model of Chapter 5, with the pyroxenite parameters presented in that Chapter and the peridotite melt productivity parametrisation and thermal properties of Katz *et al.* (2003) and Shorttle *et al.* (2014), respectively. The calculated *P* steps were then used to calculate melt compositions at $F = 0.01$ intervals for a given bulk composition in THERMOCALC, without imposing *T*. The *T* calculated by THERMOCALC was then used to test how well the two models match, and so how applicable the imposed *PTF* structure actually is in model fractional melting. The

results (Fig. 4.19) show that the two paths generally match well, with a maximum difference at a given P and F of 20 °C. Additionally, the two paths do not diverge at higher melt fractions. This means that the imposed equilibrium thermal structure is close to the model fractional melting thermal structure, and is an adequate way of imposing a dynamic melting regime in THERMOCALC. The output PT path is really tracking the shift in the solidus to higher temperatures as the bulk composition depletes, and inflections in the output PT path, seen in Fig. 4.19, reflect changes in residual mineral composition (usually the loss of a phase). Once cpx is lost from the residue at $F \sim 0.2$, the output temperature increases with a decrease in pressure. This indicates a natural break in melting, where further decompression does not result in further melting over some subsequent pressure interval. The melting path for KG1 is much longer because this point is not reached until $F \sim 0.6$.

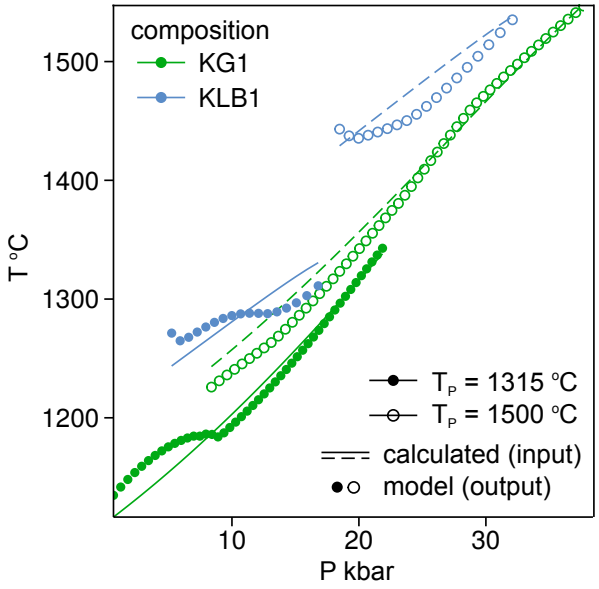

Figure 4.19: Calculated (input, calculated with model presented in Chapter 5) and model (output, temperature results from THERMOCALC) for fractional melting model. Blue, KLB-1; green, KG1; solid line, T_P = 1315 °C input PT path; dashed line, T_P = 1500 °C input PT path; filled points, output PT path at T_P = 1315 °C; open points, output PT path at T_P = 1500 °C. All points in $F = 0.01$ steps.

Melt composition

It is thought that fractional melts accumulate and mix at the base of the crust, and that basalts are generally well mixed averages of fractional melts (Kelemen *et al.*, 1997), although examples of incomplete mixing are also found in melt inclusions and larger length-scale sample heterogeneity (e.g. Maclennan *et al.*, 2003a). Melt inclusion evidence indicates that primitive picrites and ferropicrites from the Etendeka and Karoo provinces are well-mixed aggregations of mantle melts (see Chapter 3). Because of this, the incremental melt compositions retrieved along the polybaric fractional melt-

ing paths (described above) can be integrated, which simulates the pooling process and makes the calculated incremental compositions comparable with primitive melts erupted at the Earth's surface.

The integration is performed here using a 1D melting column geometry without compaction, for simplicity, such that a given melt fraction is the average of the cumulative melt fractions (e.g. a melt given as $F = 0.03$ is the average of the first three incremental melts, where the calculation is performed in steps of $F = 0.01$). The resultant melt composition is known as an 'accumulated fractional melt'. The evolution of these accumulated fractional melts with further decompression, so increasing F, is shown in terms of four oxides in Fig. 4.20. T_P is a proxy for pressure, as decompressing mantle will intersect the solidus and begin to melt at a higher pressure if it is hotter. As was also indicated by Fig. 4.18, Fig. 4.20 shows that the melt composition is a function of both source composition and pressure, making it more difficult to interpret source lithology from the major element composition of erupted magmas. In general, higher pressure melts will be lower in Al_2O_3 and higher in CaO (at low melt fractions), MgO and FeO for a given lithology. Melts from pyroxenite are higher in FeO and lower in CaO, MgO and Al_2O_3 than melts from peridotite at a given pressure. The fraction of melting reached has some importance, for example high fraction pyroxenite melts ($F > 0.4$) will have a similar composition to low fraction peridotite melts in terms of FeO and CaO. Interestingly, low pressure peridotite partial melts will become more enriched in MgO with increased melting and source depletion, whereas high pressure peridotite and all pyroxenite melts decrease in MgO with continued melting. This reflects the competing effects of source composition (which would produce more MgO-rich melts with depletion) and pressure (which would produce less MgO-rich melts as it decreases) on the melt.

Al_2O_3 and MgO appear to be more sensitive to pressure than source composition, whereas CaO and FeO are more sensitive to source composition than to pressure. CaO and FeO may therefore be the more useful indicators of source lithology, although their concentrations are still affected by the pressure of melting. Fig. 4.20 also shows the suggested primary melt compositions of Etendeka picrites and ferropicrites. These do not perfectly coincide with any given source lithology, T_P and F, reflecting both the large uncertainty associated with determining a primary composition, as well as the simplistic nature of the model. However, for every oxide shown, the general sense of the difference between the picrite and ferropicrite primary melt is consistent with the derivation of ferropicrite from a source more similar to KG1 pyroxenite, whereas picrite is more consistent with a peridotite source (e.g. ferropicrite is higher in FeO and lower in the other elements), and is generally consistent with a high T_P in the region of ~ 1500 °C.

Fig. 4.21 shows the composition of accumulated fractional melts plotted in terms of the co-variation of two compositional features. Fig. 4.21(a) gives CaO and MgO, because this combination of oxides was suggested by Herzberg and Asimow (2008) to be useful in discriminating between peridotite and pyroxenite sources. The grey dashed line was given by Herzberg and Asimow (2008)

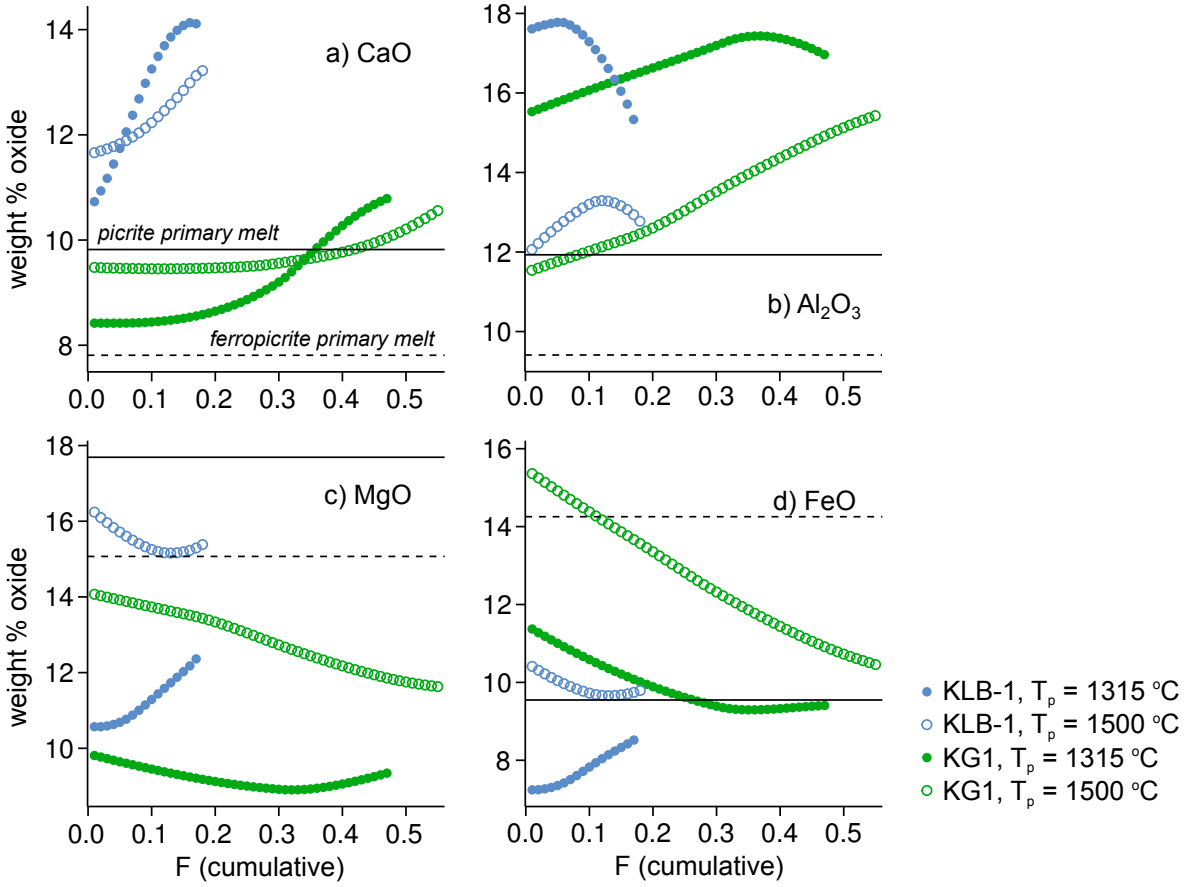

Figure 4.20: Composition of accumulated fractional melts as a function of melt fraction F. a) CaO, b) Al_2O_3, c) MgO, d) FeO, for polybaric fractional melting of peridotite KLB-1 (blue) and silica-deficient pyroxenite KG1 (green) and T_P = 1315 and 1500 °C. Each point represents an $F = 0.01$ calculation step. Melts shown are integrated cumulative compositions of all melt fractions up to the one shown. A 1D melt column is assumed, i.e. the composition of an $F = 0.03$ melt is the average of the first three incremental melt compositions. Lines show the Etendeka picrite (solid) and ferropicrite (dashed) suggested primary melt compositions of Chapter 2, assuming $Fe^{3+}/Fe_T = 0.1$.

to discriminate between peridotite-sourced melts (which plot above the line) and pyroxenite-sourced melts (which plot below it) in the PRIMELT software (Herzberg and Asimow, 2008, 2015). Fractionation of olivine will shift melts parallel to the line, so will not cause liquids to cross it. The line was suggested on the basis of a parametrisation of melting experiments. However, in the polybaric fractional melting calculations, this line is too simplistic. Although KG1-derived melts do indeed plot beneath it, it is difficult to discriminate between high fraction pyroxenite melts and low-fraction, low pressure peridotite melts. Melting of pyroxenite at $T_P > 1500$ °C would likely produce melts that cross this line. In addition, the compositional change from peridotites through to pyroxenites is not a sharp boundary, and partial melts from an intermediate composition would plot closer to the line. Finally, instantaneous fractional melts have more extreme MgO and CaO compositions than their integrated counterparts, and if incomplete mixing of fractional melts occurred, the CaO-MgO boundary could

also be crossed. This discriminatory boundary is useful, however, in that it is insensitive to olivine fractionation and does not need a good estimate of primary composition.

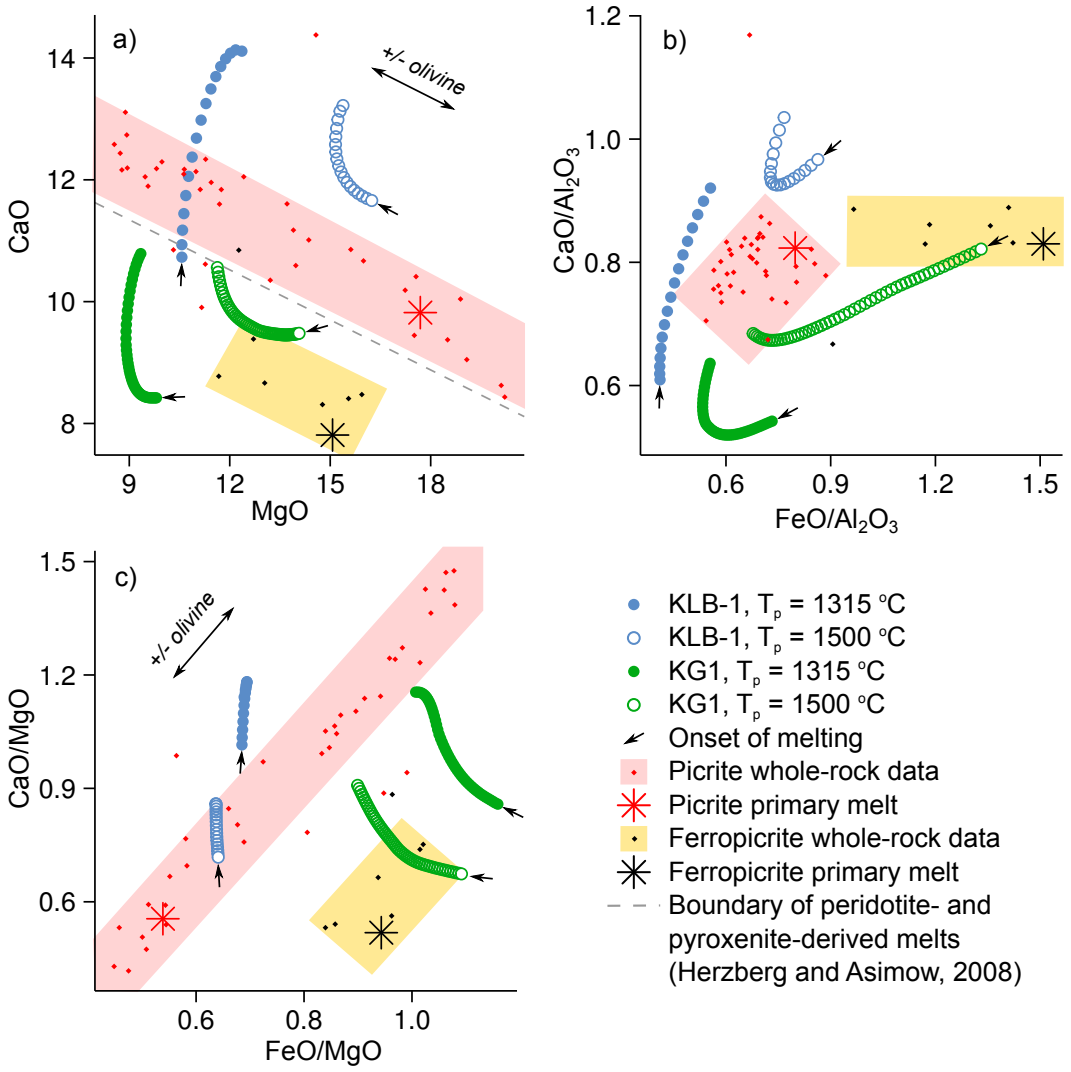

Figure 4.21: Composition of accumulated fractional melts compared with whole-rock data. Points are accumulated (integrated) melt compositions at $F = 0.01$ intervals; see caption to Fig. 4.20 for detail. Small arrows indicate the location of the $F = 0.01$ melt, i.e. the onset of melting. Small dots represent unfiltered whole-rock data (Etendeka samples only, assuming $Fe^{3+}/\Sigma Fe = 0.1$), enclosed by coloured fields to highlight the general trend and location of most of the samples, and stars show the suggested primary melt composition of Chapter 2. Vectors calculated for olivine fractionation/accumulation are shown, and explain most of the spread in the whole-rock data. The dashed line in a) is the boundary given by Herzberg and Asimow (2008) to differentiate between peridotite-derived melts (above the line) and pyroxenite-derived melts (below the line), where change parallel to the line is caused by olivine loss or gain.

As discussed above, CaO and FeO are somewhat more sensitive to source composition than pressure, and the reverse is true for MgO and Al_2O_3. The pressure component of CaO and FeO concentrations can be reduced by normalising to MgO or Al_2O_3, as is shown in Figs. 4.21(b) and (c). The

result is an increased importance of source composition in controlling the melt composition, so a bigger separation between the KG1 and KLB-1 results. Fig. 4.21(b) does not require MgO, which means that compositional changes in a magma caused by olivine fractionation have only a small effect on a primitive composition, and the accurate estimation of a primary melt is not required to discriminate between a peridotite source (which is indicated by melts with low FeO/Al_2O_3 and high CaO/Al_2O_3) and a pyroxenite source. In Fig. 4.21(c), the effect of olivine fractionation is pronounced, but despite this, a good separation of peridotite and pyroxenite-sourced melts is still achieved, with only small differences in melt composition resulting from different T_Ps. It is concluded that CaO and FeO of a magma are the best major elements for discriminating between source compositions, and that normalising to either MgO or Al_2O_3 is an effective means of reducing the complicating effect of pressure on magma composition. This is in agreement with previous studies. For example, isotopically enriched samples from Iceland have been shown to derive from more fusible mantle lithologies by their correlation with glacial cycles (Sims *et al.*, 2013); such isotopically enriched samples have higher FeO and lower CaO and SiO_2 than isotopically depleted samples (Shorttle and Maclennan, 2011). Additionally, Lambart *et al.* (2013) show from experimental data that pyroxenite-derived melts can have high FeO and/or low SiO_2 relative to peridotite-derived melts. In the modelled fractional accumulated melts of this chapter, SiO_2 is similar for KG1 pyroxenite and KLB-1 peridotite, although it is lower at higher pressure.

Fig. 4.21 also shows Etendeka picrite and ferropicrite whole-rock compositions and suggested primary compositions. It is clearer here than in Fig. 4.20 that i) ferropicrites are similar to low to moderate-fraction melts of high pressure (high T_P) silica-deficient pyroxenite KG1 and ii) picrites are similar to partial melts of KLB-1, although the T_P and F are less clear. The dominating effect of olivine loss or gain on the whole-rock compositions is clear in (a) and (c). In every plot, the sense of the change in chemistry of picrites and ferropicrites is matched by the sense of the change between accumulated fractional melts of KLB-1 and KG1. The chemistries of the natural samples could probably be better matched by calculating over wider range of T_P and adjusting the bulk composition, although the examples shown clearly illustrate that ferropicrites can be explained by the high pressure melting of a predominantly pyroxenitic source (i.e. close to 100% pyroxenite). There is little consensus about the most appropriate composition for mantle pyroxenite, and KG1 by no means represents the only option; being a synthetic mixture of MORB and peridotite, it is not entirely clear how such a blended composition would be created in the mantle.

4.6 Summary

4.6.1 Model uses, bounds and limitations

The new thermodynamic model of Jennings and Holland (2015) is tested in this chapter for applicability to a range of potential mantle compositions, and is used to make original observations and to explore the origin of the unusual ferropicrite composition. The model was calibrated on a rather small number of experimental constraints enabling it to be tested over a wide set of experimental and natural observations. It is concluded that this simple model provides an effective means of examining mantle phase equilibria and melting behaviour. The effect of varying T_P on the major element composition of basalts and other primitive melts can be assessed, and parameters which inform trace element models can be derived. The model was calibrated for peridotite partial melting, and it was demonstrated that it is indeed effective for this purpose, successfully reproducing the results of experimental studies. This includes the solidus and liquidus positions and melt productivity, modal mineralogy, and low fraction melt compositions. This final point is important; mantle melting is fractional, and in order to realistically model it, the model has to be effective at low melt fractions.

The model should primarily be used to interpolate between *PTX* conditions of experimental studies of upper mantle lithologies (depleted peridotite through to eclogite). It is suggested that the model be used only in the pressure range of 0.001–60 kbar and from 800 °C to liquidus temperatures, that reflects the range of experimental data used in the calibration and is the range over which the model is tested and validated in this chapter. Some aspects, such as the solidus position and mineral modes, are valid to higher pressures in peridotite, and others, such as solid-liquid Mg-Fe partitioning, work less well at high pressures. The model, although originally calibrated for peridotite melting, reproduced experimental pyroxenite and eclogite melt compositions well, although less well than for peridotite melting, and it is concluded that the model is applicable to a range of mantle compositions from depleted harzburgite through to silica-excess eclogite, although for silica-excess compositions it should be used with caution.

The model is presented in the simple NCFMASOCr system. This begins to approximate a real, complex system, unlike the MAS, CMAS and CFMAS predecessors. However, the effects of Ti and K are not examined, and will have a minor effect on phase equilibria and liquid composition (Davis and Hirschmann, 2013). Volatiles such as H_2O and CO_2 have been shown to have important effects on phase equilibria, melt compositions and the pressure and temperature of melt onset (Dasgupta and Hirschmann, 2010; Eggler, 1976; Gaetani and Grove, 1998; Green, 1973). This becomes a more important limitation when considering pyroxenite and eclogite, which contain higher concentrations of K, Ti and volatiles than peridotite. These extra components will reduce the source solidus temperature and increase melt productivity at low melt fraction. Some experimental studies on eclogite melting have stabilised rutile and K-feldspar close to the solidus, although these phases are lost shortly after

the onset of melting (Spandler *et al.*, 2008). Because TiO_2, K_2O and H_2O are higher in ferropicrites than in picrites (up to 3.9% in the Ahlmannryggen samples), the system limitation is particularly important when using the present model to investigate their origin. There is scope for future developments to the model to incorporate more components, more end-members and more complex mixing models.

Thermodynamic models such as this are useful as they allow the exploration of parameter space that is impractical to investigate experimentally, for example subsolidus and/or low temperature conditions that are difficult to equilibrate and are important for understanding the xenolith record, and low melt fractions that are important for understanding fractional melting. The present model performs well in the task of reproducing experimental melt compositions, solidus mineralogy and solidus location, relative to previously published thermodynamic and empirical models; a detailed review and comparison with other methods is given in Jennings and Holland (2015).

4.6.2 The effect of mantle source composition on melting

The effect of varying source composition on partial melt compositions were modelled. The compositions of partial melts of mantle enriched by the addition of basalt were to some extent buffered by an increased relative stability of clinopyroxene. This means that partial melts of a more enriched (pyroxenitic to eclogitic) mantle may be difficult to distinguish from peridotite partial melts, especially given the strong effect that melting pressure has on melt composition. However, there are exceptions to this. At pressures above that of the thermal divide, silica-saturated compositions have quartz in the melting assemblage. This exerts a dominating effect both on the solidus temperature and the melt composition, producing a distinctive dacitic composition that, were it to reach the surface without reacting, would be easy to identify. Over a broad range of bulk compositions from depleted harzburgite to eclogite, the pressure of the garnet-spinel transition (or the first appearance of garnet) on the solidus varied little, meaning that the use of a 'garnet signature' in trace element compositions as a pressure proxy is robust to changes in source composition, although the modal proportion of garnet in more enriched compositions is higher.

4.6.3 The origin of ferropicrite

Polybaric fractional melting simulations were performed on peridotite (KLB-1) and a silica-deficient pyroxenite composition (KG1) in order to assess melt compositions from a more realistic melting scenario. The accumulated partial melt compositions from an ambient T_P (1315 °C) and an elevated T_P (1500 °C) were compared with whole-rock compositions and the suggested primary composition of Etendeka picrites and ferropicrites. Pyroxenite accumulated melts were found to be higher in FeO, similar in SiO_2 and lower in MgO, CaO and Al_2O_3 than peridotite partial melts, although the effect

of the pressure of melting on MgO and Al_2O_3 in particular is greater than the effect of source lithology. However, FeO and CaO proved effective in discriminating between melts of the two sources, particularly when the effect of pressure was reduced by normalising to MgO or Al_2O_3. The Etendeka picrites best match the elevated T_P (1500 °C) partial melts of peridotite, whereas the ferropicrites are better explained by elevated T_P melting of the pyroxenite KG1. This is consistent with the sense of change in every oxide between picrite and ferropicrite. However, inconsistencies between the simplistic model results and the sample compositions make it difficult to quantify these results precisely. Because the Karoo and other Phanerozoic ferropicrites have similar major element compositions, the same conclusion is suggested for their petrogenesis.

These results strongly argue for a pyroxenite-bearing peridotite plume as the source of the Etendeka CFBs. Although ferropicrites appear to be partial melts of close to 100% pyroxenite, this does not mean that the source is 100% pyroxenite. Rather, in the mixed lithology mantle, pyroxenite begins to melt a little deeper and much more productively than peridotite, meaning that the earliest melts will reflect a high contribution of pyroxenite melting. Later melting of the more voluminous peridotite would swamp the pyroxenite melts, and highly refractory pyroxenite would also cease to melt once peridotite melting is extensive; this explains the lack of a clear pyroxenite melt contribution in the later picrites in the Etendeka. These results are in agreement with previous studies of the major element origin of ferropicrite (Gibson, 2002) and it is argued that the modelling approach presented here is more robust than comparison with equilibrium compositions of single pressure melting experiments. This is also consistent with the liquidus-type experiments of Tuff *et al.* (2005), which identified a high pressure garnet and clinopyroxene-bearing source for the ferropicrites. However, this chapter highlights a limitation of such experiments; if they worked perfectly (i.e. if magmas represented primary and unaltered equilibrium melts), a three phase multiple saturation point including olivine would be expected at high pressure for samples derived from both peridotite and olivine-bearing pyroxenite.

To quantitatively solve the origin of ferropicrite from a major element perspective, more fractional melting simulations are required over a range of T_P and starting compositions. Results of such simulations could also help to understand the controversial major element composition of OIBs (e.g. Putirka *et al.*, 2011). Such simulations are not currently convenient to perform in THERMOCALC.

Chapter 5

The potential temperatures of the Paraná-Etendeka and Karoo CFB mantle sources

Collaborative work statement

The olivine-spinel pair data and corresponding crystallisation temperatures for the DML Ahlmannryggen group 3 samples in this chapter were analysed during research for this thesis and are published in Heinonen *et al.* (2015); they were not heavily interpreted in the publication, which mainly focuses on a dataset from a meimechite sample from the 'Vestfjella depleted ferropicrite' suite (not studied in this thesis) to look at the temperature of the Karoo CFB mantle source.

5.1 Introduction

Estimating the temperature of the mantle from geochemistry

Since the conception of the mantle plume model (Morgan, 1971), the temperature of the mantle source of magmatic provinces has been widely debated (e.g. Foulger and Anderson, 2005; Herzberg *et al.*, 2007; Hole, 2015; Keiding *et al.*, 2011; McKenzie and O'Nions, 1998; Putirka *et al.*, 2007; Richards *et al.*, 1989; Thompson and Gibson, 2000; White and McKenzie, 1989, 1995). Mantle plumes are upwelling columns of mantle that are significantly hotter than ambient mantle and result from thermal instabilities at depth. If a plume partially melts, it will begin to do so deeper than ambient mantle. To test whether a plume was responsible for melt production in CFB province settings, the mantle temperature at the time of melting must be estimated. Mid-ocean ridges distal to hotspots are considered to sample ambient mantle with no extra heat input (Parsons and Sclater, 1977). In the absence

of melting, upwelling mantle will follow an abiabat such that it will be at higher temperature when compressed. Its temperature is therefore conveniently expressed as potential temperature (T_P), which is the temperature of the mantle extrapolated along an adiabatic to the pressure at the Earth's surface (McKenzie and Bickle, 1988).

The link between modern off-axis volcanism and magmatic seamount chains (such as the Hawaiian-Emperor seamount chain and modern volcanic activity on Hawaii) was an early piece of evidence that lead to the idea of tectonic plates moving over fixed, long-lived hotspots, interpreted as thermal plumes from the lower mantle (Morgan, 1971). This has frequently been confirmed through estimates of T_P at hotspots which are elevated relative to that of MORB (e.g. Herzberg *et al.*, 2007), although there is still not a universal consensus; see Foulger and Anderson (2005). Richards *et al.* (1989) first suggested that the enormous volumes of melt observed in CFB provinces were also related to plume activity, specifically to the arrival of buoyant mantle plume starting-heads. It remains unclear whether plume heads need to be hotter, or just more voluminous, than their long-lived tails (Farnetani *et al.*, 2002; Herzberg and Gazel, 2009; Richards *et al.*, 1989; Thompson and Gibson, 2000; White and McKenzie, 1995). However, the link between continental magmatism and plumes is made more complex by the often concurrent extensive rifting and the observation that not all CFB provinces are associated with a hotspot track (e.g. Siberian Traps). White and McKenzie (1989) demonstrated that a combination of elevated T_P and lithospheric thinning through rifting is required to produce voluminous CFB melts, and Campbell and Griffiths (1990) suggested that the rifting is often a consequence of subsidence following the impact of a mantle plume starting head.

Geochemical methods that have been applied to primitive melts in CFB provinces in order to constrain the T_P of their mantle plume source are:

1. Olivine-liquid MgO-FeO equilibria geothermometry on melt crystallisation temperatures, which is converted to T_P (Beattie, 1993; Ford *et al.*, 1983; Putirka, 2005; Putirka *et al.*, 2007; Roeder and Emslie, 1970).

2. Parametrisations of peridotite melting as a function of P and T, which allow the forward modelling of melt compositions for comparison with primary melt compositions (e.g. Langmuir *et al.*, 1992; McKenzie and Bickle, 1988), including MELTS/pMELTS (Ghiorso *et al.*, 2002; Ghiorso and Sack, 1995), and the PRIMELT2/PRIMELT3 software, which simultaneously solves for primary melt composition and mantle melting conditions (Herzberg and Asimow, 2008, 2015).

3. REE inversion, where, for an assumed mantle source composition, a melt REE composition is inverted to solve for melt fraction (F) as a function of depth. This can be compared with forward models of peridotite melting to estimate T_P (McKenzie and O'Nions, 1991).

These methods all require a good knowledge of the melt chemistry and extrapolation to the primary melt composition. Primitive CFB samples are not glassy and not always fresh, so assuming a liquid composition adds an extra level of uncertainty. The Al-in-olivine crystallisation geothermometer was recently calibrated, which relies on the temperature-dependent exchange of Al between olivine and spinel (Coogan *et al.*, 2014; Wan *et al.*, 2008) and does not require an estimate of the melt composition. Crystallisation temperatures obtained by this technique provide a minimum constraint for mantle T_P, and thermal models can be used to back-calculate these to source T_P. This chapter presents a series of such calculations.

Although there are still large discrepancies between the findings of the various methods (Herzberg *et al.*, 2007), CFB province sources appear to have elevated T_P relative to ambient mantle, which is usually interpreted in the context of the thermal plume paradigm. Alternatively, specific to rifted CFB provinces, a thermal insulation model has also been invoked (Coltice *et al.*, 2007; Hole, 2015; Rolf *et al.*, 2012) in which a supercontinent insulates underlying mantle, allowing it to build up heat and then partially melt in the event of subsequent rifting. This would be difficult to distinguish from a plume model on the basis of temperature alone.

The temperature of the Paraná-Etendeka and Karoo CFB mantle sources: Previous work

Early work on the Paraná-Etendeka CFB province explored mantle T_P from the perspective of melt volume generation and relied on assumptions about lithospheric thickness and the relative timing of rifting and melt generation (Gallagher and Hawkesworth, 1994). More recently, geochemical methods have been applied to constrain the mantle source temperature. The Etendeka picrites are similar to the parental melts of the voluminous Paraná-Etendeka CFBs, and because the picrites and the lower MgO CFB lavas sample the same mantle plume source, knowing the temperature of the picrite source sheds light on the origin of the CFB.

Thompson *et al.* (2001) use both forward models of major element compositions (after Langmuir *et al.*, 1992) and REE inversion modelling to infer a mantle T_P of 1470–1560 °C from the Etendeka picrite whole-rock compositions. This required a lithospheric thickness of 55–95 km and corresponds to $F \sim 0.12$–0.22 (the lithosphere acts as a lid and prevents further mantle upwelling). The picrites were suggested by Thompson and Gibson (2000) to have a bimodal olivine compositional population, where the higher Fo_{91-93} olivines were suggested to derive from crystallisation of the 'Horingbaai parental komatiite' (a more magnesian primary liquid of 24 wt.% MgO) deeper in the system, which represents melting of a $\sim T_P$ = 1700 °C plume.

If the interpretation of Thompson and Gibson (2000) is correct, the crystallisation temperatures recorded by the olivine population should be strongly bimodal. Keiding *et al.* (2011) tested this theory with MgO-FeO equilibria (after Putirka *et al.*, 2007) between olivine-hosted melt inclusions and their

host olivines in a similar suite of Horingbaai picrites. They estimated olivine-melt equilibrium temperatures (interpreted as crystallisation temperatures) to be 1246–1395 °C and a T_P (calculated from inclusion MgO content according to the equation $T_P = 1463 + 12.7\text{MgO} - 2924/\text{MgO}$ of Herzberg *et al.*, 2007) of 1520 °C. Keiding *et al.* (2011) dispute the method used by Thompson and Gibson (2000) to extrapolate melt MgO from olivine Fo, citing this to largely overestimate melt MgO. However, the method of Keiding *et al.* (2011) is also problematic. They used melt inclusions that have been rehomogenised at 1350 °C to represent the liquid composition. As shown in Chapter 3, the rehomogenisation processes significantly alters the major element composition of olivine-hosted melt inclusions, and this is especially true of Mg and Fe, which exchange with the host olivine both immediately after inclusion formation, and again at the high temperatures used in rehomogenisation. Changes to MgO and FeO concentrations in melt inclusions are dismissed by Keiding *et al.* (2011), but it is demonstrated in Chapter 3 that they are significant. Therefore, the results of Keiding *et al.* (2011) should be interpreted with caution. The relationship between host olivine Fo and apparent T_P (or MgO) is not discussed, but their data indicate that there is no correlation.

The Karoo mantle source T_P is still poorly resolved and highlights the discrepancies between different methods. Recently, Hole (2015) calculated the T_P of several CFB provinces from published whole-rock compositions using PRIMELT2 (Herzberg and Asimow, 2008). He finds that, for the Etendeka picrites, T_P = 1490–1563 °C with a final equilibration pressure at 1.3–3.7 GPa (39–111km), and for Karoo samples from DML, T_P = 1529–1650 °C with a final equilibration pressure of 3.7 to >7 GPa (111 to > 217 km). The final equilibration pressure implies that the mantle stopped upwelling at this pressure, i.e. it is a proxy for the palaeo lithospheric thickness. The results of Hole (2015) are at odds with the evidence from one DML meimechite sample (AL/B7-03), that Hole (2015) find to have the highest temperature (T_P = 1650 °C) on the basis of whole-rock chemistry, whereas Heinonen *et al.* (2015) measure a maximum Al-in-olivine crystallisation temperature in that sample of 1481 °C, corresponding to T_P = 1495. Primary melt compositions calculated for this sample group previously yielded a T_P of $\sim$ 1700 °C (Heinonen and Luttinen, 2010, after Putirka *et al.*, 2007), although T_P obtained by the method of Putirka (2005) and Putirka *et al.* (2007) tend to overestimate T_P and crystallisation temperature relative to other methods (Herzberg *et al.*, 2007).

In summary, the mantle T_P for the Paraná-Etendeka and Karoo CFBs have been examined in several studies but the estimates vary widely (Paraná-Etendeka: 1470–1700 °C; Karoo: 1495–1700 °C). Previous methods required a good knowledge of the primary liquid composition, or the actual liquid composition corrected for fractionation, with a particular focus on MgO and FeO. As discussed in Chapter 2, the liquid composition is obscured by olivine macrocryst loss or gain, and the magnitude of the fractionation correction required to define a primary melt is not well constrained. The recent development of the Al-in-olivine crystallisation thermometer provides the opportunity to reassess the crystallisation temperature distribution and mantle T_P, and represents an improvement over previous

methods for the samples of this study because it requires no knowledge of the melt composition and, unlike olivine-melt Mg-Fe equilibria, is robust against subsolidus re-equilibration.

Because ferropicrite is probably not a peridotite partial melt, its mantle source T_P is difficult to determine. It is argued in this thesis and in previous publications (Gibson, 2002; Heinonen *et al.*, 2014, 2013; Tuff *et al.*, 2005) that ferropicrite derives from the high pressure melting of mantle pyroxenite. Therefore, methods involving parametrisations of peridotite primary melts as a function of *PT* are not applicable, although olivine saturation in liquids should still give valid crystallisation temperatures. REE inversions are made difficult by the different source composition and partitioning behaviour during pyroxenite melting, as well as the fact that fractionation correction is done on the basis of a major element parametrisation of primary peridotite melts in the method of McKenzie and O'Nions (1991). Gibson *et al.* (2000) estimate a T_P for the ferropicrites of 1550 °C with a lithospheric thickness of 115 km and $F = 0.10$ on the basis of peridotite or Fe-rich peridotite melting. Additionally, crystallisation experiments performed on an Etendeka ferropicrite sample (Tuff *et al.*, 2005) locate the 1 atm liquidus, or the highest crystallisation temperature, at 1375 °C. There is scope for a reassessment of the mantle melting conditions of ferropicrite production (in both the Etendeka and Karoo provinces) on the basis of pyroxenite melting.

5.2 Crystallisation temperatures

5.2.1 The Al-in-olivine thermometer

Like other geothermometers, the Al-in-olivine of Wan *et al.* (2008) and Coogan *et al.* (2014) is based on the premise that equilibrium partitioning of certain elements (in this case aluminium) between phases (here spinel-liquid and olivine-liquid pairs) is sensitive to pressure and/or temperature. Al is primarily incorporated into olivine by a coupled substitution into the M and T sites, although other mechanisms also operate (Coogan *et al.*, 2014; Wan *et al.*, 2008). At higher temperature, more Al is incorporated by the olivine structure.

The Al-in-olivine thermometer was first developed by Wan *et al.* (2008) in order to determine the equilibrium temperature based on Al partitioning between co-existing Cr-bearing spinel and olivine. Experimental temperatures were fitted to a small number of parameters: the Cr# (molar Cr/(Cr+Al)) of spinel and the distribution of Al between olivine and spinel. The thermometer was updated by Coogan *et al.* (2014), who performed additional experiments to extend the calibration range to higher fO_2. The updated thermometer, including uncertainties on coefficients in brackets, is given as:

$$T(K) = \frac{10000}{0.575(0.162) + 0.884(0.043)\text{Cr\#} - 0.897(0.025)\ln(\text{k}_\text{d})} \tag{5.1}$$

where $\text{k}_\text{d} = \text{Al}_2\text{O}_3^{\text{ol}} / \text{Al}_2\text{O}_3^{\text{sp}}$, in wt. %.

Cr-spinel and olivine tend to be the liquidus phases in primitive melts, so the recorded temperature can be taken as a proxy for the liquidus temperature. The two phases must have each been in equilibrium with the liquid, and hence each other, as they co-saturated. The very slow diffusion of trivalent Al in olivine (Spandler and O'Neill, 2010) means that re-equilibration at lower temperatures should not be a problem, even in slower cooling systems (Coogan *et al.*, 2014).

This thermometer has the advantage over traditional Mg-Fe olivine saturation thermometry in that it requires no knowledge of the melt composition. Samples in this study contain abundant Cr-rich spinels, which are preserved in a closed system trapped within olivine phenocrysts (Fig. 5.1). Assuming that the two phases co-crystallised or were in equilibrium at the moment of entrapment, the Etendeka and DML samples are a suitable material for application of the Al-in-olivine thermometer. Oxide phases in the groundmass tend to be ilmenite, or less commonly, magnetite; liquidus Cr-spinel crystals may have settled out or been resorbed.

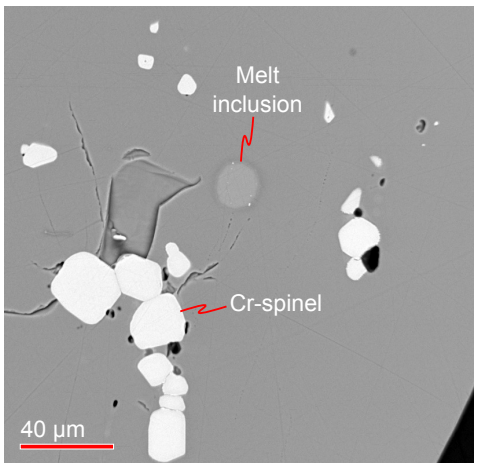

Figure 5.1: BSE image of olivine grain with abundant Cr-spinel inclusions and a rehomogenised melt inclusion (note that analyses for this chapter were only performed on unheated samples).

5.2.2 Spinel and olivine chemistry

Analytical methods: EPMA and XANES

Spinel and olivine compositions for the Etendeka and DML samples were obtained from polished, unheated samples by EPMA (analytical details are provided in Appendix A). All spinels are inclusions within olivine, and olivine analyses were obtained in a triangle around a spinel, at least 20 µm away from the interface.

Spinel $Fe^{3+}/\Sigma Fe$ and Fe^{3+} per formula unit (p.f.u.) were initially calculated stoichiometrically by EPMA according to the method of Droop (1987) on a four oxygen basis. Nine spinel standards analysed in the same session indicated that the spinel $Fe^{3+}/\Sigma Fe$ calculated from EPMA data had

low accuracy and precision, and often significantly overestimated $Fe^{3+}/\Sigma Fe$. The $Fe^{3+}/\Sigma Fe$ of the spinel standards and a subset of 11 of the spinel inclusions were subsequently analysed by Fe-Kα x-ray absorption near edge spectroscopy (XANES). A detailed account of the XANES procedure and the EPMA data corrections are given in Appendix A. The XANES measurements showed that the published Fe^{3+} contents of two of the nine standards used were probably incorrect, and that the Fe^{3+} EPMA estimates of remaining standards were inaccurate but not too imprecise. XANES measurements of these seven standards were used to calibrate the subset of spinels measured by XANES. The standards and spinel samples together showed that the EPMA data overestimated the true $Fe^{3+}/\Sigma Fe$ by 1.69, although there was scatter in this value (see Appendix A). A correction factor of 0.59 was therefore applied to the EPMA $Fe^{3+}/\Sigma Fe$ estimate of all spinel samples. The calibration and correction procedure has many limitations and caveats, and the final Fe^{3+} values should be considered approximate values. However, they indicate that the spinel samples fall within the $Fe^{3+}/\Sigma Fe$ calibration range of the Al-in-olivine thermometer (Coogan *et al.*, 2014; Wan *et al.*, 2008). The spinel Fe^{3+} contents shown in this chapter are the EPMA values adjusted as above.

Spinel and olivine compositions

The distribution of host olivine Fo used in the Al-in-olivine thermometry is similar to the distribution of compositions of olivine cores in thin section described in Chapter 4. Fo and Al_2O_3 in olivine are correlated for a given sample type, where the highest Fo olivine is also the most Al-rich (Fig. 5.2), which is consistent with a higher crystallisation temperature.

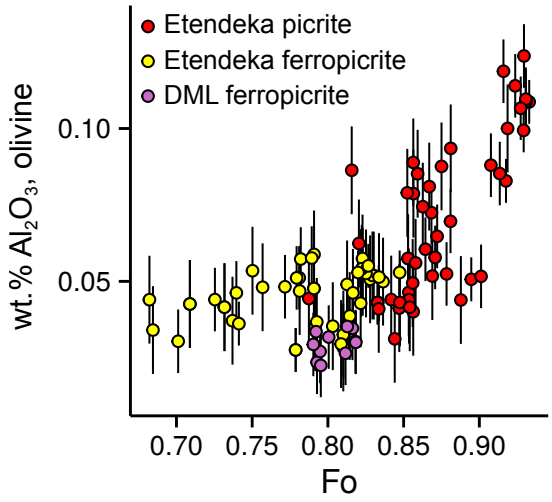

Figure 5.2: Olivine wt.% Al_2O_3 as a function of Fo (only those olivines considered in this chapter are shown). Error bars are $\pm 1\sigma$.

Because spinels form solid solutions between a range of end-members, simple trends are not expected. The inclusion compositions are approximately consistent with a global compilation of similar

samples (Barnes and Roeder, 2001) and are shown in Fig. 5.3 and Fig. 5.4. Picritic spinels tend to have the highest Mg# and the highest proportion of chromite and spinel endmembers. Cr# does not vary systematically between groups and is not dependent on Fo; however, Cr and Al concentrations are correlated and decrease systematically from the most to the least forsteritic. Ferropicritic spinels appear more evolved, with more Fe^{2+}, Fe^{3+} and Ti-rich compositions, towards magnetite and ülvospinel end-members. DML ferropicrite spinels are especially TiO_2 rich at a given Fe^{3+} and Fo, reflecting the unusually high whole-rock Ti content; a similar offset to higher Ti in some Etendeka ferropicrite spinels is also observed. Finally, spinel inclusions from sample 97SB67 have rather different compositions and are found in much lower Fo olivine. These spinels are often very magnetite and/or Ti-rich, and fall well outside of the calibration range of the Al-in-spinel thermometer, so are not included in the thermometry. Mg# and Ni in all spinels are tightly correlated with host olivine Fo, indicating re-equilibration between these faster diffusing elements.

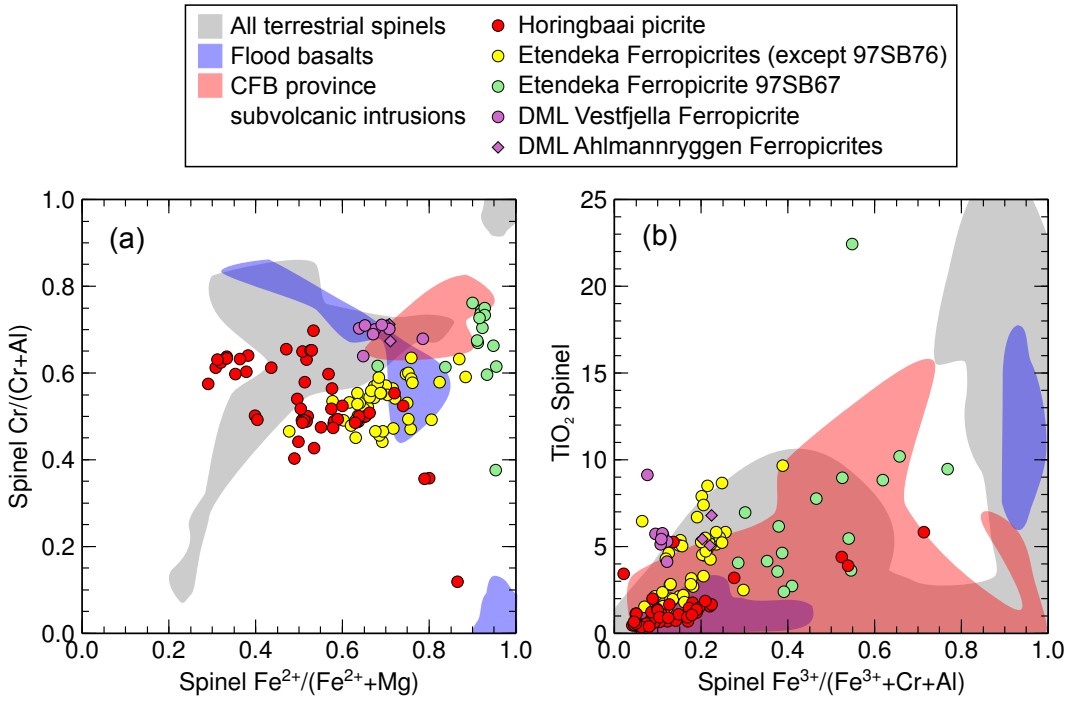

Figure 5.3: Spinel inclusion compositions: (a) 1-Mg# (molar $Mg/(Mg+Fe^{2+})$) vs. Cr# (= molar Cr/(Cr+Al)); (b) molar $Fe^{3+}/(Fe^{3+}+Cr+Al)$ vs. TiO_2 (wt. %). Shaded fields are the global compilations of Barnes and Roeder (2001), where fields in (a) show the 90th percentile of data density and fields in (b) show the 50th percentile of data density. Fe^{3+} determined by EPMA and adjusted according to the findings of XANES analyses; see section 5.2.2.

5.2.3 Thermometer calibration range and sample suitability

The Al-in-olivine thermometer was derived by regressing experimental data to relate temperature to chemistry (Coogan *et al.*, 2014; Wan *et al.*, 2008). The experiments were performed over a limited

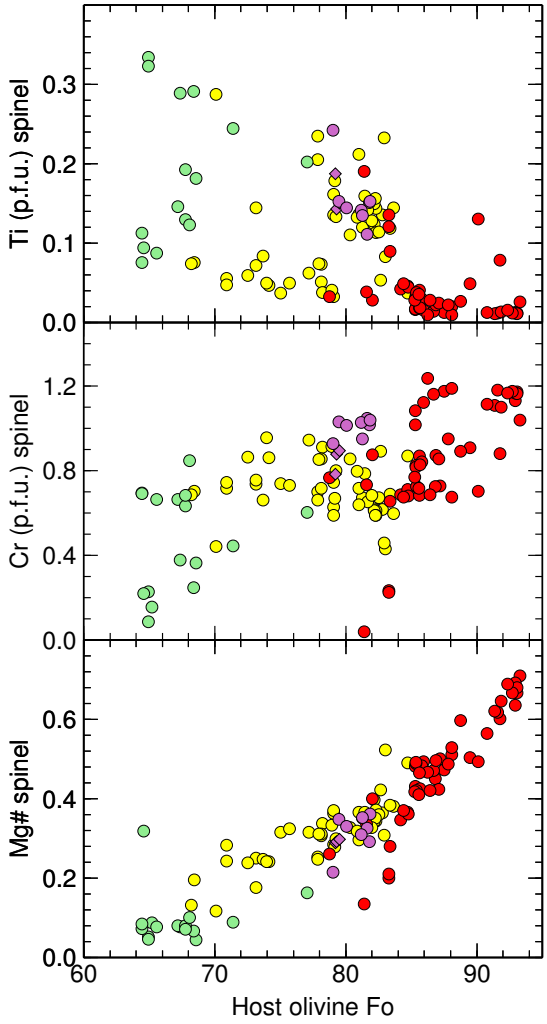

Figure 5.4: Spinel inclusion compositions plotted against host olivine Fo: Ti and Cr (both calculated per formula unit, p.f.u) and Mg#. Legend as for Fig. 5.3.

range of bulk compositions, fO_2 and temperature, and as such, it is unknown whether the thermometer behaves correctly at conditions or compositions outside of the investigated range. Wan *et al.* (2008) perform experiments at a low fO_2 of -1.8 to -1.5 log units below the QFM buffer, which was extended up to FMQ +1.3 by Coogan *et al.* (2014), who noted that the thermometer was not very sensitive to ferric iron over this fO_2 range. The calibration ranges of spinel compositional features are: Ti (p.f.u.) = 0–0.023; $Fe^{3+}/\Sigma Fe$ = 0–0.330; Fe^{3+} (p.f.u.) = 0–0.104; Cr# = 0–0.695 (Coogan *et al.*, 2014; Wan *et al.*, 2008).

Ti and Fe^{3+} (along with Cr and Al) occupy the tetrahedral sites in spinel, which can lead to an apparent increase in k_d, resulting in an overestimated temperature (Coogan *et al.*, 2014). In this study, the calibration ranges of Wan *et al.* (2008) and Coogan *et al.* (2014) have been exceeded in some samples. The Ti contents of the experimental spinels used in the thermometer calibration were very low; most natural spinels exceed the upper calibration limit, including those to which the thermometer

were applied by Coogan *et al.* (2014). This is more problematic for the ferropicrite samples, because the primary melts, and thus spinels, have high Ti relative to normal MORB and LIP samples for which the thermometer was designed. Fig. 5.5 shows the frequency with which different (a) Ti contents and (b) Fe^{3+} contents were measured. The calibration limits of the Al-in-olivine thermometer are shown as blue lines. Whereas all samples fall within the $Fe^{3+}/\Sigma Fe$ calibration limit, most samples are above the upper Ti limit. Dashed lines show the upper limit cutoffs in spinel Ti (p.f.u.) for the different sample groups as applied in this chapter. Spinels with Ti contents above this limit are not used in further thermometry. The temperature calculated with equation 5.1 is plotted as a function of Ti in Fig. 5.5c. If Ti has a large impact on the thermometer, a positive correlation between T and Ti would be expected. Given that this is not observed, the effect of Ti on T appears to be within the thermometer error for these samples, justifying a higher Ti threshold in this study (L. Coogan, pers. comm.).

Similarly, there is no clear correlation between $Fe^{3+}/\Sigma Fe$ and T (the three spurious picrite data points at $Fe^{3+}/\Sigma Fe > 0.29$ and $T > 1500$ are high in Ti and thus not used in the following thermometry). This is consistent with the observation of Coogan *et al.* (2014) that in all of their experiments, Fe^{3+} does not strongly affect the thermometer. Because they contain more ΣFe than the experimental spinels, spinel samples in this chapter are mostly outside the limit of $Fe^{3+} = 0.104$, although the nine picrite spinels which give the highest crystallisation temperatures (with Ti < 0.05 p.f.u.) have $Fe^{3+} < 0.104$. Because of the lack of apparent effect of Fe^{3+} on calculated T in the sample range, no Fe^{3+} p.f.u. cutoff is applied. In general, spinel-olivine pairs which give the highest crystallisation temperatures in this chapter have the lowest Ti and Fe^{3+} and the highest Al contents.

Coogan *et al.* (2014) also investigated the effect of a_{SiO_2} and P_2O_5 on the thermometer. They found only a weak positive correlation between the temperature offset between the experimental and calculated temperatures (ΔT), and a_{SiO_2}, so concluded that most of the Al is not incorporated in olivine through vacancy creation (which would result in an Al partitioning dependency on a_{SiO_2}). Over the calibration range, a_{SiO_2} accounts for < 20 °C error. P_2O_5 in olivine is found to have a bigger effect, where it enables an increased Al concentration; if the two are positively correlated then Al in olivine should be extrapolated to $P_2O_5 = 0$. Olivines in this study have much lower P concentrations than the experimental ones and show no correlation with P, so the effect of P on the thermometer is discounted. The effects of other species on the thermometer are not fully investigated by Coogan *et al.* (2014), although they should be accounted for by the large thermometer uncertainty. Finally, it is noted that Coogan *et al.* (2014) apply the thermometer to a range of MORB and LIP samples with a range of compositions extending outside of the thermometer compositional calibration range. They found crystallisation temperatures of 1122-1485 °C. After filtering the data to remove high Ti spinels according to the limits in Fig. 5.5a, the thermometer should be applicable to the range of compositions in this study.

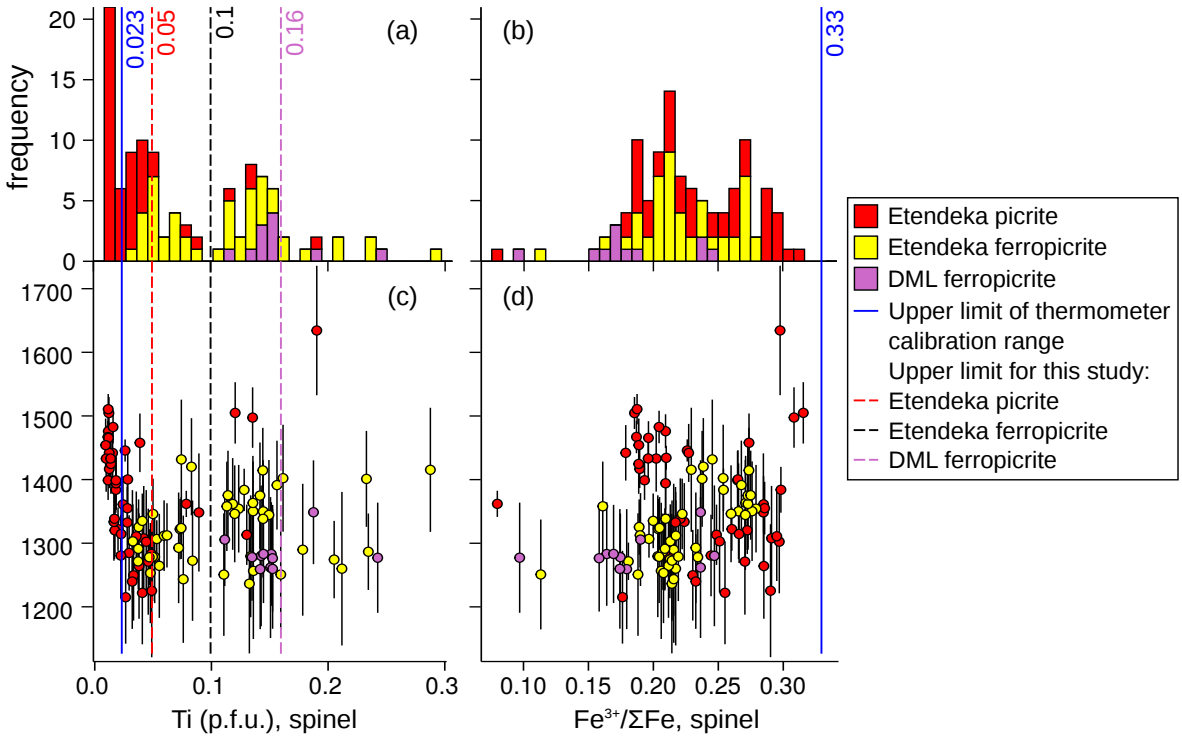

Figure 5.5: (a) Spinel Ti (p.f.u.) and b) spinel $Fe^{3+}/\Sigma Fe$ distribution from Etendeka picrites and ferropicrites and DML ferropicrites. Shown in solid blue lines are the calibration limits of Coogan *et al.* (2014); shown in dashed lines are the upper Ti limits for spinels selected for thermometry in this study (Etendeka picrites limited to < 0.05, Etendeka ferropicrites to < 0.1 and DML ferropicrites to < 0.16). Spinels with higher Ti are shown here to illustrate the effect on calculated temperature, but are not used in subsequent thermometry. c) and d): Al-in-olivine temperature plotted as a function of spinel Ti (p.f.u.) and $Fe^{3+}/\Sigma Fe$, respectively. Spurious temperature results are seen from some high Ti picrite spinels, which are outside of the acceptable picrite Ti limits.

Thermometer uncertainty

The thermometer reproduced the temperatures of 42 of the 45 calibration experiments to within 20 °C (Coogan *et al.*, 2014), indicating an inherent 1σ uncertainty of 13 °C. The published uncertainties of thermometer coefficients (shown in equation 5.1) equate to an uncertainty of around ± 55 °C when calculated by Monte Carlo simulation. This is higher than the inherent thermometer 1σ and implies that the coefficient uncertainties are correlated. The Monte Carlo method therefore overestimates uncertainty and is not used. Instead, 1σ error is estimated according to the analytical uncertainty in Al in olivine. Al is a trace element in olivine, and even with long counting times the relative uncertainty in Al measured by EPMA in samples from this study is high (and much larger than that in spinel Al or Cr). Olivines were anaysed in three analytical sessions with different counting times for Al. Details of these measurements are given in Appendix A. It was noted that, within a given analytical session, the absolute uncertainty of the Al measurement remained near-constant with olivine composition. For this reason, constant absolute uncertainties are applied here (shown in Fig. 5.2). As an

example, a counting time of 30 s gave an uncertainty of very close to ± 0.014 (1σ) wt.% Al_2O_3 in all olivines. This translates to a lower relative uncertainty in higher Al olivines. Therefore, olivines with the highest crystallisation temperatures and/or olivines measured with the longest counting times give temperature estimates with the lowest uncertainties. Temperature uncertainties are calculated from Al analyses by Monte Carlo simulations with 6000 calculations per spinel-olivine pair. The uncertainties determined were always greater than the inherent thermometer uncertainty. It is assumed that temperature changes resulting from other compositional effects are within the calculated error bracket.

5.2.4 Crystallisation Temperatures

Al-in-olivine crystallisation temperatures are shown as a function of host olivine Fo in Fig. 5.6. Only spinel compositions filtered according to the limits of Fig. 5.5a are used, and their compositions and calculated crystallisation temperatures are given in Appendix C. The highest crystallisation temperatures are recorded by the Etendeka picrites, with two extremely high temperatures (1505 ± 25 and 1511 ± 24 °C) calculated from spinel-olivine pairs in sample 97SB33. The Etendeka picrites show a weak positive correlation between Fo and T, which is expected from concurrent cooling and crystallisation. Except for the very highest temperatures, the range in temperatures can be explained by fractional crystallisation of a primitive picrite, represented by sample 97SB33 (red line on Fig. 5.6). The lowest temperature picrite measurements can be related to the highest temperature data points along a vector parallel to the calculated fractionation trend. However, a cluster of > 1400 °C measurements from Fo_{85-88} do not relate to higher Fo olivines by fractionation. These are mostly from sample 97SB56, and perhaps indicates that the primary melt for that particular sample had higher Fe/Mg ratio than 97SB33.

Ferropicrite samples have a cluster of temperatures at around 1300 °C, where the DML ferropicrites are on average slightly cooler than, but within error of, the Etendeka ferropicrites. No clear correlation is seen between temperature and Fo for these rocks. The spurious 1427 °C temperature recorded by a spinel in Fo_{68} olivine from sample 97SB80, along with a few other anomalous data points, are from spinels with Ti contents approaching the upper limit.

Fig. 5.7 shows the frequency distribution of temperatures from the same filtered dataset. Histograms a-c incorporate all of the filtered data for that sample group whereas d-h are for individual samples that have at least 10 measurements. Each temperature measurement has some uncertainty. The kernel density estimate (KDE) overlay in Fig. 5.7 incorporates this uncertainty. Mean temperatures, standard deviations and the number of observations are given in Table 5.1. In the summed distribution, a weakly bimodal temperature distribution is seen in picrite samples. A mean of 1361 ± 103 °C for all of the Etendeka Horingbaai picrites is estimated from the density distribution. If only the 11 Fo > 90 olivines are considered, an average $T = 1457 \pm 44$ °C is calculated (average for Fo < 90

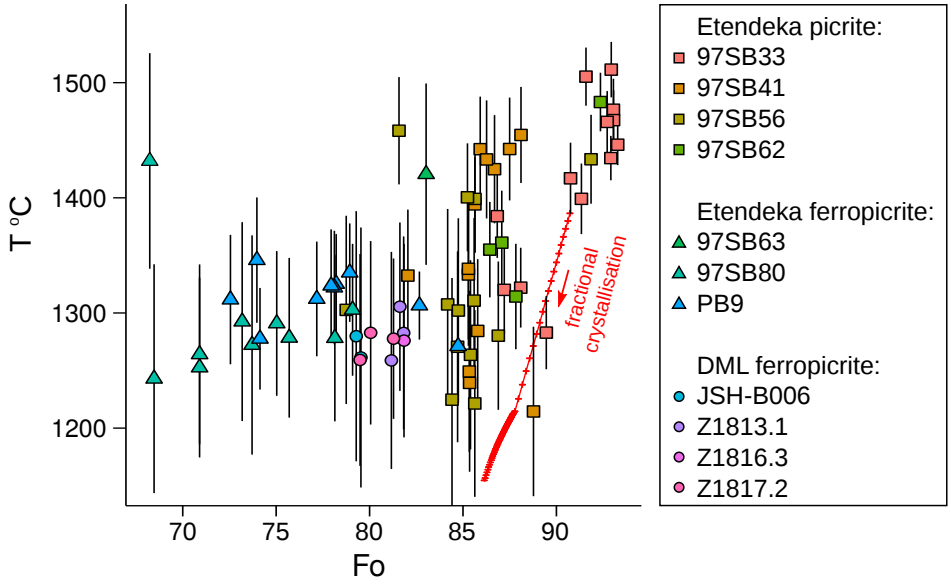

Figure 5.6: Temperature estimates from Al-in-olivine thermometry. Error bars are 1σ calculated from analytical uncertainty of Al in olivine and filtered for data with Ti below that shown in Fig. 5.5. Red line shows the modelled temperature change with Fo, calculated in Petrolog3 (Danyushevsky and Plechov, 2011), with crosses at $F = 0.01$ intervals. Calculation performed at QFM using the whole-rock composition of picrite sample 97SB33 after correction for olivine accumulation.

= 1339 °C). The high Fo cluster average temperature of 1457 °C is similar to the 1 atm crystallisation temperature of 1477 °C of this high Fo olivine group estimated using olivine Fo-whole-rock MgO systematics (Thompson and Gibson, 2000), although once corrected to the pressure at the base of the 50 km lithosphere, the crystallisation temperature cited by Thompson and Gibson (2000) is > 1527 °C, assuming a komatiite liquidus. Conversely, the maximum crystallisation temperature identified for the Horingbaai picrites by Keiding *et al.* (2011) of 1395 °C is lower, and was calculated from the relationship between melt inclusion MgO and the host olivine Fo. The Etendeka and DML ferropicrite samples do not have bimodal temperature distributions. A mean of 1312 ± 103 °C is similarly calculated for the Etendeka ferropicrites, and 1264 ± 91 °C for the DML ferropicrites. The mean of i) all Etendeka ferropicrite measurements and ii) the > 90 Fo Etendeka picrite olivine-spinel pairs are used in modelling the source T_P in the next part of this chapter. The Fo > 90 olivines are chosen because they are the least affected by fractionation and so most closely represent crystallisation on the picrite liquidus. For the ferropicrites, fractionation is not considered because its effects are difficult to resolve in this small dataset.

Global comparison of crystallisation temperatures

Coogan *et al.* (2014) determined Al-in-olivine crystallisation temperatures for samples from several global LIPs, and this database has been expanded by the addition of analyses from this chapter and

Sample group	Mean T (°C)	σ	n
All Etendeka picrites	1361	103	43
Etendeka picrites, >Fo_{90}	1457	44	11
Etendeka ferropicrites	1312	103	24
DML Karoo ferropicrites	1264	91	9

Table 5.1: Mean crystallisation temperature for each sample group, where analyses used to calculate means are filtered according to limits in Fig. 5.5.

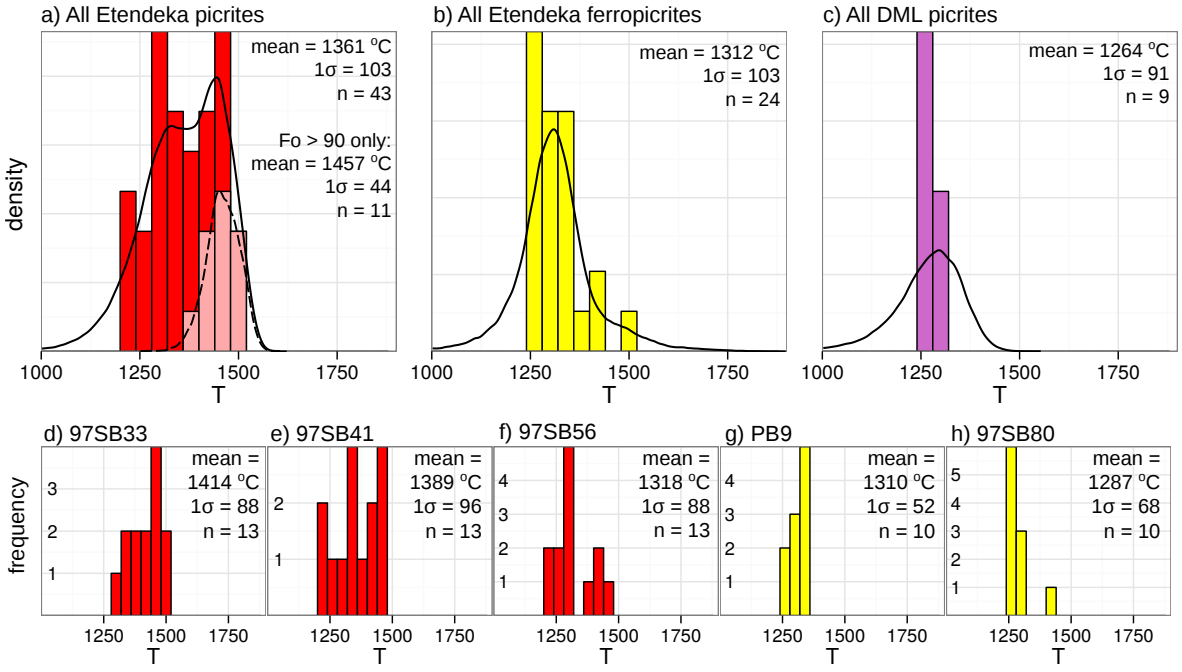

Figure 5.7: Crystallisation temperature estimates from Al-in-olivine thermometry, filtered to exclude spinels above the Ti limits of Fig. 5.5. a-c) Histograms of whole sample groups (normalised to density) with KDE overlay calculated with a bandwidth equal to the 1σ temperature uncertainty. The pale pink part of the histogram in a) and dashed KDE shows the temperatures of Fo > 90 olivines. d-h) Histograms of the frequency of temperature measurements for individual samples, for samples with at least 10 measurements.

from a primitive meimechite and ferropicrite from the DML (Karoo; Heinonen *et al.*, 2015), with the resultant distribution shown in Fig. 5.8. Both the Etendeka and Karoo rocks have crystallisation temperatures towards the high end of the global LIP distribution. Two Etendeka picrites have crystallisation temperatures of > 1500 °C, which are the highest terrestrial crystallisation temperatures measured by this technique. The Etendeka picrite peak is at least 100 °C hotter than the Gorgona komatiites, in agreement with the interpretation of Thompson and Gibson (2000). Ferropicrites crystallise within the normal temperature spectrum of other LIP samples.

To understand the origin of LIPs, it is useful to compare their Al-in-olivine crystallisation temperature distribution to that of MORB samples known to originate from ambient mantle T_P (Fig. 5.9). MORB has an average crystallisation temperature that around 160 °C lower than that of LIPs and

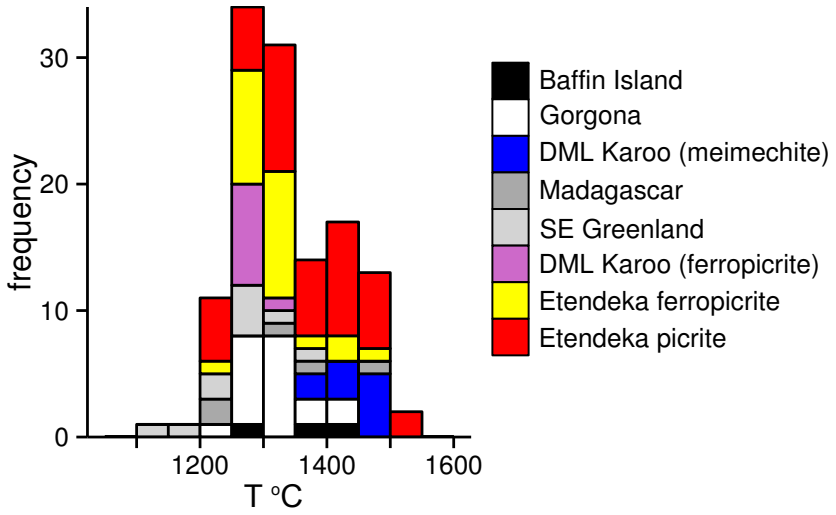

Figure 5.8: Global LIP Al-in-olivine crystallisation temperatures. Etendeka picrites and ferropicrites, this study; Karoo, Heinonen *et al.* (2015); all others, Coogan *et al.* (2014).

a narrower temperature distribution, presumably reflecting a common T_P, lithospheric thickness and mechanism of formation in samples from different ocean ridges. The lower temperature is not accounted for by extensive fractionation, as this thermometer requires the crystallisation of Cr-spinel, which only occurs close to the liquidus of primary melts. The much broader temperature distribution in LIPs reflects differences in T_P, lithospheric thickness and crystallisation depth between and within different LIP settings. The crystallisation temperature defines a minimum mantle T_P, and the higher crystallisation temperatures recorded by LIPs than MORBs must, to some extent, reflect a higher T_P.

5.2.5 Summary: Crystallisation temperature

The crystallisation temperatures of the Etendeka picrites are hotter than ferropicrites, and are also high with respect to the published LIP range. The LIP range is itself significantly hotter than MORB, implying that an elevated mantle T_P is required in LIP formation. Average crystallisation temperatures of different samples groups are given in Table 5.1. Although the temperature distribution for Etendeka picrites appears bimodal and split according to host olivine Fo, resolution on this bimodality is lost and temperatures merge into a single peak once thermometer errors are taken into account. In addition, trends between crystallisation temperature and Fo content are unclear, so it is uncertain what proportion of the temperature distribution is accounted for by crystallisation and cooling as opposed to a different parental melts for the high and low Fo groups (cf. Thompson and Gibson, 2000). T_P will be calculated in the following section to match the mean crystallisation temperatures of entire sample groups, neglecting the effect of fractionation. This limitation means that T_P calculated may be low, representing a minimum.

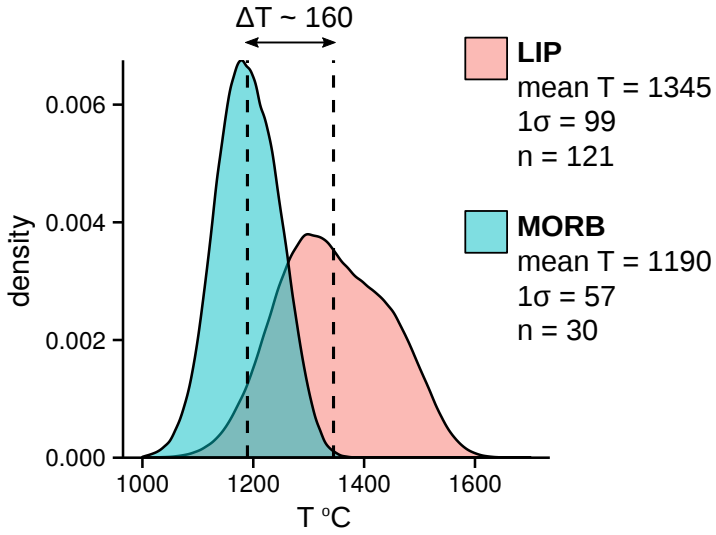

Figure 5.9: MORB vs. LIP crystallisation temperature probability distributions. KDE includes a thermometer error estimate derived from an assumed average analytical uncertainty of ±20% Al in olivine for published and new analyses. LIP samples as in Fig. 5.8, MORB samples from Coogan *et al.* (2014). Dashed lines are means, ΔT refers to the temperature difference between the two means. LIP samples exclude ferropicrite samples.

5.3 Mantle potential temperature

5.3.1 Thermal model

Melt productivity

Katz *et al.* (2003) parametrised the equilibrium melt productivity of peridotite from published experimental data and provide a general method for calculation. To account for the effect of the loss of cpx in the melting residue on melting behaviour, Katz *et al.* (2003) divide melting into two segments: a high productivity cpx-bearing interval, and a low productivity cpx-absent interval. The melting model presented here is based on the method and equations of Katz *et al.* (2003) but using an updated set of parameters. Only anhydrous melting is considered. The solidus, lhz-liq and liquidus are parametrised as quadratic functions by Katz *et al.* (2003). In this chapter, a quadratic parameterisation is added for $T_{cpx-out}$ (the temperature at which clinopyroxene is exhausted from the solid residue by melting, at $F \sim 0.20$):

$$T_{solidus} = A_1 + A_2 P + A_3 P^2 \tag{5.2}$$

$$T_{lhz-liq} = B_1 + B_2 P + B_3 P^2 \tag{5.3}$$

$$T_{liquidus} = C_1 + C_2P + C_3P^2 \tag{5.4}$$

$$T_{cpx-out} = D_1 + D_2P + D_3P^2 \tag{5.5}$$

The melt productivity over the cpx-bearing interval ($T_{solidus} < T < T_{cpx-out}$) is described by Katz *et al.* (2003) as F_{cpx}, and is a function of T' and P:

$$F_{cpx}(T') = [T'(T,P)]^{\beta_1} \tag{5.6}$$

where T' is the dimensionless scaled temperature between the solidus and the lhz-liq:

$$T' = (T - T_{solidus})/(T_{lhz-liq} - T_{solidus}) \tag{5.7}$$

The lherzolite-liquidus is a hypothetical liquidus defined by Katz *et al.* (2003) as the temperature at which 100% melting would occur were cpx never to be exhausted, i.e. by extrapolating the lherzolite (cpx-present) melt productivity to $F = 1$. Once clinopyroxene is exhausted (at $F_{cpx-out}$, the melt fraction at $T_{cpx-out}$), the melt productivity decreases. In the interval $T_{cpx-out} < T < T_{liquidus}$, F (known as F_{opx}) is given by:

$$F_{opx}(T) = F_{cpx-out} + (1 - F_{cpx-out})\left[\frac{T - T_{cpx-out}}{T_{liquidus} - T_{cpx-out}}\right]^{\beta_2} \tag{5.8}$$

A new parametrisation for peridotite and pyroxenite melt productivity

The above set of equations are potentially applicable to any cpx-bearing mantle lithology. The parameters and values given by (Katz *et al.*, 2003), however, are parametrised from experiments on peridotite and thus are only applicable to peridotite melting. It was suggested by Hirschmann and Stolper (1996) on the basis of experimental studies that garnet pyroxenite would melt both deeper and more productively than peridotite, which would explain the garnet signature apparent in some MORB. Knowledge of the melt productivity of pyroxenite has since been refined in a large number of melting experiments on various eclogite and pyroxenite compositions (e.g. Hirschmann *et al.*, 2003; Keshav *et al.*, 2004; Kogiso *et al.*, 1998; Lambart *et al.*, 2009; Pertermann and Hirschmann, 2003a; Yaxley, 2000). The thermodynamic model described in Chapter 4 reproduces pyroxenite and eclogite experimental melt compositions and melt productivities well. It is used here to parametrise pyroxenite melting following the style of the peridotite parametrisation of Katz *et al.* (2003). The bulk composition KG1, which is a 50:50 mixture of KLB-1 peridotite and average MORB (Kogiso *et al.*, 1998), is used to represent mantle pyroxenite. Additionally, a new parameterisation for peridotite melting is also created, using the same model and a KLB-1 bulk composition, so that the two models being used

are comparable. The newly parametrised KLB-1 peridotite and KG1 pyroxenite parameters are given in Table 5.2.

Value	KLB-1 per.	KG1 pyx.	Unit	Notation
A_1	993.7	941.1	°C	constant to determine $T_{solidus}$
A_2	206.4	208.9	°C GPa^{-1}	
A_3	-12.3	-12.8	°C GPa^{-2}	
B_1	1475.0	1293.7	°C	constant to determine $T_{lhz-liq}$
B_2	80.0	67.7	°C GPa^{-1}	
B_3	-3.2	5.3	°C GPa^{-2}	
C_1	1769.2	1507.8	°C	constant to determine $T_{liquidus}$
C_2	59.6	64.2	°C GPa^{-1}	
C_3	-3.7	0	°C GPa^{-2}	
D_1	1149.0	1115.5	°C	constant to determine $T_{cpx-out}$
D_2	144.8	152.2	°C GPa^{-1}	
D_3	-5.3	-6.4	°C GPa^{-2}	
β_1	1.0	1.0		melting function exponent, cpx-bearing
β_2	1.5	1.5		melting function exponent, cpx-absent
c_p	1187*	1140*	Jkg^{-1}K^{-1}	heat capacity (constant pressure)
α_{solid}	32** $\times 10^{-6}$	32** $\times 10^{-6}$	K^{-1}	thermal expansitivy (solid)
α_{liq}	80** $\times 10^{-6}$	80** $\times 10^{-6}$	K^{-1}	thermal expansitivy (liquid)
ρ	3300*	3300*	kg m^{-3}	density, solid mantle
ρ_{crust}	2800	2800	kg m^{-3}	density, average continental crust, after (Rudnick and Fountain, 1995)
ρ_{liq}	2900*	2900*	kg m^{-3}	density, liquid
ΔS	407*	380*	Jkg^{-1}K^{-1}	entropy of fusion

Table 5.2: Parameters and values for melting models. Constants A_i–D_i, β_1 and β_2 calculated for KLB-1 and KG1 in NCFMASOCr using the model of Jennings and Holland (2015) (see Chapter 4). *from Shorttle *et al.* (2014). **thermal expansivity of the solid is recalculated in this study from Ghiorso (2004) and for the liquid from volume estimates by the method of Lange and Carmichael (1990).

For $T_{solidus}$, $T_{cpx-out}$ and $T_{liquidus}$ of KLB-1 and KG1, polynomial fits were calculated to the relevant lines on the their respective pseudosections (Figs. 4.1 and 4.10). Only the portions of the solidi at pressures greater than the upper limit of plagioclase stability were used. The KG1 liquidus bears several inflections but is approximately straight, so C_3 is set to zero. Katz *et al.* (2003) suggest β_1 and $\beta_2 = 1.5$ (β is the exponent of the melting function) for peridotite, although they acknowledge that this parameter is not well known. The isobaric melting productivities of KLB-1 and KG1 are shown in Fig. 4.16. In the cpx-present interval, F varies approximately linearly with T in both compositions, i.e. $\beta_1 = 1.0$. In a more complex system, the presence of volatile elements and K_2O may give a low F tail ($\beta > 1.0$), which should have little impact except at very low melt fractions. Above $F_{cpx-out}$, dF/dT in KLB-1 is approximately matched using $\beta_2 = 1.5$. The same value is used for KG1.

B_1, B_2 and B_3, used in the formula for $T_{lhz-liq}$, are calculated for KLB-1 and KG1 in the following steps. As an example, the details for the KG1 fit are shown.

1. Isobaric melt productivities are calculated to the temperature at which clinopyroxene is exhausted ($F \sim 0.6$) at several pressures in THERMOCALC using the model of Chapter 4.

2. At the various pressures, melt fraction plotted against normalised temperature is approximately linear; it can be slightly concave-up, concave-down, or sigmoidal (Fig. 5.10). Therefore, $\beta = 1.0$ is chosen.

3. $T_{lhz-liq}$ at each pressure is calculated by extrapolating to $F = 1$ using $\mathrm{d}F/\mathrm{d}T$ from the difference between the solidus and the temperature at which clinopyroxene is exhausted (Fig. 5.10).

4. The pressure dependence of $T_{lhz-liq}$ is fitted with equation 5.3 (Fig. 5.11).

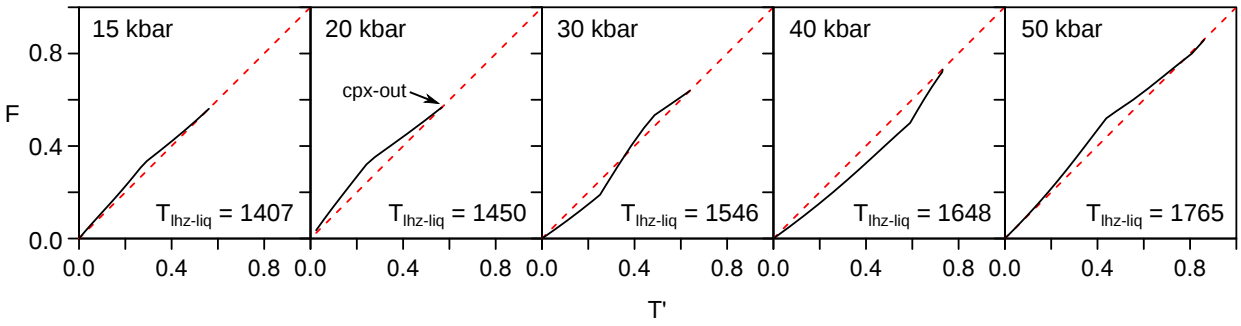

Figure 5.10: KG1 isobaric melt productivity as a function of normalised temperature. The black line represents the melt productivity calculated in THERMOCALC using the model of Chapter 4 and the red dashed line is the parametrised version; it is constrained by the origin and cpx-out, where F and T' at cpx-out in the parametrisation match those values in the modelled isobaric path. $T' = 1$ corresponds to the temperature at which $F = 1$ (the lherzolite liquidus).

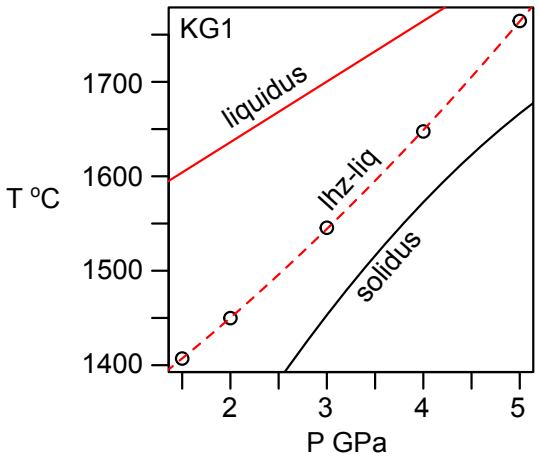

Figure 5.11: KG1 solidus, liquidus and lherzolite-liquidus parametrisation. Open circles represent $T_{lhz-liq}$ calculated for the isobaric melt productivities of Fig. 5.10, where the dashed line is a quadratic fit to these points.

The peridotite $T_{lhz-liq}$ was difficult to fit to a pressure dependence as it is highly sensitive to melting assemblage and so the pressure dependence is non-linear. It is simplified for the purpose of this model by calculating an average melting productivity for cpx-bearing peridotite across all pressures, and setting $T_{lhz-liq}$ to be offset from $T_{solidus}$ accordingly.

Thermal model setup

A forward thermal model is set up to predict the isentropic PT path and final liquid temperatures of mantle melting; the approach is after Katz *et al.* (2003) and is outlined below.

A solid adiabatic gradient for the mantle is calculated according to:

$$\left.\frac{\mathrm{d}T}{\mathrm{d}P}\right|_S = \frac{T\alpha_{solid}}{\rho c_p} \tag{5.9}$$

where parameters values and notation are given in Table 5.2. T_P is the temperature at $P = 0$, and $\mathrm{d}T/\mathrm{d}P$ allows extrapolation to depth (McKenzie and Bickle, 1988). Melting commences when the adiabat, calculated for a given T_P, intersects the solidus. If the melt stays in thermal equilibrium with the upwelling solid, the PT path will deviate from the adiabat towards lower temperatures due to the latent heat of fusion. In this case, $\mathrm{d}F/\mathrm{d}T$ must be found by simultaneously integrating expressions for $\mathrm{d}F/\mathrm{d}P$ and $\mathrm{d}T/\mathrm{d}P$, with the assumption that melting is isentropic. These expressions, originally from McKenzie (1984) are given by Katz *et al.* (2003) along with the derivatives $(\mathrm{d}T/\mathrm{d}F)|_P$ and $(\mathrm{d}T/\mathrm{d}P)|_F$.

$$\left.\frac{\mathrm{d}F}{\mathrm{d}P}\right|_S = \frac{-\frac{c_p}{T}\frac{\partial T}{\partial P}|_F + F\frac{\alpha_{liq}}{\rho_{liq}} + (1-F)\frac{\alpha_{liq}}{\rho_{liq}}}{\Delta S + \frac{c_p}{T}\left.\frac{\partial T}{\partial F}\right|_P} \tag{5.10}$$

$$\left.\frac{\mathrm{d}T}{\mathrm{d}P}\right|_S = T\left(\frac{F\frac{\alpha_{liq}}{\rho_{liq}} + (1-F)\frac{\alpha_{solid}}{\rho} - \Delta S\left.\frac{\mathrm{d}F}{\mathrm{d}P}\right|_S}{c_p}\right) \tag{5.11}$$

A PTF path is calculated using a fourth-order Runge-Kutta scheme with a small $\mathrm{d}P$ from the pressure at which the adiabat intersects the solidus to the pressure at the top of the melting column (the base of the lithosphere, where adiabatic upwelling ceases). F is calculated according to equations 5.6 or 5.8, depending on T. Expressions for hydrous melting are ignored, as water is not accounted for in the thermodynamic model of Chapter 4 and exists only at trace concentrations in the convecting mantle.

This calculation relies on the assumption that melt stays in thermal equilibrium with its decompressing mantle source, i.e. it is retained to the top of the melting region in pore spaces. A residual melt mass fraction of above $\sim 3\%$ (McKenzie, 1984, 1985), or much less according to the U-series disequilibrium modelling of (Spiegelman and Elliott, 1993), may not be stable in pore spaces and in

reality a fractional melting scenario is likely. An end-member regime of fractional melting would involve thermal disequilibrium, and is modelled by an extracted incremental melt fraction following a liquid adiabat to the surface, which assumes that no heat is lost to its surroundings. The liquid adiabat dT/dP is calculated as for the solid mantle but by substituting in the appropriate liquid parameters of Table 5.2. It is higher than that of solid mantle, but lower than when latent heat is considered in equilibrium melting. Fractional melting should produce thermally heterogeneous liquids. For simplicity, the thermal evolution of the upwelling fractionally melting mantle is assumed to be similar to that of the equilibrium melting scenario, which is demonstrated in Chapter 4 to be a reasonable approximation.

5.3.2 T_p of the proto-Tristan mantle plume

Calculating a potential temperature from a crystallisation temperature relies on the assumption that a) spinel-olivine pairs represent liquidus crystallisation of a primary melt, and b) that the melt was at the liquidus temperature when it accumulated and began to crystallise. Although the spinel-olivine pairs in the Fo > 90 olivines from picrites probably are close to the primary melt liquidus phases, there is no constraint on any superliquidus cooling interval. Therefore, T_P calculated from crystallisation temperature represents a minimum estimate.

The crystallisation temperature of a magma is not only a function of T_P, but is also affected by the lithospheric thickness, i.e. the depth at which adiabatic decompression melting stops, and the crystallisation pressure of the magma, i.e. the calculated T_P which produces a given crystallisation temperature is non-unique. This is illustrated by a general example in Fig. 5.12. For a given T_P, a thicker lithosphere would limit mantle upwelling and cause melt extraction at higher pressure. This would result in a higher crystallisation temperature, as would a deeper magma chamber. For a crystallisation pressure of 0.5 GPa ($\sim$ 15 km depth) and using a lithospheric thickness of 55 km (Thompson *et al.*, 2001), the average crystallisation temperature of Fo > 90 olivines from Etendeka picrite samples (1457 °C) is reproduced with a mantle $T_P = 1582$ °C and corresponds to a melt fraction of 0.23. This assumes equilibrium isentropic melting; the maximum temperature expected from fractional melting of that same mantle T_P, where an incipient melt is extracted from the solidus pressure to the surface along a liquid adiabat, is 1464 °C, which is within the uncertainty of the mean crystallisation temperature.

Fig. 5.12 highlights the error propagation associated with calculating T_P and especially the pressure at the onset of melting from a crystallisation temperature. The isentropic melting path intersects the adiabat at a shallow angle in PT space, so a small change in crystallisation temperature translates to a large change in the pressure at which the solidus is intersected. The mean picrite Fo > 90 crystallisation 1σ is 44 °C. However, when converted to a T_P estimation, the 1σ range translates to a error envelope of 102 °C, corresponding to a range in the pressure at the onset of melting of 3.8 to 5.1

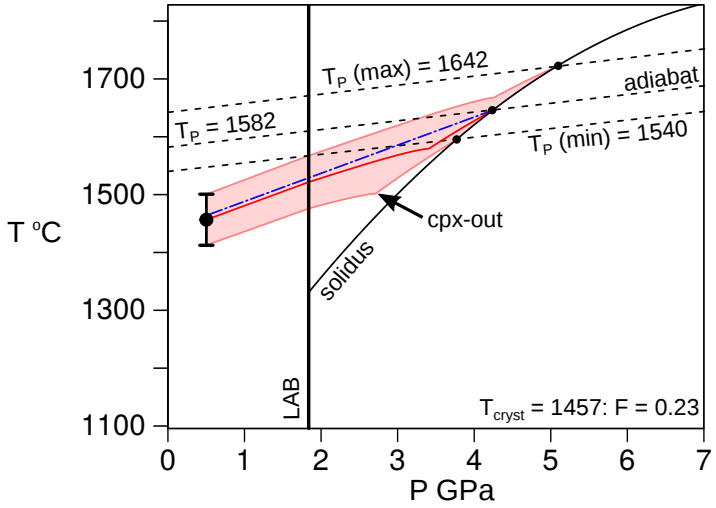

Figure 5.12: Example calculation linking mantle T_P to crystallisation temperature. Point indicates the mean Etendeka picrite crystallisation temperature of Fo > 90 olivines $\pm 1\sigma$ (see Table 5.1). The red line is the modelled equilibrium path of the liquid during melting and subsequent adiabatic rise through the lithosphere, and the pink field shows the error bracket extrapolated from the crystallisation temperature. The dot-dashed blue line indicates the path of the maximum temperature fractional melt, created at the solidus, assuming that it is thermally isolated and extracted to the surface along a liquid adiabat. Dashed black lines are the solid mantle adiabats required to produce the mean, upper and lower limit crystallisation temperatures, where T_P is their y-axis intercept; the thin black line is the peridotite solidus; the thick black line is the lithosphere-asthenosphere boundary (LAB). Other parameters: lithospheric thickness, 55 km (after Thompson *et al.*, 2001), crystallisation pressure, 0.5 GPa, using the peridotite melting model parameters (Table 5.2).

GPa. Melting of T_P above around 1710 °C is not possible because the solidus becomes parallel to the adiabatic gradient. This is a limitation of the solidus parametrisation at high pressures. Uncertainties in thermal properties (for example, the entropy of fusion is not well constrained) also contribute error in the calculation of T_P.

With the large uncertainties as a caveat, the T_P of the picrite and ferropicrite crystallisation temperatures are calculated as a function of crystallisation pressure and lithospheric thickness (Fig. 5.13). Results are represented both as a function of F and as a function of lithospheric thickness. The mean of all ferropicrite olivines is modelled, whereas the mean of only temperatures measured from Fo > 90 olivines from picrites are modelled.

Results using the peridotite model are shown in Figs. 5.13a and b. The picrite crystallisation temperature is matched by quite a narrow T_P range, with answers within around 20 °C of $\sim$ 1550 °C for crystallisation at 1 GPa, or $\sim$ 1590 °C if crystallisation was shallower at 0.5 GPa. A melt fraction of 0.2 corresponds to a lithospheric thickness of around 65 km and T_P =1550–1580.

The ferropicrite crystallisation temperature is matched by a larger T_P range of around 1350–1480 °C, but a narrower range of acceptable lithospheric thicknesses (20–70 km), which result in 0–40% melting. The shallow lithospheric thickness limit in all results is defined by the depth corre-

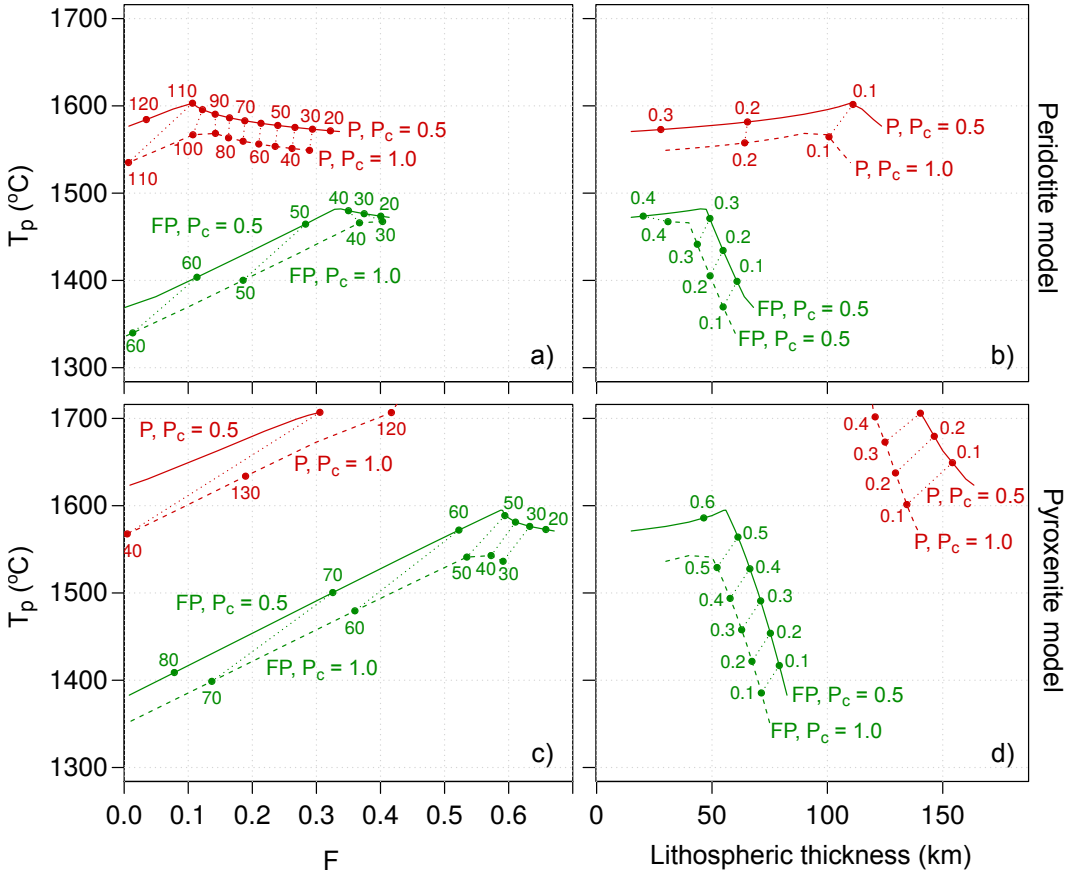

Figure 5.13: Modelled T_P using the peridotite melting model (a and b) and the pyroxenite melting model (c and d; model parameters given in Table 5.2 and a lithospheric density (crust plus lithospheric mantle) of 3050 kg m^{-3} is used. The T_P shown is the best fit solution for the measured crystallisation temperatures, calculated for 0.5 GPa (solid lines) and 1 GPa (dashed lines) crystallisation pressures (P_c). The crystallisation temperatures modelled are: i) in dark red, the mean of the Fo > 90 olivines from the Etendeka picrites (P, 1457 °C); ii) in dark green, the mean of all Etendeka ferropicrites (FP, 1312 °C). Best fit T_P is shown as a function of melt fraction F in a) and c) and as a function of lithospheric thickness (km) in b) and d). for a given T_P, F and lithospheric thickness are linked. This is indicated by the numbered points: in a) and c), 10 km intervals of lithospheric thickness are shown, and in b) and d), 0.1 intervals of F are shown.

sponding to the crystallisation pressure, whereas the deep limit is at the solidus, i.e. where $F = 0$. The prominent kink at $F = 0.1$ in the picrite result and $F = 0.55$ in the ferropicrite result is a consequence of clinopyroxene exhaustion changing the melting productivity, and thus the amount of cooling during upwelling.

If, as previously suggested, ferropicrite derives from partial melting of pyroxenite, then the peridotite thermal model is not suitable for interpreting its crystallisation temperature. Figs. 5.13c and d show the modelling results of the same data using the KG1 pyroxenite melting model. The cpx-bearing melting interval is much larger here, so most of the results shown are from the high productivity melting phase. The T_P required to match the ferropicrite average crystallisation temperature has

shifted up relative to those found using the peridotite model. This reflects the excess cooling effect of the higher melt productivity, meaning that a higher temperature is required at the solidus intersection to produce the same final crystallisation temperature. A ferropicrite crystallisation pressure of 1.0 GPa is most likely, on the basis of the olivine and clinopyroxene phenocryst assemblages and their high density (so deep neutral buoyancy). At this condition, the ferropicrite temperature reflects a melt fraction of 0–0.5, lithospheric thickness of 50–75 km, and T_P of 1360–1530 °C. These melt fractions and T_P estimates seem reasonable, although the modelled lithospheric thickness is shallower than the published estimate of 115 km of Gibson *et al.* (2000).

The same cooling effect from high melting productivity means that it is very difficult to reproduce the picrite temperature without using an excessively high T_P with the pyroxenite melting model. Note that, in this model, the solidus cannot be intersected above 1710 °C, so higher temperature results were not obtained. To produce the high picrite temperatures, a very high lithospheric thickness of around 140 km is required.

A summary of calculated T_P for a range of variable choices is given in Table 5.3. In the concluding chapter (Chapter 7), the range of T_P, F and lithospheric thickness solutions here are combined with trace element modelling results in order to identify a likely set of melting conditions in the Tristan mantle plume starting head.

Sample group	T_{cryst}	P_{cryst}	Model	Lith. (km)	F	T_P	T_P, P07
Picrite Fo > 90 mean	1457	0.5	peridotite	15 (min)	0.34	1574	1677
				66	0.20	1586	1561
				125 (max)	0.00	1584	1401
Picrite +1σ	1501			84	0.20	1652	1597
Picrite -1σ	1413			66	0.20	1544	1517
Picrite, Keiding '11	*1395*	-	-	-	-	*1520*	-
Etendeka ferropicrite mean	1312	1.0	peridotite	30 (min)	0.41	1466	1572
				60 (max)	0.00	1332	1285
			pyroxenite	30 (min)	0.58	1529	1685
				66	0.20	1414	1416
				74 (max)	0.00	1344	1279

Table 5.3: Selected T_P calculation results. The crystallisation temperature and T_P of Keiding *et al.* (2011) is shown for comparison, as is P07, the T_P calculated by equation 5.12 after Putirka *et al.* (2007), which is explained in the following section. (min) and (max) denote the minimum (the depth of crystallisation) and maximum (the depth of the solidus) permissible lithospheric thickness for the melting regime. $F = 0.2$ is shown for each scenario for direct comparison, not because it is the best solution.

T_P estimation by alternative methods

Several alternative methods for estimating T_P on the basis of geochemical data have been published. For comparison, results using these models are discussed below. A simplified method for calculating

T_P from crystallisation temperature and F is presented by Putirka *et al.* (2007), who assume a two-step process: 1) the crystallisation temperature is corrected for the temperature drop from the enthalpy of fusion; 2) temperature is then corrected back to 1 atm. along an adiabat, using the equation:

$$T_P = T^{ol-liq} + \Delta T_{fus} - P[\partial T/\partial P] \tag{5.12}$$

The temperature correction for fusion $\Delta T_{fus} = F(\Delta H_{fus}/c_p)$ can be approximated for a lherzolite source using c_p = 192.4 J/mol K^{-1} and ΔH_{fus} = 128.3kJ/mol, and $[\partial T/\partial P]$, the adiabatic gradient, is approximated as 13.3 °C/GPa (Putirka *et al.*, 2007). P is the pressure at the top of the melting region. In the method of Putirka *et al.* (2007), a crystallisation temperature (T^{ol-liq}) is obtained through olivine-liquid Fe-Mg equilibria, which requires the liquid composition to be known. As discussed above, the liquid compositions are not well known and only approximated by whole-rock data. Thus, the Al-in-olivine measured crystallisation temperature is used instead, and substitutes T^{ol-liq} in equation 5.12. T_P results (Table 5.3) somewhat resemble the T_P results of this chapter, where the simplification of the (Putirka *et al.*, 2007) method overestimates T_P at high melt fractions and underestimates it at low melt fractions, relative to the present method.

PRIMELT2 and PRIMELT3 (Herzberg and Asimow, 2008, 2015) calculate a primary melt by correcting a liquid composition for olivine fractionation, and match this to parametrised mantle melt compositions. Using the picrite composition 97SB33, a primary melt is calculated (Chapter 2, Table 2.1) in PRIMELT3, that corresponds to a crystallisation temperature of 1396 °C (somewhat lower than Al-in-olivine crystallisation temperatures of picrite high Fo picrite olivines), T_P = 1505 °C, and $F = 0.26$. The PRIMELT3 solution is not too dissimilar to the results presented here, although the T_P is a little low for a fairly high F. This method is only applicable to dry peridotite melting and cannot be applied to the ferropicrites.

The approach in this chapter (forward modelling of mantle melting to match Al-in-olivine crystallisation temperatures) gives similar results to other methods, but, as it is based on direct measurement rather than inferred primary composition, it is more robust. All methods predict that the T_P of the Etendeka source mantle was significantly elevated above ambient mantle.

5.3.3 Limitations of the approach

Does the Al-in-olivine crystallisation temperature represent the temperature of the primary melt?

A superliquidus interval would exist if the melts were emplaced in crustal magma reservoirs at temperatures higher than their liquidus. The high degree of mixing observed in melt inclusions in the most forsteritic olivines provide evidence for convective mixing prior to the onset of crystallisation (see Chapter 3). The presence of such an interval would mean that the crystallisation temperatures are

lower than the actual melt temperature, making T_P estimates a minimum. The crystallisation temperatures of DML ferropicrites are not modelled. They are around 50 °C lower than the Etendeka ferropicrites, although the DML and Etendeka ferropicrites have similar whole-rock and olivine phenocryst major element compositions. The DML ferropicrites were emplaced in the same magmatic episode as very hot meimechites (maximum crystallisation temperature of 1481 °C, Heinonen *et al.*, 2015) and must also derive from an elevated mantle T_P. The low crystallisation temperatures of the DML ferropicrites may therefore reflect the presence of a modest superliquidus cooling interval before they began to crystallise. A superliquidus cooling interval would be promoted by a thick lithosphere, i.e. a large pressure difference between the top of the melting column and crystallisation pressure, because the basaltic liquid adiabat has a shallower slope than the basalt liquidus.

If the olivine-spinel pairs are not true liquidus phases, i.e. if they did not grow from a primary melt, T_P estimates derived from them would also be high. It seems unlikely that Fo_{93} olivines derive from a melt which had already cooled and fractionated, so for the high Fo picrite group this effect is negligible. However, the uncertain major element composition of the ferropicrite primary melt provides scope for potentially higher Fo olivines having crystallised, and thus the T_P being somewhat underestimated. However, as discussed in Chapter 2, the amount of previous fractionation was probably small.

Finally, the recorded crystallisation temperatures in the Etendeka and DML ferropicrite samples could be overestimates of their true crystallisation temperatures because their Ti contents are high relative to the thermometer calibration range. As discussed earlier in this chapter, this does not seem to be too problematic.

Other model limitations

The solidus and liquidus positions and melt productivity are parameterised using a thermodynamic model in the system NCFMASOCr. This system lacks K_2O, TiO_2 and volatiles, all of which will reduce the solidus temperature by varying amounts. Pyroxenite probably has a higher volatile and K_2O content than peridotite and so the pyroxenite melting model is more susceptible to this limitation. The presence of solidus-lowering species would create a high-P 'tail' of melting which begins deeper in the mantle. However, because these elements behave incompatibly and have low abundance, their presence will have little effect on the productivity and melting pressure of the bulk of the solid mantle, especially during fractional melting where they are quickly lost from the system. Because the melts in this chapter are moderate to high fraction, using a parameterisation based on a more complete system would have little effect on the results presented.

Finally, the thermal model used here is for a solid and liquid in thermal equilibrium. Fractional melting would result in incipient melts with a range of temperatures. In general, the deepest fractional

melts would be a little hotter than equilibrium melts after decompressing along an adiabat (as shown by the dot-dashed blue line in Fig. 5.12). A hiatus in melting would also occur during fractional melting when clinopyroxene is lost. A fractional melting model based on the thermal model of this chapter is used in Chapter 4, and it shows the equilibrium melting mantle temperature to be a good approximation of the fractional melting mantle temperature.

Melting of a lithologically heterogeneous source in the convecting mantle

In this chapter, T_P was modelled from melts by assuming pure peridotite and pyroxenite mantle sources. The proto-Tristan mantle plume is believed to have contained both, and given the likelihood that pyroxenite in plumes exists as sheared filaments with a large surface area (Farnetani *et al.*, 2002), the pyroxenite and peridotite may be in thermal equilibrium but lithologically distinct. The thermodynamics of melting a mixed source rather than a single lithology are more complex and are not quantified in this chapter. In an adiabatically upwelling heterogeneous mantle, pyroxenite will intersect its solidus at higher pressure and so will begin to melt first (Hirschmann and Stolper, 1996). To compensate for the enthalpy of fusion, heat will flow from the surrounding peridotite, increasing pyroxenite melt productivity and cooling the peridotite, which will consequently reduce the peridotite solidus pressure. A complete description of this process along with appropriate equations are given by Phipps Morgan (2001). Although these effects are not quantitatively modelled here, their consequence for the calculated temperatures are worth considering. If the Etendeka picrites represent peridotite melting in a mixed mantle, then the calculated T_P will be an underestimate of the true T_P, because the peridotite source would have cooled to some extent prior to melting. Conversely, if ferropicrite represents mostly pyroxenite melting, the calculated T_P would be overestimated. Being thermally buffered by peridotite will increase the melt productivity of the pyroxenite, giving a higher melt fraction per unit of pressure change than an unbuffered pyroxenite. Refractory harzburgite domains may also be present in the plume, as they are required to balance the buoyancy reduction caused by denser pyroxenite domains; the harzburgite further thermally buffers peridotite and pyroxenite melting, without melting (Shorttle *et al.*, 2014). In this case, both the pyroxenite and peridotite will melt a little more productively.

If the Etendeka ferropicrite does not represent a pure pyroxenite partial melt, but rather represents a mixture of peridotite and pyroxenite-derivied melts, then the correct source T_P will be somewhere between the values derived from the peridotite model and the pyroxenite model. The lithology from which ferropicrite derives is investigated in Chapters 4 and 6.

5.4 Summary

Al-in-olivine crystallisation temperatures were obtained from olivine-hosted spinel inclusions for Etendeka picrites and ferropicrites and DML ferropicrites. After filtering the samples for thermometer suitability, means were calculated for the different magma types (given in Table 5.1). A maximum crystallisation temperature of 1511 $\pm$ 24 °C was obtained from a spinel-olivine pair from picrite sample 97SB33. The crystallisation temperatures from picrites have a large range, which is explained at least in part by fractionation. A cluster of Fo > 90 olivines define a high average crystallisation temperature of 1457 °C. Etendeka ferropicrite average crystallisation temperatures had a mean value of 1312 °C, around 50 °C lower than the mean of all picrite samples (1361 °C).

The temperature paths for decompression melting were modelled using the method of Katz *et al.* (2003). For this, a new parametrisation of peridotite and pyroxenite melt productivities was created, based on the thermodynamic model of Chapter 4. This forward model was used to examine the T_P required to match the observed crystallisation temperatures, where the T_P solution and associated F is non-unique and depends on the lithospheric thickness and crystallisation pressure. For $F = 0.2$ and a crystallisation pressure of 0.5 GPa, a $T_P = 1586$ is calculated for the Etendeka picrites, corresponding to a lithospheric thickness of 66 km. This T_P and associated parameters are in good agreement with those of Thompson *et al.* (2001) and Keiding *et al.* (2011). No evidence is found of the excessively high crystallisation temperature and associated T_P ($\sim$ 1700 °C) in the Etendeka picrites suggested to exist by Thompson and Gibson (2000).

The error associated in calculating T_P from crystallisation temperature is large, for many reasons, including a lack of consensus on the most appropriate thermal properties, and the fact that thermal equilibrium between peridotite and pyroxenite in a mixed source mantle is not accounted for. In addition, the uncertainty in measuring olivine Al concentrations by EPMA is also high, resulting in a significant uncertainty in the crystallisation temperatures. A large range in temperatures is recorded by the olivines in samples in this study. The potential temperatures and lithospheric thicknesses calculated in this chapter therefore suffer a reasonably high uncertainty. Incompatible trace elements are more sensitive to the degree of melting than crystallisation temperature. As such, a tighter constraint is placed on F (and so T_P) by considering the trace element modelling in Chapter 6.

Despite the uncertainties, the picrite mantle source T_P is still much higher than ambient mantle T_P (1315 °C). Similarly, the mean crystallisation temperature for basalts and picrites from all LIPs is 160 °C higher than that of MORB (Fig. 5.9). This elevated crystallisation temperature and associated elevated mantle source T_P is interpreted to show that mantle plumes are responsible for the genesis of the Paraná-Etendeka CFB province and other LIPs. The picrites represent magmas which are similar to the parental melts of the voluminous CFB units, so it can be inferred that the CFBs formed from melting of a large volume of similarly hot peridotite.

The ferropicrites record cooler crystallisation temperatures than the picrites and, in the Etendeka CFB province, are known to represent the earliest magmatism. Their cooler temperature is in part explained by their lower mantle source T_P. However, if ferropicrites are partial melts of pyroxenite, then even if their source T_Ps were identical, the ferropicrites would still be cooler than the picrites. This is because pyroxenite melts more productively than peridotite over a greater melt fraction range. The latent heat of fusion serves to cool the pyroxenite and its equilibrium partial melt during upwelling more so than a peridotite melting under the same conditions. Ferropicrites may also be recording a cooler crystallisation temperature if there is a superliquidus cooling interval (i.e. the liquid is originally hotter than its liquidus), or if it had fractionated hotter olivine that was not sampled in this study.

The main advantage of the method used in this chapter is that no assumptions need to be made about the liquid composition. Directly measuring equilibrium mineral-mineral partitioning negates the requirement to correct the composition of a fully crystalline sample for macrocryst accumulation or fractionation. In addition, this method is more convenient for suspected pyroxenite-derived melts as it does not depend on a parameterisation of peridotite partial melt compositions and an assumption about the peridotite bulk chemistry (cf. PRIMELT3). Although discrepancies are found in the results of different methods for determining T_P, they all indicate a high T_P for the Etendeka picrite mantle source.

Chapter 6

Trace element modelling of melting conditions and source mineralogy

6.1 Introduction

Incompatible trace elements are present in such low concentration in the convecting mantle that, like isotopes, they act as passive tracers of the melting process (Hofmann, 2003). However, unlike isotopes, their concentration in a melt varies as a function of partition coefficient, source mineralogy, melting reaction and extent of melting. These features can be exploited and allow the trace element compositions of natural magmatic samples to be used in solving for various aspects of their source melting conditions. Trace element modelling relies on the fact that mineral-melt trace element partitioning is highly systematic and predictable (e.g. Blundy and Wood, 1994; Onuma *et al.*, 1968). The rare earth elements (REE) in particular have been extensively studied and their partitioning behaviour in a range of phases is well understood (Draper and van Westrenen, 2007; Evans *et al.*, 2008; Sun and Liang, 2013; Wood and Blundy, 1997). The light REE (LREE), along with other highly incompatible elements, are most sensitive to the extent of melting. In contrast, the heavy REE (HREE) and Y, which are compatible in garnet, are useful in resolving the melting pressure. Both the melting pressure and extent relate to mantle temperature and lithospheric thickness. Tetravalent cations (Ti, Zr, Hf) have moderately well constrained partition coefficients and will also vary as a function of pressure, modal mineralogy and melt extent.

Trace element modelling of natural compositions can be either forward or inverse. By assuming a composition of either primitive or depleted mantle, McKenzie and O'Nions (1991) apply an inverse modelling technique to solve for the depth and extent of melting of natural samples. The same technique was used by Thompson *et al.* (2001) to calculate a lithospheric thickness of 55 km and T_p of 1470-1500 °C for the mantle source of the Horingbaai picrites. This chapter uses a forward modelling approach, which takes an assumed mantle composition and produces a model melt composition. If

the model melt has a similar composition to the natural samples, the model melting conditions should represent the mantle melting event that produced those samples. This chapter investigates whether the source mineralogy can be resolved from the trace element composition of the picrite and ferropicrite samples. Mantle T_P and lithospheric thickness are also examined from a trace element perspective, which gives a result independent of, and complementary to, the thermometry data of Chapter 5.

6.2 Model setup

6.2.1 Definitions

In addition to those previously defined, the following symbols are used in this chapter:

c_0 Bulk concentration (mass)

c_L Liquid concentration (mass)

c_S Solid residue concentration (mass)

D Partition coefficient:

- D_i Partition coefficient of element i between solid and melt
- D^i Partition coefficient between phase i and melt
- D^b Bulk partition coefficient
- D^w Weighted bulk partition coefficient
- D_0 Maximum lattice site partition coefficient

W_i^0 Mass fraction of phase i in the initial solid

p_i Mass fraction of phase i in the melt (i.e. the melting reaction coefficient for i)

r_0 Lattice site radius (m)

r_i Cation radius (m)

E Young's modulus for lattice site (Pa)

N_A Avogadro constant (6.02214×10^{23} mol^{-1})

R gas constant (8.31446 JK^{-1}mol^{-1})

6.2.2 Model overview

The model presented here is a non-modal, polybaric, accumulated batch melting model which uses PTX-dependent partition coefficients where available. It is a forward model, used to predict mantle melt compositions. Two versions of this model are presented: one optimised for peridotite melting and the other for pyroxenite. They have the same structure, but use different parameters. They are intended to be used for garnet and spinel bearing melting assemblages and are not calibrated for plagioclase-bearing assemblages. Melting which begins at high pressure can, however, be followed

through to pressures below that of the spinel-plagioclase transition because the solid residue quickly becomes too depleted to stabilise plagioclase.

At some pressure, upwelling mantle will intersect its solidus and begin to melt. The amount of melting per unit of pressure change during upwelling is determined by the thermal model described in detail in Chapter 5. Melts are buoyant and easily extracted from the solid residue, so melting cannot be modelled as a one-step equilibrium process. Although close to fractional melting, there is probably a residual porosity regime where a small threshold melt fraction must be reached in order for an interconnected permeable network to exist for melt extraction to occur (Kelemen *et al.*, 1997). This threshold is suggested from experiments in analogue systems to occur at melt fraction $F =$ 0.005–0.027 (Wark and Watson, 1998). U-series modelling of MORB by McKenzie (1985) suggests a residual porosity of 0.02, whereas more recent estimates which consider transport velocities give much lower values (Spiegelman and Elliott, 1993). This process is simulated in the present model with an accumulated batch melting regime, in which melting is treated as a polybaric series of equilibrium 1% melting steps. The model was run with a range of threshold porosities; they were found to have almost no effect on the integrated melt composition, except at very low cumulative melt fractions or very high threshold F, so 1% was considered acceptable. After extracting a 1% fraction melt, the resultant more depleted solid composition is used as the starting composition in the next melting step.

The following equations (from Shaw, 1970) relate c_0, c_S and c_L in the equilibrium melting steps, where F is the melt fraction of an increment of melting, $D^\mathrm{b} = \Sigma W_i^0 D^i$ and $Q = \Sigma p_i D^i$:

$$\frac{c_\mathrm{L}}{c_0} = \frac{1}{D^\mathrm{b} + F(1-Q)} \tag{6.1}$$

$$\frac{c_\mathrm{S}}{c_0} = \frac{D^\mathrm{b} - QF}{(1-F)(D^\mathrm{b} + F(1-Q))} \tag{6.2}$$

These are are linked to the weighted bulk partition coefficient D^w according to:

$$D^\mathrm{w} = \frac{D^\mathrm{b} - QF}{1-F} \tag{6.3}$$

The use of D^b and Q accounts for the fact that the phases present do not melt in their modal proportions. If the melting reaction is written such that $p_\mathrm{liq} = -1$ then the above equations may be used for peritectic melting by giving the precipitation phase(s) a negative p value. Mineral modes in the solid residue are adjusted and normalised to account for material lost during each melting step. The model is described as polybaric for several reasons. Firstly, the pressure-sensitive garnet-spinel phase transition is accounted for. Secondly, the initial mineral modes, melting reactions and some partition coefficients used are pressure-sensitive. The individual melt fractions extracted at different pressures are integrated to give a single primary melt composition, which is then corrected for olivine

fractionation to be comparable with the natural picrite and ferropicrite samples. The integration is performed assuming a dome-shaped melting region, as is suggested for a plume impacting upon an upper boundary layer by Ito and Mahoney (2005b).

REE, Y, Nb, Ti, Zr and Hf are modelled. These elements are chosen because they have well characterised partition coefficients, have fairly consistent concentrations within sample groups, and are not readily fluid-mobile (cf. Rb, Ba, Sr), so are insensitive to the minor hydrothermal alteration present in some samples. If the modal mineralogy of known peridotite or pyroxenite is used, then natural sample compositions can be reproduced by the model to solve for T_P and lithospheric thickness. Alternatively, if T_P and lithospheric thickness are taken as known, then the modal mineralogy of the source can be interrogated, in order to investigate the lithology.

6.2.3 Model details

The peridotite and pyroxenite models have the same structure but different thermal properties, melt productivities, modal mineralogies and mineral chemistries are used. The following describes the sequence of calculations in the model:

1. A PTF structure is calculated for a given T_P and lithospheric thickness by simultaneously solving dT/dP and dF/dT using the equations of McKenzie (1984), as described in Chapter 5 and using the thermal properties for peridotite and pyroxenite listed in Table 5.2. This is done at a small P step size (0.001 GPa), resampled at $F = 0.01$ intervals. The density of the lithosphere is taken to be a 1:1 mix of average continental crust (2800 kg m^{-3}, Rudnick and Fountain, 1995) and peridotitic mantle (3300 kg m^{-3}), to account for the presence of crust and lithospheric mantle in approximately equal proportions.

2. Initial mineral modes are defined.

3. For each pressure step and $F = 0.01$ increment:

   (a) Some aspects of mineral chemistry are calculated as a function of P and/or F.

   (b) D^b is calculated, using PTX-sensitive D_i values where possible.

   (c) Melting reactions are calculated as a function of pressure and phase assemblage.

   (d) Liquid (c_L) and solid residue (c_S) compositions are calculated from equations 6.1 and 6.2, where initial $c_0 = 1$ (i.e c_L is determined relative to the initial mantle concentration).

   (e) The bulk composition for the next iteration is set: $c_0^{m+1} = c_\mathrm{S}^m$, where there are M melting steps from $m = 0$ at the solidus to $m = M$ at the top of the melting column.

   (f) The phase proportions for the following iteration are set: $W_i^{m+1} = (W_i^m - p_i F)/(1 - F)$

4. Incremental melt compositions are integrated in a range of geometries.

5. Olivine is subtracted from the resultant mixed melt at low P to simulate fractionation.

6. Natural samples of interest are normalised to an appropriate mantle bulk composition.

7. The misfit between the final model melt and natural sample of interest is quantified.

Choice of bulk mantle compositions

The composition used to represent peridotitic mantle could be either a depleted MORB-source mantle composition (DMM, e.g. that of Salters and Stracke, 2004), representing an upper mantle reservoir, or a more primitive composition (PRIMA), e.g. that of (McDonough and Sun, 1995), which may represent a lower mantle plume-source reservoir. Plume melts are often thought to sample a more primitive mantle reservoir (e.g. O'Nions *et al.*, 1979), which has been strengthened by the identification of high $^{3}He/^{4}He$ ratios in OIBs such as Hawaii (Kurz *et al.*, 1982) and some CFB provinces such as Baffin Island and the Ethiopian flood basalt province (Pik *et al.*, 2006; Starkey *et al.*, 2009). However, high $^{3}He/^{4}He$ ratios are not always present in plume melts, and MORB-like ratios were recently measured in the most primitive Karoo rocks (Heinonen and Kurz, 2015). Melting of more depleted mantle in plume starting heads could occur as the result of entrainment and heating of ambient mantle (Griffiths and Campbell, 1990; although more recent geodynamic models indicate that entrainment does not occur in plume heads, e.g. Farnetani *et al.*, 2002). An alternative theory states that CFB provinces derive from upper mantle that becomes stagnant and superheated beneath supercontinents (Coltice *et al.*, 2007). In this case, depleted, MORB-like melts would be produced. This theory is difficult to test by geochemistry and is not considered in this study to be the origin of the Paraná-Etendeka CFB province. Alternatively, the composition of mantle from which plume starting heads originate may be depleted in some plumes but not others. The composition of 'primitive' lower mantle also depends on assumptions made about the composition of the bulk silicate Earth, which may in fact be non-chondritic and thus more depleted, as many authors now propose (e.g. Campbell and O'Neill, 2012; Caro *et al.*, 2008; Jackson and Jellinek, 2013; O'Neill and Palme, 2008).

The Etendeka picrites are plume melts with slightly enriched, but essentially similar, isotopic characteristics to MORB (εNd = 3.7-8.7). The least contaminated samples are the most MORB-like. The observation that the isotopic characteristics are MORB-like means that the Paraná-Etendeka CFB likely formed from melting of a composition similar to depleted upper mantle. In this chapter, the Etendeka picrites are modelled both with the DMM of Salters and Stracke (2004) and PRIMA of McDonough and Sun (1995), and the implications of using different source compositions are discussed.

There is little consensus on the composition of potential pyroxenites in the convecting mantle. Throughout this thesis, the composition KG1 is used to represent the major element composition of

pyroxenite. This composition is a 1:1 mixture of peridotite KLB-1 and average MORB (Kogiso *et al.*, 1998). Using the same idea, a trace element composition for KG1 pyroxenite can be approximated by a 1:1 mixture of peridotitic mantle and MORB. As pyroxenite is formed by the interaction of plume peridotite with melts of subducted eclogite, the primitive mantle composition of McDonough and Sun (1995) is mixed with the theoretical composition of subduction-modified MORB of Stracke *et al.* (2003), i.e. MORB that has lost some proportion of its more fluid-mobile elements.

Phase transitions

The pressure of phase transitions on the peridotite (KLB-1) and pyroxenite (KG1) solidi are calculated in THERMOCALC and given in Table 6.1. Four changes in phase assemblage occur along the solidus, which must be accounted for in the modal mineralogy terms of equations 6.1 and 6.2. The phase transitions are also associated with non-linear changes in melt reactions and phase compositions. From lowest to highest pressure, these transitions are: plagioclase-out, garnet-in, spinel-out and orthopyroxene-out. The geometry of these boundaries is seen in Figs. 4.1 and 4.10. Lower pressure phase transitions are ignored because the model is not intended to be used for plagioclase-bearing assemblages. Spinel-out and orthopyroxene-out are taken to occur simultaneously in pyroxenite. For simplicity, the transitions are considered to occur at a fixed pressure, so a temperature or melt fraction dependence is not defined.

Lithology	$P_{\mathrm{pl-out}}$	$P_{\mathrm{g-in}}$	$P_{\mathrm{sp-out}}$	$P_{\mathrm{opx-out}}$
Peridotite	1.06	2.14	2.17	4.19
Pyroxenite	1.23	2.19	2.36	2.36

Table 6.1: Pressure at which new phases enter or leave the assemblage on the solidus, in GPa, from Figs. 4.1 (KLB-1 peridotite) and 4.10 (KG1 pyroxenite). $P_{\mathrm{sp-out}}$ is set to match $P_{\mathrm{opx-out}}$ in pyroxenite.

As the mantle decompresses and passes through a phase transition, a reaction takes place involving other phases. These are defined in the model, so that the residual solid modes are adjusted through the transition. The orthopyroxene-in transition is continuous and is accounted for by orthopyroxene precipitation in the melting reactions. If $P_{\mathrm{solidus}} < P_{\mathrm{opx-out}}$, orthopyroxene is already present. If $P_{\mathrm{solidus}} > P_{\mathrm{opx-out}}$, orthopyroxene is made to precipitate from $P = P_{\mathrm{opx-out}}$ with a new melting reaction. Garnet is lost and replaced by spinel between $P_{\mathrm{g-in}}$ and $P_{\mathrm{sp-out}}$; both garnet and spinel are consumed by melting. The reaction of garnet to spinel also consumes olivine and precipitates clinopyroxene and orthopyroxene (Robinson and Wood, 1998) in a ratio defined by the composition of the reacting garnet. The following stoichiometric reaction is used in the model, and the only compositional variable is $X^{\mathrm{g}}_{\mathrm{Ca\ p.f.u.}}$ (Ca cations per formula unit of garnet on a 12 oxygen basis):

$$1\mathrm{ol} + 1\mathrm{g} = (2 - X^{\mathrm{g}}_{\mathrm{Ca\ p.f.u.}})\mathrm{opx} + (X^{\mathrm{g}}_{\mathrm{Ca\ p.f.u.}})\mathrm{cpx} + 1\mathrm{sp} \tag{6.4}$$

It is assumed for simplicity that $X_{\mathrm{Ca}}^{\mathrm{M2}}$ in cpx = 1 (although the true value is lower), so all Ca in garnet is accounted for by cpx precipitation. In the pressure interval between $P_{\mathrm{g-in}}$ and $P_{\mathrm{sp-out}}$, garnet and spinel are both present. This is accounted for by a linear scaling of the coefficients in equation 6.4. It is assumed that the bulk composition is too depleted by melting to precipitate any plagioclase below $P_{\mathrm{pl-out}}$.

Phase modes

The initial phase modes (W_i) are those at the mantle solidus. When the solidus phase modes are defined as an input (rather than solved for), they are calculated according to a pressure-dependent parametrisation from KLB-1 peridotite and KG1 pyroxenite (Table 6.2). The parametrisation is a polynomial fit to the phase proportions along the KLB-1 and KG1 solidi of Chapter 4. Each solidus assemblage (e.g. garnet and and opx bearing, $\mathrm{P_{sp-out}}$ to $\mathrm{P_{opx-out}}$) was fitted separately, because the pressure-dependence of phase proportions is sensitive to the assemblage (e.g. the mode of orthopyroxene, Fig. 4.3c). At each calculation step during melting, modes are adjusted to account for phases lost or gained in the melting reaction and for reaction through the garnet-spinel transition.

		KLB-1 Peridotite			KG1 Pyroxenite		
Pressure interval	Phase	a	b	c	a	b	c
$P_{\mathrm{pl-out}} < P \leqslant P_{\mathrm{g-in}}$	cpx	0.147	0.011	0.005	0.422	0.113	0
	ol	0.599	0.008	-0.001	0.097	0.003	0
	sp	0.020	-0.008	0.001	0.063	-0.003	0
	g	0	0	0	0	0	0
	opx	0.234	-0.011	-0.005	0.418	-0.113	0
$P_{\mathrm{g-in}} < P \leqslant P_{\mathrm{sp-out}}$	cpx	0.777	-0.273	0	1.265	-0.273	0
	ol	-0.080	0.322	0	-0.470	0.264	0
	sp	0.699	-0.322	0	0.631	-0.264	0
	g	-3.061	1.430	0	-2.653	1.220	0
	opx	2.668	-1.157	0	2.228	-0.947	0
$P_{\mathrm{sp-out}} < P \leqslant P_{\mathrm{opx-out}}$	cpx	0.113	0.026	0.003	-	-	-
	ol	0.619	0	0	-	-	-
	sp	0	0	0	-	-	-
	g	-0.114	0.091	-0.009	-	-	-
	opx	0.382	-0.116	0.006	-	-	-
$P > P_{\mathrm{opx-out}}$	cpx	0.333	-0.019	0.001	0.680	-0.043	0.003
	ol	0.619	0	0	0.160	0	0
	sp	0	0	0	0	0	0
	g	0.048	0.019	-0.001	0.161	0.043	-0.003
	opx	0	0	0	0	0	0

Table 6.2: Coefficients for equilibrium weight mode W of phase i along the KLB-1 peridotite and KG1 pyroxenite solidi, in the form $W_i = a_i + b_i P + c_i P^2$. Coefficients are fitted separately for different assemblages from from calculations in THERMOCALC, where each pressure interval is defined by the boundaries given in Table 6.1. Modes calculated in this way always add up to 1 ± 0.001.

Melting reactions

Melting reactions are set according to the phase assemblage present. Before any phases are exhausted through melting, the reactions used are those calculated in THERMOCALC along the KLB-1 peridotite solidus from the mode changes between $F = 0$ and $F = 0.01$. Again, these are parametrised as a function of pressure for a specific phase assemblage. The calculated melting reactions are shown in Fig. 6.1a, where they are scaled such that the reaction coefficient of liquid = -1. In the present model, opx is precipitated during melting at pressures above 5 kbar until it vanishes from the solidus, at which point it precipitates only after a threshold melt fraction is reached. Olivine is precipitated during spinel lherzolite melting and is consumed at higher pressures. Although the sign and pressure dependency of the reacting phase is usually in agreement with experimental values (in the experiments of Walter, 1998, opx is consumed, olivine is precipitated and the direction of the pressure dependencies match those of this study) the coefficient is often different. This reflects a combination of experimental uncertainty (including phase proportion determinations), model shortcoming, and the mismatch in bulk composition.

For a given assemblage, the melting reactions for pyroxenite KG1 were found to be very similar to those of KLB-1 (Fig. 6.1b), with the only important difference being the shift in phase boundary pressure. For this reason, the KLB-1 parametrisation is used for both the peridotite and pyroxenite models, and the reaction used at a given pressure is determined by the relevant phase boundary positions. The reaction coefficients as a function of P and assemblage (or pressure interval) are given in Table 6.3.

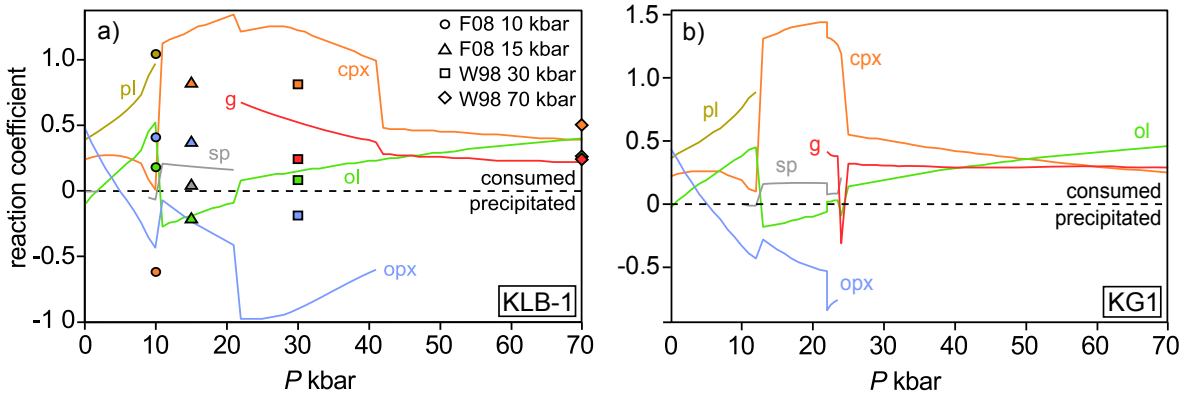

Figure 6.1: Melt reaction coefficients (p_i) for near-solidus melting plotted against pressure, calculated for a) KLB-1 peridotite and b) KG1 pyroxenite. Reaction coefficients are given such that negative values correspond to precipitation and liq = -1. Reactions are calculated over the melt fraction range $F = 0$ to $F = 0.01$. Selected experimentally-derived values are given for comparison for peridotite: W98 (Walter, 1998, KR4003) and F08 (Falloon *et al.*, 2008, MM-3, plagioclase lherzolite reaction only is shown at 10 kbar), which were determined on slightly different bulk compositions.

Pressure interval	Phase	a	b	c
$P_{\mathrm{pl-out}} < P \leqslant P_{\mathrm{g-in}}$	cpx	0.889	0.217	0
	ol	-0.458	0.179	0
	sp	0.258	-0.047	0
	g	0	0	0
	opx	0.287	-0.336	0
$P_{\mathrm{g-in}} < P \leqslant P_{\mathrm{sp-out}}$	cpx	1.284	0	0
	ol	-0.002	0	0
	sp	0.080	0	0
	g	0.339	0	0
	opx	-0.703	0	0
$P_{\mathrm{sp-out}} < P \leqslant P_{\mathrm{opx-out}}$	cpx	0.537	0.553	-0.109
	ol	-0.149	0.118	-0.006
	sp	0	0	0
	g	1.269	-0.333	0.028
	opx	-0.707	-0.312	0.084
$P > P_{\mathrm{opx-out}}$	cpx	0.615	-0.033	0
	ol	-0.125	0.105	-0.004
	sp	0	0	0
	g	0.510	-0.074	0.005
	opx	0	0	0

Table 6.3: Coefficients (p) for phase i in the melting reaction along the KLB-1 peridotite solidus, in the form $p_i = a_i + b_i P + c_i P^2$. Coefficients are fitted separately for different assemblages, where each pressure interval is defined by the boundaries given in Table 6.1 and represents a different assemblage.

The residual solid is corrected at each melt step for phases consumed and precipitated by melting. At some melt fraction, the residual solid will have exhausted a phase (usually cpx, garnet or spinel are lost first). Each new assemblage has a different associated melting reaction, so a reaction is defined according to the solid phases present. Melt reaction coefficients are a mixture of published values and new suggested values and are given in Table 6.4. Although some of the solid phase combinations in Table 6.4 are unrealistic (e.g. for garnet dunite [ol, g]), they are given for completeness (so that when the model is used to solve for initial mineralogy, unusual phase combinations still produce a result). Except for orthopyroxene, single phases are assumed to melt congruently.

Partition coefficients

Mineral-melt partition coefficients (D_i) used in this model are, where possible, PTX sensitive. Only elements with well known partitioning behaviour in all phases are used. The incompatible trace elements modelled are: 1+ valence, Na; 3+ valence, REE+Y; 4+ valence elements, Ti, Zr, Hf; 5+ valence, Nb.

For most elements, the lattice strain model (equation 6.5; Blundy and Wood, 1994) can be used to predict the partition coefficients D_i by using published parametrisations of r_0 (the ideal site radius),

Assemblage	p_{ol}	p_{cpx}	p_{opx}	p_{sp}	p_g	Source
ol, opx, cpx, g $\pm$ sp ol, opx, cpx, sp ol, cpx, g	$a_i + b_i P + c_i P^2$; see Table 6.3					
ol, opx, g	0.13	0	0.62	0	0.25	Walter (1998)
ol, opx, cpx	0.094	1.469	-0.563	0	0	Walter (1998)
ol, opx	0.03	0	0.97	0	0	Walter (1998)
ol, cpx	0.11	0.89	0	0	0	Sorbadere *et al.* (2013)
ol, g	0.1	0	0	0	0.9	This study
ol	1	0	0	0	0	congruent melting
cpx, g	0	$0.061P + 0.219$	0	0	$-0.061P + 0.781$	Hirschmann *et al.* (2003) and Kogiso *et al.* (2003)
opx, cpx	-0.12	0.50	0.62	0	0	This study
g	0	0	0	0	1	congruent melting
cpx	0	1	0	0	0	congruent melting
opx	-0.24	0	1.24	0	0	Wasylenki *et al.* (2003)

Table 6.4: Melt reaction coefficients for all phase combinations. These are normalised such that liq = -1. Reaction coefficients calculated from Hirschmann *et al.* (2003) and Kogiso *et al.* (2003) are fitted with a linear pressure dependence. Except for near-solidus melt reactions given in Table 6.3, spinel is assumed to be inert during melting. This assumption is acceptable given that spinel will not significantly fractionate any elements considered, and that the low spinel mode should only have a minimal effect on the incompatible trace element composition of melts.

D_0 (the strain-free partition coefficient), and E (the site's apparent Young's modulus), which is a measure of the stiffness of the site:

$$D_i = D_0 \times \exp\left[\frac{-4\pi E N_A \left[\frac{r_0}{2}(r_i - r_0)^2 + \frac{1}{3}(r_i - r_0)^3\right]}{RT}\right] \tag{6.5}$$

where P is in GPa, T in K, r in m, E in Pa, N_A is the Avogadro constant and R is the gas constant in $JK^{-1}mol^{-1}$. This model states that, for cation i, D_i is a parabolic function of the difference between r_i and r_0, where D_0 is the maximum possible D. The width of the parabolic distribution of D when plotted against ionic radius is controlled by E. D_0, E and r_0 must be specified for a given site, coordination number and charge in a phase. Some elements, such as the REE, often have well-known D_0, E and r_0 in different phases because a large number of elements are available for fitting. Others cannot be so easily fitted by a lattice strain model. For example, there are few 5+ trace elements, and their associated E tends to be high, meaning that the site is stiff and the parabola is narrow, so a small error in r_0 results in a large error in D_i (Hill *et al.*, 2000). It is also easier to determine D_i in some phases than others. Clinopyroxene and garnet, for example, have relatively high partition coefficients in many elements, meaning that they can be analysed precisely. However, olivine and spinel have much lower partition coefficients, so published D_i have a larger uncertainty. For these reasons, not all

partition coefficients in all phases are predicted according to equation 6.5, and fixed values are used instead.

The T term in equation 6.5 gives calculated partition coefficients a temperature dependence. Additionally, for some elements, published values for E, D_0 and/or r_0 are reported with a pressure, temperature or phase composition term, which are used here. Phase compositions are calculated, sometimes as a function of P and/or F, in THERMOCALC. The compositional notation $X_{\mathrm{Ca}}^{\mathrm{M2}}$, as an example, refers to the molar proportion of Ca in the M2 site of that phase. Ionic radius is charge- and coordination- dependent and is taken from Shannon (1976) in this study and the experimental studies cited in Table 6.5. The various parameters and equations used to predict D_i for different phases are given in Table 6.5, including the source references. If r_0, E and D_0 are specified, they are for use with equation 6.5.

Table 6.5: Methods used to calculate partition coefficients (D) in the model. Units: P, GPa; T, K; r_0, Å; E, Pa; X denotes a cation fraction; Fo is the forsterite content of olivine expressed as a mole fraction. When r_0, E and D_0 are given, these are for use with equation 6.5. The cations column states both the cations calculated and their valence state, and the Site column gives the crystallographic site in which that cation is thought to reside, and the coordination of that site (which must be known for selecting the appropriate cation radius from Shannon, 1976). In some models, such as 3+ and 4+ cations in opx, some cations are thought to partition into more than one site. In these cases, D_i calculated for the different sites are added together (Frei *et al.*, 2009). The calculation for 4+ cations in cpx is complicated; for a detailed description of the terms, see Hill *et al.* (2011) (note that terms and equations are from the erratum: Hill *et al.*, 2012).

Phase	Cations	Site(Coordination)	Details	Reference
cpx	1+: Na	M2(VIII)	$D_{\mathrm{Na}} = \mathrm{e}^{((10367+2100P-165P^2)/T)-10.27+0.358P-0.0184P^2}$	Blundy *et al.* (1995)
	3+: Y+REE	M2(VIII)	$r_0 = 0.974 + 0.067X_{\mathrm{Ca}}^{\mathrm{M2}} - 0.051X_{\mathrm{Al}}^{\mathrm{M1}}$	Wood and Blundy (1997)
			$E = 318.6 + 6.9P - 0.036T$	
			$D_0 = (Mg\#_{melt}/\mathrm{X}_{\mathrm{Mg}}^{\mathrm{M1}})\mathrm{e}^{(88750-65.644T+7050P\tilde{}770P^2)/(RT)}$	
	4+: Ti, Zr, Hf	M1(VI)	$r_0 = 0.659 - 0.008P + 0.028\mathrm{X}_{\mathrm{Al}}^{\mathrm{M1}}$	Hill *et al.* (2011); Hill *et al.* (2012)
			$E = 11228 - 5.74T + 15204X_{\mathrm{Al}}^{\mathrm{T}}$	
			$\Delta G_{elec}^{cpx} = 14000$	
			$\varnothing = [X^{4+}] + [X^{3+}]\mathrm{e}^{-\Delta G_{\mathrm{elec}}^{\mathrm{cpx}}/(RT)} + [X^{2+}]\mathrm{e}^{(-4\Delta G_{\mathrm{elec}}^{\mathrm{cpx}})/(RT)}$	
			$D_{\mathrm{Ti}} = \varnothing\mathrm{e}^{(-35730+2183P+1457P^2)/(-RT)}$	
			D_{Zr} and D_{Hf} calculated relative to D_{Ti} with adapted version of equation 6.5	
	5+: Nb	M1(VI)	$r_0 = 0.587$	Hill *et al.* (2000)
			$E = 8463 \times 10^9$	
			$D_0 = 3.6$	
opx	1+: Na	M2(VI)	$D_{\mathrm{Na}} = 0.0107\mathrm{e}^{0.7447}$	fitted to data from Frei *et al.* (2009)
	3+: Y+REE	M1(VI) & M2(VI)	$r_0^{\mathrm{M1}} = 0.656$; $E^{\mathrm{M1}} = 992.4 \times 10^9$; D_0^{M1}=2.542	Frei *et al.* (2009)
			$r_0^{\mathrm{M2}} = 0.832$; $E^{\mathrm{M2}} = 498.4 \times 10^9$; D_0^{M2}=0.149	
			$D_i = D_i^{\mathrm{M1}} + \mathrm{D}_i^{\mathrm{M2}}$	
	4+: Ti, Zr, Hf	M1(VI) & M2(VI)	$r_0^{\mathrm{M1}} = 0.642$; $E^{\mathrm{M1}} = 2360 \times 10^9$; D_0^{M1}=0.2712	Frei *et al.* (2009)

Table 6.5 – *Continued on next page*

Phase	Cations	Site(Coordination)	Details	Reference
			$r_0^{M2} = 0.832$; $E^{M2} = 335 \times 10^9$; D_0^{M2}=0.00278	
			$D_i = D_i^{M1}$+D_i^{M2}	
	5+: Nb	M1(VI)	$D_{Nb} = 0.001516$	Frei *et al.* (2009); average of 5 runs
sp	1+: Na		$D_{Na} \approx 0$	-
	3+: Y+REE		$D_i = e^{-259.4r_i^2+483.8r_i-231.5}$	Fit to data of Elkins *et al.* (2008)
	4+: Ti, Zr, Hf		$D_{Ti} = 0.095$; $D_{Zr} = 0.0011$; $D_{Hf} = 0.0011$	Wijbrans *et al.* (2015), exp. sp5_05
	5+: Nb		$D_{Nb} = 0.0005$	Wijbrans *et al.* (2015), exp. sp5_05
g	1+: Na	X(VIII)	$D_{Na} = 0.069$	Tuff *et al.* (2005); average of all g-liq pairs
	3+: Y+REE	X(VIII)	$r_0^{M1} = 0.780 + 0.155$Ca(p.f.u.)	Sun and Liang (2013)
			$E = (-1.62 + 2.29r_0) \times 10^3$	
			$D_0 = e^{-2.05+((9.17\times10^4-91.35P(38-P))/(RT))-1.02}$Ca(p.f.u.)	
	4+: Ti, Zr, Hf	Y(VI) & X(VIII)	$r_0^Y = 0.67$; $E^Y = 939 \times 10^9$; $D_0^Y = 2.6$	van Westrenen *et al.* (2001), values fitted to experimental data of Hauri *et al.* (1994)
			$r_0^X = 0.89$; $E^X = 1510 \times 10^9$; $D_0^X = 2.1$	
			$D_i = D_i^X + D_i^Y$	
	5+: Nb	Y(VI)	$D_{Nb} = 0.0007$	Fulmer *et al.* (2010)
ol	1+: Na	M(VI)	$D_{Na} = 0.0120P - 0.0042$	fit to data of Taura *et al.* (1998)
	3+: Y+REE	M(VI)	$D_0 = e^{-0.45-0.11P+1.54X_{Al}^{liq}-(1.94\times10^{-2})Fo}$	Sun and Liang (2013)
			$r_0 = 0.720$	
			$E = 426 \times 10^9$	
	4+: Ti, Zr, Hf	T(IV)	$r_0 = 0.479$	Canil and Fedortchouk (2001), exp. 132adk1
			$E = 202 \times 10^9$	
			$D_0 = 0.032$	
	5+: Nb	T(IV)	$D_{Nb} = 0.0004$	Wijbrans *et al.* (2015), exp. sp5_10

Phase compositions

Certain aspects of phase compositions are required to calculate partition coefficients (see Table 6.5). As with mineral modes and melting reactions, these have been parametrised from THERMOCALC calculations on KLB-1 peridotite and KG1 pyroxenite. The composition of minerals will depend both on pressure and prior melting. For example, cpx($X_{\mathrm{Na}}^{\mathrm{M2}}$) will be sensitive to F because Na is moderately incompatible in clinopyroxene. The parametrisation of phase compositions therefore includes P and F and is given in Table 6.6. F is calculated from equilibrium melting but is applied as cumulative F (rather than the instantaneous F for a particular calculation step) in the model, as an approximation for the general way in which a phase will increase or decrease in a given component with melting.

Compaction correction and incremental melt integration

Before recombining the individual incremental melts, a compaction correction is applied. This corrects for the fact that during each melting step, a finite volume of solid material is lost (phase modes must be renormalised to calculate trace element partitioning), and so a smaller melt volume is produced in the subsequent step. Each incremental melt fraction is multiplied by $1 - F_{\mathrm{total}}^{m}$ to achieve this ($F_{\mathrm{total}}^{m} = \sum_{i=1}^{m} F_i$, the sum of melt fractions from all previous melting increments, m).

The calculated melt fractions are then combined as a single liquid composition, to replicate the natural process whereby fractional mantle melts combine and homogenise in crustal magma chambers. It is demonstrated in Chapter 3 that the picrites and ferropicrites represent fully homogenised mantle melts. It is assumed that the accumulated melt will reflect the geometry of the melting region, i.e. that melts will escape all locations within the melting region with equal efficiency. The idea of a triangular melting region existing beneath ridge settings is well established, and integrating melts according to this geometry creates a final melt that is biased towards the composition of deeper, lower fraction melts (Plank and Langmuir, 1992), as illustrated in Fig. 6.2a. The limits of the melting region are defined by the point at which the flow streamlines lose their vertical component, when no further decompression melting can occur.

When an upwelling plume impinges on the base of the lithosphere, the melting region is also bounded by a surface defining the loss of vertical flow. However, because the plume outflow is not bounded by a linear rift, it will spread in three dimensions. Ito and Mahoney (2005a) suggest that the upper limit of this melt-bearing region in a steady-state plume has the shape of a dome (Fig. 6.2b). Plumes have the additional complication over ridges of being thermally stratified. Therefore, the solidus will be deepest in the hottest centre of the plume rather than the solidus being a flat surface (Watson and McKenzie, 1991). Modelling melting in a thermally stratified plume is computationally complex and beyond the scope of this thesis. The model in this chapter is simplified by using a single plume T_P, which is assumed to represent an average melting condition within the upwelling plume.

Lithology	Phase	Cation	Pressure interval	Intercept	$p_1(P)$	$p_2(P^2)$	$f_1(F)$	$f_2(F^2)$
Peridotite	cpx	$X_{\mathrm{Na}}^{\mathrm{M2}}$	$P_{\mathrm{pl-out}} < P \leqslant P_{\mathrm{g-in}}$	0.116			-0.847	
			$P_{\mathrm{g-in}} < P \leqslant P_{\mathrm{opx-out}}$	0.139	-0.015		-0.154	
			$P > P_{\mathrm{opx-out}}$	0.059	0.0032			
		$X_{\mathrm{Al}}^{\mathrm{M1}}$	$P_{\mathrm{pl-out}} < P \leqslant P_{\mathrm{g-in}}$	0.249	-0.034		-0.369	
			$P > P_{\mathrm{g-in}}$	0.267	-0.051	0.0039	-0.252	
		$X_{\mathrm{Ca}}^{\mathrm{M2}}$	$P_{\mathrm{pl-out}} < P \leqslant P_{\mathrm{opx-out}}$	1.019	-0.130			
			$P > P_{\mathrm{opx-out}}$	0.514			-1.271	5.066
		$X_{\mathrm{Al}}^{\mathrm{T}}$	$P > P_{\mathrm{g-in}}$	0.078	-0.015	0.0009		
			$P_{\mathrm{pl-out}} < P \leqslant P_{\mathrm{g-in}}$	0.022	0.013		0.246	
		$X_{\mathrm{Mg}}^{\mathrm{M1}}$	$P > P_{\mathrm{opx-out}}$	0.747	0.0088		0.422	
			$P_{\mathrm{g-in}} < P \leqslant P_{\mathrm{opx-out}}$	0.658	0.026		0.499	
			$P_{\mathrm{pl-out}} < P \leqslant P_{\mathrm{g-in}}$	0.740	-0.021		0.398	
	g	Ca p.f.u.	$P > P_{\mathrm{pl-out}}$	0.346				
	ol	Fo	$P > P_{\mathrm{pl-out}}$	0.900	-0.0006		0.076	
	liq	X_{Al}	$P > P_{\mathrm{g-in}}$	0.302	-0.072	0.0054		
			$P_{\mathrm{pl-out}} < P \leqslant P_{\mathrm{g-in}}$	0.232	-0.026		-0.107	
		Mg#	$P_{\mathrm{pl-out}} < P \leqslant P_{\mathrm{g-in}}$	0.760	-0.041	0.0112	0.083	-0.858
			$P > P_{\mathrm{g-in}}$	0.685	0.016		0.149	
Pyroxenite	cpx	$X_{\mathrm{Na}}^{\mathrm{M2}}$	$P > P_{\mathrm{opx-out}}$	0.165	0.016	-0.0010	-0.325	0.318
			$P_{\mathrm{pl-out}} < P \leqslant P_{\mathrm{opx-out}}$	0.189			-0.239	
		$X_{\mathrm{Al}}^{\mathrm{M1}}$	$P > P_{\mathrm{opx-out}}$	0.245	-0.012	0.0008	-0.122	
			$P_{\mathrm{pl-out}} < P \leqslant P_{\mathrm{opx-out}}$	0.218			-0.182	
		$X_{\mathrm{Ca}}^{\mathrm{M2}}$	$P > P_{\mathrm{opx-out}}$	0.415	0.013	-0.0011	-0.138	
			$P_{\mathrm{pl-out}} < P \leqslant P_{\mathrm{opx-out}}$	0.622	-0.089		0.558	-0.409
		$X_{\mathrm{Al}}^{\mathrm{T}}$	$P > P_{\mathrm{opx-out}}$	0.070	-0.016	0.0010	0.016	
			$P_{\mathrm{pl-out}} < P \leqslant P_{\mathrm{opx-out}}$	0.004	0.014		0.067	
		$X_{\mathrm{Mg}}^{\mathrm{M1}}$	$P > P_{\mathrm{opx-out}}$	0.602	0.014	-0.0006	0.354	-0.319
			$P_{\mathrm{pl-out}} < P \leqslant P_{\mathrm{opx-out}}$	0.649			0.219	
	g	Ca p.f.u.	$P > P_{\mathrm{pl-out}}$	0.219	0.039	0.0019		
	ol	Fo	$P > P_{\mathrm{pl-out}}$	0.839	-0.0025		0.106	
	liq	X_{Al}	$P > P_{\mathrm{pl-out}}$	0.238	-0.040	0.0024		
		Mg#	$P > P_{\mathrm{opx-out}}$	0.613	-0.0066	0.0022	0.213	
			$P_{\mathrm{pl-out}} < P \leqslant P_{\mathrm{opx-out}}$	0.609			0.141	

Table 6.6: Coefficients for calculating the aspects of phase composition required for the calculation of partition coefficients, as stated in Table 6.5. Coefficients are given in the format $X = p_1P + p_2P^2 + f_1F + f_2F^2 + \text{intercept}$. Coefficients are fitted over different pressure intervals (corresponding to Table 6.1) from THERMOCALC calculations on KLB-1 for peridotite and KG1 for pyroxenite. $X_{\mathrm{Na}}^{\mathrm{M2}}$ for cpx is the molar proportion of Na in the cpx M2 site; p.f.u. is per formula unit; X_{Al} is the cation fraction of Al in the liquid.

The shape of the melting region is therefore approximated as having a horizontal base at the solidus. Ito and Mahoney (2005a) suggest from fluid dynamical modelling that the thickness of the plume outflow is 100 km, i.e. plume material below this will be rising vertically in a column. In most cases, the difference between the solidus depth and the lithospheric thickness is < 100 km, so fractional melts are integrated according to a domed (half sphere) melt region geometry. If melting is at very high temperature below thin lithosphere, the melt region may be more than 100 km deep, in which case, a columnar melt region is appended at the base, as illustrated in Fig. 6.2c.

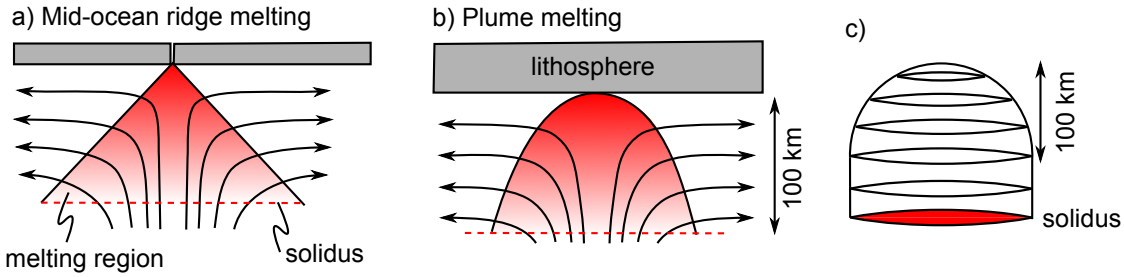

Figure 6.2: Melting regions geometries of a) a spreading ridge, and b) an isoviscous upwelling mantle column restricted by an upper boundary layer, after Ito and Mahoney (2005b). Red dashed line, solidus; coloured area, melting region; black arrows, flow lines; grey box, lithosphere. Melting ceases where flow lines have no vertical component. Plume outflow thickness is 100 km. c) Melting region geometry used in this chapter, based on b), where a half-sphere dome of radius 100 km underlain by a columnar geometry is used.

Comparison with natural data

An olivine fractionation correction is applied to the accumulated melt composition to increase the incompatible trace element concentrations of the modelled melt and make it directly comparable with natural picrite and ferropicrite samples. This is done according to the suggested extents of olivine fractionation in Table 2.1. Model melts are calculated relative to the initial mantle composition. In order to make the natural samples comparable, they must be normalised to an appropriate source composition. This composition is that of either primitive mantle PRIMA, depleted MORB-source mantle DMM or theoretical pyroxenite KG1; see above for details. In order to quantify the misfit between a model melt and the natural samples, a function is defined based on the root mean square (RMS) of difference, using quantities normalised to the sample concentration rather than absolute values:

$$\mathrm{RMS} = \sqrt{\frac{\sum_{i=1}^{n} \left((c^i_{\mathrm{model}} - c^i_{\mathrm{sample}}) / c^i_{\mathrm{sample}} \right)^2}{n}} \tag{6.6}$$

6.3 Trace element modelling results

In this thesis, both the melting conditions (T_P and lithospheric thickness) and the source modal mineralogy of the picrites and ferropicrites are of interest. Trace element modelling has the ability to address both. To reduce the number of unknowns being solved for by trace elements, the model will be used in two ways. Firstly, the melting conditions are investigated whilst assuming a known source mineralogy. Then, the source mineralogy is investigated by imposing melting conditions. These results are then considered alongside the results of previous chapters in the concluding chapter (7).

6.3.1 Melting conditions

Model melt example

Melting conditions were examined using solidus phase modes calculated from the parametrisations given in Table 6.2. The results of an example calculation are shown in Fig. 6.3. Fig. 6.3a shows the residual mineralogy as melting progresses. Melting begins deep and continues to a moderate cumulative melt fraction of around 14.5%. Garnet is exhausted from the solid residue at slightly higher pressure than the garnet-spinel transition, so no spinel is produced. Orthopyroxene is precipitated until 2.25 GPa, at which point the other phases are exhausted and it melts. The final residue is a harzburgite with 70% olivine, 25% orthopyroxene and 5% clinopyroxene. The effect of the changing mineralogy and partition coefficients on the incipient melt compositions is shown in Fig. 6.3b. Low fraction melts are very enriched in highly incompatible elements, and the loss of garnet from the melting residue causes a small spike in the HREE as they suddenly become more incompatible in the solid. The final melt composition is shown in Fig. 6.3c. This consists of the individual melt increments integrated according to the geometry described in Section 6.2.3. A correction has been applied to account for the effect of 12% olivine fractionation. The model result shows a good, but not perfect, fit to the composition of picrite sample 97SB33, where 97SB33 is normalised to the depleted MORB-source mantle of Salters and Stracke (2004). The HREE are more fractionated in the model melt than the natural sample.

Best fit T_P and lithospheric thickness solution

The optimum lithospheric thickness and T_P required to model the natural sample compositions is investigated by using the RMS (equation 6.6) to quantify the mismatch between a model output and a sample composition. Fig. 6.4 shows the results as contoured surfaces of 1/RMS as a function of lithospheric thickness and T_P.

The sample chosen to represent picrites is 97SB33 (corrected for 12% olivine fractionation), which contains the highest temperature spinel-olivine (Fo_{93}) pairs of Chapter 5 and has $\varepsilon Nd = 6.4$, so is not thought to be much affected by crustal assimilation. To illustrate the effect of the choice of source composition on the result, Fig. 6.4a shows the misfit when 97SB33 is normalised to primitive mantle (McDonough and Sun, 1995), whereas in Fig. 6.4c, 97SB33 is normalised to the depleted MORB-source upper mantle (DMM) of Salters and Stracke (2004). With a primitive mantle source, a high fraction of melting of $F = 0.3$–0.4 is required to best match the primitive picrite composition. Melting must have occurred under a thinned lithosphere ($<\sim 40$ km) at $T_P = 1450$–1600 °C. However, the mantle source of the Etendeka picrites is likely to be more similar to DMM, given the depleted, MORB-like Nd and Sr isotopic ratios of the least contaminated samples (Thompson *et al.*, 2001). With a more depleted mantle composition, a lower fraction of melting is required to match

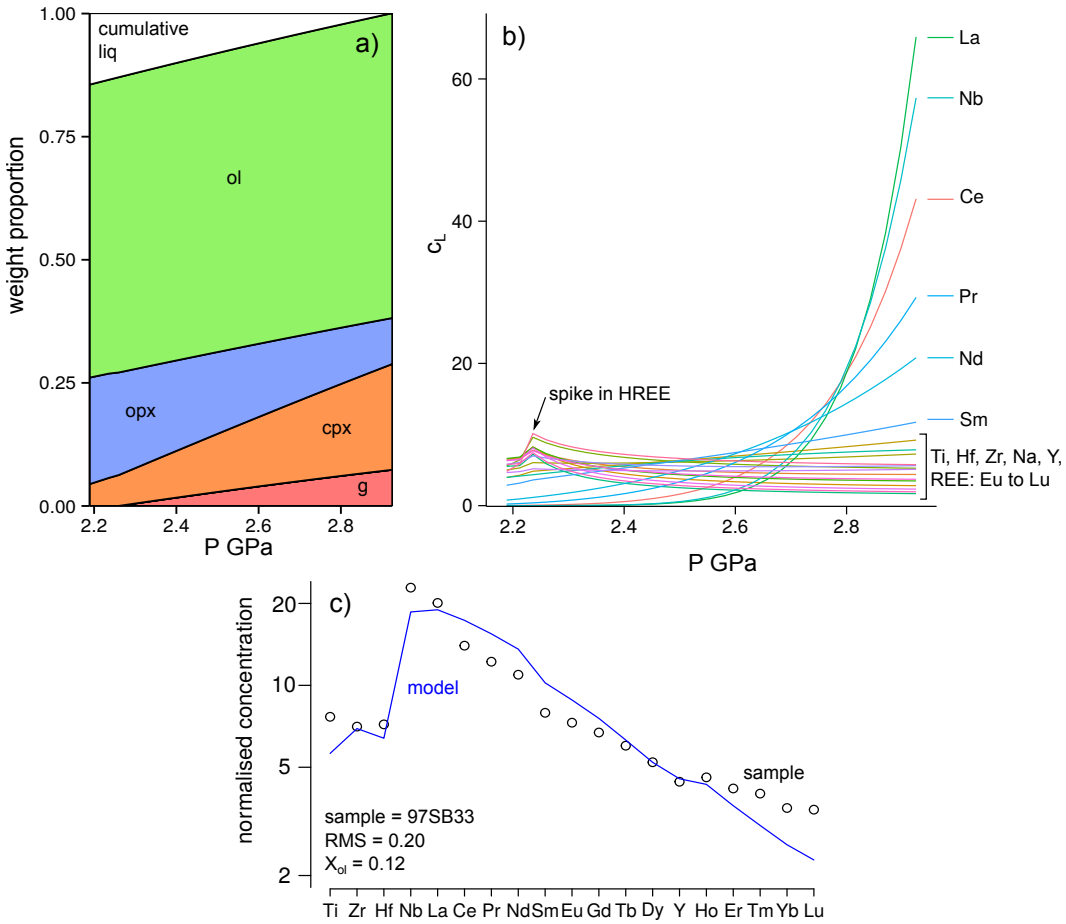

Figure 6.3: Example of a trace element model melt calculation, performed using the peridotite melting model with $T_P = 1450$ °C and lithospheric thickness = 65 km, corresponding to a cumulative melt fraction of 14.5%. a) Weight proportion of phases in the solid residue as a function of P along the melting path, normalised to include the cumulative liquid fraction; b) c_L of various elements in the incremental melt produced along the melting path; c) integrated model melt composition, with 12% olivine fractionation simulated (blue line) plotted with the whole-rock composition of sample 97SB33 (black circles), both normalised to the depleted upper mantle (DMM) composition of Salters and Stracke (2004). The trace elements in c) are grouped according to valence state, and the group Y+REE is ordered according to increasing compatibility. This is to prevent spurious peaks, which can occur because the partition coefficients for different valence state groups of cations are calculated by different methods.

the relatively depleted picrite sample. This is achieved with a somewhat lower T_P combined with a thicker lithospheric lid. Fig. 6.4c shows a 'valley' of best fit solutions at $F = 0.16$–0.20 at any depth, although the best solution is found at $T_P = 1400$–1475 °C and a lithospheric thickness of 50–60 km, corresponding to $F \sim 0.2$. Some examples of model melts produced at different melting conditions are compared to DMM-normalised picrite sample 97SB33 in Fig. 6.5. They show that it is difficult to reproduce the slightly concave-up pattern seen in the REE in sample 97SB33. This tends to be true at any T_P and lithospheric thickness combination that match the MREE and LREE well.

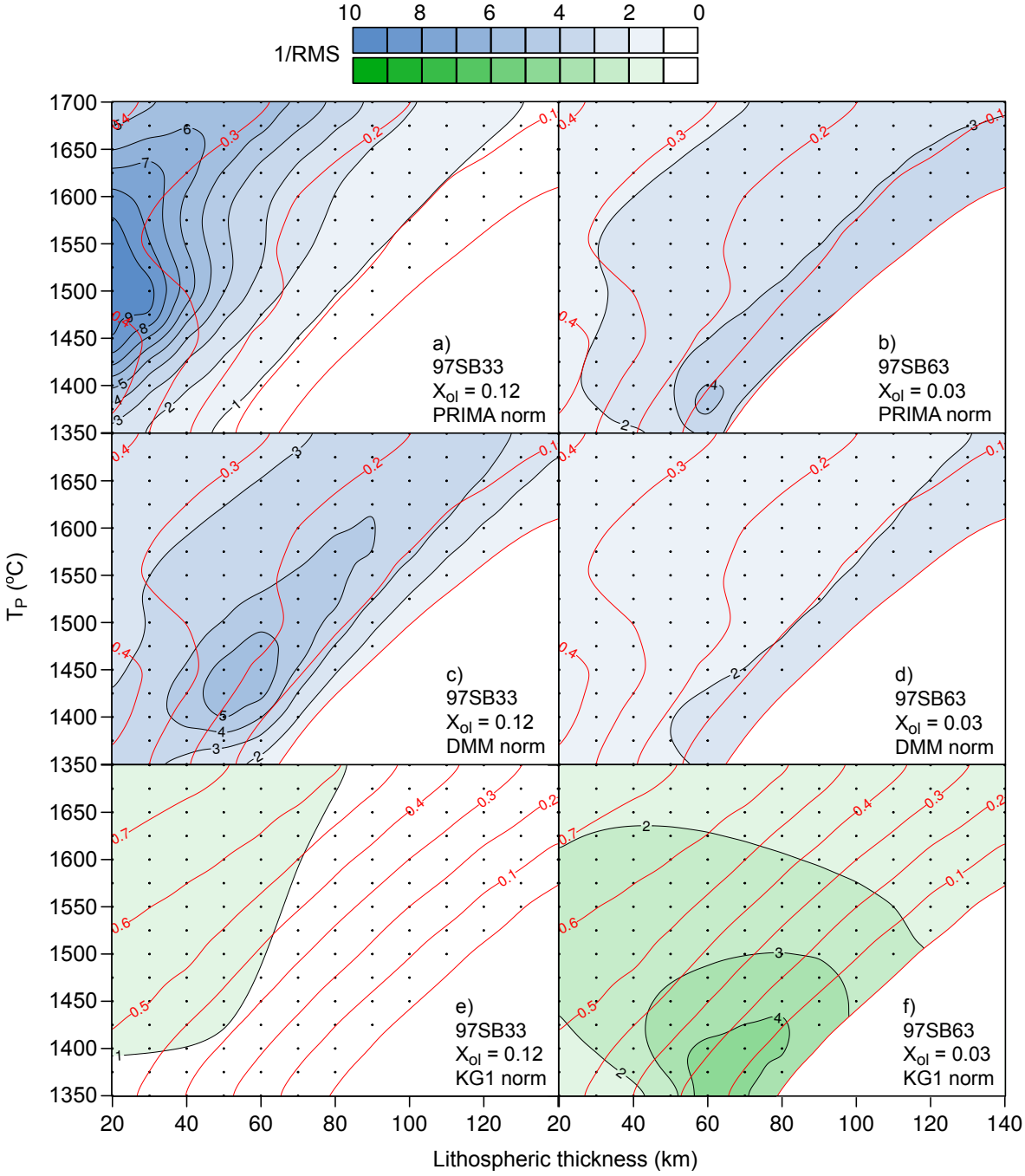

Figure 6.4: 1/RMS misfit between model melts and natural samples, contoured as a function of lithospheric thickness and T_P. Red lines are melt fraction contours. a)–d) use the peridotite melting model (blue), e)–f) use the pyroxenite melting model (green). Natural samples used are 97SB33 corrected for 12% olivine fractionation, to represent the Etendeka picrites (plots a, c, e) and 97SB63 corrected for 3% fractionation, to represent the Etendeka ferropicrites (plots b, d, f). Mantle normalisation used: a) and b): PRIMA (primitive mantle of McDonough and Sun (1995); c) and d): DMM (depleted upper mantle of Salters and Stracke, 2004); e) and f) KG1, discussed in text. Points show the grid of calculated model melts used for contouring, at T_P intervals of 25 °C and lithospheric thickness intervals of 10 km.

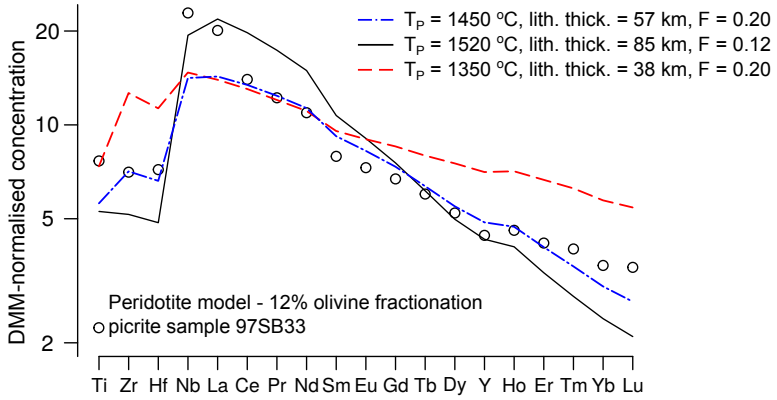

Figure 6.5: Model melt trace element patterns for some T_P and lithospheric thickness conditions, normalised to DMM (Salters and Stracke, 2004). Open symbols are sample 97SB33. The three lines are the model results with 12% olivine fractionation.

By comparison, Fig. 6.4b shows the solution for the Etendeka ferropicrite sample 97SB63 normalised to primitive mantle, and Fig. 6.4d shows the same but normalised to depleted upper mantle. These were also calculated using the peridotite model. 97SB63 corrected for 3% olivine fractionation is used to represent the Etendeka ferropicrite primary melt (in accordance with Table 2.1), as this sample is both the most primitive and least altered. Two things are clear. Firstly, the fit of the model to the data is much poorer than for the picrite sample for either mantle composition, where the best fit solution has a higher RMS than that of the picrite (indicated by paler colour fill in Figs. 6.4b and d). Secondly, a much lower melt fraction is required to create the enriched ferropicrite from a peridotite composition. For a primitive mantle source, $F \sim 0.08$ is required, and an even lower F is needed to make ferropicrite from depleted upper mantle. However, the major element composition of ferropicrite strongly suggests a pyroxenite mantle source (Chapter 4), so this solution is not an accurate representation of ferropicrite source melting conditions.

To investigate the melting conditions in the ferropicrite source, the pyroxenite model was used, with samples normalised to a KG1-like mantle source. This includes a KG1 pyroxenite solidus mineralogy, which is rich in clinopyroxene (52–67%). The resultant fits of the model to samples are shown in Fig. 6.4f, with the picrite sample 97SB33 modelled under the same conditions in 6.4e for comparison. The misfit between picrite sample 97SB33 and model melts is much worse than that found using the peridotite model (Figs. 6.4a and c), and no real solution is found. This is because no amount of melting of such an enriched source can produce a melt as depleted as the picrites. A better match is found for ferropicrite sample 97SB63 from the pyroxenite model (Fig. 6.4f) than the picrite sample, and this solution also represents an improvement over the result found with the peridotite model (Fig. 6.4b and d). The best fit is at low T_P ($\sim$ 1350-1425 °C) and at moderate melt fraction ($\sim$ 0.1), requiring a lithospheric thickness of 60–80 km. This is consistent with findings from the crystallisation temperature of ferropicrite, but seems inconsistent with major element evidence, which indicates a

higher T_P. Unlike picrite, the best fit does not match one melt fraction regardless of the pressure of melting.

Figs. 6.4a–f show that the greatest control on the trace element composition, and so the fit of the model melts to the data, is the length of the melting column. The best fit solutions tend to be smeared out parallel to contours of F. The pressure of melting is of secondary importance. Trace element modelling can therefore constrain F well, but cannot constrain an exact T_P or lithospheric thickness so well when used in isolation.

6.3.2 Source mineralogy

The mineralogy of the mantle source of picrite sample 97SB33 and ferropicrite sample 97SB63 are investigated by assuming a depth and extent of melting (by fixing T_P and lithospheric thickness). The weight modes of phases at the initiation of melting (i.e. at the solidus) can then be varied to find the lowest RMS mismatch (defined by equation 6.6) between the sample and model melt composition. These mineral modes represent the initial solid and do not stay constant throughout the melting run; in many cases an initial orthopyroxene-free and olivine-poor pyroxenite will end up as an orthopyroxene and olivine-rich pyroxenite after partial melting. For ease of calculation and displaying of results, the weight mode of orthopyroxene (X_{opx}) is fixed at 5% in the peridotite melting model runs and at 0% in the pyroxenite melting runs, because at the pressures of interest, a KLB-1-like peridotite contains a low mode of opx and a KG1-like pyroxenite contains none (see Chapter 4). The mode of opx will cause a shift towards or away from olivine (approximately) as the trace elements investigated are similarly incompatible in both. The results of these calculations are displayed on ternary diagrams in terms of initial phase modes, which are projected from orthopyroxene in Fig. 6.6.

The first row (Fig. 6.6a) shows the picrite sample 97SB33, which is corrected for 12% olivine fractionation, compared with a model accumulated fractional melt using the peridotite model and a DMM source. A fixed melt fraction of $F = 0.2$ is modelled, based on Fig. 6.4c, which indicates that the best solution at any T_P is found over a narrow melt fraction range. At $T_P = 1450$ °C, the best fit solution for this picrite sample is similar to a typical lherzolite, with 66.5 wt.% olivine, 19 wt.% clinopyroxene and 9.5 wt.% garnet (5% orthopyroxene was fixed). A higher starting mode of orthopyroxene would be approximately compensated for by a lower olivine mode in the best solution, i.e. a solution with 10% orthopyroxene would contain 61.5 wt.% olivine. For comparison, KLB-1 peridotite has 9.3 wt.% orthopyroxene, 61.9 wt.% olivine, 21.5 wt.% clinopyroxene and 7.3 wt.% garnet on the solidus when $T_P = 1450$ °C. Lherzolite solutions are also found at $T_P = 1550$ and 1650 °C, although without a clear distinction between olivine- and clinopyroxene-rich solutions. At $T_P = 1350$ °C, the solidus is intersected at a slightly lower pressure than the garnet-spinel transition,

so the results cannot distinguish between different proportions of garnet in the solid (which is instantly converted to spinel). A lherzolitic proportion of olivine is present at $X_g = 0$.

The effect of bulk composition on this result is examined in Fig. 6.6b by using the same melting conditions as Fig. 6.6a and normalising to primitive mantle source composition (McDonough and Sun, 1995). The same proportion of garnet is found to produce the best fit to the picrite composition, but the ratio of olivine to clinopyroxene is reduced. A clinopyroxene-rich peridotite through to a clinopyroxenite produces the best fit to the melts. This is explained by the fact that highly incompatible trace elements are less incompatible in clinopyroxene than in other mantle phases. In order to produce a melt of the same trace element composition as a depleted mantle melt, more clinopyroxene is needed to counteract the higher trace element composition of primitive mantle. However, Fig. 6.4a indicates that a higher melt fraction of 0.3–0.4 better fits the picrite sample when a primitive mantle composition is considered. A higher melt fraction will produce more depleted melts, and so to reproduce the same picrite composition, a lower fraction of clinopyroxene would be required. At higher F, the required source mineralogy would therefore be more olivine-rich, i.e. a lherzolite.

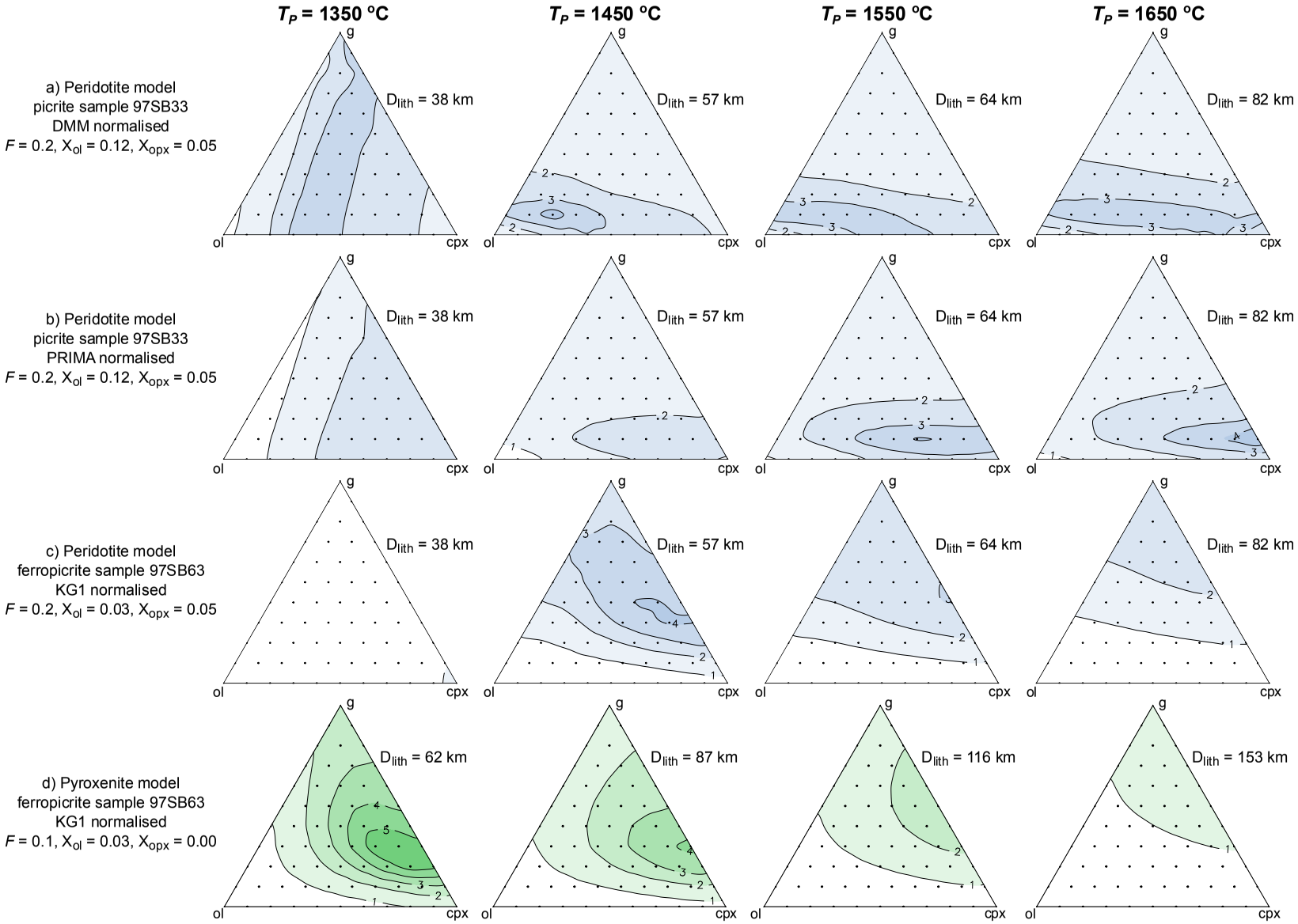

e) Pyroxenite model, picrite sample 97SB33, KG1 normalised F = 0.1, X_{ol} = 0.12, X_{opx} = 0.00: No solutions with 1/RMS > 1

f) Peridotite model, ferropicrite sample 97SB63, DMM normalised, F = 0.2, Xol = 0.03, Xopx = 0.05: No clear solution, no solution with 1/RMS > 2

Figure 6.6: 1/RMS misfit as a function of solidus mineralogy (i.e. the initial mineralogy at the onset of melting, in weight proportion of phases), for picrite sample 97SB33 and ferropicrite sample 97SB63 using the peridotite and pyroxenite melting models. Contours are at 1/RMS intervals of 1, darker colours show higher 1/RMS (so lower misfit between model data and sample data). Ternary diagrams are grouped such that diagrams in the same column are calculated for the same T_P and diagrams in the same row are calculated using the same model, sample, F, X_{ol} (weight proportion of olivine added to sample to correct for fractionation) and X_{opx} (weight proportion of orthopyroxene from which the ternary is projected). D_{lith} is the lithospheric thickness (depth to top of melting column) used in the calculation, in km. Blue fill is used for the peridotite melting model and green fill is used for the pyroxenite melting model. a-e) conditions are stated on the figure. Small points show the calculation grid from which the contours were calculated.

The Etendeka ferropicrite sample 97SB63 (+3% olivine fractionation correction) was first modelled using the peridotite model with a DMM source composition and identical parameters as the picrite sample 97SB33 result of Fig. 6.6a. No solutions with 1/RMS > 2 were found, and no particular modal mineralogy solution was indicated. This is a result of the difficulty in producing a strongly enriched melt from such a depleted bulk composition. The same ferropicrite was then modelled with the peridotite model at the same conditions, but this time using a KG1 mantle trace element composition. The result is shown in Fig. 6.6c, and at any T_P indicates an olivine-poor clinopyroxenitic source, which contains a large fraction of garnet (except at $T_P = 1350$ °C, where melting is shallower than the garnet-spinel transition). This result strongly indicates a garnet clinopyroxenite source for the ferropicrites. However, if this is the case, then it is not appropriate to model the ferropicrite composition using the peridotite model. A similar calculation is thus performed using the pyroxenite melting model (Fig. 6.6d) and a melt fraction F = 0.1, which is the most appropriate melt fraction for modelling the ferropicrite origin according to Fig. 6.4f. This time, X_{opx} is set to zero to reflect the low upper pressure limit of orthopyroxene stability in pyroxenites. The resulting best fit mineralogy is a garnet clinopyroxenite at all T_P conditions, which may or may not contain a small fraction of olivine. At $T_P = 1450$ °C, the best fit mineralogy is 60% clinopyroxene and 40% garnet. By comparison, KG1 pyroxenite is 16.0 wt.% olivine, 56.7 wt.% clinopyroxene and 27.3 wt.% garnet at the solidus at $T_P = 1450$ °C. The proportion of garnet to clinopyroxene in the solution increases with increasing pressure of melting and the best fits are obtained at lower T_P conditions. For comparison, the same conditions and pyroxenite melting model were used to model the picrite sample 97SB33. No solutions with 1/RMS > 1 were found for any mineralogy combination at any potential temperature.

6.4 Discussion

6.4.1 Model sensitivities and effect of bulk composition

Effect of bulk composition

When modelling the natural samples, the composition of the mantle source, which is used to normalise the natural sample data and make it comparable to the model results, is the parameter to which the result is most sensitive. This effect is clearly seen when using a depleted mantle source rather than a primitive one for modelling picrite sample 97SB33. A primitive mantle source requires a higher fraction of melting and/or a lower fraction of olivine to reproduce the natural sample relative to a depleted mantle source (Figs. 6.4 and 6.6).

The difference in normalisation values on the sample composition being modelled is shown in Fig. 6.7, in this case illustrated by ferropicrite sample 97SB63. The three normalisations previously used are shown. A more depleted source will result in a higher normalised concentration of incompatible trace elements in the sample. In order to model the elevated normalised concentrations, either a lower melt fraction or a higher mode of olivine or orthopyroxene (so a lower D^{b}) in the source are required. Modelling a natural sample with a more enriched source composition will therefore lead to an interpretation of a higher melt fraction or more depleted mineralogy. This effect serves to make the detection of a pyroxenite mantle source through incompatible trace element concentrations more difficult; although the mantle source is more enriched, the increased mode of clinopyroxene and garnet will reduce D^{b}, counteracting the effect of source enrichment on the melt composition. For this reason, the conclusion from Fig. 6.6 that the ferropicrite sample derives from a pyroxenite source is only true if the source composition is KG1, which is somewhat circular. However, when this ferropicrite sample is modelled with either primitive or depleted peridotite source compositions, the mismatch is always greater and the model is less effective. The misfit is lower for pyroxenite-derived model melts because the RMS parameter is affected by the shape of the multielement pattern as well as the average concentration. The distinctive high LREE/HREE ratio, concave-up REE pattern and large step between the 4+ HFSE and the highly incompatible elements in the ferropicrite sample are better reproduced by pyroxenite melting. In combination with the major element modelling, this is taken as evidence that melting of garnet clinopyroxenite is the most likely origin for the ferropicrites.

Other sensitivities and limitations

Factors other than the bulk composition of the source have a lesser impact on the model results. An equivalent modelling run was performed to that shown in Fig. 6.6d, with all parameters identical but using the peridotite model rather than the pyroxenite model (not shown). At T_P =1450–1650 °C, the mineralogy results were almost identical. At T_P = 1350 °C they are not, because the solidus is

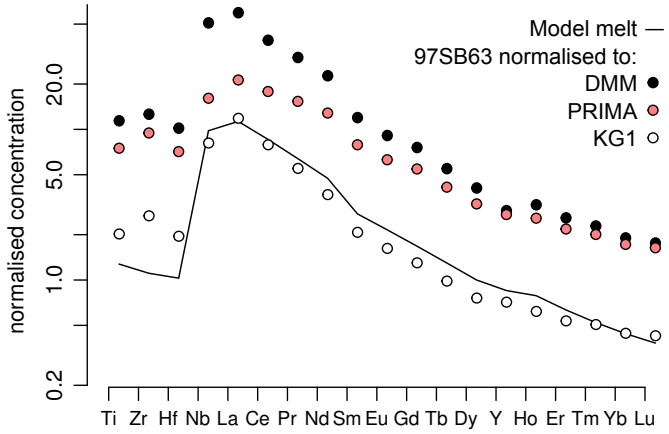

Figure 6.7: Normalised multielement plot showing the effect of normalisation values on sample composition (in this case ferropicrite sample 97SB63, corrected for 3% olivine fractionation), with a model melt for comparison. Model melt calculated at T_P = 1450 °C and lithospheric thickness = 90 km (F = 0.08) using the pyroxenite model with KG1 equilibrium mineralogy. Points show the sample normalised to primitive mantle (PRIMA, McDonough and Sun, 1995), depleted MORB-source mantle (DMM, Salters and Stracke, 2004) and KG1 (1:1 mixture of average MORB and PRIMA; see text).

intersected shallower than the garnet-spinel transition in the peridotite model. It may therefore be an acceptable approximation to use simpler melting models with partition coefficients and thermal structures calculated for peridotite to examine pyroxenite melting, as long as an appropriate modal mineralogy and bulk composition are used.

The method of fractional melt integration is not explored in the results section, where a dome geometry is used in every case. The approach in this model is simplistic and assumes a constant upwelling rate throughout the melting region. In accumulated fractional melting models, the weighting given to melts derived from different depths in the melting column has a noticeable effect on the final melt composition (Fig. 6.8). It is commonly accepted that a triangular melting region is the correct geometry for modelling MORB petrogenesis (Plank and Langmuir, 1992). However, the geometry within a spreading and thermally stratified plume is less clear. If a simple column is used instead of a dome (i.e. melts from all depths are equally represented in the final integrated melt), then the accumulated melt will contain a greater contribution from shallow melts and will be more depleted. To model a natural sample with this geometry, a lower melt fraction, a more trace element enriched source or a more olivine-rich source would be required. Fig. 6.8 shows that the melt resulting from a columnar geometry is too depleted to match the data at the given conditions, whereas that from a conical geometry is too enriched. The choice of integration is a source of uncertainty. The effect is weaker for lower cumulative melt fractions, so the choice of integration method makes little difference when modelling the ferropicrite composition.

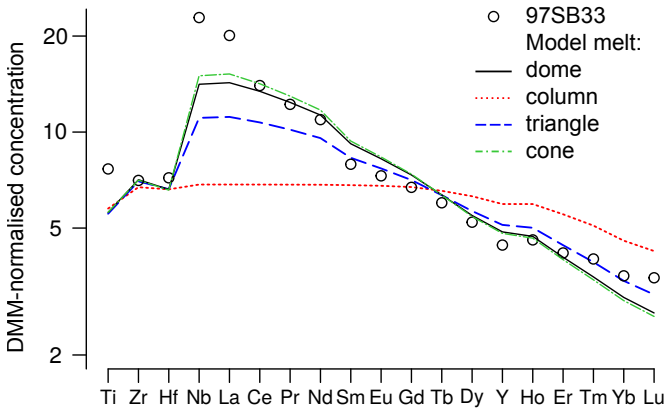

Figure 6.8: Primitive-mantle normalised multielement plot showing the effect of integration geometry on the model melt trace element composition. Model runs performed at T_P = 1450 °C, lithospheric thickness = 57 km (F = 0.2) using the peridotite model with KLB-1 equilibrium mineralogy. Sample 97SB33 is corrected for 12% olivine fractionation. Lines show the fractional melts (1% melt fraction intervals) integrated in a column, triangle, cone or dome geometry.

A final limitation is in the published partition coefficients. The 4+ elements are parametrised to the lattice strain model by a different set of studies to the 3+ elements, from different sets of experimental data. Fig. 6.5 shows that the conditions which match the 3+ REE well do not necessarily give the closest fit to the 4+ elements. The partition coefficients of the tetravalent cations have less well known PTX dependencies than those of the trivalent cations: 4+ elements are more difficult to fit with Onuma diagrams because there are fewer of them than 3+ elements (e.g. Hill *et al.*, 2000). In addition, Sun and Liang (2015) claim deficiencies in the model of Hill *et al.* (2011, 2012) (used in this study) and give a new parametrisation, the details of which are not yet published. This may be important because clinopyroxene is a major host of tetravalent trace elements.

The limitations involved in incompatible trace element modelling are in part due to a lack of precise knowledge of the PTX-sensitivity of partition coefficients, as well as uncertainties in the melting reactions, primary melt compositions of the samples modelled and the thermal structure of the model. When modelling T_P and lithospheric thickness in this chapter, assuming a mantle mineralogy introduces uncertainty, and vice versa when modelling modal mineralogy. However, the biggest sources of uncertainty cannot be quantified and result from choices made with respect to the mantle source composition used for normalisation and the shape of the melting region.

6.4.2 The sensitivity of REE to the pressure of melting

If garnet is exhausted by melting, or if the garnet-spinel transition occurs above the top of the melting column, REE modelling will not be very sensitive to the pressure of melting. Although fractionated MREE/HREE in melts from these depths will indicate a minimum pressure of origin, the variability of partition coefficients with pressure is subject to uncertainty and is not large enough to easily re-

solve the depth of the melting column. For this reason, the Etendeka picrites can be modelled by a wide range of T_P and lithospheric thickness combinations (Fig. 6.4) where those two parameters are linked by a narrow range of permissible melt fractions, and no tightly defined pressure of melting is indicated. Trace element inversion modelling (e.g. McKenzie and O'Nions, 1991) suffers the same limitation. Conversely, if the melt column straddles the garnet-spinel transition, and especially if the onset of melting is just deeper than the transition, then the resolution on the pressure of melting from trace element modelling should be good and incompatible trace element compositions can be used effectively as a lithospheric thickness and/or mantle potential temperature probe. For example, REE patterns have successfully been used to model regional variations in lithospheric thickness in the Galápagos (Gibson and Geist, 2010). Unfortunately, the picrite primary melt derives from too deep for the spinel-garnet transition to have much impact on the trace element composition of the integrated melt, and thus incompatible trace element modelling cannot easily be used in isolation to determine the palaeo-lithospheric thickness of the Etendeka province.

6.5 Conclusion

The incompatible trace element composition of the Etendeka picrites is best modelled at high melt fraction for any source mineralogy, and if a depleted mantle composition is assumed, a cumulative melt fraction of ~ 0.2 is most effective. By fixing F to 0.2 and again assuming a depleted mantle source, the composition of the melt primary to the Etendeka Horingbaai-type picrites and basalts (represented by the composition of sample 97SB33, corrected for olivine fractionation) is best modelled by an olivine-rich lherzolite similar to KLB-1 at all T_P conditions examined. The best fit lithology becomes richer in clinopyroxene at higher pressure. If a primitive mantle source is assumed instead, the production of Etendeka picrites requires higher F and/or more modal clinopyroxene relative to a depleted source. The derivation of the picrites from high fraction melting of mantle peridotite is consistent with previous interpretations of the Etendeka picrites (Keiding *et al.*, 2011; Peate, 1997; Thompson and Gibson, 2000; Thompson *et al.*, 2001), and the major element modelling of Chapter 4. However, the best fit mantle potential temperatures determined in this chapter are somewhat lower than those suggested in previous studies and from the olivine crystallisation temperatures.

After a small olivine fractionation correction, the composition of ferropicrite sample 97SB63 is used to represent the primary ferropicrite composition. The incompatible trace element concentrations and pattern are best modelled by around 10% partial melting of pyroxenite in the mantle, taken to be the hypothetical composition KG1. When the mineralogy is fixed to that of KG1, a low to moderate T_P range of 1350-1425 (which intersects the solidus at 79–100 km), combined with a melting column top at 60–80 km (corresponding to F = 10–15%) best match the data, where a similar range is found for peridotite melting. When the melt fraction is fixed to 10%, the best fit solution is given by a garnet

clinopyroxenite source mineralogy. The ratio of garnet to clinopyroxene increases with pressure of melting, and the goodness of fit decreases. This is in good agreement with the experiments of Tuff *et al.* (2005) on a similar ferropicrite composition, who found that garnet and clinopyroxene co-saturate on the liquidus at 5–7 GPa, and so inferred a garnet clinopyroxenite mantle source for the Etendeka ferropicrites. There is some discrepancy in the pressure range, where trace element modelling points to a lower melting pressure. If a depleted or primitive peridotite mantle bulk composition is used instead, a more olivine-rich source mineralogy better models the sample data, although the fit of the model melt to the natural sample is poorer than for a more enriched mantle composition, making peridotite less likely to be the mantle source of ferropicrite. The similarity between 97SB63, other Etendeka ferropicrites and the single Vestfjella (DML) ferropicrite means that the results of this trace element modelling are also applicable to those other samples. The Ahlmannryggen ferropicrites are similar to the Etendeka ones except in the highly incompatible trace elements, which are less enriched. This could perhaps be explained by a KG1-like mantle source, except consisting of depleted upper mantle mixed with MORB rather than primitive mantle. This would still give a pyroxenitic mineralogy and Fe-rich major element composition, but partially melt to produce lower incompatible trace element compositions. This is not modelled quantitatively here.

The results must be interpreted in the context of the uncertainties associated with trace element modelling, which include the assumptions made in the model setup. The trace element modelling of picrites and ferropicrites gives good constraints on their melt fractions; the conclusion that picrites are from $\sim 20\%$ melting (assuming a depleted mantle source) and ferropicrites from $\sim 10\%$ are not very model dependent and are more robust than constraints on melt fraction from major element modelling. Using a model optimised for pyroxenite melting rather than peridotite melting gives similar results when using the same input parameters and mantle source compositions. Although it is demonstrated in this chapter that incompatible trace elements can be used to interrogate the source mineralogy, the result is dependent on the choice of source composition and thus should be treated with caution when interpreted in the absence of other lines of evidence.

Chapter 7

Conclusions

7.1 Ferropicrites: the case for high pressure pyroxenite partial melts

The most commonly stated hypothesis for the origin of Phanerozoic ferropicrites is the partial melting of silica-undersaturated mantle pyroxenite (Gibson, 2002; Heinonen *et al.*, 2013; Ichiyama *et al.*, 2006; Tuff *et al.*, 2005), although this is not, as yet, universally agreed upon (reviewed in Chapter 1, section 1.3). The observations and arguments presented in this thesis support this hypothesis. This has important implications for the deep cycling of ancient subducted oceanic crust and its return to the surface in deep-seated mantle plumes, or alternative methods of pyroxenite formation.

7.1.1 Summary of the evidence

Major element chemistry

The strongest evidence for a pyroxenite source is in the major element composition of ferropicrites. In comparison with picrites (which derive from melting of normal mantle peridotite at elevated T_P conditions), ferropicrites have high FeO_T, low Al_2O_3 and low CaO, despite the two magma types having similar whole-rock MgO concentrations (Gibson *et al.*, 2000). This thesis uses the thermodynamic melting model of Jennings and Holland (2015), summarised in Chapter 4, to place new constraints on the partial melt compositions of peridotite, silica-undersaturated pyroxenite and silica-saturated eclogite. Eclogite partial melting produces low-Fe dacitic liquids which are not the source of ferropicrite. However, olivine-bearing garnet clinopyroxenite will partially melt to produce liquids which are similar to those of peridotite melting, but higher in FeO and lower in CaO. A realistic fractional melting scenario is considered, using the pyroxenite composition KG1 of Kogiso *et al.* (1998). The integrated fractional melts are indeed high in FeO and low in CaO relative to those of peridotite melting at the same T_P. In addition, they have low Al_2O_3 relative to peridotite melts. Al_2O_3 is more sensitive to the pressure of melting than to bulk composition; its depletion in pyroxenite-derived melts

is in response to the elevated melt productivity of pyroxenite close to the solidus, i.e. a greater average melting depth.

Hypothetical pyroxenite accumulated fractional melt compositions are compared with the Etendeka ferropicrite compositions in Fig. 4.21, Chapter 4. KG1 partial melting at elevated T_P (1500 °C) reproduces the Etendeka ferropicrite major element compositions well. The oxides in the ferropicrites whole-rock compositions which deviate from values expected for peridotite melting are well-matched by KG1 aggregated fractional melts. This is strong evidence that ferropicrites derive from high pressure melting of pyroxenite. With the same model, melting of normal mantle peridotite better matches the Etendeka picrites. The whole-rock major element compositions of Karoo ferropicrites from both Ahlmannryggen and Vestfjella (Antarctica) have similar major element compositions as the Etendeka ferropicrites, so the same conclusion is drawn for them. The Ahlmannryggen ferropicrites have higher TiO_2, which unfortunately cannot yet be quantitatively investigated, as the model is restricted to a Ti-free eight component system. Different pyroxenite compositions or different T_P condition to those examined may provide better or worse fits to the ferropicrite compositions, although the software requires development to conveniently perform such simulations.

Trace element chemistry

Relative to the picrites, the ferropicrites are enriched in highly incompatible trace elements and depleted in trace elements that are compatible in garnet. Chapter 6 investigates the source mineralogy of the Etendeka ferropicrites based on their incompatible trace element composition. Incompatible trace elements in mantle melts are controlled by the bulk partition coefficient (which is a function of mineralogy, as well as mineral-melt partition coefficients and melting reaction), source composition, and melting conditions. To investigate the source mineralogy, the other parameters must be set. With a KG1-like bulk composition and a 10% melt fraction, the ferropicrite trace element composition is best modelled by a garnet clinopyroxenite mineralogy, regardless of the depth of melting. At lower pressure melting conditions, the required clinopyroxene to garnet ratio is higher, and a greater mode of olivine or orthopyroxene may be present. If a peridotite-like bulk composition and a higher melt fraction is used, the best fit source becomes more olivine-rich (i.e. peridotitic). However, the mineralogy that produces a melt which best fits the sample composition has a worse fit than when a pyroxenite-like source composition is used. Therefore, a garnet clinopyroxenite source seems more likely for ferropicrites. At the very least, trace element chemistry does not rule out a garnet clinopyroxenite source.

Zn/Fe in magmas has been suggested by Le Roux *et al.* (2010) to be an effective indicator of a pyroxenite mantle source. This ratio should not fractionate during melting of olivine and orthopyroxene, but should be higher in pyroxenite-derived melts because Zn is relatively less compatible in garnet

and clinopyroxene. Heinonen *et al.* (2014) identify pyroxenite-derived 'group 3' Ahlmannryggen DML ferropicrites by applying the peridotite-pyroxenite melt boundary of Herzberg and Asimow (2008), and assigning a proportion of peridotite- to pyroxenite-derived melt to each sample based on whole-rock CaO and MgO concentrations. This boundary is shown in Fig. 4.21a and its usefulness in distinguishing between the two melt sources is discussed in Chapter 4; it is unlikely to be able to accurately quantify peridotite to pyroxenite melt contributions. Nevertheless, Heinonen *et al.* (2014) found that the Ahlmannryggen ferropicrite samples that had 'pyroxenitic' CaO and MgO also had high whole-rock Zn/Fe. This finding is compatible with a garnet pyroxenite source composition. Another ratio, Fe/Mn, is also suggested as a marker of recycled crust

, with alternative mechanisms suggested for generating elevated values (Balta *et al.*, 2011; Rogers *et al.*, 2010).

The compatible element concentrations in ferropicrite are not modelled in this thesis but can be qualitatively discussed. Ni contents in olivine phenocrysts in both the Etendeka and the Karoo ferropicrites are as high as they are in the most primitive picrite olivines, despite the ferropicrite olivines being around 9 Fo units lower than the picrite ones (Fig. 2.11). Both groups are high in Ni relative to MORB olivines. Elevated Ni in olivine has been explained by two competing hypotheses. The model of Matzen *et al.* (2013) states that $D^{\mathrm{ol}}_{\mathrm{Ni}}$ is temperature sensitive, such that if crystallisation occurs at a lower temperature than melting, the crystallising olivine will have a higher Ni concentration than the olivine in the melt source region. This means that increasing the pressure difference between melting and crystallisation will increase the Ni concentration in the liquidus olivine. Alternatively, Sobolev *et al.* (2007, 2005) suggest that high Ni is indicative of an olivine-free pyroxenite mantle source. Because Ni is compatible in olivine, it is compatible in bulk peridotite. If no olivine is present, Ni behaves incompatibly and thus has an increased concentration in the melt for a given bulk composition, resulting in the crystallisation of high Ni liquidus olivine. The high Ni in the ferropicrite olivine phenocrysts could be explained by either, or both, of these mechanisms. Melting under thick lithosphere would favour high Ni olivine phenocrysts, and if the source was pyroxenitic, the Sobolev *et al.* (2007, 2005) model also predicts higher Ni olivines (although this second mechanism only becomes significant when the source is olivine-*free*, as a low mode of olivine still has some buffering effect on Ni). With both models, the effect is somewhat counteracted by the lower bulk concentration of Ni expected in pyroxenite relative to peridotite.

Sc is compatible in garnet and mildly incompatible to mildly compatible in clinopyroxene (Hill *et al.*, 2011; Tuff and Gibson, 2007). It is moderately incompatible in olivine (Sun and Liang, 2013). It is therefore expected to behave more compatibly during melting of a garnet clinopyroxenite than in peridotite melting. Both the Etendeka and the DML ferropicrites have low Sc/Zr ratios of around 0.12, which is around a third that of the Etendeka picrites (0.4); this is consistent with their derivation from a more clinopyroxene- and garnet-rich source. Although clinopyroxene fractionation would

also reduce this ratio, extensive fractionation would be required to reduce it to enough, which is not consistent with other forms of evidence (e.g. high Ni olivine).

Crystallisation temperatures

The highest Fo phenocrysts of ferropicrite samples from both Etendeka and DML record substantially lower crystallisation temperatures than the highest Fo olivines of the Etendeka picrites (Chapter 5). This is in part explained by their formation at a lower T_P (see below). However, the difference in crystallisation temperatures between the picrite and ferropicrite samples is too great for it to be due to differences in T_P alone. The remaining difference is best explained by pyroxenite melting. Pyroxenite melts more productively than peridotite over a larger melt fraction interval, because clinopyroxene is more abundant and is not lost from the melting assemblage until a very high fraction of melting. This high melt productivity means that the effect of the enthalpy of fusion during pyroxenite melting is greater than for peridotite: during decompression melting, pyroxenite would melt and cool more than peridotite. The resultant crystallisation temperature from a given T_P would thus be lower. This effect is somewhat reduced if the pyroxenite is in thermal equilibrium with peridotite (Phipps Morgan, 2001). It is shown in Chapter 5 that the ferropicrite crystallisation temperatures can be modelled using a lower T_P than the picrites in conjunction with a pyroxenite melting regime (a difference in T_P of 130 °C between the two groups) if $F = 0.2$. If a peridotite melting regime is used, the difference in T_P between the picrite and ferropicrite source would be much larger (190 °C).

Radiogenic isotopes

Radiogenic isotopes are passive traces of source composition and provide complementary evidence to that described above. Isotopic ratios have been measured and modelled both from the Etendeka ferropicrites (Gibson *et al.*, 2000; Thompson *et al.*, 2001) and from the Ahlmannryggen and Vestfjella ferropicrites (Heinonen *et al.*, 2010, 2014; Riley *et al.*, 2005). Whilst the primary purpose of radiogenic isotope ratio modelling of the Etendeka samples is to quantify the extent of crustal contamination, the recent study of Heinonen *et al.* (2014) models the isotopic characteristics of the Ahlmannryggen DML ferropicrites in order to identify their mantle source characteristics. They identified a subset of the group 3 Ahlmannryggen samples similar to those considered in this study, with depleted mantle-like εNd (+9) and $^{187}Os/^{188}Os$ (0.1244-0.1252) that were not contaminated by lithospheric assimilation. These samples have Sr and Pb isotopic ratios which are more enriched than would be expected for depleted mantle. They can be modelled with a mixed peridotite-pyroxenite mantle source containing 10-30% seawater-altered subduction-modified MORB recycled < 1 Ga prior to the ferropicrite formation (Heinonen *et al.*, 2014).

Experimental studies

Tuff *et al.* (2005) performed liquidus-type experiments on ferropicrite sample 97SB68 at a range of pressures from 0.001–7 GPa, which elucidate its *PT* phase diagram (Fig.7.1). The phases along the liquidus are of particular interest. At pressure, they are assumed to be in equilibrium with the mantle source of that sample (e.g. Bender *et al.*, 1978). Above 5 GPa, the composition of 97SB68 co-saturates garnet and clinopyroxene, providing evidence that, if 97SB68 is derived from high pressure melting, then the mantle source contained clinopyroxene and garnet. At 2.2 GPa, olivine and clinopyroxene co-saturate. The fractionated HREE require a garnet-bearing source, so the > 5 GPa multiple saturation point was chosen to represent the mantle source by Tuff *et al.* (2005). Because primary melts are not equilibrium melts from one single *PT* condition, and because this composition may have fractionated some olivine, these experiments do not necessarily preclude olivine from having been present in the melting residue of ferropicrite 97SB68 alongside clinopyroxene and garnet. The experimental results support the above conclusions.

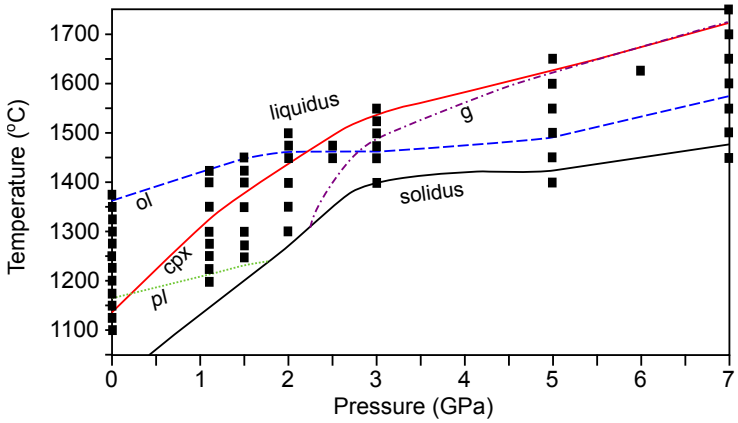

Figure 7.1: The experimentally determined phase diagram for ferropicrite 97SB68, reproduced from Tuff *et al.* (2005), Fig. 4a. Squares, experimental runs; lines, phase boundaries, labelled: g, garnet; ol, olivine; cpx, clinopyroxene; pl, plagioclase.

7.1.2 Origin of Phanerozoic and Precambrian ferropicrites: implications for whole-mantle crustal recycling

Some of the evidence listed does not strongly argue for a pyroxenite source for ferropicrites when considered in isolation. The exception to this is the major element evidence, which does not rely heavily on other assumptions. Taken together, however, the evidence builds a strong and self-consistent case for garnet clinopyroxenite mantle source for the Etendeka and DML ferropicrites, and ferropicrites from other Phanerozoic CFBs, which all have similar characteristics (reviewed by Gibson *et al.*, 2000 and Heinonen, 2011). Other mechanisms for the petrogenesis of Phanerozoic ferropicrites reviewed

in Chapter 1, section 1.3, are firmly rejected by this thesis. The Proterozoic Pechenga ferropicrites are similar to Phanerozoic samples (Gibson, 2002; Hanski and Smolkin, 1989) and are proposed to have formed by the same mechanism.

The conclusion implies that eclogite and pyroxenite deeply subducted eclogitic oceanic crust is entrained by mantle plumes and returned close to the Earth's surface, or at least that crustal eclogite or pyroxenite is present in mantle melting regions. Partial melting of eclogite and reaction of the resultant dacitic melt with ambient peridotite could produce the pyroxenite identified as the ferropicrite source (Herzberg, 2011b; Yaxley and Green, 1998). Given that rising plume heads are not thought to entrain significant amounts of ambient mantle (Farnetani *et al.*, 2002), this supports the hypothesis that subducted plates are present in the regions where mantle plumes nucleate, and that denser oceanic crust can be advected in hot plumes to the surface. If plume nucleation really is associated with LLSVPs (Torsvik *et al.*, 2006), then the 'slab graveyard' or thermochemical pile hypothesis for their origin (Tackley, 2012) is consistent with the geochemical observations from CFB settings.

The implications for the origin of the Archaean ferropicrites is less clear. Archaean ferropicrites have similar major and trace element features as Phanerozoic ones, but offset to higher MgO (often ferrokomatiites) with correspondingly higher FeO and even lower Al_2O_3 ($\sim$ 6 wt.%, reviewed by Gibson, 2002). Because the Earth has been cooling over time, the mantle is thought to have been hotter in the Archaean than at present (Bickle, 1978). The pyroxenite solidus would have been intersected at greater pressure, resulting in melts that were higher in MgO and FeO and lower in Al_2O_3, which is consistent with Archaean ferropicrites. However, for Phanerozoic ferropicrites, this metasomatic pyroxenite and its eclogite predecessor are assumed to originate from subducted oceanic crust. The oldest Archaean ferropicrites are from the Onverwacht Group, part of the Barberton Belt in South Africa, at 3.5 Ga (Gibson, 2002; Lowe and Byerly, 1999). The onset of modern-style tectonics (large-scale subduction, plumes and the supercontinent cycle) is uncertain and heavily debated, with estimates ranging from the early Hadaean based on evidence provided by zircons (Harrison *et al.*, 2005), through to the Neoproterozoic, based on interpretations of blueschists and ultra-high pressure metamorphic terranes (Stern, 2005). A recent estimate of 3.0 Ga was proposed, based on changes in the chemistry of the SCLM (Shirey and Richardson, 2011). Either the oldest Archaean ferropicrites provide evidence for a minimum age of the onset of modern-style tectonics, or they are formed through some other process. Eclogite is dense and could be returned to the mantle through a range of other mechanisms, including: delamination at the base of continents (e.g. Bédard, 2006; Zegers and van Keken, 2001), hydrothermal alteration of volcanic piles, and 'vertical tectonics', all of which are listed by Shirey and Richardson (2011) as ways in which to explain early evidence of crustal recycling. A flat, wedge-free subduction regime is another option (Smithies *et al.*, 2003). Alternative modes of petrogenesis proposed for Archaean ferropicrite petrogenesis (reviewed in Chapter 1, section 1.3), have either already had inconsistencies highlighted by other published studies or are

considered less feasible than the simple hypothesis presented by Gibson (2002) and supported in this thesis.

7.2 Melting conditions in the proto-Tristan mantle plume starting head

The potential temperature of the proto-Tristan mantle plume starting head, thought to be responsible for the origin of the Paraná-Etendeka CFB province, has been investigated by previous studies and in this thesis. A high T_P would establish the magmatism as being plume-related rather than occurring as a passive response to rifting. The Etendeka primitive melts are little altered since their creation in the mantle and are thus well suited to exploring the plume T_P. An additional difficulty in working with magmatic samples from extinct and rifted magmatic systems is that the lithospheric thickness, so depth of melting, is unconstrained. To fully constrain the depth and temperature of melting, the lithospheric thickness must be solved for simultaneously with T_P, where these two parameters are always linked by the total extent of melting, F. No single method used in this thesis gives an answer when considered in isolation. The modelled T_P and lithospheric thicknesses from crystallisation temperatures (Chapter 5), trace element chemistry (Chapter 6) and major element chemistry (Chapter 4) are shown together in Fig. 7.2.

T_P, F and lithospheric thickness: Etendeka picrites and ferropicrites

The best constraint on T_P for the Etendeka picrites comes from the crystallisation temperature of the highest Fo olivines. The average temperature of this group, 1457 °C, provides both an absolute minimum T_P constraint, and is modelled in Chapter 5 to determine the T_P and lithospheric thickness conditions of their formation. The results of that chapter are shown as black lines on Fig. 7.2a. Above $F = 0.1$, the T_P of 1550–1590 °C (depending on crystallisation pressure) is nearly independent of lithospheric thickness. The crystallisation temperature also provides a good constraint for the ferropicrite source melting conditions, although should be treated more cautiously because of both the uncertainty in the composition of the source pyroxenite (and thus its melting productivity and solidus pressure), and the increased potential for a superliquidus cooling interval. Still, the crystallisation temperature of 1312 °C indicates an absolute minimum T_P and the crystallisation temperature is modelled to indicate a T_P which is highly dependent on lithospheric thickness and crystallisation pressure; the result is shown on Fig. 7.2b.

Trace element geochemistry is also useful in constraining source melting conditions and is particularly sensitive to F (Chapter 6). This evidence is independent of, and complementary to, the crystallisation temperatures, which are more sensitive to T_P and lithospheric thickness. Forward modelling was used in Chapter 6 to identify melting conditions which produce melts with trace element characteristics most similar to those of the natural samples. Grids of calculations in $T_P - F$ space

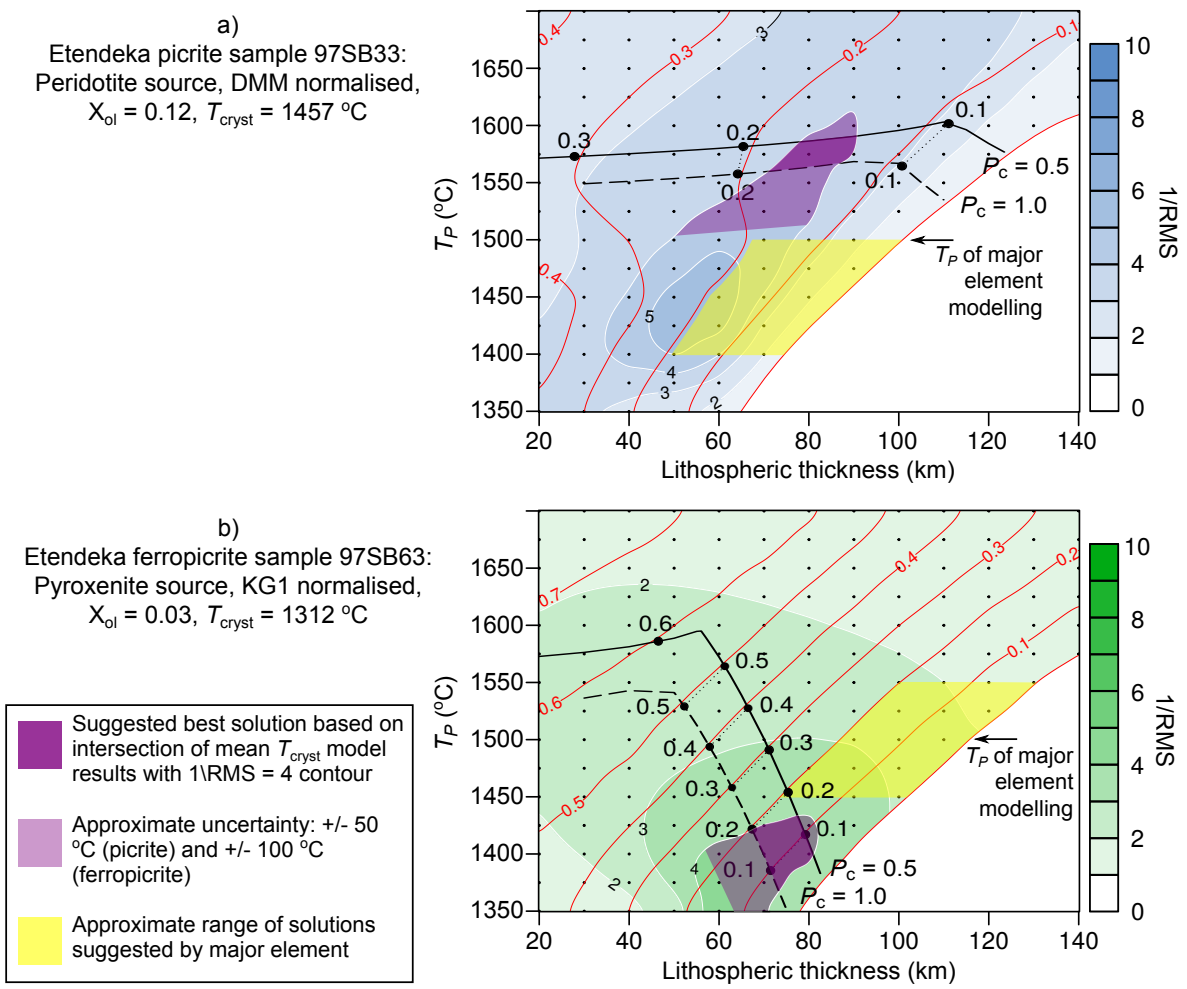

Figure 7.2: T_P and lithospheric thickness during a) Etendeka picrite sample 97SB33 production and b) Etendeka ferropicrite sample 97SB63 production (both are assumed to represent primary melts after correction for 12% and 3% olivine fractionation, respectively). a) is calculated assuming that the picrite mantle source is a depleted peridotite with the trace element composition of Salters and Stracke (2004). b) is calculated assuming that ferropicrite derives from partial melting of pyroxenite with the major element composition of KG1 (Kogiso *et al.*, 1998) and a trace element composition of 1:1 primitive mantle (McDonough and Sun, 1995) and subduction-modified MORB (Stracke *et al.*, 2003). Red lines are melt weight fraction isopleths. This plot summarises the modelling results of previous chapters. i) Black lines are from average Al-in-olivine crystallisation temperatures (T_{cryst}), where the solid and dashed lines assume respective crystallisation pressures (P_c) of 0.5 and 1 GPa (from Chapter 5, Fig. 5.13) and numbers are melt fractions. ii) Faint blue and green fields with white contour lines show fit of modelled trace element compositions from the different T_P and lithospheric thickness conditions to the samples, expressed as 1/RMS (from Chapter 6, Figs. 6.4c and f; see caption of Fig. 6.4). The darkest field represents the best fit modelling results to the respective natural samples. iii) The yellow shaded field shows an approximate T_P and lithospheric thickness from the major element modelling of Chapter 4, with limits visually inferred from Fig. 4.21. The dark purple shaded field shows the suggested best solution and is defined by an intersection of crystallisation temperature and incompatible trace element modelling results, where 1/RMS < 4, or RMS < 0.25, is taken as the threshold for best fit. The pale purple field shows an upper and lower error bracket, based on $\pm$50 and $\pm$100 °C in the T_P estimate from crystallisation temperatures for picrite and ferropicrite, respectively.

are contoured according to the RMS (from equation 6.6), a metric of the goodness of fit between the model and natural samples. Results are shown again in this chapter in Fig. 7.2, where darker filled contours correspond to better fit solutions. The 'best' answers can be pinpointed by arbitrarily applying a cutoff RMS $= 0.25$ ($1/\text{RMS} = 4$), where all trace element concentrations are, on average, within $\pm 25\%$ of the sample concentrations.

The major element chemistry approach of Chapter 4 gives the least clear constraints on the melting conditions of both the picrites and the ferropicrites, for several reasons. Firstly, major elements are less sensitive to melt fraction than trace elements. Secondly, the melt composition is dependent on the choice of source composition. Finally, few modelling runs are performed (two fractional melting simulations are performed for each of peridotite and pyroxenite, compared with a full grid of model melts produced in the trace element modelling). The way in which the integrated melt composition varies in response to changing the pressure or temperature of melting is therefore not quantified. THERMOCALC is designed for single equilibrium calculations and fractional melting must be calculated manually by incrementally imposing new conditions. The model used in Chapter 4 is not implemented in other software. As such, modelling at this level of detail is not performed. Semi-quantitative statements can be made about the T_P of melting and the melt fraction by examining Fig. 4.21, Chapter 4. The picrite melt composition appears to be matched by the model melts from a T_P a little cooler than 1500 °C. The melt fraction is not clearly constrained, but melting stopped at $F = 0.19$ in the $T_P = 1500$ °C calculation due to the loss of clinopyroxene from the melting residue. This constraint is indicated by the yellow field on Fig. 7.2a.

On Fig. 7.2a and b, fields showing the best solution for the source melting conditions are given in dark purple and summarised in Table 7.1. They are defined by the intersection of the crystallisation temperature modelling results (at crystallisation pressures of 0.5–1 GPa) and the trace element modelling results (the area within the $1/\text{RMS} = 4$ contour). The major element results are not considered when constructing the best estimates, because of the limitations stated above. The T_P and lithospheric thickness combinations which best explain the Etendeka picrites are 1565–1585 °C and 72–90 km, respectively, which correspond to $F = 0.15$–0.18. This is based on the chemistry of primitive picrite sample 97SB33 corrected for 12% olivine fractionation, used to represent the primary magma for all Etendeka Horingbaai-type picrites and basalts. The uncertainty bracket extends down to around $T_P = 1500$ °C and a slightly shallower lithosphere and larger melt fraction range.

Sample group	T_P (°C)	lithospheric thickness (km)	F
Etendeka picrites	1565–1585	72–90	0.15–0.18
Etendeka ferropicrites	1370–1430	68–80	0.07–0.19

Table 7.1: Summary of melting conditions which best fit the Etendeka picrite and ferropicrite data. The ranges given are those of the dark purple fields in Fig. 7.2.

If the assumption that ferropicrites derive from a KG1-like pyroxenite source are correct, then the melting conditions which best explain the data are as follows: T_P = 1370–1430 °C, lithospheric thickness = 68–80 km, and F = 0.07–0.19, as shown by the dark purple field in 7.2b. The error bracket extends to slightly lower lithospheric thickness and T_P, and up to $F = 0.22$. These results are for the Etendeka ferropicrite sample 97SB63, which is corrected for 3% olivine fractionation to represent the ferropicrite primary melt. It is not necessarily correct for all Etendeka ferropicrites, given that the small number of samples are not easily linked by fractionation and do not clearly define a liquid line of descent (Fig. 2.8).

Uncertainty in results

There is clearly some discrepancy in the results found by the different methods. These are the combined effect of the uncertainties, assumptions and shortcomings of each technique, which are described throughout this thesis. These discrepancies indicate that studies that determine melting conditions from just one type of data may give misleading results. For the picrites, a lower T_P is indicated by the trace element composition than by the crystallisation temperatures. The best fit result shown by the purple field is only correct assuming that crystallisation temperature is more likely to show the correct T_P whereas trace element modelling is more likely to indicate true extent of melting. The two lines of evidence provide more convergent results for the ferropicrite source conditions (Fig. 7.2b). For both sample groups, the major element evidence points to a rather different answer: a lower T_P for the picrites and a higher T_P and lithospheric thickness for the ferropicrites (yellow fields on Fig. 7.2). This discrepancy may partly be due to the difficulties in deriving these values from the major element chemistry, as described above. They are also due to uncertainty in the primary melt major element composition, uncertainty in the source composition, the simplified way in which the incremental melts are integrated, and uncertainty deriving from the simplified 8-component system used in the modelling.

The source composition is probably the most important assumption is all methods. Assuming a less depleted primitive mantle source for the picrites would cause the solution to shift to higher melt fraction ($F \sim 0.3$) and much lower lithospheric thickness ($\sim$ 20 km) at a similar T_P. The composition of pyroxenite in the mantle is not well known, and if it is produced through reaction between peridotite and a silica-rich melt, then its composition will depend on the melt/rock ratio. A less enriched pyroxenite source for the ferropicrites, from a lower melt/rock ratio, would yield higher T_P, lower F results from incompatible trace element modelling whereas the crystallisation temperatures would imply lower source T_P.

A final important limitation in the approach is in the assumption that picrite and ferropicrite derive from two seperate mantle sources, which are chemically and thermally unrelated. In reality, a range

of pyroxenite compositions and a continuum through to peridotite are permissible, and thermal equilibrium between the different lithologies will affect their melting behaviour. Depleted harzburgite, which does not melt, may also be present in the mantle source and thermally buffer melting (Shorttle *et al.*, 2014). This behaviour depends on the length scale of heterogeneity and the proportions of the different lithologies involved.

The results presented here are indicative of the source melting conditions, but are subject to as yet unquantifiable uncertainty from the numerous assumptions made.

Comparison with published estimates

The melting conditions found in this thesis (summarised in Table 7.1) are approximately similar to those previously determined for the Etendeka samples. For the picrites, T_P = 1470–1560 °C was estimated with a lithospheric thickness of 55-95 km, corresponding to $F = 0.12 - 0.22$ (Thompson *et al.*, 2001). These were calculated from major elements using the approach of Langmuir *et al.* (1992) and from REE elements using the inversion technique of McKenzie and O'Nions (1991). The results from the trace element approach are more sensitive to melting and do not require an assumption about the MgO content of the primary melt. The results of this approach are at the shallow and cool end of the above ranges (T_P = 1470–1500 and lithospheric thickness = 55 km, corresponding to $F = 0.22$). This T_P is cooler than the one found in this thesis and lithosphere is shallower; it approximately matches the best fit trace element modelling result of Fig. 7.2a, which is unsurprising given that both used trace element concentrations. Evidence for the elusive $T_P > 1680$ °C 'Horingbaai parental komatiite' of Thompson and Gibson (2000) was not found in this thesis.

The ferropicrite source T_P, lithospheric thickness and F were estimated by Gibson *et al.* (2000) to be $\sim$ 1550 °C, 115 km and 0.10, respectively. The suggested temperature and pressure of melting are therefore much higher than those calculated in this study, although the extent of melting is similar. However, these values were based on the major element modelling approach of Langmuir *et al.* (1992) assuming an Fe-rich peridotite mantle source (bulk composition PHN1611). Since this view of the mantle source has been revised by Gibson (2002), these values no longer hold true.

The experimental study of (Tuff *et al.*, 2005) finds clinopyroxene and garnet co-crystallising close to the solidus at pressures above 5 GPa for ferropicrite sample 97SB68 (the experimentally determined phase diagram of 97SB68 of Tuff *et al.*, 2005 is reproduced in Fig. 7.1). This was interpreted to mean that the top of the melting column, so the base of the lithosphere, was at $\sim$ 165 km. This requires a deep solidus intersection by mantle at $T_P \sim 1550$ °C. This conclusion is very different to that of this thesis. However, closer inspection of the study of Tuff *et al.* (2005) reveals that the experiments and the findings of this thesis are not actually mutually exclusive. In the experiments, the pressure at which garnet and clinopyroxene co-saturate is not tightly constrained: clinopyroxene is the liquidus phase at

3 GPa, whereas at 5 GPa garnet and clinopyroxene are both absent at 1650 °C but present at 1600 °C (by which point 74% crystallisation has occurred). Garnet is not isolated as the liquidus phase in any experiment. The co-saturation, which represents the crossover of the clinopyroxene-in and garnet-in boundaries, is therefore not tightly constrained and can occur anywhere above > 3 GPa. This assertion is verified by thermodynamic modelling in THERMOCALC. If orthopyroxene is suppressed to mimic the phases present in the experiments, the composition 97SB68 produces a metastable phase diagram with a similar topology as that inferred from experiments, and clinopyroxene and garnet co-saturate on the liquidus at 3.3 GPa. If, however, orthopyroxene is considered, then it tends to crystallise in place of clinopyroxene on the liquidus and co-saturates with garnet at 3.7 GPa. At high temperature, clinopyroxene and orthopyroxene have similar compositions and the Gibbs free energy contrast between the two phases is small, which may explain the discrepancy between the thermodynamic model and the experiments. Regardless of this detail, the pressure and T_P ranges suggest a pressure at the solidus of 2.7–3.2 GPa and a pressure at the base of the lithosphere of 2.3–2.7 GPa (Table 7.1). Although not comfortably explained by the experiments of Tuff *et al.* (2005), this is also not fully precluded by those experimental findings. Although 97SB68 is not a primary ferropicrite (it contains maximum Fo 67.3 olivine), it appears to have accumulated enough olivine that its bulk composition is close to that of 97SB63, i.e. its bulk composition is effectively primary.

7.2.1 Implications of results for mantle plumes and the origin of CFBs

Was there really a mantle plume?

The Etendeka picrites are the hottest, most primitive and most depleted samples in the Paraná-Etendeka CFB province, so they are the samples best suited to defining the temperature in the mantle source of the province. Despite the limitations and uncertainty, this temperature (T_P = 1565–1585 °C, Table 7.1) is elevated well above the ambient mantle T_P (defined as 1315 °C, after McKenzie *et al.*, 2005). Elevated T_P is frequently used to infer the presence of a mantle plume (e.g. Herzberg *et al.*, 2007; Putirka, 2005), where a plume is the upwelling of anomalously hot mantle, i.e. it is a thermal feature. The temperature difference between the source of the Etendeka picrites and ambient upper mantle is Δ 250–270 °C. This temperature offset is strongly indicative of a mantle plume origin for the Paraná-Etendeka CFB province. It follows that the voluminous flood basalts formed by melting of that same plume source and were not produced by rifting alone. Likewise, the DML ferropicrites and the hotter DML meimechites (crystallisation T = 1464–1481 °C, Heinonen *et al.*, 2015) indicate similarly elevated Karoo mantle T_P.

Mantle plumes are thought to be thermally zoned, with a hot core and cooler periphal regions (e.g. Watson and McKenzie, 1991). The leading edge of a plume starting head, which is wider than the tail, should also be thermally zoned. The temperature gradients within a plume mean that

melts of different temperatures can conceivably form in different points in space and time (Campbell and Griffiths, 1990; Griffiths and Campbell, 1990; Richards *et al.*, 1989). Ferropicrites represent the earliest magmatic activity in the Etendeka. The findings here agree with the model of Gibson *et al.* (2000), where ferropicrite melt forms at the cooler leading edge or sides of the plume head and picrites form from melting in the hotter plume head core.

Although elevated mantle T_P is usually interpreted as a mantle plume, it has also been interpreted in CFB provinces (particularly with respect to the breakup of the Gondwana supercontinent) as a result of continental insulation (also known as internal heating), where mantle heats as it is thermally insulated beneath the thick and continuous lithosphere of a supercontinent (e.g. Coltice *et al.*, 2007; Hole, 2015; Rolf *et al.*, 2012). Rifting, which is frequently observed in CFB settings, allows this hot mantle to upwell and partially melt. If plumes are purely thermal feature, then it is difficult to discriminate between these scenarios on the basis of geochemical data and melt temperature. Other Karoo samples from DML are isotopically depleted with low $^{3}He/^{4}He$, which has been used to argue for a thermally insulated upper mantle source for the Karoo, assuming that plumes are expected to advect material from a more enriched, distinct lower crustal reservoir to the surface (Heinonen *et al.*, 2010; Heinonen and Kurz, 2015). However, the effect of continental insulation is only expected to be able to raise mantle T_P by around 100 °C. The potential temperature of both the Paraná-Etendeka and Karoo CFB provinces are much higher than this, indicating that a mantle plume is a better explanation for these two CFB provinces. The presence of symmetrical hotspot tracks (the Walvis Ridge and Rio Grande Rise) emanating from the Paraná and Etendeka provinces is strong evidence for this interpretation in the case of the Paraná-Etendeka CFB province.

Are plume heads hotter than plume tails?

Whether plume starting heads are hotter than plume tails, as well as being more voluminous, is a long-standing question (e.g. Campbell and Griffiths, 1990). Thompson and Gibson (2000) argued on the basis of extremely high inferred crystallisation temperatures of the Fo_{92-93} olivine cluster that the Etendeka picrites formed from melting of a mantle with T_P = 1680 °C, and that because this temperature is much higher than any long lived hotspot temperature estimates, plume heads are indeed hotter than tails. Although such high temperatures are not supported by the present study, the Etendeka picrite mantle source was hot relative to that of many hotspots.

The temperature offset of the Etendeka picrite mantle source relative to ambient upper mantle of ΔT_p = +250 to 270 °C is higher than the average T_P obtained from <100 Ma melts from the modern Tristan plume by REE inversion (1414 °C or ΔT_P +99 °C; Gibson *et al.*, 2005). This implies that the Tristan plume has cooled through the head to tail transition. The Etendeka mantle source estimate is also higher than estimates for the Iceland plume (ΔT_P +165, Slater *et al.*, 2001; >+130 °C,

Shorttle *et al.*, 2014; +85–180 °C Brown and Lesher, 2014; +162–184 °C, Putirka, 2005; Putirka *et al.*, 2007; +145 °C, Herzberg *et al.*, 2007; values expressed relative to ambient T_P, as stated in the reference or taken as 1315 °C). However, the Etendeka picrite mantle source is not much hotter than the Hawaiian mantle plume, which is both long-lived and is regarded as one of the hottest modern plumes (ΔT_P +243, Watson and McKenzie, 1991; +213–268 °C, Putirka, 2005; Putirka *et al.*, 2007; +235 °C, Herzberg *et al.*, 2007). The current range of T_P estimates and their high associated uncertainties means that it is not easy to assess whether all CFBs are from hotter mantle than all OIBs. In addition, it is difficult to evaluate the T_P responsible for the generation of the voluminous CFBs, given their fractionated nature (e.g. Morrison *et al.*, 1985). Their large volumes must reflect the additional volume of heated mantle in an upwelling plume starting head, where melting is greatly exacerbated by rifting (White and McKenzie, 1989).

The importance of rifting in CFB generation

CFB provinces are often rifted, and the relative importance of rifting (thinning lithosphere) vs. elevated mantle T_P in causing the melting is uncertain. If an initial lithospheric thickness of 125 km is assumed (appropriate for mobile belts, McKenzie and Bickle, 1988), no melting can have occurred at any $T_P < 1577$ °C, approximately the temperature of the Etendeka picrite plume source. However, the Etendeka picrites indicate that the lithosphere thinned to 72–90 km, allowing 15–18% melting. Therefore, even at these very high T_P conditions, extensive rifting must have occurred to allow melting to occur, so rifting is an important process in CFB generation. If a thicker lithosphere is assumed (e.g. the modern lithospheric thickness at the Horingbaai coast is $\sim$ 160 km, Fernàndez *et al.*, 2010), no melting could occur at any realistic Phanerozoic plume T_P without significant rifting. Partial melting will not initiate in ambient T_P mantle (1315 °C) until the lithosphere has thinned to 57 km, or shallower still if the mantle source is depleted.

7.3 Mantle melt aggregation in CFB provinces

Olivine-hosted melt inclusions in primitive melts from oceanic settings are frequently observed to have highly heterogeneous incompatible trace element and isotopic compositions (e.g. Gurenko and Chaussidon, 1995; Maclennan, 2008b; Maclennan *et al.*, 2003b; Saal *et al.*, 1998; Shimizu, 1998; Slater *et al.*, 2001; Sobolev and Shimizu, 1993; Sours-Page *et al.*, 2002). Although much of the incompatible trace element variability has been explained by fractional melting processes in the mantle, the isotopic variability at least must reflect melting of a heterogeneous source. Melt inclusion variability indicates that the melts from which those melt inclusions were trapped were poorly mixed at the time of entrapment, in contrast with the homogeneity observed in the erupted host lavas (Maclennan, 2008a).

CFBs consist of large volume inflated flows which are usually considered to be internally homogeneous, and sequences of related flows tend to be petrographically and geochemically similar to one another (Arndt *et al.*, 1993; Cox, 1980; Duncan *et al.*, 1997; Erlank *et al.*, 1984; Reidel and Tolan, 2013; Wooden *et al.*, 1993). Localised isotopic heterogeneity identified within a flow from the Columbia River CFB by Vye-Brown *et al.* (2013) was ascribed to varying degrees of crustal assimilation rather than reflecting mantle source variability. The parental magmas of CFBs must have originated from fractional melting in the mantle (e.g. McKenzie, 1984), and thus have originally been heterogeneous. It follows that during CFB province generation, fractional mantle melts must accumulate and homogenise in crustal magma chambers prior to eruption. The timing of this process was examined with olivine-hosted melt inclusions from both the Paraná-Etendeka and Karoo CFB provinces. (Chapter 3). Even in the most primitive olivines ($\sim Fo_{93}$), the melt inclusion populations from single hand specimens were found to be remarkably uniform. This is especially true in the ferropicrite samples. This implies that in CFB provinces, mantle melts mix very early and prior to the onset of crystallisation. This could occur during melt transport through the relatively thick lithosphere, or perhaps by convective mixing in a superliquidus cooling interval in deep crustal magma chambers. This early mixing means that the CFBs derive from a homogeneous primitive melt. Subsequent differences in the assimilation and fractionation histories of magma batches must develop as they travel through complex CFB plumbing systems, explaining the variability between the different eruptive products (Morrison *et al.*, 1985).

An analysis of a global dataset of ridge, OIB and CFB olivine-hosted inclusions indicates that melt inclusion variability by sample group is as follows: ferropicrites < CFB province melts (excluding ferropicrites) < Iceland and OIB < MAR (Mid Atlantic Ridge). The extreme homogeneity of melt inclusions in ferropicrite samples may reflect the physical properties of ferropicritic liquids, which are particularly low viscosity at a given temperature. For the other groups, there appears to be a tectonic setting control, where elevated mantle T_P and thicker lithosphere promotes the early mixing of mantle melts. This may explain the difference in olivine-hosted melt inclusion variability between Icelandic samples and the Paraná-Etendeka and Karoo CFB province ones, despite the fact that Icelandic volcanic systems are regarded as analogous to CFB ones in some respects (Thordarson and Self, 1993).

7.4 Summary: a revised model for the evolution of the Paraná-Etendeka CFB

If the origin of ferropicrite is in melting of pyroxenite and if the values of Table 7.1 are to believed, then the geodynamic model of the early evolution of the Paraná-Etendeka CFB can be updated from

the model of Thompson *et al.* (2001), Gibson (2002) and Tuff *et al.* (2005) and is summarised by the schematic diagram (not to scale) of Fig. 7.3.

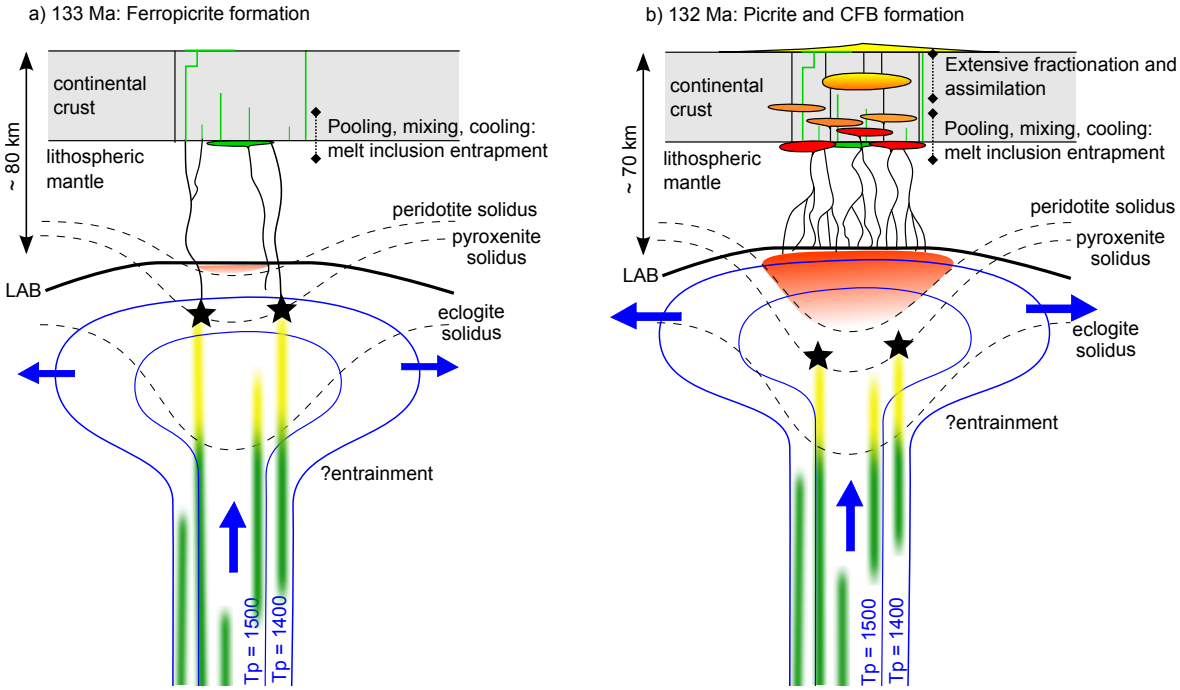

Figure 7.3: A summary schematic diagram showing a model for the origin of picrite and ferropicrite in the Paraná-Etendeka CFB, not drawn to scale. Black stars represent pyroxenite partial melting. Pyroxenite (shown as blurred yellow regions) occurs at discrete locations above sheared eclogite units (represented as green blurred streaks), where eclogite has partially melted deeper and metasomatised adjacent peridotite. Picrite melting is shown by the red gradient filled region. Dashed lines show the solidi of different lithologies. Blue lines are isopotential temperatures, and blue arrows show the direction of mantle motion. The thick back lines represent the asthenosphere-lithosphere boundary (LAB). Within the lithosphere, lines and blobs represent a complex plumbing system of sills, dykes and magma chambers, where ferropicrites are green and flow is channelised in the lithospheric mantle. The left diagram (a) shows a cross-section through the province at 133 Ma and b) at 132 Ma. See text for details.

> 133 Ma Prior to the onset of rifting, the lithosphere has an unconstrained thickness. It may be around 125 km or thicker, based on general estimates for mobile belts and measurements of the modern lithosphere (Fernàndez *et al.*, 2010; McKenzie and Bickle, 1988). In the proposed model, the upwelling proto-Tristan mantle plume head contains sheared filaments of eclogite, that may be the remnants of ancient subducted oceanic slabs and may have been advected from the core-mantle boundary. The plume passes through the eclogite solidus, which is offset to higher pressure in the higher temperature upwelling mantle. Eclogite partially melts to produce a high-Si liquid, which metasomatises the overlying and adjacent peridotite to increase its modal pyroxene and form pyroxenite. A depleted residue remains. In the meanwhile, rifting of the overlying Gondwanan lithosphere was already underway. The development of the

Etjo Sandstone Formation (onto which the basal ferropicrites go on to erupt) was syntectonic and recorded local rifting: evidence includes increasing sediment load upwards through the formation, dunes thickening towards the basin centre, and evidence for syndepositional active normal faulting, which indicate that rifting pre-dated the onset of magmatism (Mountney *et al.*, 1999). Small fraction lithospheric melting produced alkaline magmas in the west of the province (Gibson *et al.*, 2006).

133 Ma Fig. 7.3a: The lithosphere has significantly thinned from its initial state to around 80 km by rifting and perhaps thermal erosion. The upwelling plume head reaches the base of the lithosphere and its cooler leading edge (average $T_P = \sim 1400$ °C) passes through the pyroxenite solidus (almost none of the mantle has passed through the peridotite solidus yet). The pyroxenite fractionally melts to produce high-FeO, trace-element enriched liquids in the presence of residual garnet, where the total extent of melting is 7–19 %. These melts rise and pool close to the Moho and have an average temperature of 1312 °C. Efficient mixing even before the onset of crystallisation results in a primary ferropicrite, and the first olivine to crystallise ($\sim Fo_{85}$) capture melt inclusions which record the well-mixed nature of the liquid. A few dykes manage to carry ferropicritic magma to the surface and erupt thin basal flows onto aeolian dunes of the Etjo Sandston Fm. (Jerram *et al.*, 1999), although a large proportion of the ferropicrite may remain in the lower crust due to its high density and deep neutral buoyancy.

132 Ma Further lithospheric thinning has occurred to around 70 km and the plume head spreads laterally beneath the lithospheric base. The peridotite solidus, which is much deeper in the hot plume core, is intersected. Large volumes of peridotite now melt in the thermally stratified plume and the hottest picrites derive from melting in the central core, at $T_P = 1575$ °C, to a total extent of up to 18 %. Pyroxenite also melts, but the melts are not detectable because i) they are volumetrically insignificant relative to the peridotite melts and ii) high fraction pyroxenite melts will have less FeO-rich major elements and more depleted trace elements, similar to those of peridotite. Again, the melts rise to the lower crust, aggregate and mix. Fo_{93} olivine crystallises at 1457 °C, capturing inclusions of well homogenised melts. A proportion of this melt is transported to the surface as dykes. Another portion first fractionates olivine and some plagioclase in the mid to upper crust before being transported to the surface. Both of these groups are the 'Horingbaai-type' picrites and basalts. Most of the mantle melt volume, however, pools in either large crustal sill-like magma chambers or a complex series of smaller intrusions, fractionates extensively and accumulates host country rock to become the main CFB lavas and sills and the accompanying silicic magmatism (Thompson *et al.*, 2007).

Eventually, rifting and melting result in a much thinner lithosphere and a transition to an oceanic spreading regime, where the plume switches to a stem melting regime and forms the age-progressive

Walvis Ridge and Rio Grande Rise. This model explains the spatial and temporal relationship between the picrites, the ferropicrites and the CFB. It is suggested that a similar sequence of events occurred in the Karoo at $\sim$ 188 Ma. The reason for no picrite-ferropicrite mixed composition samples having been found is unclear in the context of the presented model. It could be explained in several ways. Firstly, there is an obvious sampling deficiency in the ferropicrites; intermediate mixed outcrops may exist. Secondly, intermediate samples may be present, but are less primitive, so may be difficult to identify as such. The Nil Desperandum magma type is a candidate for this, which formed off-axis from the plume centre under thicker lithosphere (Thompson *et al.*, 2001). Finally, the volume ratio of peridotite to eclogite in the upwelling plume may have been so large that as soon as peridotite passed its solidus at $\sim$ 120 km, the pyroxenite-derived melts were instantly swamped.

The Paraná-Etendeka province was rifting and the picrites must have formed under a thinner lithosphere, given that they are younger than the ferropicrites. The lack of resolvable pressure drop between the Etendeka picrites and ferropicrites may be masked by uncertainties in the lithospheric thickness estimates. However, the required pressure drop may be reduced as a result of the vertical temperature gradient in the leading edge of the upwelling plume head. As the plume head rises, the solidus at the centre simultaneously drops. This reduces the additional upwelling required to cross the peridotite solidus after the onset of pyroxenite melting (Fig. 7.3). In long-lived mantle plumes with no vertical temperature gradient (hotspots), a larger offset in the pressure of the onset of melting would be expected between peridotite and pyroxenite.

7.5 Suggestions for future work

Many studies, and many measurements, have already been made on ferropicrites and Horingbaai-type picrites and basalts from the Paraná-Etendeka CFB province (Chapter 2). However, some questions still remain unanswered. Firstly, the number of ferropicrite samples is very small and they do not form a coherent liquid line of descent. Their crustal fractionation history is poorly constrained, as is the composition of melts which have evolved from ferropicritic primary magmas. The existence of a single ferropicrite primary magma remains unclear, as does the question of whether different ferropicrites have substantially varying post-melting histories. More basic petrology work needs to be performed on larger ferropicrite sample suites from different CFBs in order to understand the behaviour of these magmas in the crust. Different ferropicrites from the Etendeka province may represent different ratios of peridotite to pyroxenite-derived melt mixtures. The origin of the Etendeka ferropicrites could be further probed with other measurements, for example radiogenic Os isotopes (e.g. as has been done for the Karoo ferropicrites, Heinonen *et al.*, 2014). Given the conclusion about the origin of ferropicrite and the extent to which mantle pyroxenite is debated, these samples provide an excellent opportunity to test predictions of markers of pyroxenite-derived melts. In particular,

many minor and trace elements in olivine and melts have recently been proposed as markers of a pyroxenite-derived component, such as Ni, Mn, Sc, Co, Zn, and various ratios involving these and other elements (e.g. Foley *et al.*, 2013; Le Roux *et al.*, 2011, 2010; Sobolev *et al.*, 2007, 2005). Quantitative examination of these would be an obvious next step in the Etendeka ferropicrites.

Another question which remains open for the Paraná-Etendeka CFB province is the composition and origin of the peridotite mantle component. Picrites derive from an isotopically depleted source and similarly, meimechites in the Karoo are isotopically depleted (Heinonen *et al.*, 2010). Conversely, many OIBs, which are also thought to derive from melting in mantle plumes, are isotopically enriched and appear to incorporate some melt from a distinct reservoir, perhaps advected from deeper in the mantle (Hanan and Graham, 1996; Hofmann, 1997). Why is this not the case in all CFBs? He isotope measurements for the Horingbaai picrites would be a powerful tool in better understanding the origin of the CFB-source mantle and whether an 'undegassed' primordial lower mantle source is sampled (e.g. after Hofmann, 1997; Kurz *et al.*, 1982).

Beyond the Paraná-Etendeka CFB province, the tools and methods used in this thesis (e.g. Jennings and Holland, 2015) are applicable to other settings. For example, alongside its trace element and isotope geochemistry, the major element composition of OIB has been heavily debated in relation to the potential presence of recycled eclogite or pyroxenite in its source (Dasgupta *et al.*, 2010; Davis *et al.*, 2011; Herzberg, 2006; Kogiso *et al.*, 2003; Lambart *et al.*, 2013; Prytulak and Elliott, 2007). The thermodynamic model itself needs to be developed into a more useful tool by adding Ti, K and volatile elements, and/or with software improvements to make it more flexible for igneous petrology purposes.

References

Albarède, F. (1992). How deep do common basaltic magmas form and differentiate? *Journal of Geophysical Research: Solid Earth*, 97(B7):10997–11009. 00230.

Albarède, F. (1996). High-resolution geochemical stratigraphy of Mauna Kea flows from the Hawaii Scientific Drilling Project core. *Journal of Geophysical Research: Solid Earth*, 101(B5):11841–11853.

Andres, M., Blichert-Toft, J., and Schilling, J.-G. (2002). Hafnium isotopes in basalts from the southern Mid-Atlantic Ridge from 40°S to 55°S: Discovery and Shona plume–ridge interactions and the role of recycled sediments. *Geochemistry, Geophysics, Geosystems*, 3(10):8502.

Arndt, N. T., Czamanske, G. K., Wooden, J. L., and Fedorenko, V. A. (1993). Mantle and crustal contributions to continental flood volcanism. *Tectonophysics*, 223(1–2):39–52.

Ballmer, M. D., Ito, G., Wolfe, C. J., and Solomon, S. C. (2013). Double layering of a thermochemical plume in the upper mantle beneath Hawaii. *Earth and Planetary Science Letters*, 376:155–164.

Balta, J. B., Asimow, P. D., and Mosenfelder, J. L. (2011). Manganese partitioning during hydrous melting of peridotite. *Geochimica et Cosmochimica Acta*, 75(20):5819–5833.

Barnes, S. J. and Roeder, P. L. (2001). The range of spinel compositions in terrestrial mafic and ultramafic rocks. *Journal of Petrology*, 42(12):2279–2302.

Barry, T. L., Kelley, S. P., Reidel, S. P., Camp, V. E., Self, S., Jarboe, N. A., Duncan, R. A., and Renne, P. R. (2013). Eruption chronology of the Columbia River Basalt Group. *Geological Society of America Special Papers*, 497:45–66.

Beattie, P. (1993). Olivine-melt and orthopyroxene-melt equilibria. *Contributions to Mineralogy and Petrology*, 115(1):103–111.

Bédard, J. H. (2006). A catalytic delamination-driven model for coupled genesis of Archaean crust and sub-continental lithospheric mantle. *Geochimica et Cosmochimica Acta*, 70(5):1188–1214.

Bender, J., Hodges, F., and Bence, A. (1978). Petrogenesis of basalts from the project FAMOUS area: experimental study from 0 to 15 kbars. *Earth and Planetary Science Letters*, 41(3):277–302.

Bickle, M. (1978). Heat loss from the earth: A constraint on Archaean tectonics from the relation between geothermal gradients and the rate of plate production. *Earth and Planetary Science Letters*, 40(3):301–315.

Blundy, J. and Wood, B. (1994). Prediction of crystal melt partition coefficients from elastic moduli. *Nature*, 372:452–454.

Blundy, J. D., Falloon, T. J., Wood, B. J., and Dalton, J. A. (1995). Sodium partitioning between clinopyroxene and silicate melts. *Journal of Geophysical Research: Solid Earth*, 100(B8):15501–15515.

Bohrson, W. A. and Spera, F. J. (2001). Energy-Constrained Open-System Magmatic Processes II: Application of Energy-Constrained Assimilation–Fractional Crystallization (EC-AFC) Model to Magmatic Systems. *Journal of Petrology*, 42(5):1019–1041.

Borghini, G., Fumagalli, P., and Rampone, E. (2010). The stability of plagioclase in the upper mantle: Subsolidus experiments on fertile and depleted lherzolite. *Journal of Petrology*, 51(1-2):229–254.

Boschi, L., Becker, T. W., and Steinberger, B. (2007). Mantle plumes: Dynamic models and seismic images. *Geochemistry, Geophysics, Geosystems*, 8(10):Q10006.

Brown, E. L. and Lesher, C. E. (2014). North Atlantic magmatism controlled by temperature, mantle composition and buoyancy. *Nature Geoscience*, 7(11):820–824.

Bryan, S. E. and Ernst, R. E. (2008). Revised definition of Large Igneous Provinces (LIPs). *Earth-Science Reviews*, 86(1-4):175–202.

Bryndzia, L. T. and Wood, B. J. (1990). Oxygen thermobarometry of abyssal spinel peridotites; the redox state and C-O-H volatile composition of the Earth's sub-oceanic upper mantle. *American Journal of Science*, 290(10):1093–1116.

Campbell, I. and Griffiths, R. (1990). Implications of mantle plume structure for the evolution of flood basalts. *Earth and Planetary Science Letters*, 99(1-2):79–93.

Campbell, I. H. (2007). Testing the plume theory. *Chemical Geology*, 241(3–4):153–176.

Campbell, I. H. and O'Neill, H. S. C. (2012). Evidence against a chondritic Earth. *Nature*, 483(7391):553–558.

Canil, D. (1992). Orthopyroxene stability along the peridotite solidus and the origin of cratonic lithosphere beneath southern Africa. *Earth and Planetary Science Letters*, 111(1):83–95.

Canil, D. and Fedortchouk, Y. (2001). Olivine–liquid partitioning of vanadium and other trace elements, with applications to modern and ancient picrites. *The Canadian Mineralogist*, 39(2):319–330.

Canil, D., O'Neill, H. S. C., Pearson, D. G., Rudnick, R. L., McDonough, W. F., and Carswell, D. A. (1994). Ferric iron in peridotites and mantle oxidation states. *Earth and Planetary Science Letters*, 123(1–3):205–220.

Caro, G., Bourdon, B., Halliday, A. N., and Quitté, G. (2008). Super-chondritic Sm/Nd ratios in Mars, the Earth and the Moon. *Nature*, 452(7185):336–339.

Chauvel, C., Hofmann, A., and Vidal, P. (1992). HIMU-EM: the French Polynesian connection. *Earth and Planetary Science Letters*, 110(1-4):99–119.

Chung, S.-L. and Jahn, B.-m. (1995). Plume-lithosphere interaction in generation of the Emeishan flood basalts at the Permian-Triassic boundary. *Geology*, 23(10):889.

Coffin, M., Duncan, R., Eldholm, O., Fitton, J. G., Frey, F., Larsen, H. C., Mahoney, J., Saunders, A., Schlich, R., and Wallace, P. (2006). Large Igneous Provinces and Scientific Ocean Drilling: Status Quo and A Look Ahead. *Oceanography*, 19(4):150–160.

Coffin, M. F. and Eldholm, O. (1994). Large igneous provinces: Crustal structure, dimensions, and external consequences. *Reviews of Geophysics*, 32(1):1–36.

Coltice, N., Phillips, B. R., Bertrand, H., Ricard, Y., and Rey, P. (2007). Global warming of the mantle at the origin of flood basalts over supercontinents. *Geology*, 35(5):391–394.

Coogan, L. A., Saunders, A. D., and Wilson, R. N. (2014). Aluminum-in-olivine thermometry of primitive basalts: Evidence of an anomalously hot mantle source for large igneous provinces. *Chemical Geology*, 368:1–10.

Cottrell, E. and Kelley, K. A. (2011). The oxidation state of Fe in MORB glasses and the oxygen fugacity of the upper mantle. *Earth and Planetary Science Letters*, 305(3–4):270–282.

Cottrell, E., Kelley, K. A., Lanzirotti, A., and Fischer, R. A. (2009). High-precision determination of iron oxidation state in silicate glasses using XANES. *Chemical Geology*, 268(3–4):167–179.

Courtillot, V. E. and Renne, P. R. (2003). On the ages of flood basalt events. *Comptes Rendus Geoscience*, 335(1):113–140.

Cox, K. G. (1980). A model for flood basalt vulcanism. *Journal of Petrology*, 21(4):629–650.

Danyushevsky, L. V., Della-Pasqua, F. N., and Sokolov, S. (2000). Re-equilibration of melt inclusions trapped by magnesian olivine phenocrysts from subduction-related magmas: petrological implications. *Contributions to Mineralogy and Petrology*, 138:68–83.

Danyushevsky, L. V. and Plechov, P. (2011). Petrolog3: Integrated software for modeling crystallization processes. *Geochemistry, Geophysics, Geosystems*, 12(7):Q07021.

Dasgupta, R. and Hirschmann, M. M. (2010). The deep carbon cycle and melting in Earth's interior. *Earth and Planetary Science Letters*, 298(1–2):1–13.

Dasgupta, R., Jackson, M. G., and Lee, C.-T. A. (2010). Major element chemistry of ocean island basalts — Conditions of mantle melting and heterogeneity of mantle source. *Earth and Planetary Science Letters*, 289(3–4):377–392.

Davies, D. R., Goes, S., Davies, J. H., Schuberth, B. S. A., Bunge, H. P., and Ritsema, J. (2012). Reconciling dynamic and seismic models of Earth's lower mantle: The dominant role of thermal heterogeneity. *Earth and Planetary Science Letters*, 353–354:253–269.

Davis, F. A. and Hirschmann, M. M. (2013). The effects of K2O on the compositions of near-solidus melts of garnet peridotite at 3 GPa and the origin of basalts from enriched mantle. *Contributions to Mineralogy and Petrology*, 166(4):1029–1046.

Davis, F. A., Hirschmann, M. M., and Humayun, M. (2011). The composition of the incipient partial melt of garnet peridotite at 3 GPa and the origin of OIB. *Earth and Planetary Science Letters*, 308(3–4):380–390.

Davis, F. A., Tangeman, J. A., Tenner, T. J., and Hirschmann, M. M. (2009). The composition of KLB-1 peridotite. *American Mineralogist*, 94(1):176–180.

Deines, P., Nafziger, R., Ulmer, G., and Woermann, E. (1974). Temperature-oxygen fugacity tables for selected gas mixtures in the system C-H-O at one atmosphere total pressure. *Bulletin of the Earth and Mineral Sciences Experiment Station*, 88:1–129.

DePaolo, D. J. (1981). Trace element and isotopic effects of combined wallrock assimilation and fractional crystallization. *Earth and Planetary Science Letters*, 53(2):189–202.

Desta, M. T., Ayalew, D., Ishiwatari, A., Arai, S., and Tamura, A. (2014). Ferropicrite from the Lalibela area in the Ethiopian large igneous province. *Journal of Mineralogical and Petrological Sciences*, 109:191–207.

Dodd, S. C., Mac Niocaill, C., and Muxworthy, A. R. (2015). Long duration (>4 Ma) and steady-state volcanic activity in the early Cretaceous Paraná–Etendeka Large Igneous Province: New palaeomagnetic data from Namibia. *Earth and Planetary Science Letters*, 414:16–29.

Draper, D. S. and van Westrenen, W. (2007). Quantifying garnet-melt trace element partitioning using lattice-strain theory: assessment of statistically significant controls and a new predictive model. *Contributions to Mineralogy and Petrology*, 154(6):731–746.

Droop, G. T. R. (1987). A general equation for estimating Fe3+ concentrations in ferromagnesian silicates and oxides from microprobe analyses, using stoichiometric criteria. *Mineralogical magazine*, 51(361):431–435.

Duncan, R. A., Hooper, P. R., Rehacek, J., Marsh, J. S., and Duncan, A. R. (1997). The timing and duration of the Karoo igneous event, southern Gondwana. *Journal of Geophysical Research: Solid Earth*, 102(B8):18127–18138.

Eggler, D. H. (1976). Does CO2 cause partial melting in the low-velocity layer of the mantle? *Geology*, 4(2):69–72.

Elkins, L. J., Gaetani, G. A., and Sims, K. W. W. (2008). Partitioning of U and Th during garnet pyroxenite partial melting: Constraints on the source of alkaline ocean island basalts. *Earth and Planetary Science Letters*, 265(1–2):270–286.

Ellam, R. M. and Cox, K. G. (1991). An interpretation of Karoo picrite basalts in terms of interaction between asthenospheric magmas and the mantle lithosphere. *Earth and Planetary Science Letters*, 105(1–3):330–342.

Elliott, T. R., Hawkesworth, C. J., and Grönvold, K. (1991). Dynamic melting of the Iceland plume. *Nature*, 351(6323):201–206.

Erlank, A. J. (1984). *Petrogenesis of the volcanic rocks of the Karoo province: Presenting results of the South African Geodynamics Project on the Karoo volcanics*, volume 13 of *Geological Society of South Africa: Special publication*. Geological Society of South Africa.

Erlank, A. J., Marsh, J. S., Duncan, A. R., Miller, R. M., Hawkesworth, C. J., Betton, P. J., and Rex, D. C. (1984). Geochemistry and petrogenesis of the Etendeka volcanic rocks from SWA/Namibia. In *Petrogenesis of the Volcanic Rocks of the Karoo Province*, volume 13 of *Geological Society of South Africa: Special publication*, pages 195–245. Geological Society of South Africa.

Evans, T., C. O'Neill, H., and Tuff, J. (2008). The influence of melt composition on the partitioning of REEs, Y, Sc, Zr and Al between forsterite and melt in the system CMAS. *Geochimica et Cosmochimica Acta*, 72(23):5708–5721.

Ewart, A., Marsh, J. S., Milner, S. C., Duncan, A. R., Kamber, B. S., and Armstrong, R. A. (2004). Petrology and geochemistry of early Cretaceous bimodal continental flood volcanism of the NW Etendeka, Namibia. Part 1: Introduction, mafic lavas and re-evaluation of mantle source components. *Journal of Petrology*, 45(1):59–105.

Ewart, A., Milner, S. C., Armstrong, R. A., and Dungan, A. R. (1998). Etendeka volcanism of the Goboboseb Mountains and Messum Igneous Complex, Namibia. Part I: Geochemical evidence of early Cretaceous Tristan plume melts and the role of crustal contamination in the Paraná–Etendeka CFB. *Journal of Petrology*, 39(2):191–225.

Falloon, T. J., Green, D. H., Danyushevsky, L. V., and McNeill, A. W. (2008). The composition of near-solidus partial melts of fertile peridotite at 1 and 1.5 GPa: Implications for the petrogenesis of MORB. *Journal of Petrology*, 49(4):591–613.

Farnetani, C. G. (2005). Beyond the thermal plume paradigm. *Geophysical Research Letters*, 32(7):2–5.

Farnetani, C. G., Hofmann, A. W., and Class, C. (2012). How double volcanic chains sample geochemical anomalies from the lowermost mantle. *Earth and Planetary Science Letters*, 359–360:240–247.

Farnetani, C. G., Legras, B., and Tackley, P. J. (2002). Mixing and deformations in mantle plumes. *Earth and Planetary Science Letters*, 196(1-2):1–15.

Farnetani, C. G., Richards, M. A., and Ghiorso, M. S. (1996). Petrological models of magma evolution and deep crustal structure beneath hotspots and flood basalt provinces. *Earth and Planetary Science Letters*, 143(1–4):81–94.

Fernàndez, M., Afonso, J., and Ranalli, G. (2010). The deep lithospheric structure of the Namibian volcanic margin. *Tectonophysics*, 481(1–4):68–81.

Fiorentini, M., Beresford, S., Deloule, E., Hanski, E., Stone, W., and Pearson, N. (2008). The role of mantle-derived volatiles in the petrogenesis of Palaeoproterozoic ferropicrites in the Pechenga Greenstone Belt, northwestern Russia: Insights from in-situ microbeam and nanobeam analysis of hydromagmatic amphibole. *Earth and Planetary Science Letters*, 268(1–2):2–14.

Foley, S. F., Prelevic, D., Rehfeldt, T., and Jacob, D. E. (2013). Minor and trace elements in olivines as probes into early igneous and mantle melting processes. *Earth and Planetary Science Letters*, 363:181–191.

Ford, C., Russell, D., and Craven, J. (1983). Olivine-liquid equilibria: temperature, pressure and composition dependence of the crystal/liquid cation partition coefficients for Mg, Fe2+, Ca and Mn. *Journal of Petrology*, 24:256–265.

Foulger, G. R. and Anderson, D. L. (2005). A cool model for the Iceland hotspot. *Journal of Volcanology and Geothermal Research*, 141(1–2):1–22.

Fram, M. S. and Lesher, C. E. (1997). Generation and polybaric differentiation of East Greenland early Tertiary Flood Basalts. *Journal of Petrology*, 38(2):231–275.

Francis, D., Ludden, J., Johnstone, R., and Davis, W. (1999). Picrite evidence for more Fe in Archean mantle reservoirs. *Earth and Planetary Science Letters*, 167(3–4):197–213.

Frei, D., Liebscher, A., Franz, G., Wunder, B., Klemme, S., and Blundy, J. (2009). Trace element partitioning between orthopyroxene and anhydrous silicate melt on the lherzolite solidus from 1.1 to 3.2 GPa and 1,230 to 1,535°C in the model system Na2O–CaO–MgO–Al2O3–SiO2. *Contributions to Mineralogy and Petrology*, 157(4):473–490.

Frost, B. R. (1991). Introduction to oxygen fugacity and its petrologic importance. *Reviews in Mineralogy and Geochemistry*, 25(1):1–9.

Fulmer, E. C., Nebel, O., and van Westrenen, W. (2010). High-precision high field strength element partitioning between garnet, amphibole and alkaline melt from Kakanui, New Zealand. *Geochimica et Cosmochimica Acta*, 74(9):2741–2759.

Gaetani, G. and Watson, E. (2000). Open system behavior of olivine-hosted melt inclusions. *Earth and Planetary Science Letters*, 183:27–41.

Gaetani, G. A. and Grove, T. L. (1998). The influence of water on melting of mantle peridotite. *Contributions to Mineralogy and Petrology*, 131(4):323–346.

Gale, A., Dalton, C. A., Langmuir, C. H., Su, Y., and Schilling, J.-G. (2013). The mean composition of ocean ridge basalts. *Geochemistry, Geophysics, Geosystems*, 14(3):489–518.

Gallagher, K. and Hawkesworth, C. (1994). Mantle plumes, continental magmatism and asymmetry in the South Atlantic. *Earth and Planetary Science Letters*, 123(1–3):105–117.

Garland, F., Turner, S., and Hawkesworth, C. (1996). Shifts in the source of the Paraná basalts through time. *Lithos*, 37(2–3):223–243.

Garnero, E. J., Lay, T., and McNamara, A. (2007). Implications of lower-mantle structural heterogeneity for the existence and nature of whole-mantle plumes. *Geological Society of America Special Papers*, 430:79–101.

Gasparik, T. and Newton, R. C. (1984). The reversed alumina contents of orthopyroxene in equilibrium with spinel and forsterite in the system MgO-Al2O3-SiO2. *Contributions to Mineralogy and Petrology*, 85(2):186–196.

Gast, P. W. (1968). Trace element fractionation and the origin of tholeiitic and alkaline magma types. *Geochimica et Cosmochimica Acta*, 32(10):1057–1086.

Ghiorso, M. S. (2004). An equation of state for silicate melts. III. Analysis of stoichiometric liquids at elevated pressure: shock compression data, molecular dynamics simulations and mineral fusion curves. *American Journal of Science*, 304(8-9):752–810.

Ghiorso, M. S., Hirschmann, M. M., Reiners, P. W., and Kress, V. C. (2002). The pMELTS: A revision of MELTS for improved calculation of phase relations and major element partitioning related to partial melting of the mantle to 3 GPa. *Geochemistry, Geophysics, Geosystems*, 3(5):1–35.

Ghiorso, M. S. and Sack, R. O. (1995). Chemical mass transfer in magmatic processes IV. A revised and internally consistent thermodynamic model for the interpolation and extrapolation of liquid-solid equilibria in magmatic systems at elevated temperatures and pressures. *Contributions to Mineralogy and Petrology*, 119(2-3):197–212.

Gibson, S., Thompson, R., and Dickin, A. (2000). Ferropicrites: geochemical evidence for Fe-rich streaks in upwelling mantle plumes. *Earth and Planetary Science Letters*, 174:355–374.

Gibson, S. A. (2002). Major element heterogeneity in Archean to Recent mantle plume starting-heads. *Earth and Planetary Science Letters*, 195(1-2):59–74.

Gibson, S. A. and Geist, D. (2010). Geochemical and geophysical estimates of lithospheric thickness variation beneath Galápagos. *Earth and Planetary Science Letters*, 300(3–4):275–286.

Gibson, S. A., Geist, D. G., Day, J. A., and Dale, C. W. (2012). Short wavelength heterogeneity in the Galápagos plume: Evidence from compositionally diverse basalts on Isla Santiago. *Geochemistry, Geophysics, Geosystems*, 13:Q09007.

Gibson, S. A., Thompson, R. N., and Day, J. A. (2006). Timescales and mechanisms of plume–lithosphere interactions: 40Ar/39Ar geochronology and geochemistry of alkaline igneous

rocks from the Paraná–Etendeka large igneous province. *Earth and Planetary Science Letters*, 251(1–2):1–17.

Gibson, S. A., Thompson, R. N., Day, J. A., Humphris, S. E., and Dickin, A. P. (2005). Melt-generation processes associated with the Tristan mantle plume: Constraints on the origin of EM-1. *Earth and Planetary Science Letters*, 237(3–4):744–767.

Gibson, S. A., Thompson, R. N., Leonardos, O. H., Dickin, A. P., and Mitchell, J. G. (1999). The limited extent of plume-lithosphere interactions during continental flood-basalt genesis: geochemical evidence from Cretaceous magmatism in southern Brazil. *Contributions to Mineralogy and Petrology*, 137(1-2):147–169.

Goldstein, S. B. and Francis, D. (2008). The petrogenesis and mantle source of Archaean ferropicrites from the Western Superior Province, Ontario, Canada. *Journal of Petrology*, 49(10):1729–1753.

Grand, S. P. (2002). Mantle shear-wave tomography and the fate of subducted slabs. *Philosophical Transactions of the Royal Society of London A: Mathematical, Physical and Engineering Sciences*, 360(1800):2475–91.

Green, D. H. (1973). Experimental melting studies on a model upper mantle composition at high pressure under water-saturated and water-undersaturated conditions. *Earth and Planetary Science Letters*, 19(1):37–53.

Green, E. C. R., Holland, T. J. B., Powell, R., and White, R. W. (2012). Garnet and spinel lherzolite assemblages in MgO–Al2O3–SiO2 and CaO–MgO–Al2O3–SiO2: thermodynamic models and an experimental conflict. *Journal of Metamorphic Geology*, 30(6):561–577.

Griffiths, R. and Campbell, I. (1990). Stirring and structure in mantle starting plumes. *Earth and Planetary Science Letters*, 99(1-2):66–78.

Grove, T. L., Holbig, E. S., Barr, J. A., Till, C. B., and Krawczynski, M. J. (2013). Melts of garnet lherzolite: experiments, models and comparison to melts of pyroxenite and carbonated lherzolite. *Contributions to Mineralogy and Petrology*, 166(3):887–910.

Gurenko, A. and Chaussidon, M. (1995). Enriched and depleted primitive melts included in olivine from Icelandic tholeiites: origin by continuous melting of a single mantle column. *Geochimica et Cosmochimica Acta*, 59(14):2905–2917.

Gurenko, A. A., Sobolev, A. V., Hoernle, K. A., Hauff, F., and Schmincke, H.-U. (2009). Enriched, HIMU-type peridotite and depleted recycled pyroxenite in the Canary plume: A mixed-up mantle. *Earth and Planetary Science Letters*, 277(3–4):514–524.

Hanan, B. B. and Graham, D. W. (1996). Lead and Helium Isotope Evidence from Oceanic Basalts for a Common Deep Source of Mantle Plumes. *Science*, 272(5264):991–995.

Hanski, E. and Smolkin, V. (1989). Pechenga ferropicrites and other early Proterozoic picrites in the eastern part of the Baltic Shield. *Precambrian Research*, 45(1–3):63–82.

Hanski, E. and Smolkin, V. (1995). Iron- and LREE-enriched mantle source for early Proterozoic intraplate magmatism as exemplified by the Pechenga ferropicrites, Kola Peninsula, Russia. *Lithos*, 34(1–3):107–125.

Harris, C., le Roux, P., Cochrane, R., Martin, L., Duncan, A. R., Marsh, J. S., le Roex, A. P., and Class, C. (2015). The oxygen isotope composition of Karoo and Etendeka picrites: High δ18O mantle or crustal contamination? *Contributions to Mineralogy and Petrology*, 170(1):1–24.

Harrison, T. M., Blichert-Toft, J., Müller, W., Albarede, F., Holden, P., and Mojzsis, S. J. (2005). Heterogeneous Hadean Hafnium: Evidence of Continental Crust at 4.4 to 4.5 Ga. *Science*, 310(5756):1947–1950.

Hart, S. R., Hauri, E. H., Oschmann, L. A., and Whitehead, J. A. (1992). Mantle plumes and entrainment: Isotopic Evidence. *Science*, 256(5056):517–520.

Hauri, E. H. (1996). Major-element variability in the Hawaiian mantle plume. *Nature*, 382(6590):415–419.

Hauri, E. H., Wagner, T. P., and Grove, T. L. (1994). Experimental and natural partitioning of Th, U, Pb and other trace elements between garnet, clinopyroxene and basaltic melts. *Chemical Geology*, 117(1-4):149–166.

Hawkesworth, C., Kelley, S., Turner, S., Le Roex, A., and Storey, B. (1999). Mantle processes during Gondwana break-up and dispersal. *Journal of African Earth Sciences*, 28(1):239–261.

Hawkesworth, C. J., Gallagher, K., Kelley, S., Mantovani, M., Peate, D. W., Regelous, M., and Rogers, N. W. (1992). Paraná magmatism and the opening of the South Atlantic. *Geological Society, London, Special Publications*, 68(1):221–240.

Heinonen, J. S. (2011). *Geochemistry and petrology of the ferropicrite dikes and associated rocks of Vestfjella, western Dronning Maud Land, Antarctica*. Thesis, University of Helsinki.

Heinonen, J. S., Carlson, R. W., and Luttinen, A. V. (2010). Isotopic (Sr, Nd, Pb, and Os) composition of highly magnesian dikes of Vestfjella, western Dronning Maud Land, Antarctica: A key to the origins of the Jurassic Karoo large igneous province? *Chemical Geology*, 277:227–244.

Heinonen, J. S., Carlson, R. W., Riley, T. R., Luttinen, A. V., and Horan, M. F. (2014). Subduction-modified oceanic crust mixed with a depleted mantle reservoir in the sources of the Karoo continental flood basalt province. *Earth and Planetary Science Letters*, 394:229–241.

Heinonen, J. S., Jennings, E. S., and Riley, T. R. (2015). Crystallisation temperatures of the most Mg-rich magmas of the Karoo LIP on the basis of Al-in-olivine thermometry. *Chemical Geology*, 411:26–35.

Heinonen, J. S. and Kurz, M. D. (2015). Low-3He/4He sublithospheric mantle source for the most magnesian magmas of the Karoo large igneous province. *Earth and Planetary Science Letters*, 426:305–315.

Heinonen, J. S. and Luttinen, A. V. (2008). Jurassic dikes of Vestfjella, western Dronning Maud Land, Antarctica: Geochemical tracing of ferropicrite sources. *Lithos*, 105(3-4):347–364.

Heinonen, J. S. and Luttinen, A. V. (2010). Mineral chemical evidence for extremely magnesian subalkaline melts from the Antarctic extension of the Karoo large igneous province. *Mineralogy and Petrology*, 99:201–217.

Heinonen, J. S., Luttinen, A. V., Riley, T. R., and Michallik, R. M. (2013). Mixed pyroxenite–peridotite sources for mafic and ultramafic dikes from the Antarctic segment of the Karoo continental flood basalt province. *Lithos*, 177:366–380.

Herzberg, C. (2011a). Basalts as temperature probes of Earth's mantle. *Geology*, 39(12):1179–1180.

Herzberg, C. (2011b). Identification of source lithology in the Hawaiian and Canary Islands: Implications for origins. *Journal of Petrology*, 52(1):113–146.

Herzberg, C. (print November 30, 2006). Petrology and thermal structure of the Hawaiian plume from Mauna Kea volcano. *Nature*, 444(7119):605–609.

Herzberg, C. and Asimow, P. D. (2008). Petrology of some oceanic island basalts: PRIMELT2.XLS software for primary magma calculation. *Geochemistry, Geophysics, Geosystems*, 9(9).

Herzberg, C. and Asimow, P. D. (2015). PRIMELT3 MEGA.XLSM software for primary magma calculation: Peridotite primary magma MgO contents from the liquidus to the solidus. *Geochemistry, Geophysics, Geosystems*, 16(2):563–578.

Herzberg, C., Asimow, P. D., Arndt, N., Niu, Y., Lesher, C. M., Fitton, J. G., Cheadle, M. J., and Saunders, A. D. (2007). Temperatures in ambient mantle and plumes: Constraints from basalts, picrites, and komatiites. *Geochemistry, Geophysics, Geosystems*, 8(2):Q02006.

Herzberg, C., Asimow, P. D., Ionov, D. A., Vidito, C., Jackson, M. G., and Geist, D. (2013). Nickel and helium evidence for melt above the core-mantle boundary. *Nature*, 493(7432):393–397.

Herzberg, C., Gasparik, T., and Sawamoto, H. (1990). Origin of mantle peridotite: Constraints from melting experiments to 16.5 GPa. *Journal of Geophysical Research: Solid Earth*, 95(B10):15779–15803.

Herzberg, C. and Gazel, E. (2009). Petrological evidence for secular cooling in mantle plumes. *Nature*, 458(7238):619–622.

Herzberg, C. and O'Hara, M. J. (2002). Plume-associated ultramafic magmas of Phanerozoic age. *Journal of Petrology*, 43(10):1857–1883.

Herzberg, C., Raterron, P., and Zhang, J. (2000). New experimental observations on the anhydrous solidus for peridotite KLB-1. *Geochemistry, Geophysics, Geosystems*, 1(11):1051.

Herzberg, C. and Zhang, J. (1996). Melting experiments on anhydrous peridotite KLB-1: compositions of magmas in the upper mantle and transition zone. *Journal of Geophysical Research*, 101(B4):8271–8295.

Hill, E., Blundy, J. D., and Wood, B. J. (2011). Clinopyroxene–melt trace element partitioning and the development of a predictive model for HFSE and Sc. *Contributions to Mineralogy and Petrology*, 161(3):423–438.

Hill, E., Blundy, J. D., and Wood, B. J. (2012). Erratum to: Clinopyroxene–melt trace element partitioning and the development of a predictive model for HFSE and Sc. *Contributions to Mineralogy and Petrology*, 163(3):563–565.

Hill, E., Wood, B. J., and Blundy, J. D. (2000). The effect of Ca-Tschermaks component on trace element partitioning between clinopyroxene and silicate melt. *Lithos*, 53(3–4):203–215.

Hill, R. I. (1991). Starting plumes and continental break-up. *Earth and Planetary Science Letters*, 104(2–4):398–416.

Hirose, K., Fei, Y., Ma, Y., and Mao, H.-K. (1999). The fate of subducted basaltic crust in the Earth's lower mantle. *Nature*, 397(6714):53–56.

Hirose, K. and Kushiro, I. (1993). Partial melting of dry peridotites at high pressures: Determination of compositions of melts segregated from peridotite using aggregates of diamond. *Earth and Planetary Science Letters*, 114(4):477–489.

Hirose, K., Takafuji, N., Sata, N., and Ohishi, Y. (2005). Phase transition and density of subducted MORB crust in the lower mantle. *Earth and Planetary Science Letters*, 237(1–2):239–251.

Hirschmann, M. M. (2000). Mantle solidus: Experimental constraints and the effects of peridotite composition. *Geochemistry, Geophysics, Geosystems*, 1(10):1042.

Hirschmann, M. M., Kogiso, T., Baker, M. B., and Stolper, E. M. (2003). Alkalic magmas generated by partial melting of garnet pyroxenite. *Geology*, 31(6):481–484.

Hirschmann, M. M. and Stolper, E. M. (1996). A possible role for garnet pyroxenite in the origin of the "garnet signature" in MORB. *Contributions to Mineralogy and Petrology*, 124(2):185–208.

Hofmann, A. (1997). Mantle geochemistry: the message from oceanic volcanism. *Nature*, 385(6613):219–229.

Hofmann, A. W. (2003). Sampling mantle heterogeneity through oceanic basalts: Isotopes and trace elements. *Treatise on Geochemistry*, 2:61–101.

Hofmann, A. W. and White, W. M. (1982). Mantle plumes from ancient oceanic crust. *Earth and Planetary Science Letters*, 57(2):421–436.

Holden, J. C. and Vogt, P. (1977). Graphic solutions to problems of plumacy. *Eos, Transactions American Geophysical Union*, 58(7):573–580.

Hole, M. J. (2015). The generation of continental flood basalts by decompression melting of internally heated mantle. *Geology*, 43(4):311–314.

Holland, T. and Powell, R. (2001). Calculation of phase relations involving haplogranitic melts using an internally consistent thermodynamic dataset. *Journal of Petrology*, 42(4):673–683.

Holland, T. J. B., Hudson, N. F. C., Powell, R., and Harte, B. (2013). New thermodynamic models and calculated phase equilibria in NCFMAS for basic and ultrabasic compositions through the transition zone into the uppermost lower mantle. *Journal of Petrology*, 54(9):1901–1920.

Holland, T. J. B. and Powell, R. (2011). An improved and extended internally consistent thermodynamic dataset for phases of petrological interest, involving a new equation of state for solids. *Journal of Metamorphic Geology*, 29(3):333–383.

Ichiyama, Y., Ishiwatari, A., Hirahara, Y., and Shuto, K. (2006). Geochemical and isotopic constraints on the genesis of the Permian ferropicritic rocks from the Mino–Tamba belt, SW Japan. *Lithos*, 89(1–2):47–65.

Ionov, D. (2004). Chemical variations in peridotite xenoliths from Vitim, Siberia: Inferences for REE and Hf behaviour in the garnet-facies upper mantle. *Journal of Petrology*, 45(2):343–367.

Ionov, D. A. and Wood, B. J. (1992). The oxidation state of subcontinental mantle: oxygen thermobarometry of mantle xenoliths from central Asia. *Contributions to Mineralogy and Petrology*, 111(2):179–193.

Ito, G. and Mahoney, J. J. (2005a). Flow and melting of a heterogeneous mantle: 1. Method and importance to the geochemistry of ocean island and mid-ocean ridge basalts. *Earth and Planetary Science Letters*, 230(1–2):29–46.

Ito, G. and Mahoney, J. J. (2005b). Flow and melting of a heterogeneous mantle: 2. Implications for a chemically nonlayered mantle. *Earth and Planetary Science Letters*, 230(1):47–63.

Jackson, M. G. and Dasgupta, R. (2008). Compositions of HIMU, EM1, and EM2 from global trends between radiogenic isotopes and major elements in ocean island basalts. *Earth and Planetary Science Letters*, 276(1–2):175–186.

Jackson, M. G. and Hart, S. R. (2006). Strontium isotopes in melt inclusions from Samoan basalts: Implications for heterogeneity in the Samoan plume. *Earth and Planetary Science Letters*, 245(1–2):260–277.

Jackson, M. G., Hart, S. R., Konter, J. G., Kurz, M. D., Blusztajn, J., and Farley, K. A. (2014). Helium and lead isotopes reveal the geochemical geometry of the Samoan plume. *Nature*, 514(7522):355–358.

Jackson, M. G. and Jellinek, A. M. (2013). Major and trace element composition of the high 3He/4He mantle: Implications for the composition of a nonchonditic Earth. *Geochemistry, Geophysics, Geosystems*, 14(8):2954–2976.

Jahn, B.-m., Gruau, G., and Glikson, A. Y. (1982). Komatiites of the Onverwacht Group, S. Africa: REE geochemistry, Sm/Nd age and mantle evolution. *Contributions to Mineralogy and Petrology*, 80(1):25–40.

Jakobsen, J. K., Veksler, I. V., Tegner, C., and Brooks, C. K. (2005). Immiscible iron- and silica-rich melts in basalt petrogenesis documented in the Skaergaard intrusion. *Geology*, 33(11):885–888.

Jennings, E. S. and Holland, T. J. B. (2015). A simple thermodynamic model for melting of peridotite in the system NCFMASOCr. *Journal of Petrology*, 56(5):869–892.

Jerram, D., Mountney, N., Holzförster, F., and Stollhofen, H. (1999). Internal stratigraphic relationships in the Etendeka group in the Huab Basin, NW Namibia: understanding the onset of flood volcanism. *Journal of Geodynamics*, 28(4–5):393–418.

Jochum, K. P., Nohl, U., Herwig, K., Lammel, E., Stoll, B., and Hofmann, A. W. (2005). GeoReM: A New Geochemical Database for Reference Materials and Isotopic Standards. *Geostandards and Geoanalytical Research*, 29(3):333–338.

Kamenetsky, V. S., Chung, S.-L., Kamenetsky, M. B., and Kuzmin, D. V. (2012). Picrites from the Emeishan Large Igneous Province, SW China: A compositional continuum in primitive magmas and their respective mantle sources. *Journal of Petrology*, 53(10):2095–2113.

Kamenetsky, V. S., Eggins, S. M., Crawford, A. J., Green, D. H., Gasparon, M., and Falloon, T. J. (1998). Calcic melt inclusions in primitive olivine at 43°N MAR: evidence for melt–rock reaction/melting involving clinopyroxene-rich lithologies during MORB generation. *Earth and Planetary Science Letters*, 160(1–2):115–132.

Karlstrom, L. and Richards, M. (2011). On the evolution of large ultramafic magma chambers and timescales for flood basalt eruptions. *Journal of Geophysical Research*, 116(B8):1–13.

Katz, R. F., Spiegelman, M., and Langmuir, C. H. (2003). A new parameterization of hydrous mantle melting. *Geochemistry, Geophysics, Geosystems*, 4(9):1073.

Katz, R. F. and Weatherley, S. M. (2012). Consequences of mantle heterogeneity for melt extraction at mid-ocean ridges. *Earth and Planetary Science Letters*, 335–336:226–237.

Kawabata, H., Hanyu, T., Chang, Q., Kimura, J.-I., Nichols, A. R. L., and Tatsumi, Y. (2011). The petrology and geochemistry of St. Helena alkali basalts: Evaluation of the oceanic crust-recycling model for HIMU OIB. *Journal of Petrology*, 52(4):791–838.

Keiding, J., Trumbull, R., Veksler, I., and Jerram, D. (2011). On the significance of ultra-magnesian olivines in basaltic rocks. *Geology*, 39(12):1095–1098.

Keiding, J. K., Frei, O., Renno, A. D., Veksler, I. V., and Trumbull, R. B. (2013). Conditions of magma crystallization in the Henties Bay-Outjo dyke swarm, Namibia: Implications for the feeder system of continental flood basalts. *Lithos*, 179:16–27.

Kelemen, P. B., Hirth, G., Shimizu, N., Spiegelman, M., and Dick, H. J. (1997). A review of melt migration processes in the adiabatically upwelling mantle beneath oceanic spreading ridges. *Philosophical Transactions of the Royal Society of London A: Mathematical, Physical and Engineering Sciences*, 355(1723):283–318.

Kent, A. J., Baker, J. A., and Wiedenbeck, M. (2002). Contamination and melt aggregation processes in continental flood basalts: constraints from melt inclusions in Oligocene basalts from Yemen. *Earth and Planetary Science Letters*, 202:577–594.

Kent, A. J. R. (2008). Melt inclusions in basaltic and related volcanic rocks. *Reviews in Mineralogy and Geochemistry*, 69(1):273–331.

Keshav, S., Gudfinnsson, G. H., Sen, G., and Fei, Y. (2004). High-pressure melting experiments on garnet clinopyroxenite and the alkalic to tholeiitic transition in ocean-island basalts. *Earth and Planetary Science Letters*, 223(3–4):365–379.

Kinzler, R. J. (1997). Melting of mantle peridotite at pressures approaching the spinel to garnet transition: Application to mid-ocean ridge basalt petrogenesis. *Journal of Geophysical Research: Solid Earth*, 102(B1):853–874.

Kinzler, R. J. and Grove, T. L. (1992). Primary magmas of mid-ocean ridge basalts 1. Experiments and methods. *Journal of Geophysical Research: Solid Earth*, 97(B5):6885–6906.

Klein, E. M. and Langmuir, C. H. (1987). Global correlations of ocean ridge basalt chemistry with axial depth and crustal thickness. *Journal of Geophysical Research: Solid Earth*, 92(B8):8089–8115.

Klemme, S. (2004). The influence of Cr on the garnet–spinel transition in the Earth's mantle: experiments in the system MgO–Cr2O3–SiO2 and thermodynamic modelling. *Lithos*, 77(1–4):639–646.

Kogiso, T., Hirose, K., and Takahashi, E. (1998). Melting experiments on homogeneous mixtures of peridotite and basalt: application to the genesis of ocean island basalts. *Earth and Planetary Science Letters*, 162(1–4):45–61.

Kogiso, T. and Hirschmann, M. M. (2006). Partial melting experiments of bimineralic eclogite and the role of recycled mafic oceanic crust in the genesis of ocean island basalts. *Earth and Planetary Science Letters*, 249(3–4):188–199.

Kogiso, T., Hirschmann, M. M., and Frost, D. J. (2003). High-pressure partial melting of garnet pyroxenite: possible mafic lithologies in the source of ocean island basalts. *Earth and Planetary Science Letters*, 216(4):603–617.

Kogiso, T., Hirschmann, M. M., and Pertermann, M. (2004a). High-pressure partial melting of mafic lithologies in the mantle. *Journal of Petrology*, 45(12):2407–2422.

Kogiso, T., Hirschmann, M. M., and Reiners, P. W. (2004b). Length scales of mantle heterogeneities and their relationship to ocean island basalt geochemistry. *Geochimica et Cosmochimica Acta*, 68(2):345–360.

Koleszar, A. M., Saal, A. E., Hauri, E. H., Nagle, A. N., Liang, Y., and Kurz, M. D. (2009). The volatile contents of the Galapagos plume; evidence for H2O and F open system behavior in melt inclusions. *Earth and Planetary Science Letters*, 287(3–4):442–452.

Konter, J. G. and Becker, T. W. (2012). Shallow lithospheric contribution to mantle plumes revealed by integrating seismic and geochemical data. *Geochemistry, Geophysics, Geosystems*, 13(2):Q02004.

Koornneef, J. M., Stracke, A., Bourdon, B., Meier, M. A., Jochum, K. P., Stoll, B., and Grönvold, K. (2012). Melting of a two-component source beneath Iceland. *Journal of Petrology*, 53(1):127–157.

Kreissig, K., Nägler, T. F., Kramers, J. D., van Reenen, D. D., and Smit, C. A. (2000). An isotopic and geochemical study of the northern Kaapvaal Craton and the Southern Marginal Zone of the Limpopo Belt: are they juxtaposed terranes? *Lithos*, 50(1–3):1–25.

Kress, V. C. and Carmichael, I. S. E. (1991). The compressibility of silicate liquids containing Fe2O3 and the effect of composition, temperature, oxygen fugacity and pressure on their redox states. *Contributions to Mineralogy and Petrology*, 108(1-2):82–92.

Kurz, M. D., Jenkins, W. J., and Hart, S. R. (1982). Helium isotopic systematics of oceanic islands and mantle heterogeneity. *Nature*, 297(5861):43–47.

Lambart, S., Laporte, D., and Schiano, P. (2009). An experimental study of pyroxenite partial melts at 1 and 1.5 GPa: Implications for the major-element composition of Mid-Ocean Ridge Basalts. *Earth and Planetary Science Letters*, 288(1–2):335–347.

Lambart, S., Laporte, D., and Schiano, P. (2013). Markers of the pyroxenite contribution in the major-element compositions of oceanic basalts: Review of the experimental constraints. *Lithos*, 160–161:14–36.

Lange, R. L. and Carmichael, I. S. E. (1990). Thermodynamic properties of silicate liquids with emphasis on density, thermal expansion and compressibility. *Reviews in Mineralogy and Geochemistry*, 24(1):25–64.

Langmuir, C. H., Klein, E. M., and Plank, T. (1992). Petrological systematics of mid-ocean ridge basalts: Constraints on melt generation beneath ocean ridges. In Morgan, J. P., Blackman, D. K., and Sinton, J. M., editors, *Geophysical Monograph Series*, volume 71, pages 183–280. American Geophysical Union, Washington, D. C.

Lassak, T. M., McNamara, A. K., Garnero, E. J., and Zhong, S. (2010). Core–mantle boundary topography as a possible constraint on lower mantle chemistry and dynamics. *Earth and Planetary Science Letters*, 289(1–2):232–241.

Laubier, M., Gale, A., and Langmuir, C. H. (2012). Melting and crustal processes at the FAMOUS segment (Mid-Atlantic Ridge): New insights from olivine-hosted melt inclusions from multiple samples. *Journal of Petrology*, 53(4):665–698.

Le Bas, M. J. (2000). IUGS Reclassification of the High-Mg and Picritic Volcanic Rocks. *Journal of Petrology*, 41(10):1467–1470.

Le Bas, M. J. L., Maitre, R. W. L., Streckeisen, A., Zanettin, B., and Rocks, I. S. o. t. S. o. I. (1986). A chemical classification of volcanic rocks based on the total alkali-silica diagram. *Journal of Petrology*, 27(3):745–750.

Le Roux, V., Dasgupta, R., and Lee, C. T. A. (2011). Mineralogical heterogeneities in the Earth's mantle: Constraints from Mn, Co, Ni and Zn partitioning during partial melting. *Earth and Planetary Science Letters*, 307(3–4):395–408.

Le Roux, V., Lee, C. T. A., and Turner, S. J. (2010). Zn/Fe systematics in mafic and ultramafic systems: Implications for detecting major element heterogeneities in the Earth's mantle. *Geochimica et Cosmochimica Acta*, 74(9):2779–2796.

Li, Y., Deschamps, F., and Tackley, P. J. (2014). The stability and structure of primordial reservoirs in the lower mantle: insights from models of thermochemical convection in three-dimensional spherical geometry. *Geophysical Journal International*, 199(2):914–930.

Lightfoot, P. C., Naldrett, A. J., Gorbachev, N. S., Doherty, W., and Fedorenko, V. A. (1990). Geochemistry of the Siberian Trap of the Noril'sk area, USSR, with implications for the relative contributions of crust and mantle to flood basalt magmatism. *Contributions to Mineralogy and Petrology*, 104(6):631–644.

Lin, S.-C. and van Keken, P. E. (2006a). Dynamics of thermochemical plumes: 1. Plume formation and entrainment of a dense layer. *Geochemistry, Geophysics, Geosystems*, 7(2):Q02006.

Lin, S.-C. and van Keken, P. E. (2006b). Dynamics of thermochemical plumes: 2. Complexity of plume structures and its implications for mapping mantle plumes. *Geochemistry Geophysics Geosystems*, 7(3).

Longhi, J. (2002). Some phase equilibrium systematics of lherzolite melting: I. *Geochemistry, Geophysics, Geosystems*, 3(3):1–33.

Lowe, D. R. and Byerly, G. R. (1999). *Geologic Evolution of the Barberton Greenstone Belt, South Africa*. Geological Society of America.

Luttinen, A. V. and Furnes, H. (2000). Flood basalts of Vestfjella: Jurassic Magmatism across an Archaean–Proterozoic lithospheric boundary in Dronning Maud Land, Antarctica. *Journal of Petrology*, 41(8):1271–1305.

Luttinen, A. V., Heinonen, J. S., Kurhila, M., Jourdan, F., Mänttäri, I., Vuori, S. K., and Huhma, H. (2015). Depleted mantle-sourced CFB magmatism in the Jurassic Africa–Antarctica rift: Petrology and 40Ar/39Ar and U/Pb chronology of the Vestfjella dyke swarm, Dronning Maud Land, Antarctica. *Journal of Petrology*, page egv022.

Macdonald, G. A. (1968). Composition and origin of Hawaiian lavas. *Geological Society of America Memoirs*, 116:477–522.

Maclennan, J. (2008a). Concurrent mixing and cooling of melts under Iceland. *Journal of Petrology*, 49(11):1931–1953.

Maclennan, J. (2008b). Lead isotope variability in olivine-hosted melt inclusions from Iceland. *Geochimica et Cosmochimica Acta*, 72(16):4159–4176.

Maclennan, J., McKenzie, D., Grönvold, K., Shimizu, N., Eiler, J. M., and Kitchen, N. (2003a). Melt mixing and crystallization under Theistareykir, northeast Iceland. *Geochemistry, Geophysics, Geosystems*, 4(11):8624.

Maclennan, J., McKenzie, D., Hilton, F., Gronvold, K., and Shimizu, N. (2003b). Geochemical variability in a single flow from northern Iceland. *Journal of Geophysical Research*, 108(B1):2007.

Mallik, A. and Dasgupta, R. (2012). Reaction between MORB-eclogite derived melts and fertile peridotite and generation of ocean island basalts. *Earth and Planetary Science Letters*, 329–330:97–108.

Marschall, H. R., Hawkesworth, C. J., Storey, C. D., Dhuime, B., Leat, P. T., Meyer, H.-P., and Tamm-Buckle, S. (2010). The Annandagstoppane Granite, East Antarctica: Evidence for Archaean intracrustal recycling in the Kaapvaal–Grunehogna craton from zircon O and Hf isotopes. *Journal of Petrology*, 51(11):2277–2301.

Marsh, J. S., Ewart, A., Milner, S. C., Duncan, A. R., and Miller, R. M. (2001). The Etendeka Igneous Province: Magma types and their stratigraphic distribution with implications for the evolution of the Paraná-Etendeka flood basalt province. *Bulletin of Volcanology*, 62(6-7):464–486.

Matzen, A. K., Baker, M. B., Beckett, J. R., and Stolper, E. M. (2011). Fe–Mg partitioning between olivine and high-magnesian melts and the nature of Hawaiian parental liquids. *Journal of Petrology*, 52(7-8):1243–1263.

Matzen, A. K., Baker, M. B., Beckett, J. R., and Stolper, E. M. (2013). The temperature and pressure dependence of nickel partitioning between olivine and silicate melt. *Journal of Petrology*, page egt055.

McDonough, W. and Sun, S.-s. (1995). The composition of the Earth. *Chemical Geology*, 120(3–4):223–253.

McKenzie, D. (1984). The generation and compaction of partially molten rock. *Journal of Petrology*, 25(3):713–765.

McKenzie, D. (1985). 230Th238U disequilibrium and the melting processes beneath ridge axes. *Earth and Planetary Science Letters*, 72(2-3):149–157.

McKenzie, D. and Bickle, M. J. (1988). The volume and composition of melt generated by extension of the lithosphere. *Journal of Petrology*, 29(3):625–679.

McKenzie, D., Jackson, J., and Priestley, K. (2005). Thermal structure of oceanic and continental lithosphere. *Earth and Planetary Science Letters*, 233(3-4):337–349.

McKenzie, D. and O'Nions, R. K. (1983). Mantle reservoirs and ocean island basalts. *Nature*, 301:229–231.

McKenzie, D. and O'Nions, R. K. (1991). Partial melt distributions from inversion of rare earth element concentrations. *Journal of Petrology*, 32(5):1021.

McKenzie, D. and O'Nions, R. K. (1998). Melt production beneath oceanic islands. *Physics of the Earth and Planetary Interiors*, 107(1–3):143–182.

McNamara, A. K. and Zhong, S. (2005). Thermochemical structures beneath Africa and the Pacific Ocean. *Nature*, 437(7062):1136–1139.

Mibe, K., Fujii, T., Yasuda, A., and Ono, S. (2006). Mg–Fe partitioning between olivine and ultramafic melts at high pressures. *Geochimica et Cosmochimica Acta*, 70(3):757–766.

Milner, S. C. and le Roex, A. P. (1996). Isotope characteristics of the Okenyenya igneous complex, northwestern Namibia: constraints on the composition of the early Tristan plume and the origin of the EM 1 mantle component. *Earth and Planetary Science Letters*, 141(1–4):277–291.

Milner, S. C., Roex, A. P. L., and O'Connor, J. M. (1995). Age of Mesozoic igneous rocks in northwestern Namibia, and their relationship to continental breakup. *Journal of the Geological Society*, 152(1):97–104.

Morgan, W. J. (1971). Convection plumes in the lower mantle. *Nature*, 230(5288):42–43.

Morrison, M. A., Thompson, R. N., and Dickin, A. P. (1985). Geochemical evidence for complex magmatic plumbing during development of a continental volcanic center. *Geology*, 13(8):581–584.

Moune, S., Sigmarsson, O., Schiano, P., Thordarson, T., and Keiding, J. K. (2012). Melt inclusion constraints on the magma source of Eyjafjallajökull 2010 flank eruption. *Journal of Geophysical Research: Solid Earth*, 117(B9):B00C07.

Mountney, N., Howell, J., Flint, S., and Jerram, D. (1999). Climate, sediment supply and tectonics as controls on the deposition and preservation of the aeolian-fluvial Etjo Sandstone Formation, Namibia. *Journal of the Geological Society*, 156(4):771–777.

Neave, D. A., Maclennan, J., Edmonds, M., and Thordarson, T. (2014a). Melt mixing causes negative correlation of trace element enrichment and CO2 content prior to an Icelandic eruption. *Earth and Planetary Science Letters*, 400:272–283.

Neave, D. A., Maclennan, J., Hartley, M. E., Edmonds, M., and Thordarson, T. (2014b). Crystal storage and transfer in basaltic systems: The Skuggafjöll eruption, Iceland. *Journal of Petrology*, 55(12):2311–2346.

Neave, D. A., Passmore, E., Maclennan, J., Fitton, G., and Thordarson, T. (2013). Crystal–melt relationships and the record of deep mixing and crystallization in the ad 1783 Laki eruption, Iceland. *Journal of Petrology*, 54(8):1661–1690.

Neumann, E.-R., Svensen, H., Galerne, C. Y., and Planke, S. (2011). Multistage evolution of dolerites in the Karoo Large Igneous Province, Central South Africa. *Journal of Petrology*, 52(5):959–984.

Nielsen, R. L., Michael, P. J., and Sours-Page, R. (1998). Chemical and Physical Indicators of Compromised Melt Inclusions. *Geochimica et Cosmochimica Acta*, 62(5):831–839.

Nielsen, T., Turkov, V., Solovova, I., Kogarko, L., and Ryabchikov, I. (2006). A Hawaiian beginning for the Iceland plume: Modelling of reconnaissance data for olivine-hosted melt inclusions in Palaeogene picrite lavas from East Greenland. *Lithos*, 92(1-2):83–104.

Niu, Y. (2003). Origin of ocean island basalts: A new perspective from petrology, geochemistry, and mineral physics considerations. *Journal of Geophysical Research*, 108(B4).

Norman, M. D., Garcia, M. O., Kamenetsky, V. S., and Nielsen, R. L. (2002). Olivine-hosted melt inclusions in Hawaiian picrites: equilibration, melting, and plume source characteristics. *Chemical Geology*, 183(1–4):143–168.

O'Hara, M. J. (1968). The bearing of phase equilibria studies in synthetic and natural systems on the origin and evolution of basic and ultrabasic rocks. *Earth-Science Reviews*, 4:69–133.

O'Neill, H. S. C. and Palme, H. (2008). Collisional erosion and the non-chondritic composition of the terrestrial planets. *Philosophical Transactions of the Royal Society of London A: Mathematical, Physical and Engineering Sciences*, 366(1883):4205–4238.

O'Nions, R. K., Evensen, N. M., and Hamilton, P. J. (1979). Geochemical modeling of mantle differentiation and crustal growth. *Journal of Geophysical Research: Solid Earth*, 84(B11):6091–6101.

Onuma, N., Higuchi, H., Wakita, H., and Nagasawa, H. (1968). Trace element partition between two pyroxenes and the host lava. *Earth and Planetary Science Letters*, 5:47–51.

Parsons, B. and Sclater, J. G. (1977). An analysis of the variation of ocean floor bathymetry and heat flow with age. *Journal of Geophysical Research*, 82(5):803–827.

Peate, D. (1997). The Paraná-Etendeka province. *Geophysical Monograph-American Geophysical Union*, 100:217–246.

Peate, D. W., Hawkesworth, C. J., Mantovani, M. M. S., Rogers, N. W., and Turner, S. P. (1999). Petrogenesis and Stratigraphy of the High-Ti/Y Urubici Magma Type in the Paraná Flood Basalt Province and Implications for the Nature of 'Dupal'-Type Mantle in the South Atlantic Region. *Journal of Petrology*, 40(3):451–473.

Peate, D. W., Peate, I. U., Rowe, M. C., Thompson, J. M., and Kerr, A. C. (2012). Petrogenesis of high-MgO lavas of the Lower Mull Plateau Group, Scotland: Insights from melt inclusions. *Journal of Petrology*, 53(9):1867–1886.

Perkins III, D. and Newton, R. C. (1980). The compositions of coexisting pyroxenes and garnet in the system CaO-MgO-Al2O3-SiO2 at 900°–1,100°C and high pressures. *Contributions to Mineralogy and Petrology*, 75(3):291–300.

Pertermann, M. and Hirschmann, M. M. (2003a). Anhydrous partial melting experiments on MORB-like eclogite: Phase relations, phase compositions and mineral-melt partitioning of major elements at 2–3 GPa. *Journal of Petrology*, 44(12):2173–2201.

Pertermann, M. and Hirschmann, M. M. (2003b). Partial melting experiments on a MORB-like pyroxenite between 2 and 3 GPa: Constraints on the presence of pyroxenite in basalt source regions from solidus location and melting rate. *Journal of Geophysical Research*, 108(B2):2125.

Pertermann, M., Hirschmann, M. M., Hametner, K., Günther, D., and Schmidt, M. W. (2004). Experimental determination of trace element partitioning between garnet and silica-rich liquid during anhydrous partial melting of MORB-like eclogite. *Geochemistry, Geophysics, Geosystems*, 5(5):Q05A01.

Phipps Morgan, J. (2001). Thermodynamics of pressure release melting of a veined plum pudding mantle. *Geochemistry, Geophysics, Geosystems*, 2(4):2000GC000049.

Pietruszka, A. J., Norman, M. D., Garcia, M. O., Marske, J. P., and Burns, D. H. (2013). Chemical heterogeneity in the Hawaiian mantle plume from the alteration and dehydration of recycled oceanic crust. *Earth and Planetary Science Letters*, 361:298–309.

Pik, R., Marty, B., and Hilton, D. R. (2006). How many mantle plumes in Africa? The geochemical point of view. *Chemical Geology*, 226(3–4):100–114.

Pilet, S., Hernandez, J., Sylvester, P., and Poujol, M. (2005). The metasomatic alternative for ocean island basalt chemical heterogeneity. *Earth and Planetary Science Letters*, 236(1–2):148–166.

Plank, T. and Langmuir, C. H. (1992). Effects of the melting regime on the composition of the oceanic crust. *Journal of Geophysical Research: Solid Earth*, 97(B13):19749–19770.

Powell, R., Holland, T., and Worley, B. (1998). Calculating phase diagrams involving solid solutions via non-linear equations, with examples using THERMOCALC. *Journal of Metamorphic Geology*, 16(4):577–588.

Powell, R., White, R., Green, E., Holland, T., and Diener, J. (2014). On parameterizing thermodynamic descriptions of minerals for petrological calculations. *Journal of Metamorphic Geology*, 32(3):245–260.

Prytulak, J. and Elliott, T. (2007). TiO2 enrichment in ocean island basalts. *Earth and Planetary Science Letters*, 263(3–4):388–403.

Putirka, K., Ryerson, F. J., Perfit, M., and Ridley, W. I. (2011). Mineralogy and composition of the oceanic mantle. *Journal of Petrology*, 52(2):279–313.

Putirka, K. D. (2005). Mantle potential temperatures at Hawaii, Iceland, and the mid-ocean ridge system, as inferred from olivine phenocrysts: Evidence for thermally driven mantle plumes. *Geochemistry Geophysics Geosystems*, 6(5):Q05L08.

Putirka, K. D., Perfit, M., Ryerson, F. J., and Jackson, M. G. (2007). Ambient and excess mantle temperatures, olivine thermometry, and active vs. passive upwelling. *Chemical Geology*, 241(3–4):177–206.

Regelous, M., Niu, Y., Abouchami, W., and Castillo, P. R. (2009). Shallow origin for South Atlantic Dupal Anomaly from lower continental crust: Geochemical evidence from the Mid-Atlantic Ridge at 26°S. *Lithos*, 112(1–2):57–72.

Reidel, S. P. and Tolan, T. L. (2013). The Grande Ronde Basalt, Columbia River Basalt Group. *Geological Society of America Special Papers*, 497:117–153.

Ren, Z.-Y., Ingle, S., Takahashi, E., Hirano, N., and Hirata, T. (2005). The chemical structure of the Hawaiian mantle plume. *Nature*, 436(7052):837–840.

Renne, P. R., Glen, J. M., Milner, S. C., and Duncan, A. R. (1996). Age of Etendeka flood volcanism and associated intrusions in southwestern Africa. *Geology*, 24(7):659–662.

Richards, M. A., Duncan, R. A., and Courtillot, V. E. (1989). Flood basalts and hot-spot tracks: Plume heads and tails. *Science*, 246(4926):103–107.

Rickwood, P. C. (1989). Boundary lines within petrologic diagrams which use oxides of major and minor elements. *Lithos*, 22:247–263.

Ridley, V. A. and Richards, M. A. (2010). Deep crustal structure beneath large igneous provinces and the petrologic evolution of flood basalts. *Geochemistry Geophysics Geosystems*, 11(9).

Riley, T. R. and Knight, K. B. (2001). Age of pre-break-up Gondwana magmatism. *Antarctic Science*, 13(02):99–110.

Riley, T. R., Leat, P. T., Curtis, M. L., Millar, I. L., Duncan, R. A., and Fazel, A. (2005). Early-middle Jurassic dolerite dykes from western Dronning Maud Land (Antarctica): Identifying mantle sources in the Karoo Large Igneous Province. *Journal of Petrology*, 46(7):1489–1524.

Robinson, J. A. C. and Wood, B. J. (1998). The depth of the spinel to garnet transition at the peridotite solidus. *Earth and Planetary Science Letters*, 164(1–2):277–284.

Robinson, J. A. C., Wood, B. J., and Blundy, J. D. (1998). The beginning of melting of fertile and depleted peridotite at 1.5 GPa. *Earth and Planetary Science Letters*, 155(1–2):97–111.

Roeder, P. L. and Emslie, R. F. (1970). Olivine-liquid equilibrium. *Contributions to Mineralogy and Petrology*, 29(4):275–289.

Rogers, N. (2006). Basaltic magmatism and the geodynamics of the East African Rift System. *Geological Society, London, Special Publications*, 259(1):77–93.

Rogers, N. W., Davies, M. K., Parkinson, I. J., and Yirgu, G. (2010). Osmium isotopes and Fe/Mn ratios in Ti-rich picritic basalts from the Ethiopian flood basalt province: No evidence for core contribution to the Afar plume. *Earth and Planetary Science Letters*, 296(3–4):413–422.

Rolf, T., Coltice, N., and Tackley, P. J. (2012). Linking continental drift, plate tectonics and the thermal state of the Earth's mantle. *Earth and Planetary Science Letters*, 351–352:134–146.

Rosenthal, A., Yaxley, G. M., Green, D. H., Hermann, J., Kovács, I., and Spandler, C. (2014). Continuous eclogite melting and variable refertilisation in upwelling heterogeneous mantle. *Scientific Reports*, 4.

Rudge, J. F., Maclennan, J., and Stracke, A. (2013). The geochemical consequences of mixing melts from a heterogeneous mantle. *Geochimica et Cosmochimica Acta*, 114:112–143.

Rudnick, R. L. and Fountain, D. M. (1995). Nature and composition of the continental crust: A lower crustal perspective. *Reviews of Geophysics*, 33(3):267–309.

Rudolph, M. L. and Zhong, S. (2013). Does quadrupole stability imply LLSVP fixity? *Nature*, 503(7477):E3–E4.

Saal, A. E., Hart, S. R., Shimizu, N., Hauri, E. H., and Layne, G. D. (1998). Pb isotopic variability in melt inclusions from oceanic island basalts, Polynesia. *Science*, 282(5393):1481–1484.

Sakyi, P. A., Tanaka, R., Kobayashi, K., and Nakamura, E. (2012). Inherited Pb isotopic records in olivine antecryst-hosted melt inclusions from Hawaiian lavas. *Geochimica et Cosmochimica Acta*, 95:169–195.

Salters, V. J. M. and Stracke, A. (2004). Composition of the depleted mantle. *Geochemistry, Geophysics, Geosystems*, 5(5):Q05B07.

Schmitt, A. K., Emmermann, R., Trumbull, R. B., Bühn, B., and Henjes-Kunst, F. (2000). Petrogenesis and 40Ar/39Ar geochronology of the Brandberg Complex, Namibia: Evidence for a major mantle contribution in metaluminous and peralkaline granites. *Journal of Petrology*, 41(8):1207–1239.

Schoene, B., Samperton, K. M., Eddy, M. P., Keller, G., Adatte, T., Bowring, S. A., Khadri, S. F. R., and Gertsch, B. (2015). U-Pb geochronology of the Deccan Traps and relation to the end-Cretaceous mass extinction. *Science*, 347(6218):182–184.

Self, S., Schmidt, A., and Mather, T. A. (2014). Emplacement characteristics, time scales, and volcanic gas release rates of continental flood basalt eruptions on Earth. *Geological Society of America Special Papers*, 505:SPE505–16.

Shannon, R. D. (1976). Revised effective ionic radii and systematic studies of interatomic distances in halides and chalcogenides. *Acta Crystallographica Section A*, 32(5):751–767.

Shaw, D. M. (1970). Trace element fractionation during anatexis. *Geochimica et Cosmochimica Acta*, 34(2):237–243.

Shimizu, N. (1998). The geochemistry of olivine-hosted melt inclusions in a FAMOUS basalt ALV519-4-1. *Physics of the Earth and Planetary Interiors*, 107(1–3):183–201.

Shirey, S. B. and Richardson, S. H. (2011). Start of the Wilson Cycle at 3 Ga Shown by Diamonds from Subcontinental Mantle. *Science*, 333(6041):434–436.

Shorttle, O. and Maclennan, J. (2011). Compositional trends of Icelandic basalts: Implications for short–length scale lithological heterogeneity in mantle plumes. *Geochemistry Geophysics Geosystems*, 12(11):Q11008.

Shorttle, O., Maclennan, J., and Lambart, S. (2014). Quantifying lithological variability in the mantle. *Earth and Planetary Science Letters*, 395:24–40.

Shorttle, O., Maclennan, J., and Piotrowski, A. M. (2013). Geochemical provincialism in the Iceland plume. *Geochimica et Cosmochimica Acta*, 122:363–397.

Sides, I. R., Edmonds, M., Maclennan, J., Swanson, D. A., and Houghton, B. F. (2014). Eruption style at Kilauea Volcano in Hawai/'i linked to primary melt composition. *Nature Geoscience*, 7(6):464–469.

Sims, K. W. W., Maclennan, J., Blichert-Toft, J., Mervine, E. M., Blusztajn, J., and Grönvold, K. (2013). Short length scale mantle heterogeneity beneath Iceland probed by glacial modulation of melting. *Earth and Planetary Science Letters*, 379:146–157.

Slater, L., McKenzie, D., Grönvold, K., and Shimizu, N. (2001). Melt generation and movement beneath Theistareykir, NE Iceland. *Journal of Petrology*, 42(2):321–354.

Sleep, N. H. (2006). Mantle plumes from top to bottom. *Earth-Science Reviews*, 77(4):231–271.

Smith, P. M. and Asimow, P. D. (2005). Adiabat_1ph: A new public front-end to the MELTS, pMELTS, and pHMELTS models. *Geochemistry, Geophysics, Geosystems*, 6(2):Q02004.

Smithies, R. H., Champion, D. C., and Cassidy, K. F. (2003). Formation of Earth's early Archaean continental crust. *Precambrian Research*, 127(1–3):89–101.

Sobolev, A. (1996). Melt inclusions in minerals as a source of principle petrological information. *Petrology*, 4(3):228–239.

Sobolev, A. V., Hofmann, A. W., Jochum, K. P., Kuzmin, D. V., and Stoll, B. (2011). A young source for the Hawaiian plume. *Nature*, 476(7361):434–437.

Sobolev, A. V., Hofmann, A. W., Kuzmin, D. V., Yaxley, G. M., Arndt, N. T., Chung, S.-l., Danyushevsky, L. V., Elliott, T., Frederick, A., Garcia, M. O., Gurenko, A. A., Kamenetsky, V. S., Kerr, A. C., Krivolutskaya, N. A., Matvienkov, V. V., Nikogosian, I. K., Sigurdsson, I. A., Sushchevskaya, N. M., Teklay, M., and Frey, F. A. (2007). The amount of recycled crust in sources of mantle-derived melts. *Science*, 316:412–417.

Sobolev, A. V., Hofmann, A. W., and Nikogosian, I. K. (2000). Recycled oceanic crust observed in 'ghost plagioclase' within the source of Mauna Loa lavas. *Nature*, 404(6781):986–990.

Sobolev, A. V., Hofmann, A. W., Sobolev, S. V., and Nikogosian, I. K. (2005). An olivine-free mantle source of Hawaiian shield basalts. *Nature*, 434(7033):590–7.

Sobolev, A. V., Krivolutskaya, N. A., and Kuzmin, D. V. (2009). Petrology of the parental melts and mantle sources of Siberian trap magmatism. *Petrology*, 17(3):253–286.

Sobolev, A. V. and Shimizu, N. (1993). Ultra-depleted primary melt included in an olivine from the Mid-Atlantic Ridge. *Nature*, 363:151–154.

Sorbadere, F., Médard, E., Laporte, D., and Schiano, P. (2013). Experimental melting of hydrous peridotite–pyroxenite mixed sources: Constraints on the genesis of silica-undersaturated magmas beneath volcanic arcs. *Earth and Planetary Science Letters*, 384:42–56.

Sours-Page, R., Nielsen, R. L., and Batiza, R. (2002). Melt inclusions as indicators of parental magma diversity on the northern East Pacific Rise. *Chemical Geology*, 183(1–4):237–261.

Spandler, C. and O'Neill, H. (2010). Diffusion and partition coefficients of minor and trace elements in San Carlos olivine at 1,300°C with some geochemical implications. *Contributions to Mineralogy and Petrology*, 159(6):791–818.

Spandler, C., Yaxley, G., Green, D. H., and Rosenthal, A. (2008). Phase relations and melting of anhydrous K-bearing eclogite from 1200 to 1600°C and 3 to 5 GPa. *Journal of Petrology*, 49(4):771–795.

Spera, F. J. and Bohrson, W. A. (2001). Energy-Constrained Open-System Magmatic Processes I: General Model and Energy-Constrained Assimilation and Fractional Crystallization (EC-AFC) Formulation. *Journal of Petrology*, 42(5):999–1018.

Spiegelman, M. and Elliott, T. (1993). Consequences of melt transport for uranium series disequilibrium in young lavas. *Earth and Planetary Science Letters*, 118(1–4):1–20.

Spiegelman, M. and Kelemen, P. B. (2003). Extreme chemical variability as a consequence of channelized melt transport. *Geochemistry, Geophysics, Geosystems*, 4(7):1055.

Starkey, N. A., Fitton, J. G., Stuart, F. M., and Larsen, L. M. (2012). Melt inclusions in olivines from early Iceland plume picrites support high 3He/4He in both enriched and depleted mantle. *Chemical Geology*, 306–307:54–62.

Starkey, N. A., Stuart, F. M., Ellam, R. M., Fitton, J. G., Basu, S., and Larsen, L. M. (2009). Helium isotopes in early Iceland plume picrites: Constraints on the composition of high 3He/4He mantle. *Earth and Planetary Science Letters*, 277(1–2):91–100.

Steinberger, B. and Torsvik, T. H. (2012). A geodynamic model of plumes from the margins of Large Low Shear Velocity Provinces. *Geochemistry, Geophysics, Geosystems*, 13(1):Q01W09.

Stern, R. J. (2005). Evidence from ophiolites, blueschists, and ultrahigh-pressure metamorphic terranes that the modern episode of subduction tectonics began in Neoproterozoic time. *Geology*, 33(7):557–560.

Stone, W. E., Crocket, J. H., Dickin, A. P., and Fleet, M. E. (1995). Origin of Archean ferropicrites: geochemical constraints from the Boston Creek Flow, Abitibi greenstone belt, Ontario, Canada. *Chemical Geology*, 121(1–4):51–71.

Storey, M., Mahoney, J. J., and Saunders, A. D. (1997). Cretaceous basalts in Madagascar and the transition between plume and continental lithosphere mantle sources. In J.honey, J. and Coffin, M. F., editors, *Large Igneous Provinces: Continental, Oceanic, and Planetary Flood Volcanism*, pages 95–122. American Geophysical Union.

Stracke, A., Bizimis, M., and Salters, V. J. M. (2003). Recycling oceanic crust: Quantitative constraints. *Geochemistry Geophysics Geosystems*, 4(3):8003.

Stracke, A. and Bourdon, B. (2009). The importance of melt extraction for tracing mantle heterogeneity. *Geochimica et Cosmochimica Acta*, 73(1):218–238.

Stracke, A., Hofmann, A. W., and Hart, S. R. (2005). FOZO, HIMU, and the rest of the mantle zoo. *Geochemistry Geophysics Geosystems*, 6(5):Q05007.

Styles, E., Goes, S., van Keken, P. E., Ritsema, J., and Smith, H. (2011). Synthetic images of dynamically predicted plumes and comparison with a global tomographic model. *Earth and Planetary Science Letters*, 311(3–4):351–363.

Sun, C. and Liang, Y. (2013). The importance of crystal chemistry on REE partitioning between mantle minerals (garnet, clinopyroxene, orthopyroxene, and olivine) and basaltic melts. *Chemical Geology*, 358:23–36.

Sun, C. and Liang, Y. (2015). HFSE partitioning in pyroxenes and olivine: Parameterized models with implications to HFSE fractionation in the upper mantle. In *Goldschmidt Abstracts*, page 3030, Prague.

Svensen, H., Corfu, F., Polteau, S., Hammer, Ø., and Planke, S. (2012). Rapid magma emplacement in the Karoo Large Igneous Province. *Earth and Planetary Science Letters*, 325–326:1–9.

Tackley, P. J. (2011). Living dead slabs in 3-D: The dynamics of compositionally-stratified slabs entering a "slab graveyard" above the core-mantle boundary. *Physics of the Earth and Planetary Interiors*, 188(3-4):150–162.

Tackley, P. J. (2012). Dynamics and evolution of the deep mantle resulting from thermal, chemical, phase and melting effects. *Earth-Science Reviews*, 110(1–4):1–25.

Takahashi, E. (1986). Melting of a dry peridotite KLB-1 up to 14 GPa: Implications on the Origin of peridotitic upper mantle. *Journal of Geophysical Research: Solid Earth*, 91(B9):9367–9382.

Takahashi, E. and Kushiro, I. (1983). Melting of a dry peridotite at high pressures and basalt magma genesis. *American Mineralogist*, 68(9-10):859–879.

Takahashi, E. and Nakajima, K. (2002). Melting Process in the Hawaiian Plume: An Experimental Study. In Takahashi, E., Lipman, P. W., Garcia, M. O., Naka, J., and Aramaki, S., editors, *Hawaiian Volcanoes: Deep Underwater Perspectives*, pages 403–418. American Geophysical Union.

Takahashi, E., Nakajima, K., and Wright, T. L. (1998). Origin of the Columbia River basalts: melting model of a heterogeneous plume head. *Earth and Planetary Science Letters*, 162(1–4):63–80.

Takahashi, E., Shimazaki, T., Tsuzaki, Y., and Yoshida, H. (1993). Melting study of a peridotite KLB-1 to 6.5 GPa, and the origin of basaltic magmas. *Philosophical Transactions of the Royal Society of London A: Mathematical, Physical and Engineering Sciences*, 342(1663):105–120.

Taura, H., Yurimoto, H., Kurita, K., and Sueno, S. (1998). Pressure dependence on partition coefficients for trace elements between olivine and the coexisting melts. *Physics and Chemistry of Minerals*, 25(7):469–484.

Thiede, D. S. and Vasconcelos, P. M. (2010). Paraná flood basalts: Rapid extrusion hypothesis confirmed by new 40Ar/39Ar results. *Geology*, 38(8):747–750.

Thompson, R. N. and Gibson, S. (2000). Transient high temperatures in mantle plume heads inferred from magnesian olivines in Phanerozoic picrites. *Nature*, 407(6803):502–506.

Thompson, R. N., Gibson, S. A., Dickin, A. P., and Smith, P. M. (2001). Early Cretaceous basalt and picrite dykes of the southern Etendeka region, NW Namibia: Windows into the role of the Tristan mantle plume in Paraná–Etendeka magmatism. *Journal of Petrology*, 42(11):2049–2081.

Thompson, R. N., Riches, a. J. V., Antoshechkina, P. M., Pearson, D. G., Nowell, G. M., Ottley, C. J., Dickin, a. P., Hards, V. L., Nguno, a.-K., and Niku-Paavola, V. (2007). Origin of CFB magmatism: Multi-tiered intracrustal picrite-rhyolite magmatic plumbing at Spitzkoppe, western Namibia, during early Cretaceous Etendeka magmatism. *Journal of Petrology*, 48(6):1119–1154.

Thomson, A. and Maclennan, J. (2013). The distribution of olivine compositions in Icelandic basalts and picrites. *Journal of Petrology*, 54(4):745–768.

Thordarson, T. and Self, S. (1993). The Laki (Skaftár Fires) and Grímsvötn eruptions in 1783–1785. *Bulletin of Volcanology*, 55(4):233–263.

Till, C. B., Grove, T. L., and Krawczynski, M. J. (2012). A melting model for variably depleted and enriched lherzolite in the plagioclase and spinel stability fields. *Journal of Geophysical Research: Solid Earth*, 117(B6):B06206.

Toplis, M. J. (2005). The thermodynamics of iron and magnesium partitioning between olivine and liquid: criteria for assessing and predicting equilibrium in natural and experimental systems. *Contributions to Mineralogy and Petrology*, 149(1):22–39.

Torsvik, T. H., Smethurst, M. A., Burke, K., and Steinberger, B. (2006). Large igneous provinces generated from the margins of the large low-velocity provinces in the deep mantle. *Geophysical Journal International*, 167(3):1447–1460.

Tuff, J. and Gibson, S. (2007). Trace-element partitioning between garnet, clinopyroxene and Fe-rich picritic melts at 3 to 7 GPa. *Contributions to Mineralogy and Petrology*, 153:369–387.

Tuff, J., Takahashi, E., and Gibson, S. (2005). Experimental constraints on the role of garnet pyroxenite in the genesis of high-Fe mantle plume derived melts. *Journal of Petrology*, 46(10):2023–2058.

Turner, S., Regelous, M., Kelley, S., Hawkesworth, C., and Mantovani, M. (1994). Magmatism and continental break-up in the South Atlantic: high precision 40Ar-39Ar geochronology. *Earth and Planetary Science Letters*, 121(3–4):333–348.

Ueki, K. and Iwamori, H. (2014). Thermodynamic calculations of the polybaric melting phase relations of spinel lherzolite. *Geochemistry, Geophysics, Geosystems*, 15(12):5015–5033.

van der Hilst, R. D., Widiyantoro, S., and Engdahl, E. R. (1997). Evidence for deep mantle circulation from global tomography. *Nature*, 386(6625):578–584.

van Keken, P. E., Hauri, E. H., and Ballentine, C. J. (2002). Mantle mixing: The generation, preservation, and destruction of chemical heterogeneity. *Annual Review of Earth and Planetary Sciences*, 30(1):493–525.

Van Kranendonk, M. J. (2011). Onset of plate tectonics. *Science*, 333(6041):413–414.

van Westrenen, W., Blundy, J. D., and Wood, B. J. (2001). High field strength element/rare earth element fractionation during partial melting in the presence of garnet: Implications for identification of mantle heterogeneities. *Geochemistry, Geophysics, Geosystems*, 2(7):1039.

Veksler, I., Dorfman, A., Danyushevsky, L., Jakobsen, J., and Dingwell, D. (2006). Immiscible silicate liquid partition coefficients: implications for crystal-melt element partitioning and basalt petrogenesis. *Contributions to Mineralogy and Petrology*, 152(6):685–702.

Vye-Brown, C., Gannoun, A., Barry, T. L., Self, S., and Burton, K. W. (2013). Osmium isotope variations accompanying the eruption of a single lava flow field in the Columbia River Flood Basalt Province. *Earth and Planetary Science Letters*, 368:183–194.

Walter, M. J. (1998). Melting of garnet peridotite and the origin of komatiite and depleted lithosphere. *Journal of Petrology*, 39(1):29–60.

Wan, Z., Coogan, L. A., and Canil, D. (2008). Experimental calibration of aluminum partitioning between olivine and spinel as a geothermometer. *American Mineralogist*, 93(7):1142–1147.

Wark, D. A. and Watson, E. B. (1998). Grain-scale permeabilities of texturally equilibrated, monomineralic rocks. *Earth and Planetary Science Letters*, 164(3–4):591–605.

Wasylenki, L. E., Baker, M. B., Kent, A. J. R., and Stolper, E. M. (2003). Near-solidus melting of the shallow upper mantle: Partial melting experiments on depleted peridotite. *Journal of Petrology*, 44(7):1163–1191.

Watson, S. and McKenzie, D. (1991). Melt generation by plumes: A study of Hawaiian volcanism. *Journal of Petrology*, 32(3):501–537.

Weatherley, S. M. and Katz, R. F. (2012). Melting and channelized magmatic flow in chemically heterogeneous, upwelling mantle. *Geochemistry Geophysics Geosystems*, 13(null):Q0AC18.

Weaver, B. L. (1991). Trace element evidence for the origin of ocean-island basalts. *Geology*, 19(2):123–126.

Weis, D., Garcia, M. O., Rhodes, J. M., Jellinek, M., and Scoates, J. S. (2011). Role of the deep mantle in generating the compositional asymmetry of the Hawaiian mantle plume. *Nature Geoscience*, 4(12):831–838.

White, R. and McKenzie, D. (1989). Magmatism at rift zones: The generation of volcanic continental margins and flood basalts. *Journal of Geophysical Research: Solid Earth*, 94(B6):7685–7729.

White, R. S. and McKenzie, D. (1995). Mantle plumes and flood basalts. *Journal of Geophysical Research: Solid Earth*, 100(B9):17543–17585.

White, W. M. (2010). Oceanic island basalts and mantle plumes: The geochemical perspective. *Annual Review of Earth and Planetary Sciences*, 38(1):133–160.

White, W. M. and Hofmann, A. W. (1982). Sr and Nd isotope geochemistry of oceanic basalts and mantle evolution. *Nature*, 296(5860):821–825.

Wignall, P. B. (2001). Large igneous provinces and mass extinctions. *Earth-Science Reviews*, 53(1–2):1–33.

Wijbrans, C. H., Klemme, S., Berndt, J., and Vollmer, C. (2015). Experimental determination of trace element partition coefficients between spinel and silicate melt: the influence of chemical composition and oxygen fugacity. *Contributions to Mineralogy and Petrology*, 169(4).

Wilke, M., Farges, F., Petit, P.-E., Brown, G. E., and Martin, F. (2001). Oxidation state and coordination of Fe in minerals: An Fe K-XANES spectroscopic study. *American Mineralogist*, 86(5-6):714–730.

Willbold, M. and Stracke, A. (2006). Trace element composition of mantle end-members: Implications for recycling of oceanic and upper and lower continental crust. *Geochemistry Geophysics Geosystems*, 7(4):Q04004.

Wolfe, C. J., Solomon, S. C., Laske, G., Collins, J. A., Detrick, R. S., Orcutt, J. A., Bercovici, D., and Hauri, E. H. (2009). Mantle shear-wave velocity structure beneath the Hawaiian hot spot. *Science*, 326(5958):1388–1390.

Wood, B. J. and Blundy, J. D. (1997). A predictive model for rare earth element partitioning between clinopyroxene and anhydrous silicate melt. *Contributions to Mineralogy and Petrology*, 129(2-3):166–181.

Wood, B. J. and Virgo, D. (1989). Upper mantle oxidation state: Ferric iron contents of Iherzolite spinels by 57Fe Mössbauer spectroscopy and resultant oxygen fugacities. *Geochimica et Cosmochimica Acta*, 53(6):1277–1291.

Wooden, J. L., Czamanske, G. K., Fedorenko, V. A., Arndt, N. T., Chauvel, C., Bouse, R. M., King, B.-S. W., Knight, R. J., and Siems, D. F. (1993). Isotopic and trace-element constraints on mantle

and crustal contributions to Siberian continental flood basalts, Noril'sk area, Siberia. *Geochimica et Cosmochimica Acta*, 57(15):3677–3704.

Woodland, A. B. (2009). Ferric iron contents of clinopyroxene from cratonic mantle and partitioning behaviour with garnet. *Lithos*, 112, Supplement 2:1143–1149.

Yasuda, A., Fujii, T., and Kurita, K. (1994). Melting phase relations of an anhydrous mid-ocean ridge basalt from 3 to 20 GPa: Implications for the behavior of subducted oceanic crust in the mantle. *Journal of Geophysical Research: Solid Earth*, 99(B5):9401–9414.

Yaxley, G. and Sobolev, A. (2007). High-pressure partial melting of gabbro and its role in the Hawaiian magma source. *Contributions to Mineralogy and Petrology*, 154(4):371–383.

Yaxley, G. M. (2000). Experimental study of the phase and melting relations of homogeneous basalt + peridotite mixtures and implications for the petrogenesis of flood basalts. *Contributions to Mineralogy and Petrology*, 139(3):326–338.

Yaxley, G. M. and Green, D. H. (1998). Reactions between eclogite and peridotite: Mantle refertilisation by subduction of oceanic crust. *Schweizerische Mineralogische Und Petrographische Mitteilungen*, 78(2):243–255.

Yaxley, G. M., Kamenetsky, V. S., Kamenetsky, M., Norman, M. D., and Francis, D. (2004). Origins of compositional heterogeneity in olivine-hosted melt inclusions from the Baffin Island picrites. *Contributions to Mineralogy and Petrology*, 148(4):426–442.

Zegers, T. E. and van Keken, P. E. (2001). Middle Archean continent formation by crustal delamination. *Geology*, 29(12):1083–1086.

Zhang, J. and Herzberg, C. (1994). Melting experiments on anhydrous peridotite KLB-1 from 5.0 to 22.5 GPa. *Journal of Geophysical Research: Solid Earth*, 99(B9):17729–17742.

Zhang, Z., Mahoney, J. J., Mao, J., and Wang, F. (2006). Geochemistry of picritic and associated basalt flows of the western Emeishan Flood Basalt Province, China. *Journal of Petrology*, 47(10):1997–2019.

Zhao, D. (2004). Global tomographic images of mantle plumes and subducting slabs: insight into deep Earth dynamics. *Physics of the Earth and Planetary Interiors*, 146(1–2):3–34.

Zindler, A. and Hart, S. (1986). Chemical geodynamics. *Annual Review of Earth and Planetary Sciences*, 14(1):493–571.

Appendix A

Experimental and Analytical Methods

A.1 Experimental methods and sample preparation

A.1.1 Melt inclusion rehomogenisation

Olivine separates were hand-picked from sieved size fractions from hand- and jaw-crushed rocks. The most useful size fraction (that with the highest proportion of single olivine crystals) was almost always 250-500 μm; although phenocrysts are larger in thin section, they are invariably fractured and presumably break into non-euhedral pieces.

Grains were then treated in a gas-mixing (controlled-atmosphere) furnace in order to melt the crystalline inclusions. Weighed batches of grains from each sample were wrapped in Pt foil and placed in a Pt crucible (Fig. A.1). This was suspended at the top of the pre-heated furnace column, where, due to large temperature gradients present in the furnace, they were kept relatively cool (< 600 °C). The furnace was then sealed and the gas mix was fluxed through for at least ten minutes to flush out residual air. The sample was then quickly lowered to the hot-spot and held at the experimental temperature for 20 minutes. Temperature was monitored with a type-R thermocouple (accuracy at the relevant temperature range is < ±1.5%) located < 10 mm from the sample. Temperature could be stabilised to within 3 °C of that required and the internal temperature gradient should be < 5 °C per 10 mm. The samples were instantly quenched in water by breaking a Pt fuse wire. This allowed for complete control over the fO_2 condition and heating rate.

The CO-CO_2 total gas pressure was approximately atmospheric and the ratio was set to fix $\log(fO_2)$ = FMQ-1 (one log unit below the Fayalite-Magnetite-Quartz buffer). Fixing the gas composition imposed a reducing environment on the olivine grains, preventing their deterioration by oxidation, where olivine would convert to haematite and forsterite. FMQ+0 through to FMQ-2 is a commonly used fO_2 range for this task (e.g. Kent *et al.*, 2002; Peate *et al.*, 2012). The position of

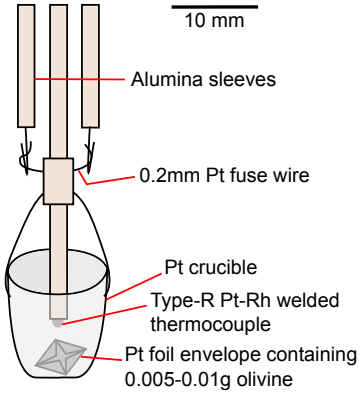

Figure A.1: Experimental setup, where olivine grains are held within Pt foil envelopes in a Pt crucible. Thermocouple distance to grains is generally < 10mm.

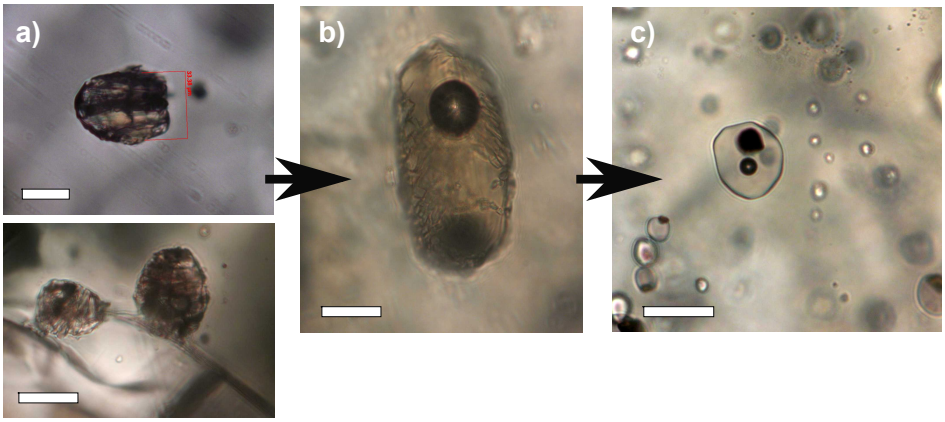

Figure A.2: Photomicrographs of a) two non-homogenised melt inclusions, b) a partially homogenised inclusion and c) a fully homogenised inclusion. Scale bars all 20 µm.

FMQ on the absolute log fO_2 scale is temperature dependent, as is the speciation of CO-CO_2. The log(fO_2) of FMQ at a given temperature is calculated from Frost (1991):

$$\text{FMQ} : \log(fO_2) = -25096.3/T + 8.735 + 0.110(P-1)/T \tag{A.1}$$

where T is in K and P is in bars. If the log(fO_2) at a given temperature is known, the CO-CO_2 ratio at that temperature can be found in the tables of Deines *et al.* (1974).

The temperature required for homogenisation was determined experimentally. Initially, low volume batches of $\sim$ 0.005 g were run at temperature intervals of 40 °C; grains were mounted and examined under an optical microscope (Fig. A.2). The 'homogenisation temperature' was reached when an arbitrary threshold of 95% of melt inclusions had homogenised. Large-volume grain batches ($\sim$ 0.02 g) were then run at this temperature. Experimental conditions for individual experiments are provided in Table A.1.

Table A.1: Run conditions of the homogenisation experiments performed. CO/CO_2 is a pressure ratio where the total gas pressure is $\sim$ 2 bar. Run products were given a binary classification of homogenised (yes or no), based on a criteria of > 95% of inclusions being visually homogenised. Three experiments where a gas mix failure caused grains to oxidise have been excluded.

Experiment	T	±	CO/CO_2	$\log(fO_2)$	mass (g)	t (mins)	% homogenised
97SB62-exp1	1170	3	0.099	-9	0.0135	20	< 95
97SB62-exp2	1210	3	0.111	-9	0.0147	20	100
97SB62-exp3	1250	3	0.215	-9	0.0127	20	100
97SB62-exp4	1210	2	0.146	-9.19	0.0199	20	98
97SB33-exp1	1246	3	0.203	-8.79	0.0131	20	98
97SB34-exp1	1185	3	0.139	-9.48	0.0198	20	95
97SB41-exp1	1174	2	0.134	-9.61	0.0189	20	5
97SB46-exp1	1163	2	0.126	-9.73	0.0159	20	5
97SB41-exp2	1214	2	0.150	-9.14	0.0184	20	95
97SB46-exp2	1203	4	0.150	-9.27	0.0092	20	98
97SB62-exp5	1350	5	0.186	-7.73	0.0152	15	100
97SB79-exp1	1210	3	0.146	-9.19	0.0053	22	50
97SB56-exp1	1210	3	0.146	-9.19	0.0044	22	85
97SB29-exp1	1210	3	0.146	-9.19	0.0048	22	60
97SB75-exp1	1210	3	0.146	-9.19	0.0051	22	90
97SB56-exp2	1230	3	0.153	-8.96	0.0065	20	100
97SB75-exp2	1230	3	0.153	-8.96	0.0053	20	100
97SB79-exp3	1250	2	0.160	-8.74	0.0046	20	95
97SB29-exp3	1250	2	0.160	-8.74	0.0064	20	98
97SB34-exp2	1165	4	0.133	-9.72	0.0054	20	90
97SB33-exp2	1216	2	0.149	-9.12	0.0058	20	30
97SB68-exp2	1220	4	0.150	-9.07	0.0049	20	< 95
97SB68-exp3	1260	4	0.163	-8.63	0.0053	20	> 95
97SB68-exp4	1300	3	0.177	-8.22	0.0028	20	> 95
97SB63-exp1	1200	3	0.143	-9.3	0.0048	20	< 95
97SB63-exp2	1240	2	0.156	-8.85	0.0046	20	> 95
97SB63-exp3	1280	4	0.170	-8.42	0.0044	20	> 95
97SB67-exp1	1200	4	0.143	-9.3	0.006	20	80
97SB73-exp1	1200	4	0.143	-9.3	0.005	20	< 95
97SB80-exp1	1200	4	0.143	-9.3	0.0051	20	80
97SB67-exp2	1240	3	0.156	-8.85	0.0046	20	80
97SB73-exp2	1240	3	0.156	-8.85	0.0049	20	100
97SB80-exp2	1240	3	0.156	-8.85	0.0043	20	100
97SB63-exp4	1240	3	0.156	-8.85	0.0137	20	100

Table A.1 – *Continued from previous page*

Experiment	T	±	CO/CO_2	$\log(fO_2)$	mass (g)	t (mins)	% homogenised
97SB80-exp3	1240	3	0.156	-8.85	0.0119	20	98
97SB73-exp3	1220	5	0.156	-9.07	0.0174	20	100
97SB41-exp3	1220	5	0.156	-9.07	0.021	20	100
97SB67-exp3	1260	4	0.163	-8.63	0.0253	20	> 95
97SB68-exp5	1260	4	0.163	-8.63	0.0242	20	100
97SB56-exp3	1230	3	0.153	-8.96	0.0222	20	95
97SB75-exp3	1230	3	0.153	-8.96	0.0207	20	100
97SB34-exp3	1200	2	0.143	-9.3	0.0245	20	100
97SB46-exp3	1210	2	0.146	-9.19	0.0108	20	100
97SB63-exp5	1240	4	0.156	-8.85	0.0101	20	100
97SB80-exp4	1280	4	0.170	-8.42	0.0127	21	99
97SB67-exp4	1260	4	0.163	-8.63	0.0158	20	100
97SB56-exp4	1260	4	0.163	-8.63	0.0192	20	100
97SB80-exp5	1280	4	0.170	-8.42	0.0152	20	100
97SB41-exp4	1220	3	0.150	-9.07	0.0165	20	99
97SB46-exp4	1210	3	0.146	-9.19	0.0145	20	99
Z1813.1-exp1	1180	4	0.137	-9.54	0.0068	21	80
Z1817.2-exp1	1180	4	0.137	-9.54	0.0063	21	70
JSH-B006-exp1	1180	3	0.137	-9.54	0.0059	20	80
Z1816.3-exp1	1180	3	0.137	-9.54	0.0108	20	50
Z1813.1-exp2	1220	4	0.150	-9.07	0.006	20	98
Z1817.2-exp2	1220	4	0.150	-9.07	0.0067	20	70
JSH-B006-exp2	1220	3	0.150	-9.07	0.0057	20	100
Z1816.3-exp2	1220	3	0.150	-9.07	0.0119	20	100
Z1813.1-exp3	1260	3	0.163	-8.63	0.0061	20	100
Z1817.2-exp3	1260	3	0.163	-8.63	0.0057	20	100
JSH-B006-exp3	1260	3	0.163	-8.63	0.005	20	100
Z1816.3-exp3	1260	3	0.163	-8.63	0.0119	20	100
Z1813.1-exp4	1220	4	0.150	-9.07	0.0199	20	100
Z1816.3-exp4	1220	3	0.150	-9.07	0.024	20	100
JSH-B006-exp4	1220	3	0.150	-9.07	0.0191	20	100
Z1817.2-exp4	1260	4	0.163	-8.63	0.0222	20	100
Z1816.3-exp5	1220	4	0.150	-9.07	0.0202	20	100
Z1813.1-exp5	1220	4	0.150	-9.07	0.0114	120	100
Z1813.1-exp6	1220	3	0.150	-9.07	0.0119	5	100
Z1813.1-exp7	1300	3	0.177	-8.22	0.01	20	100
Z1813.1-exp8	1220	4	0.150	-9.07	0.0145	20	100
JSH-B006-exp5	1220	4	0.150	-9.07	0.0153	20	100

Table A.1 – *Continued from previous page*

Experiment	T	±	CO/CO_2	$\log(fO_2)$	mass (g)	t (mins)	% homogenised
Z1817.2-exp5	1260	3	0.163	-8.63	0.0164	20	100
PB009-exp1	1260	3	0.163	-8.63	0.0106	20	100
PB009-exp2	1220	3	0.150	-9.07	0.0182	20	100
PB009-exp3	1180	3	0.137	-9.54	0.0064	20	< 95

A.1.2 Sample preparation

Grains were dried and mounted in grids in 25 mm diameter epoxy rings (Buehler EpoThin or Struers EpoFix), set for several days, ground to an arbitrary depth with successively finer silicon-carbide paper, and polished with 9 µm, 3 µm and 1 µm diamond laps. Melt inclusions of interest for analysis by Electron Probe Microanalyser (EPMA) and Secondary Ion Mass Spectrometry (SIMS) were imaged by transmitted and reflected light optical microscopy and by SEM (back-scattered electrons) in order to assess whether they were homogeneous, as well as to identify the presence and severity of fractures, both on the polished surface and beneath it. For example, a minor fracture caused by the quench process is not problematic. However, a fracture present before the furnace treatment (a 'breached' inclusion) may have allowed open-system behaviour of the melt inclusion both in the furnace and over its prior geological history (Nielsen *et al.*, 1998). Breached inclusions tend to have more irregular shapes and/or anomalous chemistries. They can sometimes be identified through glass or other material being present in the fracture, occasionally visible by Mg-Fe diffusion profiles that appear on either side of the fracture.

A.2 EPMA analysis

EPMA analysis was performed on a Cameca SX100 electron microanalyser in wavelength-dispersive (WDS) mode in the Department of Earth Sciences at the University of Cambridge, with the assistance of Dr. Iris Buisman. Analyses were performed with an accelerating voltage of 15 keV on five spectrometers. Counting times, beam current and spot size were varied to be appropriate to the phase analysed. Na and Si were always measured first on their respective spectrometers and Si was sometimes measured on two spectrometers to decrease 'Si-drift'. Any analyses of phases that should have an oxide weight total of 100% (i.e. no significant Fe^{3+} or unanalysed volatiles) were excluded if their totals fell outside of the range $99\% > x < 102\%$.

Primary standards for the EPMA calibration of major elements in all phases were as follows: K-Kα on K-feldspar; P-Kα on apatite; Na-Kα on jadeite; Fe-Kα on fayalite; Ni-Kα on NiO or Ni; Si-Kα

Ca-Kα on diopside; Mg-Kα on olivine (St. Johns); Al-Kα on corundum; Cr-Kα and Mn-Kα on pure metals; Ti-Kα on rutile. PAP sequences were used for interference and matrix corrections. A range of appropriate secondary standards were used to check calibrations. The following specific variations of the setup were used: Glass, 4–6 µm beam diameter and 6 nA beam current; olivine, pyroxene, other silicates, 1 µm beam diameter and 10–20 nA beam current; spinel, 1 µm beam diameter and 40 nA beam current. Average standard deviations from some analytical sessions with the described setup are given in Table A.2; these are calculated from count rates by the Cameca EPMA software.

Phase	SiO_2	TiO_2	Al_2O_3	FeO	MnO	MgO	CaO	P_2O_5	Na_2O	K_2O	Cr_2O_3	NiO
olivine	1.60	0.03	0.04	0.83	0.13	1.96	0.04				0.09	0.13
cpx/opx	1.51	0.07	0.12	0.45	0.09	0.72	0.87	0.02	0.05	0.02	0.10	0.06
glass	1.76	0.08	0.41	0.72	0.16	0.55	0.37	0.06	0.20	0.08	0.13	0.15
spinel 20kV	0.02	0.12	0.30	0.71	0.03	0.23	0.01				0.57	0.03
spinel 15kV	0.02	0.10	0.21	1.56	0.07	0.14	0.01				1.71	0.07

Table A.2: Average uncertainty for different oxides and phases measured by EPMA, calculated from the uncertainty of all measurements as determined by the Cameca EPMA software from count rates (which appear somewhat overestimated relative to repeat analyses). All values are absolute standard deviations given in wt.% oxide.

For the purpose of Al-in-olivine thermometry, a variation of the setup described above was used, a higher precision analysis was required for measuring Al in the olivine host. Olivine-spinel pairs were analysed in three analytical sessions on different dates. A shorter counting time was used in the first session, from which it was apparent that a longer counting time would be preferable in subsequent analytical sessions. In addition, a 20 keV accelerating voltage was used in the first session, whereas 15 keV was used in subsequent sessions. This should have little effect on the precision because the Al K-α line energy is well below the accelerating voltage, and analyses from other analytical sessions with a 15 keV accelerating voltage and the same counting times produced identical uncertainties. Olivine hosts were always analysed at 20 nA with a 1 µm beam diameter, with Al measured with an LTAP crystal to increase the precision. The uncertainties were calculated for each point analysis by the in-house Cameca EPMA software and are based on counting statistics during the measurement. It was found that the absolute uncertainty of Al in olivine was similar regardless of the olivine analysed in a given analytical session. For this reason, an average absolute uncertainty was chosen, leading to a lower relative uncertainty for higher Al crystals. The analytical conditions for measuring Al in olivine hosts are summarised in Table A.3. The average Al concentration was taken from three spot analyses of a single olivine host, measured in a triangular configuration around the spinel, in order to smooth any potential natural variability. Although natural variability increases the uncertainty, Al in averaged olivine has effectively been analysed for triple the time, meaning that the uncertainty used (given in Table A.3) is likely somewhat overestimated.

Date	KeV	Count time (s)	Average $AlO_{1.5}$ 1σ (wt. %)	Relative error for 0.05 wt. % Al_2O_3 olivine (%)
07/03/13	20	30	0.014	28.7
13/12/13	15	60	0.010	20.8
12/01/15	15	140	0.007	14.4

Table A.3: Analytical configuration for measuring Al in olivine by EPMA (for Al-in-olivine thermometry). The absolute uncertainty was very close to the average for every measurement in a given session. Uncertainties calculated from counting statistics. As an example, the relative error for a 0.05 wt. % olivine is also shown.

A.3 SIMS analysis

Rare earth elements (REE) and other trace elements (Rb, Ba, Sr, K, Nb, Ti, Zr, Y, Sc) were analysed by SIMS using the Cameca ims-4f ion microprobe at the NERC microanalysis facility at the University of Edinburgh, with the assistance of Dr. Cees-Jan de Hoog. Analyses were performed over two five day sessions, one in October 2012 and one in October 2013. Similar setups were used in the two sessions. Inclusions were bombarded with a 15 kV primary O^- ion beam, with a secondary voltage of 4500 V minus an offset of 75 V. The beam current used was 3-5 nA, with a spot size of approximately 15 µm. Peak positions were verified before each analysis; mass 130.5 was measured as background in each cycle and was always zero. Six analytical cycles were used per analysis.

NIST-610 was used as a primary calibration standard, and to correct for daily machine drift, where the maximum drift was 16% in ^{175}Lu. Absolute abundances were fixed by normalising ^{42}Ca to the CaO concentration determined by EPMA. Total ^{42}Ca was chosen to counteract the effect of including some host olivine in the analysis of smaller melt inclusions. Oxide interferences were corrected for, with minor adjustment made by using the composition of BCR-2G. A matrix correction was applied using measurements of GSD-1G, BCR-2G, BHVO-2G, BIR-1G, GOR132-G and ML3B-G, where a correction factor was calculated for each element using a linear regression through all standards for analysed vs. published values (from GeoReM, Jochum *et al.*, 2005), with a maximum correction of +25% for Rb. Precision was calculated using repeat analyses of some standards, with relative 1σ = 0.01-0.12 for the range of elements analysed. There was fairly good agreement between the two sessions, as seen in the standard analyses (given in Appendix C) although precision and/or accuracy does vary in some elements. The magnitude of the corrections applied and the precision and accuracy of concentrations as determined from standards are shown in Table A.4 (October 2012 values) and Table A.5 (October 2013 values). Trace element data was collected from 76 picrite inclusions and 84 ferropicrite inclusions. All SIMS analyses of the standards and of the melt inclusions are given in Appendix C.

Element	Drift correction						Matrix correction	Precision*	Accuracy*
Date	08/10/12 am	09/10/12	10/10/12	11/10/12	12/10/12	13/10/12	08/10/12		
Si	-1.30	-2.44	-0.40	-1.83	-2.51	-1.48	1.76	0.87	8.89
K	2.26	-0.03	2.36	7.18	14.06	15.69	20.95	2.92	1.55
Ca	0.00	0.00	0.00	0.00	0.00	0.00	0.00	0.00	0.00
Sc	-0.63	-0.96	-0.18	-0.30	-0.48	-0.66	-4.84	1.26	5.46
Ti	0.09	-0.58	-0.12	1.12	1.81	1.98	11.24	1.04	0.88
Rb	NA	5.60	2.05	7.81	15.90	13.88	17.33	9.72	23.77
Sr	-1.55	-1.37	-2.45	0.85	4.14	2.20	15.51	0.80	1.42
Y	-1.04	-2.19	-2.21	-0.19	2.14	0.49	10.43	1.86	6.16
Zr	0.27	0.18	-1.93	0.48	3.77	4.47	2.08	1.38	3.08
Nb	1.97	2.60	-2.13	2.71	10.34	9.40	15.35	2.97	1.79
Ba	0.44	2.17	-0.92	5.04	12.33	9.12	23.44	1.54	3.15
La	-1.70	0.98	-3.78	0.67	5.73	3.14	13.48	1.26	6.98
Ce	0.50	0.48	0.14	2.75	7.55	5.73	16.39	2.74	2.33
Pr	-1.53	-2.34	-2.68	0.36	5.32	3.18	16.62	3.32	5.19
Nd	-0.72	-0.97	-4.66	1.35	6.24	0.75	13.39	5.71	3.03
Sm	-1.73	-2.38	-0.97	2.23	6.74	3.05	16.91	7.09	6.00
Eu	-1.08	-2.76	-2.42	1.37	6.58	4.69	13.27	6.14	1.49
Gd	-0.57	-1.32	3.15	8.23	15.42	9.85	-1.39	6.02	5.55
Tb	-1.08	-1.54	-1.77	1.62	7.87	5.68	11.76	7.11	9.24
Dy	-0.57	-1.06	-1.76	1.70	9.47	6.45	13.62	4.24	9.63
Ho	-0.35	-1.10	-1.70	1.17	8.93	6.92	10.12	5.39	7.61
Er	-1.05	-1.07	-1.14	1.79	9.22	7.58	10.65	6.53	7.30
Tm	-0.36	-0.62	-1.78	1.51	9.80	7.30	7.36	12.75	12.94
Yb	-1.26	-0.11	-2.01	0.44	7.90	6.80	8.27	10.61	16.51
Lu	0.14	1.37	-1.46	0.96	11.40	9.60	-1.61	20.68	3.87
								n=8	n=8

Table A.4: SIMS data corrections and statistics, October 2012. All values given in %, n indicates the number of analyses used in the calculation. *Precision and Accuracy (%) calculated from combined repeat analyses of BCR, BHVO and ML3B

Element	Drift correction				Matrix correction	Precision*	Accuracy**
	22/10/13	23/10/13	24/10/13	25/10/13			
Si	0.00	0.00	0.00	0.00	0.02	0.02	0.05
K	3.59	-4.71	-9.43	-6.66	17.07	4.28	4.45
Ca	1.95	2.21	1.84	3.05	9.06	1.39	7.71
Sc	0.53	-0.28	0.33	1.85	-2.41	2.06	3.91
Ti	0.72	-1.45	-0.94	-0.23	18.26	1.30	1.53
Rb	5.16	-7.03	-11.02	-6.98	24.81	7.12	2.41
Sr	2.70	-1.55	-3.78	0.11	18.71	1.88	0.42
Y	0.01	-3.39	-3.14	0.86	9.38	2.24	0.01
Zr	1.95	-1.78	-1.23	1.27	4.36	1.97	0.11
Nb	4.59	-4.29	-6.46	0.92	11.37	5.30	6.04
Ba	8.97	-1.43	-3.16	3.32	20.87	3.79	0.56
La	5.34	0.53	-0.93	6.86	2.37	3.37	4.38
Ce	5.51	-1.23	-2.32	6.72	12.45	4.14	2.69
Pr	6.45	-2.00	-1.97	5.11	4.58	3.02	8.91
Nd	8.32	-0.11	-0.54	6.51	3.06	4.98	5.67
Sm	5.10	-3.07	-2.76	4.34	10.43	5.50	4.25
Eu	7.20	-2.35	-1.45	4.65	6.16	8.26	6.46
Gd	1.64	-11.44	-10.12	-4.26	14.16	11.05	5.25
Tb	6.98	-5.80	-3.88	3.25	5.75	9.90	1.32
Dy	8.48	-3.63	-4.18	3.72	9.56	10.53	2.26
Ho	7.03	-6.24	-5.66	1.73	5.06	5.86	7.55
Er	6.84	-7.78	-8.81	0.76	12.12	6.81	2.39
Tm	5.35	-9.24	-10.29	-0.89	4.52	8.28	0.81
Yb	1.98	-12.47	-13.33	-5.47	7.44	9.94	1.44
Lu	1.22	-14.79	-16.20	-8.76	4.00	12.01	3.92
						n=22	n=9

Table A.5: SIMS data corrections and statistics, October 2013. All values given in %, n indicates the number of analyses used in the calculation.
*Precision calculated from combined repeat analyses of BCR, BHVO and ML3B
**Accuracy calculated from repeat analyses of BCR only

A.4 XANES analysis

A.4.1 Analytical method

For Fe-Kα X-ray absorption near edge structure (XANES) spectroscopy, olivines were not heat treated in a furnace. Instead, a 250-500 μm size fraction of various samples was separated from crushed material, mounted and polished down to a 1 μm diamond grit in order to expose spinel inclusions at the surface for analysis. 19 pristine-looking spinel inclusions > 10 μm diameter at the exposed surface were selected for analysis. Standards were similarly prepared. EPMA major element data was collected prior to XANES spectroscopy.

Fe-Kα XANES spectroscopy was performed in fluorescence mode at beamline I18 at Diamond Light Source, with the assistance of Dr. Konstantin Ignatyev. An experimental geometry was used where the sample was at 80° to the incident beam and 10° to the detector, thus minimising detection of X-rays fluoresced from deeper within the sample, which may derive from olivine if the boundary with the spinel inclusion is shallow. The X-ray beam had an area of 2x3.5 μm on the sample and was monochromatised using a double Si(333) crystal for improved energy step resolution. A germanium detector with nine elements was used with a maximum count rate of no greater than 200 kHz. The energy step sizes and dwell times used were chosen to maximise resolution in the pre-edge and edge structures (Table A.6).

Energy range (eV)	Step size (eV)	Dwell time (s)
7020.0-7100.0	10	1
7100.0-7106.0	1.0	2
7106.0-7110.0	0.25	2
7110.0-7126.0	0.1	2.5
7126.0-7148.0	0.5	1
7148.0-7410.0	2	1
7410.0-7500.0	5	1

Table A.6: Energy step sizes and dwell times

Nine standards were measured in order create an empirical calibration for the oxidation state of Fe in spinels from Fe-Kα XANES spectra. The standards used were KLB 8311, BAR 8601-9, MHP 79-4, MBR 8307, IM 8703, Mo 103, DB 8802-1, DB 8803-1 and Vi-314-580, with Mössbauer spectroscopy analyses of $Fe^{3+}/\Sigma Fe$ published by Wood and Virgo (1989) and Ionov and Wood (1992). Standards were donated by Prof. Bernie Wood (Oxford University). It should be noted that some of the $Fe^{3+}/\Sigma Fe$ values have since been disputed, and as such, the $Fe^{3+}/\Sigma Fe$ of spinel standard DB8803-1 was adjusted by -0.10, according to an unpublished recent measurement (F. Davis, pers. comm.).

Repeat analyses of standard KLB-8311 were used to check data reproducibility; the results show that the data is highly reproducible and that no drift correction is required (Fig. A.3a). Beam damage, i.e. the self-oxidation or reduction of Fe under the X-ray beam, was tested by analysing the first

pre-edge peak (which is sensitive to Fe^{2+}) at 7113 eV of sample KLB-8311 for 80 seconds, where collection commenced slightly prior to the shutter being opened. The results suggest that in this initial time period, no change in Fe oxidation occurs (Fig. A.3b). Repeats of the full $\sim$ 20 minute analysis on the same spot show that there is also no change in oxidation state or other features of the spectrum over longer exposure times.

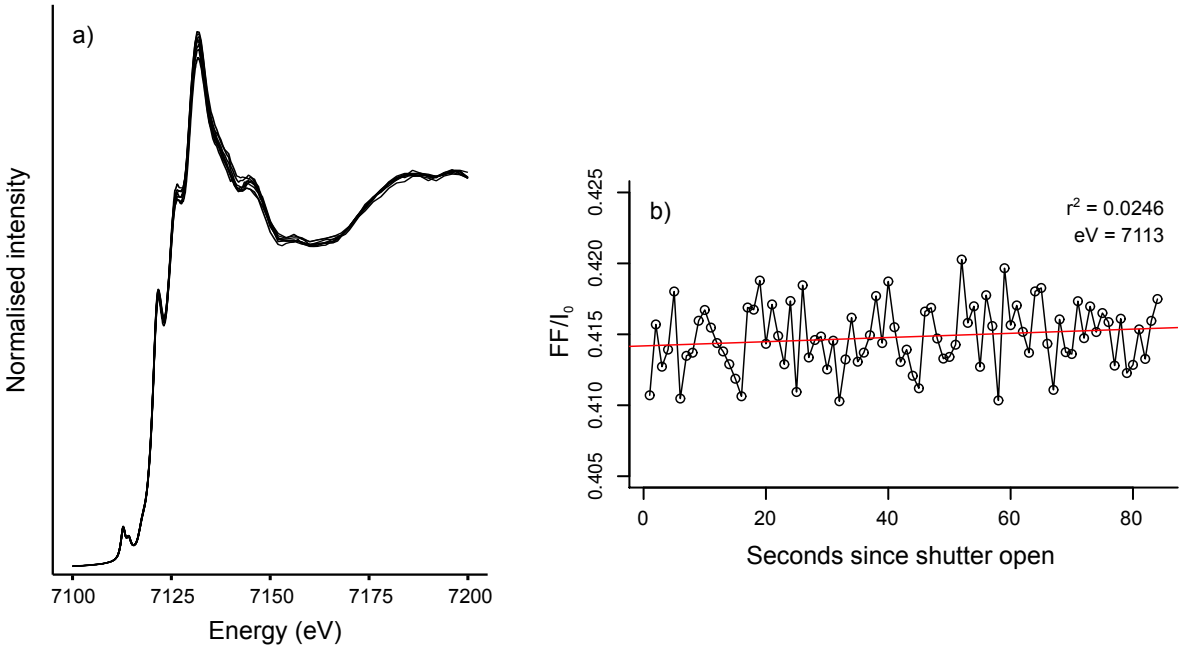

Figure A.3: a) Eight spectra (normalised intensity as a function of energy) of standard KLB-8311 analysed at various points throughout the 48 hour experimental session at beamline I18. b) Time series of fluoresced intensity (FF) normalised to I_0 analysed at 1s intervals over the first 84s of X-ray beam exposure at 7113 eV.

Raw spectra were normalised in two stages. Firstly, a linear baseline was fitted by regression of FF/I_0 (fluoresced intensity (FF) normalised to I_0) in the energy window 7020 to 7090 eV, before the pre-edge peaks. This baseline was subtracted from the spectra, which were then normalised to an edge-step of 1 by a fitting a curve through the 7170-7500 eV region (Fig. A.4).

A.4.2 Valence state calibration

An empirical valence state calibration was created, linking $Fe^{3+}/\Sigma Fe$ of the standards to certain features of the XANES spectra. No detailed studies of Fe-Kα XANES spinel spectra exist in the literature, although four spectra of spinel end-members were published by Wilke *et al.* (2001). Spinel is a solid solution of many end-members and its chemistry is highly varied in natural samples (Barnes and Roeder, 2001). For the calibration, one or more features of the sample spectra had to be identified that vary systematically with $Fe^{3+}/\Sigma Fe$ but are insensitive to changes in other aspects of the spinel

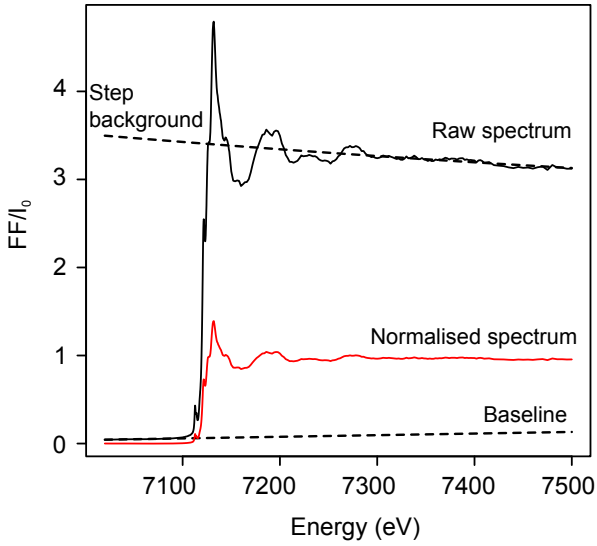

Figure A.4: KLB-8311 spectrum illustrating the baseline in the pre-edge region, which is subtracted from the raw spectrum, and the background in the edge step, to which the spectrum is normalised.

chemistry. The general appearance of the spectra of spinels from different samples is quite varied and is clearly controlled by differences in their chemistry. Although the expected $Fe^{3+}/\Sigma Fe$ range in the spinel samples lies mostly within and a little above the standard range, the sample set unfortunately is not well bracketed by the standards in terms of other aspects of their chemistry, such as Cr/(Cr+Al), Mg/(Mg+Fe) and TiO_2. The analyses of spinel samples which were very different to the standards were discarded. Molar Cr+Al (on a per formula unit basis) tends to be around 1.9 in the standards and is a measure of the proportion of spinel and chromite end-members in the solid solution. For the purpose of this study, 1.5 is an arbitrary cut off, below which less than 3/4 of the spinel constitutes these end-members. 11 samples were kept and eight discarded. The mismatch between standard and sample compositions is because the samples are magmatic whereas the standards are from mantle xenoliths, reflecting the lack of availability of magmatic standards.

Peak fitting was performed in order to extract quantitative information from the spectra. The most common spectral feature used to calibrate $Fe^{3+}/\Sigma Fe$ in both natural minerals and glasses is the ratio of the areas of the two major peaks in the pre-edge region (Cottrell *et al.*, 2009; Wilke *et al.*, 2001). The analyses of some end-member compositions of Wilke *et al.* (2001) indicate that the same is likely to be true for spinel. To test this, all spectra (both standards and samples) were fitted with three Lorentzian peaks (P1, P2, P3) in the pre-edge region plus a fourth, the shoulder of which was used for the edge background and provided an excellent fit (Fig. A.5a). Additionally, the differential spectrum was fitted by three Lorentzian peaks (D1, D2, D3) over the region 7104.5-7120.98 eV to capture the immediate edge features (Fig. A.5b). As opposed to glasses, which have a single, sharp edge (Cottrell *et al.*, 2009), spinel has a stepped edge, that gives three peaks when differentiated. This

stepped edge is clearly seen in Fig. A.3a. The origin of these steps is unknown, but they appear to change in spacing and size with spinel composition.

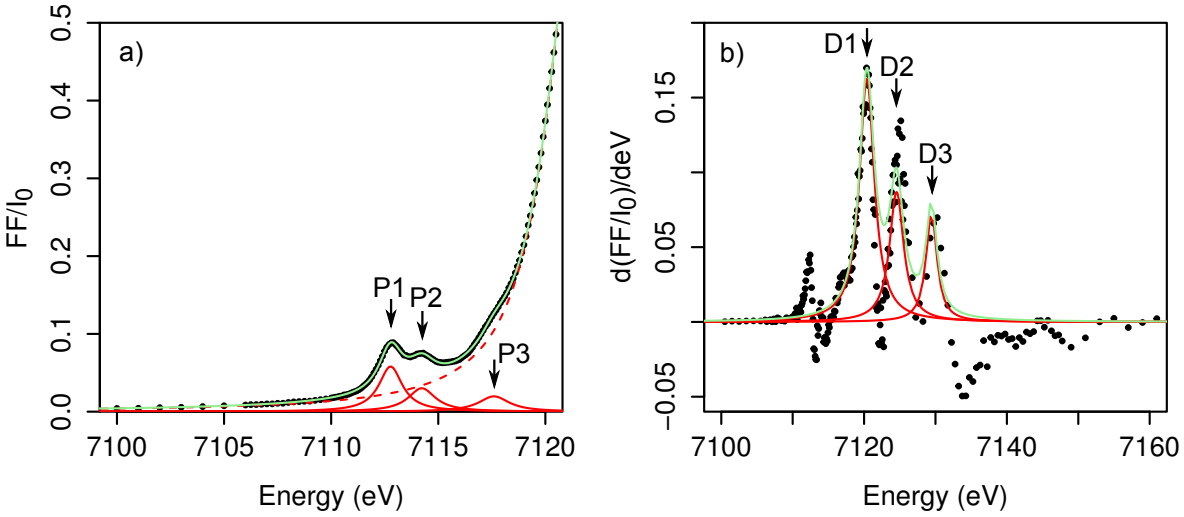

Figure A.5: An example showing the peaks used to fit the XANES spectra, in this case of sample 23-97SB33-02. a) Lorentzian peaks (red lines) P1, P2 and P3 fitted to FF/I_0 (black points) as a function of energy (eV). The left-hand shoulder of a fourth Lorentzian peak was used to fit the edge baseline (red dashed line). The resultant spectrum is shown in green. b) Lorentzian peaks D1, D2 and D3 (red lines) fitted to the differential form of (a), with a scale expanded into the post-edge region.

Testing for correlation between all elements of the spinel standards and all features of the above mentioned peaks showed that the ratio of the areas of the two major pre-edge peaks ($P1_{area}/P2_{area}$) strongly correlates with oxidation state and is insensitive to all other elements. $Fe^{3+}/\Sigma Fe$ in the spinel standards only weakly co-varies with other aspects of their chemistry. $Fe^{3+}/\Sigma Fe$ is also strongly linked to the area of the second differential peak ($D2_{area}$). When plotting $Fe^{3+}/\Sigma Fe$ against both of these features, it was clear that two of the nine published spinel $Fe^{3+}/\Sigma Fe$ values were outliers, from what would otherwise be tightly defined curves ($P1_{area}/P2_{area}$ shown in Fig. A.6). Other workers have noticed some inconsistencies in the published spinel dataset, and for this reason, an error in the published values is suspected and these two standards are discounted. The compositional range of the spinel samples (where $Fe^{3+}/\Sigma Fe$ is unknown but other aspects of the chemistry are known) is much broader. The sensitivity of $P1_{area}/P2_{area}$ to other aspects of the composition was tested by examining all analysed spinels (standards and samples) together. No important dependency was found, with a small positive correlation existing with MgO and a small negative correlation with FeO (FeO and MgO being linked by Mg#).

Discounting the two suspected erroneous standards (unfilled circles on Fig. A.6), a power-law fit was calculated by non-linear least squares regression of $Fe^{3+}/\Sigma Fe$ as a function of $P1_{area}/P2_{area}$ (Fig. A.6):

$$Fe^{3+}/\Sigma Fe = 0.340 \pm 0.011 (P1_{area}/P2_{area})^{-1.229 \pm 0.082} \quad (A.2)$$

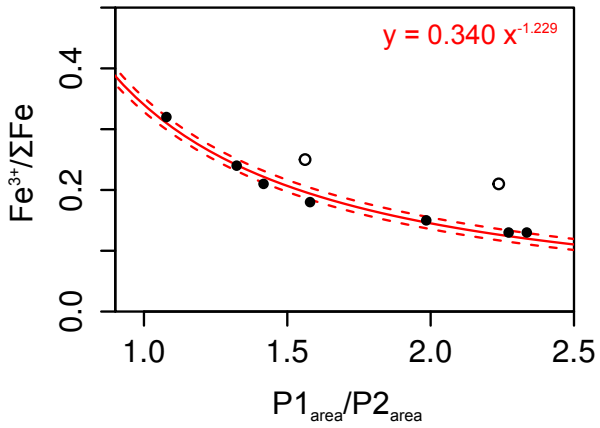

Figure A.6: Known $Fe^{3+}/\Sigma Fe$ of standards plotted as a function of $P1_{area}/P2_{area}$. Open circles, standards which are outliers both in this curve and in a similar curve of $Fe^{3+}/\Sigma Fe$ as a function of $D2_{area}$. These are not included in the curve fit and are assumed to have erroneous published values. Closed circles are the accepted standards. The red curve is fitted by non-linear least squares regression and dashed lines show the 1σ uncertainty bracket calculated a Monte Carlo method.

The fit was slightly improved by adding a linear MgO term (FeO and Mg# are not used as, to know them accurately, $Fe^{3+}/\Sigma Fe$ must be known), but this extra term was not significant to the 95% confidence level. The area of D2 was not used because it is strongly correlated with many other aspects of the spinel chemistry such as Mg#, Al_2O_3 and Cr_2O_3. Because of the mismatch in sample and standard compositions, the error bracket shown in Fig. A.6 does not encompass the full error for the samples, where uncertainty is imposed by other aspects of the spinel composition also affecting $P1_{area}/P2_{area}$.

A.4.3 $Fe^{3+}/\Sigma Fe$ correction for EPMA data

The spinel standards and samples were all previously measured by EPMA. $Fe^{3+}/\Sigma Fe$ was determined by recalculating the EPMA data as a mineral formula on a four oxygen basis. Comparing the EPMA estimates of $Fe^{3+}/\Sigma Fe$ of the nine standards with published values showed that the former overestimated the Mössbauer estimates in a non-systematic way. Even after removing the two standards with suspected incorrect published $Fe^{3+}/\Sigma Fe$ values, the offset is difficult to determine. The EPMA data may suffer both low accuracy and precision because the stoichiometric method means that the uncer-

tainty on every element measured will combine in the estimation Fe^{3+}. Additionally, other elements such as V may be present in significant proportions, but were not analysed.

The $Fe^{3+}/\Sigma Fe$ ratio for the spinel samples obtained by XANES is compared with the previous EPMA data along with the standards in Fig. A.7. These data almost all fall below unity. Most spinel samples have $Fe^{3+}/\Sigma Fe$ of around 0.2-0.3, where the EPMA data indicated them to be 0.3-0.4. Fig. A.7 indicates that the EPMA method consistently overestimates Fe^{3+}, and that a correction factor of 0.59 (least squares regression to both samples and standards) brings the EPMA data in line with the XANES data. The offset seen in Fig. A.7 is not perfectly consistent and the uncertainty on the magnitude of the correction is quite large. Additionally, for spinels with major-element chemistries or $Fe^{3+}/\Sigma Fe$ far outside of the range of the spinel standards, the correction to $Fe^{3+}/\Sigma Fe$ may not be quite right, and for these samples the final $Fe^{3+}/\Sigma Fe$ estimation should be regarded as semi-quantitative (but still a significant improvement on the EPMA estimate). This correction factor is applied to the full dataset of more than 100 spinels analysed by EPMA to improve the determination of their $Fe^{3+}/\Sigma Fe$ ratios. $P1_{area}/P2_{area}$, $Fe^{3+}/\Sigma Fe$ and some aspects of major element chemistry of the seven accepted standards and 11 accepted samples are given in Table A.7.

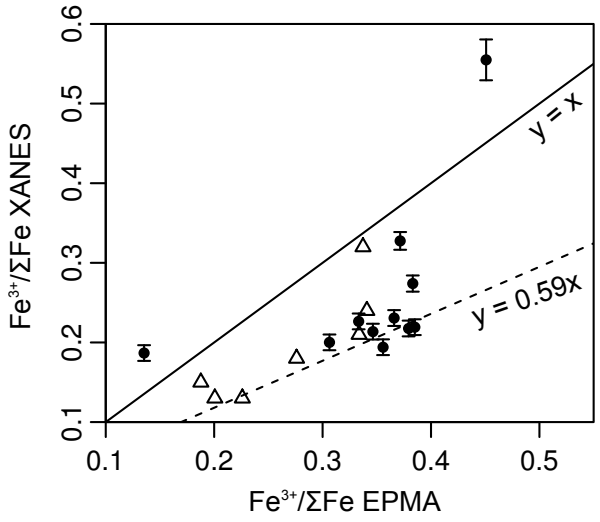

Figure A.7: $Fe^{3+}/\Sigma Fe$ estimate by XANES plotted against $Fe^{3+}/\Sigma Fe$ estimate by EPMA. Standards, open triangles (open symbols of Fig. A.6 excluded); samples, closed circles (subset with (Al + Cr) > 1.5). Error bars are 1σ uncertainty in the calibration curve fit (A.6) but are underestimates due to compositional mismatch between samples and standards. Points mostly fall well below the 1:1 line; the 1:0.59 line is fitted by least squares regression and is used as a correction factor to bring the EPMA $Fe^{3+}/\Sigma Fe$ estimates of all of the spinel samples in line with that suggested by XANES.

Code	Mg#	Cr#	Cr+Al	TiO_2	$\frac{P1_{area}}{P2_{area}}$	EPMA $Fe^{3+}/\Sigma Fe$	
Standard							Mössbauer $Fe^{3+}/\Sigma Fe$
KLB-8311	0.66	0.53	1.93	0.12	2.24	0.23	(0.21)
MO-103	0.74	0.20	1.96	0.10	2.34	0.20	0.13
Vi-314-580	0.72	0.20	1.90	0.41	1.32	0.34	0.24
DB-8802-1	0.76	0.12	1.93	0.14	1.42	0.33	0.21
MHP-79-4	0.79	0.09	1.96	0.11	2.27	0.23	0.13
BAR-8601-9	0.76	0.14	1.94	0.10	1.58	0.28	0.18
MBR-8307	0.74	0.20	1.94	0.08	1.56	0.28	(0.25)
IM-8703	0.70	0.13	1.91	0.07	1.08	0.34	0.32
DB-8803-1	0.68	0.49	1.94	0.19	1.98	0.19	0.15
Sample							XANES $Fe^{3+}/\Sigma Fe$
06-97SB62-09	0.41	0.58	1.64	0.90	0.67	0.45	0.55
06-97SB62-11	0.64	0.63	1.85	0.66	1.46	0.35	0.21
17-97SB41-01	0.37	0.60	1.70	0.65	1.44	0.38	0.22
17-97SB41-05	0.43	0.65	1.73	0.62	1.43	0.39	0.22
17-97SB80-14s2	0.27	0.46	1.57	1.96	1.03	0.37	0.33
23-08SB33-06	0.44	0.54	1.68	1.99	1.37	0.37	0.23
23-97SB33-01	0.65	0.57	1.81	1.13	1.19	0.38	0.27
23-97SB33-02	0.64	0.61	1.85	0.53	1.58	0.36	0.19
23-97SB33-05	0.58	0.50	1.76	3.42	1.63	0.14	0.19
23-PB009-01	0.37	0.54	1.66	2.14	1.39	0.33	0.23
23-PB009-02	0.44	0.50	1.75	1.54	1.54	0.31	0.20

Table A.7: Major element compositions, $P1_{area}/P2_{area}$ and $Fe^{3+}/\Sigma Fe$ of spinel standards and samples (Al + Cr > 1.5 per formula unit (p.f.u.) only). For the standards, the published Mössbauer value is given, with the two suspected erroneous values indicated in brackets. For the samples, $Fe^{3+}/\Sigma Fe$ calculated from $P1_{area}/P2_{area}$ according to equation A.2. Cr+Al is in cations p.f.u. DB8803-1 was adjusted by -0.10 from the published value of 0.25.

Appendix B

Modelling input files

THERMOCALC calculations, Chapter 4

Version 288 (updated 24/01/15) dataset of Holland and Powell (2011) was used, with calculations performed in THERMOCALC version 340L. The mixing models and dataset used are provided on the attached cd and online as supplementary material to Jennings and Holland (2015):

Dataset tc-ds622.txt

AX file (mixing models) tc-NCFMASCrO.txt

pMELTS calculations, Chapter 4

Calculations were performed using the MELTS and pMELTS models (Ghiorso *et al.*, 2002; Ghiorso and Sack, 1995) in alphaMELTS (v.1.3.1, (Smith and Asimow, 2005)). The new garnet model is used and fO_2 is not imposed. Input files details are documented below.

KLB-1 solidus

These calculations are performed on a 'nominal' solidus (F=0.005). The KLB-1 bulk composition of Davis et al. (2009) is used, with Fe_2O_3 set to 0.3 wt.%. Components considered are those in the system NCFMASOCrTi, i.e. the components used in the NCFMASOCr model (Jennings and Holland, 2015) plus TiO_2; results were then normalised, excluding TiO_2. Input files are as follows:

MELTS file

```
Title:  KLB-1, majors Davis et al., 2009
Initial Composition:  SiO2 44.84
Initial Composition:  Al2O3 3.51
Initial Composition:  FeO 7.93
```

```
Initial Composition:  Fe2O3 0.3
Initial Composition:  MgO 39.52
Initial Composition:  CaO 3.07
Initial Composition:  Na2O 0.3
Initial Composition:  TiO2 0.11
Initial Composition:  Cr2O3 0.32
Initial Temperature:  1500.0
Initial Pressure:  40000.00
Final Pressure:  1
Increment Pressure:  -500
```

Settings file

n.b. ! = line not read i.e. variable set to FALSE

```
ALPHAMELTS_VERSION pMELTS
!ALPHAMELTS_OLD_GARNET true
!ALPHAMELTS_ALTERNATIVE_FO2 true
!ALPHAMELTS_IMPOSE_FO2 true
ALPHAMELTS_MODE isentropic
ALPHAMELTS_DELTAP -500
ALPHAMELTS_DELTAT 0
ALPHAMELTS_MAXP 40000
ALPHAMELTS_MINP 1
ALPHAMELTS_MAXT 2400
ALPHAMELTS_MINT 500
```

Batch file

```
1, KLB1.melts, 10, 1 , 4, 1, liquid, 1, 0.005, 0, 0
```

Isobaric melting calculations

Isobaric calculations were performed on the bulk composition KLB-1, using the composition given above, and MM-3, Falloon *et al.* (2008) with Fe_2O_3 set to 0.3 wt.%. Components considered are as above. Input files are as follows:

MELTS file

```
Title:  MM-3, Falloon 2008
Initial Composition:  SiO2 45.50
Initial Composition:  Al2O3 3.98
```

```
Initial Composition:  Fe2O3 0.30
Initial Composition:  FeO 6.85
Initial Composition:  MgO 38.30
Initial Composition:  CaO 3.57
Initial Composition:  Na2O 0.31
Initial Composition:  Cr2O3 0.68
Initial Composition:  TiO2 0.11
Initial Temperature:  2000.0
Final Temperature:  1300
Initial Pressure:  15000
Final Pressure:  15000
Increment Temperature:  -10
Increment Pressure:  0
```

Settings file

```
ALPHAMELTS_VERSION pMELTS
!ALPHAMELTS_ OLD_GARNET true
ALPHAMELTS_MODE isobaric
!ALPHAMELTS_ALTERNATIVE_FO2 true
!ALPHAMELTS_IMPOSE_FO2 true
!ALPHAMELTS_FRACTIONATE_SOLIDS true
ALPHAMELTS_DELTAP 0
ALPHAMELTS_DELTAT -10
ALPHAMELTS_MAXP 40000
ALPHAMELTS_MINP 1
ALPHAMELTS_MAXT 2400
ALPHAMELTS_MINT 500
```

Appendix C

Data tables

Data tables printed in this appendix are as follows:

C.1 Whole-rock data, part 1

C.2 Whole-rock data, part 2

C.3 Summary of olivine forsterite contents

C.4 New olivine phenocryst core EPMA data from thin sections

C.5 Average pyroxene compositions per sample

C.6 EPMA compositions of spinel inclusions and host olivine pairs, for Al-in-olivine thermometry, including calculated temperatures and error brackets

C.7 SIMS analyses of natural and synthetic basaltic standards

C.8 Major elements of melt inclusions, analysed by EPMA

C.9 Trace element (except REE) compositions of olivine-hosted melt inclusions, analysed by SIMS

C.10 REE element compositions of olivine-hosted melt inclusions, analysed by SIMS

C.11 XANES peak fitting results

The above data is provided in .csv format on the accompanying cd. Additional data tables and other materials provided in electronic format are:

1. Picrite and ferropicrite pyroxene phenocryst major element compositions
2. Compilation of olivine data, both new and unpublished, which is summarised in C.3.
3. Raw XANES spectra

4. THERMOCALC input files and dataset used in this thesis

5. R script for trace element and thermal modelling script

Table C.1: Whole-rock data, part 1. References for data sources: 1, Thompson *et al.* (2001); 2, Gibson *et al.* (2000); 3, Riley *et al.* (2005); 4, Heinonen *et al.* (2010). Sample types: P, Horingbaai-type picrite; Fp, ferropicrite; Ahl., Ahlmannryggen; Vest., Vestfjella. Subsctipt t denotes the time of emplacement. Number of significant figures as published.

Sample	Sample type	Ref.	SiO_2	TiO_2	Al_2O_3	$Fe_2O_3^T$	MnO	MgO	CaO	Na_2O	K_2O	P_2O_5	LOI	Ba	Cr	Hf	Nb	Ni	Pb	Rb	Sc	Sr
97SB79	Etendeka P	1	46.62	0.8	10.56	12.09	0.16	19.7	8.22	1.32	0.34	0.07	0.76	67	1472	1.5	3.6	744	1.8	12.0	19	142
97SB34	Etendeka P	1	46.15	1.02	10.97	12.11	0.16	18.45	8.75	1.32	0.34	0.09	0.76	67	1302	1.64	4	770	0.9	16.9	19	156
97SB41	Etendeka P	1	47	1.07	11.56	11.96	0.16	17	9.17	1.42	0.27	0.09	0.67	92	1209	1.78	4.3	696	1.0	22.3	22	174
97SB37	Etendeka P	1	46.65	1.09	13.19	11.52	0.16	15.29	10.63	1.63	0.3	0.11	0.64	73	1011	1.61	6.9	556	0.9	10.3	22	201
97SB33	Etendeka P	1	47.27	1.02	13.28	11.86	0.17	13.56	10.9	1.7	0.23	0.09	0.76	69	795	1.43	4.8	478	0.9	28.2	29	177
97SB56	Etendeka P	1	47.54	1.04	13.09	12.07	0.16	13.56	10.28	1.55	0.3	0.08	0.72	60	993	1.59	4	441	1.3	11.1	29	159
97SB51	Etendeka P	1	47.78	1.22	13.36	12.52	0.17	11.44	11.53	1.83	0.29	0.1	0.96	58	596	1.66	5.6	337	0.6	12.0	30	184
97SB62	Etendeka P	1	48.27	1.3	13.44	12.26	0.17	11.39	11.3	1.8	0.26	0.11	0.38	71	583	1.94	5.8	318	1.3	8.2	30	199
97SB35	Etendeka P	1	47.44	1.16	13.9	12.43	0.17	11.18	11.68	2.12	0.29	0.1	0.76	58	610	1.63	5.5	309	0.5	9.6	33	163
97SB53	Etendeka P	1	46.84	1.19	14.08	12.24	0.17	10.57	11.67	1.82	0.2	0.11	1.03	83	585	1.71	7.2	306	0.7	5.7	31	196
97SB29	Etendeka P	1	47.64	1.13	14.01	12.62	0.18	10.37	11.86	2.02	0.33	0.1	0.42	83	548	1.57	7.3	272	0.7	4.0	32	173
97SB61	Etendeka P	1	48.4	1.3	13.4	12.13	0.18	10.29	11.71	1.94	0.21	0.11	1.31	69	596	2.15	5.9	376	2.0	7.1	30	222
97SB42	Etendeka P	1	50.69	0.79	14.43	10.95	0.17	10.09	10.61	1.96	0.27	0.08	1.49	157	833	2.28	5.5	273	2.9	34.4	31	143
97SB75	Etendeka P	1	47.83	1.22	14.15	12.63	0.17	9.63	11.87	1.52	0.44	0.09	0.47	38	510	1.7	4.1	234	0.5	4.0	35	159
97SB46	Etendeka P	1	49.07	1.33	14.43	12.02	0.17	9.6	11.92	1.83	0.13	0.1	1.13	54	424	1.81	3.6	242	0.7	6.5	31	182
97SB64	Etendeka P	1	49.77	1.2	14.05	11.87	0.17	8.51	11.79	1.97	0.17	0.11	0.27	97	407	2.35	5.3	157	8.3	11.0	35	215
97SB44	Etendeka P	1	48.77	1.31	14.76	11.64	0.16	8.5	12.11	2.6	0.44	0.11	0.63	59	381	1.89	5.3	191	1.0	11.3	31	200
97SB70	Etendeka P	1	49.33	1.15	14.66	11.4	0.19	8.3	12.21	2.13	0.27	0.1	1.61	82	634	1.98	5	305	4.4	7.2	33	216
97SB28	Etendeka P	1	48.37	1.41	14.85	12.03	0.17	7.5	12.58	1.85	0.46	0.12	0.42	98	243	-	6	111	-	20.0	33	254
97SB27	Etendeka P	1	52.69	1.75	14.62	11.24	0.16	5.87	10.07	2.18	0.55	0.21	0.42	148	207	3.76	11	55	1.6	14.4	30	329
97SB32	Etendeka P	1	52.65	1.75	14.33	11.36	0.15	5.62	10.31	2.53	0.59	0.21	0.42	164	213	3.75	11	53	1.8	33.1	32	336
97SB26	Etendeka P	1	51.4	2.21	13.33	15.25	0.22	4.76	7.24	2.36	0.86	0.44	0.42	504	7	5	34.6	27	8.9	91.7	29	261
97SB31	Etendeka P	1	51.33	2.16	13.41	14.85	0.24	4.49	7.72	3.61	1.87	0.45	0.42	566	6	4.88	34.1	25	6.5	157.0	28	372
96SB48	Etendeka Fp	2	46.14	1.91	9.52	16.7	0.19	15.39	8.18	2.03	0.63	0.17	0.22	267	494	3	12.8	866	3.3	13.4	24	488
97SB63	Etendeka Fp	2	45.66	2.32	9.5	17.46	0.19	14.04	7.9	2.01	0.88	0.3	0.89	353	412	3.1	16.3	681	3.3	18.5	13	439
97SB67	Etendeka Fp	2	49.23	2.16	10.04	15.19	0.15	12.54	8.33	2.12	0.84	0.24	0.53	324	520	3.1	12.1	478	3.0	19.0	19	474
97SB68	Etendeka Fp	2	46.91	1.75	9.09	16.56	0.17	14.94	8.08	1.94	0.68	0.19	0.43	144	601	2.73	10.5	660	2.5	12.9	16	319

Table C.1 – *Continued on next page*

Sample	Sample type	Ref.	SiO_2	TiO_2	Al_2O_3	$Fe_2O_3^T$	MnO	MgO	CaO	Na_2O	K_2O	P_2O_5	LOI	Ba	Cr	Hf	Nb	Ni	Pb	Rb	Sc	Sr
97SB73	Etendeka Fp	2	46.63	2.91	10.3	15.75	0.17	12.01	8.87	2.3	1.13	0.33	1.59	437	441	4.01	24	482	3.7	21.0	18	584
97SB66	Etendeka Fp	2	47.03	2.79	15.18	15.63	0.17	5.1	7.57	4.13	1.08	0.37	0.22	492	8	4.07	21	15	3.3	28.0	19	781
97SB72	Etendeka Fp	2	48.51	1.99	13.88	15.46	0.18	6.8	9.78	3.55	0.45	0.16	2.55	337	129	2.43	10.6	273	1.2	10.2	17	1064
97SB76	Etendeka Fp	2	50.68	2.41	12.73	14.75	0.16	6.9	7.87	3.79	1.12	0.26	1.86	475	706	3.79	14.9	207	3.6	23.0	23	513
97SB80	Etendeka Fp	2	48.17	1.6	12.71	14.88	0.18	11.28	8.48	2.4	0.54	0.18	1.22	206	575	2.75	7.5	276	2.0	9.0	16	286
PB9	Etendeka Fp	1	46.36	1.89	11.68	14.58	0.19	11.71	10.35	2.01	0.88	0.21	0.05	222	728	3.2	12.7	275	2.3	12.6	25	403
Z1813.1	DML Ahl. Fp	3	45.22	3.5	9.59	14.73	0.17	12.19	9.87	1.65	0.32	0.22	1.93	79	728	6.19	9.6	597	1.3	6.5	32	282
Z1816.3	DML Ahl. Fp	3	45.78	3.25	8.14	12.27	0.18	21.61	7.67	1.25	0.55	0.19	1.28	53	823	5.76	7.91	727	1.0	4.0	32	230
Z1817.2	DML Ahl. Fp	3	46.54	3.86	10.22	14.44	0.17	12	9.91	1.57	0.27	0.24	0.77	65	683	6.93	10.1	578	1.1	6.2	36	283
JSH/B006	DML Vest. Fp	4	44.86	3.01	8.19	17.99	0.21	15.54	9.02	1.75	0.87	0.36	2.42	225	579	4.04	18.54	660	2.3	20.8	19	520

Table C.2: Whole-rock data, part 2. Caption as for Table C.1.

Sample	Ta	Th	U	Y	Zr	La	Ce	Pr	Nd	Sm	Eu	Gd	Tb	Dy	Ho	Er	Tm	Yb	Lu	$(\frac{^{87}Sr}{^{86}Sr})_t$	εNd	$(\frac{^{206}Pb}{^{204}Pb})_t$	$(\frac{^{207}Pb}{^{204}Pb})_t$	$(\frac{^{208}Pb}{^{204}Pb})_t$
97SB79	0.24	1.03	0.34	15	54	4.9	11.7	1.72	8.1	2.22	0.69	2.45	0.42	2.50	0.50	1.38	0.22	1.29	0.2	0.70610	3.72	18.75	15.69	38.29
97SB34	0.22	0.39	0.11	16	66	4.4	11.1	1.72	8.3	2.35	0.81	2.69	0.44	2.64	0.53	1.43	0.23	1.3	0.21	0.70488	5.44	18.26	15.54	37.77
97SB41	0.23	0.43	0.12	18	73	4.7	11.8	1.83	9.0	2.49	0.84	2.97	0.46	2.81	0.57	1.54	0.24	1.4	0.22	0.70742	5.59	18.38	15.64	38.09
97SB37	0.35	0.56	0.16	18	67	5.3	12.7	1.89	9.2	2.46	0.84	2.75	0.45	2.71	0.56	1.48	0.23	1.37	0.21	-	-	-	-	-
97SB33	0.26	0.59	0.15	18	56	4.7	10.8	1.60	7.8	2.14	0.78	2.65	0.45	2.77	0.56	1.55	0.24	1.42	0.22	0.70499	6.43	18.55	15.61	38.04
97SB56	0.23	0.7	0.23	18	63	4.3	10.6	1.65	8.0	2.32	0.80	2.83	0.47	2.82	0.57	1.56	0.24	1.44	0.22	0.70454	5.43	18.60	15.67	38.15
97SB51	0.3	0.44	0.12	20	65	4.7	11.4	1.75	8.6	2.52	0.89	3.08	0.51	3.08	0.62	1.70	0.27	1.55	0.24	0.70547	8.35	18.04	15.54	37.56
97SB62	0.31	0.64	0.22	21	78	5.3	13.3	2.07	10.2	2.89	0.98	3.32	0.55	3.26	0.65	1.72	0.27	1.58	0.24	0.70365	7.33	18.50	15.67	38.00
97SB35	0.3	0.36	0.1	22	64	4.3	10.5	1.61	8.2	2.46	0.90	3.10	0.54	3.32	0.69	1.90	0.31	1.79	0.27	-	-	-	-	-
97SB53	0.37	0.55	0.15	21	67	5.4	12.5	1.85	9.0	2.60	0.92	3.09	0.51	3.22	0.65	1.75	0.27	1.66	0.25	0.70326	9.07	18.08	15.59	37.69
97SB29	0.38	0.49	0.13	22	63	5.2	11.7	1.71	8.4	2.43	0.89	3.08	0.53	3.31	0.69	1.92	0.30	1.8	0.27	0.70320	7.84	18.03	15.56	37.63
97SB61	0.35	0.73	0.24	21	81	5.8	14.9	2.32	11.5	3.24	1.09	3.58	0.61	3.67	0.73	1.98	0.30	1.78	0.27	-	-	-	-	-
97SB42	0.34	2.46	0.32	24	84	9.8	20.9	2.83	12.2	2.95	0.83	3.33	0.60	3.74	0.79	2.27	0.37	2.22	0.34	-	-	-	-	-
97SB75	0.22	0.33	0.09	22	66	3.6	9.1	1.45	7.6	2.52	0.92	3.18	0.56	3.44	0.70	1.90	0.29	1.75	0.26	0.70319	8.72	17.98	15.56	37.56
97SB46	0.21	0.43	0.12	21	73	3.8	10.4	1.71	8.8	2.68	0.92	3.23	0.54	3.27	0.67	1.80	0.28	1.63	0.25	0.70350	7.98	18.29	15.63	37.70
97SB64	0.34	1.49	0.49	23	84	7.3	17.6	2.63	12.6	3.43	1.08	3.83	0.65	3.93	0.80	2.17	0.34	1.96	0.3	0.70630	4.05	18.95	15.68	38.46
97SB44	0.28	0.47	0.16	22	75	4.5	11.8	1.90	9.6	2.85	0.99	3.42	0.56	3.47	0.70	1.87	0.29	1.73	0.26	0.70366	8.01	18.27	15.59	37.76

Table C.2 – *Continued on next page*

Sample	Ta	Th	U	Y	Zr	La	Ce	Pr	Nd	Sm	Eu	Gd	Tb	Dy	Ho	Er	Tm	Yb	Lu	$(\frac{^{87}Sr}{^{86}Sr})_t$	εNd	$(\frac{^{206}Pb}{^{204}Pb})_t$	$(\frac{^{207}Pb}{^{204}Pb})_t$	$(\frac{^{208}Pb}{^{204}Pb})_t$
97SB70	0.32	0.92	0.3	20	71	5.5	13.7	2.13	10.4	2.94	0.97	3.34	0.57	3.49	0.69	1.90	0.29	1.74	0.27	-	-	-	-	-
97SB28	-	-	-	17	67	-	-	-	-	-	-	-	-	-	-	-	-	-	-	-	-	-	-	-
97SB27	0.71	1.39	0.33	28	149	14.0	31.9	4.54	20.7	5.09	1.61	5.19	0.84	4.85	0.96	2.54	0.38	2.23	0.34	-	-	-	-	-
97SB32	0.72	1.37	0.29	28	149	14.2	32.2	4.53	20.8	5.07	1.62	5.39	0.86	4.95	0.97	2.56	0.39	2.24	0.34	-	-	-	-	-
97SB26	1.87	4.85	1.32	52	195	29.6	60.5	7.84	33.7	7.79	2.40	8.57	1.42	8.71	1.79	5.00	0.79	4.65	0.73	-	-	-	-	-
97SB31	1.85	4.78	1.28	51	192	29.2	59.8	7.78	33.1	7.61	2.37	8.39	1.39	8.54	1.76	4.84	0.77	4.55	0.7	-	-	-	-	-
96SB48	0.78	1.71	0.46	19	116	14.5	33.2	4.07	19.7	4.53	1.52	4.80	0.71	3.78	0.66	1.58	0.23	1.22	0.18	0.70420	2.60	17.83	15.54	37.75
97SB63	0.73	2.08	0.45	18	153	21.2	46.0	6.00	24.7	4.94	1.49	4.58	0.63	3.32	0.59	1.47	0.21	1.17	0.17	0.70513	0.52	18.00	15.57	38.06
97SB67	0.8	2.01	0.42	23	118	17.1	36.6	4.90	21.1	5.06	1.77	5.48	0.81	4.28	0.76	1.76	0.25	1.3	0.18	0.70496	-2.90	17.70	15.55	37.80
97SB68	0.68	1.69	0.43	19	107	14.0	31.3	4.30	18.5	4.26	1.38	4.41	0.64	3.50	0.63	1.54	0.22	1.19	0.17	0.70445	2.20	17.88	15.54	37.87
97SB73	1.55	2.95	0.62	21	163	25.5	52.4	6.90	29.2	6.30	2.11	5.82	0.81	4.07	0.68	1.51	0.21	1.1	0.16	0.70417	1.60	17.36	15.49	37.56
97SB66	0.82	1.72	0.42	25	180	19.7	45.2	6.00	26.5	6.07	2.05	5.60	0.86	4.67	0.86	2.41	0.36	2.11	0.32	-	-	-	-	-
97SB72	0.6	0.85	0.21	25	70	8.7	20.9	3.10	15.0	4.36	1.70	4.96	0.81	4.71	0.88	2.13	0.30	1.67	0.23	-	-	-	-	-
97SB76	0.98	2.06	0.45	27	155	21.6	46.6	6.10	25.7	5.62	1.84	5.66	0.84	4.60	0.85	2.18	0.32	1.77	0.26	-	-	-	-	-
97SB80	0.37	0.8	0.17	21	108	10.3	24.4	3.50	16.3	3.75	1.22	3.96	0.61	3.50	0.68	1.79	0.27	1.6	0.24	0.70723	-1.44	-	-	-
PB9	0.7	1.3	0.3	20	123	15.3	36.4	5.03	22.3	4.91	1.53	4.73	0.70	3.80	0.68	1.76	0.26	1.5	0.22	0.70442	3.67	18.27	15.58	38.03
Z1813.1	0.66	0.67	0.23	37	228	10.0	27.5	4.82	25.3	7.84	2.70	9.18	1.40	7.45	1.40	3.29	0.48	2.57	0.38	0.70407	7.0	-	-	-
Z1816.3	0.55	0.55	0.18	35	216	7.5	22.1	4.08	22.5	7.18	2.48	8.44	1.31	7.10	1.31	3.09	0.44	2.39	0.35	0.70393	7.1	-	-	-
Z1817.2	0.69	0.65	0.22	42	262	9.3	27.5	5.11	27.9	8.69	3.01	10.23	1.56	8.41	1.54	3.58	0.52	2.81	0.42	0.70366	7.1	-	-	-
JSH/B006	1.24	1.69	0.45	24	151	18.9	43.7	6.10	27.4	7.12	2.47	7.21	1.10	5.93	1.02	2.29	0.28	1.42	0.2	0.70428	3.5	17.908	15.525	37.82

Table C.3: Mean, minimum and maximum olivine forsterite contents for each sample considered by this thesis (filtered for EPMA oxide totals of 98–102), where n is the number of analyses. K11 indicates Keiding *et al.* (2011). For each sample, olivine data is from a mixture of previously published thin section analyses, new thin section analyses (both of which focus on olivine core compositions) and mounted olivines used in melt inclusion work. Whole-rock Mg# is molar Mg/(Mg+Fe^{2+}, assuming $Fe^{3+}/Fe_T = 0.1$. Fo is forsterite content expressed as a %, assuming $Fe^{3+}/Fe_T = 0$ in olivine. HP is Horingbaai-type picrite, Fp is ferropicrite.

Location	Type	Sample	n	WR Mg#	Fo (mean)	Fo (min)	Fo (max)
Alhmannryggen, DML	Fp	Z1803.1	25	0.570	78.8	76.0	81.0
Alhmannryggen, DML	Fp	Z1803.5	23	0.640	79.3	75.9	80.8
Alhmannryggen, DML	Fp	Z1813.1	88	0.646	81.6	78.7	84.9
Alhmannryggen, DML	Fp	Z1816.3	101	0.795	82.5	79.8	90.3
Alhmannryggen, DML	Fp	Z1817.2	76	0.647	80.2	77.2	85.7
Alhmannryggen, DML	Fp	Z1825.3	42	0.665	85.2	82.5	88.1
Alhmannryggen, DML	Fp	Z1826.1	83	0.705	84.5	79.1	90.0
Alhmannryggen, DML	Fp	Z1826.2	63	0.710	85.3	78.8	90.5
Alhmannryggen, DML	Fp	Z1838.1	101	0.732	86.6	84.2	89.3
Vestfjella, DML	Fp	JSH-B006	18	0.655	79.8	78.3	84.2
Etendeka	Fp	96SB48	68	0.670	69.8	63.2	81.7
Etendeka	Fp	97SB63	89	0.639	82.5	77.1	85.1
Etendeka	Fp	97SB67	69	0.645	66.6	63.8	72.6
Etendeka	Fp	97SB68	42	0.665	66.0	64.4	67.3
Etendeka	Fp	97SB73	72	0.627	81.2	70.0	86.9
Etendeka	Fp	97SB80	62	0.625	74.3	60.0	80.1
Etendeka	Fp	PB9	60	0.639	75.7	68.5	84.0
Etendeka	HP	97SB29	20	0.644	85.8	83.3	90.4
Etendeka	HP	97SB33	31	0.716	90.6	83.7	93.3
Etendeka	HP	97SB34	76	0.770	85.5	82.3	92.0
Etendeka	HP	97SB35	21	0.664	89.0	85.3	92.0
Etendeka	HP	97SB37	33	0.745	85.8	83.8	88.6
Etendeka	HP	97SB41	70	0.758	85.5	83.9	90.3
Etendeka	HP	97SB44	18	0.616	87.1	83.2	89.4
Etendeka	HP	97SB46	57	0.637	87.9	86.6	91.4
Etendeka	HP	97SB53	19	0.655	88.8	81.2	92.7
Etendeka	HP	97SB56	35	0.712	85.3	80.7	90.4
Etendeka	HP	97SB62	41	0.672	87.7	80.9	93.1
Etendeka	HP	97SB75	33	0.627	87.1	85.0	90.2
Etendeka	HP	97SB79	23	0.782	87.5	82.7	90.9
Etendeka	HP, K11	377	4	0.746	84.8	82.9	86.2
Etendeka	HP, K11	412	7	0.632	81.9	77.5	84.1
Etendeka	HP, K11	417	2	0.679	83.4	81.8	84.9
Etendeka	HP, K11	419	4	0.751	86.3	84.3	87.7
Etendeka	HP, K11	DO-09-4	27	0.622	86.4	82.4	89.2
Etendeka	HP, K11	DO-09-6	31	0.615	90.0	83.3	93.1
Etendeka	HP, K11	JVT-09-08	15	0.634	88.2	84.4	90.8
Etendeka	HP, K11	JVT-09-20	14	0.643	83.3	78.1	87.6
Etendeka	HP, K11	JVT-09-21	18	0.612	86.0	84.7	88.5
Etendeka	HP, K11	JVT-09-22	23	0.721	88.5	85.5	90.9
Etendeka	HP, K11	JVT-09-23	5	0.575	83.6	82.6	84.9
Etendeka	HP, K11	JVT-09-24	35	0.640	67.2	52.8	92.8
Etendeka	HP, K11	JVT-09-26	18	0.758	86.4	85.1	89.9
Etendeka	HP, K11	JVT-09-27	15	0.773	86.5	84.7	90.9

Table C.3 – *Continued on next page*

Location	Type	Sample	n	WR Mg#	Fo (mean)	Fo (min)	Fo (max)
Etendeka	HP, K11	JVT-09-28	22	0.662	90.2	86.5	93.1
Etendeka	HP, K11	JVT-09-29	14	0.624	87.3	86.1	89.9
Etendeka	HP, K11	JVT-09-31	26	0.702	90.5	85.4	92.9
Etendeka	HP, K11	JVT-09-32	48	0.769	89.5	83.6	93.3
Etendeka	HP, K11	KPH-18a	9	0.788	77.6	75.8	78.3
Etendeka	HP, K11	Q15	6	0.792	77.4	76.5	79.7
Etendeka	HP, K11	Q18	2	0.550	79.1	78.8	79.4
Etendeka	HP, K11	Q22	10	0.755	78.8	68.8	82.7

Table C.4: New olivine phenocryst core data obtained by EPMA from thin sections in this study. FeO^T is total Fe expressed as FeO. Type: HP, Horingbaai-type picrite; Fp, ferropicrite. Analyses with oxide totals outside of 100 ± 2 are excluded. n.d. means not determined.

Location	Type	Sample	SiO_2	TiO_2	Al_2O_3	FeO^T	MnO	MgO	CaO	P_2O_5	Cr_2O_3	NiO	Total	Fo
Etendeka	HP	97SB29	39.75	0.00	0.06	14.1	0.3	45.5	0.34	0.01	0.01	0.23	100.3	85.2
Etendeka	HP	97SB29	40.1	0.00	0.04	14.1	0.3	45.8	0.34	0.01	0.02	0.24	101.0	85.3
Etendeka	HP	97SB29	40.2	0.01	0.04	14.3	0.2	46.2	0.34	0.00	0.03	0.25	101.5	85.2
Etendeka	HP	97SB29	40.0	0.02	0.03	14.5	0.3	46.0	0.35	0.01	0.06	0.20	101.5	85.0
Etendeka	HP	97SB29	40.0	0.00	0.05	14.0	0.3	45.7	0.36	0.00	0.01	0.24	100.6	85.4
Etendeka	HP	97SB29	40.1	0.00	0.07	14.2	0.3	46.3	0.35	0.00	0.00	0.28	101.7	85.3
Etendeka	HP	97SB29	40.0	0.00	0.05	14.4	0.2	45.8	0.38	0.00	0.01	0.23	101.1	85.0
Etendeka	HP	97SB29	39.5	0.03	0.07	13.9	0.3	46.0	0.38	0.00	0.07	0.37	100.7	85.5
Etendeka	HP	97SB29	40.2	0.02	0.06	13.8	0.2	45.8	0.36	0.00	0.00	0.17	100.6	85.6
Etendeka	HP	97SB29	40.4	0.02	0.07	13.6	0.2	46.3	0.34	0.01	0.02	0.25	101.2	85.8
Etendeka	HP	97SB29	40.0	0.01	0.06	13.8	0.3	46.1	0.36	0.04	0.05	0.27	101.1	85.6
Etendeka	HP	97SB29	40.1	0.01	0.07	13.7	0.3	45.6	0.33	0.01	0.05	0.28	100.5	85.5
Etendeka	HP	97SB29	40.1	0.03	0.06	14.1	0.3	46.1	0.38	0.03	0.00	0.22	101.3	85.4
Etendeka	HP	97SB29	39.8	0.03	0.05	13.7	0.2	46.0	0.36	0.02	0.06	0.17	100.4	85.7
Etendeka	HP	97SB29	39.8	0.01	0.05	13.9	0.3	45.9	0.35	0.01	0.00	0.17	100.5	85.5
Etendeka	HP	97SB29	39.5	0.01	0.09	15.9	0.3	44.4	0.43	0.09	0.01	0.17	100.9	83.3
Etendeka	HP	97SB34	39.9	0.03	0.05	14.1	0.2	44.8	0.34	n.d.	0.03	0.44	99.9	85.0
Etendeka	HP	97SB34	40.1	0.02	0.08	14.4	0.2	44.9	0.28	n.d.	0.02	0.31	100.3	84.7
Etendeka	HP	97SB34	40.3	0.01	0.05	14.3	0.2	44.6	0.32	n.d.	0.08	0.26	100.1	84.8
Etendeka	HP	97SB34	40.6	0.02	0.09	11.3	0.2	46.6	0.29	n.d.	0.13	0.47	99.8	88.0
Etendeka	HP	97SB34	40.9	0.01	0.07	11.7	0.1	47.4	0.32	n.d.	0.10	0.37	101.0	87.8
Etendeka	HP	97SB34	40.7	0.00	0.06	11.3	0.1	47.0	0.28	n.d.	0.13	0.33	100.0	88.1
Etendeka	HP	97SB34	40.0	0.03	0.10	13.5	0.2	44.8	0.30	n.d.	0.08	0.29	99.3	85.6
Etendeka	HP	97SB34	39.9	0.04	0.11	13.5	0.2	45.2	0.30	n.d.	0.10	0.33	99.7	85.7
Etendeka	HP	97SB34	40.0	0.04	0.10	14.0	0.2	44.8	0.31	n.d.	0.01	0.40	99.8	85.1
Etendeka	HP	97SB56	39.8	0.02	0.06	14.0	0.3	46.6	0.33	0.00	0.04	0.24	101.4	85.5
Etendeka	HP	97SB56	39.7	0.03	0.04	14.2	0.2	46.5	0.34	0.00	0.01	0.28	101.4	85.4
Etendeka	HP	97SB56	39.9	0.01	0.05	14.2	0.2	46.8	0.30	0.02	0.00	0.24	101.7	85.5
Etendeka	HP	97SB56	39.1	0.02	0.05	18.4	0.3	43.3	0.33	0.03	0.00	0.27	101.8	80.8

Table C.4 – *Continued on next page*

Location	Type	Sample	SiO_2	TiO_2	Al_2O_3	FeO^T	MnO	MgO	CaO	P_2O_5	Cr_2O_3	NiO	Total	Fo
Etendeka	HP	97SB56	39.6	0.01	0.04	17.2	0.3	43.8	0.34	0.00	0.00	0.19	101.5	81.9
Etendeka	HP	97SB56	39.8	0.01	0.05	14.4	0.2	46.5	0.32	0.02	0.00	0.24	101.7	85.2
Etendeka	HP	97SB56	40.2	0.00	0.02	14.0	0.3	46.5	0.36	0.00	0.00	0.27	101.7	85.5
Etendeka	HP	97SB56	40.2	0.01	0.07	14.1	0.1	46.5	0.33	0.01	0.05	0.30	101.7	85.5
Etendeka	HP	97SB56	40.0	0.00	0.05	15.4	0.3	45.5	0.33	0.00	0.07	0.24	101.9	84.0
Etendeka	HP	97SB56	39.8	0.04	0.12	14.8	0.2	45.9	0.33	0.05	0.04	0.25	101.6	84.7
Etendeka	HP	97SB56	40.3	0.01	0.05	14.3	0.2	46.0	0.31	0.00	0.09	0.30	101.6	85.1
Etendeka	HP	97SB56	39.1	0.03	0.07	18.3	0.3	43.0	0.32	0.04	0.01	0.20	101.3	80.7
Etendeka	HP	97SB56	39.5	0.02	0.07	16.9	0.3	44.1	0.32	0.00	0.00	0.23	101.5	82.3
Etendeka	HP	97SB56	39.8	0.01	0.06	14.6	0.2	46.3	0.30	0.03	0.01	0.32	101.7	85.0
Etendeka	HP	97SB56	39.4	0.00	0.07	15.2	0.3	46.0	0.34	0.00	0.01	0.32	101.6	84.4
Etendeka	HP	97SB56	40.7	-0.01	0.06	12.0	0.1	47.9	0.32	0.01	0.01	0.34	101.5	87.7
Etendeka	HP	97SB56	40.2	0.01	0.07	12.3	0.2	47.7	0.29	0.07	0.02	0.38	101.2	87.4
Etendeka	HP	97SB56	40.5	0.01	0.06	12.3	0.2	48.1	0.30	0.00	0.04	0.32	101.7	87.5
Etendeka	HP	97SB56	39.7	0.02	0.09	14.4	0.3	46.2	0.33	0.07	0.08	0.24	101.3	85.2
Etendeka	HP	97SB56	39.8	0.01	0.07	14.4	0.2	46.2	0.32	0.04	0.08	0.28	101.3	85.1
Etendeka	HP	97SB62	40.0	0.01	0.05	14.2	0.2	45.8	0.31	0.04	0.03	0.25	100.9	85.2
Etendeka	HP	97SB62	39.9	0.00	0.02	14.1	0.2	46.0	0.33	0.12	0.04	0.29	101.1	85.3
Etendeka	HP	97SB62	40.1	0.02	0.06	14.2	0.2	45.5	0.32	0.02	0.03	0.26	100.6	85.1
Etendeka	HP	97SB62	39.6	0.02	0.07	15.9	0.3	44.2	0.32	0.00	0.03	0.33	100.7	83.2
Etendeka	HP	97SB62	39.4	0.00	0.05	17.0	0.3	44.0	0.34	0.01	0.03	0.23	101.3	82.2
Etendeka	HP	97SB62	39.2	0.01	0.05	17.9	0.4	42.6	0.33	0.01	0.04	0.27	100.8	80.9
Etendeka	HP	97SB62	41.2	0.00	0.06	7.2	0.1	51.7	0.29	0.01	0.17	0.55	101.4	92.7
Etendeka	HP	97SB62	41.1	0.00	0.10	7.2	0.1	51.5	0.25	0.06	0.12	0.47	101.0	92.7
Etendeka	HP	97SB62	40.9	0.00	0.08	7.2	0.2	51.2	0.29	0.06	0.18	0.43	100.5	92.7
Etendeka	HP	97SB62	41.7	0.02	0.08	7.3	0.1	51.9	0.26	0.00	0.15	0.40	101.9	92.7
Etendeka	HP	97SB62	41.3	0.01	0.07	7.6	0.1	51.2	0.27	0.00	0.08	0.34	101.0	92.3
Etendeka	HP	97SB62	41.0	0.00	0.11	7.5	0.1	50.9	0.27	0.00	0.17	0.40	100.6	92.3
Etendeka	HP	97SB62	40.3	0.00	0.05	14.6	0.2	45.8	0.31	0.02	0.08	0.32	101.7	84.8
Etendeka	HP	97SB62	40.5	0.03	0.04	12.3	0.2	47.2	0.33	0.02	0.03	0.22	101.0	87.2
Etendeka	HP	97SB75	40.0	0.01	0.09	13.1	0.2	47.1	0.32	0.03	0.03	0.31	101.2	86.5
Etendeka	HP	97SB75	39.9	0.02	0.17	12.8	0.2	46.9	0.34	0.01	0.03	0.26	100.6	86.8

Table C.4 – *Continued on next page*

Location	Type	Sample	SiO_2	TiO_2	Al_2O_3	FeO^T	MnO	MgO	CaO	P_2O_5	Cr_2O_3	NiO	Total	Fo
Etendeka	HP	97SB75	40.3	0.04	0.17	12.5	0.3	47.1	0.36	0.02	0.10	0.22	101.1	87.0
Etendeka	HP	97SB75	39.8	-0.01	0.07	12.7	0.2	46.8	0.33	0.02	0.00	0.29	100.2	86.8
Etendeka	HP	97SB75	40.3	-0.01	0.07	12.7	0.2	47.3	0.33	0.03	0.02	0.30	101.3	86.9
Etendeka	HP	97SB75	40.4	-0.01	0.07	12.8	0.2	47.4	0.32	0.01	0.06	0.22	101.4	86.8
Etendeka	HP	97SB75	40.3	0.02	0.07	12.5	0.2	47.0	0.32	0.02	0.02	0.25	100.7	87.1
Etendeka	HP	97SB75	40.3	0.02	0.07	12.5	0.2	47.1	0.32	0.03	0.00	0.35	101.0	87.0
Etendeka	HP	97SB75	40.4	0.02	0.06	12.6	0.2	46.9	0.36	0.00	0.07	0.29	101.0	87.0
Etendeka	HP	97SB75	40.1	0.01	0.07	12.6	0.2	47.0	0.35	0.01	0.07	0.26	100.7	86.9
Etendeka	HP	97SB75	40.4	0.00	0.07	13.3	0.2	46.8	0.34	0.00	0.04	0.19	101.4	86.2
Etendeka	HP	97SB75	40.0	0.00	0.06	12.8	0.2	46.8	0.32	0.02	0.05	0.29	100.6	86.7
Etendeka	HP	97SB75	40.2	0.01	0.05	13.0	0.1	46.9	0.35	0.01	0.04	0.27	101.0	86.5
Etendeka	HP	97SB75	40.0	0.02	0.11	12.8	0.2	47.0	0.34	0.02	0.01	0.37	100.8	86.7
Etendeka	HP	97SB75	40.1	0.00	0.08	12.7	0.3	47.0	0.34	0.00	0.04	0.28	100.8	86.8
Etendeka	HP	97SB75	40.5	0.01	0.07	12.6	0.2	46.9	0.32	0.02	0.05	0.31	101.0	86.9
Etendeka	HP	97SB75	40.1	0.00	0.05	12.4	0.2	46.7	0.30	0.00	0.07	0.29	100.1	87.0
Etendeka	HP	97SB75	39.7	0.02	0.07	13.0	0.2	46.3	0.33	0.00	0.08	0.27	100.0	86.4
Etendeka	HP	97SB75	40.5	0.01	0.08	12.7	0.2	47.2	0.33	0.01	0.01	0.29	101.3	86.9
Etendeka	HP	97SB75	39.5	0.02	0.12	14.3	0.3	45.5	0.33	0.04	0.00	0.20	100.2	85.0
Etendeka	HP	97SB75	40.5	0.02	0.08	12.9	0.2	47.5	0.34	0.00	0.00	0.23	101.7	86.8
Etendeka	HP	97SB75	40.1	0.03	0.08	13.0	0.2	46.7	0.35	0.00	0.04	0.30	100.7	86.5
Etendeka	HP	97SB79	39.9	0.00	0.06	15.2	0.2	45.3	0.25	0.01	0.04	0.28	101.2	84.2
Etendeka	HP	97SB79	40.1	0.01	0.06	15.0	0.2	45.2	0.29	0.02	0.05	0.28	101.1	84.3
Etendeka	HP	97SB79	40.5	0.01	0.06	11.2	0.1	48.4	0.26	0.01	0.17	0.39	101.1	88.5
Etendeka	HP	97SB79	40.6	0.00	0.05	10.8	0.1	48.5	0.30	0.00	0.07	0.42	100.8	88.9
Etendeka	HP	97SB79	41.0	0.01	0.08	9.1	0.2	50.1	0.28	0.01	0.18	0.42	101.4	90.8
Etendeka	HP	97SB79	40.9	0.02	0.09	8.9	0.1	50.2	0.28	0.00	0.11	0.47	101.2	90.9
Etendeka	HP	97SB79	41.0	0.00	0.07	9.4	0.1	49.5	0.29	0.00	0.11	0.34	100.8	90.4
Etendeka	HP	97SB79	39.7	0.03	0.10	14.5	0.2	45.2	0.31	0.01	0.10	0.31	100.5	84.8
Etendeka	HP	97SB79	40.2	0.02	0.07	14.6	0.2	45.2	0.31	0.01	0.01	0.26	100.8	84.6
Etendeka	HP	97SB79	39.7	0.02	0.09	14.7	0.2	45.2	0.31	0.00	0.05	0.25	100.6	84.5
Etendeka	HP	97SB79	41.3	0.01	0.07	9.1	0.2	50.4	0.28	0.04	0.11	0.41	101.9	90.8
Etendeka	HP	97SB79	40.8	0.02	0.11	8.9	0.2	49.6	0.29	0.03	0.10	0.45	100.4	90.9

Table C.4 – *Continued on next page*

Location	Type	Sample	SiO_2	TiO_2	Al_2O_3	FeO^T	MnO	MgO	CaO	P_2O_5	Cr_2O_3	NiO	Total	Fo
Etendeka	HP	97SB79	40.6	0.01	0.09	9.3	0.2	49.5	0.30	0.06	0.11	0.40	100.6	90.5
Etendeka	HP	97SB79	40.3	0.01	0.05	14.2	0.3	46.0	0.30	0.00	0.05	0.19	101.5	85.2
Etendeka	HP	97SB79	39.9	-0.01	0.06	14.3	0.2	45.9	0.34	0.00	0.05	0.25	101.0	85.1
Etendeka	HP	97SB79	39.8	0.03	0.05	14.3	0.2	45.7	0.33	0.03	0.00	0.28	100.8	85.0
Etendeka	HP	97SB79	40.8	0.01	0.09	9.5	0.2	49.6	0.31	0.00	0.14	0.38	101.0	90.3
Etendeka	HP	97SB79	41.0	0.00	0.09	9.4	0.2	49.5	0.30	0.00	0.18	0.39	101.1	90.4
Etendeka	HP	97SB79	40.7	0.01	0.07	9.4	0.1	49.5	0.30	0.00	0.14	0.31	100.6	90.3
Etendeka	HP	97SB79	38.9	0.01	0.03	16.3	0.2	43.5	0.31	0.00	0.02	0.27	99.5	82.7
Etendeka	Fp	97SB80	37.0	0.01	0.04	26.7	0.4	35.1	0.29	0.02	0.01	0.16	99.8	70.1
Etendeka	Fp	97SB80	37.5	0.03	0.06	23.8	0.4	37.2	0.27	0.03	0.01	0.10	99.5	73.6
Etendeka	Fp	97SB80	37.8	0.01	0.06	21.8	0.3	39.2	0.24	0.06	0.08	0.32	99.9	76.3
Etendeka	Fp	97SB80	37.6	0.01	0.07	22.9	0.4	37.9	0.28	0.03	0.04	0.12	99.2	74.7
Etendeka	Fp	97SB80	37.7	0.00	0.05	22.0	0.3	39.4	0.27	0.01	0.02	0.20	99.9	76.1
Etendeka	Fp	97SB80	38.3	0.00	0.03	21.4	0.4	39.8	0.29	0.01	0.06	0.16	100.5	76.8
Etendeka	Fp	97SB80	37.5	0.02	0.05	27.0	0.5	34.5	0.25	0.07	0.00	0.14	100.0	69.5
Etendeka	Fp	97SB80	37.6	0.03	0.05	25.7	0.4	35.6	0.25	0.07	0.04	0.17	100.0	71.2
Etendeka	Fp	97SB80	38.4	0.03	0.06	20.6	0.4	39.9	0.27	0.14	0.04	0.22	100.0	77.6
Etendeka	Fp	97SB80	38.4	0.01	0.05	20.9	0.3	39.9	0.27	0.07	0.02	0.15	100.1	77.3
Etendeka	Fp	97SB80	38.1	0.03	0.05	24.2	0.4	37.1	0.29	0.03	0.03	0.18	100.3	73.2
Etendeka	Fp	97SB80	37.8	0.01	0.03	24.2	0.4	37.0	0.30	0.07	0.00	0.18	100.0	73.1
Etendeka	Fp	97SB80	36.5	0.02	0.04	29.6	0.5	32.8	0.32	0.03	0.02	0.08	99.8	66.4
Etendeka	Fp	97SB80	35.7	0.02	0.03	31.1	0.5	31.4	0.31	0.02	0.02	0.08	99.2	64.3
Etendeka	Fp	97SB80	38.7	0.02	0.07	19.4	0.2	41.0	0.25	0.17	0.07	0.32	100.2	79.0
Etendeka	Fp	97SB80	38.8	0.00	0.04	19.6	0.3	40.6	0.23	0.17	0.01	0.22	99.9	78.7
Etendeka	Fp	97SB80	37.8	0.03	0.06	23.1	0.3	37.8	0.28	0.18	0.02	0.20	99.7	74.5
Etendeka	Fp	97SB80	37.6	0.01	0.06	24.1	0.4	37.1	0.27	0.03	0.00	0.18	99.7	73.3
Etendeka	Fp	97SB80	36.1	0.02	0.08	29.7	0.5	32.4	0.30	0.16	0.06	0.13	99.4	66.0
Etendeka	Fp	97SB80	36.8	0.01	0.04	28.9	0.4	33.4	0.31	0.05	0.05	0.05	100.0	67.3
Etendeka	Fp	97SB80	38.4	0.01	0.04	19.9	0.3	40.7	0.24	0.06	0.06	0.25	100.0	78.5
Etendeka	Fp	97SB80	38.5	0.03	0.07	19.6	0.3	40.9	0.26	0.08	0.08	0.30	100.2	78.8
Etendeka	Fp	97SB80	37.4	0.02	0.05	25.0	0.3	36.0	0.34	0.09	0.01	0.13	99.5	72.0
Etendeka	Fp	97SB80	38.4	0.02	0.04	25.1	0.3	36.1	0.34	0.13	0.06	0.09	100.5	71.9

Table C.4 – *Continued on next page*

Location	Type	Sample	SiO_2	TiO_2	Al_2O_3	FeO^T	MnO	MgO	CaO	P_2O_5	Cr_2O_3	NiO	Total	Fo
Etendeka	Fp	97SB80	37.6	0.03	0.05	24.2	0.4	37.6	0.28	0.07	0.00	0.22	100.4	73.4
Etendeka	Fp	97SB80	37.5	0.02	0.06	23.4	0.2	38.2	0.28	0.05	0.05	0.13	99.9	74.5
Etendeka	Fp	97SB80	36.1	0.04	0.04	30.8	0.4	32.0	0.37	0.01	0.02	0.06	99.9	64.9
Etendeka	Fp	97SB80	39.5	0.05	0.26	31.1	0.6	26.1	0.49	0.04	0.00	0.09	98.2	60.0
Etendeka	Fp	96SB48	38.5	0.01	0.06	26.8	0.3	33.7	0.33	0.02	0.06	0.33	100.1	69.1
Etendeka	Fp	96SB48	38.1	0.04	0.06	24.9	0.3	36.6	0.30	0.03	0.01	0.30	100.6	72.4
Etendeka	Fp	96SB48	39.0	0.03	0.04	25.1	0.3	35.7	0.31	0.01	0.00	0.32	100.9	71.7
Etendeka	Fp	96SB48	37.9	0.02	0.02	27.3	0.3	34.3	0.31	0.01	0.01	0.29	100.5	69.1
Etendeka	Fp	96SB48	37.6	0.02	0.05	27.5	0.3	34.2	0.29	0.02	0.02	0.30	100.3	68.9
Etendeka	Fp	96SB48	37.7	0.00	0.06	26.8	0.3	34.8	0.29	0.02	0.03	0.34	100.4	69.8
Etendeka	Fp	96SB48	38.2	0.01	0.08	25.7	0.2	36.2	0.28	0.00	0.02	0.31	101.0	71.5
Etendeka	Fp	96SB48	38.4	0.05	0.03	25.4	0.2	35.8	0.27	0.00	0.00	0.27	100.5	71.5
Etendeka	Fp	96SB48	38.7	0.02	0.07	24.1	0.3	37.1	0.25	0.03	0.00	0.25	100.9	73.3
Etendeka	Fp	96SB48	38.5	0.01	0.05	24.9	0.3	36.1	0.29	0.00	0.00	0.37	100.5	72.1
Etendeka	Fp	96SB48	39.0	0.03	0.05	25.1	0.3	36.2	0.30	0.01	0.04	0.30	101.4	72.0
Etendeka	Fp	96SB48	38.5	0.02	0.05	25.4	0.3	35.1	0.31	0.01	0.06	0.33	100.1	71.1
Etendeka	Fp	96SB48	37.8	0.12	0.01	28.3	0.4	33.2	0.32	0.01	0.03	0.33	100.5	67.7
Etendeka	Fp	96SB48	37.8	0.05	0.02	29.5	0.3	32.9	0.33	0.01	0.01	0.29	101.3	66.5
Etendeka	Fp	96SB48	39.1	0.00	0.07	23.4	0.3	37.5	0.25	0.01	0.01	0.32	100.9	74.1
Etendeka	Fp	96SB48	38.6	0.03	0.06	22.9	0.3	37.7	0.28	0.04	0.00	0.37	100.4	74.6
Etendeka	Fp	96SB48	38.4	0.03	0.05	26.8	0.3	34.0	0.30	0.01	0.00	0.40	100.3	69.3
Etendeka	Fp	96SB48	38.7	0.01	0.05	24.7	0.3	35.4	0.29	0.00	0.03	0.34	99.9	71.8
Etendeka	Fp	96SB48	39.4	0.00	0.04	23.4	0.2	37.4	0.23	0.04	0.02	0.38	101.2	74.0
Etendeka	Fp	96SB48	39.7	0.04	0.03	20.0	0.3	39.7	0.23	0.07	0.00	0.43	100.5	78.0
Etendeka	Fp	96SB48	38.4	0.00	0.04	23.9	0.3	36.9	0.25	0.03	0.04	0.30	100.1	73.4
Etendeka	Fp	96SB48	40.5	0.02	0.04	17.0	0.2	42.5	0.26	0.00	0.01	0.45	101.0	81.7
Etendeka	Fp	96SB48	39.6	0.00	0.10	24.6	0.3	35.3	0.26	0.00	0.00	0.34	100.5	71.9
Etendeka	Fp	PB9	37.9	0.02	0.04	24.7	0.4	36.7	0.36	0.01	0.01	0.24	100.4	72.6
Etendeka	Fp	PB9	38.0	0.03	0.06	24.9	0.4	36.1	0.35	0.01	0.02	0.16	100.1	72.1
Etendeka	Fp	PB9	38.0	0.02	0.04	25.0	0.4	36.1	0.37	0.01	0.04	0.15	100.1	72.0
Etendeka	Fp	PB9	37.9	0.03	0.04	23.9	0.3	37.2	0.35	0.01	0.01	0.19	99.9	73.5
Etendeka	Fp	PB9	37.4	0.02	0.04	26.0	0.5	35.4	0.36	0.07	0.02	0.13	100.0	70.8

Table C.4 – *Continued on next page*

Location	Type	Sample	SiO_2	TiO_2	Al_2O_3	FeO^T	MnO	MgO	CaO	P_2O_5	Cr_2O_3	NiO	Total	Fo
Etendeka	Fp	PB9	38.1	0.01	0.02	23.8	0.3	37.3	0.35	0.00	0.01	0.19	100.2	73.6
Etendeka	Fp	PB9	37.8	0.01	0.04	25.3	0.4	36.1	0.36	0.02	0.03	0.17	100.2	71.8
Etendeka	Fp	PB9	38.1	0.02	0.04	24.8	0.4	36.3	0.36	0.04	0.02	0.19	100.3	72.3
Etendeka	Fp	PB9	37.8	0.02	0.05	24.4	0.4	36.8	0.38	0.00	0.08	0.19	100.1	72.9
Etendeka	Fp	PB9	38.0	0.02	0.04	24.5	0.3	36.8	0.37	0.01	0.03	0.19	100.2	72.8
Etendeka	Fp	PB9	38.1	0.02	0.04	24.4	0.4	36.8	0.33	0.00	0.10	0.17	100.4	72.9
Etendeka	Fp	PB9	38.3	0.02	0.05	24.2	0.3	36.8	0.32	0.02	0.03	0.14	100.2	73.0
Etendeka	Fp	PB9	38.2	0.01	0.06	22.2	0.2	38.6	0.30	0.01	0.01	0.23	100.0	75.6
Etendeka	Fp	PB9	38.6	0.03	0.04	22.4	0.4	38.1	0.31	0.01	0.07	0.23	100.1	75.2
Etendeka	Fp	PB9	37.6	0.01	0.04	24.3	0.4	37.1	0.35	0.05	0.02	0.17	100.0	73.1
Etendeka	Fp	PB9	38.4	0.01	0.03	23.9	0.3	37.0	0.33	0.00	0.06	0.16	100.1	73.4
Etendeka	Fp	PB9	37.6	0.02	0.04	24.8	0.4	36.3	0.34	0.01	0.01	0.18	99.7	72.3
Etendeka	Fp	PB9	38.2	0.02	0.07	21.7	0.3	39.7	0.31	0.02	0.07	0.23	100.5	76.5
Etendeka	Fp	PB9	39.1	0.02	0.04	17.4	0.2	42.2	0.34	0.01	0.06	0.21	99.7	81.2
Etendeka	Fp	PB9	38.8	0.02	0.06	21.5	0.3	39.7	0.30	0.01	0.04	0.18	101.0	76.7
Etendeka	Fp	PB9	38.6	0.01	0.06	20.1	0.3	40.5	0.28	0.01	0.04	0.19	100.0	78.3
Etendeka	Fp	PB9	38.3	0.02	0.03	22.5	0.3	38.1	0.32	0.02	0.02	0.18	99.9	75.1
Etendeka	Fp	PB9	37.9	0.02	0.04	22.9	0.3	38.4	0.32	0.02	0.06	0.14	100.1	74.9
Etendeka	Fp	PB9	37.7	0.02	0.03	22.2	0.3	38.7	0.36	0.00	0.02	0.19	99.5	75.6
Etendeka	Fp	PB9	37.8	0.03	0.03	21.8	0.3	38.9	0.34	0.01	0.04	0.17	99.4	76.0
Etendeka	Fp	PB9	38.1	0.02	0.05	22.7	0.3	37.6	0.32	0.02	0.04	0.16	99.5	74.7
Etendeka	Fp	PB9	37.4	0.02	0.05	24.3	0.4	37.2	0.32	0.03	0.07	0.17	99.9	73.1
Etendeka	Fp	PB9	37.9	0.03	0.02	24.6	0.4	36.5	0.31	0.03	0.04	0.17	99.9	72.5
Etendeka	Fp	PB9	37.5	0.00	0.05	24.6	0.3	36.4	0.33	0.02	0.01	0.14	99.4	72.5
Etendeka	Fp	PB9	38.5	0.02	0.05	21.3	0.3	39.2	0.30	0.01	0.03	0.23	99.9	76.7
Etendeka	Fp	PB9	37.9	0.03	0.05	22.6	0.3	38.1	0.31	0.01	0.02	0.21	99.6	75.1
Etendeka	Fp	PB9	38.1	0.00	0.03	22.9	0.3	38.1	0.31	0.02	0.07	0.21	100.1	74.8
Etendeka	Fp	PB9	37.7	0.02	0.03	23.3	0.4	37.8	0.35	0.01	0.00	0.22	99.8	74.3
Etendeka	Fp	PB9	38.2	0.01	0.04	22.2	0.3	38.5	0.32	0.00	0.05	0.24	99.9	75.6
Etendeka	Fp	PB9	38.5	0.03	0.08	22.0	0.3	38.3	0.29	0.05	0.00	0.20	99.7	75.6
Etendeka	Fp	PB9	38.8	0.02	0.05	19.7	0.2	40.4	0.34	0.01	0.06	0.23	99.8	78.5
Etendeka	Fp	PB9	38.4	0.03	0.05	22.1	0.3	38.7	0.34	0.01	0.00	0.21	100.1	75.7

Table C.4 – *Continued on next page*

Location	Type	Sample	SiO_2	TiO_2	Al_2O_3	FeO^T	MnO	MgO	CaO	P_2O_5	Cr_2O_3	NiO	Total	Fo
Etendeka	Fp	PB9	38.6	0.01	0.04	22.2	0.3	38.5	0.32	0.01	0.08	0.12	100.2	75.6
Etendeka	Fp	PB9	38.9	0.01	0.05	18.4	0.2	41.6	0.31	0.06	0.08	0.28	100.0	80.1
Etendeka	Fp	PB9	38.9	0.02	0.04	19.7	0.3	40.5	0.28	0.01	0.04	0.26	100.0	78.6
Etendeka	Fp	PB9	38.8	0.02	0.06	18.6	0.3	41.5	0.31	0.06	0.05	0.27	100.0	79.9
Etendeka	Fp	PB9	38.3	0.02	0.04	22.4	0.4	38.4	0.35	0.02	0.04	0.22	100.2	75.3
Etendeka	Fp	PB9	38.4	0.02	0.05	21.7	0.3	39.4	0.33	0.01	0.04	0.24	100.5	76.3
Etendeka	Fp	PB9	38.0	0.03	0.05	22.6	0.3	38.5	0.34	0.00	0.04	0.22	100.0	75.3
Vestfjella, DML	Fp	JSH-B006	39.3	0.05	0.02	18.8	0.2	40.7	0.40	n.d.	0.01	0.29	99.8	79.4
Vestfjella, DML	Fp	JSH-B006	39.5	0.01	0.04	18.8	0.2	41.1	0.32	n.d.	0.03	0.38	100.4	79.6
Vestfjella, DML	Fp	JSH-B006	39.2	0.02	0.05	18.9	0.2	41.0	0.39	n.d.	0.04	0.39	100.3	79.4
Vestfjella, DML	Fp	JSH-B006	39.7	0.03	0.03	17.6	0.2	42.3	0.43	n.d.	0.05	0.37	100.7	81.0
Vestfjella, DML	Fp	JSH-B006	39.9	0.00	0.07	14.8	0.2	44.2	0.19	n.d.	0.00	0.56	99.9	84.2
Vestfjella, DML	Fp	JSH-B006	39.4	0.02	0.02	18.4	0.2	41.1	0.27	n.d.	0.03	0.41	99.9	79.9
Vestfjella, DML	Fp	JSH-B006	39.4	0.01	0.03	18.5	0.3	41.5	0.46	n.d.	0.00	0.28	100.5	80.0
Vestfjella, DML	Fp	JSH-B006	39.3	0.01	0.02	19.0	0.2	41.2	0.45	n.d.	0.07	0.25	100.6	79.5
Vestfjella, DML	Fp	JSH-B006	39.3	0.02	0.04	18.9	0.2	41.3	0.41	n.d.	0.08	0.29	100.6	79.5
Vestfjella, DML	Fp	JSH-B006	39.3	0.03	0.03	20.0	0.3	40.6	0.44	n.d.	0.04	0.32	100.9	78.3
Ahlmannryggen, DML	Fp	Z1813-1	39.5	0.03	0.03	17.8	0.2	42.2	0.28	n.d.	0.06	0.41	100.6	80.8
Ahlmannryggen, DML	Fp	Z1813-1	39.6	0.02	0.03	17.3	0.2	42.5	0.28	n.d.	0.04	0.44	100.4	81.4
Ahlmannryggen, DML	Fp	Z1813-1	39.6	0.02	0.03	17.2	0.2	42.6	0.27	n.d.	0.05	0.44	100.4	81.5
Ahlmannryggen, DML	Fp	Z1813-1	39.4	0.03	0.04	18.9	0.2	41.3	0.25	n.d.	0.06	0.38	100.6	79.6
Ahlmannryggen, DML	Fp	Z1813-1	39.7	0.02	0.04	17.5	0.2	42.4	0.28	n.d.	0.04	0.42	100.7	81.2
Ahlmannryggen, DML	Fp	Z1813-1	39.6	0.02	0.03	17.5	0.2	42.3	0.27	n.d.	0.05	0.40	100.3	81.2
Ahlmannryggen, DML	Fp	Z1813-1	39.8	0.02	0.03	17.1	0.2	42.8	0.27	n.d.	0.07	0.43	100.6	81.7
Ahlmannryggen, DML	Fp	Z1813-1	39.8	0.02	0.03	17.2	0.2	42.6	0.27	n.d.	0.04	0.38	100.5	81.5
Ahlmannryggen, DML	Fp	Z1813-1	39.8	0.03	0.03	17.0	0.2	42.8	0.26	n.d.	0.03	0.45	100.5	81.8
Ahlmannryggen, DML	Fp	Z1816-3	39.5	0.01	0.03	17.1	0.1	42.7	0.30	n.d.	0.10	n.d.	99.8	81.7
Ahlmannryggen, DML	Fp	Z1816-3	39.7	0.02	0.03	17.2	0.2	42.7	0.28	n.d.	0.06	0.43	100.6	81.6
Ahlmannryggen, DML	Fp	Z1816-3	39.8	0.03	0.03	16.4	0.2	43.1	0.28	n.d.	0.07	0.47	100.4	82.4
Ahlmannryggen, DML	Fp	Z1816-3	39.7	0.02	0.02	17.0	0.2	42.7	0.27	n.d.	0.07	0.42	100.4	81.7
Ahlmannryggen, DML	Fp	Z1816-3	39.7	0.03	0.04	16.7	0.2	42.8	0.26	n.d.	0.04	0.47	100.2	82.1
Ahlmannryggen, DML	Fp	Z1816-3	39.7	0.02	0.04	16.4	0.2	43.1	0.28	n.d.	0.08	0.46	100.3	82.4

Table C.4 – *Continued on next page*

Location	Type	Sample	SiO_2	TiO_2	Al_2O_3	FeO^T	MnO	MgO	CaO	P_2O_5	Cr_2O_3	NiO	Total	Fo
Ahlmannryggen, DML	Fp	Z1816-3	39.7	0.02	0.03	17.1	0.2	42.5	0.30	n.d.	0.08	0.42	100.3	81.6
Ahlmannryggen, DML	Fp	Z1816-3	39.8	0.02	0.04	16.9	0.2	43.0	0.27	n.d.	0.08	0.46	100.8	81.9
Ahlmannryggen, DML	Fp	Z1816-3	40.9	0.02	0.04	10.2	0.1	48.0	0.19	n.d.	0.11	0.56	100.2	89.3
Ahlmannryggen, DML	Fp	Z1816-3	40.0	0.02	0.04	15.0	0.2	44.1	0.21	n.d.	0.06	0.50	100.2	84.0
Ahlmannryggen, DML	Fp	Z1816-3	39.6	0.02	0.02	17.2	0.2	42.6	0.24	n.d.	0.07	0.44	100.3	81.6
Ahlmannryggen, DML	Fp	Z1817-2	39.8	0.02	0.02	16.1	0.2	43.6	0.26	n.d.	0.07	0.54	100.7	82.8
Ahlmannryggen, DML	Fp	Z1817-2	39.3	0.02	0.03	19.7	0.2	41.0	0.28	n.d.	0.04	0.39	100.9	78.8
Ahlmannryggen, DML	Fp	Z1817-2	39.2	0.02	0.03	19.9	0.2	40.5	0.26	n.d.	0.04	0.40	100.6	78.4
Ahlmannryggen, DML	Fp	Z1817-2	39.2	0.03	0.04	19.4	0.2	41.0	0.27	n.d.	0.04	0.40	100.6	79.0
Ahlmannryggen, DML	Fp	Z1817-2	39.5	0.02	0.04	17.4	0.2	42.4	0.27	n.d.	0.04	0.51	100.4	81.3
Ahlmannryggen, DML	Fp	Z1817-2	39.7	0.02	0.04	16.9	0.2	43.0	0.24	n.d.	0.05	0.49	100.6	81.9
Ahlmannryggen, DML	Fp	Z1817-2	39.2	0.03	0.04	19.1	0.2	41.4	0.26	n.d.	0.04	0.45	100.6	79.5
Ahlmannryggen, DML	Fp	Z1817-2	39.4	0.02	0.04	18.3	0.2	42.0	0.25	n.d.	0.03	0.46	100.6	80.3
Ahlmannryggen, DML	Fp	Z1817-2	39.3	0.02	0.05	19.7	0.2	41.0	0.28	n.d.	0.04	0.40	101.0	78.8
Ahlmannryggen, DML	Fp	Z1817-2	39.0	0.03	0.03	19.9	0.3	40.6	0.28	n.d.	0.01	0.36	100.5	78.4
Ahlmannryggen, DML	Fp	Z1817-2	39.1	0.02	0.03	18.9	0.2	41.3	0.28	n.d.	0.03	0.45	100.4	79.5
Ahlmannryggen, DML	Fp	Z1817-2	39.6	0.02	0.04	17.8	0.2	42.3	0.23	n.d.	0.05	0.48	100.7	80.9

Table C.5: Average compositions of clinopyroxene and orthopyroxene in each sample (filtered for oxide totals of 97–101%). Fe^{2+}, used for calculating Mg#, is determined stoichiometrically. HP is Horingbaai picrite, Fp is ferropicrite. n.d. means not determined.

Location	Type	Sample	Phase	n	SiO_2	TiO_2	Al_2O_3	FeO^T	MnO	MgO	CaO	P_2O_5	Na_2O	Cr_2O_3	NiO	Total	Mg#
Ahlmannryggen, DML	Fp	Z1813.1	cpx	7	52.0	1.13	2.4	7.6	0.19	17.8	17.8	n.a.	0.25	0.74	n.a.	100.0	0.806
Ahlmannryggen, DML	Fp	Z1816.3	cpx	10	51.3	1.48	2.9	8.7	0.14	17.7	16.8	n.a.	0.22	0.56	n.a.	99.8	0.783
Ahlmannryggen, DML	Fp	Z1817.2	cpx	14	52.1	1.13	2.1	8.8	0.18	17.5	17.3	n.a.	0.23	0.72	n.a.	100.0	0.781
Etendeka	Fp	96SB48	cpx	22	49.5	1.40	3.4	7.6	0.14	14.7	21.0	0.01	0.46	0.61	0.05	98.9	0.775
Etendeka	Fp	97SB67	cpx	25	48.6	1.73	6.6	8.7	0.18	14.0	19.3	n.a.	0.39	0.27	n.a.	99.8	0.733
Etendeka	Fp	97SB73	cpx	44	49.8	1.45	3.2	8.0	0.15	14.7	20.4	0.01	0.42	0.37	0.03	98.6	0.765
Etendeka	Fp	97SB76	cpx	22	50.8	0.93	2.7	8.4	0.18	15.8	19.2	0.01	0.33	0.56	0.04	99.0	0.771
Etendeka	Fp	PB9	cpx	43	50.1	1.15	3.4	7.2	0.15	14.7	21.1	0.01	0.40	0.66	0.03	99.0	0.786
Etendeka	HP	97SB34	cpx	5	51.2	0.69	3.7	5.9	0.17	16.2	20.3	n.a.	0.28	0.84	n.a.	99.4	0.830
Vestfjella, DML	Fp	JSH-B006	cpx	5	50.6	1.47	2.9	8.0	0.15	14.6	21.2	n.a.	0.45	0.44	n.a.	99.9	0.763
Ahlmannryggen, DML	Fp	Z1813.1	opx	5	55.4	0.45	1.4	10.9	0.17	29.0	2.5	n.a.	0.05	0.50	n.a.	100.4	0.826
Ahlmannryggen, DML	Fp	Z1816.3	opx	12	55.8	0.42	1.1	10.6	0.19	29.5	2.4	n.a.	0.04	0.47	n.a.	100.4	0.832
Ahlmannryggen, DML	Fp	Z1817.2	opx	9	55.3	0.48	1.4	10.5	0.16	29.1	2.5	n.a.	0.05	0.48	n.a.	100.0	0.832
Etendeka	HP	97SB56	opx	4	47.9	1.41	9.4	11.2	0.20	18.2	12.0	n.a.	0.18	0.04	n.a.	100.6	0.725

Table C.6: Spinel inclusions and host olivine pairs, with compositions analysed by EPMA for Al-in-olivine thermometry, including calculated temperatures and error brackets. HP, Horingbaai-type picrite, Fp, ferropicrite. Both Fe^{3+}/Fe_T calculated by the method of Droop (1987) from EPMA data and the ratio corrected according to XANES measurements are given. p.f.u., per formula unit (on a 4 oxygen basis). Mg# refers to spinel Mg#, Cr# is spinel molar Cr/(Cr + Al), Fo is olivine forsterite content expressed as a %, T is crystallisation temperature calculated from the equation of Coogan *et al.* (2014), in °C.

Location	Sample	SiO_2	MgO	Al_2O_3	TiO_2	Cr_2O_3	FeO_T	MnO	NiO	Total	Ti p.f.u.	Fe^{3+}/Fe_T EPMA	Fe^{3+}/Fe_T XANES	Mg#	Cr#	$Al_2O_3^{ol} \pm 1\sigma$	Fo	$T \pm 1\sigma$
Etendeka HP	97SB33	0.32	17.3	21.3	1.13	42.9	16.3	0.17	0.29	100.1	0.026	0.38	0.23	0.709	0.575	0.109 ± 0.007	93.3	1446 ± 17
Etendeka HP	97SB33	0.15	16.3	19.6	0.53	46.0	16.4	0.16	0.23	99.8	0.012	0.36	0.21	0.692	0.611	0.099 ± 0.007	92.9	1434 ± 19
Etendeka HP	97SB33	0.06	6.6	8.6	4.39	7.2	67.8	0.36	0.30	97.6	0.135	0.52	0.31	0.200	0.358	0.043 ± 0.007	83.3	1498 ± 48
Etendeka HP	97SB33	0.07	7.0	8.4	3.89	7.0	68.3	0.30	0.31	97.7	0.120	0.53	0.32	0.211	0.356	0.043 ± 0.007	83.3	1505 ± 48
Etendeka HP	97SB33	0.60	14.8	24.4	3.42	36.5	19.0	0.20	0.29	99.4	0.078	0.14	0.08	0.601	0.502	0.083 ± 0.007	91.8	1362 ± 21
Etendeka HP	97SB33	0.09	12.4	20.2	1.99	35.5	27.9	0.27	0.29	99.4	0.049	0.37	0.22	0.504	0.541	0.051 ± 0.007	89.5	1283 ± 31
Etendeka HP	97SB33	0.17	14.2	17.6	0.50	46.7	19.3	0.19	0.24	99.2	0.012	0.31	0.19	0.617	0.640	0.119 ± 0.010	91.6	1505 ± 25
Etendeka HP	97SB33	0.07	4.7	5.8	5.84	1.2	76.9	0.35	0.23	97.6	0.190	0.50	0.30	0.134	0.119	0.036 ± 0.010	81.4	1635 ± 102
Etendeka HP	97SB33	0.15	15.4	17.9	0.49	46.9	17.4	0.19	0.34	99.2	0.012	0.35	0.21	0.666	0.637	0.109 ± 0.010	93.1	1476 ± 27
Etendeka HP	97SB33	0.19	14.6	18.1	0.48	46.3	18.3	0.22	0.27	98.8	0.012	0.32	0.19	0.636	0.632	0.124 ± 0.010	92.9	1511 ± 24
Etendeka HP	97SB33	0.08	13.5	18.9	5.28	27.1	33.0	0.20	0.40	99.5	0.130	0.42	0.25	0.493	0.490	0.052 ± 0.010	90.1	1313 ± 47
Etendeka HP	97SB33	0.07	13.1	26.8	0.83	26.8	30.2	0.19	0.31	99.2	0.020	0.44	0.26	0.511	0.402	0.070 ± 0.010	88.1	1322 ± 34
Etendeka HP	97SB33	0.15	14.4	19.5	0.48	44.1	19.4	0.25	0.20	98.9	0.011	0.33	0.19	0.621	0.603	0.085 ± 0.010	91.3	1399 ± 31
Etendeka HP	97SB33	0.13	13.1	18.6	0.51	43.8	22.2	0.20	0.25	99.2	0.012	0.32	0.19	0.565	0.612	0.088 ± 0.010	90.8	1417 ± 30
Etendeka HP	97SB33	0.08	12.8	24.1	0.71	28.4	31.3	0.21	0.31	98.9	0.017	0.46	0.27	0.501	0.441	0.065 ± 0.010	87.2	1320 ± 37
Etendeka HP	97SB33	0.23	11.8	20.0	0.71	26.9	36.7	0.25	0.32	98.2	0.018	0.51	0.30	0.450	0.475	0.072 ± 0.010	86.8	1384 ± 36
Etendeka HP	97SB33	0.16	15.6	18.9	0.48	46.8	16.1	0.19	0.24	98.9	0.011	0.32	0.19	0.680	0.624	0.110 ± 0.010	93.1	1467 ± 26
Etendeka HP	97SB33	0.16	15.5	18.3	0.50	47.2	17.2	0.18	0.27	99.7	0.012	0.33	0.20	0.666	0.634	0.107 ± 0.010	92.7	1466 ± 26
Etendeka HP	97SB41	0.09	10.4	17.3	0.65	38.4	31.4	0.30	0.20	99.5	0.016	0.38	0.22	0.432	0.598	0.058 ± 0.014	85.3	1333 ± 61
Etendeka HP	97SB41	0.30	11.6	16.4	0.69	41.8	28.6	0.30	0.18	100.8	0.017	0.37	0.22	0.482	0.631	0.058 ± 0.014	85.3	1338 ± 64
Etendeka HP	97SB41	0.10	11.9	15.7	0.62	43.4	28.2	0.28	0.22	101.1	0.015	0.39	0.23	0.493	0.649	0.085 ± 0.014	85.9	1442 ± 46
Etendeka HP	97SB41	0.08	9.8	20.3	1.12	33.3	33.6	0.32	0.20	99.7	0.028	0.37	0.22	0.400	0.524	0.062 ± 0.014	82.0	1332 ± 56
Etendeka HP	97SB41	0.07	10.8	16.1	0.50	45.1	26.2	0.30	0.18	99.8	0.012	0.30	0.18	0.473	0.652	0.088 ± 0.014	87.5	1442 ± 44
Etendeka HP	97SB41	0.18	11.6	22.9	0.75	34.2	28.5	0.28	0.24	99.4	0.018	0.35	0.21	0.479	0.500	0.089 ± 0.014	85.6	1394 ± 41
Etendeka HP	97SB41	0.10	11.9	23.4	1.22	33.2	28.7	0.27	0.24	99.7	0.029	0.35	0.21	0.483	0.488	0.056 ± 0.014	85.8	1284 ± 59

Table C.6 – *Continued on next page*

Location	Sample	SiO_2	MgO	Al_2O_3	TiO_2	Cr_2O_3	FeO_T	MnO	NiO	Total	Ti p.f.u.	Fe^{3+}/Fe_T EPMA	Fe^{3+}/Fe_T XANES	Mg#	Cr#	$Al_2O_3^{ol} \pm 1\sigma$	Fo	T °C $\pm 1\sigma$
Etendeka HP	97SB41	0.09	10.9	16.0	0.56	44.5	26.9	0.29	0.18	99.9	0.014	0.32	0.19	0.470	0.652	0.081 ± 0.014	86.7	1425 ± 47
Etendeka HP	97SB41	0.09	12.3	22.8	1.38	32.7	29.9	0.28	0.26	100.6	0.033	0.39	0.23	0.488	0.490	0.046 ± 0.014	85.3	1249 ± 71
Etendeka HP	97SB41	0.11	12.3	22.8	1.32	32.0	29.6	0.26	0.25	99.5	0.032	0.39	0.23	0.491	0.485	0.044 ± 0.014	85.4	1239 ± 75
Etendeka HP	97SB41	0.08	12.2	16.4	0.38	46.2	23.8	0.28	0.19	100.1	0.009	0.32	0.19	0.529	0.654	0.094 ± 0.014	88.1	1454 ± 42
Etendeka HP	97SB41	0.13	14.5	25.6	1.15	36.8	21.2	0.23	0.26	100.3	0.026	0.30	0.18	0.596	0.491	0.044 ± 0.014	88.8	1215 ± 73
Etendeka HP	97SB41	0.08	10.7	13.6	0.39	46.7	27.3	0.32	0.18	99.9	0.010	0.34	0.20	0.467	0.698	0.074 ± 0.014	86.3	1433 ± 52
Etendeka HP	97SB56	0.17	15.2	20.1	0.58	44.5	18.4	0.25	0.22	99.8	0.014	0.33	0.20	0.647	0.597	0.100 ± 0.014	91.9	1433 ± 38
Etendeka HP	97SB56	0.07	9.4	16.4	1.57	24.4	44.7	0.31	0.24	98.6	0.042	0.49	0.29	0.347	0.500	0.044 ± 0.014	84.2	1307 ± 83
Etendeka HP	97SB56	0.10	9.7	18.4	1.76	26.0	41.1	0.34	0.23	98.9	0.046	0.46	0.27	0.366	0.487	0.041 ± 0.014	84.7	1271 ± 84
Etendeka HP	97SB56	0.09	10.8	19.6	0.72	31.2	35.5	0.30	0.24	99.6	0.018	0.45	0.26	0.425	0.517	0.079 ± 0.014	85.6	1399 ± 47
Etendeka HP	97SB56	0.08	10.0	16.4	1.67	24.5	44.9	0.32	0.26	99.6	0.044	0.50	0.30	0.361	0.500	0.043 ± 0.014	84.8	1302 ± 81
Etendeka HP	97SB56	0.06	9.1	17.3	1.48	26.6	43.7	0.30	0.21	100.0	0.039	0.46	0.27	0.337	0.509	0.086 ± 0.014	81.6	1458 ± 46
Etendeka HP	97SB56	0.13	12.1	24.0	1.67	26.7	33.4	0.29	0.28	99.5	0.041	0.43	0.26	0.465	0.427	0.040 ± 0.014	85.6	1222 ± 81
Etendeka HP	97SB56	0.08	12.4	21.4	0.92	34.1	29.8	0.24	0.22	100.0	0.022	0.41	0.24	0.496	0.517	0.052 ± 0.014	86.9	1280 ± 64
Etendeka HP	97SB56	0.08	6.7	16.5	1.20	27.0	45.4	0.36	0.16	98.7	0.032	0.43	0.25	0.260	0.524	0.044 ± 0.014	78.7	1303 ± 81
Etendeka HP	97SB56	0.09	11.1	19.2	1.48	26.9	38.2	0.29	0.26	98.8	0.038	0.48	0.29	0.420	0.485	0.042 ± 0.014	85.4	1264 ± 83
Etendeka HP	97SB56	0.10	10.7	20.1	1.11	28.7	36.1	0.30	0.24	98.4	0.028	0.45	0.27	0.418	0.489	0.079 ± 0.014	85.2	1400 ± 46
Etendeka HP	97SB56	0.06	8.0	12.1	3.21	22.4	51.2	0.33	0.24	99.1	0.089	0.48	0.28	0.280	0.554	0.041 ± 0.014	83.4	1348 ± 93
Etendeka HP	97SB56	0.08	11.1	18.3	1.38	26.5	40.3	0.30	0.26	99.5	0.036	0.50	0.29	0.410	0.493	0.049 ± 0.014	85.6	1311 ± 71
Etendeka HP	97SB56	0.07	10.1	17.4	1.86	24.5	43.2	0.30	0.26	99.1	0.049	0.49	0.29	0.371	0.486	0.031 ± 0.014	84.4	1225 ± 105
Etendeka HP	97SB62	0.23	10.8	16.0	0.92	30.9	36.7	0.21	0.29	97.3	0.024	0.48	0.28	0.424	0.564	0.058 ± 0.010	87.1	1361 ± 44
Etendeka HP	97SB62	0.07	12.1	17.5	0.90	35.9	31.0	0.24	0.26	98.9	0.023	0.45	0.27	0.487	0.579	0.052 ± 0.010	87.8	1314 ± 46
Etendeka HP	97SB62	0.13	16.1	18.4	0.66	47.0	16.3	0.14	0.27	99.4	0.016	0.35	0.20	0.688	0.631	0.114 ± 0.010	92.4	1483 ± 26
Etendeka HP	97SB62	0.95	11.2	18.8	1.08	25.2	38.5	0.26	0.37	97.8	0.028	0.48	0.29	0.421	0.474	0.061 ± 0.010	86.4	1355 ± 42
Etendeka Fp	97SB63	0.30	11.7	16.2	4.87	23.3	44.0	0.27	0.42	102.3	0.123	0.47	0.28	0.397	0.491	0.053 ± 0.014	82.2	1354 ± 69
Etendeka Fp	97SB63	0.52	8.1	11.2	5.83	21.6	48.9	0.30	0.36	98.2	0.161	0.43	0.25	0.284	0.564	0.048 ± 0.014	79.1	1402 ± 84
Etendeka Fp	97SB63	0.23	10.5	14.9	5.14	21.2	45.5	0.24	0.45	99.6	0.136	0.47	0.28	0.363	0.488	0.048 ± 0.014	79.1	1350 ± 78
Etendeka Fp	97SB63	8.82	16.7	12.5	3.29	16.2	35.6	0.22	0.45	94.9	0.083	0.40	0.24	0.523	0.466	0.052 ± 0.014	83.0	1420 ± 76
Etendeka Fp	97SB63	0.16	10.4	14.8	5.12	22.2	44.3	0.24	0.44	99.0	0.136	0.46	0.27	0.364	0.502	0.051 ± 0.014	82.8	1363 ± 74
Etendeka Fp	97SB63	0.40	9.2	13.8	8.68	16.3	48.2	0.27	0.47	98.6	0.233	0.40	0.24	0.308	0.441	0.052 ± 0.014	82.9	1401 ± 76
Etendeka Fp	97SB63	0.21	10.7	15.8	5.49	21.6	42.4	0.24	0.49	98.3	0.144	0.45	0.27	0.380	0.479	0.050 ± 0.014	83.6	1350 ± 75

Table C.6 – *Continued on next page*

Location	Sample	SiO_2	MgO	Al_2O_3	TiO_2	Cr_2O_3	FeO_T	MnO	NiO	Total	Ti p.f.u.	Fe^{3+}/Fe_T EPMA	Fe^{3+}/Fe_T XANES	Mg#	Cr#	$Al_2O_3^{ol} \pm 1\sigma$	Fo	T °C $\pm 1\sigma$
Etendeka Fp	97SB63	0.14	9.9	13.4	5.34	21.5	46.3	0.28	0.41	98.7	0.144	0.46	0.27	0.343	0.518	0.057 ± 0.014	82.3	1415 ± 67
Etendeka Fp	97SB63	0.13	9.8	13.3	5.53	21.6	46.2	0.25	0.44	98.6	0.149	0.46	0.27	0.342	0.521	0.043 ± 0.014	82.2	1344 ± 87
Etendeka Fp	97SB63	0.13	10.7	14.7	4.49	24.9	42.2	0.25	0.45	99.0	0.118	0.46	0.27	0.384	0.532	0.051 ± 0.014	83.4	1362 ± 72
Etendeka Fp	97SB63	0.13	9.7	15.1	4.54	24.2	43.4	0.25	0.38	99.0	0.120	0.44	0.26	0.351	0.517	0.049 ± 0.014	81.3	1346 ± 76
Etendeka Fp	97SB63	5.31	11.0	16.0	4.64	22.9	39.6	0.25	0.39	101.0	0.113	0.27	0.16	0.371	0.489	0.053 ± 0.014	82.3	1358 ± 70
Etendeka Fp	97SB63	0.12	9.5	12.2	5.22	22.9	47.1	0.26	0.36	99.1	0.142	0.46	0.27	0.331	0.558	0.046 ± 0.014	81.7	1375 ± 84
Etendeka Fp	97SB63	0.17	10.1	14.2	4.28	23.9	44.1	0.25	0.41	98.9	0.114	0.47	0.27	0.360	0.531	0.053 ± 0.014	82.5	1375 ± 70
Etendeka Fp	97SB63	0.13	10.1	14.1	5.85	21.0	45.6	0.23	0.47	98.8	0.156	0.45	0.27	0.351	0.499	0.054 ± 0.014	82.2	1391 ± 70
Etendeka Fp	97SB63	0.31	9.0	13.6	4.74	24.1	44.2	0.26	0.42	97.9	0.128	0.43	0.25	0.327	0.542	0.053 ± 0.007	82.0	1384 ± 33
Etendeka Fp	97SB73	1.81	10.3	14.6	5.36	26.9	40.1	0.26	0.37	100.6	0.136	0.35	0.21	0.365	0.554	0.033 ± 0.014	81.0	1256 ± 107
Etendeka Fp	97SB73	0.10	8.3	16.0	4.28	31.5	37.5	0.28	0.30	99.0	0.111	0.32	0.19	0.327	0.569	0.035 ± 0.014	80.3	1250 ± 97
Etendeka Fp	97SB73	0.21	7.7	13.5	6.69	23.9	45.7	0.28	0.32	99.4	0.178	0.37	0.22	0.278	0.542	0.035 ± 0.014	79.2	1290 ± 104
Etendeka Fp	97SB73	0.09	7.8	14.5	5.06	28.8	40.9	0.29	0.31	98.6	0.134	0.34	0.20	0.300	0.571	0.037 ± 0.014	79.3	1279 ± 96
Etendeka Fp	97SB73	0.92	9.4	18.2	6.47	30.4	32.8	0.27	0.29	99.6	0.159	0.19	0.11	0.366	0.528	0.039 ± 0.014	81.4	1250 ± 87
Etendeka Fp	97SB73	0.18	8.4	12.5	7.91	22.7	45.4	0.27	0.39	98.9	0.212	0.37	0.22	0.296	0.549	0.028 ± 0.014	81.0	1260 ± 121
Etendeka Fp	97SB73	0.08	8.4	14.2	5.03	28.8	40.8	0.28	0.32	99.0	0.133	0.36	0.21	0.318	0.576	0.030 ± 0.014	80.9	1236 ± 110
Etendeka Fp	97SB73	0.08	6.9	10.8	7.40	24.0	46.3	0.26	0.30	97.2	0.205	0.36	0.21	0.253	0.598	0.028 ± 0.007	77.9	1274 ± 61
Etendeka Fp	97SB73	0.21	7.0	10.2	8.49	22.8	47.6	0.26	0.28	97.9	0.234	0.35	0.21	0.248	0.599	0.028 ± 0.007	77.9	1286 ± 60
Etendeka Fp	97SB80	0.04	4.7	12.5	5.26	25.5	50.0	0.44	0.12	99.8	0.144	0.35	0.21	0.176	0.578	0.042 ± 0.014	73.2	1338 ± 93
Etendeka Fp	97SB80	0.04	6.6	16.0	2.70	27.0	45.8	0.34	0.15	99.9	0.072	0.39	0.23	0.251	0.530	0.042 ± 0.014	73.2	1293 ± 87
Etendeka Fp	97SB80	0.06	6.2	19.9	2.14	26.4	43.9	0.37	0.11	100.2	0.055	0.36	0.21	0.243	0.471	0.043 ± 0.014	70.9	1264 ± 82
Etendeka Fp	97SB80	0.06	7.2	21.0	1.88	28.0	41.1	0.33	0.14	100.6	0.048	0.35	0.21	0.283	0.472	0.043 ± 0.014	70.9	1253 ± 79
Etendeka Fp	97SB80	1.50	6.6	16.3	3.16	23.7	45.5	0.37	0.15	98.8	0.084	0.36	0.21	0.248	0.493	0.037 ± 0.014	73.7	1272 ± 95
Etendeka Fp	97SB80	0.07	7.9	22.4	1.49	28.0	38.8	0.33	0.17	100.1	0.037	0.35	0.21	0.315	0.456	0.053 ± 0.014	75.0	1291 ± 64
Etendeka Fp	97SB80	0.72	7.8	20.6	2.01	26.7	39.6	0.33	0.20	98.9	0.051	0.35	0.20	0.307	0.465	0.047 ± 0.014	78.1	1278 ± 73
Etendeka Fp	97SB80	0.09	8.3	21.1	1.96	27.4	39.4	0.31	0.18	99.7	0.050	0.37	0.22	0.324	0.466	0.048 ± 0.014	75.7	1279 ± 70
Etendeka Fp	97SB80	0.08	5.1	17.2	2.83	24.9	47.5	0.39	0.08	99.3	0.076	0.37	0.22	0.195	0.493	0.034 ± 0.014	68.4	1243 ± 100
Etendeka Fp	97SB80	0.07	9.3	23.5	1.32	28.6	35.9	0.29	0.22	100.0	0.033	0.36	0.21	0.370	0.450	0.059 ± 0.014	79.1	1303 ± 58
Etendeka Fp	97SB80	1.50	3.6	8.6	2.50	22.0	56.7	0.40	0.13	97.0	0.074	0.42	0.25	0.131	0.632	0.044 ± 0.014	68.2	1432 ± 94
Etendeka Fp	PB009	0.06	10.4	19.9	2.14	34.1	31.5	0.26	0.15	99.2	0.053	0.33	0.20	0.422	0.535	0.055 ± 0.007	82.7	1306 ± 29
Etendeka Fp	PB009	0.08	11.8	23.3	1.54	34.2	26.8	0.21	0.13	98.7	0.037	0.31	0.18	0.490	0.496	0.053 ± 0.007	84.7	1271 ± 29

Table C.6 – *Continued on next page*

Location	Sample	SiO_2	MgO	Al_2O_3	TiO_2	Cr_2O_3	FeO_T	MnO	NiO	Total	Ti p.f.u.	Fe^{3+}/Fe_T EPMA	Fe^{3+}/Fe_T XANES	Mg#	Cr#	$Al_2O_3^{ol} \pm 1\sigma$	Fo	T °C $\pm 1\sigma$
Etendeka Fp	PB009	0.06	6.1	14.2	1.70	29.9	44.3	0.33	0.14	97.8	0.047	0.40	0.23	0.241	0.586	0.036 ± 0.007	74.1	1278 ± 44
Etendeka Fp	PB009	0.07	6.0	14.9	2.20	30.3	43.3	0.33	0.14	98.2	0.059	0.37	0.22	0.239	0.577	0.044 ± 0.010	72.5	1312 ± 56
Etendeka Fp	PB009	0.07	8.0	18.9	1.46	33.6	34.6	0.25	0.14	97.7	0.038	0.32	0.19	0.338	0.544	0.057 ± 0.010	78.2	1325 ± 44
Etendeka Fp	PB009	0.04	7.8	16.9	2.81	31.3	38.5	0.30	0.15	98.7	0.073	0.35	0.20	0.311	0.554	0.051 ± 0.010	78.1	1322 ± 48
Etendeka Fp	PB009	0.08	7.6	16.1	2.37	34.4	36.2	0.26	0.23	98.0	0.062	0.32	0.19	0.316	0.589	0.048 ± 0.010	77.2	1312 ± 51
Etendeka Fp	PB009	0.08	8.1	17.9	1.58	33.8	35.9	0.27	0.10	98.6	0.041	0.34	0.20	0.334	0.558	0.058 ± 0.010	78.9	1335 ± 43
Etendeka Fp	PB009	0.06	7.8	16.8	2.83	31.1	38.5	0.27	0.19	98.3	0.074	0.35	0.20	0.311	0.554	0.051 ± 0.010	77.9	1324 ± 49
Etendeka Fp	PB009	0.06	5.9	12.7	1.81	33.0	42.6	0.28	0.18	97.7	0.050	0.38	0.22	0.241	0.635	0.046 ± 0.010	74.0	1346 ± 56
Etendeka Fp	PB009	0.06	3.6	6.6	9.67	14.2	62.5	0.35	0.11	98.7	0.288	0.39	0.23	0.117	0.590	0.030 ± 0.010	70.1	1415 ± 98
Vest., DML Fp	JSH-B006	0.05	8.1	8.8	6.79	27.0	46.2	0.27	0.31	98.7	0.187	0.40	0.24	0.290	0.673	0.034 ± 0.010	79.2	1349 ± 82
Vest., DML Fp	JSH-B006	0.08	7.9	8.0	5.08	29.7	45.1	0.26	0.25	97.6	0.143	0.42	0.25	0.292	0.712	0.024 ± 0.010	79.3	1280 ± 111
Vest., DML Fp	JSH-B006	0.06	8.0	8.4	5.43	30.7	43.9	0.22	0.25	98.1	0.151	0.40	0.24	0.297	0.710	0.023 ± 0.010	79.5	1261 ± 111
Ahl., DML Fp	Z1813.1	0.08	7.2	10.3	5.65	36.1	37.4	0.30	0.35	98.1	0.151	0.28	0.16	0.292	0.701	0.030 ± 0.010	81.8	1283 ± 82
Ahl., DML Fp	Z1813.1	0.08	7.9	10.7	4.14	37.1	36.2	0.27	0.33	97.5	0.111	0.32	0.19	0.325	0.699	0.035 ± 0.010	81.6	1305 ± 73
Ahl., DML Fp	Z1813.1	0.07	7.8	10.0	5.31	36.6	37.5	0.25	0.35	98.7	0.142	0.30	0.18	0.310	0.711	0.026 ± 0.010	81.2	1259 ± 95
Ahl., DML Fp	Z1816.3	0.14	8.8	10.6	5.72	37.1	33.1	0.20	0.34	96.7	0.152	0.27	0.16	0.361	0.702	0.030 ± 0.010	81.8	1276 ± 84
Ahl., DML Fp	Z1817.2	0.10	8.8	13.1	5.13	34.4	34.8	0.24	0.37	97.6	0.135	0.30	0.17	0.353	0.638	0.035 ± 0.010	81.3	1278 ± 69
Ahl., DML Fp	Z1817.2	0.04	8.8	10.2	5.78	37.2	35.3	0.24	0.37	98.7	0.152	0.30	0.17	0.348	0.710	0.027 ± 0.010	79.5	1259 ± 94
Ahl., DML Fp	Z1817.2	0.06	5.4	10.5	9.14	33.2	39.3	0.31	0.31	98.7	0.243	0.16	0.10	0.215	0.679	0.029 ± 0.010	79.0	1277 ± 87
Ahl., DML Fp	Z1817.2	0.07	8.2	11.0	5.44	36.3	35.6	0.26	0.34	97.9	0.145	0.29	0.17	0.330	0.690	0.032 ± 0.010	80.1	1283 ± 77

Table C.7: SIMS analyses of standard glasses. Final concentrations in ppm following normalisation to ^{42}Ca, daily drift correction and matrix correction. Repeat analyses of standards were staggered throughout the week-long sessions. Published values from GeoReM (Jochum *et al.*, 2005).

Standard	Si	K	Ca	Sc	Ti	Rb	Sr	Y	Zr	Nb	Ba	La
Published values, ppm												
NIST-610	325778	464	81476	455	452	425.7	515.5	462	448	465	452	440
BCR-2G	254266	14900	50458	33	14100	47	342	35	184	12.5	683	24.7
BHVO-2G	230428	4270	81476	33	16300	9.2	396	26	170	18.3	131	15.2
BIR-1G	222015	183	95055	43	5400	0.197	109	14.3	14	0.52	6.5	0.609
GOR132-G	212667	256	60392	36.5	1834	2.1	15.3	12.9	9.9	0.073	0.815	0.0842
GSD-1G	248657	25300	51458	52	7433	37.3	69.4	42	42	42	67	39.1
ML3B-G	240244	3196	75044	31.6	12767	5.8	312	23.9	122	8.61	80.1	8.99
Measured October 2012												
BCR-2G	275164	14941	50458	31.3	13930	NA	340.6	35.8	185	12.6	684.5	25.2
BCR-2G	279496	15257	50458	30.8	13993	45.1	337.7	35.8	182	13.0	686.6	24.9
BHVO-2G	245822	4131	81476	31.8	16659	NA	397.4	26.7	169	17.6	132.9	15.7
BHVO-2G	251039	4247	81476	30.9	16584	7.4	392.2	26.4	164	17.3	131.5	15.7
BIR-1G	239071	204	95055	44.1	5751	NA	110.4	15.9	14	0.5	7.2	0.7
BIR-1G	242940	207	95055	43.9	5794	-0.4	109.9	15.8	15	0.6	6.6	0.6
GOR132-G	237332	268	60392	38.9	1816	1.7	14.8	15.4	11	0.1	1.0	0.1
GOR132-G	236408	293	60392	39.1	1812	1.7	14.8	15.4	11	0.1	0.9	0.1
GSD-1G	262716	25227	51458	48.0	7701	NA	72.2	44.6	41	42.1	70.7	39.1
GSD-1G	265704	25485	51458	47.8	7689	38.1	73.5	44.5	43	45.3	76.2	41.3
GSD-1G	265830	25939	51458	47.7	7790	36.1	72.0	45.2	44	43.4	72.7	40.2
GSD-1G	266318	27273	51458	48.1	7751	38.9	73.3	44.9	44	44.4	75.3	42.9
GSD-1G	256804	26371	51458	47.5	7482	35.4	74.5	45.5	42	45.5	77.5	43.2
GSD-1G	260083	26711	51458	47.9	7493	33.7	71.6	44.4	42	43.4	71.4	40.9
ML3B-G	263372	3055	75044	29.6	12787	5.4	315.3	25.3	125	8.6	82.9	10.0
ML3B-G	264311	3375	75044	29.6	13081	4.2	323.4	26.4	130	9.1	87.4	10.0
ML3B-G	259597	3243	75044	30.5	12611	4.9	318.6	27.1	128	8.5	84.6	10.3
ML3B-G	263510	3301	75044	29.7	12730	5.0	319.0	26.5	129	8.2	83.6	9.8
Measured October 2013												
BCR-2G	254306	14393	53092	31.4	14332	45.8	339.7	34.6	182	12.3	677.6	23.2
BCR-2G	254416	13773	53580	30.3	13970	42.8	328.8	33.8	177	10.8	646.7	22.7
BCR-2G	254336	14699	52856	31.0	14403	46.9	344.3	34.1	187	12.1	692.4	22.9
BCR-2G	254413	14382	55997	31.4	14700	46.3	352.6	34.9	189	12.1	683.9	23.1
BCR-2G	254416	13826	54729	32.5	14375	45.1	340.7	35.6	186	11.7	683.1	24.8
BCR-2G	254416	13955	54929	32.7	14211	46.6	343.0	34.7	181	11.2	687.6	23.2
BCR-2G	254416	14125	55036	32.3	14144	44.9	349.5	36.8	184	12.2	685.3	24.9
BCR-2G	254416	13924	54460	31.8	14054	44.1	341.6	35.4	182	11.0	663.2	23.8
BCR-2G	254416	14594	53671	30.6	14310	47.3	336.1	33.9	182	11.4	660.5	23.0
BHVO-2G	230462	4299	85076	31.1	17401	9.6	406.3	26.0	170	17.3	135.8	15.0
BHVO-2G	230561	3943	85072	31.0	16825	9.7	382.3	25.0	164	15.2	122.3	13.7
BHVO-2G	230559	3397	88080	30.7	16819	8.1	385.3	25.4	165	13.9	117.7	14.4
BHVO-2G	230561	4051	87531	32.5	17304	9.1	399.5	26.2	171	16.9	136.2	15.2
BHVO-2G	230561	4016	86524	31.1	16926	8.5	397.4	26.7	171	16.4	124.8	14.8
BHVO-2G	230561	3918	86470	31.5	16830	8.6	391.3	26.5	164	15.2	126.1	15.4
BHVO-2G	230561	4200	86919	30.7	17100	8.6	392.4	25.6	165	17.1	122.7	14.3
BIR-1G	222090	196	97883	41.6	6022	NA	111.8	15.2	14	0.6	6.7	0.5
BIR-1G	222184	151	99919	42.6	5756	0.5	104.6	15.7	14	0.4	5.5	0.6
BIR-1G	222186	171	99662	43.7	5894	0.0	105.5	16.3	14	0.5	6.2	0.7

Table C.7 – *Continued on next page*

Standard	Si	K	Ca	Sc	Ti	Rb	Sr	Y	Zr	Nb	Ba	La
BIR-1G	222148	177	100000	42.7	5923	-0.3	109.4	15.2	14	0.5	6.0	0.8
BIR-1G	222186	186	98850	41.6	5909	NA	106.1	15.4	14	0.5	6.6	0.6
GSD-1G	248725	25467	55476	49.8	8215	39.0	73.8	43.2	44	41.7	73.4	39.5
GSD-1G	248830	25060	56578	48.6	8242	37.5	73.4	43.4	45	41.4	77.3	39.3
GSD-1G	248832	25563	57441	50.1	8190	40.5	72.7	44.2	43	41.5	76.2	39.1
GSD-1G	248790	25555	57746	48.1	8197	40.1	78.0	42.6	45	41.5	74.9	39.3
GSD-1G	248832	26136	56904	48.8	8078	39.6	72.6	43.7	44	39.1	73.0	36.9
ML3B-G	240367	2954	77989	29.0	12899	5.3	302.8	24.8	123	7.2	74.2	8.2
ML3B-G	240263	3100	77205	29.3	12952	5.6	306.6	23.5	120	7.5	78.6	8.3
ML3B-G	240365	3011	79017	28.7	13144	5.2	317.8	24.7	129	7.7	84.0	8.8
ML3B-G	240367	2892	77845	29.5	12786	6.2	303.5	24.7	123	7.5	77.3	8.3
ML3B-G	240367	2934	78476	29.3	12778	4.5	310.0	24.0	126	7.2	76.4	8.8
ML3B-G	240367	3083	78174	28.5	13011	4.6	309.2	24.6	126	7.7	78.9	8.5

Table C.7 continued.

Standard	Ce	Pr	Nd	Sm	Eu	Gd	Tb	Dy	Ho	Er	Tm	Yb	Lu
Published													
NIST-610	453	448	430	453	447	449	437	437	449	455	435	450	439
BCR-2G	53.3	6.7	28.9	6.59	1.97	6.71	1.02	6.44	1.27	3.7	0.51	3.39	0.503
BHVO-2G	37.6	5.35	24.5	6.1	2.07	6.16	0.92	5.28	0.98	2.56	0.34	2.01	0.279
BIR-1G	1.89	0.37	2.37	1.09	0.517	1.85	0.35	2.55	0.56	1.7	0.24	1.64	0.248
GOR132-G	0.393	0.089	0.689	0.508	0.255	1.19	0.269	2.15	0.507	1.56	0.234	1.61	0.237
GSD-1G	41.4	45	44.7	47.8	41	50.7	47	51.2	49	40.1	49	50.9	51.5
ML3B-G	23.1	3.43	16.7	4.75	1.67	5.26	0.797	4.84	0.906	2.44	0.324	2.06	0.286
Measured October 2012													
BCR-2G	53.4	7.0	28.7	6.9	2.00	6.49	1.13	7.51	1.38	3.59	0.43	3.94	NA
BCR-2G	53.2	7.0	27.3	6.2	1.86	5.70	1.04	7.05	1.38	3.90	0.57	4.15	0.55
BHVO-2G	39.0	5.5	22.7	5.9	2.16	5.49	1.04	5.49	1.05	2.40	0.40	1.90	NA
BHVO-2G	37.4	5.2	25.5	6.8	2.11	5.66	0.88	5.68	0.97	2.96	0.31	2.64	0.29
BIR-1G	2.0	0.3	3.3	1.4	0.63	2.00	0.37	2.25	0.55	2.08	0.29	1.73	NA
BIR-1G	2.1	0.3	2.7	1.1	0.58	1.73	0.35	2.78	0.63	1.74	0.24	1.90	0.27
GOR132-G	0.5	0.1	0.8	1.1	0.46	1.48	0.32	2.82	0.59	1.85	0.30	1.80	0.22
GOR132-G	0.6	0.1	0.8	0.7	0.41	0.82	0.30	2.65	0.48	1.77	0.24	1.85	0.24
GSD-1G	40.2	45.1	45.6	48.0	41.05	50.66	47.07	51.46	49.06	40.23	49.04	51.14	49.78
GSD-1G	42.5	44.1	46.6	47.6	39.77	50.32	47.72	52.33	50.07	40.96	50.26	55.48	51.53
GSD-1G	43.4	47.0	44.1	50.0	42.06	50.14	48.32	51.76	50.58	41.04	49.77	53.33	50.25
GSD-1G	42.6	47.7	43.2	50.3	42.74	52.16	49.59	54.95	51.22	42.11	51.09	54.80	52.07
GSD-1G	42.1	48.1	47.9	52.1	44.36	51.68	48.75	55.19	51.42	41.23	51.34	54.93	53.06
GSD-1G	41.6	46.7	44.2	49.3	42.36	49.07	48.41	52.37	50.21	40.43	49.47	53.32	50.79
ML3B-G	22.7	3.7	16.6	4.7	1.48	5.16	0.87	4.86	0.96	2.61	0.46	2.62	0.36
ML3B-G	24.0	3.5	16.7	5.3	1.84	5.24	1.00	5.40	0.94	2.66	0.40	2.47	0.23
ML3B-G	24.9	3.6	19.2	5.8	1.66	5.61	0.84	5.52	0.96	2.79	0.38	2.11	0.25
ML3B-G	24.3	3.9	16.9	5.0	1.72	4.67	0.90	5.49	1.10	2.84	0.35	2.43	0.31
Measured October 2013													
BCR-2G	52.5	6.0	27.4	6.8	1.98	7.55	1.09	6.45	1.18	3.95	0.48	3.48	0.45
BCR-2G	48.7	5.9	25.9	5.7	1.90	6.05	0.81	5.81	1.25	3.70	0.45	2.96	0.48
BCR-2G	51.6	6.0	26.2	6.3	1.94	7.24	1.07	6.65	1.44	3.71	0.54	3.52	0.45
BCR-2G	52.4	6.1	26.2	5.8	1.90	6.02	1.14	5.97	1.39	3.12	0.49	3.34	0.40
BCR-2G	52.8	6.5	30.9	6.6	1.47	6.26	0.92	6.87	1.52	3.77	0.50	3.80	0.58
BCR-2G	52.6	6.0	28.2	6.4	2.00	6.39	1.01	6.12	1.43	3.30	0.48	3.43	0.56

Table C.7 – *Continued on next page*

Standard	Ce	Pr	Nd	Sm	Eu	Gd	Tb	Dy	Ho	Er	Tm	Yb	Lu
BCR-2G	51.9	6.3	27.5	6.5	1.70	6.03	1.07	6.89	1.31	3.45	0.50	3.33	0.51
BCR-2G	51.9	6.0	25.1	6.0	2.01	5.16	1.01	7.37	1.37	3.90	0.59	3.40	0.50
BCR-2G	49.3	5.9	26.6	6.1	1.74	6.21	0.96	6.37	1.29	3.71	0.47	3.21	0.42
BHVO-2G	39.1	4.8	22.6	6.3	1.78	7.08	0.97	6.65	0.95	2.57	0.35	2.03	0.23
BHVO-2G	32.6	4.7	24.0	6.0	2.00	4.49	0.77	4.71	0.94	2.23	0.29	1.76	0.21
BHVO-2G	35.9	4.6	23.0	5.5	1.70	6.09	0.90	4.87	0.86	2.27	0.32	1.74	0.20
BHVO-2G	38.8	5.1	24.3	6.2	2.00	5.74	1.00	6.17	0.99	2.63	0.37	2.58	0.23
BHVO-2G	37.8	5.1	26.3	5.5	2.08	4.99	0.88	5.28	0.91	2.55	0.34	2.08	0.27
BHVO-2G	36.8	4.8	24.2	5.7	1.70	5.95	0.84	4.82	0.96	2.51	0.36	1.98	0.31
BHVO-2G	35.6	4.9	23.8	6.0	1.81	5.47	0.77	4.74	0.84	2.25	0.29	1.75	0.29
BIR-1G	1.8	0.3	2.4	0.8	0.46	2.00	0.42	2.22	0.53	1.64	0.22	1.78	0.22
BIR-1G	1.9	0.3	2.3	1.1	0.43	1.68	0.37	2.30	0.41	1.64	0.24	1.56	0.19
BIR-1G	1.9	0.4	2.2	1.3	0.54	1.62	0.43	2.22	0.56	1.82	0.28	1.81	0.28
BIR-1G	2.0	0.3	1.8	1.2	0.58	1.70	0.33	2.38	0.61	1.49	0.24	1.05	0.29
BIR-1G	1.7	0.3	2.8	0.9	0.66	1.61	0.32	2.08	0.66	1.70	0.23	1.42	0.25
GSD-1G	43.9	44.6	45.0	47.7	40.90	50.98	47.05	51.15	49.00	40.11	48.99	50.94	51.46
GSD-1G	43.7	44.7	45.2	47.4	40.85	50.50	47.04	50.86	48.96	39.93	48.98	50.71	51.44
GSD-1G	42.0	44.8	44.3	47.8	40.88	50.40	46.98	50.92	49.09	40.03	49.00	51.07	51.52
GSD-1G	44.3	44.7	44.5	47.4	40.94	50.17	46.99	51.23	48.99	39.97	49.01	50.63	51.51
GSD-1G	40.4	41.6	43.9	45.5	39.91	47.91	43.69	49.09	46.88	36.41	46.06	47.50	48.82
ML3B-G	21.0	3.3	16.4	4.1	1.50	4.10	0.65	4.49	0.89	2.30	0.31	1.85	0.31
ML3B-G	22.3	3.0	15.9	4.4	1.53	4.69	0.81	3.93	0.92	2.34	0.29	1.92	0.29
ML3B-G	23.3	3.2	17.1	4.5	1.60	5.33	0.86	4.56	0.91	2.65	0.26	1.71	0.27
ML3B-G	22.2	3.2	17.4	4.5	1.58	5.10	0.67	3.39	0.96	2.19	0.29	1.78	0.29
ML3B-G	23.5	3.2	17.3	4.9	1.84	4.53	0.81	4.69	0.89	2.34	0.31	1.71	0.30
ML3B-G	22.4	3.1	17.7	4.6	1.51	4.93	0.85	4.43	0.85	2.19	0.26	2.17	0.25

Table C.8: Major element compositions of melt inclusions analysed by EPMA. FeO_T is total Fe expressed as FeO. SIMS shows whether that particular melt inclusion was analysed by SIMS and has a corresponding analysis in Table C.8. n.d. is not determined. Fo refers to the host olivine. Abbreviations: Fp, ferropicrite; HP, Horingbaai picrite.

Location	Type	Sample	MI code	SiO_2	TiO_2	Al_2O_3	FeO_T	MnO	MgO	CaO	P_2O_5	K_2O	Na_2O	Total	SO_2	SIMS	Fo
Ahlmannryggen	Fp	Z1813.1	exp2-04a	49.2	3.97	10.7	11.1	0.1	9.4	10.2	0.35	0.44	2.1	97.7	0.07	y	80.0
Ahlmannryggen	Fp	Z1813.1	exp2-9	49.9	3.64	11.5	10.3	0.2	9.2	10.4	0.30	0.43	2.3	98.3	0.19	y	81.0
Ahlmannryggen	Fp	Z1813.1	exp2-29	49.5	4.24	11.2	10.9	0.2	9.7	10.6	0.30	0.41	2.0	99.2	0.18	y	81.0
Ahlmannryggen	Fp	Z1813.1	exp3-29a	48.2	3.74	10.5	11.5	0.1	10.6	9.9	0.30	0.34	1.7	96.9	0.10	y	82.0
Ahlmannryggen	Fp	Z1813.1	exp4-20	51.2	3.45	9.5	10.4	0.2	10.1	12.5	0.28	0.60	1.5	100.0	0.00	n	81.7
Ahlmannryggen	Fp	Z1813.1	exp4-30b	49.2	4.34	11.3	10.2	0.2	9.6	11.0	0.32	0.43	2.2	99.2	0.10	y	82.5
Ahlmannryggen	Fp	Z1813.1	exp4-45	48.4	4.06	11.4	13.7	0.1	8.7	9.2	0.42	1.05	1.6	98.6	0.02	n	81.4
Ahlmannryggen	Fp	Z1813.1	exp4-67	49.8	4.13	11.0	11.4	0.2	9.6	10.2	0.27	0.40	1.8	98.9	0.07	n	81.7
Ahlmannryggen	Fp	Z1813.1	exp5-13	49.5	3.50	11.3	11.4	0.3	9.2	10.8	0.30	0.34	2.0	98.7	n.d.	n	82.1
Ahlmannryggen	Fp	Z1813.1	exp5-22	52.2	3.19	9.2	11.6	0.1	8.9	9.5	0.39	1.03	2.1	98.5	n.d.	y	81.8
Ahlmannryggen	Fp	Z1813.1	exp5-23	50.4	4.61	11.4	9.1	0.2	9.5	10.5	0.36	0.40	2.0	98.5	n.d.	y	84.9
Ahlmannryggen	Fp	Z1813.1	exp5-31	47.6	4.80	11.0	13.3	0.1	10.2	10.9	0.69	0.35	1.2	100.1	n.d.	y	81.5
Ahlmannryggen	Fp	Z1813.1	exp5-34	48.3	3.93	11.5	12.5	0.2	8.9	10.8	0.21	0.41	1.9	98.8	n.d.	n	81.5
Ahlmannryggen	Fp	Z1813.1	exp5-54	50.6	3.23	11.9	10.9	0.1	9.2	9.5	0.28	0.39	2.6	98.8	n.d.	n	83.2
Ahlmannryggen	Fp	Z1813.1	exp5-56a	52.8	4.18	10.2	12.8	0.1	8.4	7.3	0.39	0.83	2.1	99.1	n.d.	n	81.6
Ahlmannryggen	Fp	Z1813.1	exp5-56b	49.5	3.84	11.2	12.1	0.2	8.5	10.1	0.36	0.47	2.2	98.6	n.d.	n	80.9
Ahlmannryggen	Fp	Z1813.1	exp6-8	50.6	3.64	11.0	9.3	0.1	10.2	10.5	0.32	0.36	2.0	98.3	0.10	y	81.8
Ahlmannryggen	Fp	Z1813.1	exp6-20	50.3	3.17	11.5	9.9	0.1	9.9	12.1	0.26	0.75	1.1	99.1	0.00	n	80.7
Ahlmannryggen	Fp	Z1813.1	exp6-35	50.9	3.87	10.7	9.1	0.2	9.6	10.9	0.26	0.19	1.8	97.7	0.05	n	83.0
Ahlmannryggen	Fp	Z1813.1	exp6-44	51.1	2.86	10.5	12.1	0.1	9.0	10.7	0.25	0.84	1.3	99.0	0.02	n	81.3
Ahlmannryggen	Fp	Z1813.1	exp7-22	47.8	3.84	9.8	12.7	0.1	13.2	9.1	0.34	0.47	1.7	99.2	n.d.	y	83.5
Ahlmannryggen	Fp	Z1813.1	exp7-43	52.8	3.25	6.3	11.0	0.3	13.8	10.2	0.23	0.25	1.0	99.1	n.d.	n	82.3
Ahlmannryggen	Fp	Z1813.1	exp7-60	47.3	2.13	9.4	17.5	0.3	11.3	9.0	0.28	0.35	1.9	99.4	n.d.	n	81.0
Ahlmannryggen	Fp	Z1813.1	exp8-24	50.7	3.78	11.8	11.6	0.2	9.5	10.8	0.30	0.36	2.1	101.3	0.18	y	80.4
Ahlmannryggen	Fp	Z1813.1	exp8-40	50.5	4.34	12.0	10.6	0.1	9.8	10.4	0.30	0.58	1.4	100.0	0.01	y	81.0
Ahlmannryggen	Fp	Z1813.1	exp8-47	50.4	4.43	11.4	10.4	0.0	9.9	10.9	0.25	0.39	2.1	100.3	0.14	y	81.4
Ahlmannryggen	Fp	Z1813.1	exp8-61	50.2	4.11	10.6	10.3	0.2	9.5	13.1	0.34	0.97	1.8	101.1	0.00	y	84.1

Table C.8 – *Continued on next page*

Location	Type	Sample	MI code	SiO_2	TiO_2	Al_2O_3	FeO_T	MnO	MgO	CaO	P_2O_5	K_2O	Na_2O	Total	SO_2	SIMS	Fo
Ahlmannryggen	Fp	Z1813.1	exp8-72	50.1	4.46	11.1	12.5	0.2	9.5	10.4	0.28	0.66	1.7	101.0	0.16	n	80.9
Ahlmannryggen	Fp	Z1813.1	exp8-91	50.8	4.27	11.4	11.2	0.3	9.6	10.8	0.32	0.41	2.1	101.3	0.11	y	80.7
Ahlmannryggen	Fp	Z1816.3	exp2-02a	48.8	4.21	10.5	11.4	0.2	9.5	10.5	0.27	0.36	1.9	98.0	0.09	y	81.3
Ahlmannryggen	Fp	Z1816.3	exp2-02b	49.0	4.08	10.7	10.9	0.2	9.5	10.4	0.42	0.42	1.9	97.7	0.14	y	81.3
Ahlmannryggen	Fp	Z1816.3	exp2-02c	50.0	4.31	10.6	10.8	0.1	9.7	10.7	0.37	0.38	1.7	98.8	0.08	n	81.3
Ahlmannryggen	Fp	Z1816.3	exp2-02d	49.4	4.04	10.5	10.8	0.1	9.5	10.3	0.26	0.43	1.9	97.4	0.03	y	81.3
Ahlmannryggen	Fp	Z1816.3	exp2-5	49.3	4.24	10.6	10.6	0.2	9.5	10.8	0.27	0.35	2.0	98.1	0.19	n	82.8
Ahlmannryggen	Fp	Z1816.3	exp2-11	49.8	4.16	10.9	10.5	0.1	9.5	9.7	0.34	0.47	2.1	97.8	0.14	n	82.5
Ahlmannryggen	Fp	Z1816.3	exp2-15a	49.8	4.22	10.6	10.8	0.2	9.5	10.5	0.40	0.43	1.8	98.3	0.10	y	81.1
Ahlmannryggen	Fp	Z1816.3	exp2-16	48.9	4.12	10.6	10.4	0.0	9.7	10.7	0.32	0.38	2.0	97.3	0.10	y	82.9
Ahlmannryggen	Fp	Z1816.3	exp2-23	49.3	4.00	10.4	10.8	0.2	9.5	10.4	0.31	0.44	1.8	97.1	0.00	n	81.2
Ahlmannryggen	Fp	Z1816.3	exp2-26	49.2	4.15	11.0	10.5	0.2	9.6	10.4	0.44	0.37	2.0	98.0	0.16	y	81.8
Ahlmannryggen	Fp	Z1816.3	exp4-3	50.5	4.14	10.5	11.5	0.2	9.7	10.7	0.32	0.57	1.4	99.6	0.00	n	82.3
Ahlmannryggen	Fp	Z1816.3	exp4-06a	49.1	4.04	10.8	10.5	0.1	9.8	11.1	0.28	0.34	1.7	98.0	0.12	n	82.6
Ahlmannryggen	Fp	Z1816.3	exp4-06b	49.5	4.13	10.9	10.4	0.1	9.9	10.9	0.27	0.31	1.7	98.4	0.13	n	82.3
Ahlmannryggen	Fp	Z1816.3	exp4-08a	49.0	4.32	10.7	10.2	0.1	9.9	11.1	0.33	0.42	1.9	98.2	0.02	y	83.6
Ahlmannryggen	Fp	Z1816.3	exp4-08b	51.9	2.88	10.4	10.2	0.2	10.3	11.5	0.14	0.16	1.3	99.2	0.01	n	83.9
Ahlmannryggen	Fp	Z1816.3	exp4-12	48.9	4.18	10.1	12.4	0.2	10.1	10.3	0.24	0.36	1.6	98.7	0.04	y	83.8
Ahlmannryggen	Fp	Z1816.3	exp4-21	49.3	4.27	10.7	11.4	0.2	9.5	10.9	0.25	0.37	1.8	98.9	0.12	n	81.6
Ahlmannryggen	Fp	Z1816.3	exp4-24	50.9	3.85	10.2	10.9	0.1	9.6	10.2	0.31	0.32	1.8	98.4	0.02	n	80.3
Ahlmannryggen	Fp	Z1816.3	exp4-25	50.5	4.22	11.1	10.0	0.2	9.8	10.0	0.39	0.47	2.0	98.9	0.06	y	82.6
Ahlmannryggen	Fp	Z1816.3	exp4-30a	49.8	4.28	10.8	10.6	0.1	9.2	10.9	0.29	0.34	1.8	98.1	n.d.	n	82.6
Ahlmannryggen	Fp	Z1816.3	exp4-30b	49.4	4.59	11.0	10.8	0.1	9.4	10.9	0.27	0.29	1.8	98.5	n.d.	n	82.6
Ahlmannryggen	Fp	Z1816.3	exp4-42	49.8	4.06	10.7	11.3	0.3	9.6	10.1	0.37	0.36	2.0	98.5	n.d.	n	80.5
Ahlmannryggen	Fp	Z1816.3	exp4-43	47.7	4.00	9.9	11.3	0.2	10.4	14.1	0.31	0.20	0.9	99.1	n.d.	n	83.7
Ahlmannryggen	Fp	Z1816.3	exp4-46	49.3	4.11	9.9	11.4	0.2	9.8	11.8	0.28	0.30	1.5	98.5	n.d.	n	81.8
Ahlmannryggen	Fp	Z1816.3	exp5-1	48.3	4.41	9.9	12.8	0.1	9.0	11.7	0.47	0.26	1.1	98.0	n.d.	n	83.1
Ahlmannryggen	Fp	Z1816.3	exp5-2	49.8	3.22	10.7	11.9	0.1	9.8	10.8	0.33	0.35	2.0	99.1	n.d.	n	82.1
Ahlmannryggen	Fp	Z1816.3	exp5-4	49.3	3.92	10.7	12.0	0.2	9.4	10.4	0.33	0.33	1.8	98.6	0.03	n	80.0
Ahlmannryggen	Fp	Z1816.3	exp5-5	50.0	3.82	10.3	10.8	0.2	9.7	11.4	0.31	0.37	1.6	98.7	0.05	n	80.2
Ahlmannryggen	Fp	Z1816.3	exp5-05b	50.8	3.81	7.9	12.5	0.2	10.3	12.2	0.20	0.28	1.1	99.5	n.d.	n	80.3
Ahlmannryggen	Fp	Z1816.3	exp5-7	51.0	3.87	10.2	15.4	0.3	8.9	6.7	0.36	0.59	1.8	99.0	n.d.	n	79.8

Table C.8 – *Continued on next page*

Location	Type	Sample	MI code	SiO_2	TiO_2	Al_2O_3	FeO_T	MnO	MgO	CaO	P_2O_5	K_2O	Na_2O	Total	SO_2	SIMS	Fo
Ahlmannryggen	Fp	Z1816.3	exp5-08a	51.0	3.96	11.0	10.0	0.2	9.4	10.6	0.36	0.33	2.0	98.9	n.d.	n	83.4
Ahlmannryggen	Fp	Z1816.3	exp5-11	50.7	3.77	11.0	10.8	0.1	9.4	10.7	0.37	0.34	2.0	99.2	n.d.	n	82.1
Ahlmannryggen	Fp	Z1816.3	exp5-12	49.1	4.11	10.5	11.5	0.1	9.5	10.6	0.36	0.35	1.8	98.1	0.09	n	81.8
Ahlmannryggen	Fp	Z1816.3	exp5-13	49.2	3.43	8.5	14.0	0.3	9.0	11.9	0.30	0.33	1.0	98.1	n.d.	n	82.6
Ahlmannryggen	Fp	Z1816.3	exp5-24	50.3	4.11	10.5	10.4	0.2	10.1	10.1	0.33	0.34	1.9	98.2	0.04	n	82.8
Ahlmannryggen	Fp	Z1816.3	exp5-29	52.1	3.55	11.2	8.4	0.1	9.6	10.1	0.30	0.43	2.1	98.1	0.12	n	85.1
Ahlmannryggen	Fp	Z1816.3	exp5-36	49.3	4.12	10.5	12.2	0.2	9.3	10.2	0.35	0.34	1.9	98.3	n.d.	n	80.1
Ahlmannryggen	Fp	Z1816.3	exp5-37	50.4	4.30	10.8	10.5	0.1	9.8	10.5	0.30	0.60	1.6	99.0	0.00	y	82.7
Ahlmannryggen	Fp	Z1816.3	exp5-40a	49.8	4.20	10.9	10.2	0.1	9.8	10.9	0.39	0.33	1.7	98.5	n.d.	n	83.4
Ahlmannryggen	Fp	Z1816.3	exp5-42	49.8	3.33	10.0	10.2	0.2	10.2	13.2	0.38	0.41	1.1	98.9	0.00	n	81.4
Ahlmannryggen	Fp	Z1816.3	exp5-50	50.5	4.06	11.2	11.0	0.1	9.4	9.9	0.29	0.35	2.2	99.0	n.d.	n	81.6
Ahlmannryggen	Fp	Z1816.3	exp5-54	50.7	4.59	11.3	7.1	0.0	10.6	12.1	0.28	0.42	1.5	98.8	n.d.	n	89.3
Ahlmannryggen	Fp	Z1816.3	exp5-55a	50.3	4.37	11.3	10.0	0.2	10.0	11.1	0.31	0.56	1.4	99.6	0.01	y	82.3
Ahlmannryggen	Fp	Z1816.3	exp5-55b	50.0	4.44	11.0	10.6	0.2	9.6	10.6	0.36	0.64	1.6	99.1	n.d.	n	82.3
Ahlmannryggen	Fp	Z1816.3	exp5-60	54.1	5.80	10.6	4.7	0.1	10.2	9.9	0.35	0.59	1.9	98.4	0.00	n	85.0
Ahlmannryggen	Fp	Z1816.3	exp5-63a	50.5	4.53	10.6	11.3	0.2	9.5	9.4	0.28	0.56	1.5	98.4	0.00	y	82.4
Ahlmannryggen	Fp	Z1816.3	exp5-63b	49.7	4.15	10.9	10.6	0.1	9.4	10.6	0.32	0.32	1.8	97.8	n.d.	n	82.5
Ahlmannryggen	Fp	Z1816.3	exp5-64	49.8	4.04	10.6	10.8	0.1	9.7	10.5	0.32	0.38	1.8	98.1	0.03	y	81.3
Ahlmannryggen	Fp	Z1816.3	exp5-66	49.8	4.03	10.8	11.7	0.1	9.4	10.7	0.30	0.34	1.8	99.0	n.d.	n	81.3
Ahlmannryggen	Fp	Z1816.3	exp5-70	49.6	4.32	10.5	11.5	0.2	9.5	10.3	0.28	0.37	1.9	98.6	0.04	n	80.8
Ahlmannryggen	Fp	Z1816.3	exp5-71	50.1	3.63	10.9	11.6	0.1	9.2	9.6	0.38	0.35	2.1	98.2	0.11	n	80.9
Ahlmannryggen	Fp	Z1817.2	exp2-4	47.3	4.57	10.8	12.2	0.2	9.3	10.1	0.41	0.40	1.7	97.1	0.03	y	79.2
Ahlmannryggen	Fp	Z1817.2	exp2-18	49.1	4.32	10.5	11.1	0.1	9.8	9.8	0.32	0.38	2.1	97.8	0.11	y	83.1
Ahlmannryggen	Fp	Z1817.2	exp3-16	47.4	4.03	10.2	12.1	0.2	10.8	10.0	0.39	0.35	1.8	97.5	0.20	y	80.0
Ahlmannryggen	Fp	Z1817.2	exp3-20a	47.3	4.24	10.3	12.2	0.2	11.1	9.8	0.30	0.35	1.8	97.8	0.21	y	80.4
Ahlmannryggen	Fp	Z1817.2	exp3-29a	48.4	3.64	10.5	11.8	0.2	11.0	9.7	0.37	0.36	1.8	97.9	0.15	n	82.8
Ahlmannryggen	Fp	Z1817.2	exp3-39a	46.6	4.21	10.4	13.8	0.2	10.6	9.6	0.37	0.36	1.8	98.1	0.15	y	78.8
Ahlmannryggen	Fp	Z1817.2	exp4-9	48.2	3.97	10.6	13.0	0.1	10.9	10.1	0.23	0.29	1.7	99.2	0.05	n	80.2
Ahlmannryggen	Fp	Z1817.2	exp4-12	47.7	4.13	10.3	13.9	0.1	11.2	9.4	0.27	0.31	1.8	99.1	0.05	y	78.6
Ahlmannryggen	Fp	Z1817.2	exp4-13a	48.5	3.98	10.5	11.8	0.1	11.1	9.9	0.25	0.57	1.5	98.6	0.05	y	80.2
Ahlmannryggen	Fp	Z1817.2	exp4-13b	48.9	3.89	9.9	11.7	0.2	11.1	11.0	0.29	0.35	1.5	99.0	0.02	y	80.7
Ahlmannryggen	Fp	Z1817.2	exp4-18	48.8	3.96	11.3	11.9	0.2	10.5	9.6	0.38	0.29	2.1	99.3	0.12	n	82.3

Table C.8 – *Continued on next page*

Location	Type	Sample	MI code	SiO_2	TiO_2	Al_2O_3	FeO_T	MnO	MgO	CaO	P_2O_5	K_2O	Na_2O	Total	SO_2	SIMS	Fo
Ahlmannryggen	Fp	Z1817.2	exp4-21	47.4	4.10	10.3	14.0	0.1	10.6	9.4	0.31	0.37	1.9	98.7	0.08	n	79.1
Ahlmannryggen	Fp	Z1817.2	exp4-22a	50.8	3.50	11.9	10.3	0.1	10.8	9.6	0.31	0.46	2.2	100.1	0.07	y	84.5
Ahlmannryggen	Fp	Z1817.2	exp4-34ab	49.5	3.08	7.4	13.2	0.1	10.6	12.9	0.23	0.23	1.3	98.9	0.03	n	79.0
Ahlmannryggen	Fp	Z1817.2	exp4-38	47.4	4.14	10.5	14.6	0.2	10.1	9.6	0.33	0.35	1.8	99.0	0.04	n	78.3
Ahlmannryggen	Fp	Z1817.2	exp4-69ab	50.3	1.73	4.1	16.5	0.2	11.3	13.6	0.14	0.13	0.6	99.0	0.00	n	79.2
Ahlmannryggen	Fp	Z1817.2	exp4-75	47.9	4.56	11.0	12.8	0.1	10.7	9.4	0.34	0.33	2.1	99.4	0.12	n	81.0
Ahlmannryggen	Fp	Z1817.2	exp4-76	50.3	4.38	7.5	15.6	0.2	11.5	7.6	0.41	0.36	1.3	99.3	0.00	n	79.9
Ahlmannryggen	Fp	Z1817.2	exp4-83	47.4	4.53	11.0	13.3	0.1	11.3	8.6	0.47	0.33	1.8	98.8	0.02	y	79.5
Ahlmannryggen	Fp	Z1817.2	exp4-84	50.0	3.50	6.7	14.9	0.2	11.8	10.1	0.34	0.27	1.0	98.8	n.d.	n	78.1
Ahlmannryggen	Fp	Z1817.2	exp4-87	49.9	4.38	11.6	9.5	0.1	11.2	10.3	0.33	0.32	1.9	99.7	0.09	n	84.5
Ahlmannryggen	Fp	Z1817.2	exp4-88	47.3	4.44	10.5	12.3	0.1	11.0	9.9	0.32	0.35	1.8	98.4	0.09	y	80.2
Ahlmannryggen	Fp	Z1817.2	exp4-89	48.0	4.06	10.3	12.7	0.1	11.0	9.8	0.33	0.33	1.7	98.4	0.02	y	79.5
Ahlmannryggen	Fp	Z1817.2	exp4-98	51.9	3.52	7.2	15.4	0.2	11.3	7.9	0.23	0.37	1.3	99.6	0.03	n	78.5
Ahlmannryggen	Fp	Z1817.2	exp5-03a	45.7	4.46	10.3	14.7	0.2	8.9	9.7	0.40	0.34	1.8	96.7	n.d.	n	78.6
Ahlmannryggen	Fp	Z1817.2	exp5-03b-mean	47.0	4.37	10.4	13.9	0.3	10.6	9.6	0.41	0.33	1.9	98.8	0.08	y	78.6
Ahlmannryggen	Fp	Z1817.2	exp5-03c	49.0	4.56	10.9	10.8	0.2	11.7	11.3	0.33	0.46	1.4	100.6	0.00	y	83.4
Ahlmannryggen	Fp	Z1817.2	exp5-10a	48.7	4.21	10.7	14.2	0.3	10.5	10.0	0.31	0.26	1.8	101.1	n.d.	n	79.2
Ahlmannryggen	Fp	Z1817.2	exp5-10b	51.5	3.11	7.5	11.3	0.2	11.6	10.3	0.46	0.46	1.4	97.8	n.d.	n	79.2
Ahlmannryggen	Fp	Z1817.2	exp5-24	47.4	4.59	10.1	15.5	0.2	10.0	10.9	0.34	0.51	1.2	100.8	0.04	n	79.5
Ahlmannryggen	Fp	Z1817.2	exp5-27	50.2	2.38	5.1	14.8	0.2	11.2	12.1	0.11	0.12	0.9	97.1	n.d.	n	80.6
Ahlmannryggen	Fp	Z1817.2	exp5-33	47.7	3.74	10.0	13.2	0.2	10.1	9.9	0.36	0.32	1.9	97.6	n.d.	n	80.0
Ahlmannryggen	Fp	Z1817.2	exp5-52-mean	49.9	3.92	10.7	11.9	0.1	11.3	10.2	0.35	0.35	1.9	100.7	0.07	y	80.2
Ahlmannryggen	Fp	Z1817.2	exp5-55-mean	50.0	3.77	8.5	14.2	0.2	11.2	9.1	0.34	0.40	1.2	98.9	0.00	n	81.2
Ahlmannryggen	Fp	Z1817.2	exp5-60	49.4	4.30	9.6	14.1	0.1	10.0	11.0	0.32	0.36	1.8	101.0	n.d.	n	78.1
Ahlmannryggen	Fp	Z1817.2	exp5-68	48.3	4.26	11.0	12.0	0.2	8.9	9.8	0.24	0.35	2.0	97.2	n.d.	n	79.0
Vestfjella	Fp	JSH-B006	exp4-104	44.3	4.76	11.3	14.6	0.1	9.4	11.4	0.64	1.03	1.2	98.9	0.18	y	80.2
Vestfjella	Fp	JSH-B006	exp4-113	48.6	3.51	9.2	13.7	0.1	9.1	10.7	0.51	0.76	2.3	98.6	0.00	n	80.1
Vestfjella	Fp	JSH-B006	exp4-114	44.0	2.80	10.7	16.4	0.2	8.0	8.8	0.90	2.53	4.0	98.7	0.36	n	79.0
Vestfjella	Fp	JSH-B006	exp4-27	43.1	4.05	10.1	16.1	0.3	8.2	10.1	0.62	1.67	3.4	97.9	0.23	y	78.4
Vestfjella	Fp	JSH-B006	exp4-49	43.8	3.86	10.4	14.9	0.1	8.3	10.4	0.57	1.64	3.4	97.6	0.30	y	79.8
Vestfjella	Fp	JSH-B006	exp4-82	54.5	3.81	9.3	12.8	0.3	8.0	7.5	0.35	1.54	2.1	100.2	0.00	n	79.3
Vestfjella	Fp	JSH-B006	exp5-32-mean	43.6	3.62	10.0	15.5	0.2	7.9	11.1	0.69	1.70	3.5	98.1	0.60	n	79.3

Table C.8 – *Continued on next page*

Location	Type	Sample	MI code	SiO_2	TiO_2	Al_2O_3	FeO_T	MnO	MgO	CaO	P_2O_5	K_2O	Na_2O	Total	SO_2	SIMS	Fo
Vestfjella	Fp	JSH-B006	exp5-86	47.0	2.79	10.6	13.9	0.2	8.7	10.6	0.68	0.79	1.2	96.6	n.d.	n	78.9
Etendeka	Fp	97SB63	exp2-15	44.1	3.99	13.3	11.9	0.2	8.9	11.4	0.48	1.11	4.2	100.1	0.41	y	84.5
Etendeka	Fp	97SB63	exp3-10	48.7	3.37	10.5	13.6	0.3	12.1	10.3	0.40	0.78	1.6	101.5	0.00	y	82.5
Etendeka	Fp	97SB63	exp4-2	46.1	3.42	12.6	12.6	0.2	9.1	10.5	0.39	1.35	4.0	100.7	0.42	y	83.2
Etendeka	Fp	97SB63	exp4-3	36.0	6.06	11.5	19.2	0.2	7.7	10.3	0.40	1.10	3.8	97.1	0.71	y	82.0
Etendeka	Fp	97SB63	exp4-31	45.0	3.86	12.9	13.4	0.1	8.3	10.6	0.43	1.35	4.4	100.9	0.44	n	81.3
Etendeka	Fp	97SB63	exp4-50	48.1	3.61	9.7	15.9	0.3	8.2	11.2	0.40	0.93	2.0	100.4	0.00	n	82.8
Etendeka	Fp	97SB63	exp5-9	49.1	4.19	13.9	9.4	0.5	9.5	7.7	0.40	1.00	2.7	98.3	n.d.	y	82.3
Etendeka	Fp	97SB63	exp5-26	45.1	3.14	12.5	12.3	0.1	9.2	10.3	0.34	1.26	3.1	97.5	n.d.	y	82.4
Etendeka	Fp	97SB63	exp5-16a	43.2	3.69	12.5	14.7	0.2	9.7	10.8	0.56	0.49	2.0	97.9	0.09	y	81.6
Etendeka	Fp	97SB63	exp5-16b	42.7	3.97	13.5	12.2	0.2	8.6	11.0	0.59	1.21	4.3	98.5	0.17	n	81.3
Etendeka	Fp	97SB63	exp5-42	43.3	3.44	12.5	12.9	0.2	9.1	11.1	0.81	1.40	3.9	98.8	0.17	y	82.5
Etendeka	Fp	97SB67	exp2-9	45.6	3.04	9.6	18.7	0.2	8.8	7.5	0.19	0.55	1.9	96.3	n.d.	n	64.5
Etendeka	Fp	97SB67	exp2-10	45.4	1.30	9.8	14.1	0.3	9.6	14.8	0.18	0.31	1.4	97.3	n.d.	n	72.6
Etendeka	Fp	97SB67	exp2-9	46.8	2.92	9.7	18.7	0.3	8.9	7.6	0.24	0.63	1.9	97.5	0.00	n	64.4
Etendeka	Fp	97SB67	exp3-06a	48.3	1.37	10.3	16.6	0.3	9.6	8.3	0.09	0.60	2.4	97.8	n.d.	y	68.2
Etendeka	Fp	97SB67	exp3-06b	43.5	1.32	3.6	24.0	0.3	7.1	15.1	0.20	0.63	0.9	97.1	n.d.	n	68.2
Etendeka	Fp	97SB67	exp3-26	45.8	2.20	5.4	25.3	0.3	8.8	7.7	0.12	0.44	1.4	97.6	n.d.	y	65.1
Etendeka	Fp	97SB67	exp3-29a	46.1	1.75	4.9	26.1	0.3	8.6	8.2	0.19	0.40	1.3	98.0	n.d.	y	64.7
Etendeka	Fp	97SB67	exp3-29b	45.9	1.86	5.1	26.1	0.3	7.5	8.7	0.21	0.32	1.4	97.6	n.d.	y	64.7
Etendeka	Fp	97SB67	exp3-29c	45.7	1.89	6.9	23.8	0.2	8.3	8.0	0.13	0.42	1.6	96.9	n.d.	y	64.7
Etendeka	Fp	97SB67	exp3-42	47.6	1.34	8.3	21.0	0.2	9.3	7.3	0.16	0.49	1.7	97.4	n.d.	y	66.6
Etendeka	Fp	97SB67	exp3-56	51.1	1.45	11.3	11.1	0.3	10.3	10.7	0.08	0.64	2.0	99.0	n.d.	n	68.0
Etendeka	Fp	97SB67	exp3-66	47.3	1.84	9.0	20.9	0.2	8.4	8.1	0.10	0.54	1.9	98.4	n.d.	y	68.8
Etendeka	Fp	97SB67	exp4-123	50.5	0.68	10.2	17.1	0.2	9.3	8.0	0.08	0.58	2.1	98.6	n.d.	y	67.1
Etendeka	Fp	97SB67	exp4-22	39.9	2.42	3.9	32.7	0.4	6.0	10.4	0.28	0.37	1.2	97.6	n.d.	y	63.8
Etendeka	Fp	97SB67	exp4-88	46.5	1.29	8.7	19.8	0.3	9.4	9.6	0.09	0.35	1.4	97.5	n.d.	n	67.5
Etendeka	Fp	97SB67	exp4-10	48.9	0.68	9.8	19.4	0.1	8.3	10.0	0.09	0.38	1.7	99.4	0.00	n	70.4
Etendeka	Fp	97SB67	exp4-29	47.2	1.72	5.4	24.8	0.2	9.3	8.7	0.29	0.25	1.3	99.5	0.00	n	67.4
Etendeka	Fp	97SB67	exp4-38	47.2	1.36	8.3	22.9	0.2	9.5	7.6	0.23	0.35	1.6	99.5	0.01	n	65.3
Etendeka	Fp	97SB67	exp4-41	43.6	1.45	4.2	25.5	0.2	6.8	13.8	0.33	0.71	1.4	98.3	0.22	n	65.8
Etendeka	Fp	97SB67	exp4-61	46.7	1.66	7.8	23.8	0.3	9.5	7.4	0.21	0.48	1.5	99.4	0.01	n	65.7

Table C.8 – *Continued on next page*

Location	Type	Sample	MI code	SiO_2	TiO_2	Al_2O_3	FeO_T	MnO	MgO	CaO	P_2O_5	K_2O	Na_2O	Total	SO_2	SIMS	Fo
Etendeka	Fp	97SB68	exp5-20	46.7	0.96	7.8	22.7	0.3	8.6	8.1	0.16	0.60	1.9	98.0	n.d.	n	66.2
Etendeka	Fp	97SB68	exp5-1	38.2	3.39	9.0	31.9	0.4	4.7	10.0	0.42	0.36	1.3	99.6	0.03	n	66.0
Etendeka	Fp	97SB68	exp5-24	43.5	2.12	10.1	25.1	0.3	7.5	5.6	0.20	0.71	2.1	97.3	0.00	n	66.3
Etendeka	Fp	97SB68	exp5-32	43.5	2.10	4.6	23.9	0.3	9.2	11.8	0.17	0.42	0.9	97.0	0.00	y	65.8
Etendeka	Fp	97SB68	exp5-44	45.5	1.08	3.1	24.9	0.3	7.2	17.5	0.20	0.57	0.6	100.9	0.01	n	65.6
Etendeka	Fp	97SB73	exp3-22	51.4	4.36	9.0	12.3	0.2	8.2	8.2	0.35	1.29	1.9	97.2	0.00	n	78.5
Etendeka	Fp	97SB80	exp2-18	52.0	1.63	12.6	15.9	0.3	9.0	6.9	0.19	0.98	1.9	101.6	0.04	n	73.8
Etendeka	Fp	97SB80	exp3-01b	49.0	1.50	15.5	11.8	0.1	9.1	7.1	0.15	0.60	2.6	97.5	n.d.	n	80.0
Etendeka	Fp	97SB80	exp3-24	48.1	1.89	14.2	9.8	0.2	9.2	9.4	0.22	0.78	3.2	97.1	n.d.	y	79.4
Etendeka	Fp	97SB80	exp3-25	50.3	1.62	12.1	15.0	0.2	9.1	6.5	0.26	0.67	1.8	97.6	n.d.	y	78.5
Etendeka	Fp	97SB80	exp3-34	48.4	1.94	14.3	10.7	0.1	8.2	9.3	0.21	0.68	3.2	97.1	n.d.	y	78.3
Etendeka	Fp	97SB80	exp3-01a	51.2	1.82	14.4	10.3	0.1	9.6	9.3	0.15	0.78	3.0	100.9	0.18	y	79.8
Etendeka	Fp	97SB80	exp3-01b	51.3	1.96	14.6	10.1	0.3	9.1	9.5	0.19	0.77	3.2	101.1	0.17	n	79.8
Etendeka	Fp	97SB80	exp3-2	49.6	1.94	12.2	17.5	0.3	8.3	7.8	0.29	0.80	3.2	102.2	0.37	y	73.4
Etendeka	Fp	97SB80	exp3-39	49.0	1.81	13.8	15.8	0.2	9.9	8.8	0.20	0.39	1.4	101.7	0.17	n	76.3
Etendeka	Fp	97SB80	exp3-55	51.1	1.77	14.0	12.5	0.2	9.2	8.9	0.23	0.76	3.1	102.2	0.25	n	76.6
Etendeka	Fp	97SB80	exp3-30	50.2	2.70	9.1	15.7	0.5	11.3	6.3	0.24	0.52	1.6	98.3	n.d.	n	69.6
Etendeka	Fp	97SB80	exp4-76	48.3	1.55	12.0	15.4	0.3	9.8	7.3	0.27	0.67	3.0	98.7	n.d.	y	75.5
Etendeka	Fp	97SB80	exp4-3	52.3	1.35	9.1	16.3	0.2	10.7	5.4	0.25	0.54	1.8	98.1	0.16	n	79.0
Etendeka	Fp	97SB80	exp4-21	49.4	1.24	9.6	19.0	0.4	10.8	4.5	0.25	0.58	1.1	96.8	0.00	y	74.8
Etendeka	Fp	97SB80	exp4-27a	47.0	1.79	13.5	16.5	0.3	11.4	8.5	0.26	0.46	1.6	101.5	0.19	n	76.8
Etendeka	Fp	97SB80	exp4-27b	47.0	1.62	11.8	16.3	0.2	9.3	7.7	0.30	0.68	2.7	97.9	0.26	n	76.8
Etendeka	Fp	97SB80	exp4-28a	50.3	1.69	13.4	12.9	0.3	10.8	8.5	0.24	0.75	2.8	101.8	0.28	y	77.1
Etendeka	Fp	97SB80	exp4-28b	55.8	1.75	9.6	14.1	0.3	10.7	5.5	0.21	0.78	2.4	101.2	0.02	n	77.1
Etendeka	Fp	97SB80	exp4-46	48.6	1.63	12.0	17.7	0.2	10.2	7.6	0.17	0.73	2.7	101.8	0.29	n	73.2
Etendeka	Fp	97SB80	exp4-59	47.9	1.21	9.2	19.2	0.2	9.2	8.0	0.19	0.48	1.6	97.2	0.00	n	64.5
Etendeka	Fp	97SB80	exp4-71	45.9	1.29	2.6	28.7	0.3	6.7	13.9	0.18	0.42	0.9	100.9	0.01	n	66.7
Etendeka	Fp	97SB80	exp5-2	51.1	1.38	13.2	13.3	0.3	10.8	5.0	0.30	0.70	2.2	98.3	n.d.	y	77.9
Etendeka	Fp	97SB80	exp5-8	45.0	1.31	10.1	20.0	0.3	9.5	7.2	0.21	0.59	2.6	96.9	n.d.	y	70.2
Etendeka	Fp	97SB80	exp5-43	46.1	1.63	11.5	16.3	0.3	10.0	7.4	0.29	0.63	2.9	97.1	n.d.	y	74.1
Etendeka	Fp	97SB80	exp5-1	50.2	1.61	13.5	13.2	0.1	10.8	8.2	0.21	0.72	2.8	101.7	0.24	n	80.1
Etendeka	Fp	97SB80	exp5-2	44.5	1.62	10.4	21.1	0.4	10.0	7.0	0.13	0.49	1.6	97.5	0.21	n	75.8

Table C.8 – *Continued on next page*

Location	Type	Sample	MI code	SiO_2	TiO_2	Al_2O_3	FeO_T	MnO	MgO	CaO	P_2O_5	K_2O	Na_2O	Total	SO_2	SIMS	Fo
Etendeka	Fp	97SB80	exp5-04a	51.0	1.49	8.1	20.9	0.4	9.9	3.6	0.16	0.68	1.9	98.2	0.01	n	72.4
Etendeka	Fp	97SB80	exp5-04b	45.4	1.60	10.1	20.6	0.4	9.1	6.8	0.20	0.57	2.6	97.6	0.21	n	72.4
Etendeka	Fp	97SB80	exp5-04c	48.1	1.79	12.9	11.2	0.3	10.9	8.3	0.16	0.71	2.6	97.1	0.24	n	79.2
Etendeka	Fp	97SB80	exp5-8	47.8	1.72	13.0	12.4	0.2	10.6	8.1	0.20	0.74	2.8	97.9	0.22	y	78.6
Etendeka	Fp	97SB80	exp5-10a	43.0	1.78	13.2	18.1	0.3	10.8	8.1	0.23	0.30	0.9	96.8	0.05	n	76.5
Etendeka	Fp	97SB80	exp5-10b	49.2	1.67	12.7	15.6	0.2	10.5	7.7	0.28	0.65	2.8	101.6	0.29	n	76.5
Etendeka	Fp	97SB80	exp5-13	47.1	2.01	12.1	14.1	0.2	10.1	7.8	0.23	0.83	3.1	97.8	0.26	y	76.3
Etendeka	Fp	97SB80	exp5-54	47.1	1.86	12.5	14.0	0.2	10.1	8.2	0.22	0.79	2.8	98.1	0.31	n	76.4
Etendeka	Fp	PB9	exp1-1	51.8	2.24	14.8	8.7	0.1	10.1	10.0	0.21	1.11	3.0	102.0	n.d.	y	83.3
Etendeka	Fp	PB9	exp1-8-mean	50.1	2.37	12.7	8.3	0.1	10.9	12.4	0.27	0.59	3.7	101.6	0.25	y	83.8
Etendeka	Fp	PB9	exp1-10-mean	50.7	1.01	10.6	12.4	0.3	10.8	12.8	0.29	0.60	1.9	101.5	0.01	n	80.3
Etendeka	Fp	PB9	exp1-16	48.8	2.01	14.6	12.1	0.2	9.9	9.6	0.27	0.86	2.6	101.0	n.d.	n	80.7
Etendeka	Fp	PB9	exp1-32-mean	50.0	2.17	12.4	11.1	0.2	10.1	10.7	0.25	0.81	3.4	101.2	0.02	y	77.9
Etendeka	Fp	PB9	exp2-6-mean	48.8	2.59	13.4	13.4	0.2	8.2	10.1	0.27	0.93	3.4	101.3	0.06	y	69.6
Etendeka	Fp	PB9	exp2-7	51.7	2.17	13.6	8.3	0.2	8.7	10.9	0.26	0.98	3.8	100.8	0.09	y	79.4
Etendeka	Fp	PB9	exp2-13	48.3	2.63	14.1	8.9	0.1	9.8	14.3	0.22	0.63	1.6	100.7	0.13	n	84.0
Etendeka	Fp	PB9	exp2-28a	50.9	2.15	12.8	11.0	0.2	8.5	11.1	0.23	0.89	3.6	101.4	0.08	y	72.4
Etendeka	Fp	PB9	exp2-28b	47.3	2.43	13.2	14.7	0.2	8.3	11.1	0.31	0.74	2.5	100.9	0.24	n	72.4
Etendeka	Fp	PB9	exp2-37	49.6	2.60	15.9	11.0	0.1	7.5	8.2	0.37	1.29	4.3	100.9	0.09	n	76.0
Etendeka	Fp	PB9	exp2-50	46.9	2.57	14.8	10.1	0.3	9.4	14.4	0.36	0.40	2.1	101.3	0.01	n	82.5
Etendeka	Fp	PB9	exp2-52	49.2	2.78	15.5	9.2	0.1	9.1	12.1	0.22	1.01	2.8	102.0	0.00	n	81.5
Etendeka	Fp	PB9	exp2-66	50.8	2.05	13.8	12.1	0.2	8.1	9.4	0.26	0.89	3.7	101.4	0.13	y	74.3
Etendeka	Fp	PB9	exp2-67	44.9	4.54	6.2	21.6	0.4	8.5	11.5	0.30	0.59	1.9	100.4	0.00	n	68.5
Etendeka	Fp	PB9	exp2-83	50.3	2.52	14.5	10.1	0.1	8.4	10.4	0.30	1.04	3.6	101.3	0.11	y	78.5
Etendeka	HP	97SB29	exp3-26	36.1	1.18	13.3	6.2	0.2	8.8	11.9	0.12	0.08	1.2	79.1	n.d.	y	90.4
Etendeka	HP	97SB34	exp1-53	46.1	1.76	15.5	7.5	0.1	6.7	13.3	0.19	3.87	1.3	96.4	n.d.	y	85.1
Etendeka	HP	97SB34	exp1-76	53.0	0.88	15.1	6.7	0.1	7.4	11.6	0.14	0.33	3.1	98.4	n.d.	y	85.5
Etendeka	HP	97SB34	exp1-79a	55.0	0.78	14.8	6.0	0.1	7.7	10.8	0.09	0.22	3.3	98.8	n.d.	y	86.6
Etendeka	HP	97SB34	exp1-79b	53.7	0.80	14.6	6.0	0.2	7.5	10.7	0.16	0.25	3.3	97.5	n.d.	y	86.6
Etendeka	HP	97SB34	exp3-9	52.0	1.24	14.3	6.6	0.1	8.4	11.7	0.21	0.43	2.6	97.7	n.d.	y	86.3
Etendeka	HP	97SB34	exp3-145	48.9	1.45	15.5	6.1	0.2	8.9	13.2	0.18	0.38	2.6	97.4	n.d.	y	87.7
Etendeka	HP	97SB34	exp3-164a	51.0	2.55	14.4	7.2	0.1	8.5	11.6	0.19	0.69	2.1	98.6	n.d.	y	86.2

Table C.8 – *Continued on next page*

Location	Type	Sample	MI code	SiO_2	TiO_2	Al_2O_3	FeO_T	MnO	MgO	CaO	P_2O_5	K_2O	Na_2O	Total	SO_2	SIMS	Fo
Etendeka	HP	97SB34	exp3-164b	52.4	1.03	15.0	6.0	0.1	8.2	11.7	0.12	0.80	2.3	97.7	n.d.	y	86.2
Etendeka	HP	97SB34	exp3-72	49.4	1.62	14.3	7.2	0.1	8.7	12.5	0.18	0.38	2.6	97.2	n.d.	y	85.6
Etendeka	HP	97SB41	exp2-01a	49.2	1.86	14.8	7.7	0.1	8.8	13.2	0.14	0.71	1.9	98.6	n.d.	y	84.6
Etendeka	HP	97SB41	exp2-01b	49.0	1.46	14.1	7.6	0.1	9.2	12.2	0.19	0.34	2.6	96.9	n.d.	y	84.6
Etendeka	HP	97SB41	exp2-01c	48.7	1.45	14.0	8.0	0.2	9.1	12.2	0.16	0.27	2.5	96.6	n.d.	y	84.6
Etendeka	HP	97SB41	exp2-09a	51.8	0.87	14.9	6.9	0.1	8.9	11.3	0.17	0.26	3.0	98.2	n.d.	y	85.3
Etendeka	HP	97SB41	exp2-09b	49.8	1.08	14.5	7.4	0.2	9.1	11.9	0.14	0.34	2.6	97.2	n.d.	y	85.3
Etendeka	HP	97SB41	exp2-17	51.5	0.99	14.3	7.5	0.1	8.9	11.8	0.11	0.25	2.9	98.5	n.d.	y	85.1
Etendeka	HP	97SB41	exp2-37	48.7	1.54	15.3	8.1	0.1	7.8	11.4	0.16	2.44	1.6	97.2	n.d.	y	85.4
Etendeka	HP	97SB41	exp2-92	48.1	1.53	14.8	8.8	0.2	9.6	12.2	0.13	0.69	1.7	97.9	n.d.	y	84.8
Etendeka	HP	97SB41	exp3-117	52.4	0.76	14.1	7.5	0.2	8.7	11.1	0.14	0.25	3.1	98.3	n.d.	y	85.4
Etendeka	HP	97SB41	exp3-31	50.1	0.98	14.7	8.1	0.1	9.2	12.2	0.24	0.14	2.8	98.8	n.d.	y	85.3
Etendeka	HP	97SB41	exp3-35	52.8	1.23	13.9	6.4	0.2	9.5	11.8	0.24	0.55	2.2	99.0	n.d.	y	87.2
Etendeka	HP	97SB41	exp3-63	53.8	0.58	13.4	7.3	0.1	8.8	10.6	0.17	0.14	3.2	98.2	n.d.	y	85.3
Etendeka	HP	97SB41	exp3-77	52.5	0.53	14.3	7.6	0.1	8.9	10.9	0.05	0.15	3.2	98.5	n.d.	y	85.2
Etendeka	HP	97SB41	exp4-104	49.0	1.45	14.0	7.5	0.1	9.3	11.9	0.13	0.36	2.6	96.5	n.d.	y	84.5
Etendeka	HP	97SB41	exp4-12	50.5	1.07	15.3	7.2	0.1	9.0	11.9	0.16	0.23	2.6	98.1	n.d.	y	85.3
Etendeka	HP	97SB41	exp4-139	50.6	1.05	15.0	6.3	0.1	9.1	11.6	0.20	0.30	2.8	96.9	n.d.	y	87.7
Etendeka	HP	97SB41	exp4-143	48.2	1.35	15.7	8.2	0.3	9.0	11.8	0.17	0.44	2.1	97.3	n.d.	y	85.2
Etendeka	HP	97SB41	exp4-36	52.8	0.58	14.4	7.6	0.2	8.5	10.4	0.10	0.22	3.4	98.2	n.d.	y	85.2
Etendeka	HP	97SB41	exp4-38	49.8	1.50	14.6	7.6	0.1	9.0	11.9	0.16	0.36	2.7	97.9	n.d.	y	85.2
Etendeka	HP	97SB41	exp4-64	48.5	1.48	14.7	7.7	0.1	9.5	12.2	0.18	0.32	2.4	97.3	n.d.	y	85.2
Etendeka	HP	97SB41	exp4-67	49.2	1.44	14.5	7.2	0.2	9.4	12.1	0.14	0.39	2.6	97.3	n.d.	y	85.4
Etendeka	HP	97SB46	exp2-03a	48.5	1.43	15.0	8.8	0.0	8.4	12.2	0.13	0.24	2.5	97.3	n.d.	y	86.6
Etendeka	HP	97SB46	exp2-03b	47.8	1.43	14.6	8.6	0.2	8.3	12.1	0.11	0.26	2.7	96.1	n.d.	y	86.6
Etendeka	HP	97SB46	exp2-21	48.5	1.44	14.9	9.0	0.2	8.1	12.2	0.12	0.27	2.5	97.2	n.d.	y	86.9
Etendeka	HP	97SB46	exp2-68	48.8	1.43	14.7	8.8	0.2	8.4	12.1	0.08	0.27	2.6	97.4	n.d.	y	86.8
Etendeka	HP	97SB46	exp2-75a	49.6	1.35	14.9	9.0	0.2	8.3	11.9	0.11	0.28	2.7	98.3	n.d.	y	87.0
Etendeka	HP	97SB46	exp2-75b	49.1	1.31	14.8	8.4	0.1	8.4	12.2	0.20	0.27	2.6	97.5	n.d.	y	87.0
Etendeka	HP	97SB46	exp3-4	48.6	1.41	14.9	9.4	0.1	8.8	12.1	0.13	0.31	2.5	98.2	n.d.	y	86.9
Etendeka	HP	97SB46	exp3-8	48.9	1.59	14.7	8.9	0.3	8.5	12.1	0.13	0.31	2.6	98.0	n.d.	y	86.8
Etendeka	HP	97SB46	exp3-20	48.7	1.23	14.7	9.0	0.2	8.6	12.0	0.11	0.24	2.6	97.5	n.d.	y	86.8

Table C.8 – *Continued on next page*

Location	Type	Sample	MI code	SiO_2	TiO_2	Al_2O_3	FeO_T	MnO	MgO	CaO	P_2O_5	K_2O	Na_2O	Total	SO_2	SIMS	Fo
Etendeka	HP	97SB46	exp3-21a	48.2	1.40	15.4	9.2	0.2	9.1	12.2	0.19	0.26	1.5	97.8	n.d.	y	86.8
Etendeka	HP	97SB46	exp3-21b	49.6	1.27	14.1	9.3	0.2	8.9	11.7	0.13	0.27	2.6	98.1	n.d.	y	86.8
Etendeka	HP	97SB46	exp3-39	48.9	1.42	14.5	9.4	0.3	9.0	12.0	0.10	0.47	1.1	97.3	n.d.	y	86.8
Etendeka	HP	97SB46	exp3-43	48.5	1.46	14.8	8.9	0.1	8.6	12.1	0.13	0.30	2.6	97.5	n.d.	y	86.7
Etendeka	HP	97SB46	exp3-60	49.1	1.46	16.2	6.5	0.2	9.1	12.8	0.11	0.23	2.5	98.2	n.d.	y	91.1
Etendeka	HP	97SB46	exp4-13	48.3	1.41	15.3	8.9	0.2	8.8	12.5	0.12	0.22	2.1	97.8	n.d.	y	91.4
Etendeka	HP	97SB46	exp4-19a	47.8	1.43	15.1	9.2	0.3	8.6	12.3	0.14	0.24	2.6	97.8	n.d.	y	87.0
Etendeka	HP	97SB46	exp4-19b	48.5	1.44	14.9	9.0	0.2	8.6	12.3	0.13	0.27	2.5	97.8	n.d.	y	87.0
Etendeka	HP	97SB46	exp4-29	47.5	1.66	18.5	5.3	0.2	9.5	13.8	0.11	0.20	1.5	98.3	n.d.	y	91.2
Etendeka	HP	97SB46	exp4-63	49.6	1.54	16.9	5.7	0.3	9.3	12.7	0.17	0.30	1.8	98.3	n.d.	y	91.0
Etendeka	HP	97SB56	exp2-11	48.6	0.83	14.9	8.1	0.1	9.4	12.6	0.12	0.19	2.6	97.5	n.d.	y	85.3
Etendeka	HP	97SB56	exp2-31	52.0	1.04	14.0	5.8	0.1	9.9	12.8	0.10	0.56	1.6	98.0	n.d.	y	85.8
Etendeka	HP	97SB56	exp3-10	51.6	0.82	13.8	7.4	0.1	9.5	11.7	0.12	0.49	2.2	97.8	n.d.	y	85.2
Etendeka	HP	97SB56	exp3-118	48.1	1.37	13.8	9.6	0.2	9.5	12.4	0.09	0.29	2.5	97.9	n.d.	y	83.4
Etendeka	HP	97SB56	exp3-26	50.1	1.52	14.9	5.1	0.0	10.3	12.2	0.15	0.42	2.4	97.2	n.d.	y	90.4
Etendeka	HP	97SB56	exp3-39	49.4	1.27	13.7	9.8	0.3	10.2	12.5	0.19	0.31	0.9	98.7	n.d.	y	84.9
Etendeka	HP	97SB56	exp3-61	53.1	0.82	11.9	10.0	0.2	9.8	10.2	0.12	0.33	1.0	97.7	n.d.	y	85.3
Etendeka	HP	97SB56	exp3-79	49.8	1.09	13.8	8.2	0.1	9.8	11.8	0.17	0.44	2.4	97.7	n.d.	y	84.6
Etendeka	HP	97SB56	exp4-110	49.8	0.67	13.2	9.1	0.2	11.3	12.6	0.21	0.33	0.9	98.3	n.d.	y	85.0
Etendeka	HP	97SB56	exp4-98	50.8	1.01	12.2	11.1	0.1	11.5	11.2	0.15	0.23	0.7	99.2	n.d.	y	84.8
Etendeka	HP	97SB75	exp2-21	49.8	0.63	13.6	8.2	0.2	9.6	13.2	0.31	0.60	1.7	97.9	n.d.	y	86.9
Etendeka	HP	97SB75	exp2-27a	48.0	1.74	15.6	9.6	0.1	8.2	9.3	0.60	1.41	2.8	97.4	n.d.	y	86.3
Etendeka	HP	97SB75	exp3-14	48.7	1.10	15.2	6.7	0.2	10.1	12.9	0.10	0.08	2.2	97.3	n.d.	y	90.2
Etendeka	HP	97SB75	exp3-26	48.5	1.25	15.7	6.0	0.1	10.1	12.8	0.06	0.14	2.3	97.0	n.d.	y	90.1
Etendeka	HP	97SB75	exp3-29	50.5	0.96	15.3	6.4	0.3	10.1	12.5	0.18	0.35	1.5	98.1	n.d.	y	89.9
Etendeka	HP	97SB75	exp3-40	50.1	1.09	14.9	7.0	0.1	10.3	12.7	0.17	0.20	1.4	98.1	n.d.	y	89.2
Etendeka	HP	97SB75	exp3-53	53.1	0.86	14.5	10.8	0.1	8.4	6.6	0.12	0.52	2.8	97.9	n.d.	y	86.2
Etendeka	HP	97SB75	exp3-68	47.2	1.31	14.5	8.0	0.1	9.8	13.0	0.11	0.16	2.5	97.0	n.d.	y	86.0
Etendeka	HP	97SB79	exp3-17	49.9	0.93	14.0	8.0	0.1	10.4	11.4	0.13	0.47	2.1	97.8	n.d.	y	85.0
Etendeka	HP	97SB29	exp3-10	49.0	0.98	14.9	7.4	0.1	11.1	13.2	0.03	0.11	1.2	98.0	n.d.	n	89.5
Etendeka	HP	97SB33	exp1-10a	52.3	1.18	16.3	4.4	0.0	11.1	13.1	0.05	0.05	2.4	101.0	n.d.	n	93.0
Etendeka	HP	97SB33	exp1-22a	50.7	2.16	16.3	6.3	0.2	11.0	13.1	0.04	0.02	2.1	101.9	n.d.	n	91.0

Table C.8 – *Continued on next page*

Location	Type	Sample	MI code	SiO_2	TiO_2	Al_2O_3	FeO_T	MnO	MgO	CaO	P_2O_5	K_2O	Na_2O	Total	SO_2	SIMS	Fo
Etendeka	HP	97SB33	exp1-22b	50.4	2.29	15.9	5.7	0.2	11.0	12.9	0.04	0.02	2.1	100.7	n.d.	n	91.0
Etendeka	HP	97SB33	exp1-32a	49.3	1.90	15.6	5.8	0.1	10.5	12.6	0.13	0.21	1.8	98.2	n.d.	n	88.7
Etendeka	HP	97SB33	exp1-65a	51.5	0.85	16.6	5.8	0.1	10.1	12.6	0.06	0.15	1.9	99.8	n.d.	n	90.5
Etendeka	HP	97SB33	exp1-69a	48.7	2.82	13.7	5.9	0.1	14.2	12.5	0.03	0.05	1.9	100.0	n.d.	n	91.5
Etendeka	HP	97SB33	exp1-70a	49.5	1.22	15.2	6.5	0.2	10.0	12.3	0.11	0.02	2.3	97.4	n.d.	n	89.5
Etendeka	HP	97SB34	exp1-13a	53.1	1.59	15.7	5.8	0.1	8.4	12.1	0.29	0.21	3.2	100.5	n.d.	n	87.1
Etendeka	HP	97SB34	exp1-13a2	52.8	1.50	15.7	5.7	0.0	8.4	12.0	0.33	0.24	3.2	100.1	n.d.	n	87.1
Etendeka	HP	97SB34	exp1-13a3	50.9	1.47	15.1	5.8	0.2	7.8	11.6	0.31	0.20	3.0	96.3	n.d.	n	87.1
Etendeka	HP	97SB34	exp1-18a	49.4	1.74	16.6	8.0	0.1	8.0	13.6	0.22	0.44	2.7	100.7	n.d.	n	85.2
Etendeka	HP	97SB34	exp1-23a	53.2	0.70	14.6	5.9	0.0	7.1	10.8	0.07	0.14	3.1	95.6	n.d.	n	87.4
Etendeka	HP	97SB34	exp1-30a	52.8	0.85	14.9	6.3	0.2	7.4	10.8	0.17	0.24	3.2	96.9	n.d.	n	86.1
Etendeka	HP	97SB34	exp1-37a	52.4	0.60	14.9	6.8	0.2	7.2	11.0	0.14	0.21	3.4	97.0	n.d.	n	85.6
Etendeka	HP	97SB34	exp1-39a	55.4	0.97	14.8	4.6	0.0	7.5	10.6	0.05	0.08	3.3	97.5	n.d.	n	92.0
Etendeka	HP	97SB34	exp1-57a	51.4	1.06	15.0	6.3	0.1	7.6	11.8	0.14	0.36	3.1	97.3	n.d.	n	87.4
Etendeka	HP	97SB34	exp1-71a	50.7	1.25	15.5	6.3	0.1	7.8	11.9	0.13	0.29	2.9	97.0	n.d.	n	86.0
Etendeka	HP	97SB34	exp1-73a	50.0	3.93	15.2	9.2	0.2	5.9	7.9	0.28	2.67	4.6	100.1	n.d.	n	84.6
Etendeka	HP	97SB34	exp1-74a	51.5	0.84	14.9	6.7	0.2	7.4	11.3	0.08	0.28	3.0	96.2	n.d.	n	85.3
Etendeka	HP	97SB34	exp1-74b	54.2	0.70	16.1	7.1	0.1	7.4	11.7	0.13	0.23	3.5	101.3	n.d.	n	85.3
Etendeka	HP	97SB34	exp3-111	49.1	1.52	15.1	8.1	0.2	8.5	12.6	0.13	0.66	1.6	97.7	n.d.	n	84.8
Etendeka	HP	97SB41	exp2-1a	48.5	1.53	14.1	8.7	0.2	8.6	12.0	0.16	0.30	2.6	96.8	n.d.	n	84.4
Etendeka	HP	97SB41	exp2-9a	48.6	1.57	14.4	7.6	0.1	8.9	12.3	0.19	0.35	2.3	96.4	n.d.	n	86.3
Etendeka	HP	97SB41	exp2-19a	51.2	0.78	15.8	7.8	0.2	8.1	11.0	0.15	1.26	2.0	98.2	n.d.	n	85.3
Etendeka	HP	97SB41	exp2-32a	52.0	1.33	15.0	7.1	0.1	9.6	12.9	0.30	0.37	2.1	101.0	n.d.	n	87.5
Etendeka	HP	97SB41	exp2-32b	52.8	1.26	14.9	6.0	0.1	9.6	12.3	0.24	0.70	2.1	100.0	n.d.	n	87.5
Etendeka	HP	97SB41	exp2-35	49.8	0.96	14.8	7.6	0.2	8.7	11.5	0.14	0.28	3.1	97.2	n.d.	n	85.4
Etendeka	HP	97SB41	exp2-43a	50.6	1.73	16.8	5.6	0.1	8.7	13.1	0.16	1.76	1.9	100.7	n.d.	n	90.3
Etendeka	HP	97SB41	exp2-49a	49.1	1.60	14.5	7.9	0.1	8.8	12.2	0.18	0.39	2.4	97.2	n.d.	n	85.0
Etendeka	HP	97SB41	exp2-53a	51.8	1.36	15.5	6.9	0.1	9.3	12.6	0.18	0.26	2.6	100.8	n.d.	n	87.1
Etendeka	HP	97SB41	exp2-55a	50.0	1.67	14.8	7.6	0.1	9.2	12.5	0.19	0.40	2.5	99.1	n.d.	n	83.9
Etendeka	HP	97SB41	exp2-55b	50.6	1.66	14.9	7.8	0.2	9.1	12.5	0.22	0.45	2.6	100.1	n.d.	n	83.9
Etendeka	HP	97SB41	exp2-64a	54.9	0.69	14.9	7.5	0.1	8.6	10.9	0.09	0.17	3.2	101.2	n.d.	n	85.5
Etendeka	HP	97SB41	exp3-130	54.0	0.76	14.9	6.6	0.2	8.5	10.0	0.21	0.84	2.4	98.4	n.d.	n	86.0

Table C.8 – *Continued on next page*

Location	Type	Sample	MI code	SiO_2	TiO_2	Al_2O_3	FeO_T	MnO	MgO	CaO	P_2O_5	K_2O	Na_2O	Total	SO_2	SIMS	Fo
Etendeka	HP	97SB41	exp4-101	52.5	0.59	14.6	7.0	0.2	8.3	10.4	0.10	0.12	3.4	97.3	n.d.	n	86.9
Etendeka	HP	97SB41	exp4-58	48.6	1.67	15.4	9.0	0.2	8.4	11.1	0.17	1.76	1.6	97.7	n.d.	n	84.8
Etendeka	HP	97SB46	exp2-3a	48.3	1.42	15.0	8.0	0.2	8.4	12.4	0.13	0.28	2.6	96.7	n.d.	n	86.9
Etendeka	HP	97SB46	exp2-3b	47.9	1.43	14.9	8.7	0.2	8.5	12.0	0.11	0.29	2.5	96.7	n.d.	n	86.9
Etendeka	HP	97SB46	exp2-7a	48.9	1.37	15.6	6.4	0.0	9.0	12.9	0.13	0.22	2.6	97.2	n.d.	n	90.9
Etendeka	HP	97SB46	exp2-11a	52.0	1.45	16.0	6.1	0.0	8.8	12.8	0.23	0.21	2.7	100.4	n.d.	n	90.6
Etendeka	HP	97SB46	exp2-30a	50.9	1.37	15.7	8.1	0.2	7.8	10.4	0.15	1.00	2.6	98.4	n.d.	n	86.7
Etendeka	HP	97SB46	exp2-30b	47.1	1.50	15.9	8.4	0.1	8.6	12.8	0.14	0.43	1.5	96.7	n.d.	n	86.7
Etendeka	HP	97SB46	exp2-30c	48.1	1.60	16.5	9.2	0.2	8.7	13.6	0.16	0.65	1.9	100.6	n.d.	n	86.7
Etendeka	HP	97SB46	exp2-30d	49.5	1.49	15.6	8.8	0.1	8.6	12.7	0.16	0.29	2.7	100.2	n.d.	n	86.7
Etendeka	HP	97SB46	exp2-42a	51.9	1.44	16.6	5.8	0.1	8.9	13.1	0.22	0.26	2.7	101.1	n.d.	n	91.2
Etendeka	HP	97SB46	exp2-56a	50.6	1.49	16.5	7.8	0.1	8.6	12.8	0.15	0.50	2.3	100.9	n.d.	n	89.5
Etendeka	HP	97SB46	exp2-56a1	51.0	1.68	16.3	7.1	0.1	8.8	13.7	0.15	0.63	2.2	101.8	n.d.	n	89.5
Etendeka	HP	97SB46	exp2-56a2	50.0	1.68	15.9	6.6	0.2	8.7	13.5	0.13	0.60	2.1	99.3	n.d.	n	89.5
Etendeka	HP	97SB46	exp2-56a3	50.8	1.71	15.9	6.5	0.2	8.9	13.7	0.16	0.63	2.2	100.7	n.d.	n	89.5
Etendeka	HP	97SB46	exp2-82a	46.2	1.70	17.9	6.1	0.2	9.4	13.8	0.17	0.14	1.3	97.1	n.d.	n	91.2
Etendeka	HP	97SB46	exp4-17a	47.0	1.49	16.3	8.5	0.1	9.0	12.7	0.14	0.26	1.4	97.1	n.d.	n	86.7
Etendeka	HP	97SB46	exp4-17b	48.5	1.41	15.2	9.5	0.2	8.6	11.8	0.14	0.27	1.9	97.6	n.d.	n	86.7
Etendeka	HP	97SB46	exp4-22	49.5	1.64	12.7	9.6	0.2	8.7	11.6	0.16	0.30	1.9	96.5	n.d.	n	86.9
Etendeka	HP	97SB46	exp4-26	48.3	1.42	15.0	9.1	0.1	8.8	12.2	0.16	0.30	2.5	98.0	n.d.	n	86.9
Etendeka	HP	97SB46	exp4-68	47.7	2.11	12.4	10.3	0.3	8.7	13.6	0.15	0.23	1.8	97.5	n.d.	n	89.4
Etendeka	HP	97SB56	exp3-26	49.8	1.55	14.8	4.8	0.1	10.4	12.1	0.13	0.42	2.5	96.7	n.d.	n	90.4
Etendeka	HP	97SB56	exp4-6	47.5	1.61	13.5	8.8	0.1	11.8	13.0	0.14	0.18	0.7	97.6	n.d.	n	85.4
Etendeka	HP	97SB56	exp4-27	50.9	0.72	13.8	9.2	0.2	11.3	10.9	0.17	0.37	1.1	98.8	n.d.	n	84.8
Etendeka	HP	97SB62	exp4-12c	49.8	0.89	15.3	7.7	0.3	10.6	10.4	0.17	0.50	2.3	97.9	n.d.	n	87.3
Etendeka	HP	97SB62	exp4-12c	50.2	1.22	15.5	6.9	0.2	8.9	12.2	0.11	0.25	2.9	98.3	n.d.	n	87.3
Etendeka	HP	97SB62	exp4-13a	49.3	1.13	13.0	8.4	0.2	15.4	10.9	0.11	0.19	2.5	101.4	n.d.	n	92.6
Etendeka	HP	97SB62	exp4-15b	50.0	1.10	14.4	10.6	0.2	8.6	11.8	0.84	0.55	3.1	101.4	n.d.	n	83.6
Etendeka	HP	97SB62	exp4-19a	48.3	2.02	14.1	11.1	0.2	8.7	13.0	0.79	0.59	2.7	101.7	n.d.	n	83.4
Etendeka	HP	97SB62	exp4-38c	53.2	1.02	14.2	4.3	0.1	9.0	12.0	0.22	0.08	2.9	97.2	n.d.	n	92.4
Etendeka	HP	97SB62	exp4-43c	48.5	1.23	15.6	7.7	0.1	10.1	13.1	0.16	0.26	2.7	99.5	n.d.	n	87.3
Etendeka	HP	97SB62	exp4-43d	49.6	1.27	16.3	7.6	0.2	9.2	13.4	0.14	0.30	2.7	100.6	n.d.	n	87.3

Table C.8 – *Continued on next page*

Location	Type	Sample	MI code	SiO_2	TiO_2	Al_2O_3	FeO_T	MnO	MgO	CaO	P_2O_5	K_2O	Na_2O	Total	SO_2	SIMS	Fo
Etendeka	HP	97SB62	exp4-45a	48.6	1.05	17.9	6.8	0.1	9.2	13.9	0.76	0.15	2.7	101.1	n.d.	n	88.6
Etendeka	HP	97SB62	exp4-56a	50.7	1.25	14.8	8.0	0.1	8.6	11.4	0.11	0.71	2.2	98.1	n.d.	n	86.5
Etendeka	HP	97SB62	exp4-56b	48.9	1.48	14.8	8.4	0.3	8.9	12.6	0.12	0.43	1.8	97.7	n.d.	n	86.5
Etendeka	HP	97SB62	exp4-69a	48.9	1.67	14.3	10.6	0.3	8.6	12.5	0.61	0.80	2.9	101.1	n.d.	n	83.5
Etendeka	HP	97SB62	exp5-4a	45.8	0.98	11.2	9.1	0.2	19.2	8.1	0.13	0.17	2.0	97.0	n.d.	n	88.1
Etendeka	HP	97SB62	exp5-4b	48.5	1.19	13.5	10.2	0.2	13.9	11.3	0.14	0.24	2.3	101.5	n.d.	n	88.1
Etendeka	HP	97SB62	exp5-9a	49.1	1.11	14.3	7.4	0.2	14.6	11.4	0.33	0.13	2.2	100.8	n.d.	n	92.2
Etendeka	HP	97SB62	exp5-19a	49.3	1.09	11.0	8.4	0.2	15.5	9.1	0.17	0.18	2.2	97.5	n.d.	n	87.8
Etendeka	HP	97SB62	exp5-22a	48.4	0.63	11.8	10.0	0.1	12.8	10.5	0.28	0.09	2.3	97.2	n.d.	n	88.1
Etendeka	HP	97SB62	exp5-26a	45.5	1.13	12.4	10.9	0.0	14.9	10.2	0.13	0.21	2.1	97.6	n.d.	n	86.8
Etendeka	HP	97SB62	exp5-26b	47.9	0.73	10.7	10.2	0.3	13.6	11.4	0.07	0.22	2.0	97.4	n.d.	n	86.8
Etendeka	HP	97SB62	exp5-28a	48.8	0.82	11.0	10.0	0.2	12.1	10.8	0.00	0.02	2.3	96.9	n.d.	n	89.3
Etendeka	HP	97SB62	exp5-40a	47.4	0.86	11.0	10.4	0.2	15.3	10.9	0.09	0.17	0.7	98.2	n.d.	n	88.2
Etendeka	HP	97SB62	exp5-41b	50.4	1.09	9.3	13.7	0.2	14.6	7.5	0.20	0.54	1.4	99.3	n.d.	n	87.2
Etendeka	HP	97SB62	exp5-45a	51.4	0.90	13.0	6.7	0.1	15.0	11.0	0.47	0.11	1.9	100.8	n.d.	n	93.1
Etendeka	HP	97SB62	exp5-47a	46.3	0.99	12.2	11.5	0.1	13.1	11.3	0.19	0.22	2.0	97.9	n.d.	n	87.5
Etendeka	HP	97SB62	exp5-47b	47.1	1.13	12.9	13.4	0.3	11.4	12.2	0.26	0.13	2.2	101.4	n.d.	n	87.5
Etendeka	HP	97SB75	exp3-21	50.2	1.48	14.4	11.1	0.1	9.2	8.4	0.14	0.31	1.8	97.3	n.d.	n	89.9
Etendeka	HP	97SB75	exp3-46	55.0	0.47	1.6	14.2	0.2	26.5	1.3	0.03	0.05	0.3	99.8	n.d.	n	87.8

Table C.9: Trace element compositions (excluding REE) of melt inclusions, analysed by SIMS. Abbreviations: Fp, ferropicrite; HP, Horingbaai picrite. Session refers to data collection in October 2012 or Oct 2013.

Location	Type	Sample	Melt inclusion	Session	Sc	Rb	Sr	Y	Zr	Nb	Ba	Fo
Vestfjella	Fp	JSH-B006	exp4-104	2013	25.8	22.9	866.3	38.9	232.0	26.9	366.6	80.2
Vestfjella	Fp	JSH-B006	exp4-27	2013	25.7	38.8	986.2	33.3	224.2	34.4	508.8	78.4
Vestfjella	Fp	JSH-B006	exp4-49	2013	25.6	38.9	950.0	34.0	220.2	32.8	510.1	79.8
Ahlmannryggen	Fp	Z1813.1	exp2-04a	2013	32.2	8.4	341.6	43.5	270.0	10.3	82.7	80.7
Ahlmannryggen	Fp	Z1813.1	exp2-9	2013	31.0	7.1	334.0	44.6	256.2	9.7	74.8	81.2
Ahlmannryggen	Fp	Z1813.1	exp2-29	2013	34.2	9.3	348.7	46.3	278.1	9.9	85.1	81.0
Ahlmannryggen	Fp	Z1813.1	exp3-29a	2013	27.3	7.2	307.7	40.3	242.2	8.8	75.2	82.5

Table C.9 – *Continued on next page*

Location	Type	Sample	Melt inclusion	Session	Sc	Rb	Sr	Y	Zr	Nb	Ba	Fo
Ahlmannryggen	Fp	Z1813.1	exp4-30b	2013	32.8	9.4	379.7	44.5	291.0	10.1	87.1	82.5
Ahlmannryggen	Fp	Z1813.1	exp5-22	2013	28.3	18.0	382.4	36.7	253.3	7.9	79.1	81.8
Ahlmannryggen	Fp	Z1813.1	exp5-23	2013	27.7	8.3	364.6	45.9	293.9	10.5	86.4	84.9
Ahlmannryggen	Fp	Z1813.1	exp5-31	2013	35.6	11.2	232.8	43.8	285.8	9.8	37.4	81.5
Ahlmannryggen	Fp	Z1813.1	exp6-8	2013	33.0	6.3	345.6	44.1	268.9	9.6	76.6	81.8
Ahlmannryggen	Fp	Z1813.1	exp7-22	2013	28.8	10.7	339.6	37.9	270.0	9.2	88.8	83.5
Ahlmannryggen	Fp	Z1813.1	exp8-24	2013	32.6	7.6	322.0	45.7	254.1	9.1	77.1	80.4
Ahlmannryggen	Fp	Z1813.1	exp8-40	2013	33.8	25.1	574.7	49.8	330.6	18.9	543.3	81.0
Ahlmannryggen	Fp	Z1813.1	exp8-47	2013	33.7	8.8	359.9	47.4	287.9	10.6	88.8	81.4
Ahlmannryggen	Fp	Z1813.1	exp8-61	2013	28.4	16.8	362.1	44.6	263.4	10.1	56.1	84.1
Ahlmannryggen	Fp	Z1813.1	exp8-91	2013	34.7	9.6	374.9	46.9	283.2	10.6	86.7	80.7
Ahlmannryggen	Fp	Z1816.3	exp2-02a	2013	35.6	7.4	315.8	45.2	282.8	9.3	70.5	81.3
Ahlmannryggen	Fp	Z1816.3	exp2-02b	2013	34.9	8.3	332.2	45.8	280.4	9.6	77.8	81.3
Ahlmannryggen	Fp	Z1816.3	exp2-02d	2013	34.3	8.0	310.3	44.2	274.6	9.4	70.5	81.3
Ahlmannryggen	Fp	Z1816.3	exp2-15a	2013	34.6	8.4	312.2	45.1	275.7	9.1	75.5	81.1
Ahlmannryggen	Fp	Z1816.3	exp2-16	2013	35.5	7.9	315.7	45.2	276.4	9.3	71.3	82.9
Ahlmannryggen	Fp	Z1816.3	exp2-26	2013	32.6	7.2	317.2	44.9	281.0	9.2	72.3	81.8
Ahlmannryggen	Fp	Z1816.3	exp4-08a	2013	36.7	8.2	333.0	45.1	288.7	9.0	79.2	83.6
Ahlmannryggen	Fp	Z1816.3	exp4-12	2013	39.6	7.0	311.2	43.1	281.1	8.4	75.0	83.8
Ahlmannryggen	Fp	Z1816.3	exp4-25	2013	29.3	11.2	351.6	43.3	306.0	10.0	94.8	82.6
Ahlmannryggen	Fp	Z1816.3	exp5-37	2013	32.7	9.8	317.3	44.3	277.6	9.0	73.8	82.7
Ahlmannryggen	Fp	Z1816.3	exp5-55a	2013	33.3	12.3	331.2	46.4	293.1	9.0	88.0	82.3
Ahlmannryggen	Fp	Z1816.3	exp5-63a	2013	30.8	13.7	311.0	42.1	258.0	8.6	57.7	82.4
Ahlmannryggen	Fp	Z1816.3	exp5-64	2013	34.0	7.0	318.6	42.8	279.9	9.1	77.5	81.3
Ahlmannryggen	Fp	Z1817.2	exp2-18	2013	32.7	6.0	326.8	41.7	281.5	10.1	76.7	83.1
Ahlmannryggen	Fp	Z1817.2	exp2-4	2013	32.8	8.5	347.4	47.5	309.4	11.2	81.5	79.2
Ahlmannryggen	Fp	Z1817.2	exp3-16	2013	29.4	6.7	316.6	41.9	273.4	9.5	76.9	80.0
Ahlmannryggen	Fp	Z1817.2	exp3-20a	2013	28.7	5.7	328.2	42.3	283.9	10.1	73.4	80.4
Ahlmannryggen	Fp	Z1817.2	exp3-39a	2013	32.5	6.7	339.1	41.5	282.3	9.5	74.5	78.8
Ahlmannryggen	Fp	Z1817.2	exp4-12	2013	30.3	6.8	323.2	41.9	276.7	8.6	75.9	78.6
Ahlmannryggen	Fp	Z1817.2	exp4-13a	2013	28.7	10.5	313.8	42.7	268.7	8.3	77.2	80.2
Ahlmannryggen	Fp	Z1817.2	exp4-13b	2013	33.4	8.1	315.2	41.9	261.5	8.3	80.0	80.7

Table C.9 – *Continued on next page*

Location	Type	Sample	Melt inclusion	Session	Sc	Rb	Sr	Y	Zr	Nb	Ba	Fo
Ahlmannryggen	Fp	Z1817.2	exp4-22a	2013	23.0	8.5	361.4	39.2	290.8	10.3	86.1	84.5
Ahlmannryggen	Fp	Z1817.2	exp4-83	2013	29.8	7.0	319.9	44.7	312.0	9.9	77.4	79.5
Ahlmannryggen	Fp	Z1817.2	exp4-88	2013	29.8	5.8	338.7	44.4	289.2	9.1	74.9	80.2
Ahlmannryggen	Fp	Z1817.2	exp4-89	2013	28.8	6.0	311.1	41.6	264.9	8.3	75.3	79.5
Ahlmannryggen	Fp	Z1817.2	exp5-03b-mean	2013	29.9	6.8	336.7	44.2	295.3	10.1	81.1	78.6
Ahlmannryggen	Fp	Z1817.2	exp5-03c	2013	32.3	10.0	325.9	48.5	300.6	9.9	73.4	83.4
Ahlmannryggen	Fp	Z1817.2	exp5-52-mean	2013	29.6	6.3	309.1	42.8	265.8	9.0	75.8	80.2
Etendeka	Fp	97SB63	exp5-9	2012	11.4	27.8	759.0	28.7	274.4	27.3	574.2	82.3
Etendeka	Fp	97SB63	exp5-26	2012	24.0	27.5	745.4	30.6	225.4	21.1	585.1	82.4
Etendeka	Fp	97SB63	exp2-15	2013	22.9	22.6	747.8	25.7	204.3	18.5	334.3	84.5
Etendeka	Fp	97SB63	exp3-10	2013	32.9	26.1	400.4	27.5	230.2	16.4	303.5	82.5
Etendeka	Fp	97SB63	exp4-2	2013	23.5	24.7	776.3	27.1	210.2	19.6	540.9	83.2
Etendeka	Fp	97SB63	exp4-3	2013	24.8	20.9	740.1	25.2	203.8	19.2	413.3	82.0
Etendeka	Fp	97SB63	exp5-16a	2013	25.0	16.5	773.8	26.3	258.6	27.1	546.9	81.6
Etendeka	Fp	97SB63	exp5-42	2013	23.2	27.4	878.3	25.3	223.4	23.6	626.1	82.5
Etendeka	Fp	97SB67	exp3-06a	2012	17.8	16.5	677.0	16.7	74.9	6.8	361.4	68.2
Etendeka	Fp	97SB67	exp3-26	2012	29.4	8.1	526.5	32.9	58.1	4.3	242.4	65.1
Etendeka	Fp	97SB67	exp3-29a	2012	30.3	7.1	563.5	34.2	90.4	11.0	320.9	64.7
Etendeka	Fp	97SB67	exp3-29b	2012	30.4	8.6	572.9	34.6	87.1	10.4	326.0	64.7
Etendeka	Fp	97SB67	exp3-29c	2012	23.2	10.3	534.3	23.1	86.4	10.0	340.2	64.7
Etendeka	Fp	97SB67	exp3-42	2012	19.6	13.2	568.4	20.8	67.2	4.7	352.0	66.6
Etendeka	Fp	97SB67	exp3-66	2012	22.9	12.1	591.0	23.9	111.6	11.6	386.0	68.8
Etendeka	Fp	97SB67	exp4-123	2012	22.0	12.1	632.8	18.2	35.0	1.4	382.4	67.1
Etendeka	Fp	97SB67	exp4-22	2012	46.4	21.8	483.9	58.4	135.0	17.9	346.2	63.8
Etendeka	Fp	97SB68	exp5-32	2013	88.9	0.9	152.9	29.2	70.8	6.6	124.7	65.8
Etendeka	Fp	97SB80	exp3-24	2012	23.8	10.7	332.2	24.2	131.6	7.5	288.2	79.4
Etendeka	Fp	97SB80	exp3-25	2012	23.3	12.0	157.6	19.8	110.5	6.1	78.1	78.5
Etendeka	Fp	97SB80	exp3-34	2012	17.9	10.4	337.4	23.4	130.9	7.2	289.6	78.3
Etendeka	Fp	97SB80	exp4-76	2012	22.0	10.4	298.9	18.6	117.6	6.0	275.1	75.5
Etendeka	Fp	97SB80	exp5-2	2012	14.4	11.1	261.4	18.7	155.2	10.7	203.5	77.9
Etendeka	Fp	97SB80	exp5-8	2012	23.0	8.9	258.0	20.1	109.3	6.0	238.1	70.2
Etendeka	Fp	97SB80	exp5-43	2012	20.2	9.2	307.9	20.6	125.0	7.1	269.5	74.1

Table C.9 – *Continued on next page*

Location	Type	Sample	Melt inclusion	Session	Sc	Rb	Sr	Y	Zr	Nb	Ba	Fo
Etendeka	Fp	97SB80	exp3-01a	2013	24.7	12.4	335.6	24.0	136.8	6.9	291.0	79.8
Etendeka	Fp	97SB80	exp3-2	2013	21.9	14.5	349.4	23.9	137.1	7.2	295.1	73.4
Etendeka	Fp	97SB80	exp4-21	2013	22.8	15.0	197.4	17.1	94.9	5.0	127.2	74.8
Etendeka	Fp	97SB80	exp4-28a	2013	19.2	11.5	327.4	21.7	128.1	6.9	281.4	77.1
Etendeka	Fp	97SB80	exp5-8	2013	18.5	11.1	305.3	20.8	124.1	6.4	261.0	78.6
Etendeka	Fp	97SB80	exp5-13	2013	20.2	14.2	341.8	24.0	142.0	6.8	322.5	76.3
Etendeka	Fp	PB9	exp1-1	2013	16.8	23.9	426.7	24.0	159.5	9.0	268.8	83.3
Etendeka	Fp	PB9	exp1-8-mean	2013	39.0	11.4	546.2	18.3	118.8	7.8	160.9	83.8
Etendeka	Fp	PB9	exp1-32-mean	2013	36.8	18.7	447.5	20.5	146.2	8.9	261.8	77.9
Etendeka	Fp	PB9	exp2-6-mean	2013	19.1	18.2	495.5	25.6	168.3	12.0	307.7	69.6
Etendeka	Fp	PB9	exp2-7	2013	34.5	22.2	481.2	22.0	166.7	9.5	298.3	79.4
Etendeka	Fp	PB9	exp2-28a	2013	36.7	21.9	468.4	22.5	160.8	8.9	273.7	72.4
Etendeka	Fp	PB9	exp2-66	2013	13.9	19.3	472.5	23.7	161.2	9.3	276.2	74.3
Etendeka	Fp	PB9	exp2-83	2013	16.3	19.7	503.1	25.6	170.5	12.4	307.3	78.5
Etendeka	HP	97SB29	exp3-26	2012	41.8	1.2	105.9	27.4	74.8	6.3	42.2	90.4
Etendeka	HP	97SB34	exp1-53	2012	34.1	451.8	705.5	26.6	109.7	5.9	146.3	85.1
Etendeka	HP	97SB34	exp1-76	2012	30.9	7.0	179.0	23.5	72.9	4.3	95.6	85.5
Etendeka	HP	97SB34	exp1-79a	2012	24.6	3.6	177.2	20.0	70.5	2.7	55.0	86.6
Etendeka	HP	97SB34	exp1-79b	2012	23.4	3.8	180.5	20.4	70.5	3.0	67.2	86.6
Etendeka	HP	97SB34	exp3-9	2012	27.8	10.0	222.3	21.8	94.9	5.2	128.0	86.3
Etendeka	HP	97SB34	exp3-145	2012	42.6	3.8	236.3	23.3	91.7	3.1	54.2	87.7
Etendeka	HP	97SB34	exp3-164a	2012	30.5	40.9	186.8	26.3	169.8	7.9	59.9	86.2
Etendeka	HP	97SB34	exp3-164b	2012	25.7	47.0	198.6	23.3	77.1	3.1	65.3	86.2
Etendeka	HP	97SB34	exp3-72	2012	37.0	8.0	229.4	26.6	103.7	5.2	116.3	85.6
Etendeka	HP	97SB41	exp2-01a	2012	41.7	29.5	208.1	28.3	111.1	4.3	83.2	84.6
Etendeka	HP	97SB41	exp2-01b	2012	34.2	6.7	222.0	25.3	90.6	3.7	88.8	84.6
Etendeka	HP	97SB41	exp2-01c	2012	33.6	6.8	196.1	23.7	81.7	3.3	79.9	84.6
Etendeka	HP	97SB41	exp2-09a	2012	28.8	3.6	179.2	20.7	69.6	4.7	77.3	85.3
Etendeka	HP	97SB41	exp2-09b	2012	32.0	6.1	208.7	22.1	76.1	5.8	99.0	85.3
Etendeka	HP	97SB41	exp2-17	2012	32.0	6.5	165.6	22.3	76.2	3.3	76.7	85.1
Etendeka	HP	97SB41	exp2-37	2012	29.4	199.9	1329.1	23.6	100.6	5.2	885.2	85.4
Etendeka	HP	97SB41	exp2-92	2012	33.9	6.8	224.6	24.1	92.1	4.2	101.0	84.8

Table C.9 – *Continued on next page*

Location	Type	Sample	Melt inclusion	Session	Sc	Rb	Sr	Y	Zr	Nb	Ba	Fo
Etendeka	HP	97SB41	exp3-117	2012	25.9	3.4	196.4	20.4	83.3	2.4	66.7	85.4
Etendeka	HP	97SB41	exp3-31	2012	28.7	0.9	175.2	23.9	74.4	2.0	34.8	85.3
Etendeka	HP	97SB41	exp3-35	2012	24.3	11.9	206.6	22.4	90.8	6.4	208.0	87.2
Etendeka	HP	97SB41	exp3-63	2012	24.9	2.6	185.3	19.7	72.3	2.1	41.5	85.3
Etendeka	HP	97SB41	exp3-77	2012	25.6	2.0	148.3	20.0	58.2	1.9	30.3	85.2
Etendeka	HP	97SB41	exp4-104	2012	36.4	6.4	233.2	22.4	89.5	4.8	99.7	84.5
Etendeka	HP	97SB41	exp4-12	2012	31.6	5.5	148.4	23.5	63.6	3.2	82.5	85.3
Etendeka	HP	97SB41	exp4-139	2012	23.8	5.8	208.6	22.5	71.9	4.2	92.0	87.7
Etendeka	HP	97SB41	exp4-143	2012	30.3	8.3	184.7	24.2	85.6	4.8	106.7	85.2
Etendeka	HP	97SB41	exp4-36	2012	26.6	5.4	143.4	19.0	60.0	3.2	71.4	85.2
Etendeka	HP	97SB41	exp4-38	2012	32.1	6.7	254.5	27.2	99.8	5.7	115.0	85.2
Etendeka	HP	97SB41	exp4-64	2012	34.0	6.9	218.0	23.5	97.8	5.3	110.2	85.2
Etendeka	HP	97SB41	exp4-67	2012	32.5	6.7	226.7	22.4	91.1	5.0	102.8	85.4
Etendeka	HP	97SB46	exp2-03a	2012	38.2	6.4	204.7	22.3	74.5	3.4	55.0	86.6
Etendeka	HP	97SB46	exp2-03b	2012	36.8	6.7	194.6	20.2	68.9	2.9	51.7	86.6
Etendeka	HP	97SB46	exp2-21	2012	38.7	6.2	206.1	22.5	75.2	3.5	55.2	86.9
Etendeka	HP	97SB46	exp2-68	2012	37.3	4.9	200.4	21.9	77.7	3.7	58.2	86.8
Etendeka	HP	97SB46	exp2-75a	2012	36.2	4.7	205.6	21.5	75.3	3.5	50.4	87.0
Etendeka	HP	97SB46	exp2-75b	2012	36.0	5.4	187.4	21.6	74.4	3.2	49.7	87.0
Etendeka	HP	97SB46	exp3-4	2012	37.2	6.0	206.7	22.8	74.0	3.4	60.8	86.9
Etendeka	HP	97SB46	exp3-8	2012	37.8	5.6	197.0	21.2	74.3	3.4	56.2	86.8
Etendeka	HP	97SB46	exp3-20	2012	36.0	4.3	175.5	21.9	65.7	3.1	46.2	86.8
Etendeka	HP	97SB46	exp3-21a	2012	37.6	3.3	162.9	23.8	81.2	3.6	50.9	86.8
Etendeka	HP	97SB46	exp3-21b	2012	34.6	4.5	181.1	20.6	69.6	3.2	51.6	86.8
Etendeka	HP	97SB46	exp3-39	2012	38.0	7.8	199.3	23.6	79.7	4.1	63.5	86.8
Etendeka	HP	97SB46	exp3-43	2012	37.1	5.7	198.5	22.6	76.0	3.4	58.6	86.7
Etendeka	HP	97SB46	exp3-60	2012	32.2	5.2	199.1	22.5	74.5	3.4	59.4	91.1
Etendeka	HP	97SB46	exp4-13	2012	34.1	3.6	180.0	19.4	63.4	2.8	53.4	91.4
Etendeka	HP	97SB46	exp4-19a	2012	37.1	6.9	192.0	21.1	74.6	3.6	54.1	87.0
Etendeka	HP	97SB46	exp4-19b	2012	37.7	5.8	201.0	22.0	76.7	3.4	54.7	87.0
Etendeka	HP	97SB46	exp4-29	2012	31.1	3.3	106.2	26.8	77.5	2.8	33.0	91.2
Etendeka	HP	97SB46	exp4-63	2012	28.6	5.8	147.7	23.3	72.5	2.6	43.5	91.0

Table C.9 – *Continued on next page*

Location	Type	Sample	Melt inclusion	Session	Sc	Rb	Sr	Y	Zr	Nb	Ba	Fo
Etendeka	HP	97SB56	exp2-11	2012	30.0	2.2	134.2	21.7	55.6	2.2	37.1	85.3
Etendeka	HP	97SB56	exp2-31	2012	36.5	19.0	208.4	23.6	93.9	2.8	38.0	85.8
Etendeka	HP	97SB56	exp3-10	2012	29.2	8.8	162.2	20.1	62.8	3.6	66.4	85.2
Etendeka	HP	97SB56	exp3-118	2012	35.2	5.3	187.6	23.7	72.0	3.9	64.5	83.4
Etendeka	HP	97SB56	exp3-26	2012	30.4	13.8	209.9	25.4	81.5	5.1	92.8	90.4
Etendeka	HP	97SB56	exp3-39	2012	33.1	24.2	99.7	21.7	71.1	3.9	59.6	84.9
Etendeka	HP	97SB56	exp3-61	2012	25.4	41.2	202.1	15.9	49.1	2.4	59.8	85.3
Etendeka	HP	97SB56	exp3-79	2012	33.6	14.5	194.4	20.6	76.8	4.0	88.3	84.6
Etendeka	HP	97SB56	exp4-110	2012	34.8	62.5	156.6	23.4	50.1	2.1	23.9	85.0
Etendeka	HP	97SB56	exp4-98	2012	33.3	28.6	76.1	19.6	60.5	4.5	8.4	84.8
Etendeka	HP	97SB75	exp2-21	2012	37.5	12.3	112.1	22.8	47.1	1.2	19.7	86.9
Etendeka	HP	97SB75	exp2-27a	2012	53.0	16.7	97.2	23.8	86.7	5.1	44.6	86.3
Etendeka	HP	97SB75	exp3-14	2012	36.4	0.9	135.2	21.9	55.7	1.5	15.4	90.2
Etendeka	HP	97SB75	exp3-26	2012	32.6	1.9	152.9	23.5	59.1	2.1	29.4	90.1
Etendeka	HP	97SB75	exp3-29	2012	31.1	12.0	165.1	21.3	53.3	5.8	68.6	89.9
Etendeka	HP	97SB75	exp3-40	2012	32.2	10.7	161.7	26.0	65.5	1.8	47.3	89.2
Etendeka	HP	97SB75	exp3-53	2012	20.6	19.8	133.4	13.3	37.6	2.6	35.3	86.2
Etendeka	HP	97SB75	exp3-68	2012	38.3	2.7	176.7	24.4	68.0	3.7	46.0	86.0
Etendeka	HP	97SB79	exp3-17	2012	31.8	11.0	159.8	20.9	62.3	3.8	78.1	85.0

Table C.10: Trace element compositions (REE) of melt inclusions (SIMS). Abbreviations: Fp, ferropicrite; HP, Horingbaai picrite. Session refers to data collection in October 2012 or Oct 2013 session.

Location	Type	Sample	Melt incl.	La	Ce	Pr	Nd	Sm	Eu	Gd	Tb	Dy	Ho	Er	Tm	Yb	Lu	Fo
Vestfjella	Fp	JSH-B006	exp4-104	27.5	68.8	8.71	41.5	10.01	3.60	10.60	1.78	8.59	1.53	3.67	0.35	2.21	0.19	80.2
Vestfjella	Fp	JSH-B006	exp4-27	34.5	80.0	9.95	47.4	9.85	3.05	11.14	1.37	7.51	1.24	2.66	0.41	1.54	0.22	78.4
Vestfjella	Fp	JSH-B006	exp4-49	35.8	80.7	10.29	46.9	10.51	2.75	9.88	1.48	7.60	1.31	3.42	0.40	2.19	0.23	79.8
Ahlmannryggen	Fp	Z1813.1	exp2-04a	11.5	34.3	5.30	30.4	9.50	3.01	10.14	1.55	8.64	1.62	4.02	0.52	3.32	0.36	80.7
Ahlmannryggen	Fp	Z1813.1	exp2-9	10.7	31.7	5.04	27.6	8.87	3.18	9.27	1.47	10.03	1.71	3.74	0.46	2.72	0.41	81.2
Ahlmannryggen	Fp	Z1813.1	exp2-29	11.3	34.8	5.41	32.5	9.35	3.12	9.24	1.58	9.35	1.83	4.10	0.55	3.58	0.42	81.0
Ahlmannryggen	Fp	Z1813.1	exp3-29a	9.6	29.7	4.32	24.5	8.02	2.67	9.44	1.39	8.41	1.40	3.74	0.41	2.78	0.31	82.5

Table C.10 – *Continued on next page*

Location	Type	Sample	Melt incl.	La	Ce	Pr	Nd	Sm	Eu	Gd	Tb	Dy	Ho	Er	Tm	Yb	Lu	Fo
Ahlmannryggen	Fp	Z1813.1	exp4-30b	12.2	37.0	5.17	31.3	9.28	2.79	9.73	1.79	9.16	1.61	3.99	0.55	3.35	0.36	82.5
Ahlmannryggen	Fp	Z1813.1	exp5-22	11.3	31.2	4.70	26.5	7.49	2.97	7.73	1.28	6.77	1.45	3.33	0.48	2.38	0.28	81.8
Ahlmannryggen	Fp	Z1813.1	exp5-23	11.5	36.0	5.50	30.4	9.39	3.08	9.98	1.45	10.10	1.60	4.18	0.55	3.35	0.42	84.9
Ahlmannryggen	Fp	Z1813.1	exp5-31	12.3	33.9	5.03	26.8	9.59	2.93	9.06	1.40	9.29	1.51	3.75	0.45	2.80	0.41	81.5
Ahlmannryggen	Fp	Z1813.1	exp6-8	11.2	33.6	4.91	29.1	9.51	2.72	8.93	1.36	9.27	1.64	4.10	0.53	3.52	0.43	81.8
Ahlmannryggen	Fp	Z1813.1	exp7-22	10.5	31.3	4.92	27.3	8.34	2.58	8.96	1.10	8.49	1.22	3.41	0.41	1.98	0.39	83.5
Ahlmannryggen	Fp	Z1813.1	exp8-24	10.9	31.8	5.06	26.1	9.00	2.90	9.81	1.63	9.11	1.71	4.56	0.57	3.34	0.39	80.4
Ahlmannryggen	Fp	Z1813.1	exp8-40	14.3	40.8	6.24	32.8	10.03	2.99	10.32	1.78	10.03	1.83	4.86	0.50	3.83	0.37	81.0
Ahlmannryggen	Fp	Z1813.1	exp8-47	11.8	36.7	5.94	29.4	10.64	3.05	10.42	1.61	9.57	1.62	4.27	0.52	3.52	0.46	81.4
Ahlmannryggen	Fp	Z1813.1	exp8-61	11.5	33.8	5.07	30.8	9.33	3.01	8.78	1.50	8.14	1.48	4.19	0.53	2.81	0.35	84.1
Ahlmannryggen	Fp	Z1813.1	exp8-91	12.7	37.0	5.69	33.4	10.07	3.03	10.23	1.63	9.57	1.81	4.51	0.58	2.90	0.41	80.7
Ahlmannryggen	Fp	Z1816.3	exp2-02a	9.7	31.0	4.65	27.5	9.68	3.26	9.62	1.45	10.40	1.65	4.62	0.58	3.29	0.44	81.3
Ahlmannryggen	Fp	Z1816.3	exp2-02b	10.5	32.9	5.03	30.0	9.51	3.19	9.43	1.52	9.87	1.74	4.36	0.57	3.44	0.43	81.3
Ahlmannryggen	Fp	Z1816.3	exp2-02d	9.9	31.6	4.97	30.3	8.89	3.02	8.73	1.43	9.29	1.60	3.99	0.53	3.00	0.42	81.3
Ahlmannryggen	Fp	Z1816.3	exp2-15a	10.2	32.9	4.48	27.3	8.75	3.00	10.87	1.43	8.02	1.76	4.26	0.61	3.32	0.35	81.1
Ahlmannryggen	Fp	Z1816.3	exp2-16	10.2	31.6	5.09	28.6	9.11	2.95	9.60	1.51	8.95	1.69	4.13	0.52	3.37	0.44	82.9
Ahlmannryggen	Fp	Z1816.3	exp2-26	9.6	31.2	4.94	29.2	8.87	3.17	9.33	1.49	9.03	1.53	4.64	0.49	3.64	0.39	81.8
Ahlmannryggen	Fp	Z1816.3	exp4-08a	10.7	32.7	5.13	30.6	9.27	3.40	10.39	1.51	8.97	1.57	4.41	0.52	3.85	0.41	83.6
Ahlmannryggen	Fp	Z1816.3	exp4-12	10.0	30.9	4.73	30.0	8.56	3.19	10.50	1.57	8.19	1.53	4.32	0.54	3.05	0.47	83.8
Ahlmannryggen	Fp	Z1816.3	exp4-25	12.0	34.2	5.39	31.2	10.29	3.10	10.53	1.61	9.26	1.72	4.18	0.52	3.18	0.40	82.6
Ahlmannryggen	Fp	Z1816.3	exp5-37	9.7	28.8	4.74	30.3	8.66	3.12	9.11	1.35	9.22	1.70	3.58	0.44	3.03	0.36	82.7
Ahlmannryggen	Fp	Z1816.3	exp5-55a	10.7	31.4	4.96	30.3	9.05	3.06	9.51	1.53	8.94	1.71	4.29	0.54	3.50	0.41	82.3
Ahlmannryggen	Fp	Z1816.3	exp5-63a	8.8	27.8	4.63	26.3	8.86	2.88	8.70	1.36	8.11	1.47	3.85	0.48	3.17	0.36	82.4
Ahlmannryggen	Fp	Z1816.3	exp5-64	9.7	29.1	5.10	26.7	8.69	2.83	8.61	1.60	8.29	1.44	4.09	0.47	3.53	0.30	81.3
Ahlmannryggen	Fp	Z1817.2	exp2-18	11.0	33.6	4.87	29.0	8.52	3.11	10.25	1.63	9.21	1.44	4.40	0.52	2.99	0.31	83.1
Ahlmannryggen	Fp	Z1817.2	exp2-4	11.1	35.7	5.67	29.5	10.93	3.39	10.09	1.75	9.84	1.76	4.53	0.60	3.24	0.43	79.2
Ahlmannryggen	Fp	Z1817.2	exp3-16	10.3	30.4	4.59	26.1	8.31	2.87	9.24	1.46	8.04	1.51	4.53	0.50	3.21	0.35	80.0
Ahlmannryggen	Fp	Z1817.2	exp3-20a	10.3	30.9	4.99	26.0	8.87	3.08	10.51	1.50	9.52	1.56	4.36	0.52	2.81	0.37	80.4
Ahlmannryggen	Fp	Z1817.2	exp3-39a	10.1	31.2	4.95	26.2	9.20	2.92	10.52	1.52	9.93	1.60	4.27	0.47	2.92	0.33	78.8
Ahlmannryggen	Fp	Z1817.2	exp4-12	10.1	29.8	4.88	29.8	8.76	2.70	10.31	1.62	8.21	1.62	4.10	0.51	3.13	0.36	78.6
Ahlmannryggen	Fp	Z1817.2	exp4-13a	9.7	31.8	5.01	28.6	8.78	2.83	9.41	1.41	8.31	1.51	3.51	0.50	2.73	0.38	80.2
Ahlmannryggen	Fp	Z1817.2	exp4-13b	9.8	31.6	5.25	28.5	8.78	3.16	9.77	1.52	8.54	1.53	4.03	0.43	2.69	0.36	80.7

Table C.10 – *Continued on next page*

Location	Type	Sample	Melt incl.	La	Ce	Pr	Nd	Sm	Eu	Gd	Tb	Dy	Ho	Er	Tm	Yb	Lu	Fo
Ahlmannryggen	Fp	Z1817.2	exp4-22a	11.5	35.5	5.48	29.5	8.88	3.17	10.32	1.62	8.36	1.45	3.35	0.42	2.85	0.34	84.5
Ahlmannryggen	Fp	Z1817.2	exp4-83	11.5	33.4	5.21	32.9	9.83	3.25	11.40	1.68	9.48	1.62	3.82	0.53	2.61	0.39	79.5
Ahlmannryggen	Fp	Z1817.2	exp4-88	10.5	32.7	5.36	31.0	9.28	3.17	10.25	1.60	8.89	1.56	4.06	0.61	3.08	0.41	80.2
Ahlmannryggen	Fp	Z1817.2	exp4-89	9.8	29.9	5.07	27.2	8.59	3.09	8.58	1.58	8.33	1.37	3.09	0.48	3.03	0.27	79.5
Ahlmannryggen	Fp	Z1817.2	exp5-03b-mean	11.0	32.7	5.15	31.0	9.79	3.70	10.33	1.57	9.90	1.65	3.74	0.60	3.28	0.48	78.6
Ahlmannryggen	Fp	Z1817.2	exp5-03c	10.5	31.9	5.08	31.4	10.29	3.44	10.63	1.84	9.11	1.61	4.46	0.50	4.03	0.43	83.4
Ahlmannryggen	Fp	Z1817.2	exp5-52-mean	10.0	31.3	5.09	27.7	9.19	3.02	9.41	1.51	8.54	1.55	3.67	0.47	3.08	0.48	80.2
Etendeka	Fp	97SB63	exp5-9	56.2	109.3	13.97	48.3	9.27	3.07	7.05	1.08	5.99	1.23	2.94	0.38	2.28	0.27	82.3
Etendeka	Fp	97SB63	exp5-26	43.9	93.9	11.94	49.5	11.16	2.25	7.02	1.09	6.77	1.09	3.37	0.43	2.75	0.36	82.4
Etendeka	Fp	97SB63	exp2-15	28.1	66.6	8.26	35.3	8.69	2.13	8.56	1.01	5.59	0.98	2.85	0.32	1.78	0.20	84.5
Etendeka	Fp	97SB63	exp3-10	32.4	76.6	8.84	37.0	8.33	2.39	7.15	1.01	5.11	1.11	3.02	0.31	2.21	0.31	82.5
Etendeka	Fp	97SB63	exp4-2	36.8	83.5	9.83	44.2	8.20	2.14	8.77	1.05	5.52	1.18	2.71	0.35	1.38	0.23	83.2
Etendeka	Fp	97SB63	exp4-3	34.7	75.7	8.98	38.3	7.90	2.30	8.74	1.15	5.51	0.99	2.34	0.30	1.60	0.25	82.0
Etendeka	Fp	97SB63	exp5-16a	43.1	98.4	11.63	47.1	9.77	2.37	10.12	1.45	6.73	1.12	2.90	0.33	1.83	0.19	81.6
Etendeka	Fp	97SB63	exp5-42	42.6	98.0	11.00	45.2	9.04	2.10	9.39	1.25	6.55	0.97	2.77	0.34	1.74	0.23	82.5
Etendeka	Fp	97SB67	exp3-06a	12.0	23.0	2.49	13.9	4.11	1.59	5.16	0.54	3.07	0.68	1.68	0.22	1.19	0.14	68.2
Etendeka	Fp	97SB67	exp3-26	11.8	25.9	3.84	19.4	6.14	1.89	6.25	1.08	6.58	1.18	3.40	0.48	3.19	0.39	65.1
Etendeka	Fp	97SB67	exp3-29a	14.5	29.8	4.03	19.6	5.94	1.86	8.30	1.07	7.82	1.16	3.49	0.51	2.78	0.41	64.7
Etendeka	Fp	97SB67	exp3-29b	14.8	30.7	4.57	19.4	6.36	1.76	7.06	1.16	7.19	1.15	3.68	0.49	2.98	0.36	64.7
Etendeka	Fp	97SB67	exp3-29c	12.6	24.8	3.11	15.6	4.49	1.66	4.46	0.71	4.68	0.89	2.54	0.31	2.05	0.28	64.7
Etendeka	Fp	97SB67	exp3-42	13.2	27.4	3.60	18.6	4.64	1.72	6.00	0.66	3.64	0.87	2.24	0.34	1.83	0.26	66.6
Etendeka	Fp	97SB67	exp3-66	14.7	30.3	4.44	18.9	4.87	2.00	5.87	0.95	4.90	1.05	2.61	0.28	2.27	0.25	68.8
Etendeka	Fp	97SB67	exp4-123	9.0	18.9	2.29	11.9	3.79	1.74	4.68	0.74	3.68	0.66	1.92	0.23	1.28	0.16	67.1
Etendeka	Fp	97SB67	exp4-22	25.6	54.9	7.67	34.3	10.09	2.11	12.43	2.09	11.90	1.83	5.29	0.72	4.32	0.44	63.8
Etendeka	Fp	97SB68	exp5-32	8.8	19.6	2.65	13.2	4.81	1.13	5.58	1.06	6.40	1.11	3.04	0.38	3.17	0.41	65.8
Etendeka	Fp	97SB80	exp3-24	14.9	35.2	4.54	19.8	5.47	1.17	4.79	0.82	5.08	0.99	2.80	0.33	2.09	0.22	79.4
Etendeka	Fp	97SB80	exp3-25	12.7	29.6	3.58	16.4	4.18	1.79	4.50	0.60	4.05	0.66	1.91	0.30	1.76	0.23	78.5
Etendeka	Fp	97SB80	exp3-34	14.7	33.5	4.83	20.9	5.08	1.49	4.72	0.76	4.83	0.86	2.64	0.27	1.91	0.24	78.3
Etendeka	Fp	97SB80	exp4-76	12.7	29.6	4.06	17.6	4.59	1.18	4.25	0.66	3.93	0.78	1.67	0.22	1.80	0.14	75.5
Etendeka	Fp	97SB80	exp5-2	13.4	33.2	3.88	16.4	3.90	1.34	3.60	0.58	3.36	0.63	2.22	0.26	1.79	0.29	77.9
Etendeka	Fp	97SB80	exp5-8	11.6	27.0	3.84	17.7	4.83	1.17	4.17	0.66	3.95	0.67	1.74	0.30	2.18	0.24	70.2
Etendeka	Fp	97SB80	exp5-43	13.0	30.2	4.38	20.4	4.66	1.34	4.29	0.87	4.02	0.89	2.26	0.25	1.69	0.19	74.1

Table C.10 – *Continued on next page*

Location	Type	Sample	Melt incl.	La	Ce	Pr	Nd	Sm	Eu	Gd	Tb	Dy	Ho	Er	Tm	Yb	Lu	Fo
Etendeka	Fp	97SB80	exp3-01a	13.8	33.3	4.27	20.9	5.67	1.27	5.12	0.79	4.27	0.99	2.35	0.35	2.54	0.24	79.8
Etendeka	Fp	97SB80	exp3-2	13.1	33.8	4.09	20.4	4.93	1.57	6.32	0.91	4.70	0.88	2.47	0.32	1.94	0.23	73.4
Etendeka	Fp	97SB80	exp4-21	10.1	24.3	2.69	13.2	3.07	1.09	4.65	0.52	3.20	0.62	1.52	0.25	1.65	0.22	74.8
Etendeka	Fp	97SB80	exp4-28a	12.8	33.6	3.93	18.8	4.15	1.11	4.82	0.72	4.73	0.83	2.21	0.30	1.72	0.22	77.1
Etendeka	Fp	97SB80	exp5-8	12.0	30.2	3.71	19.0	4.65	1.22	5.13	0.67	3.59	0.82	1.88	0.24	1.27	0.21	78.6
Etendeka	Fp	97SB80	exp5-13	14.5	35.6	4.20	21.2	5.34	1.47	6.24	0.74	4.64	0.84	2.04	0.28	1.95	0.27	76.3
Etendeka	Fp	PB9	exp1-1	17.9	44.9	5.39	25.6	6.23	1.56	5.97	0.79	5.33	0.92	2.40	0.32	1.37	0.20	83.3
Etendeka	Fp	PB9	exp1-8-mean	12.8	34.2	4.49	22.9	5.44	1.45	4.70	0.67	4.24	0.75	1.62	0.22	1.06	0.14	83.8
Etendeka	Fp	PB9	exp1-32-mean	17.7	45.0	5.75	24.2	6.05	1.56	4.17	0.95	4.64	0.82	1.96	0.24	1.93	0.14	77.9
Etendeka	Fp	PB9	exp2-6-mean	20.2	51.1	6.53	29.8	6.10	1.85	6.85	0.93	5.90	0.94	2.25	0.34	1.95	0.24	69.6
Etendeka	Fp	PB9	exp2-7	20.3	50.5	6.17	28.2	6.24	1.49	6.03	0.89	4.62	0.83	2.11	0.27	1.02	0.17	79.4
Etendeka	Fp	PB9	exp2-28a	19.1	47.1	6.30	27.5	6.15	1.74	5.78	0.97	5.30	0.96	2.33	0.25	1.50	0.17	72.4
Etendeka	Fp	PB9	exp2-66	19.0	45.4	5.67	26.7	6.09	1.98	6.36	0.96	4.21	0.79	2.15	0.24	1.50	0.16	74.3
Etendeka	Fp	PB9	exp2-83	20.2	49.2	6.25	27.9	5.82	1.69	6.02	1.02	5.92	0.83	2.27	0.30	2.01	0.27	78.5
Etendeka	HP	97SB29	exp3-26	6.5	15.4	2.21	11.3	4.62	1.55	4.59	0.76	5.31	0.93	2.56	0.40	2.97	0.42	90.4
Etendeka	HP	97SB34	exp1-53	9.2	20.7	3.30	16.3	4.71	1.34	4.46	0.82	5.09	0.97	2.89	0.37	2.55	0.38	85.1
Etendeka	HP	97SB34	exp1-76	6.4	14.4	2.28	11.7	3.84	1.22	3.91	0.60	4.22	0.91	2.37	0.35	2.29	0.28	85.5
Etendeka	HP	97SB34	exp1-79a	4.1	12.1	1.86	10.7	3.31	1.32	4.81	0.65	4.41	0.84	2.12	0.22	1.83	0.16	86.6
Etendeka	HP	97SB34	exp1-79b	4.7	11.3	1.82	11.4	3.75	1.20	3.92	0.66	4.18	0.70	1.82	0.27	1.58	0.23	86.6
Etendeka	HP	97SB34	exp3-9	8.4	20.7	2.87	12.8	3.71	1.03	3.53	0.59	4.23	0.84	2.48	0.31	1.90	0.22	86.3
Etendeka	HP	97SB34	exp3-145	6.4	16.6	3.00	15.7	4.44	1.31	3.44	0.69	4.34	0.86	2.92	0.36	2.54	0.33	87.7
Etendeka	HP	97SB34	exp3-164a	4.8	14.4	2.44	12.8	4.69	1.32	4.48	0.74	5.14	1.11	2.60	0.35	2.35	0.28	86.2
Etendeka	HP	97SB34	exp3-164b	5.3	14.1	2.04	12.4	3.67	1.37	4.66	0.75	4.44	0.85	2.34	0.30	1.66	0.24	86.2
Etendeka	HP	97SB34	exp3-72	8.7	20.9	2.85	15.1	4.95	1.11	4.79	0.91	3.92	0.97	2.84	0.36	2.49	0.26	85.6
Etendeka	HP	97SB41	exp2-01a	7.2	17.1	2.75	14.5	4.89	1.30	4.41	0.88	5.43	1.11	3.27	0.42	2.95	0.40	84.6
Etendeka	HP	97SB41	exp2-01b	7.0	16.6	2.36	12.8	4.19	1.47	5.01	0.72	4.20	0.91	2.67	0.37	2.35	0.27	84.6
Etendeka	HP	97SB41	exp2-01c	6.0	15.1	2.26	13.1	3.78	1.28	4.00	0.69	4.15	0.84	2.37	0.37	2.16	0.25	84.6
Etendeka	HP	97SB41	exp2-09a	5.7	13.0	1.85	10.8	3.24	0.98	3.41	0.70	3.52	0.89	2.10	0.36	2.11	0.26	85.3
Etendeka	HP	97SB41	exp2-09b	6.7	14.4	2.10	11.4	3.56	1.16	4.06	0.66	4.14	0.88	2.39	0.28	2.54	0.28	85.3
Etendeka	HP	97SB41	exp2-17	6.0	13.8	2.21	12.7	4.00	1.20	3.50	0.74	3.81	0.85	2.74	0.36	1.86	0.33	85.1
Etendeka	HP	97SB41	exp2-37	8.6	19.8	2.96	15.1	3.51	0.29	4.72	0.72	4.86	0.94	2.44	0.35	2.02	0.28	85.4
Etendeka	HP	97SB41	exp2-92	6.6	16.0	2.69	13.1	3.28	1.18	3.45	0.71	4.72	0.95	2.15	0.28	2.28	0.36	84.8

Table C.10 – *Continued on next page*

Location	Type	Sample	Melt incl.	La	Ce	Pr	Nd	Sm	Eu	Gd	Tb	Dy	Ho	Er	Tm	Yb	Lu	Fo
Etendeka	HP	97SB41	exp3-117	5.5	16.6	2.56	13.3	3.41	1.04	3.57	0.55	4.05	0.80	2.46	0.23	1.96	0.23	85.4
Etendeka	HP	97SB41	exp3-31	3.9	12.1	2.14	12.7	3.74	1.72	4.59	0.62	4.51	0.84	2.46	0.36	2.17	0.31	85.3
Etendeka	HP	97SB41	exp3-35	9.2	20.2	2.90	11.6	3.09	0.64	3.21	0.67	3.91	0.98	2.43	0.35	2.03	0.24	87.2
Etendeka	HP	97SB41	exp3-63	4.4	14.2	1.91	9.2	2.97	1.00	4.13	0.56	3.87	0.73	2.00	0.29	1.88	0.19	85.3
Etendeka	HP	97SB41	exp3-77	3.2	9.2	1.71	8.6	3.04	1.05	3.17	0.55	3.60	0.68	1.92	0.29	2.02	0.26	85.2
Etendeka	HP	97SB41	exp4-104	7.1	18.0	2.76	13.7	3.79	1.19	3.67	0.68	4.07	0.91	2.40	0.33	2.15	0.27	84.5
Etendeka	HP	97SB41	exp4-12	5.1	11.5	1.71	8.5	3.39	1.14	3.19	0.57	4.60	0.79	2.23	0.33	2.43	0.37	85.3
Etendeka	HP	97SB41	exp4-139	5.8	13.5	2.00	10.9	3.90	1.14	4.61	0.64	4.14	0.86	2.29	0.30	1.73	0.19	87.7
Etendeka	HP	97SB41	exp4-143	7.0	18.1	2.70	12.8	4.53	1.13	3.45	0.68	4.17	0.92	2.20	0.29	2.21	0.24	85.2
Etendeka	HP	97SB41	exp4-36	4.8	10.7	1.55	9.6	2.93	1.21	3.84	0.52	3.56	0.59	2.17	0.24	1.83	0.25	85.2
Etendeka	HP	97SB41	exp4-38	7.8	20.4	3.11	14.4	4.65	1.34	4.37	0.71	5.41	0.97	2.48	0.36	2.57	0.29	85.2
Etendeka	HP	97SB41	exp4-64	7.9	19.9	2.95	13.4	4.06	1.23	3.96	0.76	3.89	0.92	2.45	0.30	2.33	0.29	85.2
Etendeka	HP	97SB41	exp4-67	6.9	18.7	2.79	13.5	4.06	1.20	3.83	0.59	4.16	0.95	2.67	0.32	2.07	0.31	85.4
Etendeka	HP	97SB46	exp2-03a	5.2	13.2	2.19	11.3	4.10	1.23	3.49	0.66	4.42	0.83	2.22	0.35	1.98	0.35	86.6
Etendeka	HP	97SB46	exp2-03b	4.3	11.7	2.06	8.1	3.52	1.23	3.78	0.59	3.84	0.85	1.93	0.33	1.81	0.24	86.6
Etendeka	HP	97SB46	exp2-21	4.8	12.7	2.15	11.2	3.27	0.98	4.25	0.61	4.06	0.76	2.26	0.31	1.75	0.29	86.9
Etendeka	HP	97SB46	exp2-68	5.0	13.8	2.12	12.0	3.27	0.98	3.49	0.71	4.06	0.77	2.25	0.35	1.98	0.26	86.8
Etendeka	HP	97SB46	exp2-75a	4.6	12.9	2.15	12.2	3.32	1.20	3.94	0.69	4.52	0.86	2.52	0.30	2.23	0.23	87.0
Etendeka	HP	97SB46	exp2-75b	5.0	12.3	2.04	11.6	3.62	1.22	4.09	0.64	4.32	0.76	2.49	0.29	2.05	0.25	87.0
Etendeka	HP	97SB46	exp3-4	5.3	13.9	2.10	11.5	3.37	1.29	4.16	0.65	4.58	0.94	2.36	0.34	2.24	0.34	86.9
Etendeka	HP	97SB46	exp3-8	5.1	13.4	2.25	10.1	3.25	1.07	3.20	0.74	4.60	0.69	2.48	0.32	1.74	0.28	86.8
Etendeka	HP	97SB46	exp3-20	4.6	11.2	1.64	10.1	3.30	0.89	4.58	0.58	4.26	0.74	2.17	0.37	1.77	0.32	86.8
Etendeka	HP	97SB46	exp3-21a	5.6	15.0	2.52	11.8	3.77	1.00	3.84	0.69	4.84	0.87	2.41	0.40	2.01	0.29	86.8
Etendeka	HP	97SB46	exp3-21b	4.5	12.4	2.09	10.7	3.37	1.19	3.93	0.52	3.40	0.83	2.30	0.26	2.04	0.22	86.8
Etendeka	HP	97SB46	exp3-39	5.1	15.1	2.07	11.4	3.91	1.37	4.60	0.77	4.44	0.84	2.58	0.38	2.53	0.25	86.8
Etendeka	HP	97SB46	exp3-43	5.0	12.8	2.12	10.7	3.89	1.14	3.21	0.69	4.40	0.75	1.89	0.32	2.20	0.25	86.7
Etendeka	HP	97SB46	exp3-60	4.4	12.4	1.88	10.9	3.68	1.14	3.72	0.66	4.30	0.85	2.55	0.34	1.77	0.24	91.1
Etendeka	HP	97SB46	exp4-13	4.3	12.3	1.72	10.0	3.05	0.92	3.19	0.57	3.77	0.74	2.45	0.28	2.14	0.22	91.4
Etendeka	HP	97SB46	exp4-19a	5.0	13.1	2.08	10.8	3.58	1.23	3.41	0.54	3.68	0.86	2.65	0.31	2.14	0.27	87.0
Etendeka	HP	97SB46	exp4-19b	5.2	13.2	2.14	11.1	3.59	1.07	3.55	0.69	4.59	0.84	2.12	0.30	2.45	0.24	87.0
Etendeka	HP	97SB46	exp4-29	4.5	12.8	2.19	11.1	4.44	1.29	3.62	0.72	5.63	1.05	2.77	0.38	2.89	0.37	91.2
Etendeka	HP	97SB46	exp4-63	4.1	11.4	1.96	10.2	3.76	1.16	3.69	0.68	4.79	0.83	2.25	0.34	2.49	0.28	91.0

Table C.10 – *Continued on next page*

Location	Type	Sample	Melt incl.	La	Ce	Pr	Nd	Sm	Eu	Gd	Tb	Dy	Ho	Er	Tm	Yb	Lu	Fo
Etendeka	HP	97SB56	exp2-11	3.3	9.3	1.49	9.5	3.22	1.04	4.19	0.70	4.44	0.87	2.49	0.34	2.38	0.22	85.3
Etendeka	HP	97SB56	exp2-31	4.5	11.9	2.17	11.5	3.77	1.08	3.90	0.63	4.23	0.89	2.64	0.39	2.14	0.33	85.8
Etendeka	HP	97SB56	exp3-10	4.8	12.2	1.80	8.4	3.02	0.87	3.43	0.52	3.86	0.77	1.91	0.28	1.70	0.24	85.2
Etendeka	HP	97SB56	exp3-118	4.9	13.0	2.01	10.5	2.95	1.11	3.71	0.62	4.60	0.88	2.06	0.31	1.96	0.22	83.4
Etendeka	HP	97SB56	exp3-26	7.3	18.0	2.75	13.2	4.93	1.03	4.65	0.87	4.95	1.02	2.88	0.35	2.51	0.26	90.4
Etendeka	HP	97SB56	exp3-39	5.8	15.2	1.96	10.7	3.45	1.26	4.12	0.62	4.33	0.68	2.00	0.29	2.02	0.20	84.9
Etendeka	HP	97SB56	exp3-61	3.5	9.0	1.36	7.1	2.50	1.46	2.43	0.52	2.64	0.54	1.62	0.22	1.73	0.15	85.3
Etendeka	HP	97SB56	exp3-79	7.0	16.5	2.36	11.5	3.22	0.86	3.84	0.59	3.72	0.82	2.38	0.30	1.87	0.26	84.6
Etendeka	HP	97SB56	exp4-110	3.5	9.7	1.53	8.7	3.15	1.19	4.42	0.64	3.79	0.82	2.30	0.29	2.13	0.27	85.0
Etendeka	HP	97SB56	exp4-98	5.1	13.0	2.01	9.9	3.14	1.42	2.51	0.53	3.69	0.67	1.95	0.29	1.96	0.29	84.8
Etendeka	HP	97SB75	exp2-21	2.1	6.5	0.97	6.2	2.47	0.89	3.47	0.63	4.05	0.78	2.51	0.33	2.31	0.28	86.9
Etendeka	HP	97SB75	exp2-27a	4.6	10.9	1.76	10.2	4.12	0.98	4.35	0.64	4.42	0.68	3.11	0.44	1.97	0.37	86.3
Etendeka	HP	97SB75	exp3-14	2.0	7.3	1.19	7.7	2.66	0.94	2.92	0.50	3.01	0.85	2.24	0.31	2.09	0.22	90.2
Etendeka	HP	97SB75	exp3-26	3.5	8.9	1.67	7.1	2.84	1.01	3.43	0.73	4.01	0.88	2.64	0.32	1.91	0.25	90.1
Etendeka	HP	97SB75	exp3-29	4.7	11.4	1.35	5.8	2.76	0.77	3.43	0.61	3.98	0.76	2.27	0.29	2.02	0.24	89.9
Etendeka	HP	97SB75	exp3-40	4.1	11.7	1.95	11.7	3.67	1.28	4.00	0.72	5.35	0.99	2.65	0.36	2.23	0.27	89.2
Etendeka	HP	97SB75	exp3-53	2.9	6.9	1.00	5.0	1.72	1.27	2.27	0.40	2.77	0.52	1.13	0.18	1.21	0.20	86.2
Etendeka	HP	97SB75	exp3-68	4.5	11.0	1.71	8.9	3.18	1.19	3.62	0.71	4.42	0.90	2.48	0.34	2.58	0.29	86.0
Etendeka	HP	97SB79	exp3-17	6.6	14.4	1.85	8.0	2.77	0.96	3.47	0.62	3.95	0.80	2.40	0.29	1.90	0.22	85.0

Table C.11: Peak fitting results for XANES spectra, performed on normalised spectra. The seven peaks (P1–4, D1–3) are explained in Appendix A. Centroid is the peak position in eV; height and area of the peaks are in normalised FF/I_0. The published $Fe^{3+}/\Sigma Fe$ Mössbauer measurements of the standards and the EPMA estimate are given along with the calibrated XANES value. *standards with suspected incorrect published $Fe^{3+}/\Sigma Fe$. ** spinels discarded because their (Cr + Al) < 1.5.

Type	sample code	P1centroid	P1area	P1height	P2centroid	P2area	P2height	P3centroid	P3area	P3height	P4centroid	P4area	P4height
standard*	KLB-8311	7112.80	0.167	0.079	7114.22	0.075	0.038	7117.76	0.111	0.036	7121.11	2.85	0.56
standard	MO-103	7112.78	0.196	0.088	7114.26	0.084	0.041	7117.81	0.020	0.012	7121.20	3.23	0.75
standard	Vi-314-580	7112.77	0.158	0.072	7114.34	0.120	0.045	7117.81	0.018	0.010	7121.26	3.07	0.69
standard	DB-8802-1	7112.80	0.186	0.087	7114.30	0.131	0.052	7117.90	0.008	0.005	7121.12	2.94	0.71
standard	MHP-79-4	7112.77	0.217	0.093	7114.29	0.095	0.044	7117.88	0.005	0.004	7121.13	3.20	0.80
standard	BAR-8601-9	7112.81	0.186	0.087	7114.28	0.118	0.050	7117.87	0.009	0.007	7121.13	2.99	0.71
standard*	MBR-8307	7112.79	0.170	0.079	7114.31	0.109	0.045	7117.78	0.014	0.009	7121.20	3.05	0.68
standard	IM-8703	7112.77	0.155	0.071	7114.35	0.144	0.049	7117.82	0.011	0.007	7121.22	2.91	0.65
standard	DB-8803-1	7112.82	0.166	0.081	7114.19	0.084	0.042	7117.81	0.077	0.027	7121.25	3.00	0.62
HP	23-08SB33-06	7112.82	0.126	0.063	7114.15	0.092	0.038	7117.58	0.046	0.016	7121.47	3.45	0.60
HP	23-97SB33-01	7112.74	0.108	0.051	7114.32	0.090	0.028	7117.69	0.071	0.021	7121.50	3.07	0.57
HP	23-97SB33-02	7112.77	0.125	0.058	7114.24	0.079	0.031	7117.61	0.069	0.022	7121.31	3.14	0.59
HP	23-97SB33-05	7112.81	0.141	0.069	7114.19	0.087	0.037	7117.84	0.128	0.030	7121.33	3.08	0.58
HP	17-97SB41-01	7112.76	0.121	0.059	7114.25	0.084	0.031	7117.75	0.155	0.032	7121.51	3.15	0.57
HP	17-97SB41-05	7112.80	0.139	0.068	7114.19	0.097	0.040	7117.76	0.175	0.039	7121.45	3.28	0.57
HP	17-97SB56-17**	7112.76	0.088	0.046	7114.36	0.174	0.049	7117.74	0.142	0.023	7121.49	3.00	0.53
HP	17-97SB56-48**	7112.75	0.062	0.035	7114.38	0.263	0.077	7117.60	0.238	0.028	7121.51	3.26	0.53
HP	17-97SB56-48**	7112.76	0.055	0.033	7114.38	0.270	0.078	7117.89	0.295	0.035	7121.52	3.07	0.51
HP	17-97SB56-51**	7112.75	0.078	0.038	7114.44	0.173	0.047	7117.49	0.059	0.013	7121.47	2.90	0.51
HP	06-97SB62-09	7112.78	0.090	0.048	7114.27	0.134	0.043	7117.68	0.107	0.023	7121.50	2.84	0.51
HP	06-97SB62-11	7112.80	0.117	0.058	7114.22	0.080	0.035	7117.77	0.105	0.029	7121.50	2.97	0.56
HP	23-97SB73-01**	7112.76	0.094	0.043	7114.36	0.112	0.032	7116.66	0.032	0.006	7121.47	3.76	0.60
HP	23-97SB73-02**	7112.80	0.091	0.051	7114.26	0.145	0.047	7118.44	0.478	0.056	7121.51	3.05	0.55
Fp	17-97SB63-80**	7112.77	0.083	0.039	7114.34	0.129	0.044	7116.25	0.152	0.015	7121.27	3.15	0.53
Fp	17-97SB80-14-sp2	7112.80	0.132	0.065	7114.22	0.128	0.045	7117.73	0.099	0.020	7121.46	3.55	0.60
Fp	23-PB009-01	7112.79	0.132	0.066	7114.22	0.095	0.036	7117.72	0.096	0.024	7121.55	3.55	0.62
Fp	23-PB009-02	7112.81	0.133	0.065	7114.20	0.087	0.036	7117.63	0.038	0.016	7121.49	3.54	0.63
Fp	23-PB009-03**	7112.82	0.113	0.050	7114.26	0.081	0.029	7117.24	0.016	0.007	7121.38	3.32	0.58

Table C.11 continued.

Type	sample code	D1centroid	D1area	D1height	D2centroid	D2area	D2height	D3centroid	D3area	D3height	$Fe^{3+}/\Sigma Fe$ Mössbauer	$Fe^{3+}/\Sigma Fe$ EPMA	$Fe^{3+}/\Sigma Fe$ XANES	1σ
standard*	KLB-8311	7120.33	0.288	0.674	7124.80	0.179	0.355	7129.58	0.195	0.417	0.21	0.232	0.126	0.009
standard	MO-103	7120.19	0.368	0.767	7124.63	0.207	0.304	7129.34	0.266	0.489	0.13	0.201	0.120	0.009
standard	Vi-314-580	7120.19	0.314	0.699	7124.56	0.164	0.279	7129.33	0.220	0.480	0.24	0.341	0.241	0.010
standard	DB-8802-1	7120.16	0.360	0.750	7124.52	0.175	0.261	7129.22	0.249	0.504	0.21	0.334	0.222	0.010
standard	MHP-79-4	7120.17	0.416	0.811	7124.57	0.208	0.283	7129.26	0.293	0.527	0.13	0.226	0.124	0.009
standard	BAR-8601-9	7120.16	0.361	0.750	7124.53	0.176	0.263	7129.25	0.248	0.497	0.18	0.276	0.194	0.010
standard*	MBR-8307	7120.18	0.332	0.718	7124.57	0.178	0.282	7129.27	0.226	0.484	0.25	0.281	0.197	0.010
standard	IM-8703	7120.17	0.302	0.683	7124.53	0.155	0.268	7129.25	0.216	0.483	0.32	0.337	0.310	0.011
standard	DB-8803-1	7120.28	0.295	0.668	7124.75	0.191	0.350	7129.51	0.210	0.431	0.15	0.188	0.147	0.010
HP	23-08SB33-06	7120.20	0.210	0.679	7124.86	0.136	0.392	7129.88	0.093	0.208	NA	0.366	0.231	0.010
HP	23-97SB33-01	7120.28	0.222	0.573	7124.92	0.158	0.445	7129.83	0.147	0.370	NA	0.383	0.274	0.010
HP	23-97SB33-02	7120.22	0.240	0.685	7124.90	0.170	0.457	7130.01	0.116	0.212	NA	0.356	0.194	0.010
HP	23-97SB33-05	7120.28	0.240	0.659	7124.82	0.153	0.376	7129.68	0.128	0.293	NA	0.135	0.187	0.010
HP	17-97SB41-01	7120.33	0.212	0.604	7124.88	0.145	0.400	7129.85	0.129	0.350	NA	0.379	0.218	0.010
HP	17-97SB41-05	7120.28	0.210	0.623	7124.89	0.133	0.358	7129.85	0.119	0.294	NA	0.385	0.219	0.010
HP	17-97SB56-17**	7120.28	0.181	0.607	7124.71	0.107	0.355	7129.54	0.104	0.313	NA	0.464	0.785	0.050
HP	17-97SB56-48**	7120.35	0.167	0.668	7124.58	0.088	0.348	7129.51	0.073	0.196	NA	0.483	2.000	0.245
HP	17-97SB56-48**	7120.39	0.163	0.650	7124.55	0.087	0.329	7129.44	0.073	0.211	NA	0.483	2.416	0.326
HP	17-97SB56-51**	7120.26	0.172	0.594	7124.78	0.113	0.481	7129.70	0.081	0.217	NA	0.500	0.903	0.065
HP	06-97SB62-09	7120.30	0.184	0.542	7124.86	0.133	0.431	7129.85	0.112	0.358	NA	0.451	0.555	0.026
HP	06-97SB62-11	7120.34	0.225	0.548	7124.94	0.173	0.435	7129.91	0.167	0.435	NA	0.346	0.214	0.010
HP	23-97SB73-01**	7120.18	0.185	0.786	7124.66	0.095	0.423	7129.98	0.079	0.060	NA	0.360	0.419	0.015
HP	23-97SB73-02**	7120.40	0.184	0.733	7124.70	0.090	0.306	7129.61	0.095	0.205	NA	0.351	0.603	0.030
Fp	17-97SB63-80**	7120.16	0.176	0.729	7124.72	0.100	0.431	7129.99	0.041	0.062	NA	0.462	0.590	0.029
Fp	17-97SB80-14-sp2	7120.21	0.204	0.715	7124.67	0.101	0.288	7129.41	0.086	0.241	NA	0.372	0.328	0.011
Fp	23-PB009-01	7120.27	0.215	0.679	7124.76	0.126	0.326	7129.62	0.106	0.272	NA	0.333	0.226	0.010
Fp	23-PB009-02	7120.23	0.225	0.711	7124.87	0.137	0.399	7129.70	0.077	0.168	NA	0.306	0.200	0.010
Fp	23-PB009-03**	7120.19	0.193	0.748	7124.86	0.125	0.545	7129.86	0.052	0.017	NA	0.397	0.226	0.010